ICHSF 2008

3rd International Conference on High Speed Forming

Proceedings

March 11 - 12, 2008
Dortmund, Germany

Institute of Forming Technology
and Lightweight Construction
technische universität
dortmund

HIGH SPEED FORMING 2008

PROCEEDINGS OF THE 3rd INTERNATIONAL CONFERENCE

MARCH 11 - 12, 2008

DORTMUND, GERMANY

Edited by:

Prof. Dr.-Ing. M. Kleiner
Prof. Dr.-Ing. A. E. Tekkaya
Institut für Umformtechnik und Leichtbau,
Technische Universität Dortmund

In corporation with:

Deutsche Forschungsgemeinschaft
DFG

For 443 EMB
Elektromagnetische Blechumformung

GDA GESAMTVERBAND DER ALUMINIUMINDUSTRIE e.V.

Scientific Committee:

T. Altan	Ohio State University (USA)
N. Asnafi	Volvo Car Corporation (Sweden)
F. P. Bariani	University of Padova (Italy)
C. Beerwald	Poynting GmbH (Germany)
J. L. Chenot	Ecole des Mines de Paris (France)
G. S. Daehn	Ohio State Univ. (USA)
J. C. Gelin	University of Franche-Comte (France)
S. Golovashchenko	Ford (USA)
F. Hollmann	German Research Found. (DFG) (Germany)
W. Homberg	Universität Paderborn (Germany)
H. Huh	Korea Adv. Inst. of Sc. and Tech. (South Korea)
E. Iriondo	Fundacoin Labein (Spain)
A. Kost	Brandenburg Technical University of Cottbus (Germany)
L. W. Meyer	Technical University of Chemnitz (Germany)
R. Neugebauer	Technical University of Chemnitz (Germany)
K. Roll	Daimler AG (Germany)
B. Svendsen	Technische Universität Dortmund (Germany)
F. Vollertsen	University of Bremen (Germany)

© 2008, Organizing committee of the 3rd International Conference on High Speed Forming, March 11 – 12 2008, Technische Universität Dortmund, Faculty of Mechanical Engineering, Institute of Forming Technology and Lightweight Construction.

All rights reserved, No part of this publication may be reproduced, stored in a retrieval system or transmitted in any form by any means, electronic, mechanical, photocopying, recording or otherwise, without the written prior permission of the authors/publisher.

The articles, diagrams, captions and photographs in this publication have been supplied by the contributors or delegates of the Conference. While every effort has been made to ensure accuracy, the editors, the organizing committee and the Dortmund University of Technology do not under any circumstances accept responsibility for errors, omissions or infringements.

INSTITUT FÜR UMFORMTECHNIK UND LEICHTBAU
Technische Universität Dortmund
Baroper Str. 301
D-44227 Dortmund
Germany

Edited by:

Institute of Forming Technology and Lightweight Construction
Technische Universität Dortmund
Prof. Dr.-Ing. M. Kleiner
Prof. Dr.-Ing. A. E. Tekkaya

ISBN 3-9809535-3-X

Table of Contents

Preface

The Institute of Forming Technology and Lightweight Construction of the Technische Universität Dortmund is honored to host the International Conference on High Speed Forming for the third time. We would like to take this opportunity to thank the authors and co-authors, the scientific committee as well as all participants of the conference for their valuable contributions.

The current worldwide discussion about CO_2 reduction illustrates the importance of a persistent implementation of lightweight construction concepts. These strategies include, among other techniques, the application of typical lightweight materials as aluminum and magnesium alloys and an optimized component design. However, the limited forming capabilities of these materials and the increased part complexity require adapted technologies and forming strategies. High speed forming represents one possibility to meet these challenges.

The large number of international participants from 15 different countries emphasizes the demand for discussions especially in this niche technology. Accordingly, the conference serves as a platform presenting research results regarding the topics process technologies, tools and equipment, energy, materials and measurement techniques, modelling and simulation, and industrial applications.

The institute is delighted to welcome you in Dortmund!

Dortmund, March 2008

M. Kleiner

A. E. Tekkaya

SESSION 1

INDUSTRIAL APPLICATIONS

Analysis of Blank-Die Contact Interaction in Pulsed Forming Processes

S. Golovashchenko[1], N. Bessonov[2], R. Davies[3]

[1] Ford Research and Advanced Engineering, Ford Motor Company, Dearborn, USA
[2] Institute of the Problems of Mechanical Engineering, Russian Academy of Sciences, St. Petersburg, Russia
[3] Pacific Northwest National Laboratory, Richland, Washington, USA

Abstract

During recent decade, significant efforts were dedicated to increasing the amount of Aluminum Alloys in automotive parts in order to reduce the net weight of cars. Processes of pulsed forming are known to expand the capabilities of traditional stamping operations. Propagation of pulsed electromagnetic field can be defined by quasi-stationary Maxwell equations, solved numerically using a non-orthogonal Lagrangian mesh. Suggested formulation included modelling of contact interaction of the blank with deformable die. Mild contact model based on introduction of acting-in-vicinity forces repelling the surfaces to be in contact was employed. It was tested by analyzing the elastic impact of bars and then was applied to the corner filling operation. This operation was analysed as a single pulse and as a multi pulse forming process. It indicated that some compromise between the blank formability enhancement and level of contact stresses on the die surface can be found. In addition, some examples of tubular parts pulsed press fitting using tube expansion with pulsed pressure were analyzed. Specific attention was paid to the analysis of factors playing important role in residual contact pressure between the exterior and interior tubes in pulsed press fitting operation.

Keywords:

Sheet metal forming, electrical discharge, tool

1 Introduction

The idea of using the high velocity and high energy rates to form metal and to assemble parts has been known for several decades. In the literature it was established that high velocity metal forming was able to form complex components with one sided dies and also to minimize the springback effect. During recent decade, significant efforts were dedicated to increasing the amount of Aluminum Alloys in automotive parts in order to reduce the net

weight of cars. Implementation of these materials into auto industry makes the issues of insufficient formability and springback even more difficult.

Processes of high rate forming, such as explosive, electromagnetic (EMF) and electro-hydraulic forming (EHF) are known to expand the capabilities of traditional stamping operations and also to provide high level short duration pulses of pressure. However, increasing the velocity of the blank leads to higher loads on the die. Taking into account deformation of the die in previously developed model of electromagnetic forming provides better understanding which forming regimes are realistic from die strength and durability point of view.

2 Theoretical Approach

Propagation of electromagnetic field within coil-blank-die-air system can defined by quazistationary Maxwell equations:

$$\nabla \times \mathbf{H} = \mathbf{j}, \tag{1}$$

$$\mu_a \frac{\partial \mathbf{H}}{\partial t} = -\nabla \times \mathbf{E}, \tag{2}$$

$$\mathbf{j} = \sigma\left(\mathbf{E} + \mu_a \mathbf{v} \times \mathbf{H}\right), \tag{3}$$

where **H** is magnetic field intensity; **j** is current density; **E** is electric field intensity; σ is electric conductivity; **v** is velocity; μ_a is magnetic permeability of medium under consideration. In EMF processes, the coil and die are almost stationary, while the blank is quickly accelerated; therefore, the equation for magnetic field intensity **H** can be transformed in Lagrangian form [1]. Dynamic elastic-plastic deformation of solid can be defined by the following equation:

$$\rho \frac{\mathrm{d}}{\mathrm{dt}} \int_{\mathrm{V}} \mathbf{v} \mathrm{dV} = \oint_{\mathrm{S}} \sigma \cdot \mathrm{d}\mathbf{s} + \int_{\mathrm{V}} \mathbf{f} \mathrm{dV}, \tag{4}$$

where σ is stress tensor; ρ is density; **f** is EM force defined from Maxwell equations. A numerical procedure of integration (1)-(4) simulating the elastic-plastic deformation of the blank was discussed in [1]. An explicit integration procedure was considered to be suitable to simulate a high-rate deformation process. Electromagnetic (EM) part of the problem was solved using an implicit integration procedure. The integration step in EM problem was n times larger than in elastic-plastic problem. The parameter n was defined for each practical case in order to represent the changes in distribution of electromagnetic field appropriately and spend appropriate computational resources.

3 Soft Contact Algorithm

The most popular method of modelling contact interaction is based on the geometrical analysis of mutual position of boundary nodes of each mesh. At every integration step, it is being verified whether a boundary node of the blank has penetrated through the certain element of the surface mesh of the die. If it happens, it is necessary to make certain

corrections bringing the node back on the surface of the die and let the node slide along the die's surface instead of penetrating through this surface. A significant downside of this approach is in occasional penetration of the node through the surface. It usually happens due to insufficient accuracy of calculations. As soon as the blank's node penetrates into the die's surface, it is unable to return back and further calculations are useless. Therefore, a different approach based on the idea of a mild contact was employed. This approach is very popular in molecular dynamics where it is employed to model thousands of atoms colliding and springing back from each other. The contact force is in inverse proportion to the distance between the interacting surfaces. From mathematical point of view, mild contact is some variable boundary of an unknown shape where we have to satisfy the non-penetration condition and equilibrium of forces between both surfaces. This idea is based on the introduction of acting-in-vicinity forces repelling the surfaces to be in contact. As a result, the surfaces do not come in contact, but stay at some very small distance from each other. The force is localized in a small neighbourhood of mesh elements, and it increases to infinity when the distance between them is approaching zero. In other words, when the blank and the die are in geometrical contact, the force between them is localized on their joint surface. Mathematically it can be considered as continuous functions where the absolute value of the force F is given by:

$$F = \begin{cases} k\left(\frac{1}{h} - \frac{1}{h_0}\right) & \text{at} \quad h < h_0 \\ 0 \quad \text{at} \quad h \geq h_0 \end{cases}, \tag{5}$$

where h is the actual distance from the node of the blank to the die surface, and h_0 is the width of the layer where the force is different from zero. The direction of the force F is aligned along the local normal to the die surface.

The described algorithm allows taking into account the Coulomb friction and other contact effects. Indeed, when we compute the interaction of the node with an object of the other mesh, we know their mutual positions and velocities. It is sufficient to find the friction directed along the tangent to the surface and opposite to the tangential part of the relative velocity vector.

4 Testing of the Contact Algorithm

The developed contact algorithm was tested for contact interaction of two elastic bodies with the following characteristics: ρ = 2800 kg/m³, G = 26.5 GPa, K = 65.1 GPa, the stress-strain curve was approximated as $\sigma_s = 0.24+0.56\varepsilon$,GPa. For simplicity, the dimensions of the colliding bodies were 2 m x 4 m. The initial velocity of the first body (shown as left in Figure1) was set equal 10 m/sec, while the velocity of the second body (right in Figure 1) was set to be zero. For one-dimensional case of bar impact, the contact stress can be calculated using the following formula (assuming that the material of both bodies is identical).

$$\sigma = \frac{\rho c v}{2}, \tag{6}$$

where c is speed of sound equal to 5000 m/sec. For the selected material and speed of impact, the contact stress σ is 70 MPa, which is below the yield stress for

chosen material. The duration of the impact is equal to 0.0016sec. Parameters of the contact force from formula (6) were set k = 0.1GN and h_0 = 0.01 m.

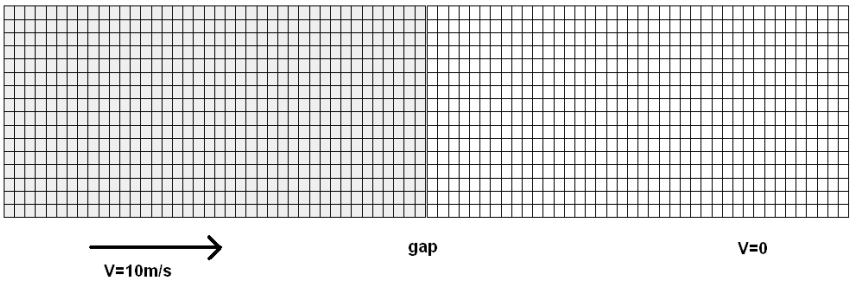

Figure 1: *Numerical meshes in bar impact test.*

In Figure 2, the stress history at the central point of the contact surface is shown with the red solid line using mild contact defined by equation (5), and the result of the analytical solution is illustrated with the dashed line. Since we are modelling the impact of two identical solids, the impact plane also serves as a symmetry plane. From this perspective, it is possible to represent the problem as an impact of one solid into the rigid wall with the velocity of 5m/sec. For the rigid wall, the boundary condition can be formulated as follows: if(x < x0) then {x = x0, v = 0}, corresponding to the simplest algorithm providing non-penetration of the nodes through the rigid contact surface. The numerical results obtained with the use of this approach are shown in Figure 2 with blue solid line. In this particular case the contact surface has a coordinate of x_0 = 4.005.

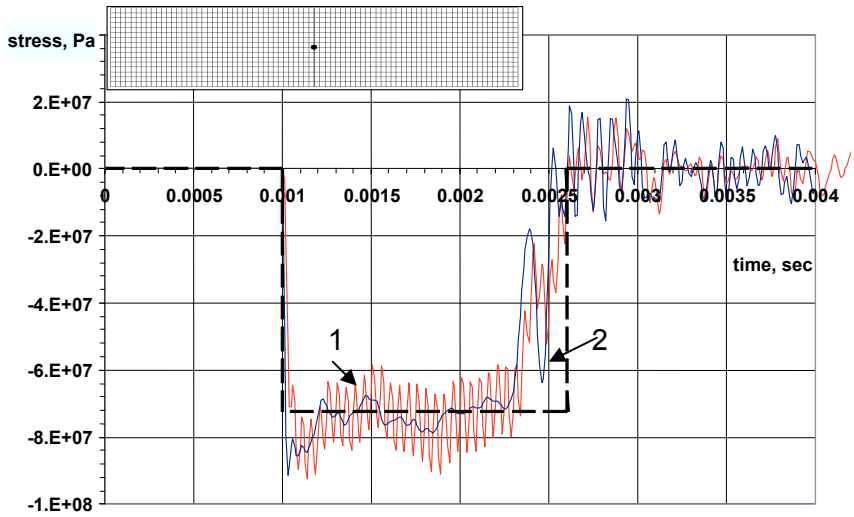

Figure 2: *Comparison of numerical results on mild contact of two elastic solids (1-red solid line), contact of elastic solid with the rigid surface with 50% less impact velocity (2-blue solid line) and analytical results (dashed line) on contact stress of two elastic bars. Contact stress is registered at the middle point of the contact zone (●).*

As it is shown in Figure 2, the duration of the impact obtained both numerically and from analytical solution (as a ratio of the double length of the bar and sound velocity in this material) is equal to 0.0016 sec. The average value of contact stress σ in selected control

point • also is identical and equal 70 MPa. The contact stress σ has "shortwave" and "longwave" variation: the "longwave" variation is related to 2D character of the problem; the "shortwave" variation is related to the formulation of the mild contact, and frequency of this variation is defined by the stiffness and width of the contact layer.

In order to reduce the amplitude of "high frequency" variation of contact stress, the artificial viscosity can be incorporated into equation (5) in such a fashion that viscous component of the contact stress acts against the direction of movement of the contact node and is equal to the value of $\nu|\mathbf{v}|^2$, where ν is coefficient of artificial viscosity. Second order of velocity module allows to affect the behaviour of the contact nodes with higher velocity more efficiently. The influence of coefficient ν on variation of the contact stress was studied: $\nu = 10^4$ reduces the variation of the contact stress; however, its further increase up to 10^6 makes it unacceptable, which indicates that an optimal range of ν exists.

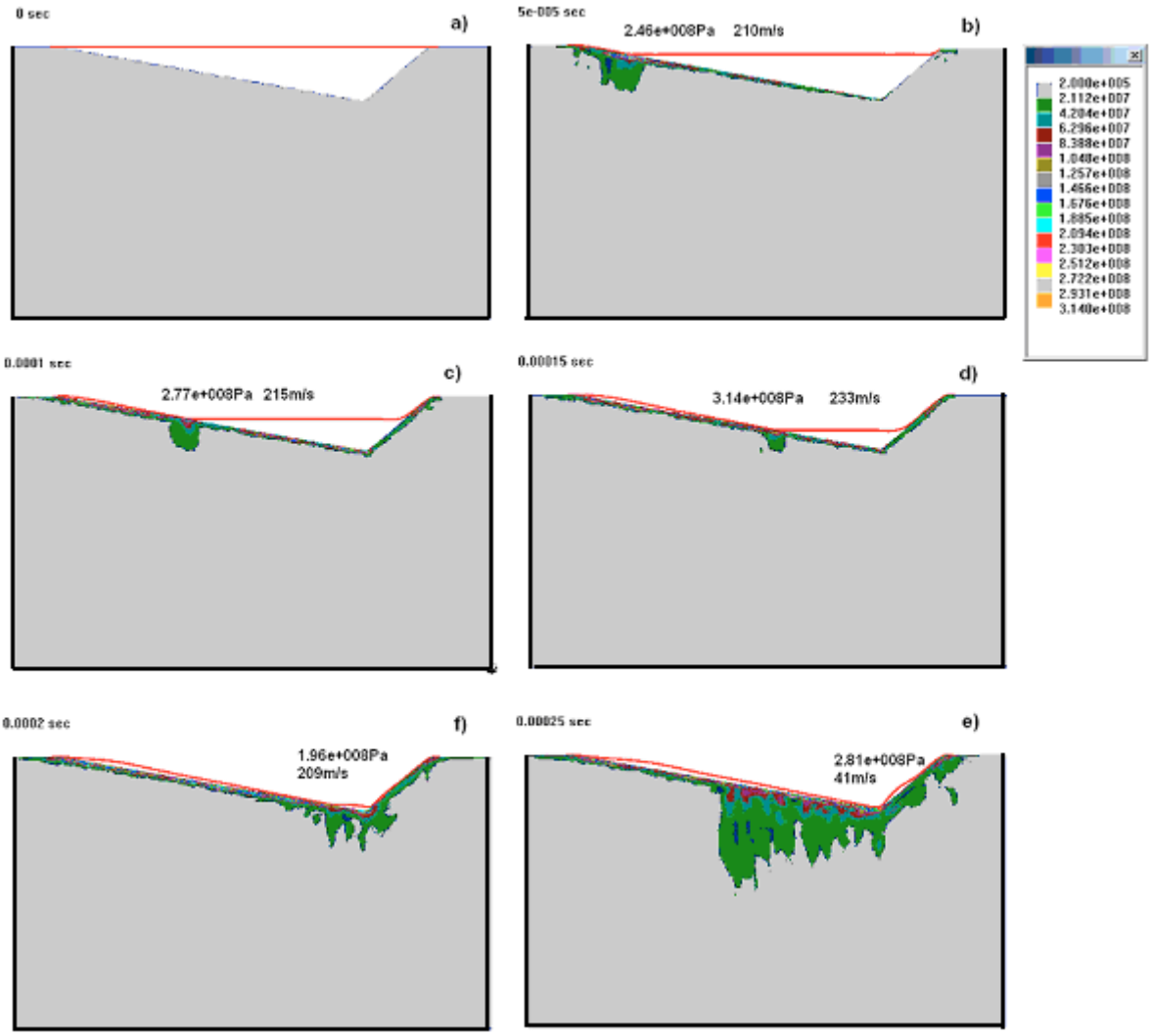

Figure 3: *Values of $J_2(\sigma)$ and velocity of the blank vs. time (P_0 = 30MPa) for a single step corner filling operation.*

5 Dynamic Contact Interaction between the Blank and the Die

The problem of dynamic contact interaction of the blank and deformable die shown in Figure 3 is under consideration. Aluminum blank is 1 mm thick and 280 mm long.

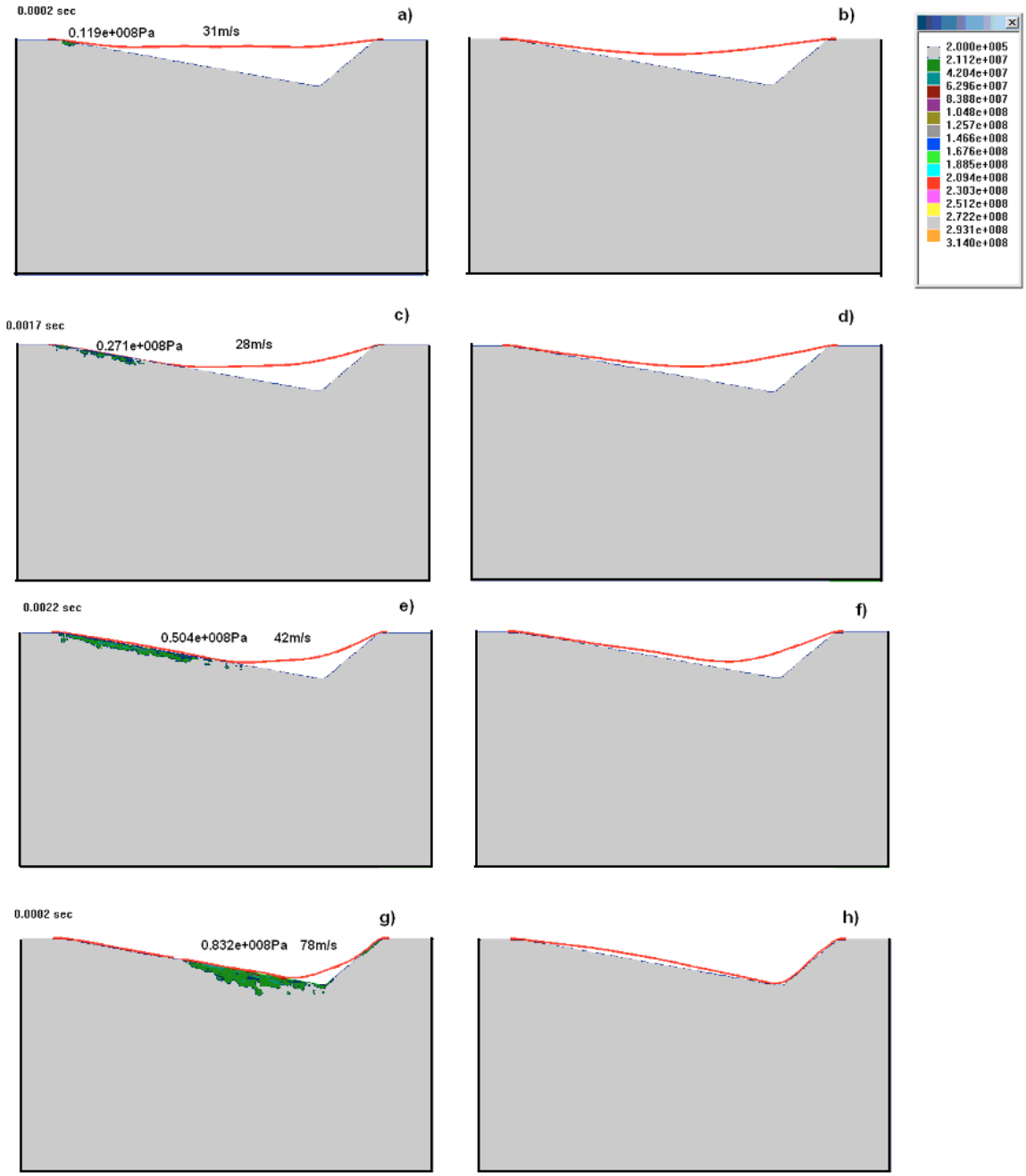

Figure 4: *Values of* $J_2(\sigma)$ *and velocity of the blank vs. time.*
a,b) - P_0 *= 5MPa; c,d) -* P_0 *= 10MPa; e,f) -* P_0 *= 15MPa; g,h) -* P_0 *= 25MPa.*

The die is made out of steel and has an angle of 130 degrees. Material properties for the die are as follows: density ρ = 7800 kg/m3; shear modulus G = 76.9 GPa, bulk modulus

K = 166 GPa, the stress-strain curve $\sigma_s = \sigma_0 + A\varepsilon$, σ_s = 620 MPa, work hardening modulus A = 1020 MPa. For the blank these properties are: ρ = 2735 kg/m³, G = 26.5 GPa, K=65.1 GPa, σ_0 = 195 MPa, and A = 520 MPa. In order to reduce the computational time, electromagnetic forces were modelled as a mechanical pressure (7) uniformly applied to the blank surface.

$$P = P_0 e^{-\beta t} \sin^2(\omega t), \tag{7}$$

where $\beta = 10^4 \sec^{-1}$; $\omega = 10^5 \sec^{-1}$; P_0 was varied to define the appropriate value to fill the die cavity with one pulse. Results of simulation are shown in Figure 3. The stress state of the die material was characterized using second invariant of the stress tensor $J_2(\sigma)$. Maximum value of $J_2(\sigma)$ in Figure 4 is coupled with maximum velocity of the blank for different time intervals at P_0 = 30MPa. For smaller values of pulsed pressure, the blank does not fill the die completely.

In Figure 4 the process of multiple loading of the blank with four pulses of pressure is described: the left column of figures (a,e,c,g) illustrates the middle portion of the process, while the right column of figures shows the final shape of the blank after corresponding forming step of the blank is completed. The pressure pulses with the following pressure amplitudes were applied: 5, 10, 15, 25 MPa. Maximum value of $J_2(\sigma)$ for the die and the impact velocity of the blank in this case are significantly lower than for a single pulse loading when the blank filled the die cavity as a result of only one forming step.

6 Dynamic Contact Interaction in Pulsed Tube Press Fitting Operation

Press fitting of tubes is another application of high-rate technologies where the advantage of pulsed pressure can be taken. In order to accomplish a tight press fit joint, the pressure pulse is applied inside the internal tube, as shown in Figure 5. Appropriate pressure pulse parameters and initial clearance between the inner and outer tubes should be identified to provide good quality joint. A practical example of joining tubes from stainless steel is discussed below. The internal tube with the external diameter of 25 mm and thickness of 2 m was expanded into the external tube from the same material with the external diameter of 50 m. The internal diameter of the external tube was varied in the range between 25.0 m and 26.25 mm in order to investigate the influence of the initial radial clearance on the residual contact pressure. This analysis is very important to formulate the requirements for tubes' accuracy. The dynamic yield stress of both inner and outer tubes material was 300 MPa , E=2x10^{11} Pa, ρ=7800 kg/m^3, Poisson's ratio was μ=0.3. The pressure pulse for such type forming processes [2] can be approximated as:

$$p(t) = p_o \, e^{-t/T} \quad , \tag{8}$$

where P_o is the pressure amplitude, which depends on the energy stored in the EHF machine capacitors; T is a decreasing period, which depends on machine characteristics. In current analysis P_o=350 MPa and T = 8.3 x 10^{-6}sec.

The numerical model, taking into account elastio-plastic deformation of both the inner and outer tubes, was used to investigate the contact interaction mechanism. During the initial stage, the internal tube is being expanded driven by the internal pressure pulse until the radial displacement reaches the initial radial clearance between the tubes. The simulation results of the impact dynamics are given in Figures 6 and 7 for rather small initial clearance of 0.006 of inner tube internal radius. Radial displacements ΔR of the tubes contact surfaces are given in dimensionless form $\Delta R / R_o$. Real time is related to the expression $R_0 / \sqrt{\sigma_{s0}/\rho}$, where R_o is the initial internal radius of the inner tube. Stresses are related to the tubes' initial yield stress σ_{so}.

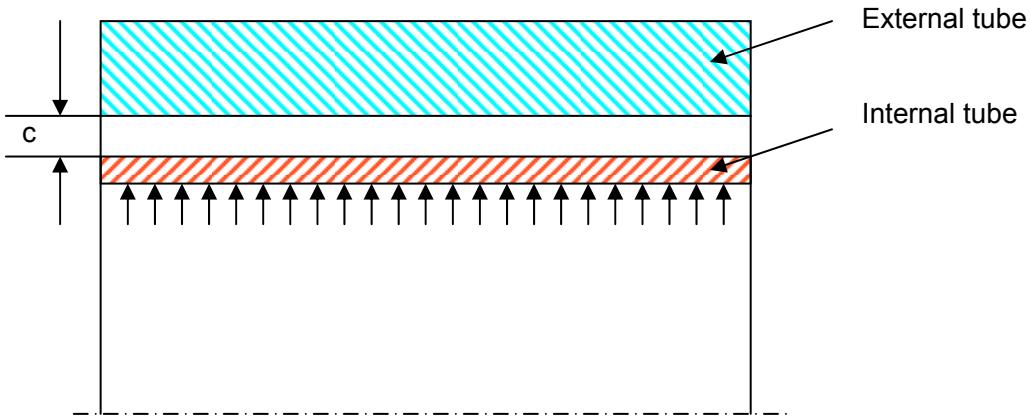

Figure 5: *Schematic of tube press fitting operation by internal tube pulsed expansion.*

At the beginning of the contact interaction, the radial compressive waves propagate inside both tubes. As long as the internal tube is much thinner than the external, the stress wave propagates through its thickness significantly faster than through the external tube. During the internal tube free expansion stage, before the first impact with the external tube, the pressure pulse is partially spent to increase the internal tube. Evidently, the larger is the initial clearance the larger is the velocity of the internal tube and the smaller is technological pressure inside it. Therefore, the radial stress on the inner surface of the internal tube during contact interaction is dependent upon the initial radial clearance between the tubes.

During the first impact, the radial stress wave propagating from the contact surface is then reflected from the inner surface of the internal tube and returns back to the tubes contact surface. At this point, the contact between the tubes is usually terminated. Contact termination may be prevented if the internal pressure is still applied to the internal surface of the internal tube. The displacements of the internal and external tubes are shown in Figure 6 with the dots and thin solid line, respectively. Their joint displacement is marked with the thick solid line. If the first impact happens at the beginning of internal tube acceleration, the technological pressure is large enough, so the reflected radial stress wave from the internal tube produces compressive radial stress at the contact surface, and both tubes move together until a reflected wave comes back from the external tube's outer surface. Due to a significantly larger thickness of the external tube, the joint motion of both tubes in this case continues substantially longer. As a result, the average velocities of both tubes are much closer to each other compared to the moment when the reflected wave from the internal tube first time reaches the contact surface. After the

contact termination, the internal tube is being accelerated by the technological pressure and impacts the external tube again.

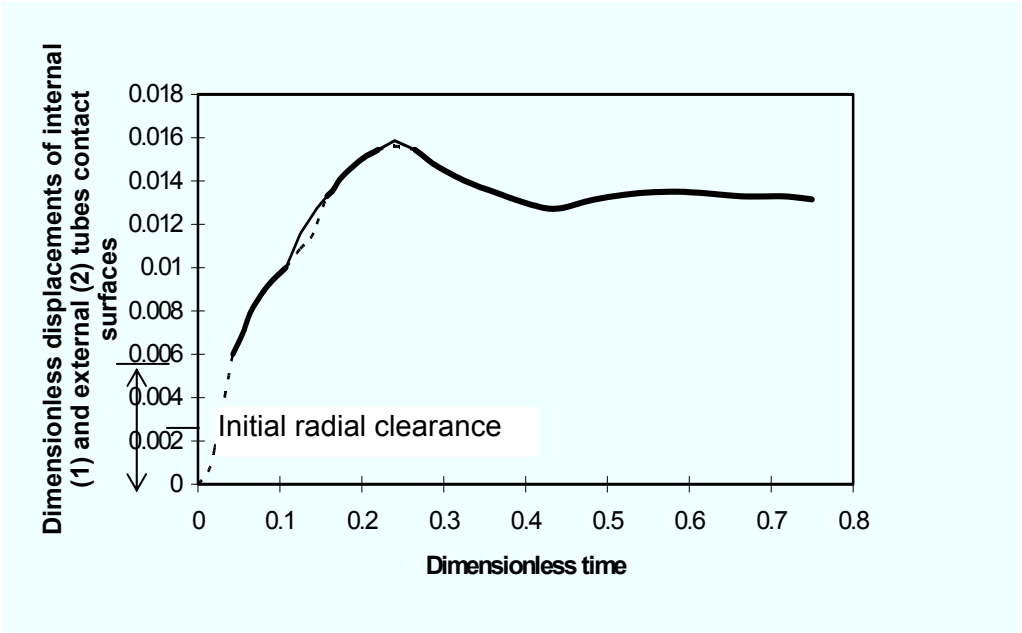

Figure 6: *Displacements of internal's tube outer surface (dotted lines), external's tube inner surface (thin solid line) and their joined displacement (thick solid line) vs. time.*

The quality of assembling process is significantly affected if both tubes start unloading from approximately the same point. In this case, residual contact pressure will be defined by the difference of elastic deformation in internal and external tubes. Evidently the elastic displacement of the external tube should prevail over the elastic displacement of the internal tube.

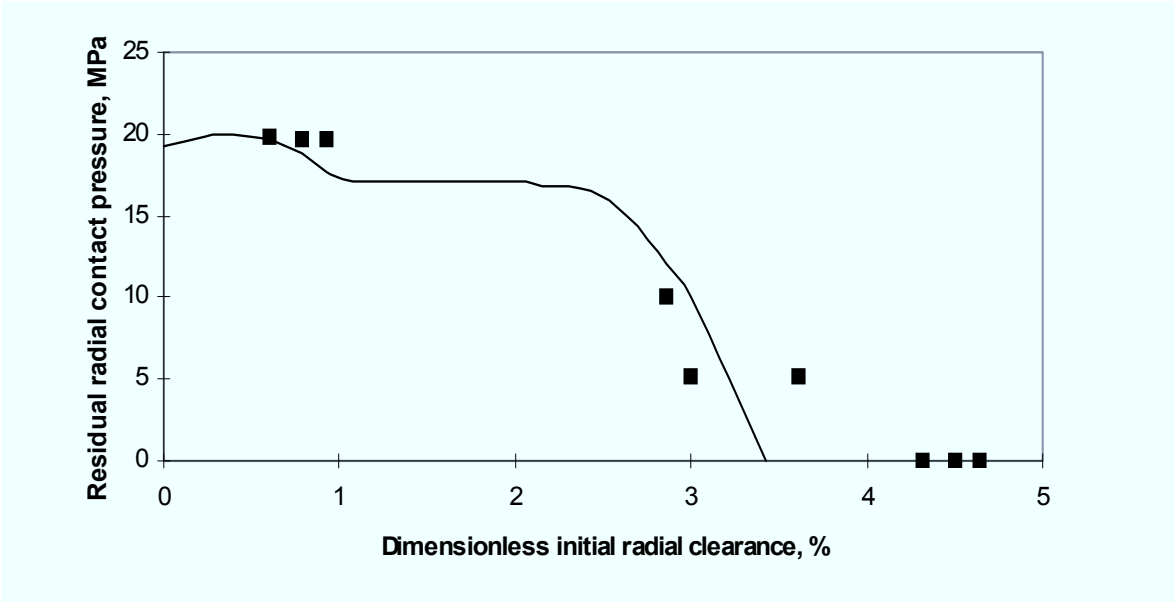

Figure 7: *Influence of initial clearance on residual contact pressure in press fitting process*

If the initial clearance between the tubes is substantial, and the pressure pulse has already diminished at the beginning of the first impact, the contact is being terminated after the reflected wave from the internal tube comes to the contact surface.

Increasing the initial clearance results in growth of the first impact velocity and descending of the technological pressure value. In this case the internal tube transfers all its velocity to the external tube, the contact between the tubes gets terminated after the reflected wave from the internal tube inner surface comes to the contact surface. In this case, the inner tube unloads after the first impact, while the external tube keeps expanding and unloads later. In such case, the unloading of internal and external tubes starts from substantially different points. This mechanism gives no residual contact pressure between the tubes and provides poor quality assembling, as indicated by the small residual contact pressure in Figure 7.

As a result of this discussion, it can be concluded that the maximum initial radial clearance between the tubes should not exceed a certain value, which is dependent on the pulse duration, geometry and material of tubes. For the discussed set of parameters the initial radial clearance should not be more than 3% of the inner tube internal radius.

7 Conclusions

1. Developed numerical model takes into account propagation of electromagnetic field, high-rate plastic deformation of the blank in contact with the deformable die, heat accumulated in the coil, and mechanical loads on the stamping die.
2. Static preforming of the blank into the die cavity combined with pulsed restrike operation or pulsed forming of the blank in several steps may substantially reduce the contact stresses on the die surface.
3. Analysis of the mechanism of contact interaction of tubes in press fitting operation indicated that initial clearance between the tubes should be minimized to provide good quality joint.

References

[1] *Golovashchenko, S.; Bessonov, N.; Davies R.:* Design and testing of coils for pulsed electromagnetic forming. Proceedings of 2nd International Conference ICHSF'2006, Dortmund, Germany, p.141-151.

[2] *Golovashchenko, S.; Mamutov, V.:* Electrohydraulic forming of automotive panels. Proceedings of TMS symposium "Trends in Materials and Manufacturing technologies for transportation industry", San-Francisco, 2005, p.65-70.

Magnetic Pulse Welding for Dissimilar and Similar Materials

V. Shribman

Pulsar Ltd, Yavne, Israel

Abstract

The Magnetic Pulse Welding (MPW) process, a cold solid state welding process, is an industrial process, operating at several high volume manufacturing facilities.

MPW is accomplished by the magnetically driven, high velocity, oblique angle, impact of two metal surfaces. At impact, the surfaces (which will always have some level of oxidation) are stripped off and ejected by the closing angle of impact. The surfaces which are then metallurgically pure, are pressed into intimate contact by the magnetic pressure, allowing valence electron sharing and atomic-level bonding. This process has been demonstrated in the joining of tubular configurations of a variety of metals and alloys [1],[2],[3]. Product designers are frequently constrained by the restrictions of traditional joining technologies, which place certain limitations on the type of joint, the materials that can be joined and the quality of the joint. Solid state welding allows manufacturers to significantly improve their product designs and production results by enabling both dissimilar and similar materials to be welded together, thus providing the opportunity to use lighter and stronger material combinations. Magnetic pulse welding is a fast, non-contact and clean solid state welding process. A review of the main elements of the process is presented here along with typical quality testing results and some applications.

Keywords

Magnetic pulse welding, dissimilar metal welding, magnetic pulse systems

1 Introduction

Magnetic pulse technology has been known and applied, for more than five decades [4], mainly in the area of forming and crimping of high conductivity metals, using low frequency pulse generators. Over that period there has been a widening interest in it, not just as an interesting research topic, but also as a well accepted production process. However, only fairly recently has equipment for magnetic pulse welding been developed, that is of a high enough standard to meet the stringent demands required by high volume manufacturers in the automotive and associated industries. Today, this process is used for production in high volume manufacturing and in addition, high frequency pulse generators have been developed, which allow the use of this process for a wider range of industrial applications.

2 Review of Principles

2.1 Process Physical Principles

Figure 1 illustrates the set-up for welding, in which a current (up to 1.3MA for larger machines) is released into the coil, creating an eddy current on the outer surface of a metal tube (outer) placed inside the coil, giving rise to a magnetic field, in addition to that produced around the coil. These magnetic fields oppose one another and cause the outer metal tube to be imploded at high velocity to impact the inner metal tube. If the impact creates the right conditions of angle of impact and velocity, jetting is created and subsequently welding.

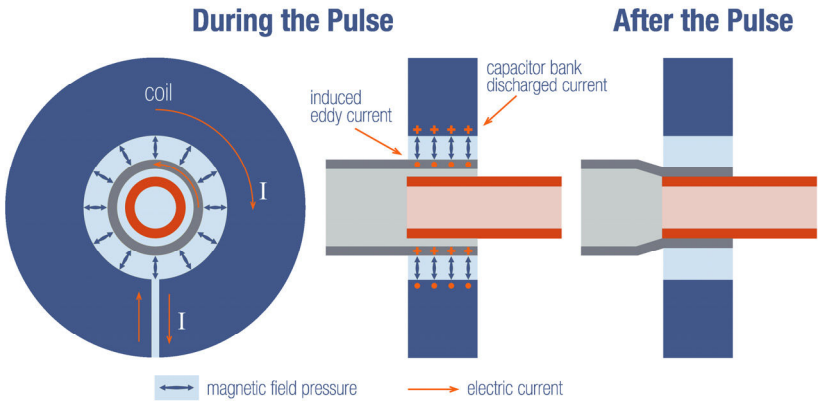

***Figure 1**: Welding Set-up*

Figure 2 show the typical part geometry before and after the welding process. Note that the welded area is always accompanied by deformation of the outer component, as shown in the figures.

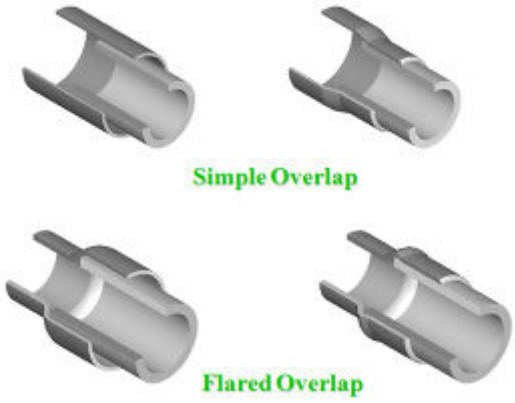

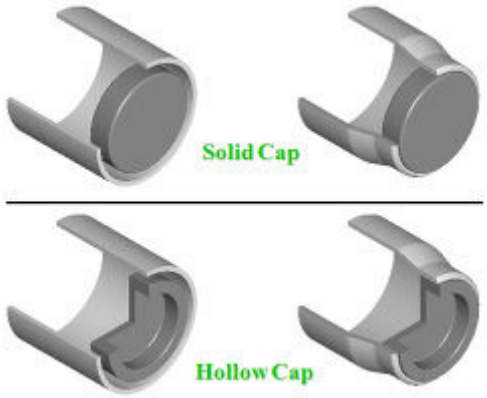

***Figure 2a**: Tube weld geometry*

***Figure 2b:** Capsule weld geometry*

2.2 The Bonding Mechanism

The detailed mechanism of an MPW weld is a complicated, and a not very widely researched subject. What is commonly known is that, as in explosive welding, a jet is created between the two bonded surfaces by the impact force acting upon them. This jetting action removes all traces of oxides and surface contaminants, allowing the magnetic pressure caused impact to plastically deform the metals for a short instant and to drive the mating surfaces together. This allows the impact of two virgin surfaces, stripped of their oxide layers, to be pressed together under very high pressure, bringing the atoms of each metal into close enough contact with each other, to allow the atomic forces of attraction to come into play. There are a number of explanations for the precise mechanism at the point of collision, but all agree that the metals momentarily behave like liquids, even though they remain solid. Due to the rapidity of the process, temperatures at the interface do not rise significantly. For this reason, it is possible to permanently bond widely dissimilar metals. The quality of the bond at the interface is a product of many parameters, among them the magnetic force, the collision angle, the collision point velocity, and the initial standoff distance between the mating surfaces (see Figure 3). Typically, the pressures at the collision point between the mating surfaces are in the order of 100,000 MPa.

In the graph in Figure 4, defined by Wittman and Deribas [5], jetting and therefore welding is only possible with parameters within the closed area abcdef. Curves 6-6 and 7-7 represent the upper and lower flyer plate velocity limits for welding to occur. A critical collision point velocity related to angle of impact 5-5 defines a curve to the right of which no jetting can occur, while jetting can occur to its left. Abscissae 3-3 and 4-4 define the minimum and maximum angles of incidence in which jetting may occur, while 1-1 and 2-2 respectively define the lowest velocity for which conditions for welding can be created and the velocity above which excessive KE is produced, which will give rise to excessive melting and thus produce unwanted intermetallic alloying. It is obvious that this envelope should be experimentally defined for all metal pairs to be welded. However, negligible work has been reported in this area.

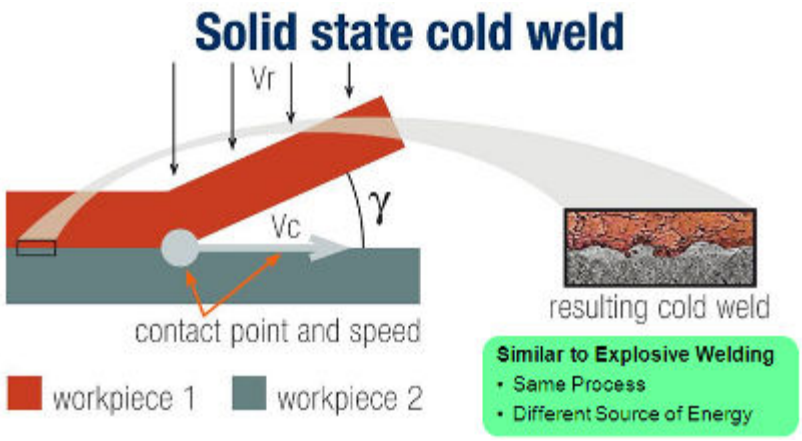

***Figure 3**: Main welding variables*

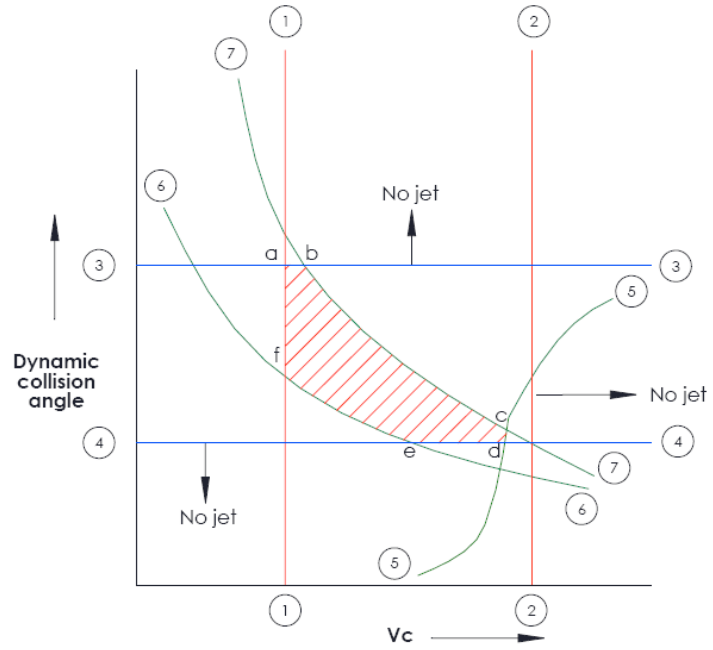

***Figure 4**: Jetting envelope for any metal pair*

2.3 Weld Interface Morphology

MPW gives rise to a wavy or waveless interface morphology, where the precise shape is determined by, among others, the properties of the metals, geometries and parameters applied. In the case of similar material pairs being welded, there is no great significance to interface differences. However, in dissimilar metal welding, there is great importance to differences eg interface with intermetallics formed, which may be brittle and reduce the acceptability of the weld. Figures 5-11 show photomicrographs of various similar and dissimilar metal interfaces with well formed waves, while Figure 6 clearly shows the extent plastic deformation that has occurred close to the interface, as a result of the welding process.

***Figure 5**: 6082-T6 weld*

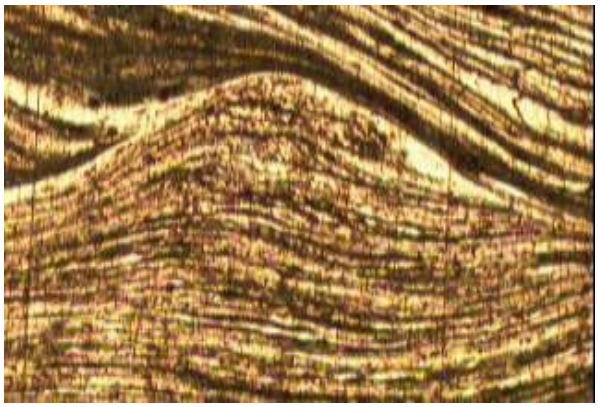

***Figure 6**: 7075-T6 weld*

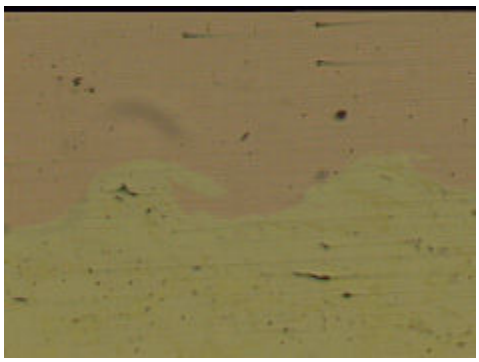

***Figure 7**: Cu/Brass 360 weld unetched x100*

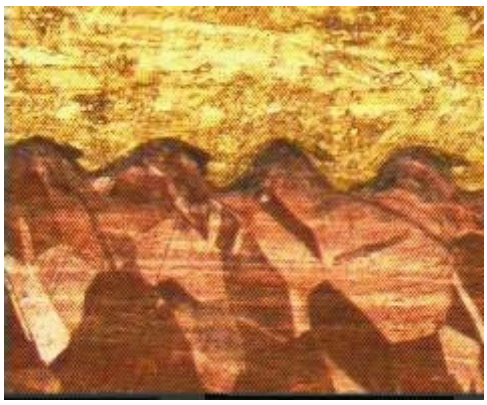

***Figure 8**: Cu/Brass 360 weld etched x100*

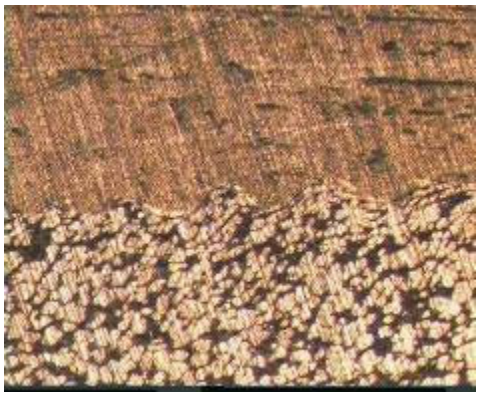

***Figure 9**: Al6063 welded to Al casting AlMg5Si2MnRE x50*

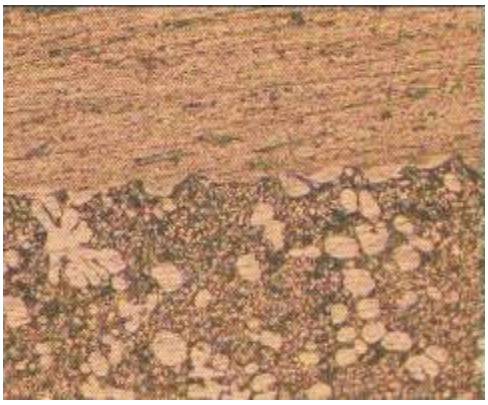

***Figure 10**: Al6082 welded to Al casting EN1706 x50*

Figures 9-12 illustrate examples of welds between wrought metals and die cast metals of various Al alloys. This is the first stage in development work being carried out

with the end target being cast to cast welds, which in its final stages will also include the welding of magnesium alloys, both wrought and cast.

Figures 12-16 show flat undulating interfaces, the latter two with the assistance of SEM.

***Figure 11**: Al6063 welded to AlMg5Si2MnRE x200*

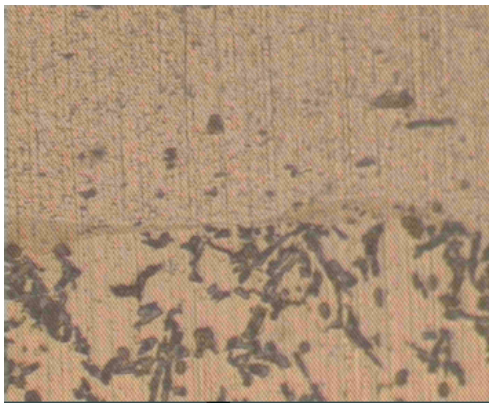

***Figure 12**: Al6082 welded to A380.1 x500*

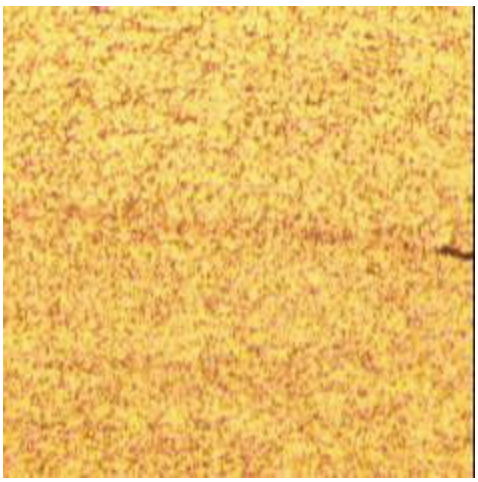

***Figure 13**: Ni200 etched x100*

***Figure 14**: Al/Cu unetched x500*

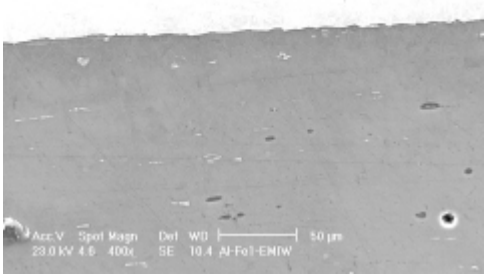

***Figure 15**: SEM Al3003/SS304 x200*

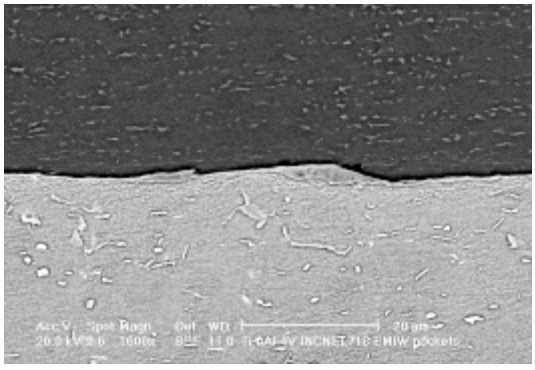

***Figure 16**: SEM Ti6Al4V/Ni Inconel 718x1600*

2.4 Weld Integrity

***Figure 17**: Peel test for Al3003-H12 to SS304*

***Figure 19**: Burst test for Al6061-T6 capsule*

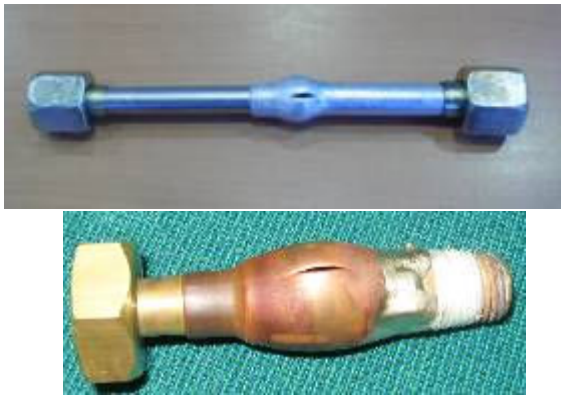

***Figure 18**: Burst test for Al5049 to SS316L and for Cu to Brass*

***Figure 21**: Torsion tested Al/Al 6061-T6 and Al/steel drive*

***Figure 20**: Tensile Test of welded 1020 steel tube*

How does MPW meet international welding specifications. The truth of the matter is that currently there are no tests defined specifically for MPW welds. However, MPW routinely meets all standards for conventional welding, such as leak test, burst test, pressure cycling, etc. In the following are some of the typical test results achieved which will show the level of joint integrity produced by the MPW process. Figure 17 shows a typical peel test of an Al to stainless steel weld, illustrating joint strength. Figures 18 and 19 show burst test results for Al to stainless steel, Cu to brass and Al/Al welds, respectively. It is

seen that the weld is not the weak link and failure occurred in the tube base material. Figure 20 shows the ductile failure of a welded steel tube, failure occurring remote from the weld, while Figures 21 illustrates torsion test results for both Al/Al and Al/steel joints, in which the weakest point is the tubeshaft and not the weld.

Typical results for helium leak test (see later Figure 29) show that the process is capable of producing hermetic seals. Routinely welded parts are required to meet a level of 5g/year at 30 bar R134a (automotive specification). Tests were carried out using a mass spectrometer and the results show 64-150 times better than the specification, as illustrated in Table 1.

Sample n° 61 = 3.9 E - 7 mbar at 30.3 bar = 0,072 g / y
Sample n° 62 = 3.3 E - 7 mbar at 30.4 bar = 0,061 g / y
Sample n° 70 = 3.2 E - 7 mbar at 30.3 bar = 0,059 g / y
Sample n° 80 = 1.8 E - 7 mbar at 30.3 bar = 0,033 g / y
Sample n° 81 = 3.9 E - 7 mbar at 30.3 bar = 0,072 g / y
Sample n° 82 = 4.2 E - 7 mbar at 30.3 bar = 0,078 g / y

***Table 1**: Helium Leak Test Results*

Testing the same item in a pressure cycling test at 1-30 bar, 1.25 Hz, with hydraulic oil at 80 deg C, gave good results after 155k cycles, when subsequently tested in water with 30 bar N_2 gas for 5 minutes.

2.5 Weld Applications

Figure 22 shows the layout of the typical system. An AC power source is transformed into DC current, which energises a bank of HV capacitors.

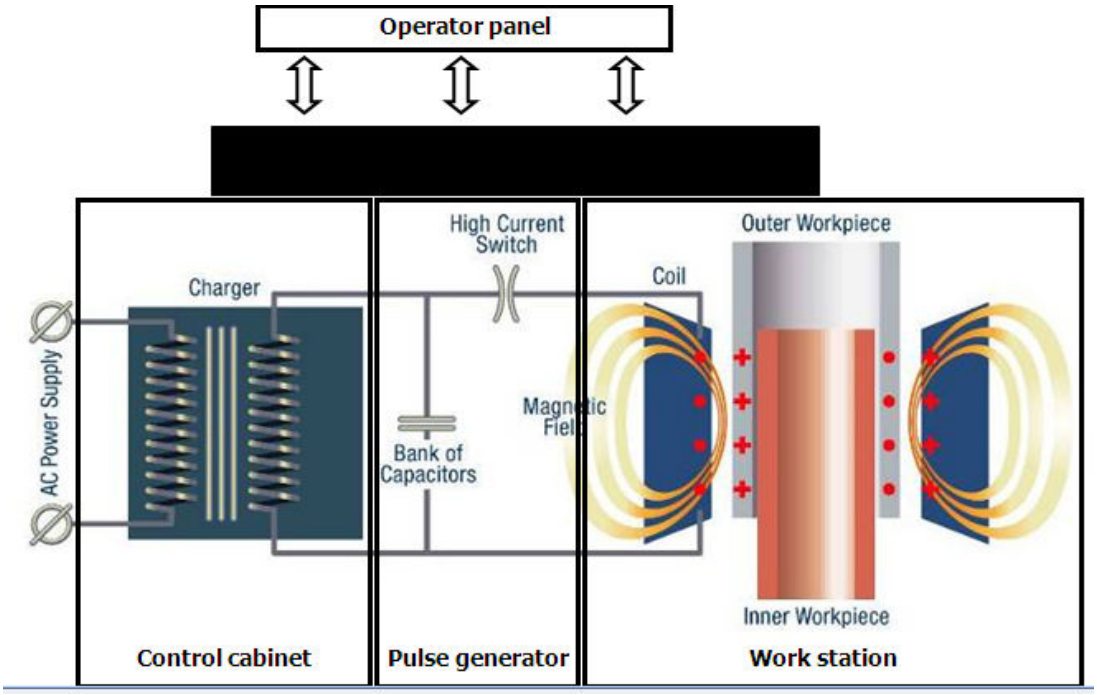

***Figure 22**: Magnetic pulse system principles*

The overall system is shown in Figure 23. It consists of a pulse generator, a control cabinet, a work station and an operator panel for remote operation of the process.

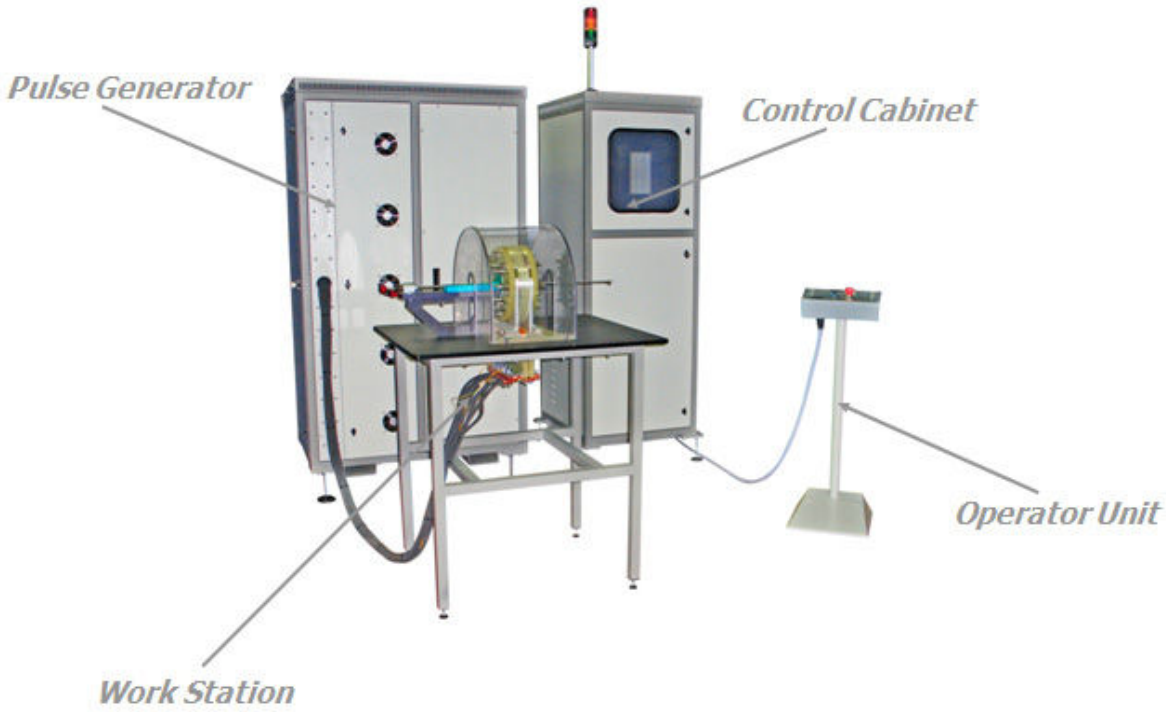

***Figure 23**: The MP System Components*

The pulse generator consists of an electrical storage module, grounding block contactor, a cooling system and a cable connector. The control cabinet consists of a 3-phase line, fuses and circuit breakers, high voltage transformers, AC to DC transformation circuits.

A typical low energy machine of 10kJ/9kV is shown opposite. This has all the components mentioned above, consolidated in a single unit, including the coil assembly being mounted directly on the machine.

***Figure 24**: Low energy pulse generator*

3 Summary

MPW is a "green" solid state welding process producing high speed versatile, high integrity weld joints, some of which, from Figs 25-30, have been incorporated in large

series industrial production. The weld produced is a cold weld, stronger than the weaker of the metal pair, good for dissimilar as well as similar metals and conventionally unweldable metals, heat treat characteristics always being preserved.

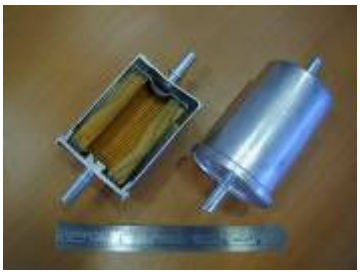

***Figure 25**: Al fuel filter*

***Figure 26**:Al/steel driveshaft*

***Figure 27**: Al/SS earth connector*

***Figure 28**: Cu/brass welds and Al/steel welds*

***Figure 29**: Al fuel filter and A/C receiver dryer*

***Figure 30**: Al7075-T6 high pressure capsule*

References

[1] *Shribman, V.; Livshitz, Y.; Gafri, O.:* Magnetic Pulse Solid State Welding. IIW/IIS Commission XII Florence, Italy Sept. 2000.

[2] *Shribman, V.; Gafri, O.; Livshitz, Y.:* Magnetumformen-Fügen und Schweissen(MPW). DVM Conference, Berlin, May 9-11, 2001.

[3] *Shribman et al.:* Magnetic Pulse Welding Produces High-Strength Aluminium Welds. AWS Welding Journal, April 2002.

[4] *Berenson, B.U.; Waichansky, S.M.; Dashuk, P.N.; Livshitz, Y.:* Development and Research of Pulsed Magnetic Forming Machine MI-1. Proceedings of the International Science -Technical Conference for Creating and Testing High Voltage Electrophysical Apparatus, Tomsk, 1967

[5] *Crossland, B.:* Explosive Welding of Metals and its Applications, Clarendon Press, Oxford, 1982

Production of Steel-Light Metal Compounds with Explosive Metal Cladding

M. Koschlig[1], M.Veehmayer[1], D. Raabe[2]

[1]DYNAenergetics GmbH&Co KG, Würgendorf
[2]MPI für Eisenforschung, Düsseldorf

Abstract

Explosive Metal Cladding is a High Speed Welding Process using the energy of an explosive to bond different metals and alloys in a 2-dimensinal areal configuration. Parameters influencing the cladding process are discussed and the potentials of the method are presented. Microscopic properties of a Cu-Al and a Steel-Ti transition zone are studied in detail to get a better knowledge of the principle mechanisms included in the bond creation. A perspective for future applications of explosive cladding in different industries like automotive and aerospace is given.

Keywords

Bonding, Titanium, Explosive Metal Cladding

1 Introduction

New applications of explosive metal cladding in the automotive and aerospace industry are thought after. Especially the possibility to create 2-dimensional areal substance-to-substance bonds between different metals and alloys is an attractive opportunity that allows the creation of light-weight compounds. As all different forgeable materials could be bond together, composites consisting of Aluminium-Steel, Titanium-Steel and Aluminium-Titanium are easily created. Even composites with Magnesium like Magnesium-Steel, Magnesium-Aluminium or Magnesium-Titanium are imaginable.

While the process of metal cladding is known since the 1960s a satisfying explanation of the bonding mechanism is still pending. A better knowledge of the processes in the transition zone and the created structures and phases is needed to further establish the method and increase the acceptance in the engineering community.

2 Explosive Metal Cladding Process Parameters

2.1 Basic Principle of the Method

Explosive Metal Cladding is a high speed welding process similar to pressure welding. In the basic setup (cmp. Fig. 1) a layer of explosive is distributed atop of a metal sheet – the clad material – which is placed at a certain stand-off from the base material to which it should be bound. When the explosive is ignited, the chemical energy is transferred to the kinetic energy of the clad material or flyer plate. The flyer plate hits the base plate at the collision point creating a material jet, if the cladding parameters are chosen correctly. This material jet cleans the surfaces of both binding partners from unwanted surface deposits like metal oxides. The two metal partners are forced close together forming the bond while a very strong plastic deformation of the interfaces is created at the transition zone.

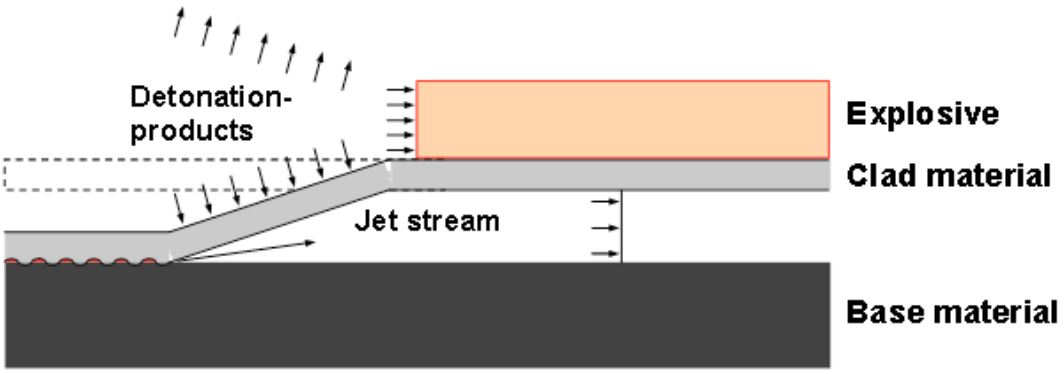

***Figure 1**: The detonating explosive accelerates the Clad material (flyer plate) to the Base Material creating a Jet Stream at the Collision Point that cleans the surfaces of the bonding partners; the kinetic energy binds the two partners together resulting in a plastic deformation of the metals in the transition zone*

In a plan parallel setup like the one shown in Fig. 1 the collision point velocity v_{coll} is equal to the detonation velocity v_d. As the formation of a shock wave inside on of the cladding partners would immediately result in the creation of cracks, this has to be avoided under all circumstances. The detonation velocity v_d must therefore be smaller than the velocity of sound of the metallic partners. To achieve this, specific cladding explosives are used, based on Ammonium Nitrate Fuel Oil (ANFO) explosives adapted to create very low detonation velocities in the range of 1800 – 3000 m/s.

2.2 Cladding Parameters

For the determination of the flyer plate velocity v_{fly} the Gurney Equation (Eq. 1) could be used [1]. In an open sandwich configuration like the one shown in Fig. 1 the flyer velocity is:

$$v_{flyer} = \sqrt{2E_G} \cdot \left(\frac{3}{1 + 5\frac{M}{C} + 4\left(\frac{M}{C}\right)^2} \right)^{\frac{1}{2}} \qquad (1)$$

Here M determines the mass of the flyer plate per unit area and C the explosive charge per unit area. As the Gurney Energy E_G is a constant of the explosive it could be easily deduced from Eq. 1 that a linear relationship between flyer plate thickness and explosive mass used for the cladding process should exist if the flyer plate velocity has to be kept constant.

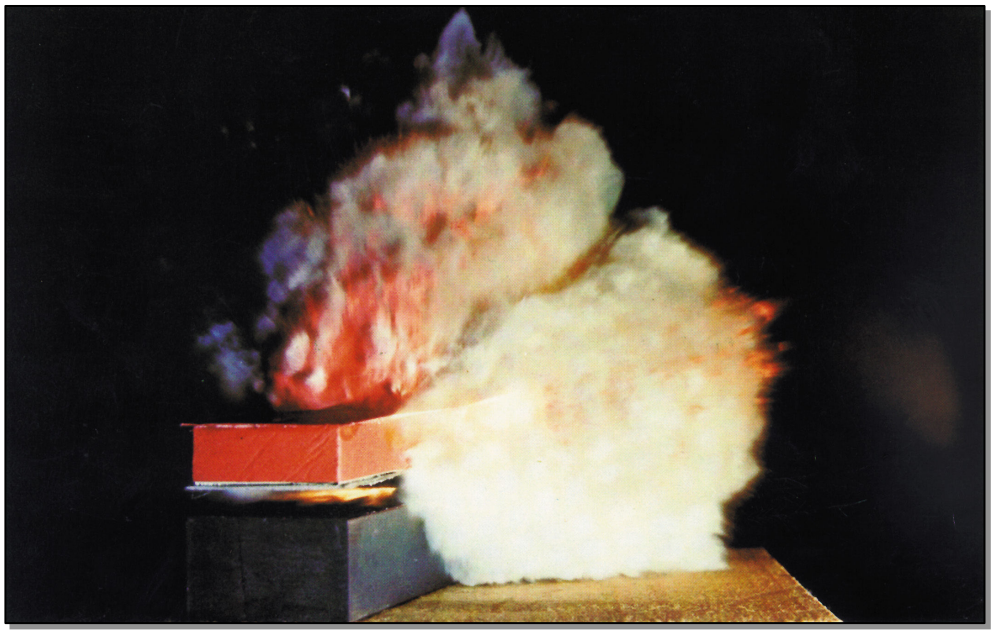

***Figure 2**: Argon Flash photograph of the detonation during explosive metal cladding*

For most explosives the Gurney velocity v_G is related to the detonation velocity v_D of the explosive [2]:

$$v_G = \sqrt{2E_G} \approx \frac{v_d}{2.97} \qquad (2)$$

Unfortunately this relation is not valid for ANFO explosives and especially cladding explosives don't follow this relation that has been deduced for High Energy (HE) explosives used in military applications.
The Gurney velocity v_G has therefore to be determined for each explosive used individually. Flash X-ray pictures could be used to do this.

2.3 Temperature in the gas gap

Combining metals with explosives, besides the impressive energy release due to the detonation, is a relative cold process. The temperatures created in the gas gap between the metal partners could be approximated, if the Mach number M_0 of the shock wave travelling through the gas is known [3].

$$M_0 = \frac{v_{Shock}}{c} \tag{3}$$

To calculate the Mach number M_0 the velocity of sound c of the gas (cmp. Eq. 4) and the shock velocity v_{Shock} (cmp. Eq. 5) have to be known. The velocity of sound depends on the adiabatic coefficient γ, the gas temperature T_0 of the unshocked gas and the molar mass μ_{mol} of the gas:

$$c = \sqrt{\frac{\gamma R T_0}{\mu_{mol}}} \tag{4}$$

The shock velocity v_{Shock} of the gas can be calculated from the Shock Hugoniot, which for most gases is given by Eq. 5 [1]:

$$v_{Shock} = 0.899 + 0.939 \cdot u \tag{5}$$

Here the particle velocity u in the gas is given by the collision point velocity v_{coll}. The temperature in the gas T_1 after the shock is given by Eq. 6 where the parameter μ^2 depends on the adiabatic coefficient γ of the gas (Eq. 7).

$$T_1 = T_0 \cdot \frac{\left(1+\mu^2\right) \cdot M_0^2 - \mu^2 + \mu^2 \left(\left(1+\mu^2\right) \cdot M_0^2 - \mu^2\right)^2}{\left(1+\mu^2\right) \cdot M_0^2} \tag{6}$$

$$\mu^2 = \frac{\gamma - 1}{\gamma + 1} \tag{7}$$

For a typical situation with a collision point velocity of v_{coll}=2000 m/s with air as the gas between the plates and an initial temperature of T_0=300°K the gas temperature in the shock front would be T_1=4000°K. As could be seen in Eq. 3 – 7 the type of gas between

the plates has a strong influence on the shock temperature T_1. If Argon would be used instead of air the shock temperature would be T_1=7250°K. For Helium the shock temperature would be reduced to T_1=970°K.

As the shock front travels very fast, the time to heat up the metal surfaces is very short and only a small zone of approximate 100 µm could be influenced through increased temperatures.

From these considerations it becomes obvious that a close study of the metal-metal interface depending on the cladding parameters like explosive amount detonated and gas in gap between the plates is necessary to prove the quality of the bond for high sophisticated applications.

2.4 General Properties of the explosive bond

The reasons to use claded metal composites are manifold. First there is the lower material costs compared with high-alloyed solid plates. In addition a combination of the properties of the binding partners could be desirable. Mechanical properties, electrical conductivity, thermal conductivity and corrosion resistance are potentially altered due to the material combination

A broad spectrum of different metal combinations (cmp. Tab. 1) is commonly bond by explosive cladding today. Nearly all forgeable metal alloys could be bond with this method creating a substance-to-substance bond. The bond is 2-dimensional and allows a further machining of the compound with standard technologies like rolling, drilling, turning, milling or welding of unmixed metals.

Base Material	**Clad Material**
Carbon Steels for Vessels	Austenitic steels
Micro-alloyed steels	High-strength steels
High-strength steels	Al + Al alloys
Austenitic steels	Cu + Cu alloys
Al + Al alloys	Ni + Ni alloys
Cu + Cu alloys	Titanium, Ta, Zr
Ni + Ni alloys	Silver
	Mo

***Table 1**: List of possible clad combinations commonly used today*

The quality of the bond is checked with destructive and non-destructive material testing. Ultrasonic testing is used to guarantee a homogenous binding quality over the complete claded area, with side bend tests, bend tests according to ASTM and shear strength tests the quality of the bond is ensured (cmp. Tab. 2). Penetration tests and Corrosion tests are further commonly used methods.

Clad Material	Base Material	Measured Shear Strength [MPa]
Stainless Steel	Carbon Steel	310-580
Nickel / Ni-Base	Carbon Steel	300-410
Copper	Carbon Steel	170-230
CuNi30Fe	Carbon Steel	265-390
Titanium Grade 1	Carbon Steel	200-480
Zirkonium 700	Carbon Steel	200-360
Tantalum	Carbon Steel	200-250
Aluminium	Carbon Steel	70-120
Aluminium	Copper	70-120
Titanium	Copper	220-280

***Table 2**: Measured Shear Strength for different material combinations*

3 Microscopic Properties of the Binding Zone Between the Metal Partners

A closer study of the interface with Scanning Electron Mircrogaphs using advanced technologies like EDAX and EBSD has been performed to better characterise the nature of the bond created.

3.1 Cu-Al Transition Zone

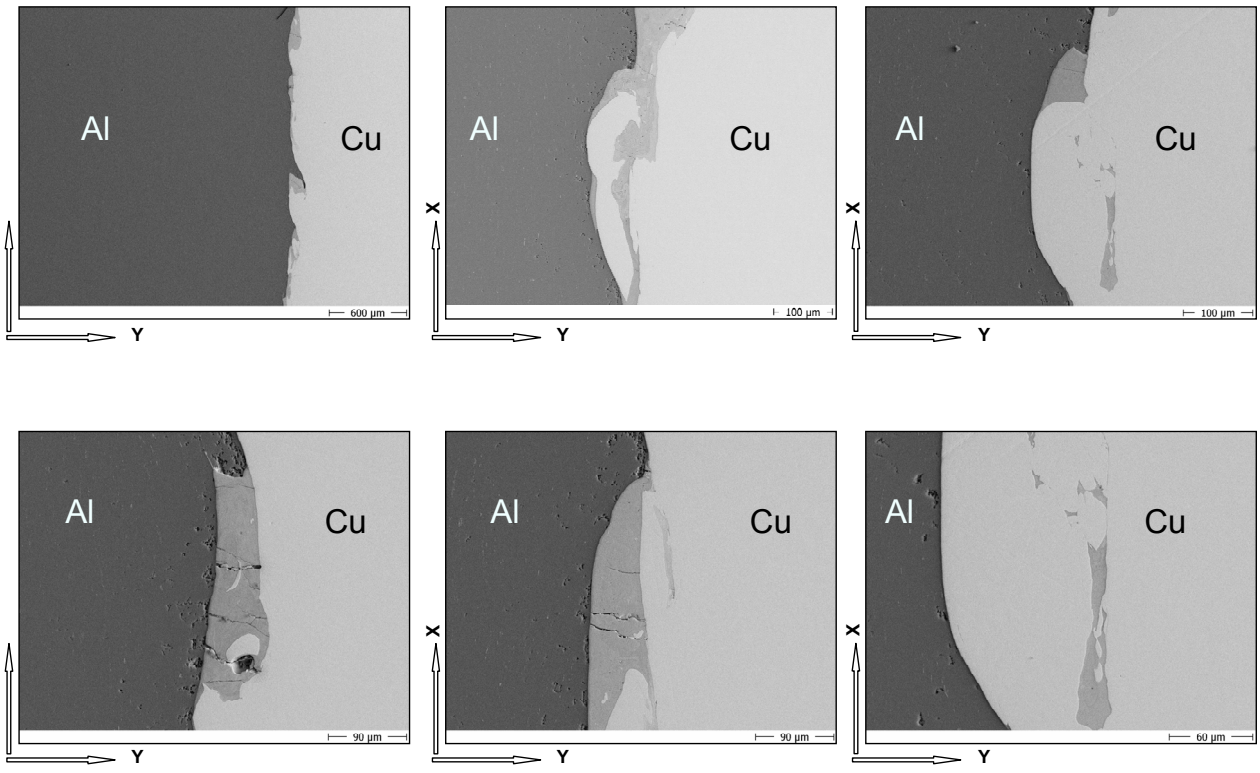

***Figure 3**: SEM of the transition zone for an Aluminium Cupper interface*

The Aluminium-Cupper Interface (Fig. 3) shows a smooth transition line and only minor, microscopic defects could be found. Most cavities were completely enclosed by pure material. In single location the occurrence of a new phase was observed. A characterisation of this phase with EDAX (Fig. 4) showed an Al-Cu compound. A statistical rating of the likelihood for the occurrence of these phases is still pending. In addition the influence of the cladding parameters on the structure of the interface is the subject of ongoing research.

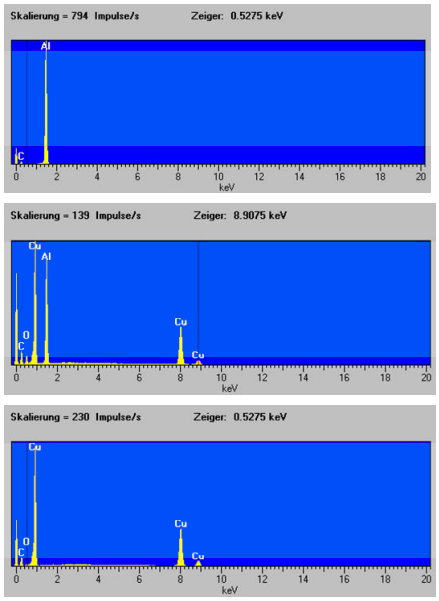

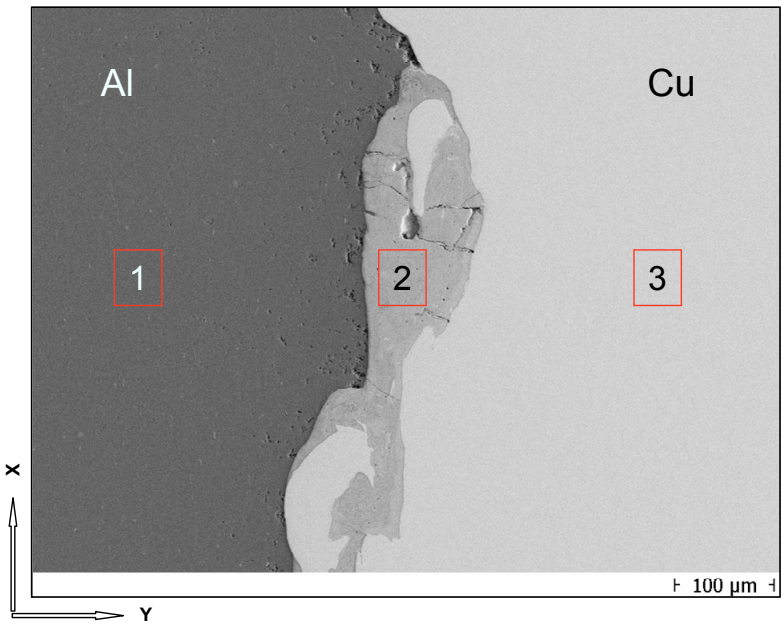

Positions of EDX measurements

Position	Al	Cu	O
1	99.15	0.04	0.81
2	20.59	76.38	3.33
3	0.09	99.32	0.59

***Figure 4**: EDAX characterisation of the metal phases in the transition zone. In position 2 an Al-Cu compound is found.*

3.2 Steel-Titanium

The Steel-Titanium Interface forms a characteristic wave shaped structure (cmp. Fig. 5). At some locations of the Interface minor defects could be found. Like in the Al-Cu case a statistical interpretation of these effects is still pending. As no continuous defect zone was found the quality of the bond is not influenced by these holes.

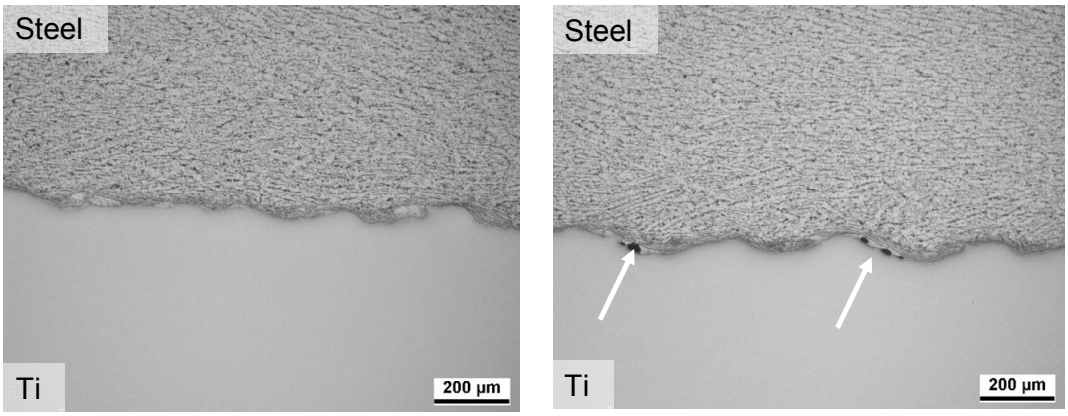

***Figure 5**: Steel-Titanium Interface with characteristic wave shaped structure. Wave length λ=250 µm, Amplitude 50 µm. In single locations minor defects could be localised at the interface of the metals.*

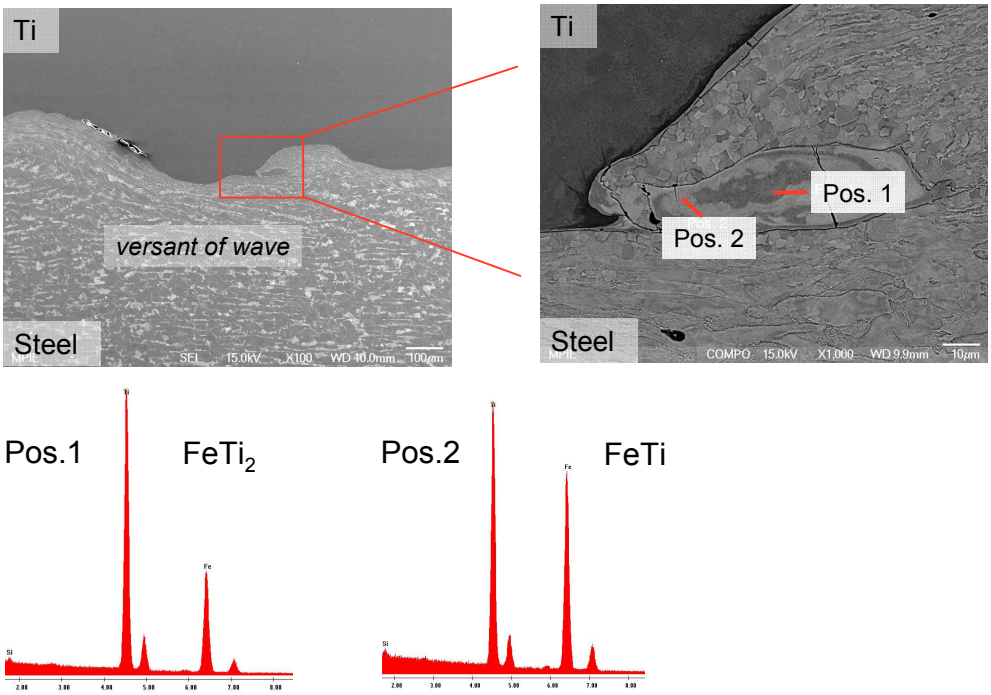

***Figure 6**: Phase characterisation in the versant of a broken wave of a Titanium-Steel interface. Compounds with 2 different chemical compositions according to FeTi and $FeTi_2$ were found.*

A closer study of the versant of a broken wave showed the occurrence of a new phase as an inclusion of the wave peak (Fig. 6). A chemical characterisation of this zone showed two different chemical compositions of the compounds according to FeTi and $FeTi_2$.

Here also a better understanding of the binding mechanism is the subject of ongoing research.

4 Industrial applications of explosive metal claded sheets

A number of well established companies – like DYNAenergetics – offer explosive metal claded products on the market. The dimensions of single plates produced could be up to 4x7 m².

***Figure 6**: Preparation of a plate sandwich for cladding in the underground mine DYNAenergetics uses. The ANFO explosive is homogenously distributed with an Aluminium lath to guarantee a homogenous layer thickness.*

Claded sheets are used today in power plants, for applications in the chemical and petrochemical industry, for construction purposes, in environmental applications, for desalination plants, in electronics and electrical applications, for electrolysis electrodes, in ship building and for medical applications.

Especially the fact that metal combinations that are difficult or impossible to bond by other means and a metallic continuity is formed are attractive for other applications like in the automotive and the aerospace industry. Light weight metals like Titanium, Aluminium and even Magnesium can be bond to other metallic partners like Steel or to each others.

5 Conclusions

The method of explosive metal cladding, which is known since the 1960s, is a well established technology in certain industries today. On the opposite it is not a standard

engineering tool in our days and in certain industries the advantages of the technology are not utilized. In this paper the effect of process parameters on the cladding results and the benefits of the technology are emphasized. To increase the acceptance of explosive metal cladding a research program to better characterise the metal-metal interface has been started. First results of the Al-Cu and the Ti-Steel interface are very promising and prove the good quality of the bond. Further improvements are likely to be achieved by adjustment of process parameters.

References

[1] *Paul W. Cooper:* Explosive Engineering, John Wiley & Sons
[2] *B.M. Dobratz, B.C. Crawford:* LLNL Explosives Handbook, Lawrance Livermore National Lab
[3] *G.F. Kinney, K.J. Graham:* Explosive Shocks in Air, Springer

SESSION 2

MATERIALS AND MEASUREMENT TECHNIQUES

Coupling Experiment and Simulation in Electro-magnetic Forming Using Photon Doppler Velocimetry*

G. S. Daehn[1], Y. Zhang[1], S. Golowin[1], K. Banik[1], A. Vivek[1], J. R. Johnson[1], G. Taber[2], G. K. Fenton[3], I. Henchi[4], P. L'Eplattenier[4]

[1]Department of Materials Science and Engineering, The Ohio State University
[2]Department of Materials Science and Engineering, Michigan State University
[3]Applied Research Associates, Albuquerque, NM
[4]Livermore Software Technology Corporation, Livermore, CA.

Abstract

Modeling electromagnetic forming processes is in many ways simpler than modeling traditional metal forming processes. In electromagnetic forming the problem is often dominated by inertial acceleration by a magnetic field. This is a much better posed problem than the more traditional ones that are often dominated by complex three dimensional constitutive behavior and frictional effects. However, important aspects of the problem are dominated by the constitutive properties of the material, and often electromagnetic forming is performed in a regime where there is little reliable material strength data. Strain rates are often high (10^2 to 10^4 s^{-1} is the typical range for electromagnetic forming). Also, heat is generated both by ohmic heating as well as by plastic deformation, and peak temperatures can be quite high. Also, while high-temperature, high-strain-rate data is scarce, there is little or no data in cases where temperature rises significantly over very short times (tens of micro-seconds) as happens in electromagnetic metal forming. This rapid temperature rise is very important to the material response because the short time scales largely preclude the material from recovery and recrystallization processes and precipitates cannot dissolve as they normally would in an age-hardening alloy in these time scales.

This presentation will show how advanced instrumentation, particularly the Photon Doppler Velocimeter (PDV) can be coupled with electromagnetic forming and provide both avenues to characterize material as well as to provide very critical tests of numerical models of the process.

---

* *Financial support for the velocimetry system was generously provided by GM R&D under the direction of John Bradley and Paul Krajewski. The Uniform pressure actuators used were manufactured by American Trim of Lima, Ohio, under Steve Hatkevich's guidance.*

Keywords

Sheet metal, Forming, Aluminum

1 Introduction

High speed and impulse metal forming methods are an ideal complement to traditional processes in stamping, cutting, hemming and welding [1]. This potential has been clear for some time, but these techniques have still seen very limited utilization to date. One of the primary issues is that while design methods for traditional processes are well-established, they are presently being developed for these impulse based methods. Once they are robust, available and have been validated, its reasonable to expect the design and implementation of impulse-based or impulse-augmented methods, such as electromagnetic forming, will become much more routine.

It can be argued that the key to effective electromagnetic forming design is related to the design of electromagnetic actuators that provide the proper spatial distribution of magnetic pressure. The temporal variation of the pressure is controlled by the electrical (LRC circuit) characteristics of the capacitor bank system. The magnetic pressure typically produces stresses in the workpiece that can exceed the flow stress in the material by a large factor. The pressure in excess of what is needed for yielding goes into accelerating the workpiece in accord with Newton's First law. To instrument the process to collect data that will provide a critical check on a model, it is probably more important to be able to measure rates of acceleration (with microsecond time resolution) than simply measuring average or peak velocities). This paper describes the use of an instrument, the Photon Doppler Velocimeter, that is capable of such measurements, which is also robust and can make measurements in tight geometric conditions, and will describe its use in the analysis of electromagnetic metal forming.

2 The Photon Doppler Velocimeter (PDV)

The traditional instrument for capturing the surface velocity has been the Velocity Interferometer for Any Reflector System (VISAR) which was developed by Barker and Hollenbach at LLNL in 1972. These instruments have been the standard for velocity measurement, but have significant shortcomings. Most importantly they essentially require dedicated technicians and data analysis is time-consuming and requires some judgment. As a result this is an expensive technique that is not suited to use in 'difficult' environments, as may be encountered in manufacturing facilities. Recently Strand and co-workers [2] at LLNL introduced a new method of measuring the velocity of free surfaces with exceptional temporal resolution, the Photon Doppler Velocimeter (PDV). This equipment leverages newly-available fiber optic lasers and components as well as higher speed oscilloscopes. The equipment represents a breakthrough in robust and inexpensive velocimetry. The equipment is durable, relatively inexpensive, and easy to use and requires very little specialized training or background. Most-importantly data analysis is has minimal ambiguity and can be performed rapidly. The technique provides sub-micron displacement resolution, temporal resolution in the nanosecond range, and it is

straightforward to collect at multiple locations with several channels. Maximum measurable velocity depends upon the speed of the oscilloscope and instrumentation, and PDV's that can measure in excess of 10km/s have been demonstrated. This equipment can also be easily packaged for use in electromagnetic forming facilities that are even in industrial environments, because only a thin fiber optic line (with an inexpensive probe on the end) needs to run between the instrumentation and the target. A schematic of the PDV system is shown in Figure 1.

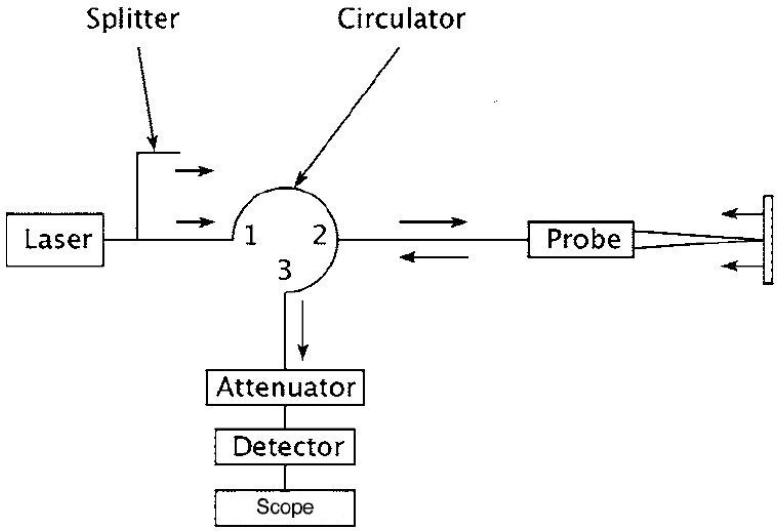

***Figure 1**: Schematic diagram of a Photon Doppler Velocimeter (PDV) system.*

This approach has been adopted at Ohio State University and the key components of the OSU PDV system include:

Laser — The heart of the system is a erbium high power fiber laser that has a very narrow spectral linewidth. The OSU system is based on an NP Photonics 1550 nm, 1000 mW output power fiber laser with a linewideth of <5kHz.

Splitters — Divide laser output to several fiber optic ports for multi channel operations or phase comparison.

Circulators — Directional fiber optic device guides light from the laser out to the probe and reflected light from the probe to the detector. We use a 1 watt JDS Uniphase device.

Detectors — Short rise time biased photodetector, high bandwidth comparable to oscilloscope. Newport model 818s detectors are used in the OSU system.

Probes — Collimating or focusing with built in reference partial reflection surface. Many types are available and used.

Oscilloscope — A 1 GHz, 5 GS/s, LeCroy Wavesrufer 104MXs with 4 channels is used in this system. This Oscilloscope has a relatively large amount of data storage, of 10 Mpts on each channel. This allows storage for periods up to 2 ms at full speed on each of the 4 channels.

The basic physics of the PDV are actually relatively simple, a moving surface produces Doppler shifted light, which is then recombined with the incident light signal to produce a beat frequency. This beat frequency is proportional to the velocity of the moving

surface, and can be analyzed with modern digitizing equipment to yield velocity vs. time profiles with good accuracy. Though the principles are simple, the actual measurements are non-trivial, and require very modern electronics.

In regards to data analysis, there are multiple methods that are possible. A full beat cycle is observed for every 775 nm of sample motion (one half of the incident wavelength, i.e. 1550/2 nm), so a simple velocity calculation can be done from the raw data (i.e. velocity = distance/time, so velocity = 775 nm/(period of one beat cycle)), also, a Fourier Transform can be performed to analyze the changes in beat frequency in order to generate velocity vs. time profiles. Due to the Nyquist limit, the minimum sampling rate is twice the bandwidth and or good analysis, it about a minimum of 5 sampling points are required for each oscillation of the beat wave. By these considerations, the basic capabilities of the OSU system are that it can measure 4 independent velocity channels at velocities from zero to about 775 m/s over a period of up to 2 ms. This can correspond to a displacement of about 1.5 m for the maximum speed acting over 2 ms. Typical measured displacements are on the order of millimeters to centimetres, as is shown in the following examples

3 Ring Expansion and Constitutive Determination

There is a great need for data on the mechanical behavior of metals at high strain rates. This is not only importan for understanding high strain rate forming processes, but also for machining, crashworthiness, armor and anti-armor studies as well as for basic scientific understanding. The Hopkinson-Kolsky bar method is the dominant approach, but this method is difficult to run in true uniaxial tension and the process of testing and data analysis is rather time consuming.

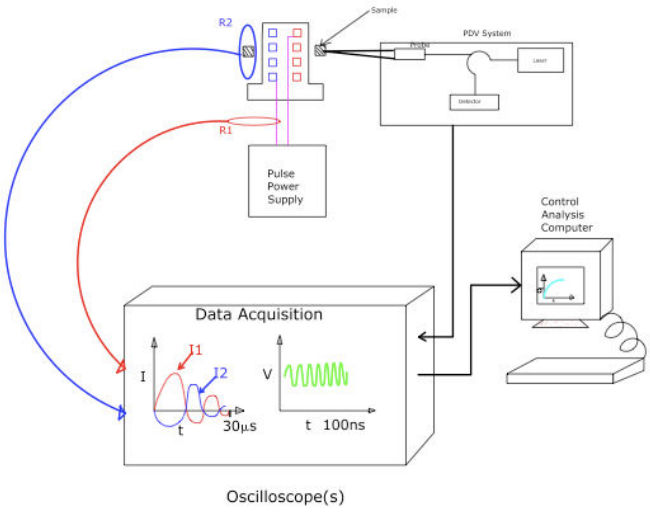

***Figure 2**: Schematic of the instrumented dynamic ring expansion test that is being developed for the measurement of tensile stress-strain relations at high strain rate.*

The electromagnetically driven expanding ring has been proposed as a test for high strain rate tensile testing by Niordson [3]and was developed to a fairly high degree of sophistication by Gourdin ([4,5]) This is a very elegant test in that it provides true uniaxial tension and can drive to strain rates over 10^4 s^{-1}. It is also a very useful test in studying

high strain rate ductility and fragmentation behavior [6, 7]). This test never became widely used for a few principal reasons: 1) The Velocity Interferometer Systems for Any Reflector (VISARs) that were used to measure expanding ring velocity (and deceleration) were very difficult to use routinely, 2) To keep the boundary conditions simple when determining constitutive tests, only very sender rings were used in testing. This limited the strain rates that could be achieved, as resistive heating is very strong in slender rings, and 3) Experimental analysis, particularly using VISAR's is rather time consuming and not typically straightforward. This section makes the case that with some modifications to Gourdin's essential test system and by using modern instrumentation and analysis, the expanding ring test can be a very efficient and effective test for acquiring high strain rate mechanical strength data in tension. In addition this test is able to work easily over a wide and controlled range of strain rates and temperatures.

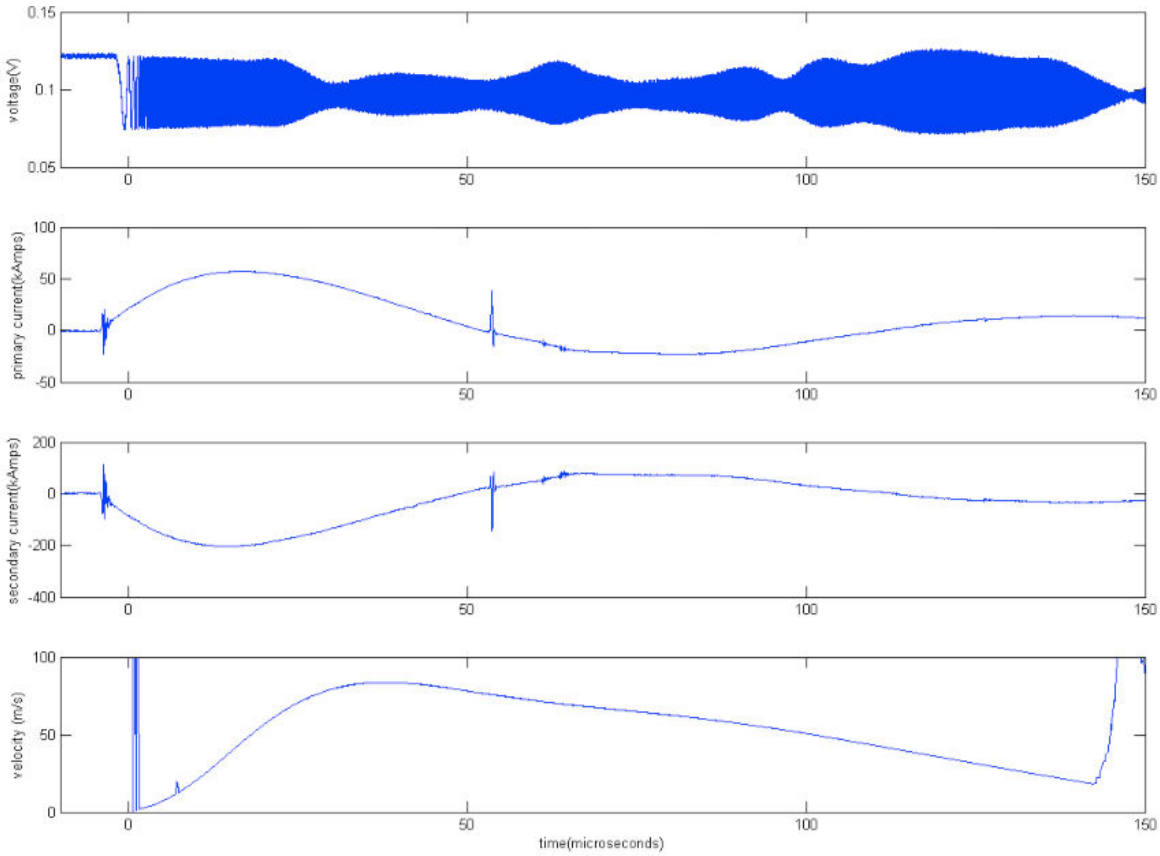

***Figure 3**. Raw data from an experiment in expanding an annealed short copper tube with a 1.44 kJ electromagnetic pulse. From top to bottom the curves respectively show: 1- the raw optical amplifier signal, 2- the primary current in the 5-turn coil, 3- the induced current in the ring and 3- the measured ring velocity as a function of time.*

The basic approach for the experiment is shown in Figure 2. Standard electromagnetic ring expansion driven by capacitor bank discharge is used to expand the test ring form a fixed solenoid coil. The instrumentation used allows precise measurements of a number of quantities with exceptional temporal resolution during the experiment. A standard commercial Rogowski coil allows measurement of the primary current. A second Rogowski coil made from fine wire loops directly around the sample ring allowing direct measurement of the induced current with time. The PDV system gives

sample position with time with temporal resolution on the order of nano-seconds and spatial resolution on the order of microns. This data can be singly or doubly differentiated with time to give velocity or acceleration with time for the ring.

The resulting data from an example launch of an annealed copper ring from a 5-turn coil at a 1.44 kJ launch is shown in Figure 3. Here the raw signal from the light detector is shown in the top graph primary and secondary currents are shown in the next two graphs and the ring velocity with time is shown in the last graph. The ring velocity is measured based on the period of each optical oscillation. Thus, this plot contains literally thousands of independent measurements of ring velocity, so acceleration values can be estimated very well. Automated methods are now being developed to turn these data into stress-strain curves for the rings.

There are two ways to analyze the deformation of the ring to determine the stress versus strain behavior of the metallic workpiece. The ring can be considered to be slender and a one-dimensional analysis can be used or for more complex situations full numerical analysis can be used. Let us consider the simpler one-dimensional approach first. The basic geometry of a short tube and the forces that act on it are shown in Figure 3. The important balance is between the magnetic pressure created by the electrical discharge and the hoop tension in the ring. Inbalance causes acceleration of the ring. The basic governing equation for this is:

$$\frac{dV_r}{dt} = \frac{P(t)}{\rho h(r)} - \frac{\sigma\left(\varepsilon\left(r\right)\right)}{\rho r} \tag{1}$$

Where t, r, h, and ρ are time, ring radius, ring width, and ring density, respectively. V_r is radial velocity. P(t) is the time-varying magnetic pressure. Ring flow stress as a function of strain is written as $\sigma(\varepsilon(r))$. When volume conservation of the ring is included, the equation can be re-cast as:

$$\frac{dV_r}{dt} = \frac{P(t)r}{\rho h_o r_o} - \frac{\sigma\left(\varepsilon\left(r\right)\right)}{\rho r} \tag{2}$$

What is important here is that every term, except for the ring flow stress can be explicitly measured or estimated at each time step. Thus, by using the kinds of data in Figure 3, each term except for the flow stress can be very closely measured or approximated and then the only remaining term, the ring flow stress, can be solved for. At each short time increment the flow stress and ring strain can be calculated and a traditional stress-strain curve can be displayed.

The approach above is largely Gourdin's original method. He strived to use very slender rings so that the equations would be nearly one-dimensional. Modern simulation software provides another method. As described in a previous publication by L'Eplattenier and co-workers [8]. Data of the type in Figure 3 can be used as input finite element simulations of ring expansion to coupled by LS-OPT and from this, the parameters for a constitutive equation can be optimized for.

This general approach offers many advantages for developing high strain rate constitutive behavior. The tests are carried out in pure tension. Tensile ductility parameters are recovered. Constitutive relations are revealed. And the geometries need not be

simple. By varying the cross section of the ring, for example, the amount of heat generation can be varied at a given strain rate. These tests are thus done under conditions that are quite faithful to those seen in electromagnetic forming.

4 Flyer Launch from the Uniform Pressure Actuator

Recently the Uniform Pressure actuator has been conceived, analyzed and shown useful for several applications [9, 10]. To present only analytical estimates of the sheet acceleration and velocity have been available and impact velocity is one of the most critical parameters in this kind of forming. Figure 4 shows schematically how a PDV system has been added to the Uniform Pressure actuator system to launch 1mm thick aluminum sheet. In these particular experiments the probe could only measure to a distance of under about 400 μm. However the example data shown in Figure 5 shows that UP actuator is able to reach velocities in excess of 50 m/s over an acceleration distance of under 400 μm, in a manner that is spatially uniform. In the future this capability will be routinely used with the UP actuator system to measure sheet-die impact velocities.

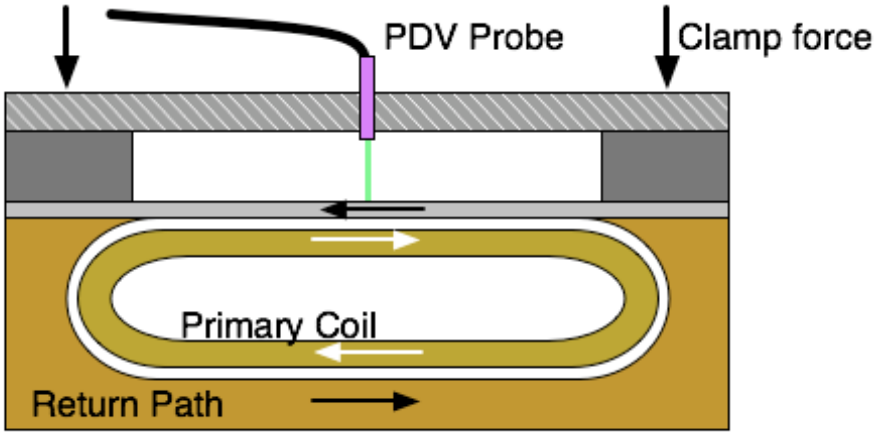

***Figure 4**: Schematic diagram of use of the PDV system to measure velocity and acceleration of a metal sheet launched using the uniform pressure actuator. The white arrows show the current in the primary coil and the black arrows shown the induced current in the return path.*

5 Flange Impact

One application of electromagnetic impulse that has received considerable attention recently is impact seam welding. The recent work of Aizawa and Kore [11-14] and their respective colleagues have shown that this can give high strength welds, can weld dissimilar metal combinations that cannot be welded by fusion and most significantly, Aizawa's work has shown that very modest energies (about 2kJ) are able to create welds in aluminum or aluminum to steel with sheet thicknesses on the order of 1mm and joint lengths of about 10 cm. This low energy requirement makes commercialization of this technique quite simple.

From work in collision welding driven by explosives (explosive welding) it is well known that collision welding takes place when the flyer and target have an sufficiently high

impact velocity (usually between 100 and 500 m/s) and an appropriate impact angle (typically 10° - 20°). Figure 6 shows schematically how sheet collision welding can be carried out in a well-packaged and efficient manner and how the PDV can be used to measure impact speed and collision angle. In this example either short focal distance or columnator probes are used and they are spaced at known distances. Since the probe signal can be analyzed both for displacement and velocity, at any time the position and velocity at each of the 3 spatial coordinates spaced along the X direction is known. Thus the impact velocity and angle can be explicitly known and compared to numerical models. Work integrating measured impact parameters with numerical models and interface microstructure development is underway currently at Ohio State.

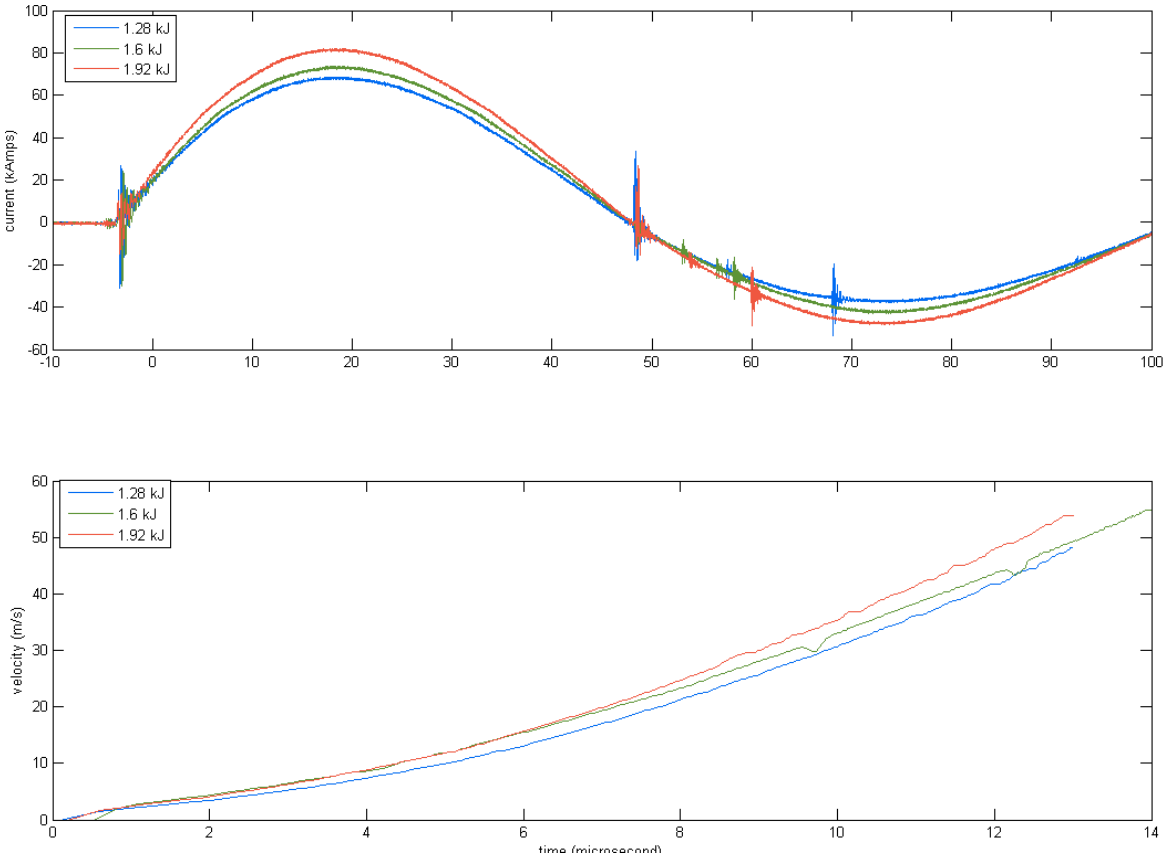

***Figure 5**: Induced current and measured velocity in the launch of a 1mm thick copper sheet from a uniform pressure actuator at launch energies of 1.28, 1.6 and 1.9 kJ respectively.*

The PDV system has been used to measure the impact velocity on one of the magnetic pulse welding actuators. A preliminary velocity profile is shown in Figure 7, which indicates the impact velocity is around 300m/s. At present signal analysis techniques are being improved. The very encouraging aspect of this is that despite the fact the flange bends and distorts in flight, a good optical beat signal can be obtained through the entire period of the experiment.

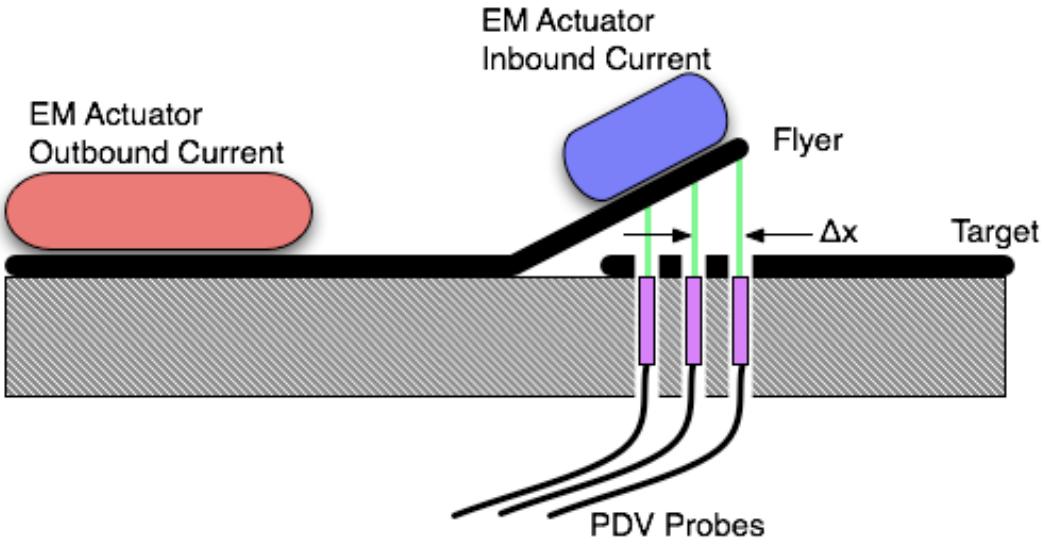

***Figure 6**: Implementation of the PDV to study impact seam welding.*

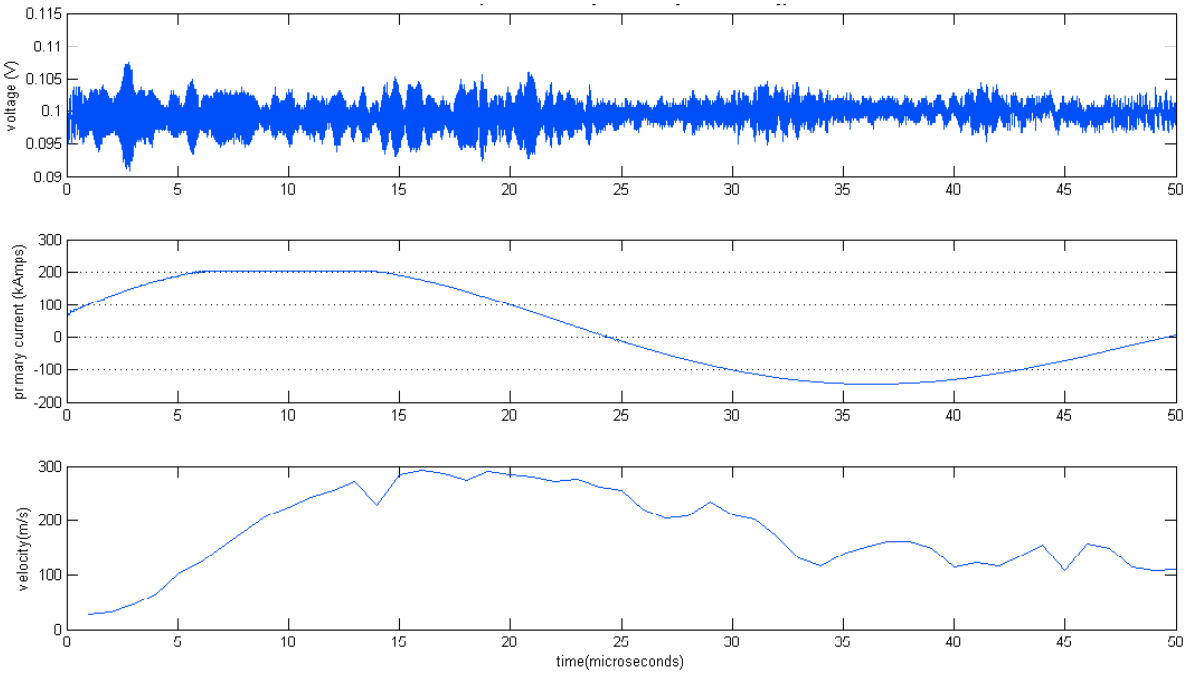

***Figure 7**: Primary current and impact velocity profile on magnetic pulse linear seam welding system. The launch energy is 4.8kJ and the stand off distance is 5.7mm.*

6 Summary / Concluding Remark

This paper details the development of a relatively low-cost, robust and easily configured photon doppler velocimeter (PDV). This device can give exceptionally precise and accurate measurements of local velocities, displacements and accelerations in

electromagnetic forming experiments. Its use has been demonstrated in several practical embodiments of electromagnetic forming.

This diagnostic tool can provide better estimates of material constitutive behavior in relevant rages of strain rates and temperatures, provide measurements of velocities and contact angles in processes such as welding and provide data sets for critical evaluation of numerical models.

References

[1] *Daehn, G.S.:* "High Velocity Metal Forming", Chapter in ASM Handbook, Volume 14, *Forming and Forging*, 2004.

[2] O. T. Strand *et al.*, in *Proceedings of SPIE*, edited by D. L. Paisley, D. R. Snyder, and B. J. Thompson ••SPIE, Bellingham, WA, 2005••, p. 593.

[3] *Niordson, F. L.*: "A Unit for Testing Materials at High Strain Rate." Experimental A Mechanics, 5, p. 23-32, 1965.

[4] Gourdin, W. H. (1987). "The Expanding Ring as a High-Strain Rate Test." *Journal of Metals*, 39(10), A65-A65.

[5] *Gourdin, W. H.*: "Analysis and Assessment of Electromagnetic Ring Expansion as a High-Strain-Rate Test." Journal of Applied Physics, 65(2), p. 411-422, 1989.

[6] *Grady, D. E.; and Benson, D. A.*: "Fragmentation of Metal Rings by Electromagnetic Loading." Experimental Mechanics, 23(4), p. 393-400, 1983.

[7] *Rusinek, A.; and Zaera, R.*: "Finite element simulation of steel ring fragmentation under radial expansion." International Journal of Impact Engineering, 34(4), 799-822, 2007.

[8] *L'Eplattenier, P.; Cook, G.; Ashcraft, C.; Burger, M.; Shapiro, A.; Daehn, G. S.; and. Seth M.*: "Introduction of an Electromagnetism Module in LS-DYNA for Coupled Mechanical-Thermal-Electromagnetic Simulations, 9th LS-DYNA Users Conference, 2007.

[9] *Kamal*, *M.:* "A Uniform Pressure Electromagnetic Actuator for Forming Flat Sheets", Ph.D. Thesis, Ohio State University, 2005.

[10] *Kamal*, *M.; and Daehn*, *G.S.:* "A Uniform Pressure Electromagnetic Actuator for Forming Flat Sheets" Journal of Manufacturing Science and Engineering 129, p. 369, 2007.

[11] *Kamal*, *M.; Cheng, V.; Sue, T.K.; Shang, J.; and Daehn*, *G.S.:* "Replication of Microfeatures by Electromagnetic Launch and Impact" Proceeding from International Conference on Micromanufacturing 2006, Urbana, IL September 13-15, 2006.

[12] *Golowin, S.; Kamal, M.; Shang, J.; Portier, J.; Din, A.; Bradley, J.; Hatkevich, S.; Daehn*, *G.S.:* "Development and Use of the Uniform Pressure Electromagnetic Actuator for Forming Sheet Metal over a Range of Length Scales, Journal of Materials Engineering and Performance, 2006.

[13] *Aizawa T.; Okogawa K.; Yoshizawa M.; Henmi N.*: "Impulse magnetic pressure seam welding of aluminum sheets" Impact Engineering and Applications 2001: p. 827-32.

[14] *Aizawa T.; Okogawa K.*: "Impact seam welding with magnetic pressure for Aluminum sheets", Material Science Forum 2004; (465): p. 231-36.

[15] *Aizawa T.*; "Methods for electromagnetic pressure seam welding of Al/Fe sheets" Welding International 2004; 18 (11): p. 868-72.

[16] *Kore, S. D.; Date, P. P.; and Kulkarni, S. V.:* International Journal of Impact Engineering, 34, 1327-1341, 2007.

Electromagnetic Compressive Split Hopkinson Bar*

C. M. A. Silva, P. A. R. Rosa, P. A. F. Martins

IDMEC, Instituto Superior Técnico, TULisbon, Portugal

Abstract

This paper proposes a new design for the compressive split Hopkinson bar that makes use of the intense pressure created in a transient magnetic field formed by the passage of a pulse of electric current through a series of coils. The proposed technology enables to characterize the behaviour of materials under high strain-rates with a small acceleration path length of the striker bar and, because propulsion is purely electromagnetic, the overall performance can be easily controlled and nearly infinitely adjustable.
The presentation is focused on the design and fabrication of the mechanical, electrical and electromagnetic components of the new compressive split Hopkinson bar and includes results from two different testing applications to demonstrate the validity of the proposed concept.

Keywords

Design, Electromagnetic, Dynamic Testing

1 Introduction

The compressive split Hopkinson bar is a device for performing the mechanical characterization of materials at high strain-rates [1-4]. Currently installed apparatuses consist of two long slender cylindrical bars of the same diameter, called the incident and the output bars, and of a shorter cylindrical bar, called the striker bar that is most

* *The authors would like to thank PTDC/EME-TME/64575/2006, FCT-Portugal and CINAMIL/Magnetic Gun for the financial support*

commonly propelled by an air gun against the incident bar. The air is generally supplied from a high pressure vessel and valves are utilized for controlling the firing pressure. The collision of the striker bar into the end of the incident bar generates a compressive stress wave that is partially transmitted throughout the specimen, placed in-between the incident and output bars, causing it to deform. The analysis of the stress wave in conjunction with the measurement of the strains in the incident and output bars by means of strain-gages makes it possible to determine the stress-strain curve of the testing material.

Major disadvantages of currently available compressive split Hopkinson bar systems can be summarized as the need for very-high air pressures for reaching high strain-rates, the lack of repeatability of the firing pressure, the high operation noise due to the instantaneous expansion of the air and the large overall length of the apparatus.

This paper proposes a new design for the compressive split Hopkinson bar that makes use of the intense pressure created in a transient magnetic field formed by the passage of a pulse of electric current through a series of coils. The magnetic field behaves like air being relief from a high pressure vessel and is capable of properly accelerating the striker bar against the incident bar. However, because the propulsion is purely electromagnetic, its overall performance can be easily controlled and is nearly infinitely adjustable. The operation conditions are very highly repeatable and, once the equipment has been set up for a particular testing method, the only extra variable to be taken into account is the material to be characterized.

The first part of the paper is focused on the design and fabrication of the main components of the electromagnetic compressive split Hopkinson bar and the last part includes a brief presentation of two different applications in the fields of material characterization and evaluation of armour vests.

2 Project, Design and Fabrication

Figure 1 presents an overall view of the compressive split Hopkinson bar installed at Instituto Superior Técnico-TULisbon. The main components can be divided into three main groups:

(i) Basic structural parts,
(ii) Specific mechanical and pneumatic parts,
(iii) Specific electrical and electromagnetic parts.

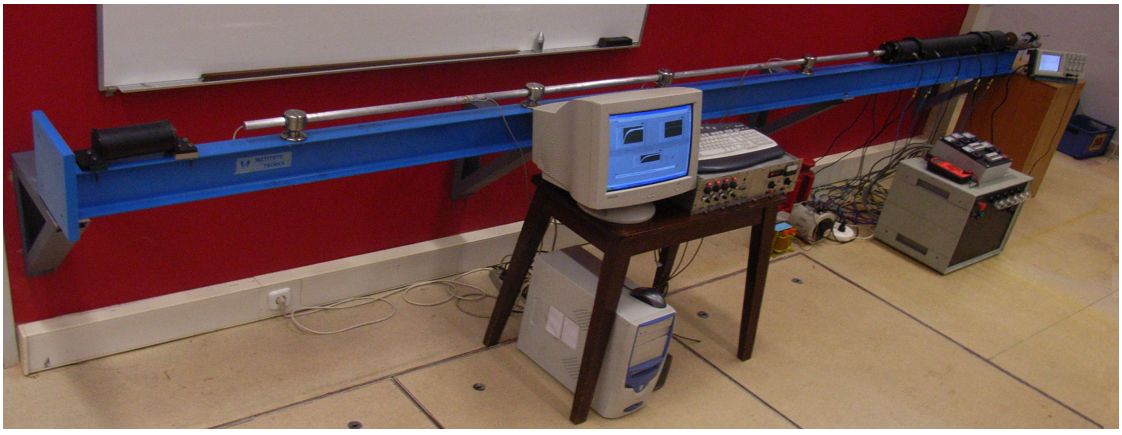

***Figure 1**: Electromagnetic compressive split Hopkinson bar installed at IST-TULisbon.*

Basic structural parts comprise components such as the structural I-beam and the support plates, which are independent of the type of testing (e.g. mechanical, fracture ...etc), operation conditions and materials to be characterized. These components are always to be utilized. Specific mechanical and pneumatic parts comprise those components such as the pressure bars, the air-bearings and the guiding tubes, whose design may be dependent on the type of testing, operation conditions and materials to be characterized. Specific electrical and electromagnetic parts include the components that provide the electrical energy to the electromagnetic actuator, e.g. the electrical circuits for charging and firing the bank of capacitors and the coils that generate the pressure to accelerate the striker bar against the incident bar. The design of the basic and specific parts will be described in what follows.

2.1 Basic Structural Parts

The Hopkinson bar is assembled on an I-beam steel structure with a length of 5 m that must account for the installation of the specific mechanical, pneumatic and electromagnetic parts. The stiffness of the I-beam is adequate for the structure of the bar because the impact and stress wave propagation preferentially occurs along the longitudinal direction of the bar. The overall length of the I-beam was chosen so that longer actuators can be added in the future with the objective of increasing the launching velocity and the kinetic energy of the striker bar. The support plates are utilized for attaching the I-beam to a concrete wall.

2.2 Specific Mechanical and Pneumatic Parts

The incident and output bars have 1.4 m length and 25 mm diameter. The bars are long in order to stabilize the one-dimensional stress wave propagation for a given pulse length and have a high length/diameter ratio so that a proper separation of the incident and reflected waves can be achieved during data acquisition.

The selection of the materials to manufacture the pressure bars is very much dependent on the materials to be tested. In fact, for increasing the signal-to-noise ratio, materials with adequate elastic modulus must be selected for the pressure bars so that high-resolution dynamic testing of low-strength materials such as lead and soft aluminium can also be performed. In addition, because the pressure bars must remain elastic during testing, the mechanical properties of the materials selected for its manufacture will greatly influence the maximum stress attainable by the test specimen. The Hopkinson bar fabricated by the authors has two different pairs of incident and output pressure bars. One pair is manufactured from high strength aluminium AA 6082-T651 (utilized in the mechanical characterization of lead, see Section 3) while the other is made of AISI M3 (tool steel).

An important advantage of the new proposed electromagnetic-based Hopkinson bar against conventional air-based Hopkinson bar systems is the possibility of easily changing the pressure bars and the striker bar because air-based systems usually require considerable amount of time and effort to open the testing apparatus and to change the bars. This advantage is particularly important for the striker bar to be loaded into the electromagnetic actuator because it provides additional control of the velocity and kinetic energy at the exit simply by changing its physical characteristics (e.g. mass).

Figure 2 shows two different types of striker bars. The first type consists of a long (1 m) and heavy (4.5 kg) bimetallic bar made of AA 6082-T651 aluminium with slotted hollow half-ring surface inserts of DIN St52.3 steel and is to be utilized when the current pulse passing through the coils is triggered by thyristor switches. The second type consists of short, low weight (250 g, 500 g and 750 g), DIN Ck45 steel bars which are to be utilized when the current pulse passing through the coils is triggered and controlled by IGBT's (insulated gate bipolar transistor). Further details on the electromagnetic actuator will be provided in Section 2.3.

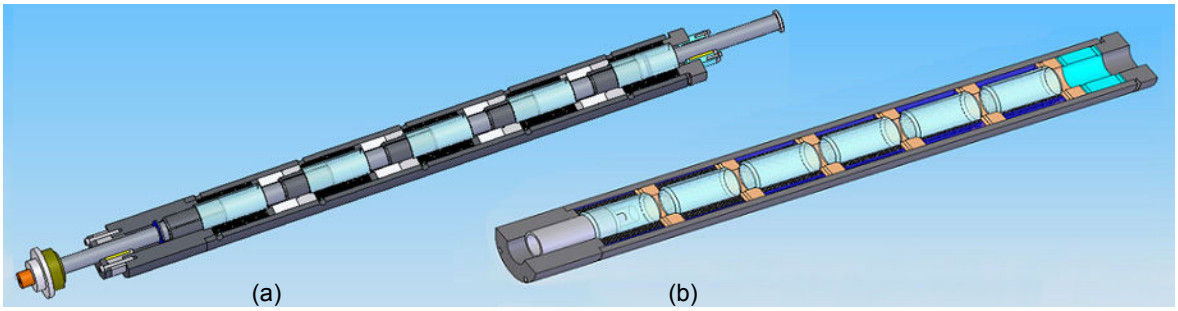

Figure 2: *Schematic representation of the coils and striker bars that are utilized when the current pulse is (a) triggered by thyristors or (b) triggered and controlled by IGBTs.*

Air-bearings (Figure 3a)) instead of contact bearings (e.g. ball-bearings, teflon-bearings... etc) were chosen to support and guide the pressure bars during high speed sliding. Unlike contact bearings, air-bearings utilize a thin film of pressurized air to provide a 'zero friction' load bearing interface between surfaces that would otherwise be in contact with each other. Being non-contact, air-bearings exhibit no starting or running friction and avoid the traditional contact bearing related problems of friction, vibration, wear, and lubricant handling, and offer distinct advantages in precision positioning and high speed sliding of the pressure bars.

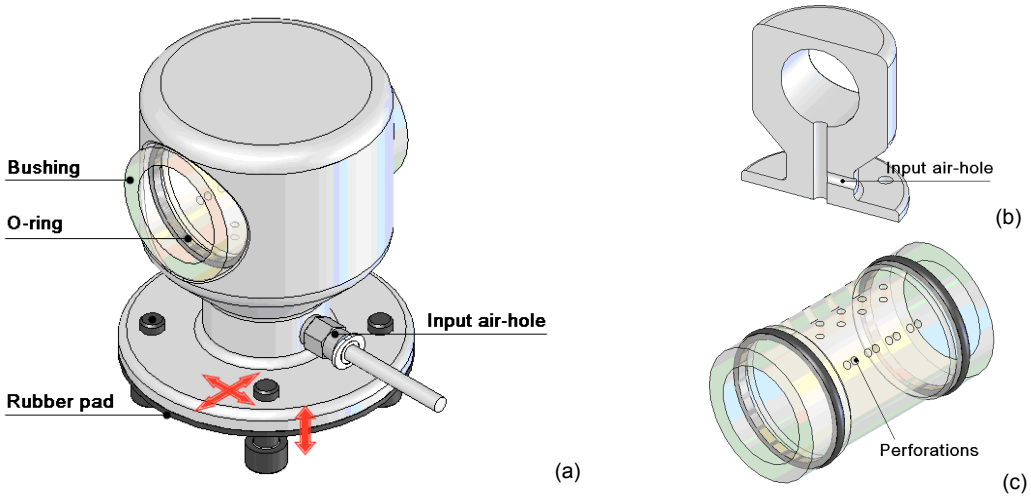

Figure 3*: Schematic representation of the air-bearing assemblies utilized in the bar.*

The air-bearings are also used as a system for aligning the electromagnetic actuator with the pressure bars and the momentum end trap (energy absorber). They are

manufactured from a non-magnetic AISI 304L stainless steel and the air (supplied by the compressed air-network of the laboratory) is pumped through an orifice that is drilled in its lower-center region (refer to Figure 3b)). Acrylic guide bushings containing holes in the longitudinal direction are included with the purpose of splitting the pressurized air flow into different directions and reducing the friction forces that are applied to the pressure bars (Figure 3c)). The location of the air-holes and the selection of the operating air-pressure were chosen after performing experimental tests for measuring the static-friction force that allows relative motion between the pressure bars and the air-bearings. The tests were made with a compression dynamometer and three alternative locations for the air-holes were considered (refer to inset pictures provided in Figure 4).

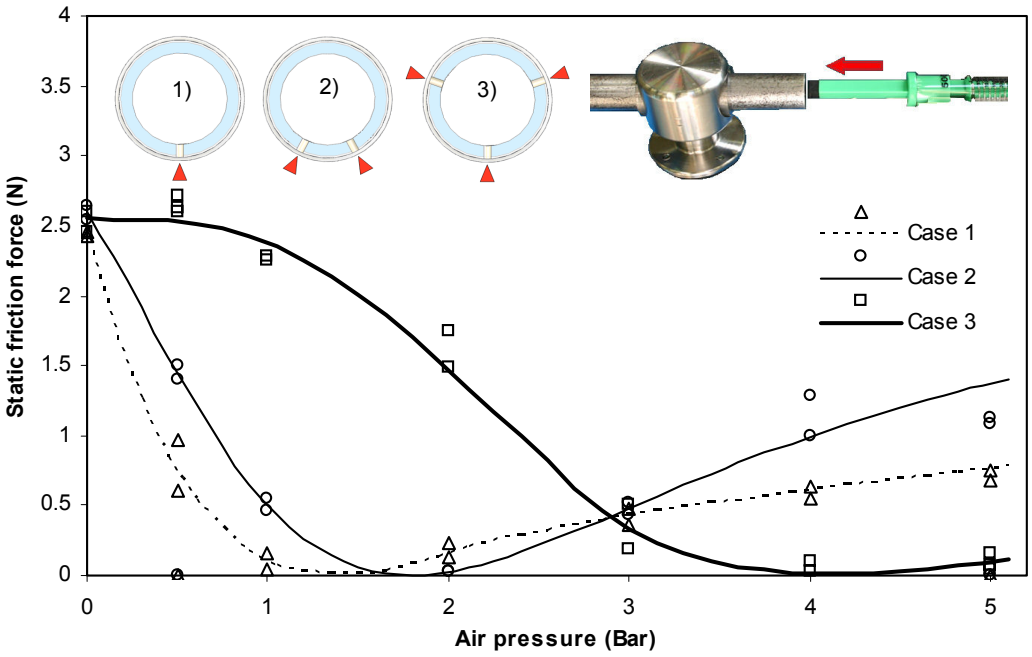

***Figure 4**: Friction force exerted on a bar as a function of the air-pressure utilized by the bearing and of the location of the air-hole perforations.*

Figure 4 shows that perforation solutions denoted as cases 1 and 2 offer low frictional opposition for air-pressures in the range 1 to 2 bar while the solution labelled as case 3 is more adequate for values of the air-pressure above 3.5 bar. Because the compressed air-network of the laboratory operates at a pressure up to 7 bar and since this case is less sensitive to air-pressure variations in the working range from 3.5 to 5 bars, it was decided to manufacture the acrylic bushings as depicted in case 3. The solution consists of three opposing perforations through which the pressurize air flows in order to build-up an air-cushion between the pressure bar and the surface of the bearing. In addition, it is worth notice that the acrylic bushings are easy to replace in case of damage and allow the utilization of pressure bars with slightly smaller and larger diameters than those initially specified in the original project of the electromagnetic Hopkinson bar.

2.3 Electrical and Electromagnetic Parts

The electromagnetic actuator consists of electrical circuits for charging and firing the banks of energy-storage capacitors (each with 6 mF) and a series of coils that generate the pressure to accelerate the striker bar against the incident bar. Two different types of electromagnetic actuators were conceived and designed by the authors (Figure 2); (i) a coil-spring and (ii) a coil-gun.

The coil-spring actuator combines the reluctance and induction electromagnetic features of the assembly between coils and striker bar. The reluctance draws from the very large positive magnetic susceptibility and attractive ferromagnetic properties of the slotted (to reduce eddy current losses) half-ring inserts of steel placed along the surface of the aluminium striker bar. The induction results from the repulsive forces originated by the eddy currents that are induced in the aluminium surface of the bimetallic striker bar when the coils are fired. The aluminium is paramagnetic and its magnetic susceptibility is much smaller than that of steel.

Figure 5 shows a schematic representation of the charging and discharging electrical circuits of the coil-spring electromagnetic actuator. To charge the capacitors, single-phase alternating current supplied with 230 V is converted to higher-voltage direct constant current by means of a charging circuit consisting of a variable-voltage transformer and a constant current rectifier system. The variable-voltage transformer is made of a variable-voltage regulator which can change the incoming line voltage from 0% to 100% and a transformer capable of producing 3.6 times the input voltage. This means that the overall rating of the variable-voltage transformer system is approximately 1000 V for a single-phase input line voltage of 230 V.

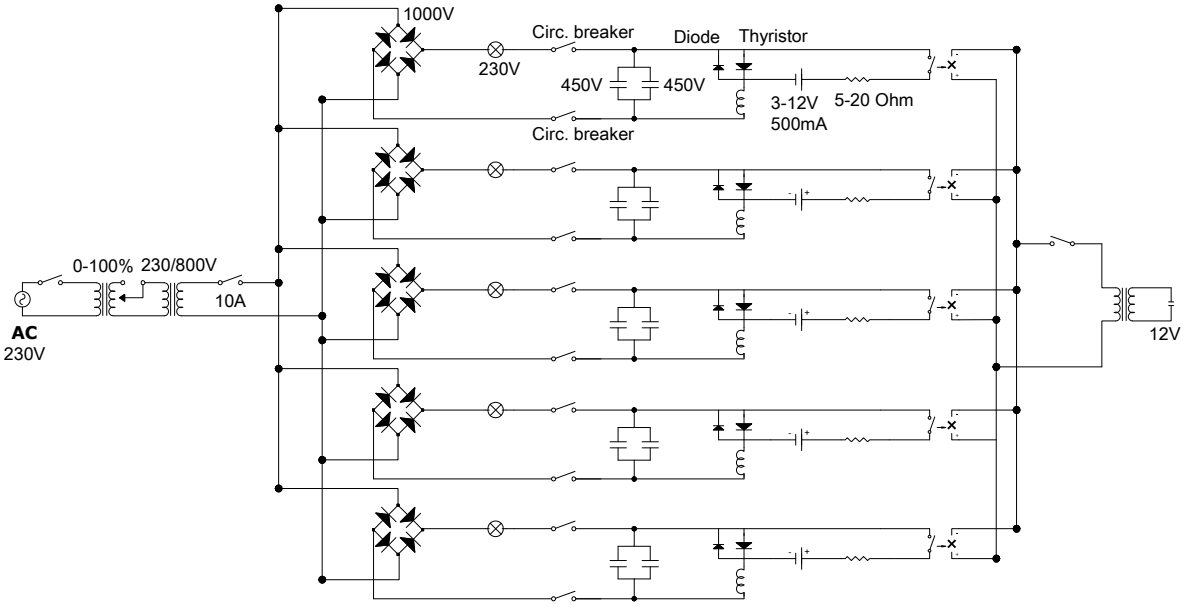

***Figure 5**: Schematic representation of the charging and discharging electrical circuits of the coil-spring electromagnetic actuator.*

Typical coils with eight windings, a total length of 92 mm, an external diameter of 80 mm and an internal diameter of 42 mm are currently being utilized.

Once the capacitors are charged the charging circuits are closed and the thyristor switches located in the discharging circuits are activated to simultaneously fire each capacitor into its associated coil. The resulting current pulse will only last for a few milliseconds and, therefore, the large switching times typical of thyristors are not capable of allowing the pulse to be terminated just as the slotted half-ring inserts of steel placed along the surface of the striker bar get to the middle of each coil. In fact, when there is no collision between the striker bar and the incident bar, the striker bar will stop and accelerate in the opposite direction into the magnetic equilibrium position – just like a spring returning to its equilibrium configuration.

When the striker bar collides against the incident bar, the striker bar achieves a large velocity very rapidly due to conservation of linear momentum. Figure 6 shows the velocity and the kinetic energy of the striker bar just before collision against the incident bar as a function of applied voltage. It is worth notice that the actual design of the electromagnetic actuator allows a single-phase 230 V directly inputted from the supply line without any intervening transformers to accelerate the 4.5 kg bimetallic striker bar to a kinetic energy level of nearly 0.5kJ (14.5 m/s) resulting in a velocity of the incident bar equal to 27.5 m/s. This gives an idea of the easy implementation-to-benefit ratio of the Hopkinson bar based on a coil-spring electromagnetic actuator.

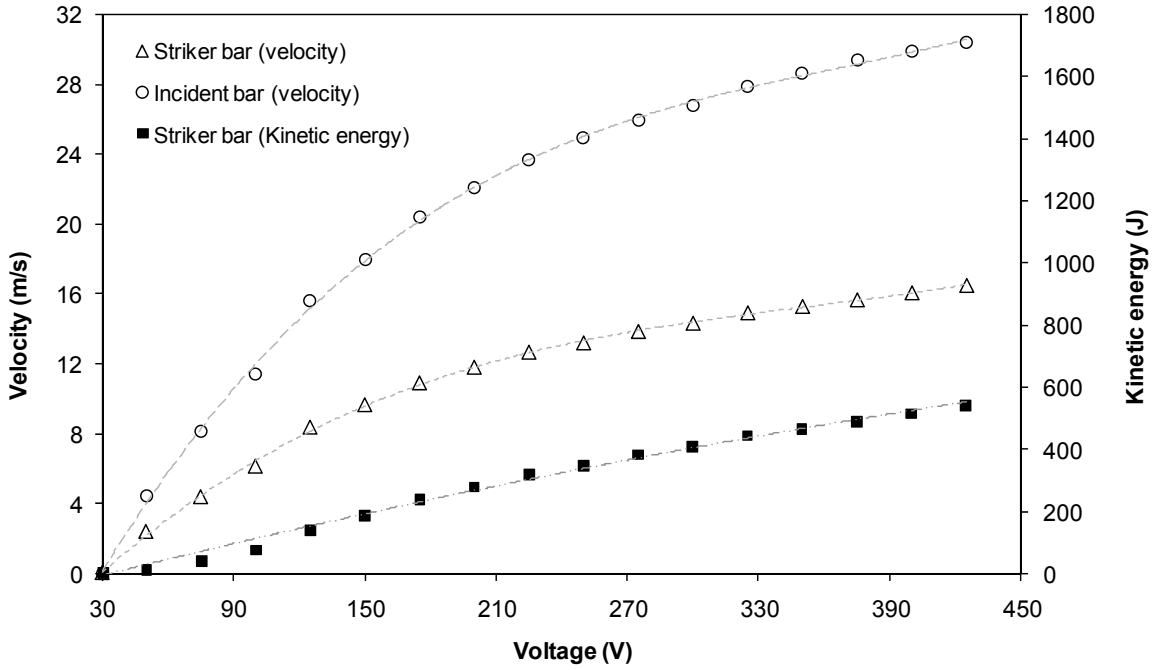

Figure 6: *Velocity and kinetic energy as a function of the applied voltage for the coil-spring electromagnetic actuator.*

The second type of electromagnetic actuator (coil-gun actuator) is based on a multi-stage reluctance actuator and is currently being fabricated by the authors. In general terms the main difference of the electrical circuit of the coil-gun actuator to that depicted in Figure 5 is to be found in the discharging circuit. IGBTs switches, faster then thyristors and intended to rapidly turn on and off, are utilized for a sequential fire of the bank of

capacitors into the coils as the striker bar exclusively made of steel accelerates throughout the coil-gun. The IGBTs switches are also expected to considerably improve the efficiency of the launching, by extinguishing the electrical current pulse in each coil before the striker bar passes through its centre. Otherwise, the remaining energy in the capacitor bank will slow down the striker bar at the exit of each coil.

To conclude this section it is worth notice that the main advantage of the proposed electromagnetic concept derives from its high flexibility. Striker bars can be easily replaced, individual coils can be easily changed or temporarily switched off and the electrical circuits for charging and firing the banks of energy-storage capacitors can be selected so that the system behaves as a coil-spring or as a coil-gun electromagnetic actuator.

3 Results and Discussion

The proposed electromagnetic Hopkinson bar system based on a coil-spring actuator was utilized in two different types of applications; for obtaining the stress-strain curve of technically pure lead at high strain-rates and for evaluating the performance of armour vests for protection of human beings.

3.1 Mechanical characterization

The stress-strain curve of technically-pure lead was obtained by means of the proposed electromagnetic Hopkinson bar system for high strain-rates, in the range of 200 to 3000 s^{-1}, and by means of quasi-static measurements performed in a fully instrumented CNC hydraulic press The tests were performed on cylindrical specimens with an initial diameter of D_0=8 mm and a height-to-diameter ratio H_0/D_0=1. Specimens were lubricated with PTFE (polymer based lubricant).

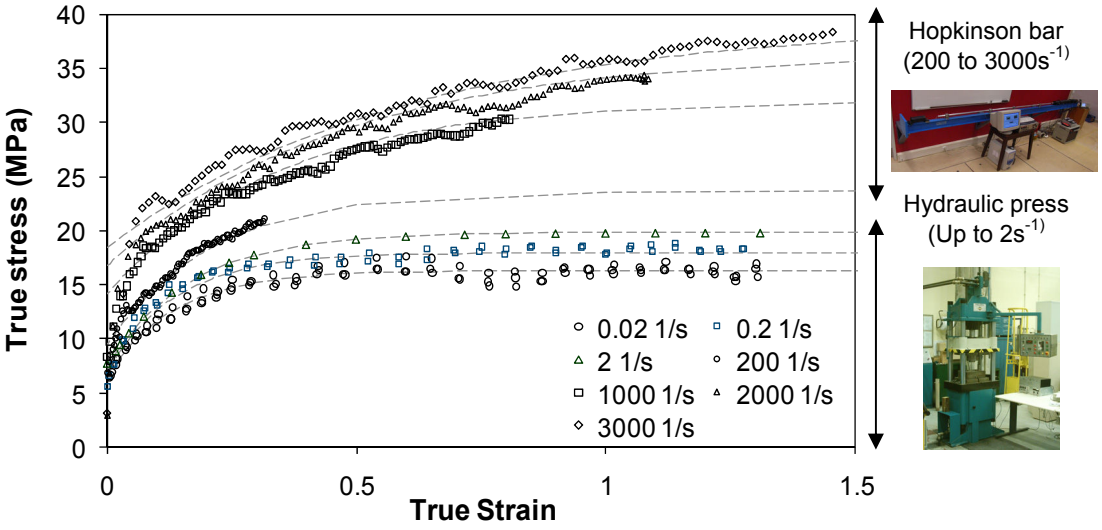

Figure 7: *Stress-strain curve of technically-pure lead obtained for different strain-rates. Pictures show the experimental apparatus utilized in the experiments.*

The experimental data resulting from the compression tests depicted in Figure 7 show good agreement with data available in the literature and indicate that technically pure lead presents significant strain-rate sensitivity.

3.2 Performance of armour vests

The performance of armour vests can be evaluated from the interaction between a projectile and a target. Classical evaluation procedures consist of qualitative observations and quantitative measurements of the impact-sustained damage. The remaining energy of the impact, not absorbed by the armours, which will be transmitted to human beings and equipments, is commonly not taken into consideration. This energy results in high forces that are applied in a very short time and its quantification is of great importance for the security of human beings and equipments.

Quantification of the remaining energy and of the magnitude of the applied forces can be performed in the proposed split compressive Hopkinson bar apparatus. The propulsion of the projectiles is achieved by means of a modified version of the tube-gun that allows shooting small projectiles. The magnetic auto-centring effect of the projectiles inside the tube-gun eliminates contact between the projectiles and the tube (unlike conventional systems propelled by air-guns) and make possible to shoot different types of projectiles and fragments.

The experiments were performed on two different types of armours with constant impact energy of 10 Joule. Figure 8 shows the magnitude of the impact force applied to the transmitted bar that result from the interaction between a 5.56 mm projectile and Kevlar and polycarbonate based armours. The magnitude of the impact force resulting from a reference shot performed without armour is include for comparison purposes. Results show that Kevlar based armours utilized in body vests perform better than polycarbonate based armours utilized in body shields.

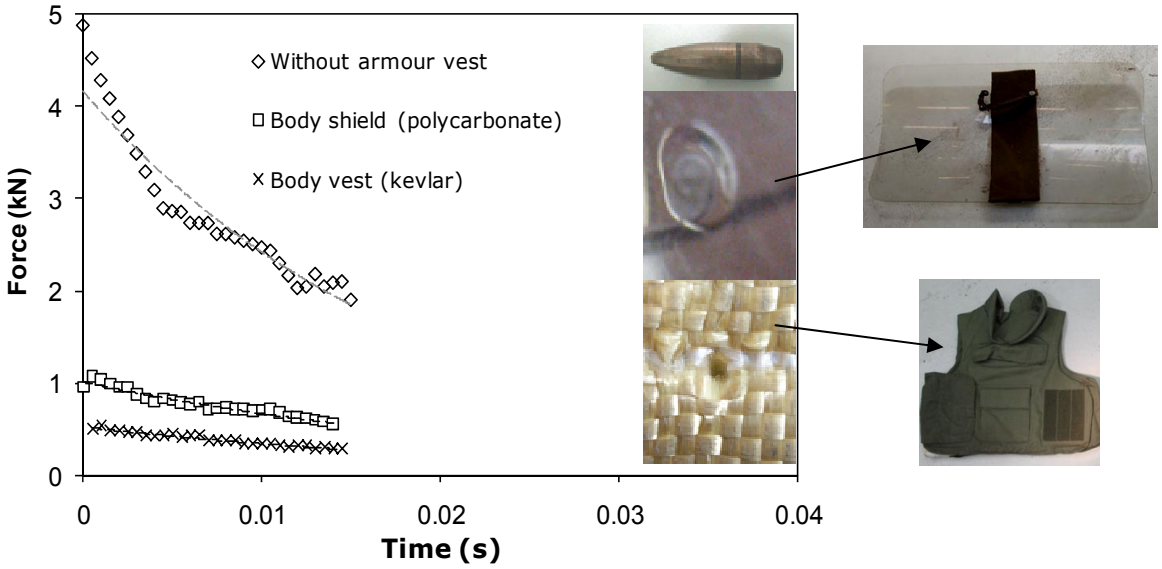

***Figure 8**: Force applied on body vests and body shields during the impact of a 5.56 mm calibre projectile with a kinetic energy of 10 J.*

4 Conclusions

This paper presents a prototype of an electromagnetic compressive split Hopkinson bar. Special purpose mechanical, pneumatic, electric and electromagnetic parts are comprehensively described and special emphasis is placed on the presentation of the main engineering details of a flexible electromagnetic actuator that allows the striker bar to be accelerated by means of a coil-spring or a coil-gun based system.

The design of the electromagnetic compressive split Hopkinson bar offers distinct advantages in positioning and changing of the pressure bars (namely the striker bar) over conventional air-based systems which require considerable amount of time and effort to perform similar operations. Repeatability of the firing velocity, low operation noise and small overall length are other important advantages of the new proposed equipment.

The performance of the electromagnetic compressive split Hopkinson bar was demonstrated by means of experiments that were designed in order to evaluate the stress-strain curve of technically pure lead for high strain rates and the performance of armour vests currently utilized in the protection of human beings.

References

[1] *Hopkinson B.:* A method of measuring the pressure produced in the detonation of high explosives or by the impact of bullets, Philos. Trans. R. Soc. (London) A, 213, 1914, p. 437-456.

[2] *Lindholm U. S.:* Some experiments with the split-Hopkinson pressure bar, Journal of the Mechanics and Physics of Solids, 12, 1964, p.317-335.

[3] *Lindholm U. S., Yeakley L. M.:* High strain rate testing: tension and compression, *Exp. Mechanics*, 8, 1968, p.1-9.

[4] *Follansbee P. S.:* The Hopkinson bar mechanical testing, ASM Handbook, American Society for Metals, 8, p.198-203, 1985.

Influence of Forming Rate on the Microstructure and Properties of Materials Subjected to Electromagnetic Forming - A Synopsis*

F.-W. Bach, D. Bormann, L. Walden

Institute of Materials Science, Leibniz Universität Hannover, Germany

Abstract

Electromagnetic high speed forming has been known since the 1960's and is successfully used for frictional connexions. In addition to joining, other applications of the process include coining, stamping and cutting. Regarding product quality and manufacturing costs, the process is superior to other methods and yet its utilisation can still be extended.

The synopsis of the material's microstructure and properties owing to electromagnetic forming, which is given by this article, clarifies the processes from a materials science point of view. This will not only represent an academic view point but also provide insight into a potential expansion of the process to other areas of application.

Keywords

Aluminium, Sheet metal Forming, Structure Analysis, High Resolution Microscope, X-ray, Texture, Residual Stress, Strain

1 Introduction

During the past few years various papers have been published in the field of the high speed forming process, however the focus was mainly on the technological aspects of metal forming. But the process is associated with a few effects on the material which are a specific consequence of the electromagnetic forming (EMF). The following conditions are

* *This work is based on the results of FOR 443; the authors would like to thank DFG for its financial support*

examples of the special features of the electromagnetic processing: the forming takes place at high speed, there is no contact with a forming tool if a die is not used and it is associated with a temperature development [1]. All these boundary conditions influence the microstructure and thus specify the specific material properties. Parameters, which characterise the product's behaviour in use, are enormously important because changes in the microstructure entail deviations of the component's properties. Technically pure aluminium shows a strong dependency on forming rate apparent strain hardening. The present investigations are the foundations for a microscopical understanding of the mechanical properties of face centred cubic materials and in particular, provide clarification of the fundamental deformation mechanisms during electromagnetic sheet forming. Examples are mentioned of distortion and premature material failure due to residual stresses. However, residual stresses are not at all invariant and can also be exploited. These exemplary descriptions give information about the material's behaviour and also present possibilities for influencing them provided the physical-chemical properties are known.

2 Metallographic and mechanical investigations

2.1 Microstructural investigations

The material investigated was 1 mm thick sheets of 99.5 % pure aluminium. The work pieces were electromagnetically deep drawn to a depth of 23 mm, figure 1. In order to fully characterise the work piece, different analyses were carried out at various radial points on the sheet. Specimens R4 to R0 were taken along the radius (figure 1 right) for the investigation. Specimen R5 is the initial state of the sheet. The designations internal and external face refer to the tool's coil where the surface of the test piece facing the tool's coil is designated as the internal face and the opposite side of the test piece surface as the external face. The abbreviations RD, TD and ND stand for the rolling direction, transverse direction and normal direction respectively. These designations are retained for all subsequent investigations and are depicted in figure 1.

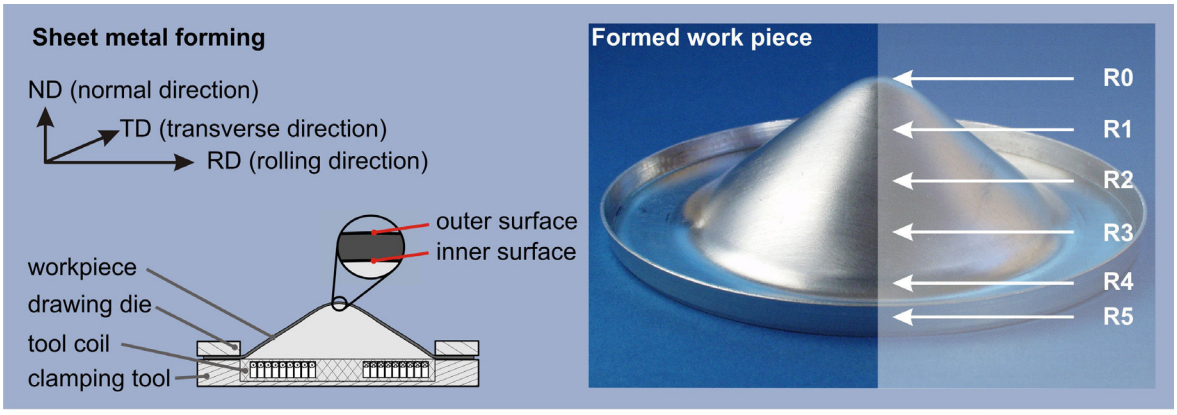

Figure 1: *Electromagnetically formed work piece; regions of interest*

Micrographs of the initial state and the formed work piece are summarised in figure 2. Since no significant differences between the surfaces and the specimen's centre

could be ascertained, the specimen's centre transverse to the rolling direction is depicted here. Analyses of the initial state as well as the formed specimens, which were subjected to variations in their process parameters, are shown in [1]. The deformed microstructure can be represented by two regions: Directly adjacent to the drawing die (R4) and the specimen's centre region (R0). Here, whilst the grain size remains unchanged, the difference in the extent of grain elongation can be metallographically clearly identified.

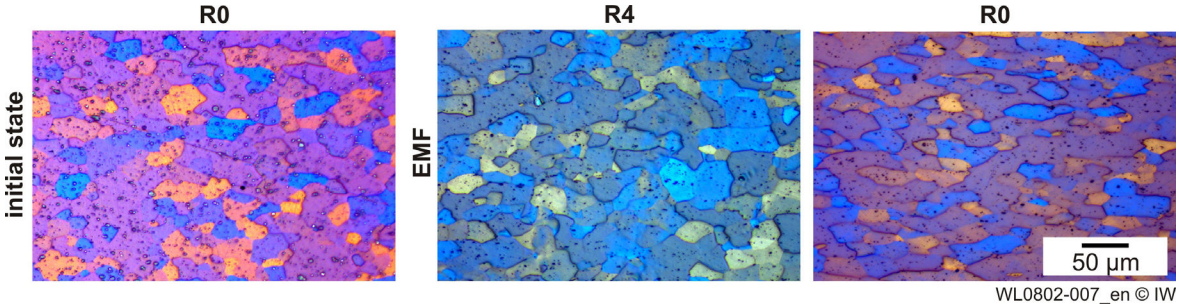

Figure 2: *Micrographs of the initial state and of the drawn work piece in TD*

The quantitative evaluation of the metallographic micrographs was carried out according to the planimetric procedure using the SIS image processing software in agreement with ASTM E112 and DIN 50601. The computing algorithm is based on a grain boundary reconstruction and is insensitive to deleterious inclusions and etching effects. The results of the grain size and grain elongation evaluation can be seen in figure 3.

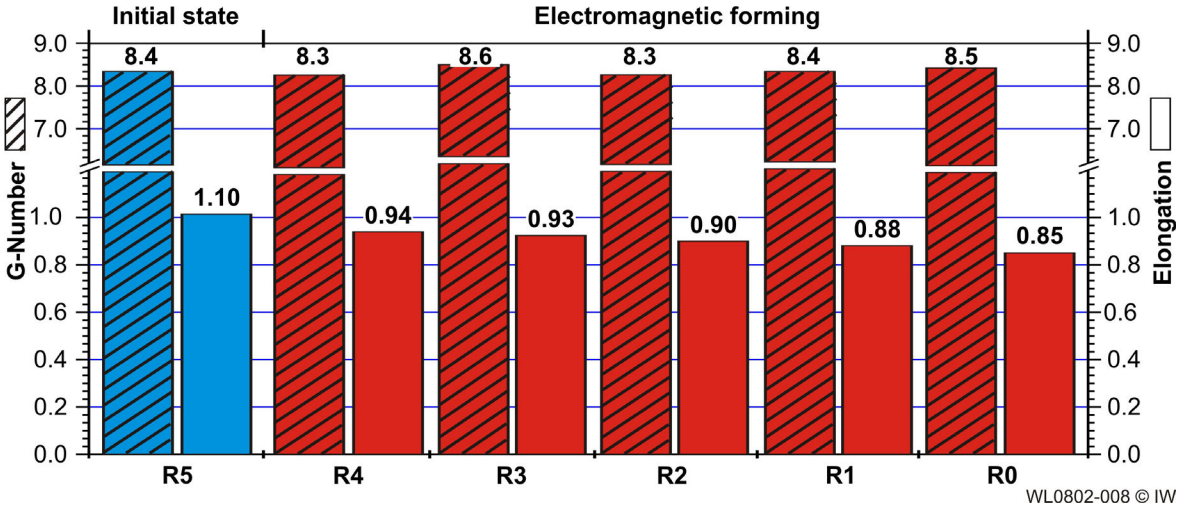

Figure 3: *Grain size and grain elongation in the initial state and in the formed work piece*

The grain size is relatively homogenous with mean values of G=8.4 ± 0.1 for the initial state and for the deformed specimens respectively, implying a grain diameter of approx. 18 µm. The grain elongation is computed as the ratio of the vertical to horizontal grain sizes and is 1.01 in the initial state (R5). For the formed work piece, the ratio continuously increases from 0.94 in the flange (R4) region up to 0.85 at the specimen's centre (R0).

2.2 Sheet metal thickness and micro hardness distribution

The wall thickness was measured along the specimen's radius in the RD and TD. No significant difference could be ascertained by comparing the RD with the TD results (figure 4 left). The continuous decrease in wall thickness along the radius towards the specimen's centre amounts to 974 ± 12 µm at the edge and 660 ± 10 µm at the specimen's centre (R0).

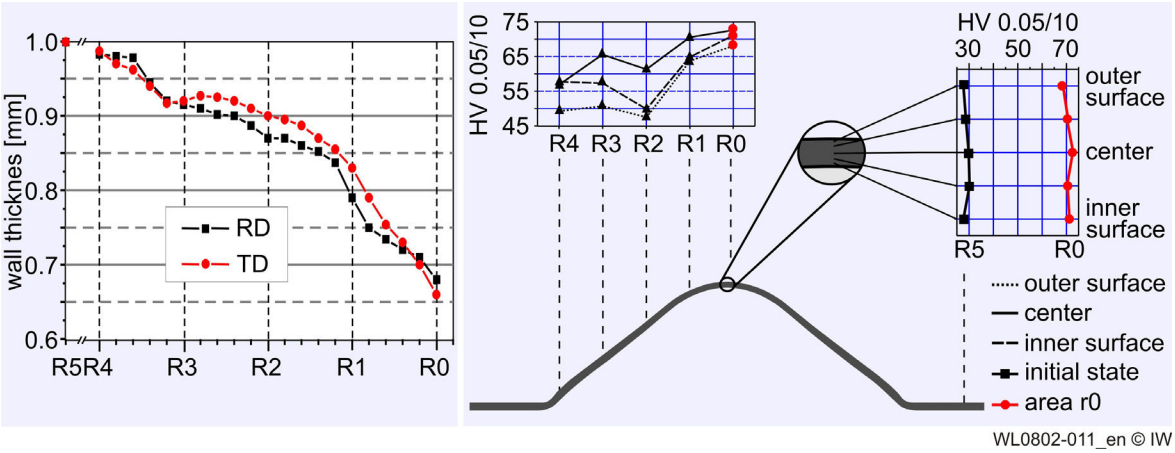

Figure 4: *Sheet metal thickness and micro hardness in the initial state (R5) and in the formed work piece (R4-R0)*

The hardness variations were measured in the sheet thickness direction (ND) in its initial state to ascertain the existing differences between the edge and the centre-line and to be able to compare these with the values from the deformed specimens. The hardness values determined show no significant differences between the external and internal faces and the specimen's centre. The mean microhardness is 29 ± 2 HV 0.5/10. A significantly higher microhardness is shown in the direction of the specimen's centre of the formed work piece. In the region R4, the microhardness has a value of 54 ± 3 HV 0.5/10 and in the region R0, a value of 71 ± 2 HV 0.5/10 (figure 4 right).

The qualitative and quantitative metallographic investigations show a microstructure with uniform grain sizes and differences in grain elongation, which increase towards the work piece's centre. The wall thickness continuously decreases towards the work piece centre-line and in this region the sheet thickness is 34 % of its initial value. Simultaneously, an increase in microhardness is measured along the specimen radius, which rises from 86 % at the edge region to 145 % at the specimen's centre.

3 Transmission electron microscopy analysis

In order to gain a comprehensive understanding of the deformation mechanisms, investigations using a transmission electron microscope (TEM) were necessary. General and detailed micrographs were taken with different magnifications at the individual sampling locations from figure 1.

Two regions are depicted in figure 5 which represent the initial state of the material. In the left portion of the figure 5, the grain boundaries of a total of five grains can be seen.

However due to their size, a whole grain cannot be recorded using the TEM. Owing to the different crystallographic orientations, etching effects occur during the specimen preparation and, as a result, geometrically arranged patterns in the microstructure can be seen. In the micrograph, several precipitates as well as isolated dislocations can also be seen. In the right portion of the figure 5, a row of dislocations can be detected next to individual dislocations. In general, the dislocation density is very low, indicating heat treatment during the sheet manufacture.

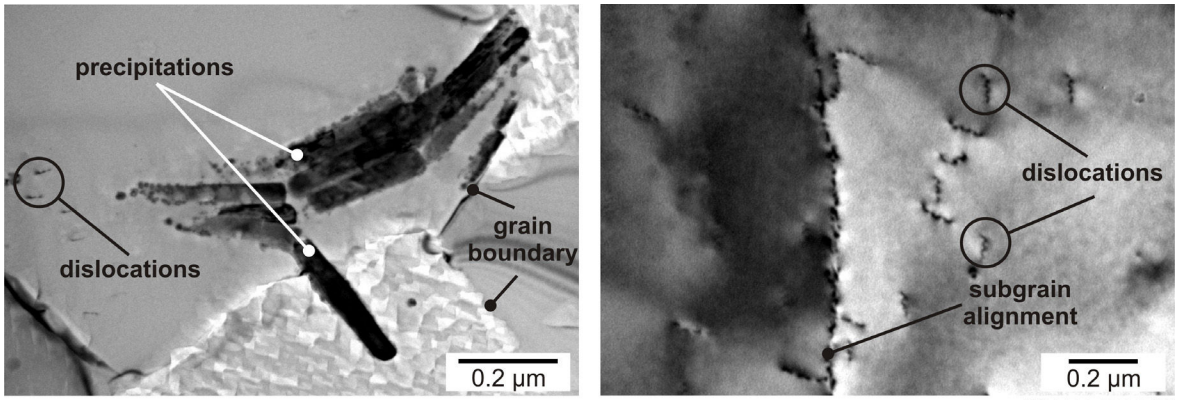

Figure 5: *Microstructure of the initial state (R5)*

The microstructures of the formed work piece from the flange region (R4) are shown in figure 6. The microstructure can be characterised as follows: In comparison to the initial state, there are regions which exhibit more individual dislocations, but the dislocation density is generally low (figure 6 left); here and there dislocation tangles and arrangements of dislocations can be observed (figure 6 right).

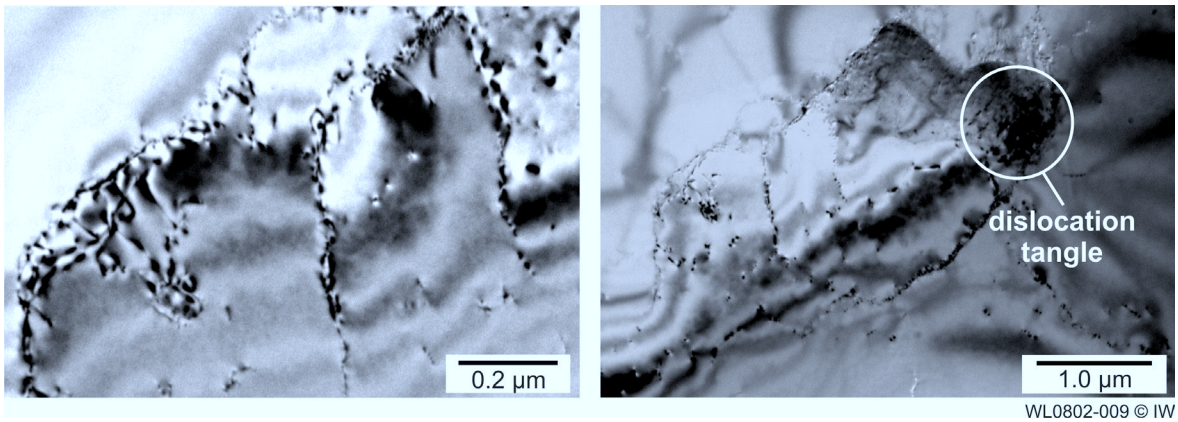

Figure 6: *Microstructure of the formed work piece, R4 region*

The microstructure from the specimen's centre is depicted in figure 7. Here, a pronounced cell structure can be seen with thin cell walls and different cell sizes. In many places, dislocation networks are still detectable; however, the cell walls already indicate sub-grain boundary character. The differences in contrast are an indication of the distinct orientations between the delineated regions (figure 7 left). This signifies that, in this case, sub-grains are involved.

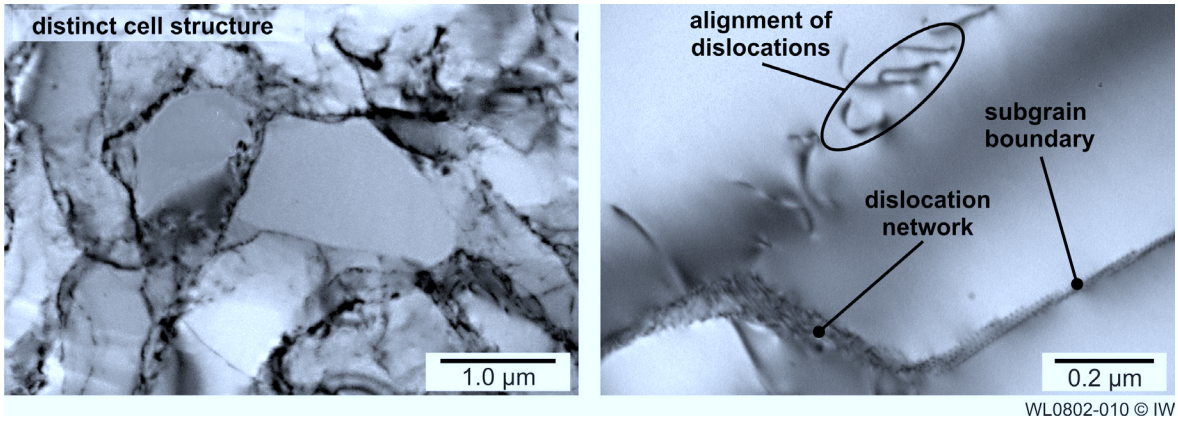

Figure 7: *Microstructure of the formed work piece, R0 region*

The TEM investigations of the forming process considered here show typical features of deformation at low temperatures; that is, temperatures below 0.4 T_s (T_s: melting point). According to the classification of Honeycombe, the electromagnetically formed specimen, depending on the level of loading, is assigned to the range I to III [2].

The TEM investigations unambiguously show that this involves cold forming. Traditionally, as is known from the theory of crystal plasticity, the dislocation density initially increases followed by observations of dislocation localisations which form tangles into cell structures with different cell wall thicknesses until sub-grains finally emerge. It is novel that all these stages of microstructural development can be observed along the radius within the work piece. The flange region exhibits a comparatively low dislocation density which indicates a smaller degree of deformation. The microstructure, depending on the degree of deformation, is evidently "frozen" into the sequential stages owing to the high deformation rate. As the degree of deformation increases, the dislocation evolution progresses until a sub-grain structure emerges in the work piece. By means of this distinct deformation history in the work piece, the differences in grain elongation and microhardness can be explained.

4 X-Ray analysis

4.1 Texture

To determine the macro-texture, X-ray diffraction techniques were employed. The orientation distribution function (ODF) was computed according to Bunge. The influences of the electromagnetic forming, related to the degree of deformation, are not uniform. Since the forming conditions can be expressed by two starkly contrasting regions (R4 and R0), these are graphically depicted in the following together with the initial state (R5).

The legend for the pole figure distribution is shown in figure 8 below left. From the sheet's pole figure in the initial state and the computed ODF, a texture becomes visible which corresponds to the ideal orientation (figure 8 above left and figure 9 left). In this case, it involves the (001) [100]-orientation or the cube alignment.

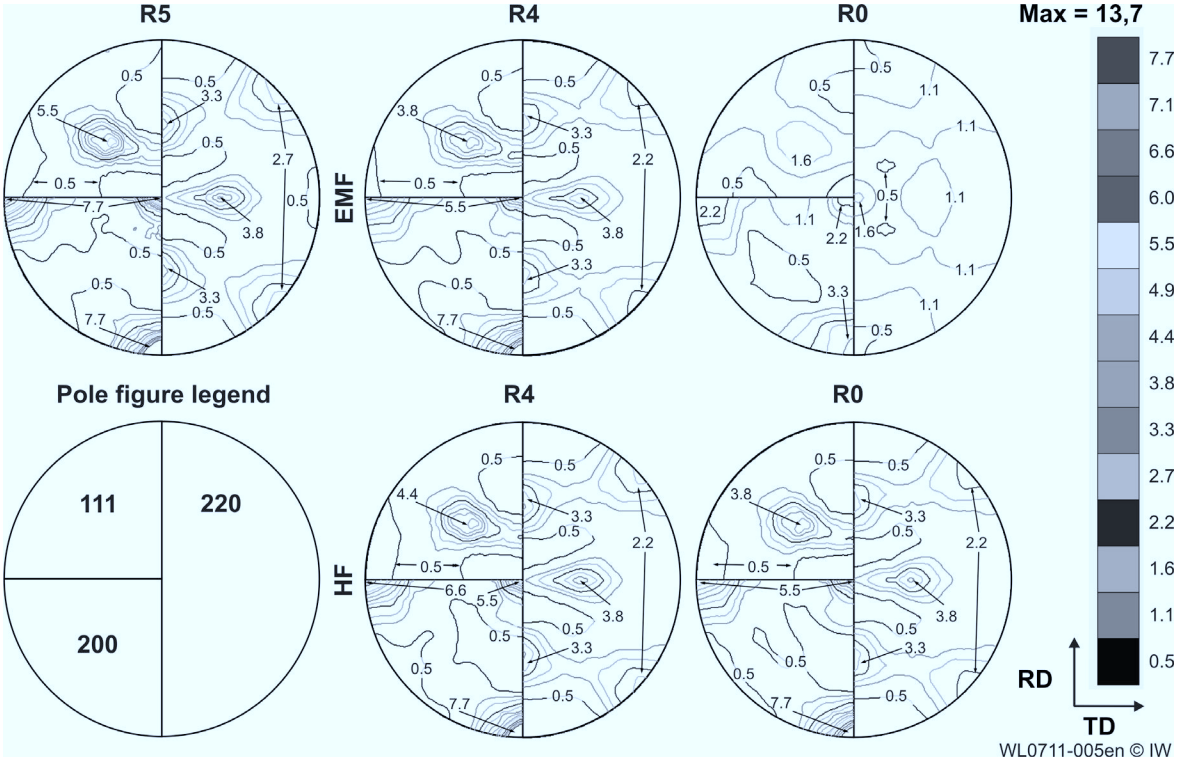

Figure 8: *Pole figures for the initial state (R5) and for the formed work pieces (R4 and R0)*

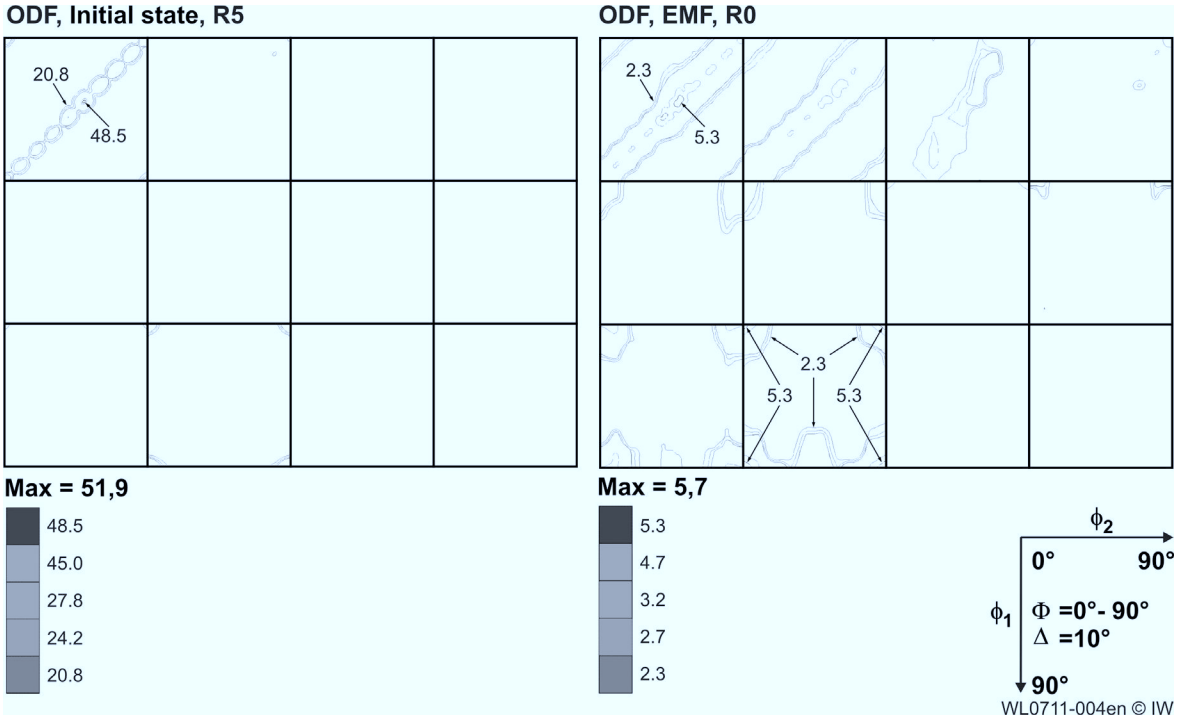

Figure 9: *ODF for the initial state (R5) and for the formed work piece (R0)*

The pole figures for the EMF specimen are depicted in figure 9 above centre and right. A reduction of the texture can be observed (see table 1) along the specimen radius from the drawing die to the cup centre. The reason for this is the sub-grain formation (see

section 3), which is discontinued by the advanced microstructural development at high deformation rates. Also, the texture type is modified with increasing degrees of deformation. Besides the attenuation of the existing cube texture, a second orientation is indicated. Using the 220 pole figure (figure 8 above right) as an example, it is clear that the four fold symmetry, recognisable from the maximum packing density along the periphery as well as both paired maximums along the RD or TD, is almost eliminated. Instead of this, a new, weakly pronounced texture component is added. To describe the new texture, the ideal orientations (0-11) [-111] and (0-11) [-211] can be taken into consideration. Owing to the attenuation of the intensity, this orientation can not quite be uniquely determined. As a comparison, hydraulically formed (HF) specimens were also investigated (figure 8 below centre and right). The measured regions of the work piece have the same nomenclature as that for the EMF specimens, and are depicted in figure 10 left. Here, an attenuation of the existing texture along the radius is also found. However, this is not as clearly pronounced as that for the EMF and no further components are observed.

Since the computation of the ODF did not result in a large difference in the function's graphical representation, the representation of the initial state is typified by the regions R5 and R4. An exception to this is the region R0 for the EMF with the highest degree of deformation (figure 9 right) for which the new component can also be seen in the ODF.

Clarification of the material's quantitative texturing is given by the maximum value of the measured or computed intensity as well as the values of the corresponding ODF's, which are summarised in the **Table 1** .

Area	Initial state, R5	EMF, R4	HF, R4	EMF, R=	HF, R0
Max. intensity	13.7	10.7	12.4	3.7	10.4
Reduction in %	-	21.9	9.5	73.0	24.0
Max. ODF- Value	51.9	30.6	42.1	5.7	28.2
Reduction in %	-	41.0	18.9	89.0	45.6

***Table 1**: Values of the intensity and the ODF*

The results of the investigations using the X-ray diffraction technique show that a cubic texture existing in the material is, with over 90 % reduction, almost eliminated. Only in regions of the highest degree of deformation (work piece centre) can a new, very weakly pronounced texture component be ascertained. The texture reduction guarantees almost isotropic material behaviour, whereas the texture is only attenuated for quasistatic processes.

4.2 Residual stress

Similar to the texture investigations (see section 4.1), the specimens were measured both in the rolling direction and along the specimen radius. The specimens were mounted such that the psi-tilting plane and the rolling direction were aligned parallel to each other. The evaluation of the measured results was carried out using the sin²-psi-procedure.

In the initial state, slight compressive residual stresses were measured (figure 10). This is a case of type I residual stresses and especially of thermal residual stresses which originated during the sheet manufacture from shrinkage effects as a result of thermal influences or heat treatment. In the formed region of the EMF, the residual stress magnitudes are both tensile as well as compressive. It can be seen that the highest tensile residual stress values occur in the region of the drawing die. The reason for this is the transition from the deep-draw loading, where insufficient continuous flowing of the material occurs, into stretch-form loading. In the work piece centre, marginally reduced tensile residual stresses were measured. Apart from the usual tensile material stresses, alternating stresses are superposed owing to the wave like movements of the sheet during forming. In these regions, material failure occurs at higher degrees of deformation, as can be expected from the values of the residual stresses. Compressive residual stresses are observed along the radius. Here, the analysis was also augmented with comparative investigations of a HF work piece. In the HF, a relatively high loading of the material in the tensile direction is observed. Along the radius, the residual stresses are continuously relieved by up to 30 %, but are retained in areas of tensile residual stresses. For both forming methods as well as their hybrids, types II or III residual stresses are involved.

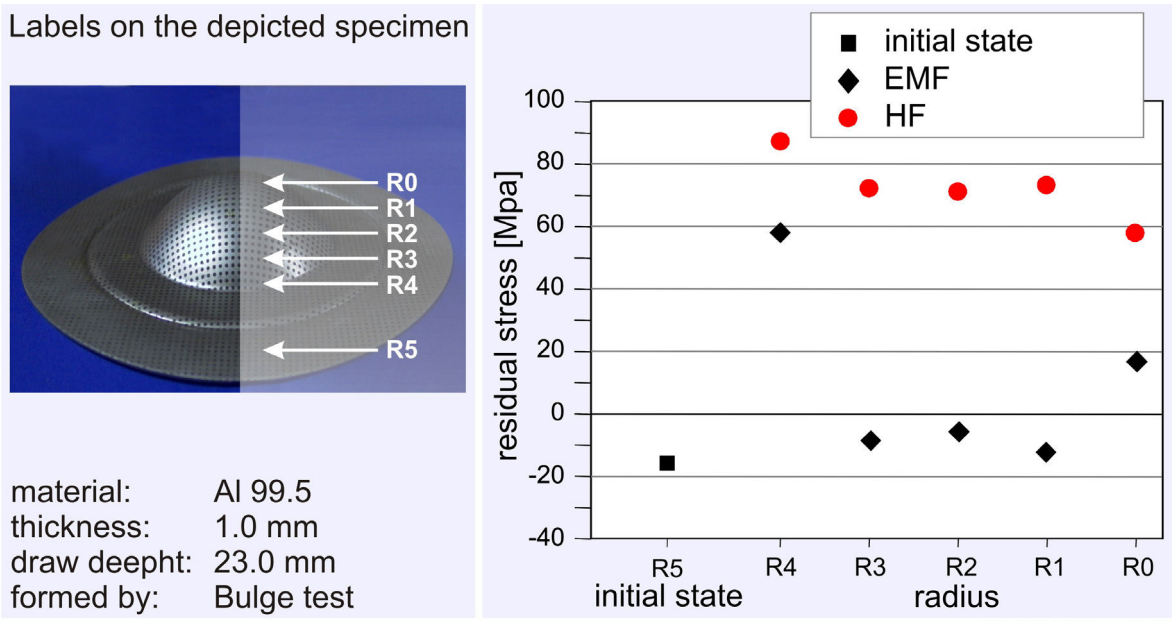

Figure 10: *Residual stress in the initial state (R5) and in the formed work piece (R4-R0)*

The measured residual stresses shed light on the failure behaviour of the sheet as a consequence of forming. Electromagnetically formed specimens have an advantageous residual stress state which lies in the region of compressive residual stresses and has a positive effect on, for example, the surface properties such as corrosion and crack formation. Tensile residual stresses were measured at only two locations: Adjacent to the drawing die (in the deep-drawing region) and in the work piece centre where a significant reduction of material occurred. In this region, material failure takes place at higher loading.

5 Conclusions

The aim of the investigations presented here is to provide an overview of electromagnetic forming, a dynamic forming process using strain rates of up to 10,000 s 1, with respect to the influences on the material.

In conclusion, it is essential to remember that the microstructural differences between conventional and electromagnetic forming processes only result from the deformation rate and the degree of deformation. From the investigations presented here, it can be derived that the changes in the work piece properties can be primarily attributed to the microstructural processes within the grain, in particular sub-grain formation. With regard to component applications, it must be taken into consideration that the deformed material exhibits almost isotropic behaviour with significantly higher microhardness which is not based on residual stresses caused by the forming, but on sub-grain formation. Possible material failure must be diagnosed or predicted, as the case may be, using appraisals of the residual stress state.

Subsequent to the forming, different microstructural analyses show a fine grained microstructure which could be clarified using a transmission electron microscope [3]. Employing a fine grained structure is an efficient method to improve the mechanical properties of materials (s. procedures like ECAP [4]). The work hardening gained by using this process creates totally new possible applications for the material. This grain refinement takes place by the formation of subgrains as a result of electromagnetic forming. These effects are due to a type of dynamic recrystallisation, which take place during the process.

The synopsis of the material's microstructure and properties owing to electromagnetic forming, which is given by this article, clarifies the processes from a materials science point of view. This will not only represent an academic view point but also provide insight into a potential expansion of the process to other areas of application.

References

[1] *Bach, Fr.-W.; Rodman, M.; Rossberg, A.; Weber, J.; Walden, L.:* Verhalten von Aluminiumwerkstoffen bei der elektromagnetischen Blechumformung. 2. Kolloquium elektromagnetische Umformung, Dortmund 2003, p. 11-19,

[2] *Honeycombe, R.:* The plastic deformation of metals. Edward Arnold Ltd. London, 2. ed., 1984

[3] *Bach, Fr.-W.; Walden L.:* Mikrostruktur und mechanische Eigenschaften von Kupferblech. Unter der Einwirkung von elektromagnetischen Kräften, ZWF, vol. 100, iss. 7/8, Hanser Verlag, p. 430-434, 2005

[4] *Hellmig, R. J.; Estrin, Y.:* Ultrafeinkörnige Kupferwerkstoffe - ein Weg zu verbesserten Eigenschaften. Metall, vol. 60 iss. 11, p. 702-704, 2006

The Mechanical Behaviour of Ultra Fine Grained Titanium Alloys at High Strain Rates

N. Herzig[1], L.W. Meyer[1], D. Musch[1], T. Halle[1], V.A. Skripnyak[2], E.G. Skripnyak[2], S.V. Razorenov[3], L. Krüger[4]

[1] Chemnitz University of Technology, Materials and Impact Engineering, Germany
[2] Tomsk State University, Russia
[3] Russian Academy of Sciences, Institute of Problems of Chemical Physics, Chernogolovka, Russia
[4] Technical University Bergakademie Freiberg, Institut für Werkstofftechnik, Germany

Abstract

Within this study the mechanical behaviour of ultra-fine grained Ti-6-22-22S titanium alloy was investigated and compared to coarse grained material. By severe plastic deformation using the cyclic channel die compression process, grain sizes between 300 and 500 nm were obtained. The mechanical behaviour was studied over a wide range of strain rates from 10^{-3} - 10^{7} s-1 under compressive loading using different experimental techniques. A significant increase of flow stress with decreasing grain size compared to the coarse grain state was found. An evaluation of the strain hardening behaviour of the UFG material shows a significant increase of the strain hardening coefficient at high strain rates for low plastic deformation. The strain rate sensitivity of the material is found to be constant within a range of strain rates from 10^{-3} to 10^{6} s^{-1} but increases at higher plastic strains. However, compressive deformability is nearly constant up to 10^{2} s^{-1} and decreased disproportionately at higher rates of strain. With decreasing grain size a significant decrease of compressive deformability was found. The strength at failure is increased with increasing strain rate.

Keywords

Impact, high strain rate, ultra-fine grain, material

1 Introduction

During the last decade, considerable efforts have been made to produce ultra-fine grained (UFG) titanium alloys due to their advantages of enhanced strength at room temperature and large deformability at elevated temperatures [1]-[4]. UFG α and α+β titanium alloys

are usually produced by various Severe Plastic Deformation (SPD) methods, such as Equal Channel Angular Pressing (ECAP), High Pressure Torsion (HPT), Twist Extrusion (TE), and Multi-Directional Forging (MDF) [5]. These methods allow receiving bulk UFG materials with a grain size down to 100 nm in diameter.

The earlier research on the mechanical behaviour of UFG titanium has shown that decreasing grain size leads to a significant increase of the yield strength, hardness, and ultimate strength but to a decrease of the strain at fracture [1]-[4]. However, mechanical properties of UFG titanium alloys under dynamic loading conditions are poorly investigated. A strong increase of the yield stress of UFG α titanium alloy VT1-0 at strain rates of 10^5 to 10^6 s^{-1} and strain hardening under shock compression loading have been shown e.g. in [6].

The objective of this research is to investigate the mechanical behaviour of UFG $\alpha+\beta$ titanium alloy (Ti-6-22-22S) within a range of strain rates from 10^{-3} up to 10^7 s^{-1} and to analyse the strain hardening behaviour, the strain rate sensitivity of the flow stress and dynamic strength compared to coarse grained material state, which was investigated in wide ranges of strain rates and temperature e.g. in [8].

2 Material and methods

2.1 Material

Within this study the $\alpha+\beta$ titanium alloy Ti-6-22-22S (Ti-6Al-2Sn-2Zr-2Cr-2Mo-Si) was investigated in two different states. Its chemical composition is shown in Table 1.

element	Al	Sn	Zr	Mo	Cr	Si	Fe	O	N	C
wt.-%	5.75	1.96	1.99	2.15	2.10	0.13	0.04	0.082	0.006	0.009

Table 1: *Chemical composition of Ti-6-22-22S (wt.-%)*

The material was studied using two different grain sizes. For the initial material state a grain size of 10 µm was observed. Additionally, the material was used in ultra-fine grained state. To reduce grain size and to obtain a nanostructured material the titanium alloy was processed by Cyclic Channel Die Compression technique (CCDC) at elevated temperatures. Due to tool design the specimen after a deformation step shows the same geometry like in initial state. Hence, the identical device can be used for several deformation steps. Performing the process according to route I or II (Fig. 1) different microstructures are observed. Hence, an accumulated plastic strain of >100% leads to a nanostructured material with a grain sizes between 300 and 500 nm. However, a non homogenous microstructure was found within a surface layer of 1 to 3 mm thickness and has to be removed before specimen manufacturing.

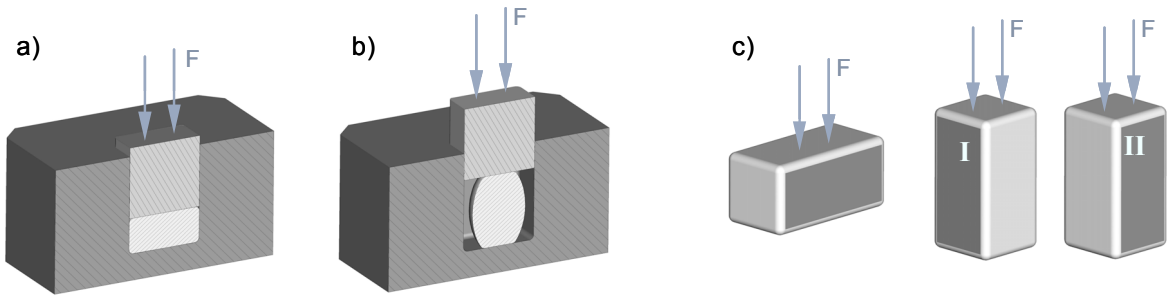

Figure 1: *Cyclic Channel Die Compression technology to produce UFG materials: (a) first and (b) second deformation step, (c) two different deformation routes*

2.2 Methods

To investigate the mechanical behaviour of coarse grained and UFG Ti-6-22-22S alloy, a variety of different testing facilities were used. The material was studied under compressive and shock loading conditions within a range of strain rates from 10^{-3} to 10^{7} s^{-1} at room temperature. Quasistatic tests were performed using a servohydraulic machine. Force was measured by a calibrated load cell. The strain response was obtained either by the use of strain gauges up to limited strains of maximum 8% plastic strain or by inductive sensors for higher deformations.

Dynamic tests at strain rates of 10^{2} s^{-1} were done using a drop weight tower device [8]. A guided mass of 600 kg impacts the specimen at a velocity of approximately 1.5 m/s and leads to deformation of the material. The force during testing is calculated from the elastic deformation of the punch obtained by strain gauges and the use of Hooke's law. The deformation was measured either by strain gauges or incremental gauges. Dynamic tests at strain rates from 10^{3} to 10^{4} s^{-1} were done using the Split Hopkinson Pressure Bar (SHPB) technique. The stress-strain response of the material is calculated using the theory of one dimensional wave propagation effects [9]. For the compression tests, cylindrical specimens with an initial diameter of Ø6 mm and an aspect ratio (ratio of specimen diameter to specimen height) of 1 were used.

Shock loading experiments were realised by Flyer Plate Impact (FPI) tests [10]. The experimental setup is shown in Fig. 2. An impactor is accelerated by an explosive lens and impacts the specimen. Hence, a planar shock wave is induced and travelling through the specimen. From measurement of the free surface velocity by using a VISAR laser Doppler velocimeter, the dynamic yield strength is calculated. The output VISAR signals were recorded with a high-frequency digital oscilloscope with a time resolution of approximately 1 ns.

Hence, applying the evaluation method described e.g. in [11] and [12], a comparison of high rate data with the mechanical behaviour at lower strain rates can be made. Within this study specimen thicknesses between 0.67 and 10 mm were used, whereby the larger specimens of 6.36 and 10 mm thickness were impacted by 2 mm aluminium plates at 660±20 m/s. For impact velocities of 1250±50 m/s specimen thicknesses of 0.67 mm and 0.835 mm and aluminium plates with 0.1 to 0.12 mm in thickness were used. The measurement accuracy of free surface velocity was better than ±5 m/s independently of its peak value. Hence, the free surface velocity histories were used for determination of

the mechanical behaviour of the UFG titanium alloy under shock compression loading. Additionally, the free surface velocity history contains information on strain hardening and strain rate effects.

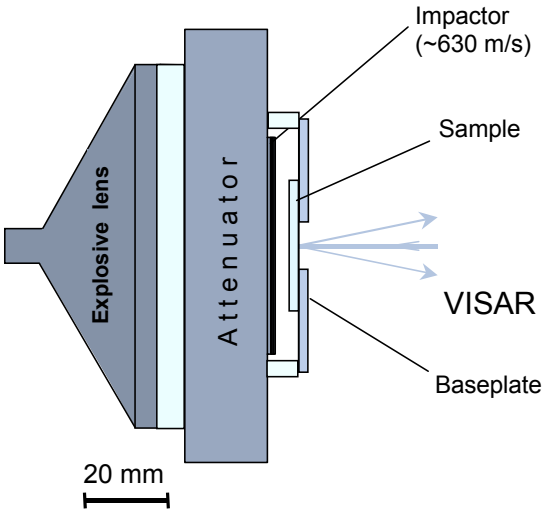

***Figure 2**: Experimental setup of flyer plate impact tests*

3 Results and discussion

3.1 Quasistatic and dynamic loading

Fig. 3 shows the stress-strain behaviour of the coarse grain and UFG titanium alloy under compressive loading at different strain rates. It can be clearly seen that with increasing strain rate an increase of flow stress for both materials can be found. For the coarse grained material a thermally activated flow stress increase in the order of 500 MPa compared to 400 MPa for the UFG state from 10^{-3} to 10^{3} s^{-1} is observed. Additionally, a significantly higher initial flow stress can be measured with decreasing grain size from 10 µm to 300 nm. Both material states tend to fail during compressive deformation under quasistatic as well as under dynamic loading conditions. However, a strong decrease of strain at fracture with decreasing grain size and increasing strain rate was observed.

From Fig. 3 a different strain hardening behaviour for the two materials can be observed. Defining the strain hardening coefficient n as the partial derivation of log σ by log ε (Eq. 1) a decrease of n with increasing strain rate is observed. Due to conversion of plastic work to heat under dynamic loading conditions thermal softening effects lead to a decrease of value n with increasing strain. However, failure initiation and occurrence lead to negative values of strain hardening coefficient which has no physical meaning but it can be used as a phenomenological value defining the start of fracture process.

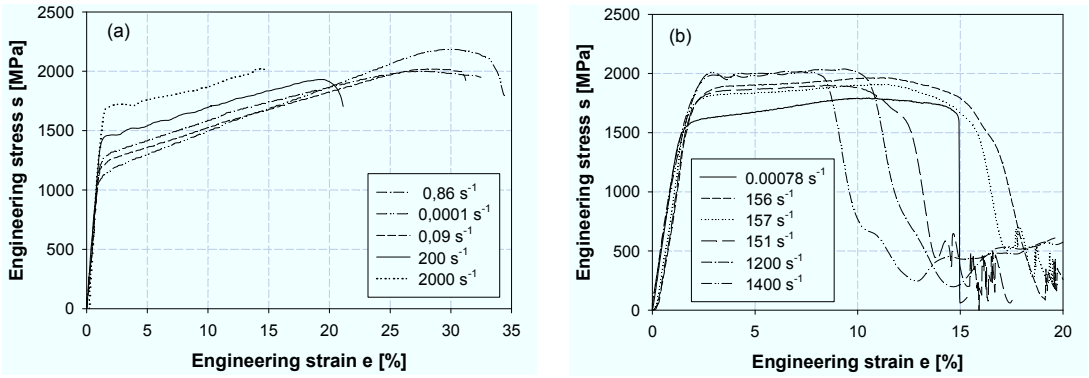

Figure 3: *Engineering stress – strain behaviour of (a) coarse grained and (b) UFG Ti-6-22-22S under compressive loading at different strain rates*

$$n = \left.\frac{\partial(\log\sigma)}{\partial(\log\varepsilon)}\right|_{\varepsilon} \tag{1}$$

Fig. 4 summarises the strain hardening coefficient for the coarse grain and UFG titanium alloy. Comparing coarse and ultra-fine grained material different strain hardening behaviour can be found. At the onset of plastic deformation the UFG material shows a 2.5 times higher strain hardening coefficient compared to the material with a grain size of 10 µm. During deformation the n-value is nearly constant for coarse grained material until failure process is initiated. The UFG material shows a strong decrease of strain hardening after low amount of plastic deformation. However, at higher strains nearly no hardening was found.

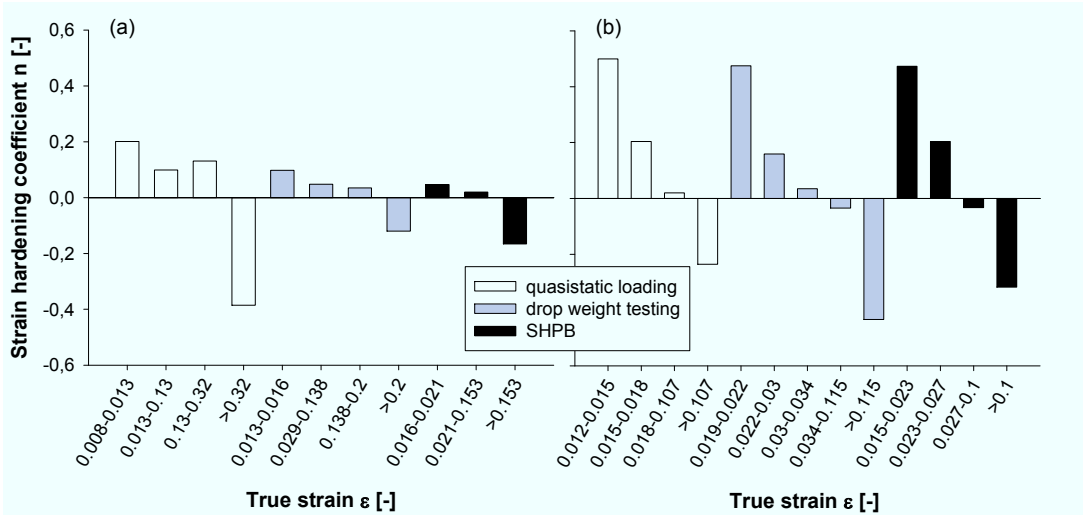

Figure 4: *Development of strain hardening coefficient with increasing deformation at different strain rates for (a) coarse grain and (b) UFG Ti-6-22-22S alloy*

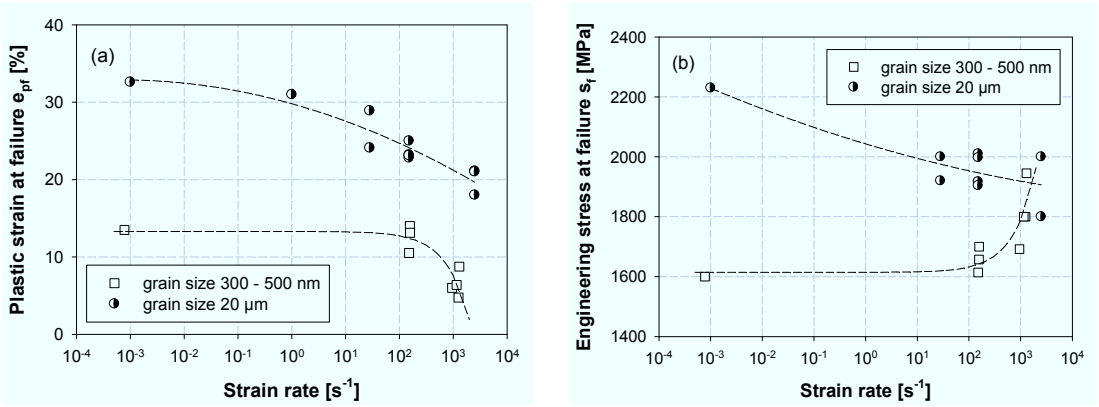

Figure 5: *(a) compressive deformability and (b) stress at failure of coarse and ultra-fine grained Ti-6-22-22S*

Fig. 5a illustrates compressive deformability of both material states. It can be seen that UFG material at room temperature is less deformable under compressive loading than coarse grain state. The plastic strain at failure is reduced at quasistatic loading from e_{pf} = 32% to 13 %. The material with 10 µm grain size shows a continuous decrease of compressive deformability with increasing strain rate, whereby the deformability behaviour of the UFG material is assumed to be nearly constant over a wide range of strain rates up to 10^2 s^{-1}. However, at higher strain rates a strong decreasing fracture strain was found. From Fig. 5b the stress at failure can be evaluated. It can be seen that coarse grained and UFG Ti-6-22-22S alloy show different behaviour. The material with a grain size of 10 µm shows a decrease of compressive strain at failure with increasing strain rate. For the UFG material the opposite behaviour was determined.

3.2 Impact loading by shock waves

Fig. 6 shows the free surface velocity history profiles measured by VISAR technique. Both material states, coarse grain and ultra fine grain, were tested with an impact velocity of ~650 and ~1250 m/s. It can be seen clearly that with increasing impact velocity increased free surface velocities are measured. The initial density of the titanium alloy was determined to 4.53 g/cm³, and the Poisson's ratio ν is 0.327. The longitudinal and the bulk sound velocities c_l and c_b are 6.01±0.04 km/s and 4.87±0.04 km/s, respectively. The amplitudes of shock waves were determined to 4.9 and 11.2 GPa for 10 µm grain size and 5.1 and 8.82 GPa for 300 nm grain size, respectively. For low impact velocity of ~650 m/s a higher value of Hugoniot Elastic Limit (HEL) σ_{HEL} for coarse grained Ti-6-22-22S was found, which was 260 MPa larger compared to UFG material. At impact velocities of ~1250 m/s the σ_{HEL} of UFG material was 400 MPa higher than for the as received state. The results are summarised in Tab. 2.

Additionally, from Fig. 6 the change of free surface velocity at spall Δu_{fs} can be determined. Δu_{fs} is evaluated as the difference between maximum of u_{fs} and the first valley after peak pressure. Hence, the spall strength σ^* was found to decrease for ultra fine grained material compared to coarse grain state. However, the difference in spall strength between the two material states increases at higher impact velocities (Tab. 2).

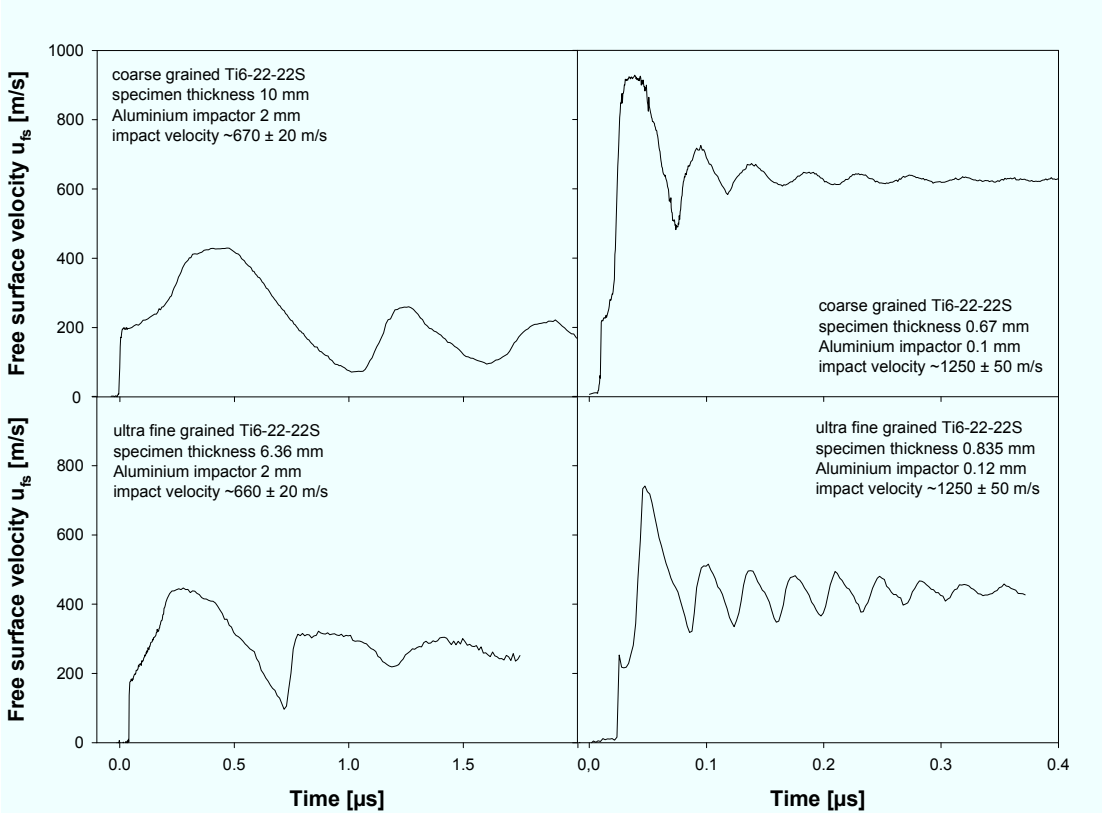

Figure 6: *Free surface velocity profiles for coarse grained and ultra fine grained Ti-6-22-22S alloy for two different impact velocities*

material	p_{max} [GPa]	σ_{HEL} [GPa]	$\sigma_{0.2}$ [GPa]	$\sigma_{0.5}$ [GPa]	σ_Y [GPa]	$h_{sp.}$ [mm]	$\dot{\varepsilon}$ 10^5 [s^{-1}]	σ^* [GPa]
cg Ti-6-22-22S	4.9	2.68	1.59	1.68	1.38	2.62	0.78	4.48
UFG Ti-6-22-22S	5.1	2.42	1.55	1.75	1.24	1.76	0.97	4.37
cg Ti-6-22-22S	11.2	3	1.81	1.93	1.55	0.17	14	5.55
UFG Ti-6-22-22S	8.82	3.4	1.8	1.92	1.75	0.16	11	5.13

Table 2: *Results of flyer plate impact experiments on Ti-6-22-22S*

To ensure comparability of impact results with quasistatic and dynamic compression tests the stress-strain response of the material have to be calculated. Therefore, the free surface velocity history profile $u_{fs}(t)$ was analysed and an approach of $u_{fs}(t) = 2u_p(t)$ and $d\sigma(t) = \rho a_\sigma \cdot du_p(t)$ was used. From the recalculated stress history profile the strain increment $d\varepsilon_x$ and the resolved shear stress τ were calculated. Assuming the uniaxial flow stress to be twice the shear stress, the stress-strain diagram of the material under shock loading can be drawn (Fig. 7). It must be emphasised that values of plastic strain under shock wave loading were less than 4%. However, at plastic strains larger than 1%,

obtained in shock loading experiments, softening effects have a strong influence on the measured material behaviour.

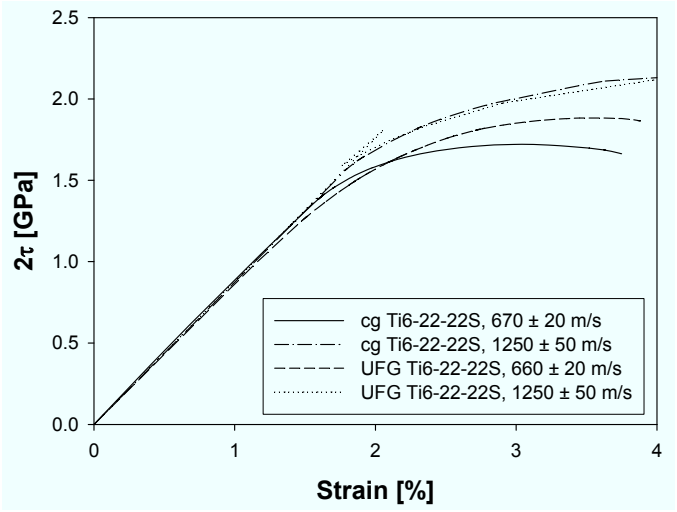

Figure 7: *Evaluation of stress-strain response of coarse grained and ultra fine grained Ti-6-22-22S alloy obtained under shock wave loading conditions.*

From Fig. 7 the 0.2% and the 0.5% flow stresses can be evaluated. Hence, for the 0.2% flow stresses similar results for both material states were observed. For larger strains, a significantly higher flow stress for UFG material at impact velocities of ~650±20 m/s compared to coarse grain material was found. However, the different flow stress behaviour for the two material states observed under uniaxial compression tests cannot be confirmed at shock wave loading conditions.

The results on flow stress behaviour of coarse grained and ultra-fine grained Ti-6-22-22S are summarised in Fig. 8. The 0.2% and 0.5% yield stress versus strain rate are shown.

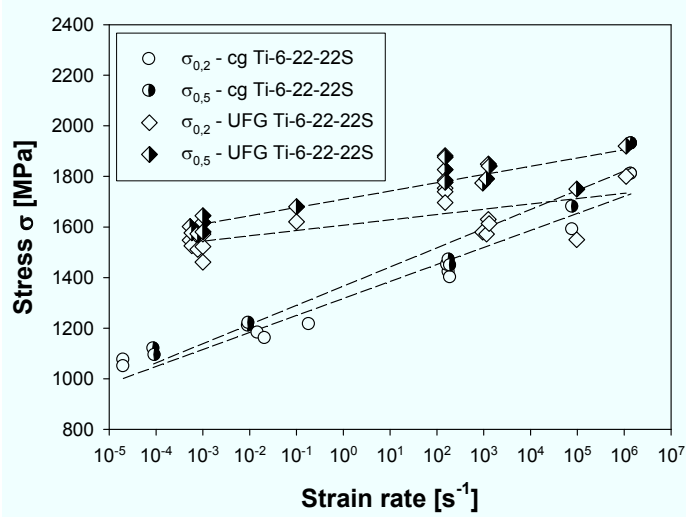

Figure 8: *Initial flow stress behaviour of coarse grained and ultra fine grained Ti-6-22-22S alloy over a range of strain rates from 10^{-4} to 10^{7} s^{-1}*

It can be seen that with decreasing grain size from ~10 µm to ~300 nm an increase of flow stresses can be measured. Under quasistatic loading conditions this difference was about 400 MPa. However, with increasing strain rate the difference between flow stresses of coarse grain and UFG material decreases, and under shock wave loading conditions nearly no different flow stresses were found. From Fig. 8 a linear dependence of flow stress on logarithmic strain rate can be evaluated for both materials. Even at high strain rates of $>10^4$ s^{-1} no alteration of strain rate sensitivity was found. Hence, the flow stress behaviour of coarse grained and ultra-fine grained Ti-6-22-22S can be assumed to be thermally activated within a range of strain rates ranging from 10^{-5} to $>10^6$ s^{-1}. Assuming the strain rate sensitivity of the material defined according to Eq. 2 different flow stress increasing increments per order of magnitude (oom) in strain rate can be found.

$$C = \left.\frac{\partial \ln \sigma}{\partial \ln \dot{\varepsilon}_p}\right|_{\varepsilon_p, T} \quad \left[\frac{MPa}{oom}\right] \tag{2}$$

	ε_p = 0.2%	ε_p = 0.5%
C_{UFG}	9.1	14.2
C_{cg}	29.2	32.9

Table 3: *Stress-strain rate sensitivity C of UFG and coarse grained Ti-6-22-22S*

In Tab. 3 the values of strain rate sensitivity obtained from Fig. 8 are shown. It can be clearly seen that ultra-fine grain Ti-6-22-22S is less sensitive on strain rate than coarse grained material. However, with increasing plastic strain, strain rate sensitivity was found to be increased.

4 Conclusions

From our work the following conclusions can be drawn:

1. Cyclic Channel Die Compression technology (CCDC) is an appropriate process to produce nanostructured titanium alloys. Grain sizes of 300 nm can be reached. However, CCDC process causes the formation of a non-homogeneous surface layer in the specimen. This layer should be removed before tests for characterising the mechanical behaviour of UFG materials.
2. Titanium alloy Ti-6-22-22S with grain sizes ~300 -500 nm shows a higher yield stress than the coarse-grained state (grain size 10 – 15 µm) within a wide range of strain rates. At quasistatic loading the UFG titanium alloy shows a 40% higher yield strength then commercial polycrystalline Ti-6-22-22S alloy.
3. The strain hardening behaviour of UFG titanium alloy differs significantly from coarse grained alloy. Within the first 1-1.5% of plastic strain, the UFG titanium alloy shows strong strain hardening which is more than at coarsed grain material. However, at larger plastic strains, no strain hardening was found for the UFG material.

4. The stress at Hugoniot elastic limit σ_{HEL} and flow stresses $\sigma_{0.2}$ and $\sigma_{0.5}$ of UFG titanium alloy at 10^6 – 10^7 s^{-1} are comparable to coarse grained material. No large difference between the two material states was found.
5. The compressive deformability of the UFG Ti 6-22-22S alloy is decreased at strain rates from 10^2 to 10^4 s^{-1} and is nearly constant at lower strain rates. However, the compressive deformability is reduced to one third and dynamically to one half of compressive failure strain of coarse grained Ti-6-22-22S.
6. For coarse grained material a decrease of compressive failure stress s_f was found. However, a different behaviour was measured for UFG material, where an increase of s_f in the order of 20% was observed.
7. For both material states a linear dependence of flow stress on logarithm of strain rate was found over the whole range of strain rates from 10^{-5} to $>10^6$ s^{-1}. However, the strain rate sensitivity is decreased with decreasing grain size. At shock wave loading the Hugoniot elastic limit and the yield stresses $\sigma_{0.2}$ and $\sigma_{0.5}$ of the UFG titanium alloy and their coarse grained counterpart are comparable.

References

[1] *Stolyarov, V.; Zhu, Y.T.; Alexandrov, I.V.; Lowe, T.C.; Valiev, R.Z.:* Grain refinement and properties of pure Ti processed by warm ECAP and cold rolling. Materials Science and Engineering, A343 (2003), 43-/50.

[2] *Ko, Y.G.; Shin, D.H.; Park, K.-T.; Lee, C.S.:* An analysis of the strain hardening behaviour of ultra-fine grained pure titanium. Scripta Mater., 54 (2006), 1785–1789.

[3] *Semenova, I.P.; Raab, G.I.; Saitova, L.R.; Valiev, R.Z.:* The effect of equal-channel angular pressing on the structure and mechanical behaviour of Ti 6Al 4V alloy. Materials Science and Engineering, A387–389 (2004), 805–808.

[4] *Sergueeva, A.V.; Stolyarov, V.V.; Valiev, R.Z.; Mukherjee, A.K.:* Superplastic behaviour of ultra-fine grained Ti–6Al–4V alloys. Materials Science and Engineering, A323 (2002), 318–325.

[5] *Valiev, R.Z.; Estrin, Y.; Horita, Z.; Langdon, T.G.; Zehetbauer, M.J.; Zhu, Y.T.:* Producing Bulk Ultrafine-Grained Materials by Severe Plastic Deformation. Journal of Material Science, April, 2006, 33-39.

[6] *Skripnyak, V.A.; Skripnyak, E.G.:* Shear strength of nanostructured and ultra-fine grained materials in shock waves. Phys. Mesomech., 2004, Vol. 7, P.1, 297-300.

[7] *Krüger, L.; Meyer, L.W.; Razorenov, S.V.; Kanel, G.I.:* Investigation of dynamic flow and strength properties of Ti-6-22-22S at normal and elevated temperatures. Int. J. of Impact Engineering, 2003, Vol. 28, 877-890.

[8] *Meyer, L.W.; Krüger, L.:* Drop-Weight Compression Shear Testing. ASM-Handbook, Vol. 8: Mech. Testing and Evaluation, ASM Int. Materials Park Ohio, 2002, 452-454.

[9] *Gray, G.T. (R.):* Classic Split-Hopkinson Pressure Bar Testing. ASM-Handbook, Vol. 8: Mech. Testing and Evaluation, ASM Int. Materials Park Ohio, 2002, 462-476.

[10] *Meyers, M.A:* Dynamic behaviour of materials. John Wiley & Sons, Inc., 1994.

[11] *Kanel, G.I.; Razorenov, S.V.; Fortov, V.E.:* Shock wave phenomena and the properties of condensed matter. Berlin-N.-Y, Springer-Verlag, 2004.

[12] *Antoun, T.; Seaman, L.; Curran, D.R.; Kanel, G.I.; Razorenov, S.V.; Utkin, A. V:* Spall fracture. Berlin-N.-Y, Springer-Verlag, 2003.

Failure Elongation of Steel Sheets for an Auto-body at the High Strain Rate

H. Huh[1], S. B. Kim[1], J. H. Song[1], J. H. Yoon[1], J. H. Lim[2]

[1] School of Mechanical, Aerospace and System Engineering, KAIST, Daeduck Science Town, Daejeon, 305-701, Korea
[2] POSCO Technical Research Laboratories 699, Gumho-dong, Gwangyang-si, Jeollanam-do, 545-090, Korea

Abstract

This paper presents the dynamic failure elongation of conventional mild steels and advanced high strength steel sheets such as TRIP and DP steels. The failure elongation has been obtained from the high speed tensile testing machine with various strain rates ranged from 0.003/s to 200/s. The experimental result demonstrates that the tensile elongation does not simply decrease as the strain rate increases, but it decreases from the quasi-static state to the strain rate of 0.1 or 1/s and increases again up to the strain rate of 100/s. Furthermore, some high strength steels have the tendency that the tensile elongation increases as the strain rate increases. This tendency has varieties depending on the microstructure and forming history of sheet metal. Moreover, the localized strain rate hardening in the necking region induces the increase of elongation. This phenomenon is very important not only in sheet metal forming but also in the crashworthiness evaluation to predict the fracture of sheet metal members.

Keywords

Fracture elongation, Sheet metal, High strain rate

1 Introduction

The sheet metal forming process is one of the most important fabrication processes for an auto-body with development of forming techniques. Due to remarkable development of forming techniques, its capabilities have been extended to very complicated sheet metal forming and multi-stage forming. Although the formability is important and indispensable for success in very complicated sheet metal forming, few studies have been done about the formability of sheet metal at the high strain rates since it was difficult to make the tensile test of sheet metal at the high strain rate ranged from several tens to hundreds per

second. The dynamic tensile properties of auto-body steel sheets are important since the range of the strain rate is under 500/s in a real auto-body crash and at which the dynamic response of steel sheets is different from static one [1-4]. Mechanical, pneumatic and servo-hydraulic loading methods have been used to measure mechanical properties of materials at this range of the high strain rates [5]. Dudder [6] and Ambur et al. [7] studied to obtain the material properties using a drop weight method and other researchers used a cam plastometer and a rotary flywheel machine and so on. Nowadays, servo-hydraulic material testing machines are employed in most research works [8, 9]. However, a few in-depth studies have been published about the dynamic material properties such as the yield and tensile strength as well as the tensile elongation at the high strain rates.

In this paper, the tensile elongation has been obtained from various steel sheets for an auto-body at the high strain rates. A high speed material testing machine was made for tensile tests at the high strain rate and the appropriate dimensions of a specimen were selected in order to induce the uniform elongation in the gauge section at the high strain rates. Dynamic tensile tests of eight different steel sheets for an auto-body such as SGACD, SPRC450R, TRIP600, DP600, TRIP800 and DP800 steels were performed to investigate the relation between the strain rate and the tensile elongation. Stress–strain curves were obtained for each steel sheet from the dynamic tensile test and used to deduce the relationship of the elongation to the strain rate.

2 Dynamic Tensile Test

2.1 High Speed Material Testing Machine

The dynamic response at the high strain rates should be obtained by adequate experimental techniques such as mechanical, pneumatic and servo-hydraulic types. Servo-hydraulic testing machines are frequently used in most recent research works due to accuracy and convenience of operation. In the present experiment, a high speed material testing machine of the servo-hydraulic type as shown in Figure 1 was utilized in order to obtain the dynamic mechanical properties at the high strain rates. The machine has the maximum stroke velocity of 7800 mm/s, the maximum load of 30 kN and the maximum displacement of 300 mm. Two electric motors are used to compress the operating hydraulic oil up to the pressure of 300 bars and two accumulators with the capacity of 5 liters are used to make the response time faster. The maximum flow rate of the servo-hydraulic unit is 4 liter/sec.

The machine equipment is set up with the Kistler 9051A piezo-electric type load cell in a specially designed loading fixture to reduce the noise level and to increase the noise frequency from the load-ringing phenomenon. The displacement is acquired by a LDT (linear displacement transducer) from Sentech company. During the operation, a function generator transmits an input signal to the servo controller to control the displacement with a feedback system by comparing the measured displacement with the input signal. Configuration file and test programs are fine-tuned for different velocities of a stroke at different strain rates. Several tests were conducted at the same condition to verify repeatability and the results were very satisfactory for repeatability with robust calibration and indicated that the machine response, testing procedure and material response were consistent.

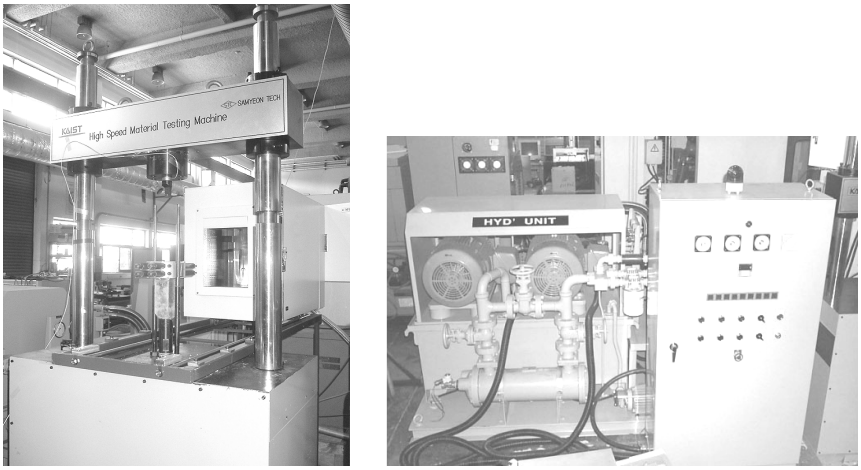

(a) (b)

Figure 1: *High speed material testing machine: (a) loading frame; (b) servo-hydraulic unit*

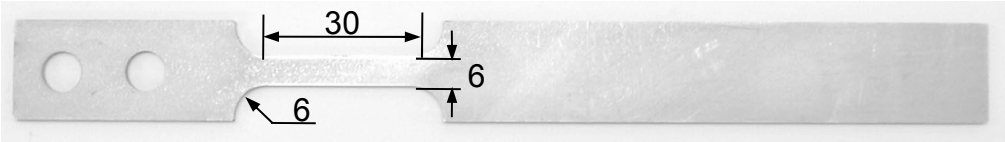

Figure 2: *Dynamic tensile specimen with the length of the parallel region of 30 mm*

2.2 Dynamic Tensile Specimen

Tensile specimens for the standard test are specified in the regulations of ASTM, BSI and KS as well as the testing method. These regulations, however, do not include the high speed tensile testing method and the corresponding specimens. Therefore, an appropriate high speed tensile testing method and specimen need to be determined for accurate tensile tests at the high strain rate ranged from 1 to 500/s. The dimension of specimen was determined from the finite element analysis result and the tensile test result considering the shape factors to induce the uniform deformation [10]. Figure 2 shows determined dynamic tensile specimen with 30 mm in length of the parallel region, 6 mm in both gauge width and fillet radius.

3 Experimental Results

3.1 Test Conditions

The materials tested were conventional steels and advanced high strength steels such as SGACD, SPRC450R, TRIP600, DP600, TRIP800 and DP800 steels prepared along the rolling direction. Experiments were carried out at room temperature of 294K at the strain rates ranged from quasi-static to the strain rate of 200/s. Quasi-static tensile tests were carried out at the strain rate of 0.003/s using the static tensile machine, Instron 5583. Dynamic tensile tests were carried out at strain rates from 0.1/s to 200/s using a high speed material testing machine developed. From the tensile test, the dynamic material

properties such as the flow stress, the strain rate sensitivity and failure elongation were investigated quantitatively.

3.2 Dynamic Tensile Characteristics of Steel Sheets

The mechanical properties of auto-body steel sheets obtained from the static test are given in Table 1. Conventional mild steel, SGACD shows high failure elongation compare to other advanced high strength steels. Comparing TRIP steel sheets with DP steel sheets having similar tensile strengths, TRIP600 and TRIP800 steels have higher elongation than DP600 and DP800 steels, respectively. TRIP steels have a good ductility compared to DP steels due to TRIP effect. This effect improves the elongation and strength of materials as the phase of remained austenite transforms into the phase of martensite during deformation. The ratio of the yield stress to the tensile strength is compared to estimate the formability of the steel sheets. SGACD steel has lower yield ratio than any other steel sheets. TRIP800 steel has a lower yield ratio than DP800 steel while TRIP600 and DP600 steels have similar ratios, which means TRIP steels have better formability than DP steels.

Dynamic tensile tests were carried out at the strain rate ranged from 0.003/s to 200/s. Tests were repeated two or three times per each strain rate. Engineering stress–strain curves of auto-body steel sheets are shown in Figure 3 at various strain rates. As the strain rate increases, the flow stress of steel sheets gradually increases. The slope of the stress–strain curve for conventional mild steel such as SGACD decreases as the strain rate increases. As a result, the ultimate tensile strength occurs at the lower strain and the hardening exponent becomes smaller with the increase of the strain rate. This phenomenon seems to occur with the mechanism of grain sliding and the heat dissipated from the plastic work at the high strain rate. The yield stress of SGACD increases by more than two times while the increases of the yield stress of the advanced high strength steel, TRIP and DP steel sheets is below 1.2 times. In general, the yield stress of the mild steel is more sensitive to the strain rate than that of the high strength steel. DP600 and DP800 are more sensitive to the strain rate than TRIP600 and TRIP800 in terms of the ultimate tensile strength. This result represents that the strain rate hardening of DP sheets is more advantageous than that of TRIP sheets because the strain rate in most auto-body crashes is under 500/s.

Material	Thickness [mm]	Yield stress [MPa]	UTS [MPa]	YS/UTS	Failure elongation [%]
SGACD	0.79	166	308	0.539	56.7
SPRC450R	1.23	324	450	0.720	33.6
TRIP600	1.45	414	612	0.676	34.0
DP600	1.43	422	632	0.668	26.9
TRIP800	1.43	480	786	0.611	25.1
DP800	1.60	555	755	0.735	19.2

Table 1: *Mechanical properties from the static test*

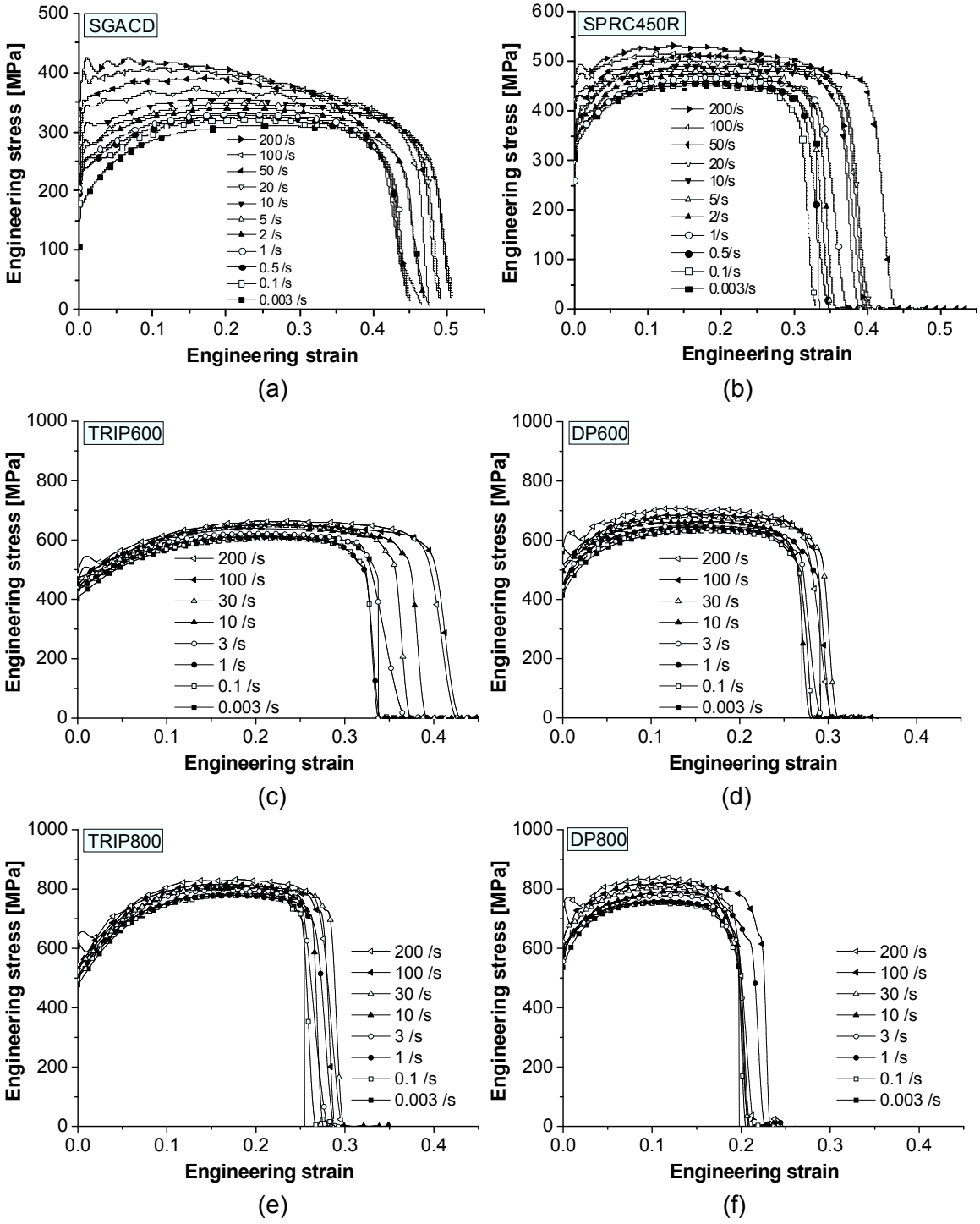

Figure 3: *Engineering stress-strain curves of auto-body steel sheets at various strain rates: (a) SGACD; (b) SPRC450R; (c) TRIP600; (d) DP600; (e) TRIP800; (f) DP800*

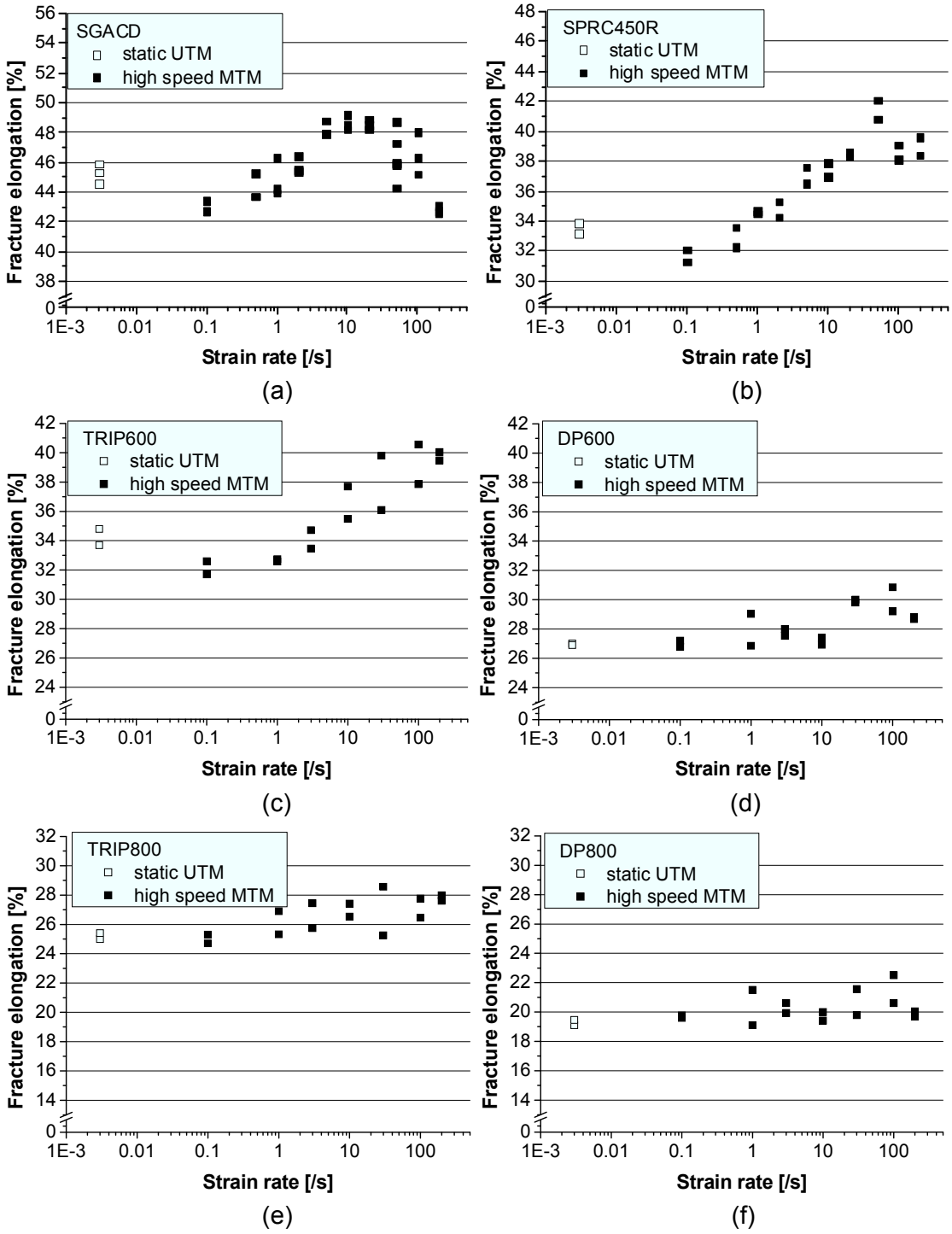

***Figure 4**: Failure elongation of auto-body steel sheets at various strain rates: (a) SGACD; (b) SPRC450R; (c) TRIP600; (d) DP600; (e) TRIP800; (f) DP800*

The failure elongation was obtained from the engineering stress-strain curves at various strain rates. Figure 4 shows the failure elongation distribution with the same elongation range of 18% against the logarithmic scale of the strain rate. It is known from classical conjecture that the strength of steel increases due to the strain rate hardening and the fracture elongation is expected to decrease as the strain rate increases. However,

the tensile test results show that the failure elongation of SGACD, SPRC450R, TRIP600 and TRIP800 steels decreases with increasing strain rate from the quasi-static state to the strain rate of 0.1/s, and then increases up to the strain rate of 50 or 100/s. On the other hand, the failure elongation of DP600 and DP800 steels increases monotonically as the strain rate increases. Peixinho et al. [11] and Choi et al. [12] obtained the similar experimental result that ductility of TRIP600 and DP600 steels does not simply decrease with increasing the tensile speed. When the necking phenomenon occurs in simple static tensile tests, deformation is concentrated at the gauge region in a narrow band of the gauge region. On the other hand, in tensile tests at the high stain rates, local strain rate hardening restrains the progress of necking and diffuse necking region expands in the adjacent region forming a wide band of necking. It is because the strain rate at the necking region becomes particularly higher than the other region and the flow stress in the necking region exceeds the flow stress in the other region due to the rapid increase of the strain rate. Consequently, the necking region becomes stronger than the neighbouring region despite thinning in the necking region, and finally the failure elongation increases as the strain rate increases. This tendency is related to the microstructure of steel sheets at various strain rates. At the quasi-static state, deformation proceeds with the rounded half-loop and V-shape dislocations. These types of dislocations still prevail at the strain rate of 0.1 and 1/s, but above the strain rate, crossing dislocations which have been investigated in literature at the strain rate over 1000/sec [13] begin to generate along the specific direction with deformation. As strain rate increases to the strain rate of 100/s, dislocation density increases significantly and most of dislocations change into the straight and crossing type which generate a dislocation net. During the forming procedure of this crossing dislocation, the failure elongation increases as strain rate increases.

This experimental result is worthy of attention for the crashworthiness of an auto-body especially in terms of the fracture and tearing of auto-body members. This result is also applicable to sheet metal forming processes of auto-body members in order to enhance the formability of sheet metals. For instance, the fracture elongation of SPRC450R and TRIP600 steels becomes 39% and 40% at the strain rate of 100/s and 33% and 34% at the quasi-static state, respectively, resulting in better formability in sheet metal forming. This increment of fracture elongation is due to the strain rate hardening in the proper strain rate range. This result reveals that forming processes at an adequate strain rate can enhance the formability compared to the static forming process.

4 Conclusion

This paper deals with the tensile failure elongation that has been obtained for various steel sheets for an auto-body at the high strain rate. The high speed material testing machine and the dynamic tensile specimen has been used for dynamic tensile tests at high strain rates ranging from 0.1/s to 200/s. Dynamic tensile tests of SGACD, SPRC450R, TRIP600, DP600, TRIP800 and DP800 steels for an auto-body were performed to investigate the relation between the strain rate and the elongation from the stress–strain curves at various strain rates. Several remarks are deduced from the experimental results as follows:

The failure elongation and the formability of TRIP steel sheets are better than those of DP steel sheets at the high strain rates. The failure elongation of conventional mild

steels and advanced high strength steels decreases with increasing strain rates from quasi-static to the strain rate of 0.1/s, and then increases up to the strain rate of 50/s or 100/s due to the local strain rate hardening. The elongation of DP600 and DP800 increases monotonically as the strain rate increases in contrast to the classical conjecture. This phenomenon is very interesting and important in sheet metal forming and the high speed deformation such as the auto-body crash from a viewpoint that the increment of the strain rate does not deteriorate the elongation.

References

[1] *Khan, A. S.; Huang, S.:* Experimental and theoretical study of mechanical behavior of 1100 aluminium in the strain rate range 10^{-5}–10^{4} s^{-1}. International Journal of Plasticity, 1992, p.397-424.

[2] *Ishikawa, K.; Tanimura, S.:* Strain rate sensitivity of flow stress at low temperatures in 304N stainless steel. International Journal of Plasticity, 1992, p.947-958.

[3] *Huh, H.; Lim, J. H.; Kim, S. B.; Han, S. S.; Park, S. H.:* Formability of the steel sheet at the intermediate strain rate. Key Engineering Materials, 2004, p.403-408.

[4] *Meyer, L. W.:* Material behaviour at high strain rates. Proceedings of International Conference on High Speed Forming, Dortmund, 2004.

[5] *Zukas, J. A.; Nicholas, T.; Swift, H. F.; Greszczuk, L. B.; Curran, D. R.:* Impact dynamics. New York: John Wiley & Sons, 1982.

[6] *Dudder, G. B.:* Drop tower compression test-metals handbook. Ohio: American Society for Metals, 1985.

[7] *Ambur, D. R.; Prasad, C. B.; Waters, W. A.:* A dropped-weight apparatus for low speed impact testing of composite structures. Experimental Mechanics, 1995, p.77–82.

[8] *Miura, K.; Takagi, S.; Furukumi, O.; Obara, T.; Tanimura, S.:* Dynamic deformation behavior of steel sheet for automobile. SAE 960019, 1996.

[9] *Kim, J. S.; Huh, H.; Lee, K. W.; Ha, D. Y.; Yeo, T. J.; Park, S. J.:* Evaluation of dynamic tensile characteristics of polypropylene with temperature variation. International Journal of Automotive Technology, 2006, p.571–577.

[10] *Huh, H.; Kim, S. B.; Song, J. H.; Lim, J. H.:* Dynamic tensile characteristics of TRIP-type and DP-type steel sheets for an auto-body. International Journal of Mechanical Sciences, 2008, (in printing).

[11] *Peixinho, N.; Pinho, A.:* Dynamic material properties of Dual-Phase and TRIP steels and constitutive equation. Proceedings of EURODYN, 2005, p.1767-1771.

[12] *Choi, I. D.; Son, D. M.; Kim, S. J.; Matlock, D. K.; Speer, J. G.:* Strain rate effects on mechanical stability of restrained austenite in TRIP sheet steels. SAE 2006-01-1434, 2006.

[13] *Mandziej, S. T.:* Low-energy dislocations and ductility of ferritic steels. Materials Science and Engineering: A, 1993, p.275–280.

SESSION 3

MODELING AND SIMULATION

Introduction of an Electromagnetism Module in LS-DYNA for Coupled Mechanical Thermal Electromagnetic Simulations

P. L'Eplattenier, G. Cook, C. Ashcraft

LSTC, 7374 Las Positas Road, Livermore, CA 94551, USA

Abstract

A new electromagnetism module is being developed in LS-DYNA for coupled mechanical/thermal/electromagnetic simulations. One of the main applications of this module is Electromagnetic Metal Forming. The electromagnetic fields are solved using a Finite Element Method for the conductors coupled with a Boundary Element Method for the surrounding air/insulators. Both methods use elements based on discrete differential forms for improved accuracy. The physics, numerical methods and capabilities of this new module are presented in detail as well as its coupling with the mechanical and thermal solvers of LS-DYNA. This module is then illustrated on an Electromagnetic Metal Forming case.

Keywords

Modelling, Finite Element Method (FEM), Boundary Element Method (BEM)

1 Introduction

LS-DYNA is a highly advanced general-purpose nonlinear finite element program that is capable of simulating complex real world problems. The distributed memory solver provides very short turn-around times on Unix, Linux and Windows clusters. The major development goal of Livermore Software Technology Corporation (LSTC) is to provide within LS-DYNA capabilities to seamlessly solve problems that require multi-physics, multiple-stages, and multi-processing. LS-DYNA is suitable to investigate phenomena that involve large deformations, sophisticated material models and complex contact conditions [1]. LS-DYNA allows running an analysis explicitly or implicitly and combining different disciplines such as coupled thermal analysis, fluid dynamics, fluid-structure interaction, SPH (smooth Particle Hydrodynamics), EFG (Element Free Galerkin). The analysis capabilities also include nonlinear dynamics, rigid body dynamics, quasi-static simulations, normal modes, eigenvalue analysis, Eulerian capabilities, ALE (Arbitrary

Lagrangian Eulerian), failure analysis, implicit spring back, adaptive re-meshing, 2D and 3D formulations. LSTC provides additional software packages for pre- and post-processing as well as for optimization. Metal forming is one of LS-DYNA's main applications, with capabilities that allow one to simulate rolling, extrusion, forging, casting, spinning, ironing, super-plastic forming, sheet metal stamping, profile rolling, deep drawing, hydro-forming, multi-stage processing, spring back, hemming.

An electromagnetism (EM) module is under development in LS-DYNA in order to perform coupled mechanical/thermal/electromagnetic simulations [2]. Electromagnetic Metal Forming (EMF) is the main application of this development, but other processes could be simulated, where magnetic pressure induces mechanical stress and deformations and/or the Joule effect induces a heating process: magnetic metal cutting, magnetic metal welding, very high magnetic pressure generation, rail-gun type apparatus, computation of the stresses and deformations in various coils, magnetic flux compression, induced heating and so forth. This module allows us to introduce some source electrical currents into solid conductors, and to compute the associated magnetic field, electric field, as well as induced currents. These fields are computed by solving the Maxwell equations in the eddy-current approximation. The Maxwell equations are solved using a Finite Element Method (FEM) [3] for the solid conductors coupled with a Boundary Element Method (BEM) [4] for the surrounding air (or insulators). Both the FEM and the BEM are based on discrete differential forms (Nedelec-like elements [5]).

In the first part, the EM module will be presented, the FEM part, the BEM part, and the coupling with external circuits. In a second part, the coupling of the EM module with the rest of LS-DYNA, and in particular with the mechanical and thermal modules will be presented. In the third part, one EMF example is presented.

2 Presentation of the Electromagnetism module

2.1 Scalar Potential and Modified Vector Potential Formulation

Let Ω be a set of multiply connected conducting regions. The surrounding insulator exterior regions will be called Ω_e. The boundary between Ω and Ω_e is called Γ, and the (artificial) boundary on Ω at the end of the meshing region (hence where the conductors are connected to an external circuit) is called Γ_c. In the following, we will denote $\vec{n}$ as the outward normal to surfaces Γ or Γ_c. The electrical conductivity, permeability and permittivity are called σ, μ and ε respectively. In Ω_e, we have $\sigma = 0$ and $\mu = \mu_0$.
The Maxwell equations read:

$$\vec{\nabla} \times \vec{E} = -\frac{\partial \vec{B}}{\partial t} \tag{1}$$

$$\vec{\nabla} \times \frac{\vec{B}}{\mu} = \vec{j} + \varepsilon \frac{\partial \vec{E}}{\partial t} \tag{2}$$

$$\nabla \bullet \vec{B} = 0 \tag{3}$$

$$\nabla \bullet \varepsilon \vec{E} = 0 \tag{4}$$

$$\nabla \bullet \vec{j} = 0 \tag{5}$$

$$\vec{j} = \sigma \vec{E} + \vec{j}_S \tag{6}$$

Where $\vec{E}$ is the electric field, $\vec{B}$ the magnetic flux density, $\vec{j}$ the total current density, and $\vec{j}_S$ is a source current density.

We consider good enough conductors with low frequency varying fields such that the condition $\varepsilon \frac{\partial \vec{E}}{\partial t} \prec\prec \sigma \vec{E}$ is satisfied. This is called the low frequency or eddy-current approximation, and is very well satisfied in EMF experiments. We thus neglect the second term of the right hand side of equation (2). The divergence condition (3) allows writing $\vec{B}$ as $\vec{B} = \vec{\nabla} \times \vec{A}$ where we introduced the magnetic vector potential $\vec{A}$ [6]. Equation (1) then implies that the electric field is given by $\vec{E} = -\vec{\nabla}\phi - \frac{\partial \vec{A}}{\partial t}$ where ϕ is the electric scalar potential. We use the Gauge condition $\nabla \bullet \sigma \vec{A} = 0$ which allows a separation of the vector potential from the scalar potential in the equations. The Maxwell equations in terms of the 2 potentials then read:

$$\nabla \bullet \sigma \vec{\nabla}\phi = 0 \tag{7}$$

$$\sigma \frac{\partial \vec{A}}{\partial t} + \vec{\nabla} \times \frac{1}{\mu} \vec{\nabla} \times \vec{A} + \sigma \vec{\nabla}\phi = \vec{j}_S \tag{8}$$

With the boundary conditions:

$$\vec{n} \bullet \vec{\nabla}\phi = 0 \text{ on } \Gamma \tag{9}$$

$$\phi = \phi_c \text{ on } \Gamma c \tag{10}$$

And

$$\vec{n} \times \vec{\nabla} \times \vec{A} = \vec{A}_e \text{ on } \Gamma \tag{11}$$

$$\vec{n} \times \vec{A} = A_c \text{ on } \Gamma \tag{12}$$

Equation (10) allows the connection of the conductors to a voltage source and equation (12) to a current source, although we will show in the following that the connection with a current source can also be done through the BEM part of the system, allowing more flexibility when using conductors with non trivial topologies.

Once the potentials are computed, the electromagnetic fields are given by:

$$\vec{E} = -\vec{\nabla}\phi - \frac{\partial \vec{A}}{\partial t} \tag{13}$$

$$\vec{B} = \vec{\nabla} \times \vec{A} \tag{14}$$

$$\vec{j} = \sigma \vec{E} + \vec{j}_S \tag{15}$$

2.2 Finite Element Method

Equations (7) and (8) are solved in the conductors with a Finite Element Method using a library called “FEMSTER” developed at the Lawrence Livermore National Laboratories [7]. FEMSTER provides discrete numerical implementations of the concepts from differential forms (often referred as Nedelec elements)[8][9]. These include in particular the exterior derivatives gradient, curl and divergence, and also the div-grad, curl-curl and grad-div operators. FEMSTER provides four forms of basis functions, called 0-forms, 1-forms, 2-forms and 3-forms, defined on hexahedra, tetrahedra and prisms. At this time, only hexahedral elements are available in the EM module of LS-DYNA. The two other types will soon be available.

0-forms are continuous scalar basis functions that have a well defined gradient, the gradient of a 0-form being a 1-form. At first order, the degrees of freedom associated with a 0-form are the values of the scalar field at the nodes of the mesh. In our particular case, the 0-forms are used for the discretization of the scalar potential ϕ.

1-forms are vector basis functions with continuous tangential components but discontinuous normal components. They have a well defined curl, the curl of a 1-form being a 2-form. At first order, the degrees of freedom of a 1-form are its line integrals along the edges of the mesh. They are used for the discretization of the electric field $\vec{E}$, the magnetic field $\vec{H}$ and the vector potential $\vec{A}$.

2-forms are vector basis functions with continuous normal components across elements but discontinuous tangential components. They have a well defined divergence, the divergence of a 2-form being a 3-form. At first order, the degrees of freedom of a 2-form are its fluxes across all the facets of the mesh. They are used for the discretization of the magnetic flux density $\vec{B}$, and the current density $\vec{j}$.

Finally, the 3-forms are discontinuous scalar basis functions which can’t be differentiated. Their degrees of freedom at first order are their integrals over the elements of the mesh.

These basis functions define spaces with an exact representation in the De-Rham sequence [7]. They also exactly satisfy numerically relations such as curl (grad)=0 or div(curl)=0, which are very important for conservation laws when solving the systems [10]. At first order, they allow one to solve partial differential equation at an integrated “Stokes theorem” level which proves to be very efficient and accurate, even on low density meshes, compared to using vector basis functions [10].

We will denote $W^0, \vec{W}^1, \vec{W}^2$, and W^3 as the basis functions associated respectively with the 0, 1, 2, and 3-forms. Equation (7) is projected against 0-forms basis functions and equation (8) against 1-forms to give, after using the appropriate Greens vector identities and the boundary conditions (9) - (12) [10].

$$\int_\Omega \sigma \vec{\nabla}\phi \bullet \vec{\nabla} W^0 d\Omega = 0 \tag{16}$$

$$\int_\Omega \sigma \frac{\partial \vec{A}}{\partial t} \bullet \vec{W}^1 d\Omega + \int_\Omega \frac{1}{\mu} \vec{\nabla} \times \vec{A} \bullet \vec{\nabla} \times \vec{W}^1 d\Omega = -\int_\Omega \sigma \vec{\nabla}\phi \bullet \vec{W}^1 d\Omega + \frac{1}{\mu} \int_\Gamma [\vec{n} \times (\vec{\nabla} \times \vec{A})] \bullet \vec{W}^1 d\Gamma \tag{17}$$

Or equivalently after decomposing $\vec{A}$ and ϕ respectively on the 0-form and 1-form basis functions:

$$S^0(\sigma)\varphi = 0 \tag{18}$$

$$M^1(\sigma)\frac{da}{dt} + S^1(\frac{1}{\mu})a = -D^{01}(\sigma)\varphi + Sa \tag{19}$$

Where we introduced the 0-form stiffness matrix S^0, the 1-form mass matrix M^1, the 1-form stiffness matrix S^1 and the 0-1 form derivative matrix D^{01}[10]. The last term of equation (19) which involves the "outside matrix stiffness" S is computed using a Boundary Element Method.

2.3 Boundary Element Method

In order to compute Sa, an intermediate variable "surface current" $\vec{k}$ is introduced. This surface current, defined on the boundary Γ is such that it produces the same vector potential (and thus $\vec{B}$ field) in the exterior regions Ω_e as the actual volume current flowing through the conductors [11]:

$$\vec{A}(x) = \frac{\mu_0}{4\pi}\int_\Gamma \frac{1}{|x-y|}\vec{k}(y)dy \text{ for all } x \in \Omega_e \text{ (and in particular for all } x \in \Gamma) \tag{20}$$

One then has:

$$[\vec{n}\times(\vec{\nabla}\times\vec{A})](x) = \frac{\mu_0}{2}\vec{k}(x) - \frac{\mu_0}{4\pi}\int_\Gamma \frac{1}{|x-y|^3}\vec{n}\times[(\vec{x}-\vec{y})\times\vec{k}(y)]dy \text{ for } x \to x_0 \in \Gamma \tag{21}$$

When projecting these equations on the 1-forms basis functions for $\vec{A}$ and the "twisted" 1-forms $\vec{V}^1(x) = \vec{n}\times\vec{W}^1(x)$ for $\vec{k}$ one gets the following matrix equations:

$$Pk = Da \tag{22}$$

$$Sa = Qk \equiv Q_S k + Q_D k \tag{23}$$

Where we introduced the BEM matrices

$$P_{i,j} = \frac{\mu_0}{4\pi}\iint_{\Gamma_x\Gamma_y}\frac{1}{|x-y|}\vec{V}_i^1(x)\bullet\vec{V}_j^1(y)d\Gamma_x d\Gamma_y \,, D_{i,j} = \int_{\Gamma_x}\vec{V}_i^1(x)\bullet\vec{W}_j^1(x)d\Gamma_x \tag{24}$$

$$Q_{Si,j} = \frac{1}{2}\int_{\Gamma_x}\vec{W}_i^1(x)\bullet\vec{V}_j^1(x)d\Gamma_x \tag{25a}$$

$$Q_{Di,j} = -\frac{1}{4\pi} \iint_{\Gamma_x \Gamma_y} \frac{1}{|x-y|^3} \vec{W}_i^1(x) \bullet \{\vec{n}_x \times [(\vec{x}-\vec{y}) \times \vec{V}_j^1(y)]\} d\Gamma_x d\Gamma_y \quad (25b)$$

The BEM method is very appealing since it does not need a mesh in the air surrounding the conductors. It thus avoids the meshing problems associated with the air, which can be significant for complicated conductor geometries. Also, for very small gaps between conductors, an air mesh could include a large number of very small and distorted elements. Even more importantly, the BEM avoid remeshing problems which arise when using an air mesh around moving conductors. Another advantage of the BEM is that it does not need the introduction of somewhat artificial infinite boundary conditions.

The main disadvantage of the BEM is that it generates full dense matrices like P and Q_D (24,25) in place of the sparse FEM matrices. This causes a-priori high memory requirement as well as longer CPU time to assemble the matrices and solve the linear systems. In order to limit the memory requirement, a domain decomposition is done on the BEM mesh, which splits the BEM matrices into sub-blocks. On the non-diagonal sub-blocks, a low rank approximation based on a rank revealing QR decomposition is performed. For sub-blocks corresponding to far away domains, the rank can be significantly smaller than the size of the sub-block, thus reducing the storage of the sub-block. We typically see reductions of by factors around 20 between the full dense matrix and the block matrix with low rank approximations. This low rank approximation also speeds up the matrix * vector operation used intensively in the iterative method to solve the BEM system (22). This method still needs the assembly of the full sub-blocks before doing the low rank approximation, generating a time consuming assembly process. We currently are working on methods generating directly the low rank approximations of the sub-blocks.

The matrices P and Q_D (24-25b) become singular or nearly singular as $x \to y$, i.e. for self face integrals or integrals over neighbour faces with a common edge or a common node. Special methods have been included such as the ones described in [12] and [13]. These methods also allow more accurate integration on inhomogeneous faces, i.e. faces with large aspect ratio.

2.4 Divergence free surface current, connection with external circuits

The surface current $\vec{k}$ is an equivalent boundary current to the actual volume current through the volume of the conductor and needs to be divergence free [11]. However, the twisted 1-forms basis functions $\vec{V}^1$ do not satisfy this divergence free constraint. We first added it as an external constraint to the BEM system (22). More recently, we introduced the so called “loop-star” solenoidal-irrotational decomposition into the divergence free “loop” basis functions and the rest [14] [15]. At first order, a twisted 1-form associated with a surface edge represents a surface current flowing across the edge, i.e. with a unit surface flux across the edge and a zero surface flux across all the other surface edges. A loop basis function associated with a node can be seen as a linear combination with coefficients +1 or -1 of 1-forms associated with all the edges originating from the node, so that it represents a (divergence-free) current flowing around the node. One can show that when using first order basis functions, the loop basis function associated with all the nodes of the surface mesh (except one) form a complete basis of the divergence free

currents for topologically simple conductors [14]. For non simple conductors, i.e. containing holes or "handles", a few extra non-local basis functions that we call "global currents" need to be added. For example in the case of a torus, two extra global currents need to be added, one corresponding to a current flowing in the toroidal direction, and one corresponding to a current flowing in the poloidal direction.

An algorithm based on the construction of a spanning tree on the surface mesh has been developed to automatically count the number of connected part, get their topologies by computing the "Betti numbers" [16], and in particular the number of global currents and then set the global current basis functions as linear combinations of the 1-form basis functions. The degrees of freedom associated with the global currents are used to impose current vs time constraints as a simple dirichlet constraint in the BEM system (one dirichlet constraint per imposed current). This method allows imposing currents in geometries where more traditional methods using dirichlet conditions on the FEM system (12) would require the introduction of cuts and/or multi-valued degrees of freedom. The above mentioned toroidal current in a torus is such an example. The use of loop and global current basis functions also gives an easy way to compute the self and mutual inductances, by solving BEM systems (22) with simple dirichlet constraints. In this manner, the conductors can be connected to a current source, a voltage source, or an R,L,C circuit.

2.5 Global integration scheme

The time integration of the FEM system (19) is done using an implicit backward euler method [10]:

$$[M^1(\sigma) + dtS^1(\frac{1}{\mu})]a^{t+1} = M^1(\sigma)a^t - dtD^{01}(\sigma)\varphi^{t+1} + dtSa^{t+1} \tag{26}$$

The BEM part of the right hand side $dtSa^{t+1}$ also is implicit which proved to substantially improve the stability, thus allowing larger time steps. It is computed by solving the BEM system (22) (23) coupled with the FEM system (19) in an iterative way:

$$Pk_{n+1}^{t+1} = Da_n^{t+1} \tag{27}$$

$$[M^1(\sigma) + dtS^1(\frac{1}{\mu})]a_{n+1}^{t+1} = M^1(\sigma)a^t - dtD^{01}(\sigma)\varphi^{t+1} + dtQk_{n+1}^{t+1} \tag{28}$$

Until convergence on both k_n^{t+1} and a_n^{t+1}.

The FEM System (28) is solved using a direct solver. The BEM system (27) is solved using a pre-conditioned gradient method. The diagonal of the matrix has been used as a pre-conditioner. More recently, the diagonal block has been used instead [17], with significant reduction in the number of required iterations (typically by a factor between 1.5 and 3).

3 Coupling of the EM module with LS-DYNA

3.1 Mechanical solver

Once the EM fields have been computed, the Lorentz force $\vec{F} = \vec{j} \times \vec{B}$ is evaluated at the nodes and added to the mechanical solver. The mechanical and electromagnetic solvers each have their own time step. For a typical EMF simulation, the mechanical time step is about 10 times smaller than the electromagnetic one. At this time, the explicit mechanical solver of LS-DYNA is used when coupled with electromagnetism. The mechanical module computes the deformation of the conductors and the new geometry is used to compute the EM fields in a Lagrangian way.

Since the EM module is fully integrated in LS-DYNA, all the material models are available. LS-DYNA provides more than 130 metallic and non-metallic material models, many of them equipped with failure criteria, such as metals, plastics, visco-elastic, elasto-viscoplastic, glass, foam, elastomers and rubbers. Included also are strain rate and temperature dependant plasticity models such as Johnson-Cook [18], Zerilli-Armstrong [19] or Steinberg [20] models, which are particularly suitable for high speed forming simulations. Numerous equations of state are also available. These models can be used on an extensive element library with both under-integrated and fully-integrated element formulations. It includes different solid elements, thick shells, different 3- and 4-node shells and beams. At this time, the EM module is only available on solid elements. It should soon be extended to shells with appropriate treatment of the diffusion of the EM fields.

Finally, efficient contact algorithms have been developed for the mechanical solver, and over 25 different contact options are available. At this time, the contact purely is mechanical and thermal, not electromagnetic, i.e. a current can not flow from one conductor to another if they come in contact during the simulation. This will be added as well as an electromagnetic sliding contact capability, necessary for rail-gun applications.

3.2 Thermal solver

The Joule heating term $\frac{j^2}{\sigma\rho}$ is added to the thermal solver allowing to update the temperature. Several thermal models are available, isotropic, orthotropic, isotropic with phase change and so forth. The temperature can be used in turn in an electromagnetic equation of state to update the electromagnetic parameters, mainly the conductivity σ. At this time, a Burgess model [21] has been introduced.

3.3 Input-output

Electromagnetic cards have been added to the standard LS-DYNA card list used to create the input deck. The LS-PREPOST software can be used to visualize the electromagnetic fields - current density, electric field, magnetic flux density, Lorentz force, joule heating, conductivity, surface current - in the same environment as the mechanical and thermal fields. These include fringe component, iso-contour, vector plots at a given time, and also time histories on chosen elements.

4 Presentation of a typical EMF case

We now present the electromagnetic forming of a 1 mm thick aluminum sheet on a conical die, with a 4.7 cm height and a 12 cm diameter. This experiment was performed at the Department of Mechanical Engineering, University Of Waterloo, Ontario, Canada [22]. The brass coil has a 10 cm diameter spiral shape with 7 turns, and a rectangular cross section 1 cm by 0.4 cm. A hexahedral 3D mesh was built for the coil and the workpiece, and shell elements were used for the die. The mesh is composed of 20736 elements for the coil, 32320 for the aluminium sheet, with 4 elements through the thickness, and 17220 shells for the die. This mesh generated 23056 BEM faces, and 23163 BEM nodes (and hence 23163 degrees of freedom in the BEM system). Figure 1 shows the mesh at initial time. The experimental current, rising to around 100 kA in 50 μs was injected in the coil. Figure 2 shows the evolution of the shape of the plate as well as the current density in a cross section of the sheet. Figure 3 shows details of the rebounding of the sheet from the die. Figure 4 shows a comparison between the numerical and experimental final shape of the sheet. The final shape shows a good agreement. One can notice that the shape does not match the shape of the die, due to rebounding of the plate from the die and a non-uniform magnetic pressure on the sheet, with a significantly lower pressure at the centre. This low pressure area is reflected in the current density plots, and is due to the shape of the coil.

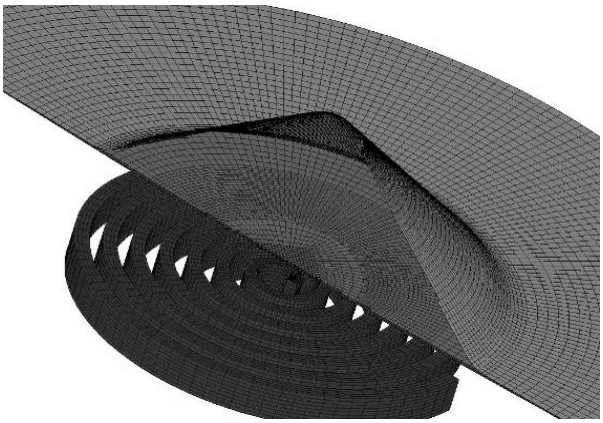

***Figure 1**: mesh of the EMF case. Only ½ of the sheet and die are represented.*

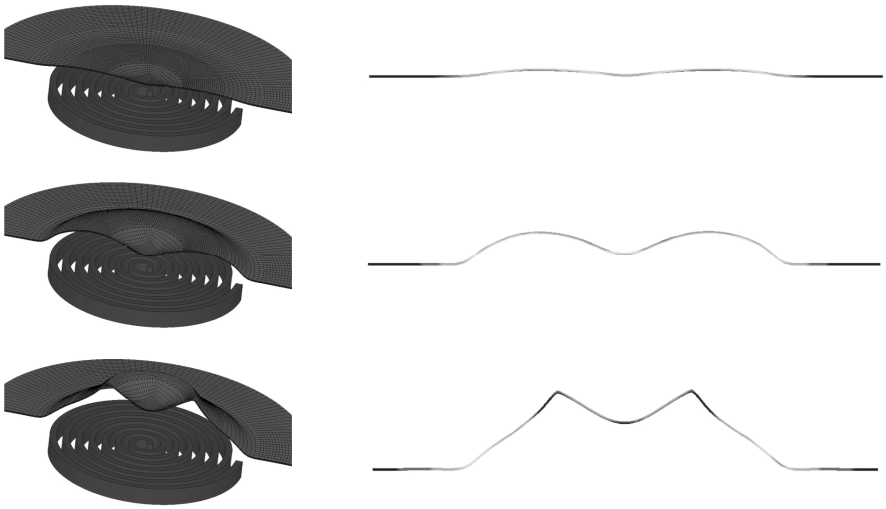

***Figure 2**: 3D shape of the sheet (left, only ½ of the sheet is represented), and current density in a cross section of the sheet (right) at 45μs (top), 70μs (middle) and 100μs (bottom). The scale in the z-direction has been increased in the cross sections for better visibility.*

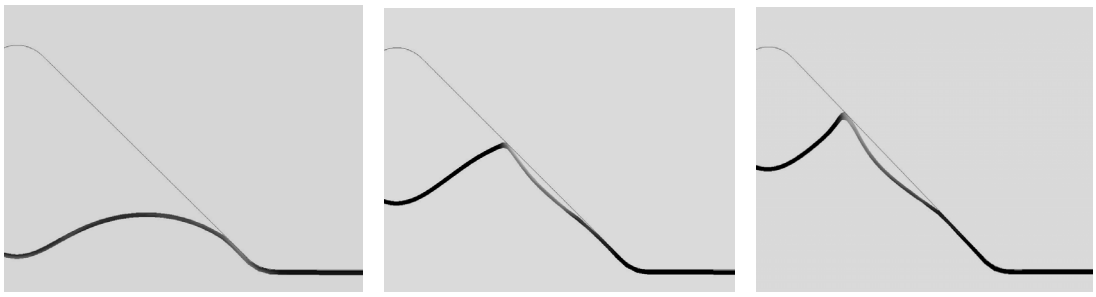

***Figure 3**: Detail of the rebounding of the sheet from the die: cross section of the sheet and die at 70μs (left), 100μs (middle) and 130μs (right). Fringes are of plastic strain.*

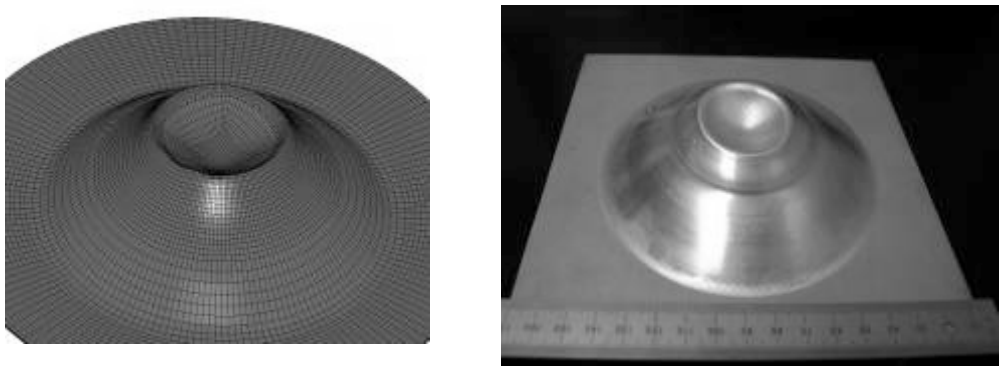

***Figure 4**: numerical (left) and experimental (right) final shape of the sheet.*

5 Conclusion

The newly introduced Electromagnetism module of LS-DYNA was presented. The electromagnetic fields are computed by solving the Maxwell equations in the eddy-current approximation, using a Finite Element Method for the conductors coupled with a Boundary Element Method for the surrounding air and insulators. Loop basis functions are used to represent the BEM surface current, allowing to handle the divergence free constraint as well as easy connection with external circuits. A 2-dimensional ax symmetric version of the EM module is also available.

This module is integrated in the “ls980” version which should be released in late 2008. In the mean time, it is available as a “beta version”. The near-term future developments for the EM module include new BEM assembly methods, introduction of tetrahedral and wedge elements, development of an Massively Parallel Processor (MPP) version (the rest of LS-DYNA is currently available in MPP, but the EM module only is serial). The planned mid-term developments include the introduction of sliding contact capabilities for the electromagnetism, remeshing capabilities, extension to other solvers (magnetostatics and so forth). Longer-term developments could include the introduction of magnetic materials.

Acknowledgment

The authors would like to thank M. Worswick and J.Imbert at the University of Waterloo, Ontario, Canada; G. Daehn, M. Seth Y. Zhang and A. Vivek at The Ohio State University, Columbus, OH, USA; G. Fenton at Applied Research Associates, Inc., Albuquerque, NM, USA; I. Ulacia at the University of Mondragon, Gipuzkoa, Spain; G. Le Blanc and G. Avrillaud at International Technologies for High Pulsed Power, Thegra, France; J. Thomas at The University of Michigan, Ann arbor, MI, USA; J. Shang at Hirotec America, Auburn Hills, MI, USA, and P.L. Hereil, P.Y. Chanal and A. Lefrancois at Centre d’Etudes De Gramat, Gramat, France, for very fruitful collaborations and for giving access to experimental or numerical data for comparisons and benchmarks.

References

[1] LS-DYNA Theory Manual, LSTC.

[2] *P. L’Eplattenier; G. Cook, C. Ashcraft; M. Burger; A. Shapir;, G. Daehn; M. Seith*: “Introduction of an Electromagnetism Module in LS-DYNA for Coupled Mechanical-Thermal-Electromagnetic Simulations”, 9th International LS-DYNA Users conference”, Dearborn, Michigan, June 2005.

[3] *J. Jin*: “The Finite Element Method In Electromagnetics”, Wiley, 1993.

[4] *J. Shen*: “Computational Electromagnetics Using Boundary Elements, Advances In Modelling Eddy Currents”, Topics in Engineering Vol 24, Series Eds: C.A. Brebbia and J.J. Connor, Southampton and Boston: Computational Mechanics Publications, 1995”.

[5] *J.C. Nedelec:* “A New Family of Mixed Finite Elements in R3”, Num. Math, 50:57-81, 1986.

[6] *O. Biro and K. Preis:* “On the use of the magnetic vector potential in the finite element analysis of three-dimensional eddy currents”, IEEE Transaction on Magnetics, 25(4)3145-3159,1989.

[7] *P. Castillo, R. Rieben and D. White:* “FEMSTER: An object oriented class library of discrete differential forms”. In Proceedings of the 2003 IEEE International Antennas and Propagation Symposium, volume 2, pages 181-184, Columbus, Ohio, June 2003.

[8] *Z. Ren and A. Razek:* “Computation of 3-D electromagnetic field using differential forms based elements and dual formulations”, International Journal of Numerical Modeling: Electronic Networks, Devices and Fields, Vol. 9, 81-98 (1996).

[9] *R. Rieben:* “A Novel High Order Time Domain Vector Finite Element Method for the Simulation of Electromagnetic Devices”, Ph-D Thesis, University of California Davis, 2004.

[10] *R. Rieben and D. White:* “Verification of high-order mixed finite element solution of transient magnetic diffusion problems”, IEEE Transaction on Magnetics, 42(1), 25-39, 2006.

[11] *Z. Ren, A. Razek:* “New technique for solving three-dimentional multiply connected eddy-current problems”, IEE Proceedings, Vol. 137, Pt. A, No 3, May 1990.

[12] *W. Wang and N. Atalla:* “A numerical algorithm for double surface integrals over quadrilaterals with a 1/r singularity”, Communications in Numerical Methods in Engineering, 13, 885-890 (1997).

[13] *S. Sauter:* “Cubature techniques for 3-D Galerkin BEM”, Boundary Elements: Implementation and Analysis of Advanced Algorithms, W. Hackbusch, G. Wittum eds, NNNFM 54, Vieweg-Verlag (1996), 29-44.

[14] *G. Vecchi:* “Loop-Star Decomposition of Basis Functions in the Discretization of the EFIE”, IEEE Transactions on Antennas and Propagation, Vol. 47, No 2, February 1999.

[15] *J.L. Volakis, D.B. Davidson:* “Iterative-Solver Convergence for Loop-Star and Loop-Tree Decompositions in Method-of-Moments Solutions of the Electric-Field Integral Equation”, IEEE Antennas and Propagation, 46(3), 80-85, June 2004.

[16] *A. Bossavit:* “Computational Electromagnetism”, Academic Press (Boston), 1998.

[17] *K.E. Chen:* “On a class of preconditioning methods for dense linear systems from boundary elements”, SIAM J. Sci. Comput. 20(2), 684-698, 1998.

[18] *G.R. Johnson, and W.H. Cook:* “Fracture Characteristics of Three Metals Subjected to Various Strains, Strain Rates, Temperatures and Pressures”, Engineering Fracture Mechanics, Vol 21, No 1, pp 31-48, 1985.

[19] *F.J. Zerilli and R.W. Armstrong:* "Dislocation-mechanics-based constitutive relations for material dynamics calculations", J. Appl. Phys. 61(5), March 1987.

[20] *D.J. Steinberg, S.G.Cochran, M.W.Guinan:* “A Constitutive Model for Metals Applicable at High-Strain Rate”, J. Appl. Phys. 51,1498 (1980)

[21] *T.J. Burgess:* “Electrical resistivity model of metals”, 4th International Conference on Megagauss Magnetic-Field Generation and Related Topics, Santa Fe, NM, USA, 1986

[22] *J. Imbert, M. Worswick, S. Winkler, S. Golovashchenko, V. Dmitriev:* “Analysis of the Increased Formability of Aluminum Alloy Sheet Formed Using Electromagnetic Forming”, Proceedings, SAE 2005, SAE Paper No. 2005-01-0082

Numerical Modelling of High Speed Blanking Considering Thermoviscoplastic Effects*

K. B. Sidhu, I. Peshekhodov, B.-A. Behrens

Institute of Metal Forming and Metal-Forming Machines (IFUM),
Leibniz University of Hannover, Germany

Abstract

To achieve the required specifications of the cut-edge profile of a blank, a time consuming trial and error procedures based on empirical information are utilized. However, the modern industry demands high quality product specifications in the shortest possible production time. Therefore, in order to predict the cut-edge profile and speed up the production process, it is essential to develop a reliable numerical model of the high speed blanking process which can predict the cut-edge profile of the blanks.

In this study, the Lagrangian based finite element (FE) approach was used to model large strain deformation that takes place in the shearzone during blanking. However, the large deformation is difficult to model using Lagrangian approach as it leads to a severe distortion of the FE mesh. Therefore, in order to overcome a premature termination of the analysis due to the mesh distortion, an adaptive remeshing and rezoning technique was developed. Furthermore, to model the ductile fracture, the discrete crack propagation method was implemented in the MSC.Marc®

Due to high speed of the cutting stamp, thermoviscoplastic material behaviour has to be taken into account. The Johnson-Cook plasticity model was used to model viscoplasticity. The results obtained from the FE analysis are presented in this paper.

Keywords

Blanking, Finite element method (FEM), Plasticity, Fracture

---

* *This work is based on the results of GRK615 / B8; the authors would like to thank DFG for its financial support*

1 Introduction

The blanking process is widely used for cutting sheet metal components in large quantities in a broad range of industries. Almost every sheet part that leaves the assembly line, either as a pre-formed piece or a finished part, undergoes blanking. During this process, the sheet is placed between the blankholder and the die, and a predefined blank shape is punched-out of the sheet with the cutting stamp. Due to the sharp stamp-edge, highly localised shear deformation takes place in the sheet leading to ductile fracture. Consequently, the cutting of sheet leads to a typical cut-edge profile of the blank which can be distinguished in four zones: rollover, shear edge, fracture and burr (Fig. 1). The quality of the cut-edge is determined based on the size of these zones, a good quality of the cut-edge implies maximum size of shear-edge and the minimum size of rollover, fracture zone and burr.

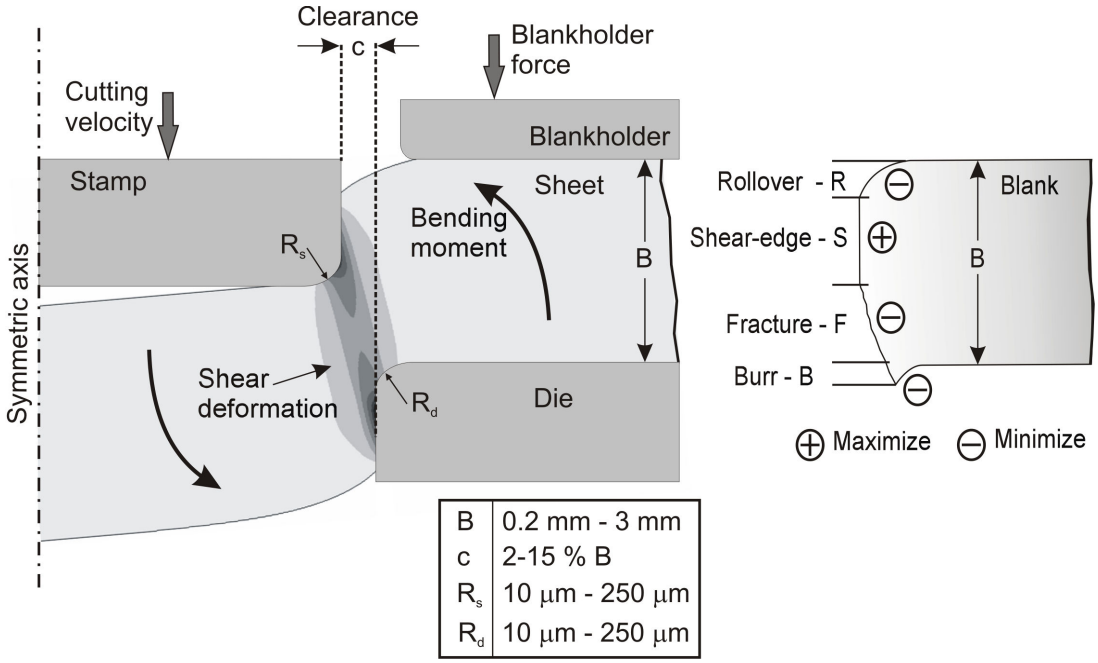

***Figure 1**: Blanking process (left) and a typical cut-edge profile (right)*

The cut-edge profile is dependent on the process parameters and the material behaviour of the sheet metal. The process parameters include the clearance, cutting velocity, tool geometry, tool wear, kinematic of the press, geometry and sheet thickness of the component. The material properties of the sheet include strain rate and temperature dependent flow behaviour and grain size [1]. To achieve a desired quality of the cut-edge, usually time consuming trial and error procedures based on empirical knowledge are used. Therefore, a development of a reliable finite element model (FEM) of the blanking process is necessary in order to predict the cut-edge profile, and consequently, speed-up the development of the production process leading to the desired quality of the cut-edge.

At present no commercial finite element package capable of simulating blanking process with a required degree of accuracy is available. In order to accurately simulate blanking, commercial finite element software should be capable of implementing adaptive remeshing technique and discrete crack propagation in order to overcome large-localised

shear deformation and ductile fracture [2]. Furthermore, the thermoviscoplastic effects due to high speed of the cutting stamp should also be taken into account to model an industrial blanking process that is usually done with high stamp velocities.

Therefore, the main objective of this paper is to present a fundamental FEM model to simulate blanking by taking into account the characteristic extremely large and local elastoviscoplastic deformation, and eventually modelling of material separation due to ductile fracture.

2 Adaptive Remeshing

The cut-edge radius of the blanking tools is usually extremely small, generally of order 10 µm to 30 µm. This leads to a very large and localised shear deformation, especially in the proximate region of the tools cutting edge, causing a severe distortion of the finite element mesh in this region. Therefore, in order to overcome the problem of severe element distortion in blanking, an adaptive remeshing technique (figure 2) given by Rank et el. [3] was implemented MSC.Marc®. The use of an adaptive mesh keeps the number of elements to the minimum required and, consequently, significantly reduces the computing time and effort due to a considerable reduction in number of degrees of freedom (DOF).

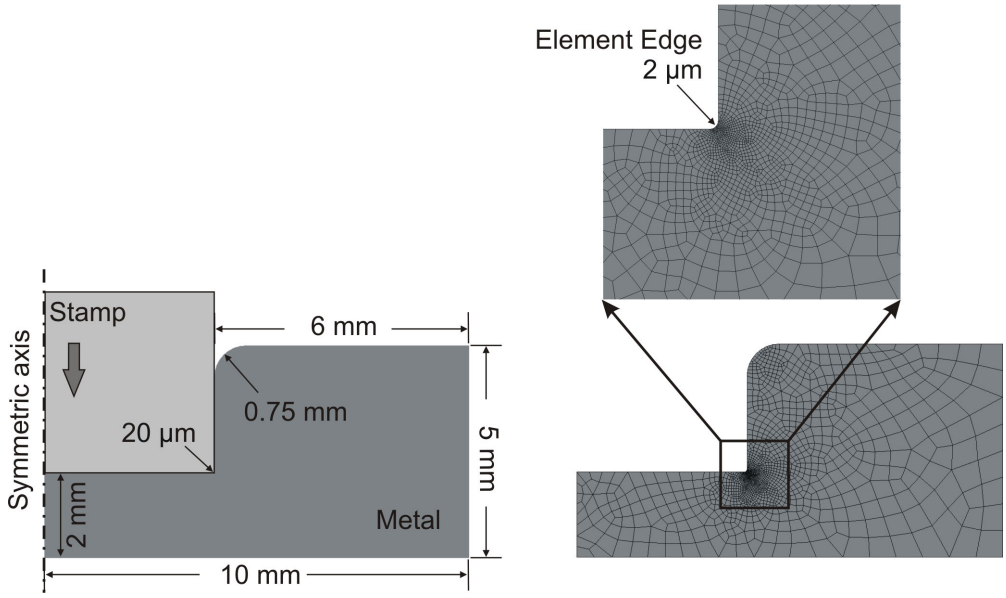

Figure 2: *Adaptive mesh*

In this study bi-linear, four-nodded, isoparametric quadrilateral elements with four integration points were implemented for two dimensional modelling of sheet continuum. The constant dilatational elements are recommended for incompressible, large strain plasticity since the conventional elements causes volumetric locking due to over constraints for nearly incompressible behaviour. Therefore, the element type 10 was selected from MSC.Marc® elements library to model axi-symmetric of blanking process.

3 Modelling of Damage and Ductile Crack Propagation

In this paper, the uncoupled damage [4,5,6] was implemented in which mechanical properties are not influenced by damage laws. The damage parameter is computed based on an integral of stress function over equivalent plastic strains. This approach is easy to implement in a finite element code, however a drawback of this method is that it does not take in account the gradual decrease of stress carrying capacity of the material due to damage evolution. Therefore, in this paper a simple fracture criterion given by Oyane et el, as given in equation 1, was used as an indicator the crack initiation and propagation [6].

$$\int_0^{\bar{\varepsilon}_p} \left(1 + 3.9\frac{\sigma_h}{\bar{\sigma}}\right) d\bar{\varepsilon}_p > C_r, \tag{1}$$

where $\frac{\sigma_h}{\bar{\sigma}}$ is the triaxiality which is hydrostatic pressure over equivalent (von Mises) stresses and C_r is the material dependent critical value.

In order to model the ductile crack propagation in blanking, the modified nodal release method [7, 8, 9] was implemented followed by rezoning of the state variables from the pervious increment to the current increment. In the modified nodal release technique, the nodes of an element near to the crack tip are moved in order to accommodate the crack extension as shown in figure 3. The advantage of this method is that it is possible to follow the predicted crack with only slight modification in the local mesh near to the crack tip.

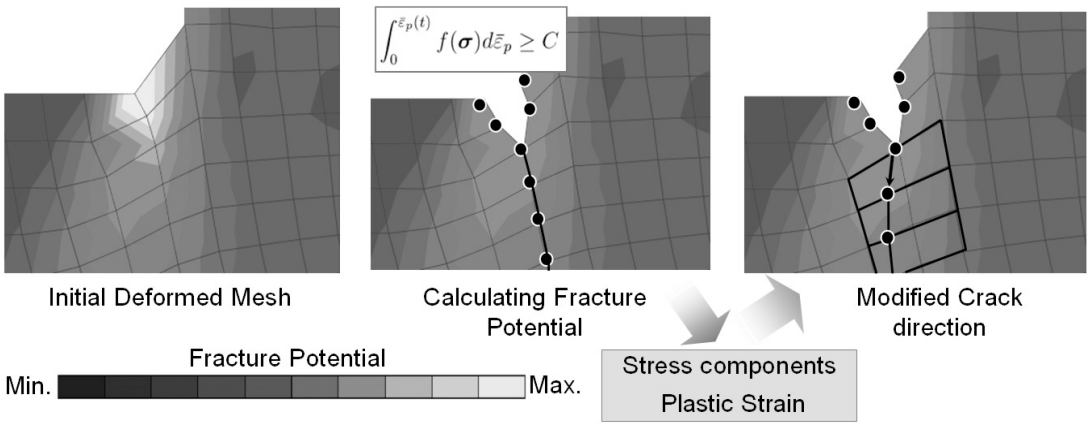

Figure 3: *Implementation of crack interface using modified nodal release method with rezoning of state variables [7, 9]*

4 State Variables Transfer

After the remeshing step, the state variables are transferred from the old mesh to the new mesh. The transfer of the state variables from the old mesh to the new mesh is also

known as rezoning. During rezoning, the values of the nodal variables are transferred from nodes of the old mesh to the new mesh, and the state variables at integration points are transferred from to the new integration points.

In this study the Inverse distance weighted method (IDW) [10] was implemented for rezoning of state variables. In IDW, the value at the new integration point or the node is interpolated from all the values at the integration points or the nodes of the old mesh that are specified in the patch, as shown in figure 4. The values at the new integration point or the node using the following equations:

$$
\begin{aligned}
R_i &= \sqrt{\left(x_p - x_i\right)^2 + \left(y_p - y_i\right)^2}, \\
SV_p &= \frac{\sum_{i=1}^{n} SV_i}{\sum_{i=1}^{n} R_i^2} \quad ; \text{if } R_i \neq 0, \\
SV_p &= SV_i \qquad ; \text{if } R_i = 0,
\end{aligned}
\tag{2}
$$

where x_p, y_p are the coordinates of new point in current mesh, and x_i, y_i are the coordinates of points in pervious mesh. R_i is the radial distance between the two points. SV_p represents the state variable at the new point, and SV_i represents the state variable at the point in the pervious mesh.

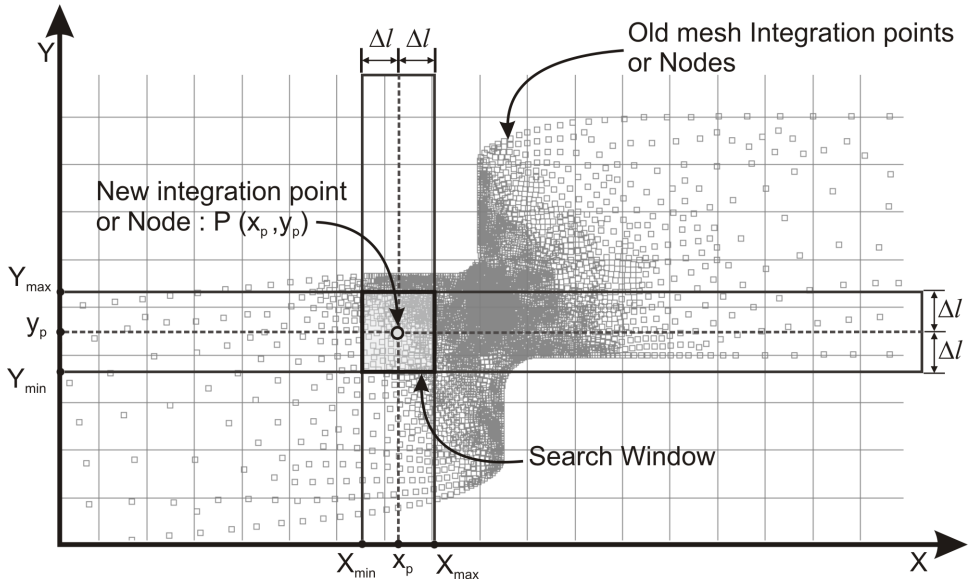

Figure 4: *Rezoning of state variables using the Inverse distance weighted method*

5 Johnson-Cook Viscoplasticity

It has been observed that the flow stresses of the metal increases as the strain rate increases and decreases as temperature increases [11]. The high stamp velocities used

in blanking performed in the industry lead to high strain rates and an increase in temperature due to plastic work dissipation in the shear zone of the sheet. Therefore, the increase in strain rate leads to viscous effects where as increase in temperature leads to thermal softening in the sheet. Hence, a temperature depended elastoviscoplastic behaviour should be taken into account to represent the sheet metal behaviour during high speed blanking.

The elastoviscoplastic model given by Johnson-Cook [12] was implemented to get an accurate representation of the strain rate and temperature dependency of material behaviour of sheet metal as given in the following equation:

$$\sigma_f = \left(A + B\varepsilon^n\right)\left(1 + C\ln\frac{\dot{\varepsilon}}{\dot{\varepsilon}_0}\right)\left(1 - T_\theta\right), \qquad (3)$$

$$T_\theta = \begin{cases} 0 & T \le T_R \\ \left(\dfrac{T - T_R}{T_{ml} - T_R}\right)^m & T_R < T < T_{ml} \\ 1 & T < T_R, \end{cases}$$

where *A, B, C, n, m* are material parameters, σ_f is the flow stresses (von Mises), $\dot{\varepsilon}$ is the actual strain rate, *T* is the actual temperature, $\dot{\varepsilon}_0$ is the initial strain rate, T_R is transition temperature, T_{ml} is the melting temperature. The transition temperature of a metal may vary from T_R = 0.2 T_{ml} to 0.4 T_{ml} [13]. This equation shows that the thermal softening takes place once the temperature of the sheet becomes higher then transition temperature T_R. The material parameter used for Ck45N is shown in the following table.

A	B	C	n	m	T_{ml} [°C]	T_R [°C]
500	693	0.0114	0.36	1	1600	320

Table 1: *Material parameters of Ck45N [14]*

The heat generation due to plastic work dissipation is calculated by the following energy balance equation [15], and due to adiabatic nature of the process heat transfer to the surrounding and in the sheet is neglected.

$$\partial T = \frac{k\ \sigma_f}{\rho\ c_p}\ \dot{\varepsilon}\ \partial t, \qquad (4)$$

where ∂T is the increase in temperature, ∂t is the infinitesimal time increment, *k is* the conversion factor and is assumed to be 0.95, ρ is the mass density, and c_p is the heat capacity.

6 Influence of Cutting Velocity on the Cut-Edge Profile

It has been experimentally observed that the cutting velocity has a significant influence on the cut-edge [16]. The size of shear-edge increases with an increase in the cutting velocity due to thermal softening of the sheet material. This thermal effect is an adiabatic process in which the heat is generated due to high strain rate; consequently, the kinetic energy is almost completely transferred into heat resulting in a sharp and localised increase in temperature of the sheet in a split second as shown in figure 5 the temperature increase at 80 % deformation of the sheet with respect to the original undeformed.

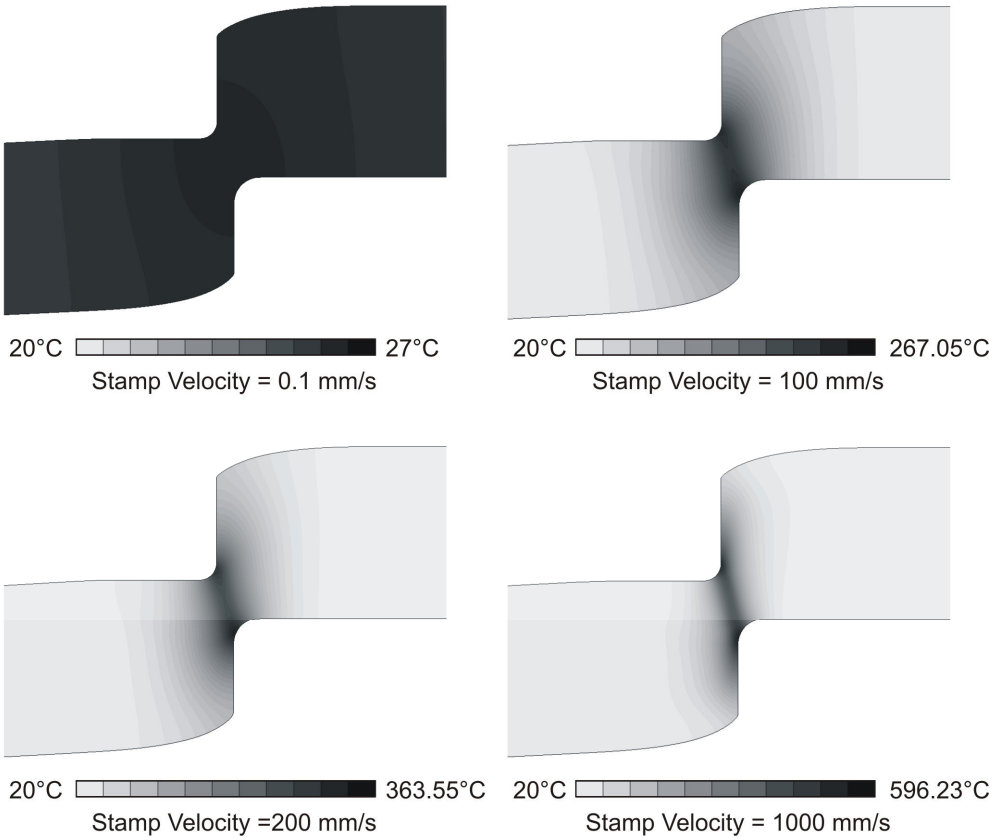

Figure 5: *Increase in temperature with the increase in stamp velocity. The deformation shown is 80 % with respect to the original undeformed sheet.*

As presented in Section 5, the thermal softening behaviour of the sheets takes place once the temperature of the sheet gets higher then transition temperature T_R and it is assumed to be 20 % of the melting temperature. Therefore, according to equation 3, as soon as heat generated due to plastic dissipation in sheet increases its temperature more then transition temperature, the term T_θ becomes non-zero. Consequently, it causes a decrease in the flow curve of the sheet metal. As shown in figure 6, the transition zone lies between the stamp velocity of 100 mm/s and 200 mm/s. In this zone, the temperature due to the heat generated becomes higher then the transition temperature. Therefore, as presented in figure 6, the von Mises stresses at 80 % deformation of the sheet increases due to the viscous effect caused by strain rates and reaches a peak and then starts

decreasing due to the thermal softening influence. Therefore, this implies that the shear edge first decreases with the increasing strain rate and after the transition zone it starts to increase again due to thermal softening of the sheet as shown in figure 6.

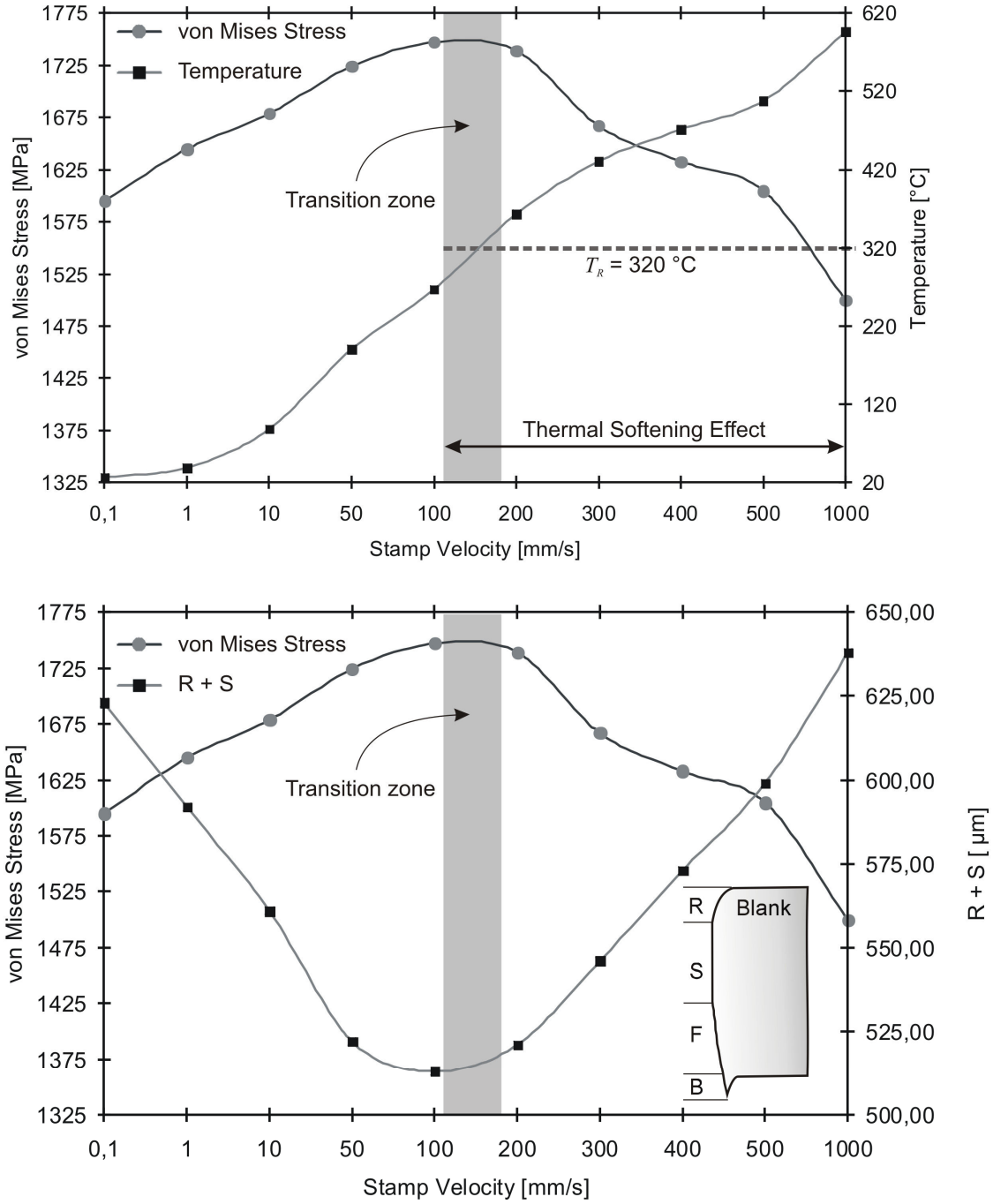

Figure 6: *Influence on stamp velocity on the cut-edge profile*

7 Conclusions

In this paper, a numerical model to simulate blanking and consequently predict the cut-edge profile of the blank was presented. An adaptive remeshing, rezoning and discrete crack propagation techniques were implemented in a commercial finite element software MSC.Marc®. The adaptive mesh based on Rank et al [3] provides a effective and robust mesh to capture a sharp edge of order 10 µm to 30 µm and at the same time keeps the number of elements to the minimum required and, thus, reducing the computational costs. Fracture criterion given by Oyane et el [6] gives relatively good results, however, it is necessary to develop a fracture criterion based on continuum damage mechanics. The elastoviscoplastic model given by Johnson-Cook [12] was implemented to get an accurate representation of the strain rate and temperature dependency of material behaviour. With the help of this model it is observed that the size of the shear-edge increases with the increase in the cutting velocity due to thermal softening of the sheet material. The thermal softening behaviour of the sheets takes place once the temperature of the sheet becomes higher then transition temperature T_R which is assumed to be 20 % of the melting temperature [13]. The prediction of rollover shape and the shear-edge can be predicted within the experimentally observed range for 0.1 mm clearance as shown in figure 7.

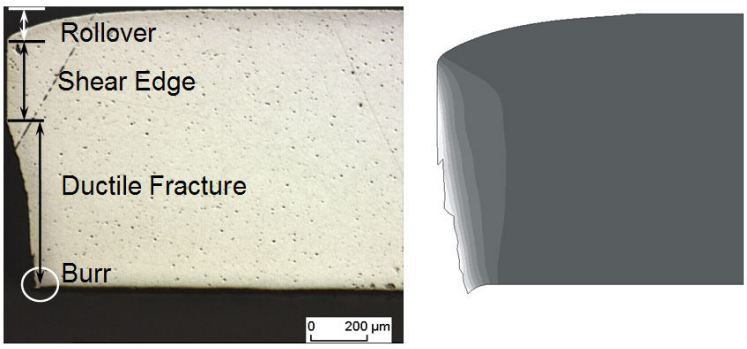

Figure 7: *Comparison of the micrograph (left) with blanking simulation at 0.1 mm clearance and 50 mm/s stamp velocity*

References

[1] *H.-H.Schmuetsch:* Einflussgroessen auf das Schneidergebnis beim Scherschneiden von Feinblechen, Ph.D thesis, IFUM, University of Hannover, 1990.

[2] *D. Brokken:* "Numerical modelling of ductile fracture in blanking", Ph.D. thesis, Technische Universiteit Eindhoven, Netherlands, 1999.

[3] *E. Rank, M. Schweingruber and M. Sommer:* Adaptive mesh generation and transformation of triangular to quadrilateral meshes, Communications on Numerical Methods in Engineering, 9 (1993), p. 121–129.

[4] *F. A. McClintock:* A criterion for ductile fracture by growth of holes subjected to multi-axial stress-states. J. of App. Mechanics. Vol. 35 (1968), p. 33-39.

[5] *J. R. Rice, D. M. Tracey:* On the ductile enlargement of voids in triaxial stress fields. J. of Mechanics and Phy. of Solids. Vol. 17 (1969), p. 201-217.

[6] *M. Oyane, T. Sato, K. Okimoto, S. Shima:* Criteria for ductile fracture and their application, J. of Mech. Work. Tech. Vol. 4 (1980), p. 65-81.

[7] *B.-A Behrens, K.B. Sidhu, O. Posse:* Different Approaches to Model the Material Separation during the Blanking Process using FEM, International Deep Drawing Research Group Conference (IDDRG '06), Porto, Portugal, June 2006.

[8] *B.-A Behrens, K.B. Sidhu:* Finite Element Analysis of Nodal Release Approach to Model Ductile Fracture in Metal Sheets. XIV Conference Computer Methods in Materials Science, KomPlasTech '07, Zakopane, Poland, January 2007.

[9] *B.-A Behrens, K.B. Sidhu:* Numerical Modeling and Analysis of Ductile Crack Propagation in Blanking Process Using Modified Nodal Release Method. 12th International Conference on Sheet Metal, SheMet '07, Palermo, Italy, April 2007.

[10] *M. Dyduch, A.M. Habraken, S. Cescotto:* Automatic adaptive remeshing for numerical simulations of metalforming, *Comp. Meth. Appl. Mech. Engrg.* 101, 283–298, 1992.

[11] *E. El-magd, C. Treppmann, M. Körthäuer:* Experimentelle und numerische Untersuchen zum thermomechanischen Stoffverhalten. 'Hochgeschwindigkeits-spanen metallischer Werkstoffe', PZH, Universität Hannover, January 2004.

[12] *G. R. Johnson and W.H. Cook:* A constitutive model and data for metals subjected to large strains, high strain rates and high temperatures. Proceedings of the seventh international symposium on ballistics. Hague, Netherlands. 1983.

[13] *C. Treppmann:* Fließverhalten metallischer Werkstoffe bei Hochgeschwindigkeits-beanspruchung Dr.-Ing. Dissertation, RWTH Aachen, 2001 .

[14] *K. Kalisch:* FEM-Beschreibung der Einflüsse der Werkzeuggeometrie bei der Hochgeschwindigkeitszerspanung, Universität der Bundeswehr Hamburg, Germany. 2006.

[15] *L.W. Meyer, T. Halle:* Ermittlung von Werkstoffkenndaten für die numerische Simulation des Hochgeschwindigkeitsspanens. 'Hochgeschwindigkeitsspanen metallischer Werkstoffe', PZH, Universität Hannover, January 2004.

[16] *M. Grünbaum, J. Breitling, T. Altan:* Influence of high cutting speeds on the quality of the blanked parts. Report No. ERC/NSM - S-96-19, NSF Engineering Research Center for Net Shape Manufacturing, Ohio State University. May 1996.

Modeling and Simulation of 3D EMF Processes[1]

J. Unger[1], M. Stiemer[2], M. Schwarze[3], B. Svendsen[1], H. Blum[2], S. Reese[3]

[1]Chair of Scientific Computing, TU Dortmund
[2]Chair of Mechanics, TU Dortmund
[3]Institute of Solid Mechanics, TU Braunschweig

Abstract

A recent interest in potential industrial applications of electromagnetic forming processes has inspired a demand for adequate simulation tools. Aiming at the virtual design of industrial applications, the purpose of this work is to develop algorithmic formulations particularly suitable to reduce the enormous computational cost inherent to 3D simulations. These formulations comprise a carefully chosen discretization, highly accurate methods for data transfer between electromagnetic and mechanical subsystems, an efficient solid shell formulation, and a termination criterion for the electromagnetic field computation. As a result the simulation time is reduced by about one order of magnitude.

Keywords:

Modeling, electromagnetic metal forming

1 Introduction

Electromagnetic forming (EMF) is a dynamic, high strain-rate forming method in which strain-rates of 10^3 s^{-1} arise. The deformation of the work piece is driven by the interaction of a pulsed magnetic field triggered by a nearby tool coil with eddy currents induced in the work piece. This interaction effects a material body force, the Lorentz force, and the electromotive power, representing an additional supply of momentum and energy to the material. On the other hand the electromagnetic part of the system is sensitively influenced by the spatio-temporal evolution of the deformation of the mechanical structure. An increasing interest

[1] *This work was carried out in the context of the German National Science Foundation (Deutsche Forschungsgemeinschaft (DFG)) Research Group FOR 443. The authors wish to thank the DFG for its financial support.*

in this forming operation, recently caused a considerable effort to simulate such coupled processes. However, approaches reported on so far were mainly restricted to axisymmetric geometries [1, 2, 3, 4, 5] or to small deformation problems [6]. Yet, it is the 3D modeling capability in combination with the large inelastic deformations that is required to advance effectively in the design of industrial EMF processes. To meet these modeling requirements the sound derivation of a physical model of the relevant magneto-mechanical phenomena has been presented in [7]. It is algorithmically implemented in [8] and [9].

While typical 2D models of EMF in general exhibit a size of between about 3000 and 10000 degrees of freedom, the number of degrees of freedom for similar 3D models is about one order of magnitude higher. Consequently, the requirements of a three dimensional simulation often exceed the computational resources contemporary computers offer. The goal of the present work is to develop new approaches to the simulation of relevant 3D models for EMF that reduce the computational cost to a range that allows for numerical simulations on contemporary computers. A main result is an accurate and efficient coupling scheme of the electromagnetic and mechanical subsystems that enables the use of solid shell elements [10] (Section 2). Further, a termination criterion for the electromagnetic part of the model leads to a significant gain in efficiency (Section 3). In Section 4 the benefit of all these methods is validated with a fully coupled forming operation. All developed methods will be demonstraded by means of a particular model problem. Although the presented forming geometry is rather exceptional (see Figure 1), dimensions and timescales carry over to other geometries. The coupled multifield model for electromagnetic forming considered here represents a special case of the general continuum thermodynamic formulation for inelastic non-polarizable and non-magnetizable materials given in [7]. In summary, this special case is based on the quasi-static approximation to Maxwell's equations, in which the wave character of the electromagnetic fields is neglected. In this case, the unknown fields of interest are the motion field $\boldsymbol{\xi}$, the scalar potential χ and the vector potential $\boldsymbol{a}$ determining in particular the magnetic field in the usual fashion [11]. Assuming Dirichlet boundary conditions for all fields, one derives the weak field relations

$$
\begin{aligned}
0 &= \int_{B_r} (\varrho_r \ddot{\boldsymbol{\xi}} - \boldsymbol{l}_r) \cdot \boldsymbol{\xi}_* + \boldsymbol{K}\boldsymbol{F}^{-\mathsf{T}} \cdot \nabla \boldsymbol{\xi}_* \,, \\
0 &= \int_R \{\dot{\boldsymbol{a}} + \boldsymbol{L}^{\mathsf{T}} \boldsymbol{a}\} \cdot \boldsymbol{a}_* + \int_R (\chi - \boldsymbol{a} \cdot \boldsymbol{v}) \operatorname{div} \boldsymbol{a}_* + \kappa_{\mathsf{EM}} \operatorname{curl} \boldsymbol{a} \cdot \operatorname{curl} \boldsymbol{a}_* \,, \\
0 &= \int_R \nabla \chi \cdot \nabla \chi_* \,,
\end{aligned}
\tag{1}
$$

for $\boldsymbol{\xi}$, $\boldsymbol{a}$, and χ, respectively. Here, $\boldsymbol{\xi}_*$, $\boldsymbol{a}_*$, and χ_* represent the corresponding test fields. Further, R represents a fixed region in Euclidean point space containing the system under consideration in which the electromagnetic fields exist and on whose boundary the boundary conditions for these fields are specified. Here, the system comprises the sheet metal consisting of the aluminum alloy AA 6060, the tool coil consisting of technically pure copper and air (see Figure 1). Electromagnetic and mechanical material properties of the system can be found in [8].

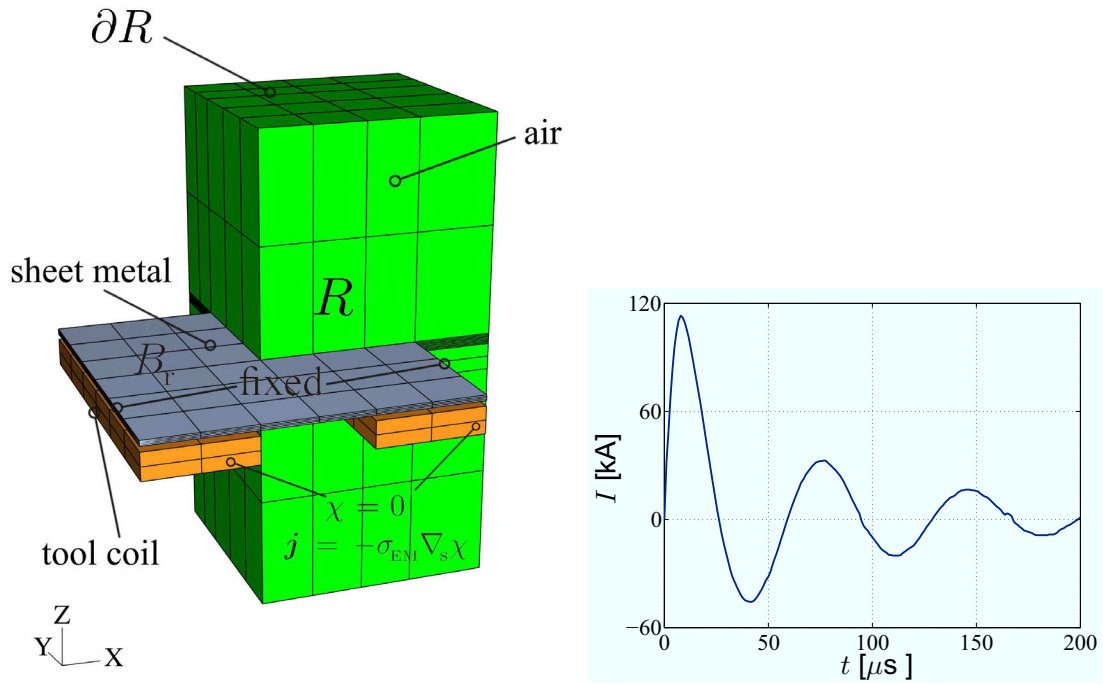

Figure 1: Exemplary forming setup including tool coil, sheet metal, and air. Here, R denotes the whole computational domain with boundary ∂R and B_r the mechanical domain. At ∂R homogeneous Dirichlet boundary conditions are assumed. The experimentally measured input current is implemented as a Neumann boundary condition for the electric scalar potential. On the mechanical side, the lateral edges of the sheet metal are fixed.

2 Mesh Adaption and Data Transfer for Solid Shell Elements

In the case of a staggered approach the solution of the coupled system is computed on two meshes. In [8] a coupled simulation has been presented where the discretization of the electromagnetic subsystem was based on an Eulerian formulation of the discrete system. This means that the Lagrangian mesh for the mechanical structure is moved over a *fixed* Eulerian mesh for the electromagnetic field. However, there are problems inherent to this approach since a contribution to the mass matrix arises as soon as a point is covered by the structure and it disappears when it is uncovered again (see Figure 2 above right). Methods that rely on this Euler-Lagrange approach are sometimes called fictitious boundary methods It has turned out that this change of the discretization causes oscillations in the time derivative of the vector potential and thus in the Lorentz force. If a good approximation to the forces is required an ALE-based method is more promising. Here, the position of the electromagnetic mesh is adapted to the current position of the structure so that the local discretizations never changes (see Figure 2 below right and left). The ALE-mesh adaption is based on a Lagrangian smoothing algorithm [12]. In the above example deformation and body force data are transferred from each single element to each element. In this respect, both discretizations can not be chosen independently. This situation can lead to an unnecessary refinement of one of the subdomains when it is necessary to refine the other

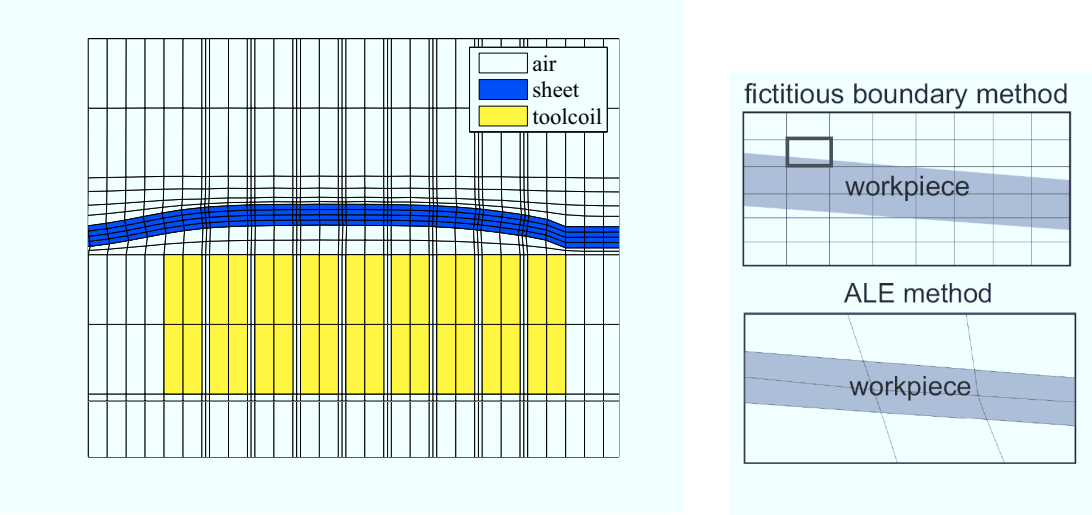

Figure 2: Interaction between the mechanical and electromagnetic mesh. Left: 2D Modeling of an EMF process by means of the ALE algorithm. Right: Schematics of the fictitious boundary method (fixed Eulerian mesh) and the ALE method (matching meshes).

(see mesh in Figure 2 left). Considering the complexity of 3D EMF simulations, there is a strong motivation to refine both meshes independently. This requirement becomes even more significant if shell elements – commonly used in sheet forming simulations – are used for the mechanical mesh. The discretization in thickness direction of the mechanical mesh is then fixed to one layer of elements, which is by far to wide for accurate electromagnetic field computation under typical situations. Here, an independent mesh refinement in thickness direction of the electromagnetic component of the sheet metal is mandatory.

The approach presented here is based on the fact that at t = 0 the boundaries of the discretized electromagnetic and mechanical domain overlap. Later the sheet deforms and the vertex positions $\tilde{\mathbf{x}}$ of the electromagnetic mesh elements have to be adopted such that mesh domains are congruent again. To achieve this, the vertex positions of the electromagnetic elements of the sheet metal are moved according to the mechanical deformation first and then the remaining vertex positions of the electromagnetic mesh are adapted. In the example shown in Figure 2 on the left, the vertices of the elements in the sheet of both the mechanical and the electromagnetic mesh match. In contrast, this is not the case when solid shell elements are used. A mapping of the mechanical deformation to those vertices of the electromagnetic mesh which are contained in the sheet metal is required. One proximate approach to achieve this is given by the simple shape function mapping of the actual nodal element positions $\mathbf{x}^e(t_n)$

$$\tilde{\mathbf{x}}^i_{\mathrm{SM}}(t_n) = \mathbf{H}(\zeta^i(\tilde{\mathbf{x}}^i_{\mathrm{SM}}(t_n))\mathbf{x}^e(t_n) \tag{2}$$

to the element vertex i contained in the sheet metal yielding its new position $\tilde{\mathbf{x}}^i_{\mathrm{SM}}(t_n)$ at t_n. Here, $\tilde{\mathbf{x}}_{\mathrm{SM}}(t_n)$ represents the positions of all element vertices of the electromagnetic mesh which are contained in the sheet, $\mathbf{H}$ the shape function matrix evaluated at the local element coordinates ζ^i which corresponds to $\tilde{\mathbf{x}}^i_{\mathrm{SM}}(t_n)$. Next, all variable positions of $\tilde{\mathbf{x}}$ are adopted to $\tilde{\mathbf{x}}_{\mathrm{SM}}$ via the aforementioned smoothing technique yielding the new mesh topology of the

electromagnetic mesh at t_n. Figure 3 shows how the electromagnetic elements are moved according to the mechanically deformed mesh. Finally, the electromagnetic loads have to be mapped correctly onto the adapted mesh. As shown in Section 4, for typical frequencies and sheet thicknesses, the Lorentz force distribution in sheet thickness direction may vary in a highly non-linear way (see Figure 10). This motivates the separation of the algorithmic form of the weak momentum balance into a component that is purely mechanical and a component resulting from the electromagnetic loads,

$$\mathbf{f}_{n+1,n} = \mathbf{f}^{\mathrm{EM}}_{n+1,n}(\mathbf{x}_{n+1}, \mathbf{a}_{n+1}) + \mathbf{f}^{\mathrm{Mech}}_{n+1,n}(\mathbf{x}_{n+1}) \,. \tag{3}$$

Here, $\mathbf{f}^{\mathrm{EM}}_{n+1,n}$ represents the part attributed to the coupling by Lorentz forces. The structural force vector can be rewritten in terms of the usual assembly relation

$$\mathbf{f}_{n+1,n} = \sum\nolimits_e \mathbf{l}^{e\mathrm{T}}_{\mathbf{x}} (\mathbf{f}^{e\ \mathrm{EM}}_{n+1,n}(\mathbf{x}^e_{n+1}, \mathbf{a}^e_{n+1}) + \mathbf{f}^{e\ \mathrm{Mech}}_{n+1,n}(\mathbf{x}^e_{n+1})) \,. \tag{4}$$

Here, $\mathbf{f}^e_{n+1,n}$ represents the element contribution to the structural right hand side $\mathbf{f}_n$ which is assembled with the help of the element connectivity matrix $\mathbf{l}^e_{\mathbf{x}}$. More precise, the electromagnetic contribution $\mathbf{f}^{e\ \mathrm{EM}}_{n+1,n}$ is obtained via the usual integration over the element domain B^e_{r}

$$\mathbf{f}^{e\ \mathrm{EM}}_{n+1,n}(\mathbf{x}^e_{n+1}, \mathbf{a}_{n+1}) = -\int_{B^e_{\mathrm{r}}} \mathbf{H}^{\mathrm{T}} \det(\boldsymbol{F}^e(\mathbf{x}^e_{n+1}))\, \boldsymbol{\ell}^e_{n+1} \,. \tag{5}$$

It is important to note that the integration of (5) needs to be accurate in the direction where $\boldsymbol{\ell}^e_{n+1}$ decays (see Figure 10 and 7). Equation (5) is integrated via Gaussian quadrature [13]. The accurate rendering of the non-linear decay is archived by choosing a high number of Gaussian points in the thickness direction of the element domain of the solid shell element. Both, mapping of the deformation and transfer of the body forces are illustrated in Figure 3. The method proposed above was tested by means of a single mechanical element. To study

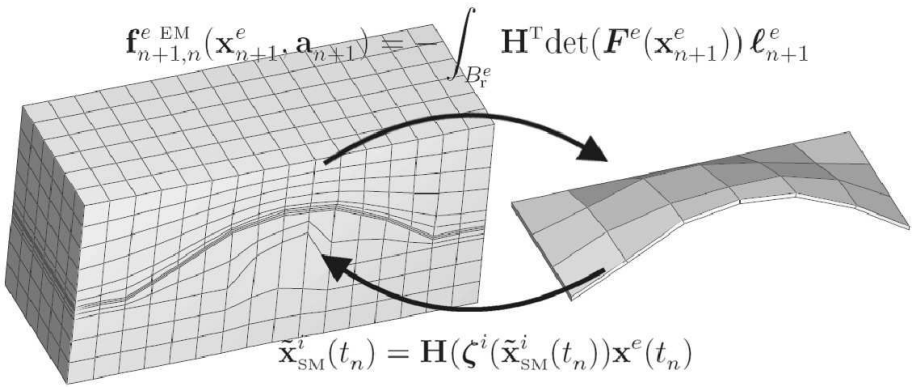

Figure 3: Data transfer in the context of the staggered solution algorithm at t_n. Body force data of the refined electromagnetic mesh are utilized to receive an accurate representation of the electromagnetic loading. The subsequent deformation of the sheet is mapped to its electromagnetic counterpart and the mesh the air is smoothly adapted.

the accuracy of $\mathbf{f}^{e\ \mathrm{EM}}_{n+1,n}$, the accuracy of both influencing factors, namely of the integration of

(5) and of ℓ^{e}_{n+1} at the integration points were investigated. For any fixed number of integration points the amount of electromagnetic elements contained in the mechanical element was increased and the corresponding sum of the vertical electromagnetic element loads was examined. Then, a current and a magnetic field distribution were imposed, both acting in the plane of the sheet metal and perpendicular to each other. Acording to the fully coupled case, both were chosen to decay exponentially. Figure 4 demonstrates the convergence of vertical loads when the number of electromagnetic elements and Gaussian points increase. Regardless of the number of Gaussian points, all curves start at the same value. If the shell contains just one electromagnetic element, the Lorentz force is assumed to be constant in the element and the nodal force result is independent of the accuracy of the integration. For the highest number of Gaussian points the nodal representation of the Lorentz force exhibits the best convergence. For lower numbers of Gaussian points the loads converge to values that are too small. A low number of Gaussian points implies that the bottom and top integration points are not located closely enough to the surface of the sheet, where body forces are maximal. This results in a pathological underestimation of the loads, which is also confirmed by an underestimation of the deformation of the sheet metal for the fully coupled simulation (see Figure 4). Since 8 Gaussian points ensure a sound integration with rather

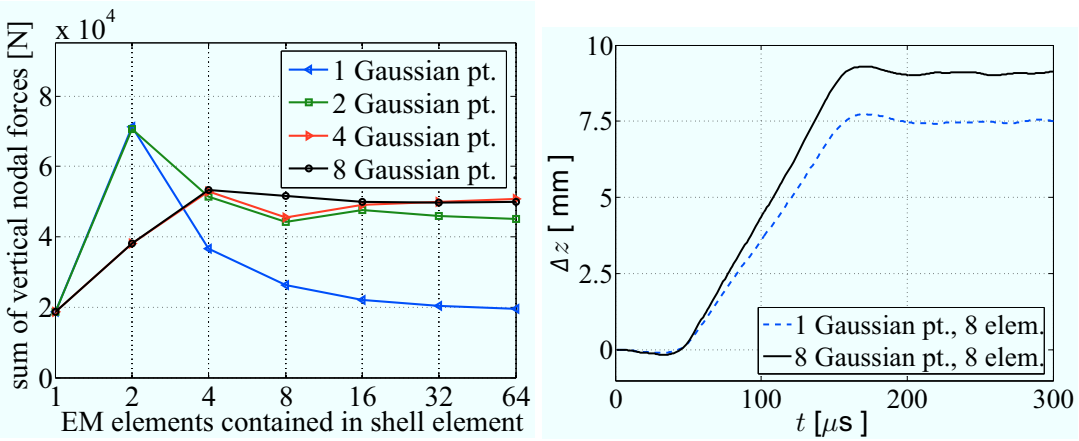

Figure 4: Accuracy of the mapping of body forces. Left: Convergence of the sum of vertical nodal forces with increasing number of elements and Gaussian points. Right: Influence of Gaussian quadrature on the vertical displacement at a specified point P2 close to the center of the plate determined by a fully coupled simulation. For a smaller number of Gaussian points electromagnetic loads are underestimated.

small additional numerical effort to integrate (5), we opt for this method, and all subsequent calculations were computed in this manner. Further, it can be seen that a good accuracy of the electromagnetic loads can be achieved by embedding at least 4 elements in the solid shell element.

3 Termination Criterion for the Electromagnetic Computation

As mentioned above, the largest computational effort is to be attributed to solving the electromagnetic part. It is important to note that external loading due to Lorentz forces typically takes place in the beginning of the process, during the first alternation of the tool coil current. Later, the amount of energy transferred to the sheet metal via electromagnetic loads is relatively small. At this time the actual forming takes place predominantly due to inertial forces. Hence a termination criterion that confidentially indicates the insignificance of the electromagnetic loads and thus enables to turn off the electromagnetic part allows for an enormous reduction in computational cost. In the field of non-linear finite element modeling convergence criteria commonly applied for the termination of global Newton Raphson schemes are usually based on the change of the energy of the corresponding Newton step in relation to the energy change of the first iteration

$$\Delta \mathbf{x}^{i}_{n+1,n} \cdot \mathbf{f}^{i}_{n+1,n} \leq \epsilon_c \Delta \mathbf{x}^{1}_{n+1,n} \cdot \mathbf{f}^{1}_{n+1,n} \, . \tag{6}$$

Here, $\Delta \mathbf{x}^{i}_{n+1,n} \cdot \mathbf{f}^{i}_{n+1,n}$ represents the energy change in terms of the deviation $\Delta \mathbf{x}^{i}_{n+1,n}$ of the nodal positions and the residual force vector $\mathbf{f}^{i}_{n+1,n}$ corresponding to the Newton step i. ϵ_c represents the tolerance for which (6) is fulfilled. Accordingly a termination criterion for the electromagnetic model is based on the energy transferred from the electromagnetic system to the mechanical one. If the amount of energy transferred after some time $t \geq t_{\text{ter}}$ is significantly smaller than the amount of energy that has been transferred up to this instance, it can be expected that an accurate representation of the mechanical deformation can be obtained without further consideration of the electromagnetic system. Therefore, with some tolerance ϵ_{EM} the electromagnetic simulation is stopped at termination time t_{ter} if

$$E_{\text{EM}}(\infty) - E_{\text{EM}}(t_{\text{ter}}) = \int_{t_{\text{ter}}}^{\infty} P_{\text{EM}} dt \leq \epsilon_{\text{EM}} \int_{0}^{t_{\text{ter}}} P_{\text{EM}} dt \tag{7}$$

is fulfilled. Here, $P_{\text{EM}}(t)$ represents the rate of energy transferred at instance t and $E_{\text{EM}}(t)$ the energy transferred from the electromagnetic system until instance t. Since the quantity $E_{\text{EM}}(\infty) - E_{\text{EM}}(t_{\text{ter}})$ is unknown, an alternative criterion based on the comparison of $P_{\text{EM}}(t)$ is employed. Here, the rate of energy at $t_{n+1,n}$ is estimated on the basis of the nodal velocities at t_{n+1} and the nodal representations of the electromagnetic loads given in (3)

$$P_{\text{EM}}(t_{n+1}) \approx \frac{(\mathbf{x}_{n+1} - \mathbf{x}_n) \cdot \mathbf{f}^{\text{EM}}_{n+1}}{t_{n+1,n}} \, . \tag{8}$$

In the particular case of EMF the rate of energy transferred to the mechanical part oscillates with decreasing amplitude as can be seen in Figure 5. This results from the oscillation of the input current. In particular during the first alternation, the largest amount of energy is transferred to the mechanical part. At later instances the intensity of the magnetic field is reduced due to the imposed input current and the expanded air gap between the sheet and the tool coil. Correspondingly, the peak values $P_{\text{EM}}(t_{Pi})$ of $P_{\text{EM}}(t)$ decay. In this case, relating the first peak value $P_{\text{EM}}(t_{P1})$ to the current peak value $P_{\text{EM}}(t_{Pi})$ represents a close match for the termination criterion given in (7) and represents a meaningful termination criterion. If the

energy contribution for $t \geq t_{Pi}$ is sufficiently small, the computation of the electromagnetic system can be terminated. In this respect the new termination criterion is denoted by

$$t_{ter} = t_{Pi} \text{ if } P_{\text{EM}}(t_{Pi}) \leq \epsilon_{\text{EM}} P_{\text{EM}}(t_{P1}) \, . \tag{9}$$

It is important to note that the value for ϵ_c in (6) can precisely be determined on the basis of the best possible numerical accuracy (usually $\epsilon_c = 1 \times 10^{-16}$). For ϵ_{EM} this is not the case. To show and quantify the effect of the termination of the electromagnetic simulation on the forming result, different values for ϵ_{EM} were chosen and the corresponding results were compared. Since the principal findings regarding the energy conversion are similar for coarse and fine meshes (see Section 4), a coarse mesh for the study of the termination criterion was chosen to save computation time.

Figure 5 shows the progression of P_{EM}. Each marker indicates the termination of the electromagnetic system corresponding to three different values for ϵ_{EM} attributed to 1.5%, 3% and 6% of the first peak value $P_{\text{EM}}(t_{P1})$. After terminating the electromagnetic simulation the total amount of energy $E_{\text{EM}}(t)$ transferred to the mechanical system remains constant which can be confirmed by the straight lines. The dotted red curve shows a simulation without termination of the electromagnetic system and serves as reference solution. Further, the graphs for the total amount of energy transferred $E_{\text{EM}}(t)$ indicate how the criteria are related to each other. As depicted in figures 5 and 6 the difference between the reference solution and the terminated one becomes smaller with decreasing ϵ_{EM} . Also interesting from the

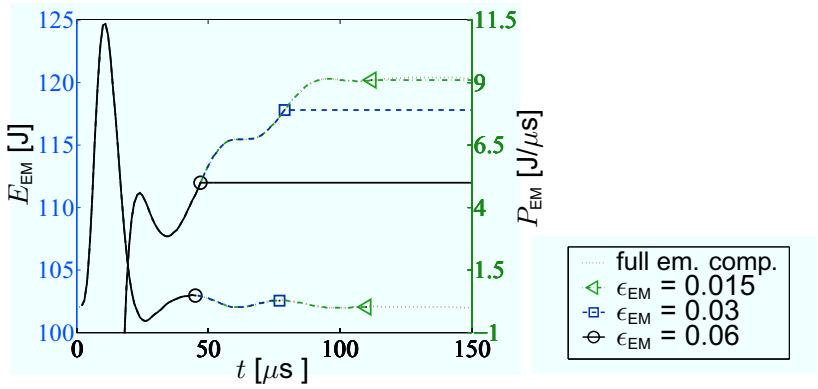

Figure 5: Termination criterion for different tolerances ϵ_{EM} corresponding to 1.5%, 3% and 6% of the first peak value $P_{\text{EM}}(t_{P1})$. To resolve the increase of E_{EM} due to subsequent alternations the left ordinate starts at 100 J. After termination of the electromagnetic part of the model P_{EM} = 0 and E_{EM} = const.

point of view of the technological process simulation is certainly the degree of deviation in terms of the deformation. To this end, the vertical displacement at a specified evaluation Point P2 close to the center of the plate was examined for the three values for ϵ_{EM}. As can be seen in the left part of Figure 6 only for ϵ_{EM} = 0.06 the deformation exhibits a significant underestimation (solid curve). For all other termination criteria the deformation is very close to the reference solution (dotted curve). To quantify this the displacement Δz and transferred energy E_{EM} at t = 300 μs were compared for the different termination criteria (see right part of Figure 6). Similar as in previous cases the relative deviation is highlighted by normalization

with the reference solution yielding the normalized values $\Delta\bar{z}$ and $\bar{E}_{\mathrm{EM}}$. Due to the nature of the termination criterion $\bar{E}_{\mathrm{EM}} < 1$. As a result of small elastic oscillations $\Delta\bar{z} > 1$ is possible for the comparison of the deformation. In view of subsequent simulations, ϵ_{EM} = 0.03 seems to represent a reasonable choice.

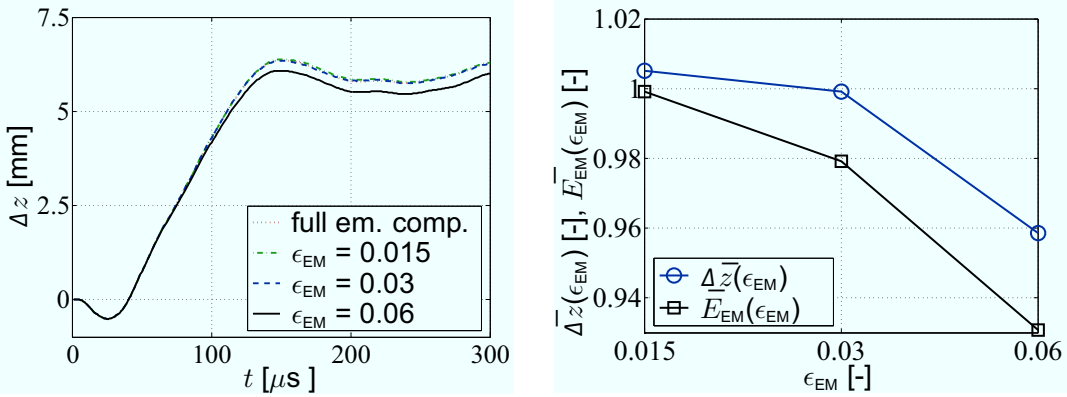

Figure 6: Influence of ϵ_{EM} on the vertical deformation at P2 and E_{EM}. Left: Vertical deformation with evolving time. Right: Normalized vertical deformation at t = 300 μs and E_{EM} depending on different values for ϵ_{EM}.

4 Discussion of Results for a Fully Coupled Simulation

With the above techniques at hand we now turn to the fully coupled simulation of the EMF process. As discussed above the energy driving the forming operation is characterized by the discharging current depicted in Figure 1 which was implemented as a Neumann boundary condition for χ. Starting from the right surface where χ = 0 is prescribed, the potential increases to a maximum value of χ = 4.1 kV to satisfy $(1)_3$ and the remaining Neumann boundary conditions. As could be expected, the *magnitude* of $\boldsymbol{j} = -\sigma_{\mathrm{EM}}\nabla_{\mathrm{s}}\chi$ inside the tool coil at t = 8 μs remains relatively unchanged, only $\boldsymbol{j}$ changes its direction following the centerline of the coil winding as can be seen in the center part of Figure 8. In the lower part of Figure 8, $\boldsymbol{j}$ is depicted for t = 40 μs. At this instance the input current has reached its second extreme value (see Figure 1) and flows in opposite direction. Accordingly the direction of $\boldsymbol{j}$ is flipped and has a reduced magnitude.

Next we turn to the development of the magnetic flux density $\boldsymbol{b}$ at the instances t = 4 μs, t = 12 μs and t = 28 μs. Up to t = 28 μs the largest portion of E_{EM} is transferred to the mechanical part of the model (see Figure 5). In this respect this period of time is significant for the forming operation. Due to the correlation of the tool coil current with the input current, also $\boldsymbol{b}$ is correlated to the input current via Ampere's law. As can be seen by comparison of Figure 7 (above) and Figure 7 (center) the increased input current at t = 12 μs results in an increase of $\boldsymbol{b}$. At t = 28 μs where I just flipped (see Figure 7 (below)) the current in the tool coil and so $\boldsymbol{b}$ are small. At all instances $\boldsymbol{b}$ is insignificant above the sheet metal. This can be attributed to the eddy currents induced in the sheet metal (see Figure 7). Here, the temporal evolution of the magnetic field becomes important. The increase

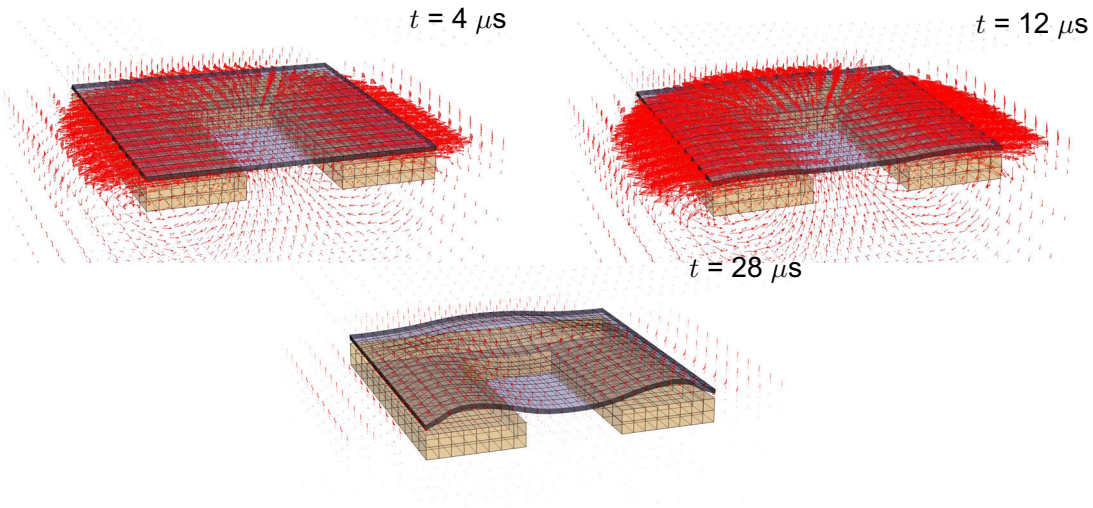

Figure 7: Magnetic flux density distribution for the instances t = 4 μs, t = 12 μs and t = 28 μs. With increasing input current I the magnetic flux density $\boldsymbol{b}$ increases as well. The shielding effect of the sheet metal becomes evident.

of I until t = 8 μs leads to an increase of $\boldsymbol{b}$ in the air in the center of the tool coil winding. The magnetic field and its increase $\partial\boldsymbol{b}$ are oriented in z-direction here. According to Faraday's law of induction, $\partial\boldsymbol{b}$ induces an electric field which drives eddy currents which proceed along the tool coil winding and are oriented in opposition to the current in the winding. Due to their orientation, these eddy currents neutralize the magnetic field above and inside the sheet metal and lead to the shielding effect. Furthermore at t = 12 μs in contrast to t = 4 μs, $\boldsymbol{b}$ begins to penetrate the sheet metal which can be seen by the vectors of $\boldsymbol{b}$ at the upper surface of the sheet metal. This is discussed below together with the development of the eddy currents in the sheet metal.

In Figure 7 the eddy current distributions for the aforementioned instances are shown. In more detail this is depicted in Figure 10 where the significant components j_y of $\boldsymbol{j}$ and b_x of $\boldsymbol{b}$ are depicted along PZ with increasing time. Since the sheet metal deforms under the influence of the Lorentz force the current flux distributions move in vertical direction with increasing time. At the beginning of the process, where the input current exhibits a significant increase, the magnetic field increases in particular close to the lower surface of the sheet metal while an increase inside the sheet metal is relatively small. Accordingly eddy currents occur close to the lower surface as well (see instance t = 4 μs Figure 10) to counter the local penetration of $\boldsymbol{b}$. Later, when the first alternation reached its peak at t = 8 μs as discussed above, $\boldsymbol{b}$ becomes maximal and remains constant outside the sheet metal and the increase close to the surface of the sheet metal is reduced. Accordingly the eddy currents induced here are reduced in comparison to t = 4 μs. *Inside* the sheet metal, however, $\partial\boldsymbol{b}$ might be larger than at previous instances due to the fact that further penetration of $\boldsymbol{b}$ in the sheet metal is facilitated. This in turn leads to an induction of eddy currents into regions which are more distant from the lower surface. As can be seen in Figure 10 at t = 4 μs the eddy currents close to the upper surface are insignificant and so is the magnetic flux density. While proceeding further to t = 8 μs inside the sheet metal, b_x has risen, consequently even close

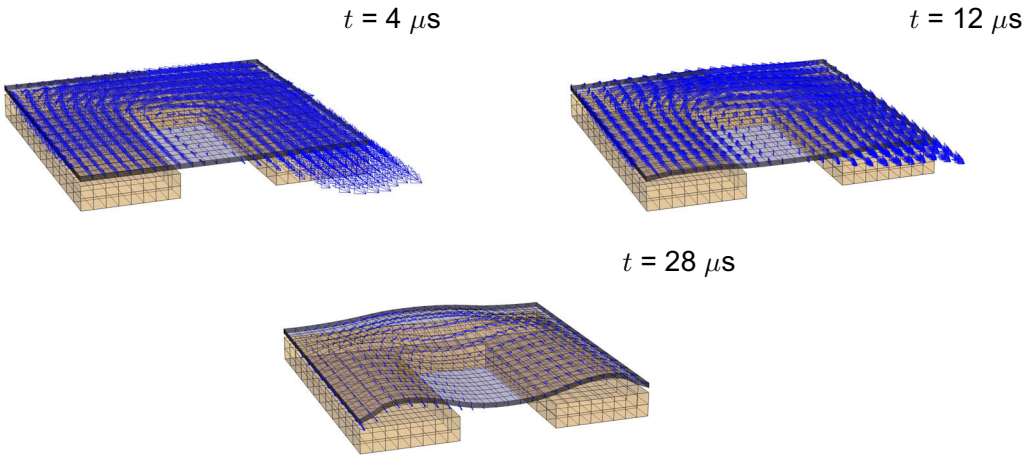

Figure 8: Eddy current distribution for the instances t = 4 μs, t = 12 μs and t = 28 μs. At the beginning of the process the increase of $\boldsymbol{b}$ in the air results in high values for the induced eddy currents at the surface of the sheet metal. At later instances $\boldsymbol{b}$ increases inside the sheet and leads to a more homogenous eddy current distribution in thickness direction.

to the upper surface j_y has become significant while close to the lower surface j_y is reduced. With increasing time (see, *e.g.*, t = 12 μs) the magnetic field in the air gap decreases, then the eddy currents close to the surface become smaller than inside the sheet metal where the penetration of the magnetic field still leads to an increase of b_x. Close to the lower surface now the effect of self induction of the sheet leads to a retention of the eddy currents although $\boldsymbol{b}$ decreases in the air gap. At t = 20 μs and later instances, the eddy current direction is even reversed close to the lower surface of the sheet metal. The flipped eddy currents at the surface of the sheet superimpose a magnetic field to that of the tool coil which leads to a further reduction of the magnetic flux density at the surface of the sheet. The maximal value for b_x is now inside the sheet (see Figure 10 instances t = 20 μs, t = 24 μs and t = 28 μs) and the maximal value for j_y at its upper surface.

Referring to the Lorentz force $\boldsymbol{l}_r$ = det($\boldsymbol{F}$)$\boldsymbol{j} \times \boldsymbol{b}$ as a coupling term to the mechanical component the above discussion underlines the fact that special care has to be taken to account for the strong variations of $\boldsymbol{b}$ and $\boldsymbol{j}$ in the sheet metal (see Section 2). Further it could be seen that $\boldsymbol{b}$ and $\boldsymbol{j}$ penetrate the sheet metal at instances where they are still significant in terms of their magnitude (see *e.g.*, t = 8 μs in Figure 10), in this respect the notion of a magnetic pressure [14] in the context of EMF is not accurate since $\boldsymbol{b}$ and $\boldsymbol{j}$ and so the Lorentz force act inside the sheet metal. Regarding the development of $\boldsymbol{b}$ and $\boldsymbol{j}$ with respect to the progression of the forming operation from figure 7 it can be seen that $\boldsymbol{l}_r$ predominantly acts in positive vertical direction and evolves below the tool coil winding. This applies to all alternations regardless of the direction of the input current, $\boldsymbol{b}$ and $\boldsymbol{j}$ basically flip simultaneously. Only at some time shortly before zero-crossing of the input current $\boldsymbol{b}$ and $\boldsymbol{j}$ are oriented such that $\boldsymbol{l}_r$ points downwards (see Figure 10, instances t = 20 μs and t = 24 μs).

The temporal development of $\boldsymbol{l}_r$ can be deduced from Figure 10. While at the very

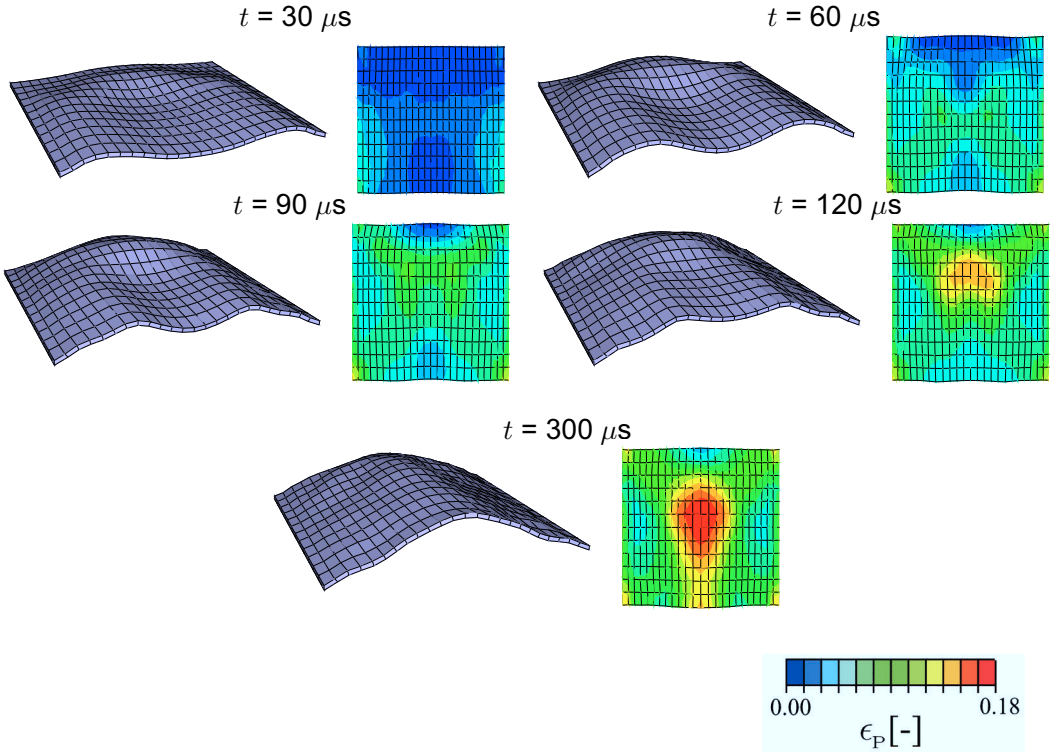

Figure 9: Forming stages of the sheet metal as a function of time and corresponding top view contour plots of ϵ_P. Initially, the part of the sheet metal lying directly over the tool coil is subject to large induced Lorentz forces and begins to accelerate. As forming proceeds, this part pulls the center of the plate along with it.

beginning of the process the largest eddy currents are induced, the magnetic flux density is still relatively small since the tool coil current is relatively small as well; moreover the sheet metal is basically at rest meaning that very little energy is transferred to the mechanical system. At some time between t = 4 μs and t = 20 μs where both, the velocity of the sheet metal and $\boldsymbol{l}_r$ = det($\boldsymbol{F}$) $\boldsymbol{j} \times \boldsymbol{b}$ are relatively large, the forming operation is most effective. In fact this motivates the redesign of the electric circuit attached to the forming setup – presently basically consisting of a switch and a capacitor – such that the efficiency of the process can be increased.

The aforementioned Lorentz force distribution is also reflected by the stages of deformation depicted in Figure 9. At the beginning of the process, the center of the plate remains at rest, whereas just above the tool coil winding, the plate experiences high Lorentz forces and begins to accelerate (see Figure 9, instance t = 30 μs). The contour plots represent the development of the accumulated inelastic deformation for this stage of deformation as a top view of the sheet metal. Due to the boundary conditions of the sheet metal for t = 30 μs the lateral regions exhibit an increase of ϵ_P, the rear part of the structure exhibits no inelastic deformation due to the fact that the sheet metal can move freely and $\boldsymbol{l}_r$ is less pronounced here The lateral fixing leads to a combined bending and stretching of the sheet caused by the body force distribution nearby. In particular at the front corners of the sheet the inelastic deformation exhibits its maximal value of $\epsilon_P \approx 0.8$. The loading of the plate leads to a lateral

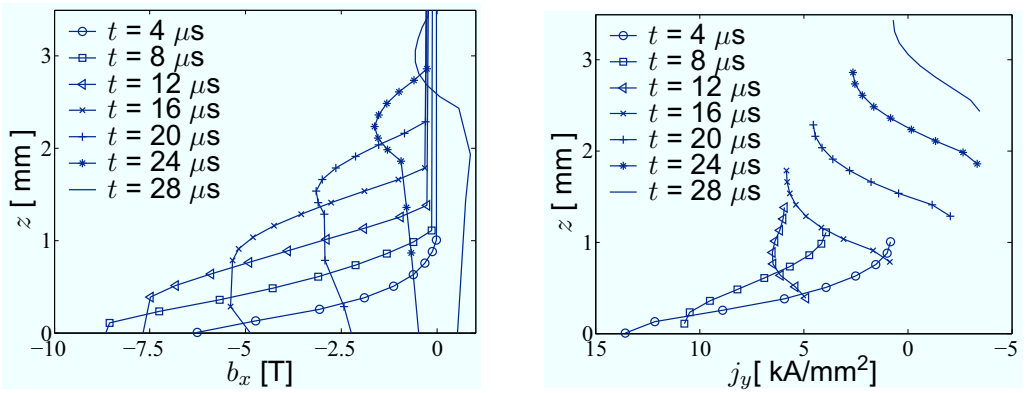

Figure 10: Development of b_x and j_y along PZ with evolving time and deformation. Left: The development of b_x in the sheet and surrounding air. Right: Development of eddy currents in the sheet. Curves for j_y move according to the vertical deformation of the sheet.

contraction of the plate which becomes zero at the fixed edge of the plate. The strains resulting from this lateral deformation, however, are maximal here and contribute to the increase of ϵ_P. With increasing time (see Figure 9, t = 60 μs) the accelerated parts of the structure continue to deform and the center of the plate – initially at rest – begins to move. In addition to the front corners of the sheet metal now the rear corners exhibit an increased inelastic deformation as well and bands of increased inelastic deformation propagate from the front corners to the center of the sheet. At t = 90 μs and t = 120 μs the center of the plate is accelerated further, the bands of deformation evolve and close to the center of the plate a maximum for ϵ_P starts to develop. The final shape of the structure for t = 300 μs is shown in the last image of Figure 9. During the last forming stages the initially downwards bent center of the structure is now pulled along with the lateral regions of the plate and bent upwards resulting in a roof-top shaped structure. The strong inelastic bending results in an additional increase of ϵ_P at the center of the plate.

References

[1] *Takatsu, N.*; *Kato, M.*; *Sato, K.*; and *Tobe, T.*: High-speed forming of metal sheets by electromagnetic forces. International Journal of the Japanese Society for Mechanical Engineering, volume 31: pp. 142–148, 1988.

[2] *Gourdin, W. H.*; *Weinland, S. L.*; and *Boling, R. M.*: Development of the electromagnetically-launched expanding ring as a high strain-rate test. Review of Scientific Instruments, volume 60: pp. 427–432, 1989.

[3] *Fenton, G.* and *Daehn, G. S.*: Modeling of electromagnetically formed sheet metal. Journal for Materials Processing Technology , volume 75: pp. 6–16, 1998.

[4] *Oliveira, D.*; *Worswick, M.*; and *Finn, M.*: Finite Element Modelling of the Electromagnetic Forming of Aluminum Alloy Sheet. In *Proceedins of 4th International ESAFORM Conference on Material Forming*, pp. pp. 773–776. Liége, Belgium, 2001.

[5] *Imbert, J.*; *Winkler, S.*; *Worswick, M.*; *Oliveira, D.*; and *Golovashchenko, S.*: Numerical Modeling of an Electromagnetic Corner Fill Operation. In *Proceedings of NUMIFORM 2004*, pp. pp. 1833–1839. Ohio State University, USA, 2004.

[6] *Schinnerl, M.*; *Schöberl, J.*; *Kaltenbacher, M.*; and *Lerch, R.*: Multigrid methods for the 3D simulation of nonlinear magneto-mechanical systems. IEEE Transactions on Magnetics, volume 38(3): pp. 1497–1511, 2002.

[7] *Svendsen, B.* and *Chanda, T.*: Continuum thermodynamic formulation of models for electromagnetic thermoinlastic materials with application to electromagnetic metal forming. Cont. Mech. Thermodyn., volume 17: pp. 1–16, 2005.

[8] *Stiemer, M.*; *Unger, J.*; *Blum, H.*; and *Svendsen, B.*: Algorithmic formulation and numerical implementation of coupled electromagnetic-inelastic continuum models for electromagnetic metal forming. Int. J. Numer. Methods Engrg., volume 68: pp. 1301–1328, 2006.

[9] *Stiemer, M.*; *Unger, J.*; *Blum, H.*; and *Svendsen, B.*: Algorithmic formulation and numerical implementation of coupled electromagnetic-inelastic continuum models for electromagnetic metal forming. In *Proceedings of ECCOMAS CFD European Conference on Computational Fluid Dynamics*, pp. pp. 362–382. Egmond aan Zee, The Netherlands, 2006.

[10] *Reese, S.*: A large deformation solid-shell concept based on reduced integration with hourglass stabilization. International Journal for Numerical Methods in Engineering, volume 69: pp. 1671–1716, 2007.

[11] *Jackson, J. D.*: *Classical Electrodynamics*. John Wiley and Sons, 1975.

[12] *Field, D.*: Laplacian smoothing and Delaunay triangulations. Communications in applied numerical methods, volume 4: pp. 709–712, 1988.

[13] *Hughes, T. J. R.*: *The Finite Element Method*. Prentice-Hall, 1987.

[14] *Mamalis, A.*; *Manolakos, D.*; *Kladas, A.*; and *Koumoutsos, A.*: Electromagnetic forming and powder processing: Trends and developments. Appl. Mech. Rev., volume 57(4): pp. 299–324, 2004.

Models for Electromagnetic Metal Forming

G. Bartels, W. Schätzing, H. P. Scheibe, M. Leone

Institute of Fundamental Electrical Engineering
and Electromagnetic Compatibility, University of Magdeburg, Germany

Abstract

This paper presents a comparison of different simulation options for electromagnetic metal forming in order to make preliminary investigations with adequate accuracy. Four simulation models are compared. The models mainly differ in their complexity, handling and necessary precondition program packages. The user has the choice to use a simple program with a defined program algorithm or to use a program with a higher programming complexity which accepts more information.

Keywords

Modelling, Computer, Simulation

1 Introduction

The lowering of costs and the reduction of the development times in view of ever larger competition is an essential objective for the producing business. Simulation tools especially for users in the range of Electromagnetic Forming (EMF) offer the opportunity to analyze the formation process and its effects already in the development stage. Compared to the expensive construction of prototypes, the variation of process parameters can be performed by simulations with significantly reduced costs.

2 Simulation Models

All presented models are suitable for the analysis of the electromagnetic field problems which results from a system configuration composed of an electromagnetic metal forming machine with installed energy storage, electromagnetic forming coil and electrically conductive tubular workpiece. The basic principle for creating the simulation models is illustrated in figure 1.

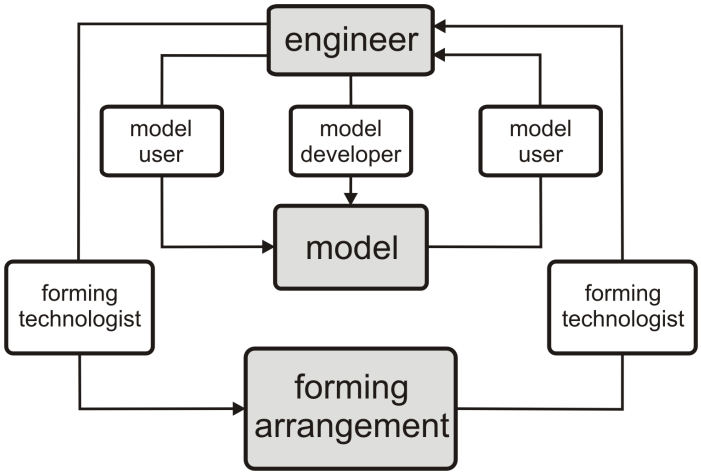

***Figure 1**: Scheme of model development*

At first, the engineer analyses the forming arrangement to get the necessary detailed insight. From the collected knowledge the engineer develops the model. In addition to the knowledge about the physical processes a great amount of training concerning the handling of model-formation software is essential for the development of computational models for electromagnetic metal forming. If the available model-formation software does not completely describe the required information in its full complexity, extensions will have to be carried out. Furthermore, knowledge of the inner function (interfaces) of commercial FEM calculation software and programming skills in higher programming languages are necessary to code and bind own routines. Such tasks were usually handled by developing groups. This leads to the creation of models which include all desired properties. The work with such model requires a certain amount of expert know-how. As a consequence, the maintenance and future extension depend on the availability of the software engineer. If the developers are not available, the further maintenance or extension won't be possible as a rule. The operation by somebody who was not involved in the development requires a great expenditure of documentation and operation introductions. For that reason the trend is to develop models which need no specific knowledge from the model user. Therefore the program has to be designed in the way that it could pass from the developer to the user. In most of the cases this requires the application of commercial model software. For simple models standard software is sufficient and does not require additional software. They can be provided to the user for training purposes and rough estimations of the expected parameters.

2.1 FEM Based Simulation Models

Complicated field problems are increasingly solved with the help of numeric computation methods in the range of electrical engineering. Instead of cost-intensive and time-consuming measurements, the modellings at the computer and a following numeric computation are being preferred today. Experimentally determined electromagnetic field values are necessary for verification of the simulation results. The FEM method transfers an electromagnetic boundary-value problem into a set of linear equations. The

electromagnetic field problem must be computed in the time domain in the case of electromagnetic metal forming. The general form of the differential equation (1) is used for this purpose [1].

$$[L(\gamma)]\begin{bmatrix}\frac{\partial \vec{A}}{\partial t}\\ \varphi\end{bmatrix}+[K(\mu)]\begin{bmatrix}\vec{A}\\ 0\end{bmatrix}=\begin{bmatrix}\vec{J}\\ 0\end{bmatrix} \quad (1)$$

$\vec{A}$: Magnetic vector potential
$\vec{J}$: Current density
$[L]$: Conductivity matrix
$[K]$: Permeability matrix
φ: Electric scalar potential

The computation of the structure-mechanical transforming process can be accomplished in a subsequent simulation step. Thereby the result of the electromagnetic field simulation is the input of the structure-mechanical simulation. The fundamental motion equation (2) which must be solved reads:

$$[M]\{u''\}+[D]\{u'\}+[C]\{u\}=\{F(t)\} \quad (2)$$

$[M]$: Mass matrix
$[D]$: Damping matrix
$[C]$: Stiffness matrix
$\{u''\}$: Vector of the node acceleration
$\{u'\}$: Vector of the node velocity
$\{u\}$: Vector of the node displacement
$\{F(t)\}$: Load vector

2.1.1 Full-access-model for commercial program combined with required routine

EMF is a high-dynamic process with high transformation velocities. The deformation results from the electric currents in the forming coil and in the workpiece. The active force is the Lorentz force. Furthermore, the electromagnetic field and so the Lorentz force depends on the temporal current, on the distance between forming coil and workpiece and their geometries. Most of the simulation tools and models for EMF are limited to 2D axial symmetrical arrangements and to small deformations. 3D simulation models become ever more important for the exact process analysis and description of the process. This gap is filled by the model. The connection between electromagnetic field and temporal displacement of the workpiece is not negligible for example working a door handle recess out for the automobile industry. Therefore the interest in coupled electromagnetic-structure mechanical simulation models which can compute 3D arrangements and larger

deformations increased in the last years. The requirements of a 3D simulation consist particularly in the increased number of nodes of the arrangement. The number of nodes drastically affects the simulation time and the necessary computer capacity. A purposeful choice of the discretisation density works against this fact [2].

The scheme of the full-access-model development for a commercial program combined with required routine is comparable with the scheme from Figure 1. This program algorithm is a very complex model for the simulation of the EMF process. The engineer is concerned with the forming arrangement and the forming process. He uses experimental results of the forming technologists. Due to analytic descriptions and such experimental results the model developer creates the model. After the model is generated, the engineer can carry out its investigations at the model. If he cannot use the model, he must contact the model developer, before conducting numerous investigations with the model. At some selected points of the arrangement the simulation results must be verified by experiments at the original forming arrangement. For the use of the model, a commercial available software package (ABAQUS/CAE) is necessary. It is to be demonstrated that the model user must have programming knowledge in handling the computation software ABAQUS/CAE based on the finite element method. Furthermore, the user must have experience in the range of the EMF. The required programming must knowledge cover the geometrical model production, the choice of a reasonable discretisation density, the definition of boundary conditions, the definition of material properties and the definition of initial conditions of the computation volume (pre-processing). Additional by the use of an embedded algorithm is required that was developed at the Chair of mechanics, University of Dortmund. This computation algorithm accomplishes the coupled electromagnetic-structure-mechanical field simulation. The representation of the computation results (post-processing) is realized in ABAQUS/CAE [3]. If the model user does not have development experiences especially of this program algorithm, the model will be unusable for the user.

2.1.2 Full-access-model for commercial program

A further possibility to simulate the EMF process offers the full-access-model for a commercial program. In this case, the commercial FEM program package (ANSYS) is necessary. It offers the possibility to analyze 2D axial symmetrical geometries or 3D geometries. The computations of 3D geometries have high requirements to the computer capacity. The typical temporal discharge current can be easily generated by an equivalent circuit that includes the machine parameters (capacity, inductance, ohmic resistance and charging voltage). Then the discharge current can be couple into the generated forming coil geometry. The coupling between the equivalent circuit and the FEM model is exemplary illustrated in Figure 2.

In the first computation step the electromagnetic field problem is calculated transiently and the magnetic body force density is determined or the magnetic pressure on the workpiece. In a next step a structure-dynamic simulation can follow to obtain the material deformation. The computations can be accomplished advantageously in the same software package. This facilitates the change between electromagnetic and structure-dynamic computation.

The scheme of the full-access-model for a commercial program is illustrated in Figure 1. There is a direct connection between model operator and model developer. The

Model developer must understand the physical background of the EMF process or cooperate with a transforming technologist. The model is noted in a typical software language. Therefore the model user must understand this language and the physical background of the process. If the model user has programming knowledge and the understanding about the forming arrangement, the direct access is not limited for this simulation model.

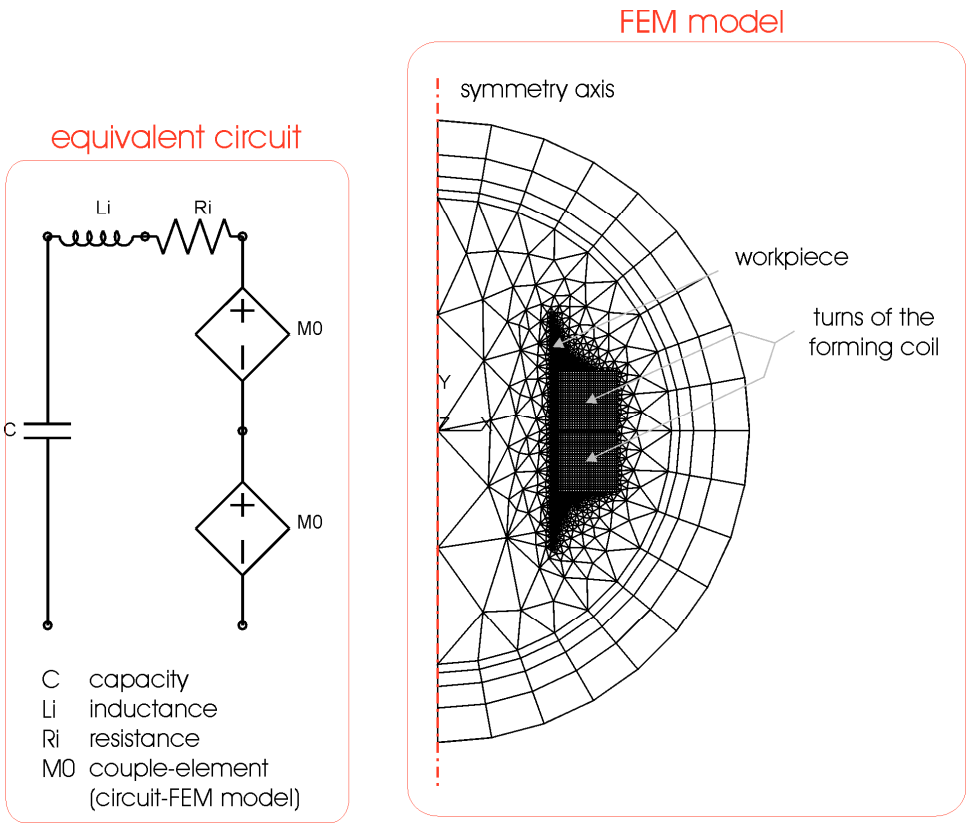

***Figure 2**: Coupling between equivalent circuit and FEM model*

2.1.3 Limited-access-model for commercial program

If there's the need for a simply operating simulation model, a model can be generated, which can used without programming knowledge and without knowledge about the forming arrangement. For this example the commercial software package (ANSYS) is needed. In this case the user operation is limited to the fact that a preassigned source code is loaded into ANSYS. The source code is programmed in such a way that a set of parameters can be entered by the model user. Thus, the model can be used for similar tasks of computation.

Figure 3 shows in contrast to the previously presented models the possibility of the model transfer from the model developer to the model user. There is no more direct connection between the model-development side and the model-user side. The possible field of application of the model is limited by the defined range of the parameters. An adjustment of the model to other computation arrangements requires a re-programming by the model developer.

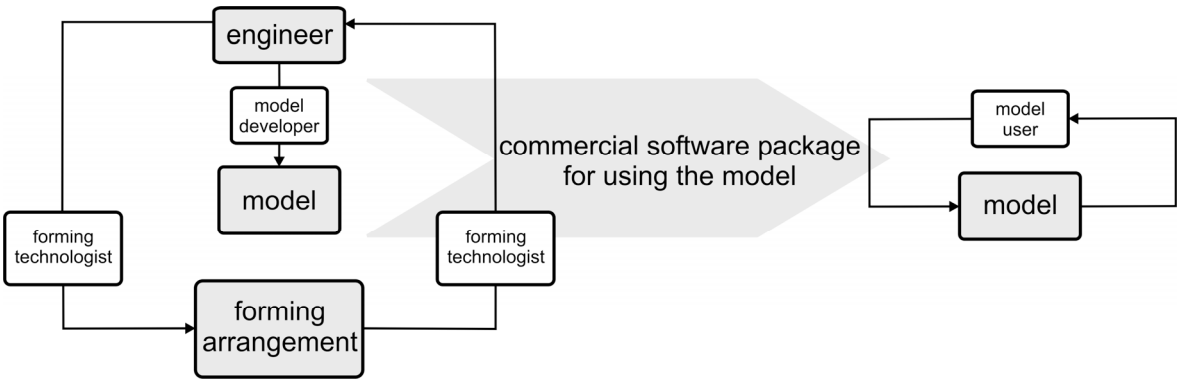

***Figure 3**: Scheme of limited-access-model development for commercial program*

2.2 Engineering Standard Software

The engineering standard software is an interactive model for the computation of the magnetic pressure at the workpiece. The magnetic pressure at the surface of the workpiece represents the fundamental value for the evaluation of the effect during the magnetic forming process. As an example a program was created at the University of Magdeburg for the determination of the magnetic pressure at the surface of the workpiece. The program runs on Windows computers and requires only small computer capacity. The computation is based on the solution of coupled differential equations. These are a result of the electrical circuit diagram, consisting of forming arrangement, forming coil and workpiece. Substantial model parameters like the internal inductance, the internal resistance and the couple factor between the forming coil and the workpiece were determined by a preceding FEM simulation. Then the differential equation problem can be numerically solved for this arrangement.

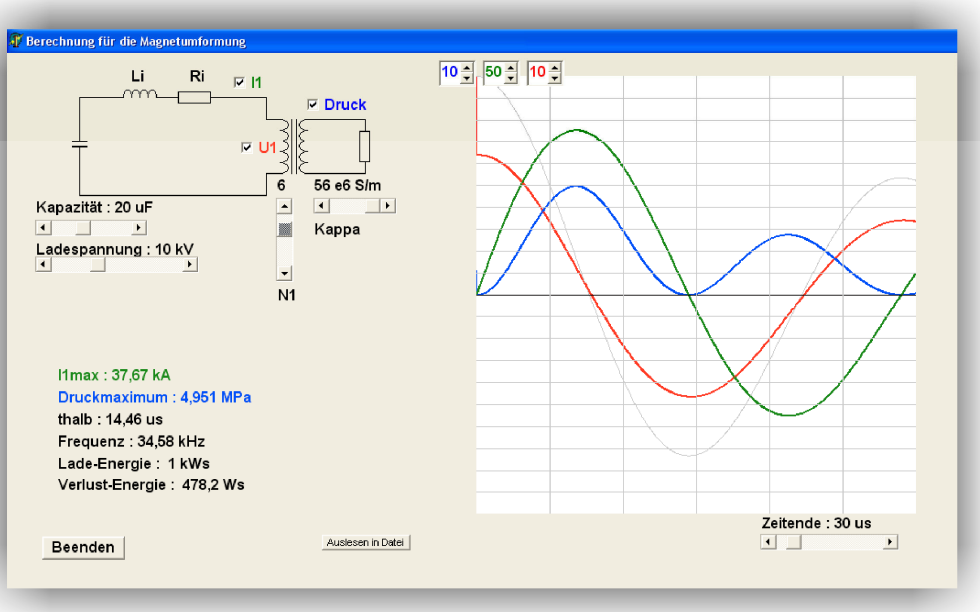

***Figure 4**: Operator interface for engineering standard software*

The development of the engineering standard software is comparable in principle with scheme from Figure 3. The model user does not require the knowledge of the model developer and the physical knowledge of the forming technologist. Furthermore, no commercial software package is necessary. The model must be generated by the model developer and by the forming technologist.

In Figure 4 the operator interface of the engineering standard software is represented. The geometry, the parameters of the forming arrangement and the material properties have influence on the magnetic pressure. The user can specify important parameters like the capacity, the charging voltage, the number of turns of the forming coil and the electrical conductivity of the workpiece within a certain range over scroll bars. A change of these parameters leads to immediate changes of the graphs, as for the charging voltage, the electrical current, the voltage of the coil and the magnetic pressure. Important maximum values are read out in a text output. Due to the fact that the geometry cannot be changed by the model operator, the applicability of the model is limited to a defined transforming arrangement.

3 Conclusions

The aim of this paper is to present different possibilities of simulation models for the EMF process. The models especially differ in the required software and in the knowledge of the model user.

model	**software**	**programming knowledge**
full-access-model for commercial program combined with required routine	commercial software package + routine	knowledge in the programming language (ABAQUS)+ knowledge of the routine
full- access -model for commercial program	commercial software package	knowledge in the programming language (ANSYS)
limited-access-model for commercial program	commercial software package	none
engineering standard software	standard software	none

***Table 1**: Characteristics of the simulation models*

In table 1 the four simulation models are compared. The customer has the possibility to decide for a suitable model in view of the operator benefit, the software requirement and the programming complexity. The model operator must simultaneously be the model developer, to use the full-access-model for a commercial program combined with required routine or the full-access-model for a commercial program. Both models can be adapted to the respective EMF process as far as possible (geometry, material and machine parameter). In these cases a commercial software package is needed. In the sense of a simple calculation of the magnetic pressure for a defined forming arrangement, the computation can be preferably accomplished with the limited-access-model with a

commercial program. However, the use of a commercial software package is needed. The engineering standard software offers a simpler operator benefit without a commercial software package.

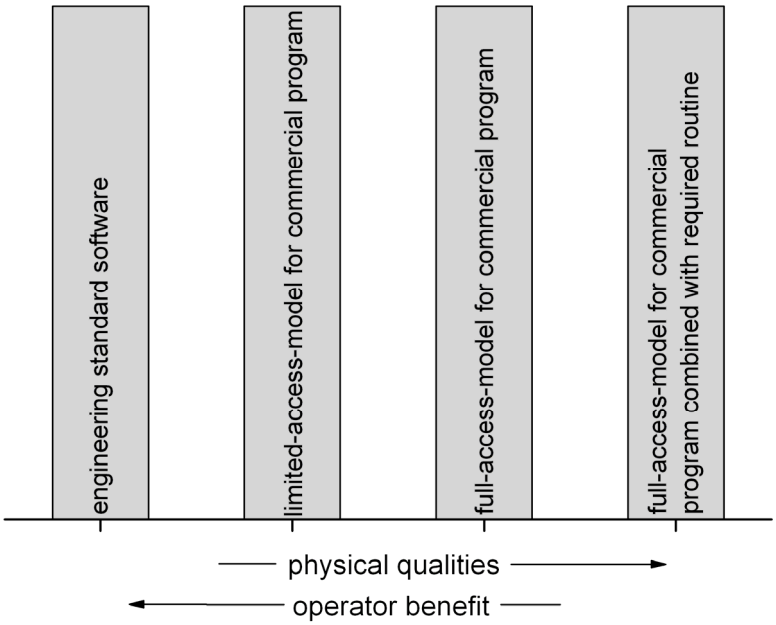

***Figure 5**: Connection between operator benefit and physical qualities*

As shown in Figure 5, a contradistinction exists between the physical quality and operator benefit with the presented simulation models. Therefore, the operator benefit decreases with rising physical quality.

Appendix

In the presentation several models are shown and demonstrated. The advantages and limitations of the respective models will be explained and evaluated.

References

[1] *Schätzing, W.; Müller, G.:* FEM für Praktiker - Band 4: Elektrotechnik. Expert-Verlag, Renningen, 2003.

[2] *Unger, J.; Stiemer, M.; Schwarze, M.; Svendsen, B.; Blum, H.; Reese, S.:* Strategies for 3D simulation of electromagnetic forming processes. Proceedings of TMS symposium "JOURNAL OF MATERIALS PRCESSING TECHNOLOGY", Volume 199 pp.341-362. , 2008.

[3] *Unger, J.; Stiemer, M., Schwarze, M.:* Magneto-mechanisch gekoppelte Finite-Elemente Modelle zur 3D Simulation von EMB Prozessen. Workshop Elektromagnetische Umformung, Dortmund, 2007.

Fast Algorithms for the Simulation of Electromagnetic Metal Forming*

M. Stiemer[1], J. Unger[2], H. Blum[1], B. Svendsen[2]

[1]Chair of Scientific Computing, TU Dortmund
[2]Chair of Mechanics, TU Dortmund

Abstract

Despite the comprehensive understanding of the modeling and numerical simulation of electromagnetic metal forming that has recently been gained, the simulation of real forming situations is still a challenging task due to the large computational resources required. A bottleneck is the computation of the electromagnetic fields, since 100.000 up to several million unknowns are required to represent the geometry of a typical forming device. The purpose of this article is to present new techniques to speed up the simulation of electromagnetic metal forming with particular emphasis on the computation of the electromagnetic fields. An acceleration of the electromagnetic field computation is a significant step towards a virtual design of electromagnetic forming processes.

Keywords:

Modeling, Electromagnetic Metal Forming

1 Introduction

The description of many phenomena in nature as well as of many engineering processes is based on multiphysical models. Consider, e.g., electromagnetic metal forming (EMF), a high speed forming process in which strain rates of over 10^3 s^{-1} arise. It is driven by he Lorentz force, a material body force, that results from the interaction of a pulsed magnetic field with eddy currents induced by the magnetic field. The magnetic field is triggered by a tool coil adjacent to the work piece which is excited by the discharging current of a capacitor bank. Although EMF offers certain advantages over other forming methods such as, e.g., an increased formability, a reduce in wrinkling, reduced tool making costs, the opportunity to

This work was carried out in the context of the German National Science Foundation (Deutsche Forschungsgemeinschaft (DFG)) Research Group FOR 443. The authors wish to thank the DFG for its financial support.

combine forming and assembly operations or the avoidance of contact, its industrial use has been limited to joining tubular semifinished materials up to know. The reason for this is the highly dynamic nature of this process inhibiting its monitoring and control. This emphasizes the significance of reliable simulations of this process to identify relevant process parameters and to optimize them.

During the last years, great progress in the simulation of coupled electromagnetic mechanical processes has been achieved. In case of electromagnetic forming, e.g., a fully coupled three dimensional simulation environment has been developed [1, 2]. It is based on the formulation of an appropriate continuum mechanical thermodynamic consistent model for electrically conducting viscoplastic solids under the influence of magnetic fields [3, 4] accounting for the rate dependency of the material typical for those strain rates arising in electromagnetic forming. Further, an algorithmic formulation for the computation of three dimensional time varying transient magnetic fields in the presence of inhomogeneous moving materials has been developed [e.g. 5, 6, 6]. Of particular importance was the implementation of a reliable coupling scheme between the electromagnetic field computation and the mechanical simulation [see 5, 6, 6]. Further, methods to correctly consider dynamical contact between the work piece and a forming tool had to be developed. A significant gain in efficiency could finally be reached by use of efficient solid shell finite elements [e.g. 7, 8] which combine the great efficiency a two dimensionally based model offers with the convenience of nodal degrees of freedom.

Although the physics behind the coupled process and its numerical requirements have been completely understood, the simulation of real forming situations represents still a scientific challenge. The reason for this is the large number of unknowns necessary to model the geometry of a real forming device sufficiently accurate. In this respect, electromagnetic forming perfectly mirrors the situation in computational electromagnetics and particularly in the numerical computation of interactions between electromagnetic fields and mechanical structures. While the scientific foundations are well understood, efficiency is a major issue of present research.

The purpose of this article is to present new approaches to increasing the computational efficiency of the simulation of electromagnetic metal forming processes. Particularly, methods to speed up the electromagnetic field computation are discussed. The paper is organized as follows. In Section 2, the mechanical model is briefly summed up and some remarks concerning its fast and accurate numerical simulation are given. Then, an efficient model for the electromagnetic subsystem is introduced (Section 3). Strategies for coupling the electromagnetic and the mechanical subsystems are then presented in Section 4. Section 5 is concerned with adaptive techniques to speed up the electromagnetic field computation. The paper ends with a discussion of applications and further perspectives (Section 6).

2 Accelerating the Mechanical Simulation

We first give a brief review of the mechanical model. Starting point for the relevant electromagnetic thermoelastic multifield model [3, 4] is the weak momentum balance

$$\int_{B_\mathrm{r}} (\varrho_\mathrm{r} \ddot{\boldsymbol{\xi}} - \boldsymbol{f}) \cdot \boldsymbol{\xi}_* + \boldsymbol{P} \cdot \nabla_\mathrm{r} \boldsymbol{\xi}_* = \int_{\partial B_\mathrm{r}} |\mathrm{cof}(\boldsymbol{F}) \boldsymbol{n}_\mathrm{r}| \, \boldsymbol{t}_\mathrm{c} \cdot \boldsymbol{\xi}_* \tag{1}$$

with respect to the referential configuration $B_\mathrm{r} \subset R$ of the work piece for all corresponding test fields $\boldsymbol{\xi}_*$ vanishing on those parts of the current boundary ∂B_c where $\boldsymbol{\xi}$ is specified. Here, $\boldsymbol{\xi}$ represents the deformation field, $\boldsymbol{f} = \det(\boldsymbol{F})\, \boldsymbol{j} \times \boldsymbol{b}$ the Lorentz force (density), $\boldsymbol{P}$ the first Piola-Kirchhoff stress, $\boldsymbol{F} := \nabla_\mathrm{r} \boldsymbol{\xi}$ the deformation gradient, and $\boldsymbol{t}_\mathrm{c}$ the current boundary traction. The mechanical model relations are completed by the specification of the material model. For a given thermodynamic state of the mechanical structure, $\boldsymbol{P}$ can, as usual, be computed from the free Helmholtz-energy stored in the material. The evolution of its density ψ_r is determined by the evolution of certain inner variables, which are, in this case, the accumulated inelastic strain, the elastic left Cauchy Green tensor and the temperature. Characteristic for the viscoplastic material model is an activation approach for modeling the evolution of the logarithmic inelastic strain. See [3, 4] for a detailed discussion.

The choice of adequate element formulations for the finite element discretization of the above mechanical model depends on geometrical properties of the structure under consideration. While continuum elements lead to satisfactory results for the simulation of tube compression, an efficient simulation of sheet metal forming requires more sophistication. Here, a solid shell formulation has been employed combining the convenience nodal degrees of freedom offer with the efficiency of a two dimensional formulation [e.g. 7, 8]. To avoid locking, modern element technology has been referred to.

3 Electromagnetic Field Computation in 3D

Electromagnetic phenomena are modeled by Maxwell's equations. This is a system of four partial differential equations for four fields, the magnetic field h, the magnetic flux density b, the electric field e and the electric displacement field d (see e.g. [9]). For the materials considered here, we have linear relations $h = \mu b$, where μ denotes the permeability of the vacuum, and $e = \epsilon_0 d$, where ϵ_0 denotes the permittivity of the vacuum. In many cases, Maxwell's equations possess wave solutions. In electromagnetic forming, however, the occurring wave lengths are much longer than the distances relevant for the forming process. Hence, the quasistatic approximation to Maxwell's equations applies (see [9, 10]), and high frequent displacement currents may be neglected. Principally, the field problem has to be solved in the whole space $\mathbb{R}^3$. However, due to the a priori known fast decay of electromagnetic dipole fields, the problem can be tackled in a large bounded open set $\Omega \subset \mathbb{R}^3$ with sufficient accuracy. In electrically conducting areas of Ω, e is related to an electric current j by a further constitutive material law. For the materials considered here, this relation simply reads $j = \gamma e$ with the electrical conductivity γ.

To compute the b and the e field, two new fields, a vector field $a = a(x, t)$ with curl $a = b$

and a scalar field $\phi = \phi(x,t)$ with

$$j = \gamma \left(-\frac{\partial a}{\partial t} - \nabla\phi - v \times \operatorname{curl} a \right) \tag{2}$$

are introduced to solve the field relations. Here, v denotes the velocity of a material point with respect to a fixed frame. The Lorentz force acting on an electrically conducting body, whose points are subject to a movement with velocity field v is given by

$$f_L = j \times b = -b \times \gamma e = \operatorname{curl} a \times \gamma \left(-\frac{\partial a}{\partial t} - \nabla\phi - v \times \operatorname{curl} a \right) . \tag{3}$$

In the case of an Eulerian formulation, the conductivity $\gamma = \gamma(x,t)$ depends on the spatial variable x and on the time t. We have $\gamma \neq 0$ if and only if the point x is covered by the work piece Σ at time t or is a point of the spatially fixed tool coil S. In the following discussion, we omit the electromotive forces $v \times \operatorname{curl} a$. From a practical point of view this is justified, since finite element simulation which consider these terms did hardly produce other results than finite element simulations omitting them (see [10]). Moreover, in the context of an arbitrary Lagrangian Eulerian reformulation of the electromagnetic subsystem, electromotive forces will implicitly be considered again. An Eulerian description of the evolution of the electromagnetic field is now given by

$$\operatorname{curl} \frac{1}{\mu} \operatorname{curl} a - \gamma \frac{\partial a}{\partial t} = \gamma \nabla\phi . \tag{4}$$

For discretization with finite elements, we consider – as usual – the week formulation, i.e., we search $a \in L^2(H_{\operatorname{curl},0}(\Omega))$ such that

$$\begin{aligned} \int_\Omega \frac{1}{\mu} \operatorname{curl} a \, \operatorname{curl} a^* + \int_\Omega \gamma \, a^* \, \frac{\partial a}{\partial t} &= -\int_S \gamma \, a^* \, \nabla\phi \\ \int_S \nabla\phi \, \nabla\phi^* &= 0 \end{aligned} \tag{5}$$

for all $a^* \in H_{\operatorname{curl},0}(\Omega)$ and for all $\phi^* \in H_0^1(\Sigma \cup S)$. Trial functions are taken from the spaces $L^2(H_{\operatorname{curl},0}(\Omega))$ of functions that map the time interval under consideration into the space $H_{\operatorname{curl},0}(\Omega)$ of spatially varying square integrable functions whose (weak) curl is still a square integrable function. On Ω, we can chose initial data $a(0) = 0$, boundary data $n \times a(x,t) = 0$, $x \in \partial\Omega$ and boundary data $\phi(x,t) = U(x,t)$, $x \in \partial\Omega \cap \partial S$.

Unfortunately, the system (5) does not provide a unique vector potential. Any temporally constant non zero field $\tilde{a}$ with $\operatorname{curl} \tilde{a} = 0$ fulfilling suitable boundary conditions may be added to a to obtain a solution different from a. Unique solvability can be granted by imposing an additional *gauge* of the vectorpotential, e.g., the Coulomb gauge, demanding $\operatorname{div} a = 0$ in Ω. The corresponding saddlepoint problem possesses a unique solution. This can e.g. be shown by proving that a suitable temporal semidiscretization leads to purely spatial problems that fulfill a Ladyshenskaya Babushka Brezzi (LBB) condition. However, saddlepoint problems of the size that is typical for practical forming problems, require large computational efforts, since both equations, equation (4) and the gauge condition need to be discretized using suitable discrete spaces. Particularly, the discrete LBB condition needs

to be fulfilled.

Hence we will now present another model for the electromagnetic subsystem: Starting point is the observation that equation (4) implies the relation

$$\text{div}\,\frac{\partial a}{\partial t} = -\Delta\phi \tag{6}$$

in electrically conducting areas. Equation (6) can now be used to introduce a Coulomb gauge implicitly in areas with a positive electrical conductivity $\gamma(x,t) > 0$. This is simply done by replacing (6) by

$$\Delta\phi = 0\,. \tag{7}$$

We solve equation (7) in areas with positive electrical conductivity first and take $\nabla\phi$ as input quantity in (4) afterwards. Then any vectorpotential fulfilling (4) is forced to have zero divergence in electrically conducting areas. The associated Lorentz forces can be computed via equation (3). The problem remains not gauged in all areas with $\gamma(x,t) = 0$. From a physical point of view, this is no problem, since any potential a fulfilling (4) in areas with $\gamma = 0$ possesses the same $b = \text{curl}\,a$, an this is the only quantity of physical significance there.

For given $\gamma \in L^2(L^2(\Omega))$ the semi-gauged electromagnetic field problem has a solution with a unique curl, and for two solutions a_1 and a_2 we always have $a_1(x,t) = a_2(x,t)$ where $\gamma(x,t) \neq 0$. The main idea of the proof of this statement is to impose an *artificial conductivity* in the air region and to control the amount of conductivity by a regularization parameter. The resulting *regularized* problems are purely parabolic and properly gauged. It can be shown that sequences of regularized problems can be chosen in such a way that they converge towards a field that represents a solution of equation 4. A detailed account of the techniques involved is given in [11] in a more abstract setting. Similar ideas have been applied by S. Zaglmayr in [12].

The lack of uniqueness in our model system (5) leads to severe numerical problems, since the linear systems of equations resulting from a finite element discretization will be singular. Hence, a straight forward application of numerical standard solvers will fail. Nevertheless, certain discretizations of the non gauged formulation can efficiently be solved [see 13]. The crucial idea is to perform an approximate Helmholtz decomposition on the discrete level and to treat the curl-free component in another way than the component with vanishing divergence. Such an algorithmic Helmholtz decomposition requires the choice of certain finite elements. From the work of R. Hiptmair, [e.g. 14], it is known that Nédélec elements [15, 16] allow for such a treatment, contrary to nodal elements.

Nédélec elements are the natural choice to discretize electromagnetic problems in three dimensions, both in the case of a saddle point formulation or in the case of an non gauged formulation. In the former case they provide a good approximation to the curl of the vector potential and simultaneously fulfill the discrete LBB-condition. In the lowest order version for hexahedral meshes, the test- and trial functions on an individual mesh element possess the form

$$b_k(x) = \begin{pmatrix} a_{11}^{(k)} + a_{12}^{(k)}x_2 + a_{13}^{(k)}x_3 + a_{14}^{(k)}x_2x_3 \\ a_{21}^{(k)}x_1 + a_{22}^{(k)} + a_{23}^{(k)}x_3 + a_{24}^{(k)}x_1x_3 \\ a_{31}^{(k)}x_1 + a_{32}^{(k)}x_2 + a_{33}^{(k)} + a_{34}^{(k)}x_1x_2 \end{pmatrix} \tag{8}$$

with $x = (x^{(1)}, x^{(2)}, x^{(3)})^\top$, $a_k, b_k \in \mathbb{R}$, $k = 1, 2, 3$. The degrees of freedom are integral means

$$M_i(b) = \int_{\Gamma_i} b \cdot t_i \tag{9}$$

over the edges Γ_i, $i = 1, \ldots, 4$ of the tetrahedron. This choice of degrees of freedom enforces only the continuity of tangential components of the resulting discretization over element faces, while normal components may jump. This corresponds to the smoothness properties of piecewise analytic functions that are globally in $H_{\mathrm{curl}}(\Omega)$, implying that Nédélec elements provide a conformal approximation. Nédélec elements for tetrahedra are constructed in a similar way.

Next, we discuss the temporal discretization, which is based on a discontinuous finite element method. These methods are on the one hand known to be particularly good suited for long-term computations and facilitate on the other hand error estimation for the fully discrete scheme, since they are Galerkin methods (e.g. [17, 18, 19, 20]).

Let $T_1 = t_0 < t_1 < \ldots < t_n = T_2$ be a partition of $I = [T_1, T_2]$ and $I_n = (t_{n-1}, t_n)$ the nth time interval with length $k_n = t_n - t_{n-1}$. Let $\mathcal{S}_n$ be the finite dimensional space used in the nth timestep for spatial discretization. Let further

$$V_q = \left\{ v \in L^2\left(H^1(\Omega) \,:\, v|_{I_n} \in V_{q,n}\right)\right\},$$

with $q \in \mathbb{N}_0$ and with

$$V_{q,n} = \left\{ v \,:\, v = \sum_{j=0}^{q} t^j \, u_j \,, u_j \in \mathcal{S}_n \right\},$$

be the time-space test- and trial space. For brevity, we will write

$$A(u, v) = \frac{1}{\mu} \int_\Omega \operatorname{curl} u \, \operatorname{curl} v \,.$$

An approximation $a^h \in V$ to the vector potential a is computed via the fully discrete scheme

$$\int_{I_n} A(a^h, v) + \int_{I_n} \left[\left(\frac{\partial a^h}{\partial t}, v \right)_{\Sigma \cup S} + \left([a^h]_{n-1}, v(\cdot, t_{n-1}+) \right)_{\Sigma \cup S} \right] = \int_{I_n} (s, v)_S \tag{10}$$

for all $v \in V_q$ and $n \in \mathbb{N}$, where $[w]_n = w(\cdot, t_n+) - w(\cdot, t_n-)$, $w_n^\pm = \lim_{s \to 0^\pm} w(t_n + s)$. Here

$$(u, v)_D = \int_D u \, v \,, \qquad u, v \in L^2(D)$$

denotes the standard scalar product of $L^2(D)$ for a domain $D \subset \mathbb{R}^3$. The source term $s \in L^2(L^2(S))$ is given by $\nabla \phi$ in equation (4).

In [11] it is shown, that the fully discrete scheme obtained by the DG(0)-Method converges to the solution of the continuous solution of a mixed elliptic-parabolic problem. Moreover, an explicit bound for the a priori error is presented. This estimate can also be established for the electromagnetic problem. We do not go into details here.

4 Coupling Strategies

The coupling between the mechanical and electromagnetic subsystems takes the form of the Lorentz force, the electromotive intensity, and the current geometry of the workpiece. The simulation of the coupled process is carried out on two meshes, one for the electromagnetic field computation and another for the mechanical structure. At a certain time step, the magnetic vector potential depending on the input amperage and the position of the structure is computed in the electromagnetic mesh and Lorentz force as well as electromotive intensity are derived. After that, these quantities are transferred into the mechanical mesh and imposed on the structure to determine its corresponding position. The altered position of the work piece is then transferred into the electromagnetic mesh and a corrected force distribution is computed. The two steps *field computation* and *structure simulation* are iterated until the electromagnetic fields and the position of the structure do not change in the scope of accuracy. This iterative scheme guarantees that the correct loads are computed for the mechanical structure, namely those connected to the new position of the work piece. When an equilibrium is attained, the next time step is started.

A natural discretization of the field equations leads to a moving mesh for the mechanical system, representing its current configuration and a fixed Eulerian mesh for the electromagnetic field. However, this approach implies serious difficulties concerning the data transfer between the two meshes: In those areas of the electromagnetic mesh currently covered by the moving structure a diffusive process with a positive finite diffusivity takes place, while outside this region the diffusivity is infinite such that the equilibrium state of the field is immediately assumed. Such a change alters the local discretization since a contribution to the mass matrix is present as soon as a point is covered by the structure and it disappears when it is uncovered again. It has turned out that this change of the discretization causes oscillations in the time derivative $\partial a/\partial t$ of the vector potential and, thus, in the Lorentz force. Newertheless, averaged quantities can sufficiently accurate be determined with this approach. In [10], it was successfully applied to compute the deformation of a mechanical structure even with relatively coarse discretizations. By the integration of Lorentz forces and due to the time stepping algorithm the above mentioned oscillations are smoothed out. However, as soon as a good and efficient approximation of the forces applied on the mechanical structure is required, an arbitrary Lagrangian Eulerian (ALE) formulation leads to much better results. In this approach, the electromagnetic mesh is adapted to the moving structure such that always the same elements are covered by the moving mechanical structure. Consequently, the character of the discretization in a particular element does never change, which avoids those jumps of a. In contrast to remeshing strategies, this approach preserves the combinatorial structure of the mesh, which allows an effective solution of the arising huge systems of linear equations. The discrete field equations on the electromagnetic mesh have to be reformulated such that the movement of the mesh is correctly considered. Surprisingly, the resulting field equations simplify. Instead of working with the partial time derivative $\partial a/\partial t$, it is convenient in this case to employ the material time derivative $\dot{a} = \partial a/\partial t + \nabla a \times v$ since its discretization is a function of the vertices of the moving mesh inside the mechanical structure rather than of spatial points. Thus, no interpolation is necessary to link past data to current data. Inside the fixed tool coil $\dot{a} = \partial a/\partial t$ applies and in

the air surrounding the tool coil and the workpiece the field assumes an equilibrium position instantaneously, which is explicitly neither depending on values of $\partial a/\partial t$ nor on values of a from a preceding time step. The weak semi-gauged form for the electromagnetic problem then takes the form

$$\int_\Omega \frac{1}{\mu} \operatorname{curl} a \operatorname{curl} a^* + \int_\Sigma \gamma_\Sigma \, a^* \, \dot{a} + \int_S \gamma_S \, a^* \, \dot{a} = -\int_S \gamma_S \, a^* \, \nabla\phi$$
$$\int_S \nabla\phi \, \nabla\phi^* = 0 \tag{11}$$

with constant conductivities γ_Σ for the work piece and γ_S for the tool coil.

5 Adaptivity

We employ two different concepts of adaptivity: The first concept is based on a precise physical understanding of the forming process at hand. Its advantage is the enormous gain in efficiency it leads to. Its drawback is that the more efficient it is the more restricted is its use to a particular forming situation. The second method is based on quantities that are dertermined from a numerical simulation. It is robust in the sense that it applies to a large class of problems without the need of any adaptations. Figure 1 shows a mesh that has automatically be adapted to the numerical requirements of a mixed elliptic-parabolic problem. The interface region between the parabolic area and the elliptic area is finely resolved [see 21].

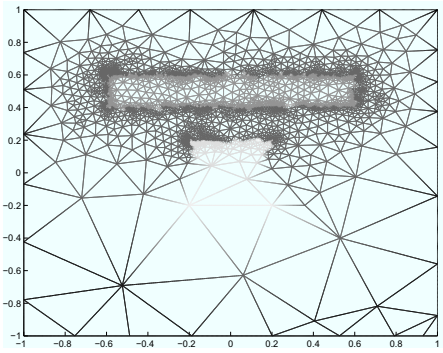

Figure 1: Automatically generated mesh adapted to the numerical requirements of a mixed elliptic parabolic problem

5.1 Adaptivity Based on a Physical Understanding of the Process

From a physical analysis of the process it is clear that after the first half wave of the triggering current has passed by, no more significant amount of energy is transmitted into the work piece. The forming process is then driven by predominantly inertial forces. To correctly meet the particular instance after which no significant energy transmission arises, criteria estimating the transmitted energy from data obtained during the simulation have been developed [1, 2]. Moreover, due to a retarded field expansion caused by magnetic diffusion, the area above the work piece is nearly free of a magnetic field. Hence we can a priori choose a very

coarse discretization there. In addition, a numerical scheme has been developed, that allows for different discretization levels for the electromagnetic and for the mechanical meshes in the context of an ALE-formulation. This is essential, when a shell formulation is coupled with th electromagnetic field computation as in [1, 2]. The influence of these modifications have thoroughly be studied [1, 2]. It has come out that the computational times could be reduced to approximately 1/10 of the original computational time.

5.2 Auto Adaptivity

Dual weighted residual error estimators represent an appropriate approach to error control for problems of the type described above. They allow a control of exactly those quantities which are of interest (see, e.g., [22]). Applied to a staggered solution algorithm, such techniques enable also to control the error of the quantities that realize the coupling between the two subsystems. Thus, error accumulation due to the coupling procedure can be reduced by mesh adaption in both subsystems. To construct a dual weighted residual error estimator for a simultaneous time- and space-adaptive scheme, we first introduce the notations

$$B(u,v) = \sum_{n=1}^{N} \int_{I_n} \left[(\dot{a}^h, v)_{\Sigma \cup S} + A(a^h, v) \right] + \sum_{n=1}^{N} ([a^h]_n \, , v(\cdot, t_{n-1}+))_{\Sigma \cup S}$$

for $u, v \in L^2(H_{\mathrm{curl}})$ and

$$L(v) = \int_I (s, v)_\Sigma$$

for $v \in L^2(H_{\mathrm{curl}})$. The forms B and L are bilinear on $L^2(H_{\mathrm{curl}})$. For the solution a^h of the discrete problem, we obtain

$$B(a^h, v) = L(v) \, , \qquad v \in V \, .$$

Since the solution of the originally problem is continuous with respect to the time variable t, all jump contributions $[a]_n$ cancel out, and we have the representation

$$B(a, v) = L(v) \, , \qquad v \in L^2(H_{\mathrm{curl}}) \, .$$

The primal residual R^p is defined by

$$R^p(v) = B(e, v) = L(v) - B(a^h, v) \, , \qquad v \in L^2(H_{\mathrm{curl}}(\Omega))$$

with $e = a - a^h$. It possesses the explicit representation

$$R^p(v) = \int_I (s, v)_S - \sum_{n=1}^{N} \int_{I_n} \left[(\dot{a}^h, v)_{\Sigma \cup S} + A(a^h, v) \right] - \sum_{n=1}^{N} ([a^h]_{n-1} \, , v(\cdot, t_{n-1}+))_{\Sigma \cup S} \, . \qquad (12)$$

With the help of the primal residual we can represent the error in a quantity of interest, which we consider as given by a linear functional J on $L^2(H_{\mathrm{curl}}(\Omega))$. Due to linearity, we have

$$J(a) - J(a^h) = J(a - a^h) = J(e) \, .$$

By the Riesz representation theorem, there exists $\zeta \in L^2(H_{\mathrm{curl}}(\Omega))$ such that

$$B(v,\zeta) = J(v)\,, \qquad v \in L^2(H_{\mathrm{curl}}(\Omega))\,. \tag{13}$$

The field ζ is the solution of the so called dual problem. This is also a well defined evolution problem with similar analytic properties as the primal problems, but with inverted course of time. If, e.g., J is a functional that only depends on $a(\cdot, t_n)$, then J defines initial conditions for the dual problem. Now let ζ^h be an approximation to the solution ζ of the dual problem (13) computed via (10) based on the same mesh as was used to determine a^h. Galerkin-orthogonality yields

$$J(e) = B(a - a^h, \zeta) = B(e, \zeta - \zeta^h) = R^p(\zeta - \zeta^h)\,, \tag{14}$$

where ζ^h is an approximation to the dual solution ζ.

Considering (12), we notice that the error representation given in (14) does not depend on the continuous primal solution a, but only on a^h and on $\zeta - \zeta^h$. The first quantity is a posteriori known, i.e. after a finite element computation has been carried out. If mesh adaptation is the major issue, an approximation of $\zeta - \zeta^h$ is sufficiently accurately determined from ζ^h by a patch-recovery technique. To avoid purely technical discussions, we confine our considerations to finite element meshes that consist of tetrahedra elements and that possess no elements T that contain both inner points of Σ and of $\Omega \setminus \Sigma$ and no elements that contain both inner points of S and of $\Omega \setminus S$. The case of hexahedral elements is treated similarly. The following localized representation of the error can now be derived: With the above notations, we have for $q = 0$ and Nédélec elements of lowest order

$$\begin{aligned} J(e) = & \sum_{\substack{1\le n\le N \\ T\in\mathcal{T}, T\subset\overline{\Sigma\cup S}}} \left[\int_{I_n\times T} s\,(\zeta - \zeta^h) + \int_T [a^h]_{n-1} \left(\zeta - \zeta^h\right)(\cdot, t_{n-1}+) \right] \\ & + \sum_{\substack{1\le n\le N \\ F\in\mathcal{F}}} \int_{I_n\times F} (\zeta - \zeta^h)\, \lfloor \mathrm{curl}\, a^h \rfloor_F\, n_F\,. \end{aligned} \tag{15}$$

Here, $\mathcal{F}$ denotes the set of all faces of the triangulation and $\lfloor \mathrm{curl}\, a^h \rfloor_F$ is the vector consisting of the jumps of $\mathrm{curl}\, a^h$ when passing over the face F. Further, n_F denotes a unit normal vector of the face E pointing outwards. Note the representation given above can be applied both if a^h and ζ^h have been computed via a problem that has explicitly been gauged in the air region or via a non gauged numerical scheme as e.g. proposed by [13]. A full exploitation of the gain in efficiency that would follow when the above error estimator is applied for local mesh adaptation requires to allow for individual time steps in different spatial areas of the discretization. Hence time stepping would become completely implicit. However, having an efficient multi-grid solver at hand, the complexity of a fully implicit treatment would not be significantly larger than that of an explicit scheme for sufficiently high numbers of unknown. Hence we consider the use of the above described technique for time-space mesh-adaptivity as promising for the simulation of large problems of technological relevance. While hanging nodes in time have pointed out to be a major problem for time-space adaptive methods for hyperbolic problem, the situation for parabolic problems looks much better. Errors entering due to mesh irregularities are damped due to the energy dissipation typical of parabolic problems. The numerical implementation and validation of the here presented techniques for a posteriori error control represents work in progress.

6 Conclusions and Future Developments

Although a scientific base for a virtual design for electromagnetic forming processes has been founded, further research is required to establish methods that cope with the large number of unknowns that result from the discretization of typical three dimensional forming situations. Many strategies to reduce computational time have been mentioned in this article. In the sense of a robust algorithm that can be applied to many situations an auto adaptive scheme seems to be very promising. Such a scheme adapts the finite element mesh to the numerical requirements. Dual weighted residual error estimators allow for the control of a quantity of interest. Such a quantity usually results from practical consideration concerning the requirements a formed work piece should match.

References

[1] *Unger, J.*: Modeling and simulation of coupled electromagnetic field problems with application to model identification and metal forming. Ph.D. thesis, Universität Dortmund, 2007.

[2] *Unger, J.*; *Stiemer, M.*; *Svendsen, B.*; and *Blum, H.*: Strategies for 3D simulation of electromagnetic forming processes. Journal of Materials Processing Technology, volume 199: pp. 341–362, 2008.

[3] *Svendsen, B.* and *Chanda, T.*: Continuum thermodynamic modeling and simulation of electromagnetic forming. Technische Mechanik, volume 23: pp. 103–112, 2003.

[4] *Svendsen, B.* and *Chanda, T.*: Continuum thermodynamic formulation of models for electromagnetic thermoinlastic materials with application to electromagnetic metal forming. Cont. Mech. Thermodyn., volume 17: pp. 1–16, 2005.

[5] *Stiemer, M.*; *Unger, J.*; *Blum, H.*; and *Svendsen, B.*: Fully-coupled 3D simulation of electromagnetic forming. In *Proceedings of the 2nd International Conference on High Speed Forming*, pp. 63–72. ICHSF 2006, 2006.

[6] *Stiemer, M.*; *Unger, J.*; *Blum, H.*; and *Svendsen, B.*: An arbitrary Lagrangian Eulerian approach to the three dimensional simulation of electromagnetic forming. 2006. Submitted.

[7] *Reese, S.*; *Svendsen, B.*; *Stiemer, M.*; *Unger, J.*; *Schwarze, M.*; and *Blum, H.*: On a new finite element technology for electromagnetic metal forming processes. Archive of Applied Mechanics (Ingenieur Archiv), volume 74: pp. 834–845, 2005.

[8] *Reese, S.*: A large deformation solid-shell concept based on reduced integration with hourglass stabilization. International Journal for Numerical Methods in Engineering, volume 69: pp. 1671–1716, 2007.

[9] *Moon, F.*: Magnetic interactions in solids. Springer-Verlag, 1980.

[10] *Stiemer, M.*; *Unger, J.*; *Blum, H.*; and *Svendsen, B.*: Algorithmic formulation and numerical implementation of coupled multifield models for electromagnetic metal forming simulations. Int. J. Numer. Methods Engrg., volume 68: pp. 1301–1328, 2006.

[11] *Stiemer, M.*: Dicontinuous Galerkin methods for mixed parabolic-elliptic partial differential equations. 2006. Submitted.

[12] *Zaglmayr, S.*: High Order Finite Elements for Electromagnetic Field Computation. Johannes Kepler Universität, Linz (Dissertation), 2006.

[13] *Sterz, O.*: Modeling and numerical methods of time harmonic eddy currents in three dimensions. (Modellierung und Numerik zeitharmonischer Wirbelstromprobleme in 3D. Whitney-Elemente, adaptive Mehrgitterverfahren, Randelemente.). Heidelberg: Universität Heidelberg, Naturwissenschaftlich-Mathematische Gesamtfakultät (Dissertation 2003). xv, 185 p. , 2003.

[14] *Hiptmair, R.*: Multigrid method for Maxwell's equation. SIAM J. Numer. Anal., volume 36(1): pp. 204–225, 1986.

[15] *Nédélec, J. C.*: Mixed Finite Elements in $\mathbb{R}^3$. Numerische Mathematik, volume 35: pp. 315–341, 1980.

[16] *Nédélec, J. C.*: A New Family of Mixed Finite Elements in $\mathbb{R}^3$. Numerische Mathematik, volume 50: pp. 57–81, 1986.

[17] *Eriksson, K.* and *Johnson, C.*: Adaptive finite element methods for parabolic problems I: A linear model problem. SIAM J. Numer. Anal., volume 28(1): pp. 43–77, 1991.

[18] *Eriksson, K.* and *Johnson, C.*: Adaptive finite element methods for parabolic problems II: Optimal error estimates in $L_\infty L_2$ and $L_\infty L_\infty$. SIAM J. Numer. Anal., volume 32(3): pp. 706–740, 1995.

[19] *Eriksson, K.* and *Johnson, C.*: Adaptive finite element methods for parabolic problems IV: Nonlinear Problems. SIAM J. Numer. Anal., volume 32(6): pp. 1729–1749, 1995.

[20] *Eriksson, K.* and *Johnson, C.*: Adaptive finite element methods for parabolic problems V: Long-Time Integration. SIAM J. Numer. Anal., volume 32(6): pp. 43–77, 1995.

[21] *Stiemer, M.*: Error control for discretizations of electromagnetic-mechanical multifield problems. In *Proceedings of the ENUMATH conference 2005*, pp. 239–246. Santiago de Compostela, 2006.

[22] *Becker, R.* and *Rannacher, R.*: A feed-back approach to error control in finite element methods: Basic analysis and examples. EAST-WEST J. Numer. Math., volume 4: pp. 137–164, 1996.

Modelling of the Mechanical Behaviour of Ultra-Fine Grained Titanium Alloys at High Strain Rates

N. Herzig[1], L.W. Meyer[1], D. Musch[1], T. Halle[1], V.A. Skripnyak[2], E.G. Skripnyak[2], S.V. Razorenov[3], L. Krüger[4]

[1] Chemnitz University of Technology, Materials and Impact Engineering, Germany
[2] Tomsk State University, Russia
[3] Russian Academy of Sciences, Institute of Problems of Chemical Physics, Chernogolovka, Russia
[4] Technical University Bergakademie Freiberg, Institut für Werkstofftechnik, Germany

Abstract

Results of numerical simulations of the mechanical behaviour of coarse grained and UFG titanium alloys under quasi-static uniaxial compression and plane shock wave loading are presented in this paper. Constitutive equations predict the strain hardening behaviour, the strain rate sensitivity of the flow stress and the temperature softening of titanium alloys with a range of grain sizes from 20 µm to 100 nm. Characteristics of the mechanical behaviour of UFG α and $\alpha+\beta$ titanium alloys in wide range of strain rates are discussed.

Keywords

Modelling, high strain rate, ultra-fine grain, material

1 Introduction

During the last decade a significant interest in production and processing of ultra-fine grained (UFG) materials arises. These materials usually show high strength and satisfactory plasticity at static loading. Designing of technology of mechanical forming of UFG metals needs constitutive equations of UFG materials with a good descriptive and predictive capability. The mechanical behaviour of UFG materials in a wide range of temperatures and strain rates is not adequately explored. Therefore, constitutive equations describing the plastic flow of such materials play an important role for computer simulations of mechanical forming processes.

The correct numerical simulation of shape changing during dynamic deformation requires the use of exactly determined physical parameters of constitutive equations. Constitutive models including grain size dependencies of metal alloys are presented e.g.

by Meyers et al. [1],[2] and Zerilli and Armstrong [3]. Khan et al. [4] modified the model of Johnson-Cook [5] by including a grain size dependent term. A suitable quantitative description of the mechanical behaviour of identical titanium alloys in coarse-grained and ultra-fine grained state is ensured by various values of model parameters. The material characteristics limit the opportunities of application of models for the prediction of the mechanical behaviour of ultra-fine grained titanium alloys under dynamic loading. The expected values of a static limit of flow of coarse grained and ultra-fine grained titanium alloys depend on the size of a grain allows receiving from Hall-Petch relation. However, obtaining realistic predictions of strain hardening and flow stress behaviour in a wide range of strain rates remains the issue of the day.

2 Materials

Constitutive equations were developed for α - titanium and $\alpha+\beta$ - titanium alloy Ti-6-22-22S (Ti-6Al-2Sn-2Zr-2Cr-2Mo-Si). The mechanical behaviour of the coarse grained and ultra-fine grained alloys were studied e.g. in [6] and [7]. The chemical composition of the alloys is shown in Table 1. The average grain size of coarse grained material is equal to 15 µm for α-Ti and 20 µm for Ti-6-22-22S. These alloys were processed by multi-axial compressions method. Hence, the average grain size of the specimens decreased to 300 nm.

Material	Al	Sn	Zr	Mo	Cr	Si	Fe	O	N	C
Ti-6-22-22S	5.75	1.96	1.99	2.15	2.10	0.13	0.04	0.082	0.006	0.009
α-Ti (VT1-0)	-	-	-	-	-	0.08	0.12	0.1	0.04	0.05

Table 1: *Chemical composition in wt.% of the grade titanium alloys*

3 Modelling

The conformity of the constitutive equations was studied by means of modelling of the mechanical behaviour of titanium alloys in a wide range of strain rates. Constitutive equations were used for simulation of the uniaxial deformation at Split Hopkinson Pressure Bar (SHPB) and the high velocity flyer plate impact. The system of constitutive equations describing the material deformation in Lagrange form can be written acc. eq. 1, where u_i is a component of particle velocity, E is the specific internal energy, ρ is a mass density, σ_{ij} is the component of the Cauchy stress tensor. Constitutive equations of the material deformation appropriate for high strain rate applications can be formulated by assuming, that the volumetric or dilatational response is governed by an equation of state (EOS), while the shear stress obeys a theory of plasticity. The stress in the material is expressed as the sum of the dilatational and deviatoric parts (eq. 2), where S_{ij} is the deviatoric part of the stress tensor, and p is the hydrostatic pressure defined to be positive in compression. S_{ij} is calculated by the eq. 3, where µ is the shear modulus, de_{ij}/dt and de_{ij}^{p}/dt are the deviatoric parts of the strain rate tensor.

$$\frac{1}{\rho}\frac{d\rho}{dt} = -\frac{\rho}{\rho_0}\nabla_i u_i\,,\ \rho\frac{du_i}{dt} = -\nabla_j \sigma_{ij}\,,\ \rho\frac{dE}{dt} = -\sigma_{ij}\frac{d\varepsilon_{ij}}{dt} \tag{1}$$

$$\sigma_{ij} = -p\,\delta_{ij} + S_{ij} \tag{2}$$

$$\frac{dS_{ij}}{dt} = 2\mu\left(\frac{de_{ij}}{dt} - \frac{de_{ij}^p}{dt}\right) \tag{3}$$

The components of S_{ij} at elastic deformation can be determined from eq. 3. The flow stress and strain relationship can be determined from a plasticity rule (eq. 4) or from an equation of plastic flow (eq. 5), where $\sigma_u = \sqrt{(3/2)\,S_{ij}S_{ij}}$, $d\dot{\varepsilon}_u^p = \sqrt{2/3\,d\dot{e}_{ij}^{(p)}d\dot{e}_{ij}^{(p)}}$, σ_s is the yield stress.

$$\sigma_u = \sigma_s(T, \varepsilon_u^p, d\varepsilon_u/dt) \tag{4}$$

$$\frac{de_{ij}^p}{dt} = \frac{3}{2}\frac{d\varepsilon_u^p}{dt}\frac{S_{ij}}{\sigma_u} \tag{5}$$

Specific features of mechanical properties of nanostructured materials are connected to distinctions of properties of matter in a crystalline phase of grains and properties of matter in the boundary of grains. The decrease of the mass density of nanostructured materials is caused by the increasing of defect density and relative volume of grain boundary phase. Significant changes of mass density of UFG titanium alloys take place at grain sizes less then 10 nm, when the relative volume of grain boundary areas of triple junction of grains sharply increases. The relative volume of grain boundary phase can amount to 20−25%, when the average sizes of a grain correspond to 10 − 20 nm. The elastic modulus of annealed UFG alloys with an average grain size exceeding 100 nm and coarse grained counterparts have no essential difference. At normal conditions the mass density of the titanium alloy Ti-6-22-22S is equal to 4.53 g/cm^3. The bulk modulus B and the shear modulus μ at the temperature T are calculated using eq. 6 and 7, where B_0 and μ_0 are the bulk and shear modulus at the room temperature T_0, γ is the Gruneisen factor, α is the coefficient of volumetric expansion.

$$B = B_0 + (T - T_0)\frac{\partial B}{\partial T}\,,\ \frac{\partial B}{\partial T} = -B_0\alpha\left(\frac{\partial B}{\partial p} - \gamma\right) \tag{6}$$

$$\mu = \mu_0 + (T - T_0)\left.\frac{\partial \mu}{\partial T}\right|_p + p\left.\frac{\partial \mu}{\partial p}\right|_T \tag{7}$$

The bulk modulus B_0 of Ti-6-22-22S alloy is equal to 105.0 GPa, $\partial B/\partial p$ is 4.37, and $\partial B/\partial T$ is –27 MPa/K. The shear modulus μ_0 is equal 46.2 GPa, $\partial\mu/\partial T$ is –2,7 MPa/K, $\partial\mu/\partial p$ 0.54, γ_0 corresponds to 1.23, α is equal to $3.3\cdot10^{-5}$ K^{-1} at 873 K and $1.4\cdot10^{-5}$ K^{-1} at 100 K. The bulk modulus and the shear modulus and their derivatives on pressure and temperature depend on the relative volume of the grain boundary phase (eq 8). Here, B and μ are the bulk and the shear modulus of nanostructured material, subscript ‘g’ corresponds to the grain boundary phase, subscript ‘cr’ corresponds to the crystalline phase, $C^{(g)}$ is the relative volume of the grain boundary phase.

$$B = B_g\, C^{(g)} + B_{cr}(1 - C^{(g)})\ ,\ \mu = \mu_g\, C^{(g)} + \mu_{cr}(1 - C^{(g)}) \tag{8}$$

The relative volume of a grain boundary phase of materials with a grain size of 300 nm and a thickness of the grain boundary region of ~5 nm is less then 0.1. The estimation of modulus leads to $B \sim 0.95 \cdot B_{cr}$ and $\mu \sim 0.95 \cdot \mu_{cr}$. The decrease of the bulk shear modulus of UFG alloys in comparison with the crystalline phase occurs, when grain sizes are smaller than 20 nm. Thus, the variation of the bulk and shear modulus of titanium alloys at grain sizes in the submicrometer range and down to 300 nm is not essential. Sound velocities of the materials can be calculated using eq. 9, where c_s, c_b and c_l are the shear, bulk and longitudinal sound velocities.

$$c_s = \sqrt{\frac{\mu}{\rho}}\ ,\ c_b = \sqrt{\frac{B}{\rho}}\ ,\ c_\ell = \sqrt{c_b^2 + \frac{4}{3}c_s^2} \tag{9}$$

At normal conditions the nominal longitudinal sound velocity of UFG titanium alloys is 6.01 km/s, and the bulk sound velocity is 4.87 km/s. The pressure in a wide range of compressibility can be described by the Mie-Gruneisen EOS (eq. 10, 11), where γ is the Gruneisen factor, E is a thermal part of the specific internal energy of material, $\xi = \rho_0/\rho$, B and B' are the bulk modulus of the material and its derivative on pressure, which is equal to 105 GPa and 4.4, respectively. The Grüneisen factor depends on the compressibility and is described by eq. 12, where γ_0 as a material constant is 1.1.

$$\mathrm{p} = \mathrm{p_c} + \gamma\, \mathrm{E} \tag{10}$$

$$\mathrm{p_c} = \frac{3}{2}\mathrm{B}(\xi^{-7/3} + \xi^{-5/3})\left(1 - \frac{3}{4}(4 - \mathrm{B}')(\xi^{-2/3} - 1)\right) \tag{11}$$

$$\gamma = \gamma_0(V/V_0) + (2/3)(1 - V/V_{0)}) \tag{12}$$

For the determination of the deviatoric part of the stress tensor S_{ij} the yield surface ought to be determined using eq. 4. The temperature dependent plastic flow stress relation in a wide range of plastic strains and strain rates can be described by the modified Johnson-Cook relation (eq. 13) or the Armstrong-Zerilli relation (eq. 14), or the relations of a micro-dynamical model (eq. 15-19).

$$\sigma_s = \left[A + B(\varepsilon_u^P)^n + k d_g^{-1/2}\right]\left[1 + C\ln\left(\dot{\varepsilon}_u / \dot{\varepsilon}_{u0}\right)\right]\left\{1 - \left(\frac{T - T_0}{T_m - T_0}\right)^m\right\} \tag{13}$$

$$\sigma_s = \sigma_{s0} + C_5\left(\varepsilon_u^p\right)^{n_1} + C_6 d_g^{-1/2} + C_2 \exp\left[-C_3 T + C_4 T \ln\left(\dot{\varepsilon}_u / \dot{\varepsilon}_{u0}\right)\right]. \tag{14}$$

Materials	A	B	n	k	C	m	$\dot{\varepsilon}_{u0}$
cg α-Ti	0.19	0.86	0.5	6.2	0.1643	0.7	1
UFG α-Ti	0.19	0.6	0.5	6.2	0.1613	0.7	1
cg Ti-6-22-22S	0.99	1.131	0.452	8.49	0.1284	0.7	1
UFG Ti-6-22-22S	0.99	1.131	0.452	8.49	0.1559	0.7	1

Table 2: *Constants of the modified Johnson-Cook model*

The material parameter of the modified Johnson-Cook and Armstrong-Zerilli equation are summarised in Table 2 and 3 for two different titanium alloys in coarse grained (cg) and ultra-fine grained (UFG) state.

Materials	σ_{s0}	C_6	C_2	C_3,	C_4	C_5	n_1
cg α-Ti	0.19	6.2	0.1843	0.000877	0.0004	0.86	0.5
UFG α-Ti	0.19	6.2	0.9298	0.000877	0.00015	0.6	0.5
cg Ti-6-22-22S	0.99	1.131	0.699	0.0024	0.01813	0.98	0.5
UFG Ti-6-22-22S	0.99	1.131	0.4464	0.0024	0.01681	1.01	0.5

Table 3: *Constants of the Armstrong-Zerilli model*

The strain hardening of titanium alloys associated with the accumulation of dislocations is described by eq. 15-17. The back stress σ_{bs} can be described using eq. 16, where α_1 is a phenomenological constant, b is the Burger's vector (for hcp titanium equal to 2.86 10-10 m), N the mobile dislocation density. The evolution of the dislocation density during deformation is described by eq. 17, where ξ=N/N_0, N_0 is the initial density of dislocations, K_0, K_1, and K_2 are phenomenological parameters of the material, q is a constant at the fixed temperature, t denotes the time, $\dot{\varepsilon}_0^p$ is equal to 1 s^{-1}. Using eq. 17 the increase of dislocation density during plastic deformation is taken into account. K_0 characterises the dislocation production during plastic flow, K_2 describes the annihilation of dislocations, K_1 characterises the emission of dislocations from the boundary of grains.

$$\sigma_s = \sigma_{s0} + \sigma_{bs} + C_6 d_g^{-1/2} + C_2 \, exp\left[-C_3 T + C_4 T \, ln\left(\dot{\varepsilon}_u / \dot{\varepsilon}_{u0}\right)\right] \tag{15}$$

$$\sigma_{bs} = \alpha_1 \mu b N^{1/2} \tag{16}$$

$$\frac{d\xi}{dt} = \frac{d\varepsilon_u^p}{dt}\left[K_0 + K_1\sqrt{\xi} - K_2\xi\left(\frac{1}{\dot{\varepsilon}_0^p}\frac{d\varepsilon_u^p}{dt}\right)^{-\frac{1}{q}}\right] \tag{17}$$

The approximation of the dependence of dislocation density versus effective plastic strain can be described using eq. 18, where N_0 is the initial density of dislocations, N^* is the largest density of dislocations, which is achieved in conditions of balance of processes of the generation and annihilation of dislocations, N' is the density of dislocations generated at dynamic loading, and G_1 is a material constant. Parameter N^* depends on temperature of the plastic deformation and is equal to ~10^{12} cm^{-2}. The initial dislocation density of UFG alloys produced by severe deformation methods is not less than ~10^9 cm^{-2}. The parameter $G_1/\mu b$ was determined to ~0.07 for coarse grained Ti-6-22-22S. Heterogeneous nucleation of dislocations under dynamic loading causes an increase of dislocation density. This rise of dislocation density is described by eq. 19, where n, η, σ_u^* are constants of the material, H is the Heaviside function, $\dot{\varepsilon}_{u0}^*$ is ~10^4 s^{-1}, and $\dot{\varepsilon}_{u0}$ =1.0 s^{-1}.

$$N = N^* - \left(N^* - N_0 - N'\right)\exp\left(-\tfrac{G_1}{\mu b}\varepsilon_u^p\right) \tag{18}$$

$$N' = \frac{1}{\eta}\left(\frac{\sigma_u}{\sigma_u^*} - 1\right)^n H(\sigma_u - \sigma_u^*)\, \mathrm{H}\left(\frac{\dot{\varepsilon}_u - \dot{\varepsilon}_{u0}^*}{\dot{\varepsilon}_{u0}}\right) \tag{19}$$

The critical stress σ_u^* of heterogeneous nucleation of dislocations depends on microstructure heterogeneity. Its value is equal to 1.45 GPa for coarse grained and 1.02 GPa for UFG Ti-6-22-22S. For α titanium σ_u^* is less than for $\alpha+\beta$ alloys and 0.63 GPa for coarse grained α-Ti and ~0.64 GPa for UFG alloy. Parameter η characterises the rate of dislocation density rise at shock loading. Its value depends on heterogeneity of microstructure. Eq. 15-19 allows the description of relaxation of the amplitude of an elastic precursor by means of taking into account of N'. It may be mentioned, that the constitutive equations (e.g. eq. 13, 14) do not allow the reception of a quantitative exact prediction of a relaxation of an elastic precursor for titanium alloys. The formation of dislocation cell substructures causes the transformation from the grain size to the average dislocation cell dimension. Fracture of titanium alloys at shock wave loading is described by the spall fracture model [7], where σ_1 is the principal stress, σ_{sp} is the spall strength and $\sigma_1 \geq \sigma_{sp}$. The spall strength of 4.7 GPa was used for simulation of spall fracture of UFG Ti-6-22-22S under shock wave loading. This value exceeds the spall strength (3.63-4.16 GPa) of its coarse grained counterpart [6]-[7].

4 Results

Variation of the grain sizes up to hundreds of nm causes a change of modulus of elasticity. Decrease of the bulk modulus leads to a change of shock adiabatic curve. The adiabatic compression curve received by eq. 10 and 11 is shown in Fig. 1. The solid curve corresponds to compression of polycrystalline titanium alloys. The dashed curve displays the calculated adiabat of UFG titanium with a grain size of 300 nm. Thus, coarse grained and UFG titanium alloys have no considerable difference in the Hugoniot adiabat. Both curves show a good correlation with experimental data in the range of intensity of dynamic compression up to 20 GPa. Differences in adiabatic curves of coarse-grained and nanostructured titanium alloy may appear at grain sizes of nanostructured alloys less than 50 nm. The influence of grain size on a plastic flow stress in a wide range of a strain rates is described by eq. 3-5 together with eq. 13-15. Fig. 2 shows the yield stress of α-Ti in a wide range of strain rates calculated using eq. 14.

Fig. 3 shows the yield stress of α-Ti in a wide range of strain rates calculated using eq. 13 and 14. The yield stress of coarse grained and UFG titanium alloys increases with the increasing strain rates in a range from 10^{-3} up to 10^{+6} s^{-1}. Eq. 13 allows receiving a suitable prediction of the yield stress at strain rates up to 10^4 s^{-1}. At grain sizes from 20 μm down to 50 nm the variation of the yield stress of titanium alloys in the range of strain rates from 10^{-4} to 10^6 s^{-1} can be described using eq. 14. Fig. 4 shows the calculated yield stress of α-Ti versus the average grain size at a strain rate of 10^{-3} s^{-1}.

It is necessary to note, experimental yield strength of titanium alloys with an average grain sizes from 5 µm down to 100 nm have a wide spacing of values, which is due to different manufacturing techniques for UFG materials. Fig. 5 and 6 show the strain rate sensitivity of the yield stress of UFG and coarse grained titanium alloys. The yield stresses at 0.2 % of plastic strain were used for estimation the strain rate sensitivity m. Factor m of UFG $\alpha+\beta$ titanium alloys increases at strain rates larger than 10^4 s^{-1}.

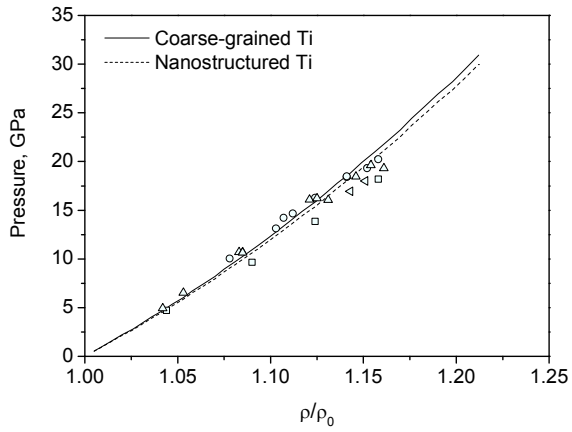

Figure 1: *Shock pressure versus relative mass density. Experimental data [9]*

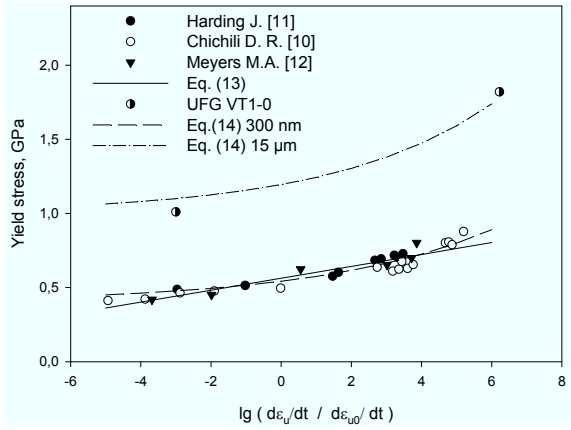

Figure 2: *Yield stress versus the logarithm of the normalized strain rate of α-Ti*

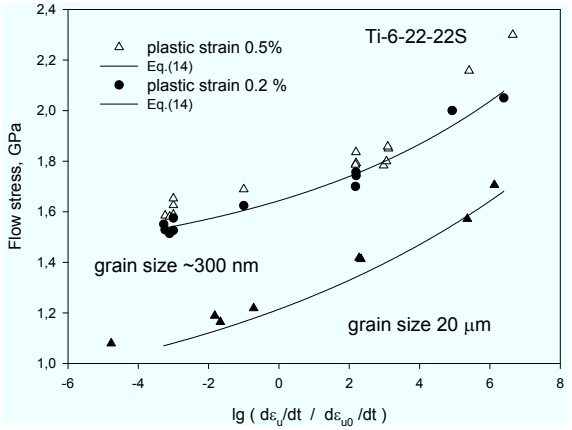

Figure 3: *Yield stress versus the logarithm of the normalized strain rate*

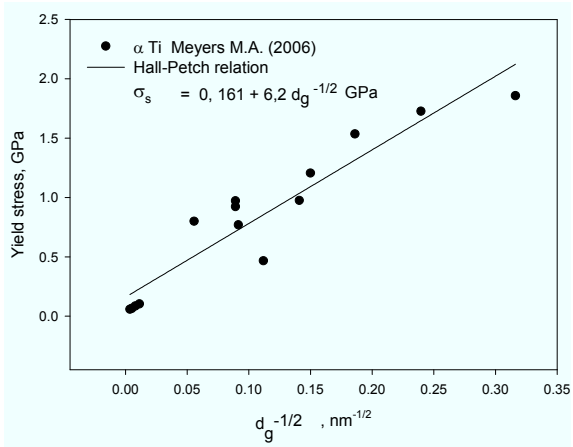

Figure 4: *Static yield stress of α titanium versus reciprocal square root of the grain size. Experimental data [1]*

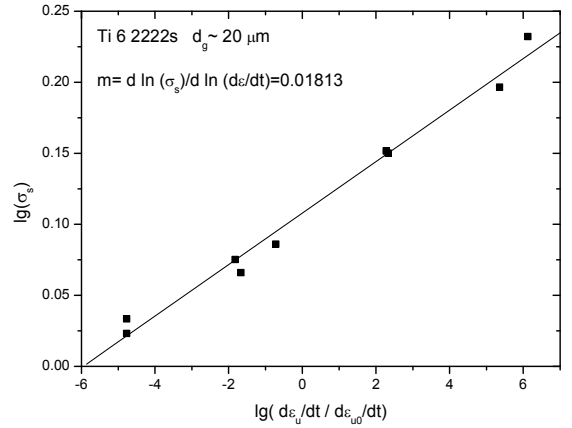

Figure 5: *Strain rate sensitivity of the yield stress of coarse-grained Ti-6-22-22S*

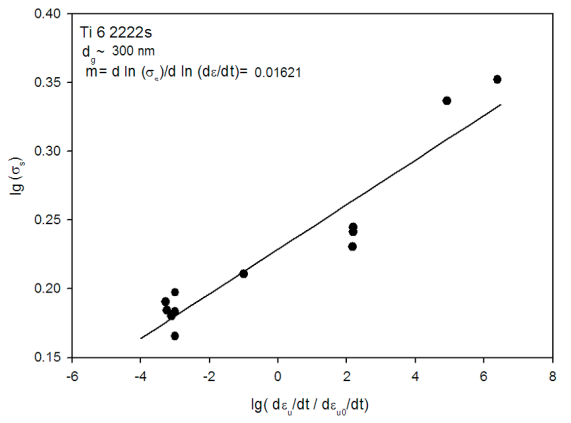

Figure 6*: Strain rate sensitivity of the yield stress of UFG Ti-6-22-22S*

Experimental results (Fig. 5 and 6) show that the strain rate sensitivity of the yield stress of UFG titanium alloys is not constant but rate dependent. Factor m of UFG titanium alloys increases in the investigated range of strain rates. This result differs from conclusions of [13] for materials with hcp, bcc and fcc lattice structure. The divergence in conclusions can be caused by using experimental data of flow stresses which correspond to different plastic strains. The strain rate sensitivity m strongly depends on the plastic strain.

Experimental and calculated yield stresses at plastic strains of 0.5% versus logarithm of strain rate are shown in Fig. 7. UFG alloys display a strong strain hardening at plastic strains up to 1% in comparison with coarse grained materials. Results of numerical simulations of strain hardening of UFG and coarse grained Ti-6-22-22S alloy are shown in Fig. 8. Strain hardening of UFG titanium alloys depends on strain rate. This effect was neglected by constitutive equations of Johnson-Cook [5] and Zerilli-Armstrong [3]. The variation of the factor B of the eq. 13 or the factor C_5 of the eq. 14 give the possibility to have a good quantitative accordance of the calculated strain hardening with experimental data. Sharp increase of dislocation density at dynamic loads can be the reason of changing in the strain hardening rate.

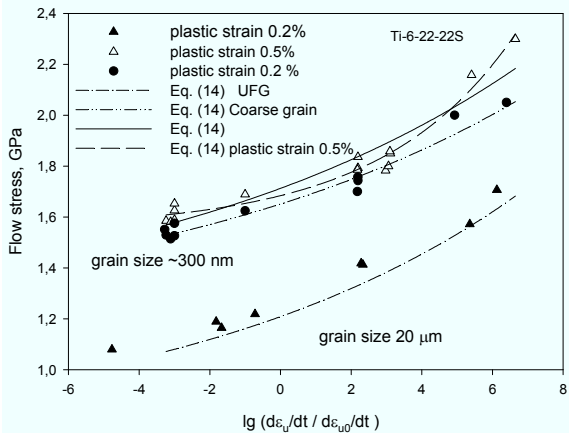

***Figure 7**: Yield stress versus the logarithm of the normalized strain rate*

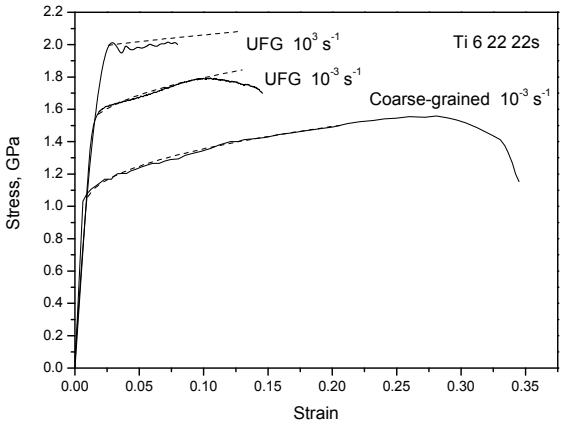

***Figure 8:** Stress versus strain of Ti-6-22-22S titanium alloy. Solid curves correspond to experimental data. Dashed curves are results of calculation*

Eq. 16-19 describe the flow stress dependence on strain rate and plastic strain. Results of numerical simulations of the deformation of α-Ti are shown in Fig. 9. The Autodyn code was used for the simulation of plane shock wave loading of coarse-grained and UFG material. Eq. 14-15 were used for describing of mechanical behaviour of Ti-6-22-22S alloy.

The results of computer simulations of the time history of the free surface velocity under plane shock wave loading are shown in Fig. 10. A good correlation of calculated shock wave amplitudes and duration of shock pulses with experimental data confirms the applicability of the equation of state (eq. 10-12) and constitutive equations of plastic flow (eq. 3-5 and 13-19) for description of the mechanical behaviour of UFG alloys. Fig 10 shows a suitable coincidence of predicted spall strength with experimental results. It can be seen that higher free surface particle velocities can be measured for higher impact

velocities and, hence, a higher spall strength can be found. There, an impact velocity of 660 m/s corresponds to shock pulse amplitudes of ~5-6 GPa and 1250 m/s to ~10 GPa, respectively. The good qualitative consent of the structures of calculated shock pulses after spall fracture of the ultra fine-grained titanium shows that the fracture model suggested in [7] is applicable for prediction of the failure under dynamic impacts.

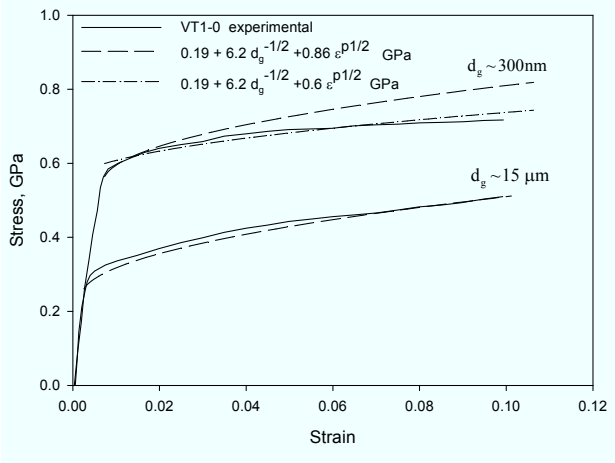

Figure 9: *Stress versus strain of α-titanium (VT1-0) at strain rate 10^{-3} s^{-1} [9]*

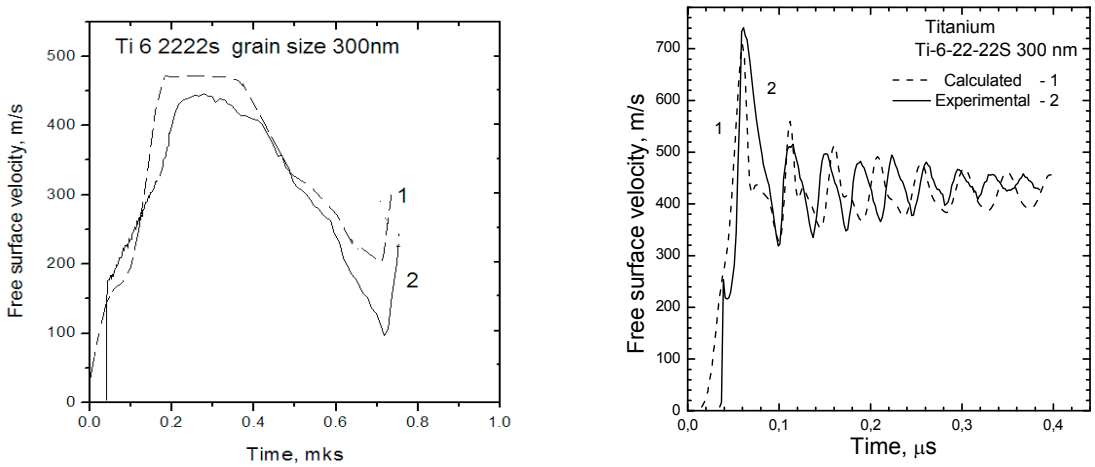

Figure 10: *Calculated (1) and experimental (2) time history of free surface velocity under plane shock wave loading. left) numerical simulation of 660 m/s impact of 2 mm aluminium impactor on 6.36 mm specimen of UFG Ti-6-22-22S. Velocity of impact is 660 m/s. right) results of simulation of impact of 0.12 mm aluminium impactor on 0.835 mm specimen. Velocity of impact is 1250 m/s*

5 Conclusions

From our work the following conclusions can be drawn:

1. The mechanical behaviour of coarse grained and UFG titanium alloys is strongly dependent on strain and strain rate.

2. Thermally activated flow stress behaviour was found for the titanium alloys up to strain rates of 10^6 s^{-1}. No drag effects were measured within the tested range of strain rates.
3. Non-linear constitutive equations have been developed for describing of the mechanical behaviour of UFG and coarse grained titanium alloys. Eq. 13-15 can be used to describe the plastic flow stress behaviour of UFG alloys as a function of the grain size, strain rate, plastic strain, and temperature.
4. Results of computer simulations show a good qualitative consent with experimental data. Simulated free surface velocity profiles can be used for further evaluation procedures.
5. A simple model of the spall fracture is suitable for prediction of the dynamic spall failure of UFG titanium alloys at shock impact loading.

References

[1] *Meyers, M.A.; Mishra, A.; Benson, D.J.:* Mechanical properties of nanocrystalline materials. Progress in Materials Science, 51 (2006), 427–556.

[2] *Meyers, M.A.; Vohringer, O.; Lubarda, V.A.:* The onset of twinning in metals: a constitutive description. Acta mater. 49 (2001), 4025–4039.

[3] *Zerilli, F.J.; Armstrong, R.W.:* Dislocation-mechanics-based relations for material dynamics calculations. J. Appl. Phys. 61 (1987), 1816-1825.

[4] *Khan, A.S.; Suh, Y.S.; Kazmi, R.:* Quasi-static and dynamic loading responses and constitutive modeling of titanium alloys. Int. J. of Plasticity 20 (2004), 2233–224.

[5] *Johnson, G.R.; Cook, W. H.:* A constitutive model and data for metals subjected to large strains, high strain rates and high temperatures. Proc. of the 7th Int. Symp. on Ballistics. Hague, Netherlands. 1983, 541-547.

[6] *Skripnyak V.A., Skripnyak E.G.* Shear strength of nanocrystalline and UFG materials under shock wave loading. Physical mesomechanics, 7 (2004), 297-300.

[7] *Krüger L., Kanel G.I., Razorenov S.V., Meyer L.W., Bezrouchko G.S.:* Yield and strength properties of the Ti-6-22-22S alloy over a wide strain rate and temperature range. In: Shock compression of condensed matter. 2002. 1327-1331.

[8] *Estrin Y.* Unified constitutive laws of plastic deformation. / Ed. by Krausz A.S., Krausz K. New York: Academic Press; 1996. 69.

[9] *Trunin R. F., Belyakova M. Yu., Zhernokletov M. V., Sutulov Yu. N.* Shock compression of metallic alloys. Izv. Akad. Nauk SSSR. Physics of the Solid Earth, 2 (1991), 99–106.

[10] *Chichili D. R. , Ramesh K. T., Hemker K. J.* The high strain-rate response of alpha-titanium: experiments, deformation mechanisms and modelling. Acta mater. 46 (1998), 1025-1043.

[11] *Harding J.* The temperature dependence and strain rate sensitivity of alpha-titanium. Arch. Mech. 27 (1975), 715- 732.

[12] *Meyers M.A. et al.* Evolution of microstructure and shear-band. Progress in Materials Science, 51 (2006), 427–556.

[13] *Kumar K.S., Van Swygenhoven H., Suresh S.* Mechanical behaviour of nanocrystalline metals and alloys. Acta Mater. 51 (2003), 5743–5774.

Towards the Contact and Impact Modeling in Finite Element Simulations of High Speed Forming*

M. Schwarze[1], C. Rickelt[1], S. Reese[1]

[1]Institute of Solid Mechanics, TU Braunschweig, Germany

Abstract

In finite element simulations of high speed sheet metal forming processes the contact between workpiece and forming tools has to be modeled very carefully. Several important aspects have to be taken into account. Robust and locking-free finite element formulations are required to model the sheet forming process, the die has to be considered as a deformable component, and the description of the contact constraints between workpiece and forming tools is a significant source of shortcomings in modeling. The contact and impact simulation makes high demands on the robustness of finite element formulations. For this reason finite elements with low order ansatz functions are preferred. Furthermore, they prove to be advantageous when automatic meshing tools are applied. To overcome the undesired effects of locking we work with an improved version of the innovative solid-shell concept proposed by [11]. It is based on the concept of reduced integration with hourglass stabilization. The use of this solid-shell finite element allows us to test the influence of the modeling of the die and the contact constraints in a very efficient way.

An overview of so-called macro and micro deformations of forming tools in sheet metal forming simulations can be found in [8]. We show that the deformation of the die has a noticeable influence in electromagnetic sheet metal forming. However, in most commercial finite element codes taking into account elastically deformable forming tools requires a full finite element discretization of the die which leads to very high computational effort. Therefore users often assume the tools as being rigid and apply node-based spring-dashpot systems to improve the modeling of the interaction between sheet metal and die. But also in this case local interactions cannot be taken into account realistically. As a possible remedy we investigate a fully elastic description of the forming tools in combination with model reduction techniques. These significantly reduce the number of degrees-of-freedom in the finite element simulation. For this reason we present different alternatives of this technique.

Keywords:

High speed forming, Solid-shell formulation, Contact modeling, Model reduction techniques

*This work is based on the results of the research group FOR 443. The authors wish to thank the German Research Foundation – DFG for its financial support.

1 Introduction

The development of shell theories, which take the three-dimensional geometry correctly into account, has been a topic of recent research in the field of finite element technology. The goal is to modify classical three-dimensional solid elements with only displacement degrees-of-freedom in such a way, that the undesired effects of locking are eliminated and only one element over the sheet thickness is sufficient for a physically correct result. From the viewpoint of industrial users two further aspects play an important role: the element has to be numerically efficient and robust in the case of large mesh distortions and contact computations. That is why many solid-shell formulations are based on the eight-node hexahedral solid element.

In the development of solid-shells the techniques of finite element technology have to be applied to avoid the undesired effect of locking. One important strategy is the method of incompatible modes. It is the basis of the enhanced assumed strain (EAS) concept, developed by Simo and co-workers [16, 14, 15]. Based on a mixed variational principle additional ”enhanced” strains are introduced to avoid non-physical constraints caused by the low order ansatz functions. In problems under compression numerical instabilities might arise [20]. In solid-shell finite element formulations this concept is often applied to avoid volumetric, thickness and membrane locking [6, 18, 1, 11]. Keeping in mind, that the number of EAS degrees-of-freedom might influence the robustness of the finite element analysis, i.e. increase the danger of hourglass instability, especially in the case of forming simulations with contact, we strive to work with a minimum number of enhanced degrees-of-freedom.

In high speed forming simulations the elasticity of the die influences the numerical results noticeably. To increase numerical efficiency we apply projection-based model reduction. Here we consider the methods of modal truncation [3, 4], load-dependent Ritz vectors (LDRV) [5, 4, 10], and proper orthogonal decomposition (POD) [2, 7, 17]. The fundamental idea is to substitute the physical model by a set of modes which well approximate the principal dynamical behaviour. This model reduction does not only reduce the size of our linear components but also preserves the sparsity of the linear part of the Schur complement.

2 Treatment of Locking in Hexahedral Finite Elements

In finite element formulations the undesired effect of locking occurs in different forms. An overview of locking in solid-shell elements with linear and quadratic ansatz functions can be found in [6]. Important strategies to cure locking are the reduced integration concept with hourglass stabilization, the assumed natural strain method, and the EAS concept. To develop a robust solid-shell formulation which allows large time increments in sheet metal forming simulations, we seek to reduce the number of EAS degrees-of-freedom to a minimum.

In sheet metal forming the structure is subject to strong bending. During plastification the material shows nearly incompressible behavior. That is why the transverse shear locking, the thickness locking, and the volumetric locking play the main role. In order to develop a robust

finite element formulation with a minimum number of EAS degrees-of-freedom we investigate here in particular thickness and volumetric locking.

2.1 Thickness Locking

Thickness locking is caused by the linear interpolation of the displacements in thickness direction. Let us consider a bending situation with respect to the η-axis. In this case the term $\mathbf{H}_{\xi\xi}$ of the local displacement gradient tensor has to be constant within the shell plane, but linear over the thickness. The same demand is required for $\mathbf{H}_{\zeta\zeta}$. Unfortunately the linear ansatz functions in ζ lead to a constant value for $\mathbf{H}_{\zeta\zeta}$ and therefore to a non-physical constraint. To avoid thickness locking it is necessary to introduce a linear strain interpolation in thickness direction. This will be done by an EAS ansatz for $\mathbf{H}_{\zeta\zeta}$.

2.2 Volumetric Locking

Volumetric locking in finite element formulations with linear ansatz functions occurs, when the material approaches incompressibility. The fulfillment of the incompressibility condition

$$\det \mathbf{F} = 1 \tag{1}$$

is not possible without artificial constraints. To demonstrate this, let us consider the compatible deformation gradient

$$\mathbf{F}_{\mathrm{comp}\star} = \mathbf{H}_{\mathrm{comp}\star} + \mathbf{1} \tag{2}$$

evaluated at the shell director. The first two columns of the compatible displacement gradient tensor evaluated at the shell director $\mathbf{H}_{\mathrm{comp}\star}$ are linear in ζ. The lack of a linear term in ζ in the third column of $\mathbf{H}_{\mathrm{comp}\star}$ leads to a constrained solution for the incompressibility condition and, consequently, to volumetric locking. So curing the volumetric locking effect means here to ensure the same order of polynoms in $\mathbf{H}_{\mathrm{comp}\star}$. One way is to compute the volumetric part of the element stiffness only in the center of the element. So all terms are constant in the considered point. However, in this case we restrict ourselves to material models with a volumetric-deviatoric split. The second possibility is to enrich the ansatz functions of the appropriate strain terms. This leads to an EAS ansatz with three enhanced degrees-of-freedom at the shell director. However, in this case we introduce artificial strain components at $\mathbf{H}_{\xi\zeta}$ and $\mathbf{H}_{\eta\zeta}$, which we attempt to avoid in the treatment of transverse shear locking. For this reason we modify the Q1SPs solid-shell element formulation and enrich only $\mathbf{H}_{\zeta\zeta}$.

3 Solid-shell Concept

Starting point of the solid-shell formulation is the two-field functional

$$g_1(\mathbf{u}^h, \mathbf{H}^h_{\mathrm{enh}}) = \int_{B_0^h} \tilde{\mathbf{P}}(\mathbf{H}^h) : \mathrm{Grad}\, \delta\mathbf{u}^h \, dV + g_{\mathrm{ext}} = 0 \tag{3}$$

$$g_2(\mathbf{u}^h, \mathbf{H}^h_{\mathrm{enh}}) = \int_{B_0^h} \tilde{\mathbf{P}}(\mathbf{H}^h) : \delta\, \mathbf{H}^h_{\mathrm{enh}} \, dV = 0 \tag{4}$$

in which the displacement vector $\mathbf{u}^h$ and the tensor of enhanced strains $\mathbf{H}^h_{enh}$ are the independent variables. The term g_{ext} includes the virtual work of the external forces. $\mathbf{P}^h$ is the first Piola-Kirchhoff stress tensor. The total strain $\mathbf{H}^h$ is additively decomposed into the compatible strain $\mathbf{H}^h_{comp}$:= Grad $\mathbf{u}$ and the enhanced part $\mathbf{H}^h_{enh}$, the interpolation of which is chosen according to the EAS concept [16, 14, 15]. The index h denotes the finite element discretization of the domain. In the following all values are given in Voigt notation. The interpolation of the total strain $\mathbf{H}^h$ does not differ from the one chosen for the hexahedral element formulation proposed by [12]:

$$\mathbf{H}^h = \underbrace{\left(\mathbf{B}_0 + \left(\mathbf{j}_0^1\,\mathbf{L}_{hg}^1 + \mathbf{j}_0^2\,\mathbf{L}_{hg}^2\right)\,\mathbf{M}_{hg}\right)\,\mathbf{U}_e}_{:=\,\mathbf{H}^h_{comp}} + \underbrace{\mathbf{j}_0^1\,\mathbf{L}_{enh}\,\mathbf{W}_e}_{\mathbf{H}^h_{enh}} \tag{5}$$

For a detailed definition of the variables used in this section see [11]. In contrast to classical finite element formulations the Jacobian matrix is always evaluated in the center of the element. $\mathbf{L}^1_{hg}$ and $\mathbf{L}_{enh}$ are linear in ξ, η and ζ, whereas $\mathbf{L}^2_{hg}$ depends bi-linearly on the local co-ordinates. The vector $\mathbf{W}_e = [W_1, W_2, ..., W_9]^T$ includes the enhanced degrees-of-freedom.

Tacitly we assume that ζ is directed along the thickness direction of the reference element. In this case the normal through the center of the reference element is given by the vector of local co-ordinates $\boldsymbol{\xi}_\star := \{\xi = 0, \eta = 0, \zeta\}$. We call it shell director. The element with the shell director is depicted in Figure 1. In the following we split the displacement gradient tensor into

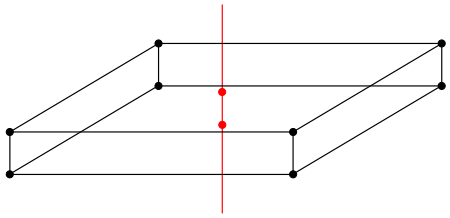

Figure 1: *Shell director on solid-shell element*

$$\mathbf{H}^h = \mathbf{H}^h_\star + \mathbf{H}^h_\triangle \tag{6}$$

in which

$$\mathbf{H}^h_\star := \mathbf{H}^h\,(\boldsymbol{\xi}_\star) \tag{7}$$

is evaluated on the shell director. The two summands of Equation 6 are given by

$$\mathbf{H}^h_\star = \underbrace{\left(\mathbf{B}_0 + \mathbf{j}_0^1\,\mathbf{L}_{hg}^{1\,\zeta}\,\mathbf{M}_{hg}\right)\,\mathbf{U}_e}_{:=\,\mathbf{H}^h_{comp\,\star}} + \underbrace{\mathbf{j}_0^1\,\hat{\mathbf{L}}^{\zeta}_{enh}\,\mathbf{W}_e^{\zeta}}_{:=\,\mathbf{H}^h_{enh\,\star}} \tag{8}$$

and

$$\mathbf{H}^h_\triangle = \underbrace{\left(\mathbf{j}_0^1\,\mathbf{L}_{hg}^{1\,\xi\eta} + \mathbf{j}_0^2\,\mathbf{L}_{hg}^2\right)\,\mathbf{M}_{hg}\,\mathbf{U}_e}_{:=\,\mathbf{H}^h_{comp\,\triangle}} + \underbrace{\mathbf{j}_0^1\,\hat{\mathbf{L}}^{\xi\eta}_{enh}\,\mathbf{W}_e^{\xi\eta}}_{:=\,\mathbf{H}^h_{enh\,\triangle}} \tag{9}$$

Following our conclusions in the previous section, we modify $\mathbf{H}^{h}_{enh\star}$ by reducing the number of enhanced degrees-of-freedom from three to one. Therefore the enhanced displacement gradient tensor, evaluated at the shell-director, simplifies to

$$\tilde{\mathbf{H}}^{h}_{enh\star} = \mathbf{j}^{1}_{0}\, \tilde{\mathbf{L}}^{\zeta}_{enh}\, W_9 \tag{10}$$

in which W_9 is the only enhanced degree-of-freedom. Furthermore $\mathbf{L}^{\zeta}_{enh}$ reduces to

$$\tilde{\mathbf{L}}^{\zeta}_{enh} = \begin{bmatrix} 0 & 0 & 0 & 0 & 0 & 0 & 0 & 0 & \zeta \end{bmatrix}^{T} \tag{11}$$

and becomes a vector. Consequently, if we work with an implicit time integration scheme, the consistent linearization of the two field variational functional simplifies noticeably. Instead of solving an three-dimensional equation system to update $\mathbf{W}^{\zeta}_{e}$, we work now with a scalar equation for W_9, which leads to a faster and more robust element formulation. The element requires a smaller memory to store the EAS variables.

A good description of the stress state over the thickness is the main point of interest for the development of the solid-shell element. For this reason a Taylor expansion with respect to the shell director is carried out, finally leading to the relation

$$\mathbf{P}^{h} \approx \mathbf{P}^{h}_{\star} + \mathbf{A}^{h}_{\star} \left(\hat{\mathbf{H}}^{h}_{comp\,\triangle} + \mathbf{H}^{h}_{enh\,\triangle} \right) \tag{12}$$

In this way the non-linear dependence on ζ is retained in the constitutive qualities, namely the stress $\mathbf{P}^{h}_{\star} := \mathbf{P}\left(\mathbf{H}^{h}_{\star}\right)$ and the tangent $\mathbf{A}^{h}_{\star} := \partial \mathbf{P}^{h}_{\star} / \partial \mathbf{H}^{h}_{\star}$. Note, that

$$\hat{\mathbf{H}}^{h}_{comp\,\triangle} = \left(\mathbf{j}^{1}_{0}\, \mathbf{L}^{1\,\xi\eta}_{hg} + \mathbf{j}^{2}_{0}\, \mathbf{L}^{2\,\zeta}_{hg} \right)\, \mathbf{M}_{hg}\, \mathbf{U}_{e} \tag{13}$$

holds. The analysis of the enhanced degrees-of-freedom is performed at the element level. They are determined separately by the non-linear scalar equation

$$R_w = \int_{\zeta=-1}^{\zeta=+1} \tilde{\mathbf{L}}^{\zeta T}\, \mathbf{j}^{1T}_{0}\, \mathbf{P}^{h}_{\star}\, d\zeta\, 4J_0 \tag{14}$$

for W_9 at the shell director, and by the linear equation

$$\mathbf{W}^{\xi\eta}_{e} = -\mathbf{K}_{ww}\, \mathbf{K}_{wu}\, \mathbf{U}_{e} \tag{15}$$

for $\mathbf{W}^{\xi\eta}_{e}$ inside the hourglass stabilization. Due to the linearity of the last equation, only the single value W_9 has to be saved as history variable.

4 Simulation of Electromagnetic Forming (EMF) with Contact

In this chapter we examine the influence of the contact parameters and the die modeling on the simulation results in EMF. Therefore we expand the three-dimensional example considered in [13] by a die made of steel. The thickness is 10 mm and the gap between the undeformed sheet metal and the die is 12 mm. The die is clamped at the upper side. In the finite element simulation of the problem we benefit from the proposed solid-shell formulation which allows us

to discretize the sheet metal with only one element over the thickness and 448 elements in the sheet plane. Further we model the contact problem by the use of the three-dimensional version of the classical node-to-segment approach in combination with the penalty method. The elastic material parameters of the die are represented by the Young's modulus E = 210.000 N/mm^2 and the Poisson's ratio ν = 0.3. Figure 2 shows the state of deformation before, during, and after the sheet impact. The simulation result of the sheet rebound depends strongly on the

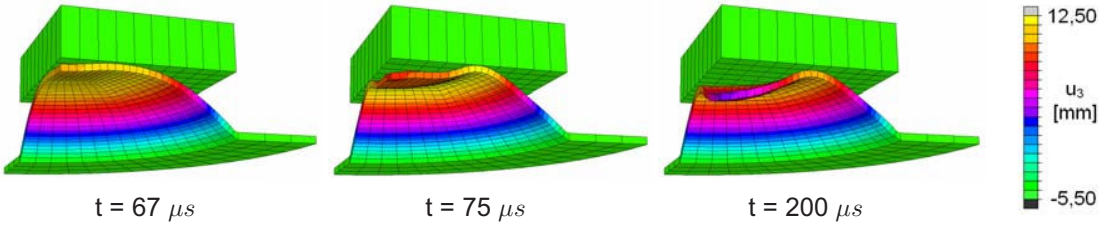

Figure 2: *Impact of the sheet metal at the die*

chosen penalty coefficient ϵ (Figure 3). By the use of small penalty coefficients the work piece penetrates the die deeply and remains there for few time increments. Due to this fact unphysically high restoring forces are introduced between sheet metal and die which lead to an overestimation of the rebound. However, if we work with an adequate value for the penalty coefficient we are able to simulate a nearly converged solution. This allows us to circumvent the application of the numerically more expensive Langrangian method of contact formulation. The second point of investigation is the die modeling. For this reason we optionally model the

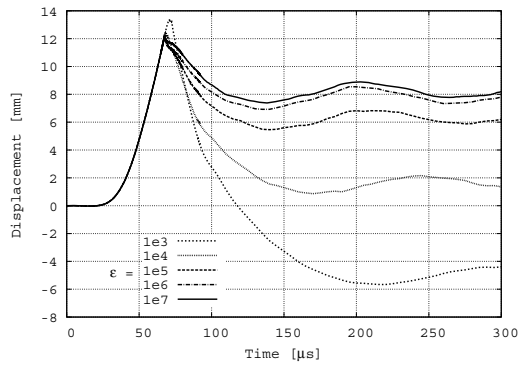

Figure 3: *Influence of pealty coefficient*

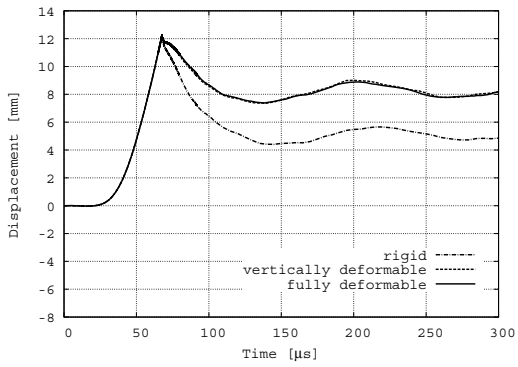

Figure 4: *Influence of die modeling*

tool as rigid, vertically deformable, and fully deformable structure. Comparing in Figure 4 the converged results of the simulated rebound the dependence of the numerical results on the die modeling becomes obvious. If we assume the tool as being rigid the entire kinetic energy of the sheet metal is reflected at the die and remains in the work piece. An overestimated rebound results. If we the die model as being vertically deformable or fully deformable we analyze a noticeable different result which seems to be more physical. However, this procedure is numerically much more expensive and let us consider the application of model reduction on the linearly elastically modeled die.

5 Model Reduction Techniques

In this section we consider model reduction techniques for linear dynamic systems. We start with the ansatz

$$\mathbf{U} = \mathbf{W}\,\mathbf{Q} \tag{16}$$

in which $\mathbf{U}$ is the displacement vector, $\mathbf{Q}$ is the vector of the reduced system and $\mathbf{W}$ a rectangular projection matrix. This approach is inserted into the linear equation of motion

$$\mathbf{K}\,\mathbf{U} + \mathbf{M}\,\ddot{\mathbf{U}} = \mathbf{P}_{\text{ext}} \tag{17}$$

in which $\mathbf{K}$ denotes the stiffness, $\mathbf{M}$ the mass matrix and $\mathbf{P}_{\text{ext}}$ the external load vector. This leads to a set of linear equations

$$\underbrace{\mathbf{W}^{\mathrm{T}}\,\mathbf{K}\,\mathbf{W}}_{\tilde{\mathbf{K}}}\,\mathbf{Q} + \underbrace{\mathbf{W}^{\mathrm{T}}\,\mathbf{M}\,\mathbf{W}}_{\tilde{\mathbf{M}}}\,\ddot{\mathbf{Q}} = \underbrace{\mathbf{W}^{\mathrm{T}}\,\mathbf{P}_{\text{ext}}}_{\tilde{\mathbf{P}}_{\text{ext}}} \tag{18}$$

of reduced order. In the following three different projection-based model reduction methods are summarized. These methods are the modal truncation, the load-dependent Ritz vectors (LDRV) and the proper orthogonal decomposition (POD). They differ in the computation of the projection matrix $\mathbf{W}$.

5.1 Modal Truncation

Modal truncation, also known as modal reduction, is the most simple and popular model reduction method. The idea is to solve a subset of the generalised eigenproblem in which $\mathbf{W}$ is the reduced modal matrix and $\mathbf{E}$ is the reduced diagonal eigenvalue matrix. After the mass normalization procedure

$$\mathbf{W}^{\mathrm{T}}\,\mathbf{K}\,\mathbf{W} = \mathbf{E}, \qquad \mathbf{W}^{\mathrm{T}}\,\mathbf{M}\,\mathbf{W} = \mathbf{I} \tag{19}$$

the reduced decoupled differential equation system

$$\mathbf{E}\,\mathbf{Q} + \mathbf{I}\,\ddot{\mathbf{Q}} = \tilde{\mathbf{P}}_{\text{ext}} \tag{20}$$

is obtained.

5.2 Load-dependet Ritz Vectors (LDRV)

The method of load-dependent Ritz vectors is based on the Lanczos algorithm in combiation with a special start vector. Here the static deflection is used as the first Ritz vector so that all following Ritz vectors may be regarded as the balancing of this initial deflection (see [19]). The advantage of this method is, that no eigenproblem has to be solved. According to [10] the method delivers the reduced coupled differential equation system

$$\mathbf{T}\,\ddot{\mathbf{Q}} + \mathbf{I}\,\mathbf{Q} = \{\beta_1,\, 0, \cdots, 0\}^T\, f(t) \tag{21}$$

wherein the stiffness matrix and the mass matrix are degenerated to an identity matrix **I** and a tridiagonal matrix **T** in generalised coordinates, respectively. If we assume that the load distribution on the structure is constant during the simulation, the projected external load vector $\mathbf{P}_{\text{ext}}$ reduces to $\{\beta_1, 0, \cdots, 0\}^T f(t)$. The scalar value $\beta_1 = \sqrt{\mathbf{w}_1^T \mathbf{M} \mathbf{w}_1}$ is given by the first not mass normalised Ritz vector $\mathbf{w}_1$.

5.3 Proper Orthogonal Decomposition (POD)

A third possibility is the POD method. This method is also known as empirical eigenvectors, Karhunen-Loève expansion, principle component analysis, empirical orthogonal eigenvectors, etc. An overview of nomenclatures used in the literature and areas of application are given e.g. in [2]. The mathematical basis for the POD method is the spectral theory of compact, selfadjoint operators which is explained e.g. in the standard text book of [7]. One problem of this ansatz is that even for small systems the eigenvectors of a large spatial covariance matrix have to be calculated. One approach to lower the computational costs is known as the ”method of snapshots”. In this case each POD basis vector

$$\mathbf{w} = \sum_{J=1}^{m} \beta_J \, \hat{\mathbf{v}}_J \tag{22}$$

is generated out of m uncorrelated zero-mean snapshots $\hat{\mathbf{v}}_J = \hat{\mathbf{u}}_J - \overline{\hat{\mathbf{u}}}$ which describe the deviation from their temporal mean $\overline{\hat{\mathbf{u}}}$. β_J are unknown coefficients which have to be determined. After some derivations and using the assumption that the investigated process is ergodic (see e.g. [9], [7]) only a reduced eigenproblem of dimension m

$$\mathbf{B}\,\boldsymbol{\beta} = \lambda\,\boldsymbol{\beta} \qquad \mathbf{B} = \frac{1}{m}\,\hat{\mathbf{V}}^{\mathsf{T}}\,\hat{\mathbf{V}} \qquad \hat{\mathbf{V}} = [\hat{\mathbf{v}}_1, \cdots, \hat{\mathbf{v}}_m] \tag{23}$$

in which $\hat{\mathbf{V}}$ contains the m snapshots, has to be solved. Finally the empirical eigenvectors **w** result from

$$\mathbf{w} = \hat{\mathbf{V}}\,\boldsymbol{\beta}. \tag{24}$$

Consequently the POD vectors are defined as a linear combination of the snapshots.

6 Conclusions

In this paper a new tree-dimensional solid-shell element has been presented to simulate the contact problem of an electromagnetic sheet metal forming process. The element formulation is free of locking and behaves numerically robustly in contact problems. This allows us to work with a strongly decreased number of elements in comparison to a discretization of the sheet metal with the classical Q1 element formulation.

The tree-dimensional contact problem was analyzed by applying the penalty method in the contact formulation. We have shown that a careful choice of the penalty coefficient allows us to circumvent the numerically more expensive Lagrangian method. An further important conclusion is the fact, that the die should be modeled as an elastically deformable structure.

To reduce the numerical effort arising from this point, we present as remedy the techniques of model reduction. The application of these methods in combination with contact problems is a topic of current research.

References

[1] R.J. Alves de Sousa, R.P.R. Cardoso, R.A.F. Valente, R.W. Yoon, J.J. Grcio, and R.M. Natal Jorge. A new one-point quadtrature enhanced assumed strain (eas) solid-shell element with multiple integration points along thickness - part ii: Nonlinear applications. *International Journal for Numerical Methods in Engineering*, 67:160–188, 2006.

[2] R.A. Bialecki, A.J. Kassab, and A. Fic. Proper orthogonal decomposition and modal analysis for acceleration of transient fem thermal analysis. *Int. J. Numer. Meth. Engng.*, 62:774–797, 2005.

[3] A.K. Chopra. *Dynamics of structures: Theory and applications to earthquake engineering*. Prentice Hall, 2001.

[4] R.W. Clough and J. Penzien. *Dynamics of structures*. McGraw-Hill, 1993.

[5] Jianmin Gu, Zheng-Dong Ma, and Gregory M. Hulbert. A new load-dependent Ritz vector method for structural dynamics analyses: quasi-static Ritz vectors. *Finite Elements in Analysis and Design*, 36:261–278, 2000.

[6] R. Hauptmann, S. Doll, M. Harnau, and K. Schweizerhof. 'solid shell' elements with linear and quadratic shape functions at large deformations with nearly incompressible materials. *Computer and Structures*, 79:1671–1685, 2001.

[7] P. Holmes, John l. Lumley, and Gal Berkooz. *Turbulence, coherent structures, dynamical systems and symmetry*. Cambridge Monographs on Mechanics, 1996.

[8] R. A. Lingbeek and T. Meinders. Towards efficient modelling of macro and micro tool deformations in sheet metal forming. *Materials Processing and Design: Modeling, Simulation and Applications, Proceedings of the 9th International Conference on Industrial Forming Processes*, pages 723–728, 2007.

[9] M. Meyer and H.G. Matthies. Efficient model reduction in non-linear dynamics using the Karhunen-Loève expansion and dual-weighted-residual methods. *Computational Mechanics*, 31:179–191, 2003.

[10] B. Nour-Omid and R.W. Clough. Dynamic analysis of structures using Lanczos coordinates. *Earthquake Engineering and Structural Dynamics*, 12:565–577, 1984.

[11] S. Reese. A large deformation solid-shell concept based on reduced integration with hourglass stabilization. *International Journal for Numerical Methods in Engineering*, 69:1671–1716, 2007.

[12] S. Reese, P. Wriggers, and B. D. Reddy. A new locking-free brick element technique for large deforamtion problems in elasticity. *Computers and structures*, 75:291–304, 2000.

[13] M. Schwarze, A. Brosius, S. Reese, and M. Kleiner. Efficient finite element and contact procedures for the simulation of high speed sheet metal forming processes. In *Proceedings of the 2nd International Conference on High Speed Forming, Dortmund, Germany*, 2006.

[14] J. C. Simo and F. Armero. Geometrically non-linear enhanced strain mixed methods and the method of incompatible modes. *International Journal for Numerical Methods in Engineering*, 33:1413–1449, 1992.

[15] J. C. Simo, F. Armero, and R. L. Taylor. Improved versions of assumed enhanced strain tri-linear elements for 3d finite deformation problems. *Computer Methods in Applied Mechanics and Engineering*, 110:359–386, 1993.

[16] J. C. Simo and M. S. Rifai. A class of mixed assumed strain methods and the method of incompatible modes. *International Journal for Numerical Methods in Engineering*, 29:1595–1638, 1990.

[17] L. Sirovitch. Turbulence and the dynamics of coherent structures part I-III. *Quarterly of Applied Mathematics*, 45:561–590, 1987.

[18] L. Vu-Quoc and X. G. Tan. Optimal solid shells for non-linear analyses of multilayer composites. i. statics. *Computer Methods in Applied Mechanics and Engineering*, 192:975–1016, 2003.

[19] E.L. Wilson, M. Yuan, and J.M. Dickens. Dynamic analysis by direct superposition of Ritz vectors. *Earthquake Engineering and Structural Dynamics*, 10:813–821, 1982.

[20] P. Wriggers and S. Reese. A note on enhanced strain methods for large deformations. *Computer Methods in Applied Mechanics and Engineering*, 135:201–209, 1996.

SESSION 4

PROCESS TECHNOLOGIES

Flanging and Hemming of Auto Body Panels using the Electro Magnetic Forming technology

P. Jimbert[1], I Eguia[1], M. A. Gutierrez[1], B. Gonzalez[1], G. S. Daehn[2], Y. Zhang[2], R. Anderson[3], H. Sundberg[4], S. O. Olsson[5], P. Brännström[6]

[1]LABEIN -Tecnalia Research Center, Automotive Unit. Derio, Spain
e-mail: pjimbert@labein.es, web: http://www.labein.es
[2]Department of Materials Science & Engineering. The Ohio State University. Columbus, OH. USA
[3]Svensk Verktygsteknik, Lulea, SWEDEN
[4]Volvo Truck, SWEDEN
[5]Saab Automobile, SWEDEN
[6]KIMAB, SWEDEN

Abstract

Electro Magnetic Forming (EMF) technology has a great number of potential applications for the automotive industry. LABEIN-Tecnalia has worked with this technology for six years and has a good understanding of the automotive industry's needs and challenges. LABEIN-Tecnalia is currently developing new applications with EMF technology. Taking into account the advantages and limitations of EMF, bending and hemming processes present good geometric conditions for the use of this technology. The study presented is based largely on hemming circular configurations which are simplifications of those commonly used on hemmed automotive parts. The parameters of this new EMF bending and hemming processes have been studied, as well as their influence on the final quality of the parts obtained. Conclusions obtained from the basic geometries were tested on a more complicated geometry in order to apply the knowledge acquired. Parallel to the experimental work, fully coupled electromechanical software by LS-DYNA has been used to simulate and extend the present hemming results.

Keywords

Sheet metal, Forming, Aluminum

1 Introduction

Hemming is one of the last operations to be used on auto body panels. Therefore, it has a critical importance on the performance and perceived quality of assembled vehicles. Due to the required precision on the hemming process and the complexity of the parts, most of the bending, flanging and hemming dies are designed based on experience and on lengthy and costly die tests. EMF can be a solution that saves time as well as money and improves the quality of the hem joint, especially when using aluminum alloys.

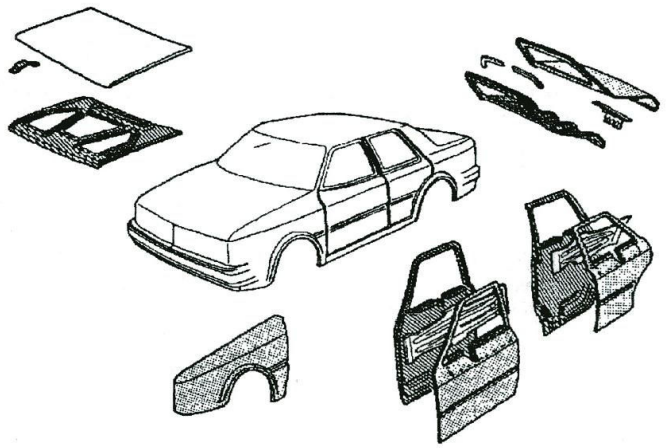

***Figure 1**: Different hemmed parts of the body and white of a car [1]*

Aluminum alloy sheet metal is more difficult to hem due to its susceptibility to strain localization during hemming, which may cause edge cracking on the hemmed edge [2], [3], [4], [5]. As a high-speed deformation method, the electromagnetic forming has some advantages. It can reduce the process time as the whole part is assembled in one rapid operation rather than two separated operations (pre-hemming and hemming). In other words, Electro Magnetic (EM) hemming can save time by not requiring a pre-hemming step.

EMF can also reduce wrinkling on curved areas of the part. This effect is especially important on small radius shrink flanges, expanding the possibilities by allowing the design of new hemming unions for the sharp corners of the parts. EMF will also reduce or avoid edge cracking on aluminum alloys due to the high strain rates achieved during the deformation process.

Before the hemming operation, the auto body panels have to be flanged. The actual mechanical hemming process carries some limitations when dealing with aluminum. For example, the minimum flange height obtained by mechanical flanging is typically greater than 4 mm. Using the EM bending process, this flange height can be reduced. This can

be done precisely and will result in an improved electromagnetic hem. This is especially important when hemming sharp edges of the parts.

The discharged energy of the capacitor bank and the relative position between the coil, the part and the tool are input parameters of EM bending and hemming processes that were investigated in this paper.

The measured output parameters are different for each application. As mentioned before, improved quality is the main objective in hemmed unions for the automotive industry. To study the feasibility of the EMF technology for bending and hemming operations these quality aspects are measured after each set of experiments.

In the flanging experiments, three output parameters are measured: the reduction of thickness of the part, the angle of the bended flange and the final diameter of the part.

For the hemmed samples the primary quality parameter measured is the edge radius (the deformation of the hem union). This is an important parameter when analyzing the quality of the hem union because it is directly related to the “Apparent Gap” (a visual effect of distance between two hemmed parts of the auto body).

2 Materials and Geometries

The aluminum alloy used for these experiments was AA6016T4, which is a widely used alloy for external auto body panels. Its mechanical properties are listed in Table 1.

	Re (MPa)	Rm (MPa)	Elongation (%)	Thickness (mm)
AA 6016 T4	123	237	20	1.1

***Table 1**: Mechanical properties of the AA6016T4 aluminum alloy.*

Three different diameter circular geometries were analyzed with two flange heights for each diameter as listed in Table 2.

	External diameter of the part (mm)			Flange height (mm)	
BENDING	30	60	90	5	7
HEMMING	30	60	90	5	7

***Table 2:** Different geometries analyzed for each process.*

3 Hemming Experiments

All the parts were flanged and then hemmed using EMF technology. The relative position between the EMF coil and the part was the process parameter studied for the two flange heights, 5 and 7mm, respectively. Two overlapping flange length percentages were studied, 15% and 60%. A schema of the EM bending experiments set-up and a picture of one of the bending coils are shown in Figure 2.

3.1 Results for the Bending Experiments

The final geometries of the flanged parts were measured. The reduction of the sheet thickness on the 1.2mm radius of the bent section of the part, the final diameter of the whole part and the final angle obtained on the bent flange were the parameters taken into account when making conclusions.

- Overlapping 15% needs more energy to reach the desired final diameter than using greater amounts of overlap, but the reduction in sheet thickness is smaller for the same final diameter. The material is less damaged after EM bending using a 15% of overlapping.
- The bigger the diameter of the whole part the easier it is to achieve this value without damaging the part.
- No rebound was observed between die and part was observed for any of the geometries.

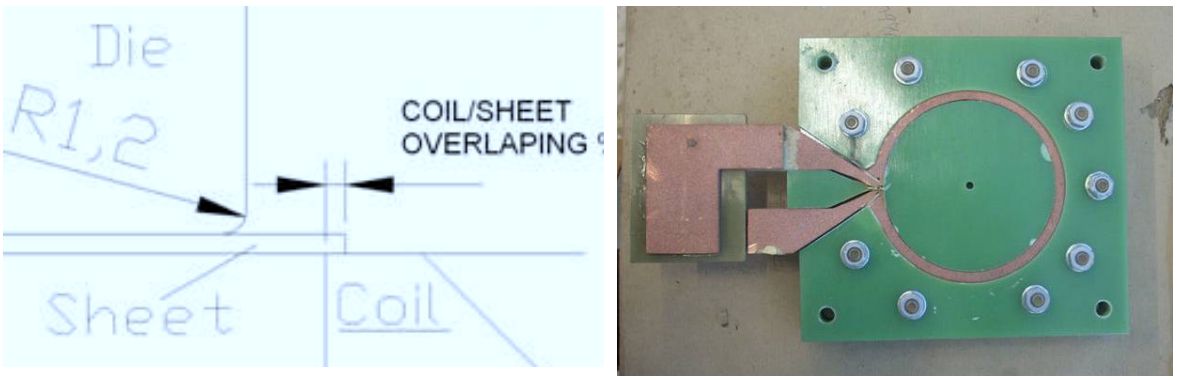

***Figure 2**: Partial section view of the circular flanging set-up (left) and one of the EM flanging coils (right) used in these experiments.*

4 Hemming Experiments

LABEIN-Tecnalia has been developing the EM hemming process for the last two years and has published several papers on this field [6], [7]. These studies have demonstrated the importance of the EM impulse application height over the flange. This EM impulse application height is closely related to the quality of the final hem union. The choice of an appropriate flange height where the EM impulse is applied is essential to ensure the inner part is not deformed in the EM hemming operation.

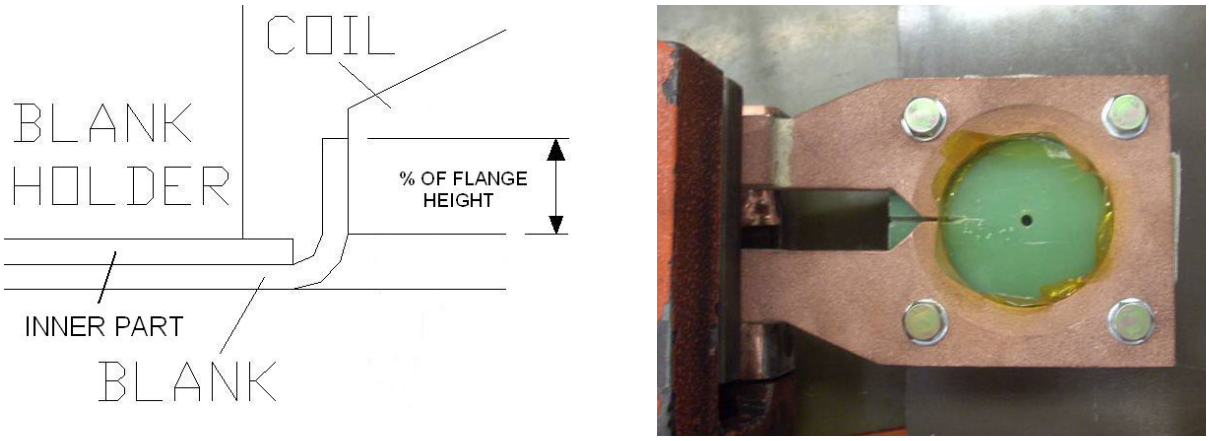

***Figure 3**: Partial section view of the circular hemming set-up with the % of flange height as input variable (left) and one of the hemming coils (right).*

Experiments were conducted with the goal of developing a methodology, which permits the design of coils for hemming complex parts (different diameters of the same geometry). The objective is to determine an EM impulse application height for different diameters avoiding the bending of the inner part and obtaining a good hem union quality. This study of simple geometries will lead us to a methodology for the design of EMF coils for hemming operations and the possibility of hemming more complex parts.

Several different diameters and flange heights were studied changing the percentage of flange where the EM impulse is applied. A schema of the EM hemming experiments set-up and a picture of one of the hemming coils are shown in Figure 3.

4.1 Results for the Hemming Experiments

After the experiments, the parts were analyzed and the most important problem was bending of the inner sheet. As a result criteria to measure and limit this were established. Parts obtained applying the EM impulse at different percentages of the flange height where measured for the same union geometry. Two different aspects of the EM hemming process cause deformation of the inner part. One is that an impact occurs due to a level of impulse that is too high. The other is that the force is applied too near the bend in the flange. The lower percent overlap is needed. To isolate the percentage of flange where the EMF impulse is applied (the scope of this study) the hemming process is performed at a low enough energy so the flange does not impact the inner. Analyzing the geometry at low energy ensures that the deformation of the inner part is caused by the inappropriate application of the EM force and not by the impact of the external part against the inner part. These results are shown in Figure 4 for the 90mm diameter and the 7mm flange height.

***Figure 4**: Optimization of the percentage of flange height where the EM impulse is applied for the 90mm diameter and 7mm flange height geometry.*

Inner part bending limits where established for the rest of the diameters and the results plotted on the graph in Figure 5.

Conclusions of the hemming experiments:

- A relation between the diameter of the part and the EM impulse application height limit has been established.
- This relation is the key factor for continuing development of a methodology for the design of a coil for hemming complex parts.
- This relationship is the same for the 5mm and 7mm flange heights.

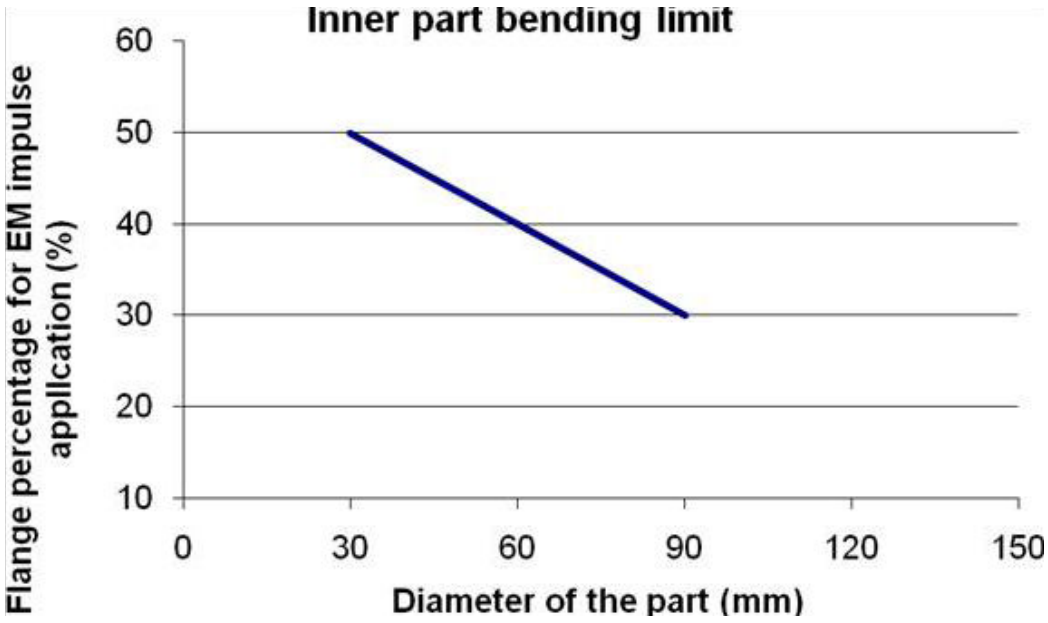

***Figure 5**: EM impulse application limit curve for avoiding the deformation of the inner part*

4.2 Simulation Results

Electromagnetic based simulation model of the process was carried out using fully coupled software by LS-DYNA developed by Pierre L'eplattenier at LSTC of Livermore,

CA. There is good correlation between the experimental and the simulation results (see Figure 6).

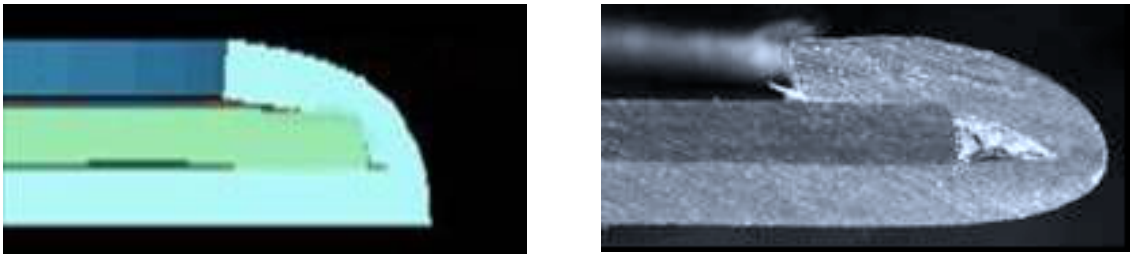

Figure 6*: FEM union obtained using the fully coupled simulation method by LS-DYNA (left) and one of the unions obtained experimentally (right).*

5 Application of the Developed EM Hemming Coil Design Methodology to a Complex Part

Using basic geometries, the first step for the characterization of the EM hemming process was accomplished by obtaining a relation between the part diameter and the coil geometry needed for obtaining a hemmed union without deforming the inner part. The next step is to prove these conclusions on a more complex part, similar to real auto body panels. For this purpose a new coil was designed and implemented containing different diameters and straight areas on the same hem flange line where conclusions from the basic geometries will be applied on the design of the coil.

A coil designed for a current collaboration project between Svensk Verktygsteknik of Sweden and Professor Daehn of The Ohio State University was used for this second approach. The geometry of this coil is shown in Figure 7.

The small number of available parts of parts and time resulted in only a small area of the part being optimized by applying the methodology developed on the design of hemming coils in this study. This area contained a straight hem line and a circular hem line of 120mm diameter for a constant 7mm flange height as shown in Figure 7.

The chosen area of this new coil was machined in such a way that the 120mm diameter flange area has 20% of the flange height applying the EM impulse over it based on an extension of the line in Figure 5. The straight section can be considered as an infinite diameter. As this is impossible, we consider a minimum of 0% overlap for the straight flange area.

To see the improvement of this method two experiments were conducted. Test 1 used 20% of flange for the EM impulse application on the 120mm diameter area and also on the straight area, and a second one. Test 2 used 20% for the 120mm diameter and 0% for the straight area accordingly to the results obtained with the basic circular geometries.

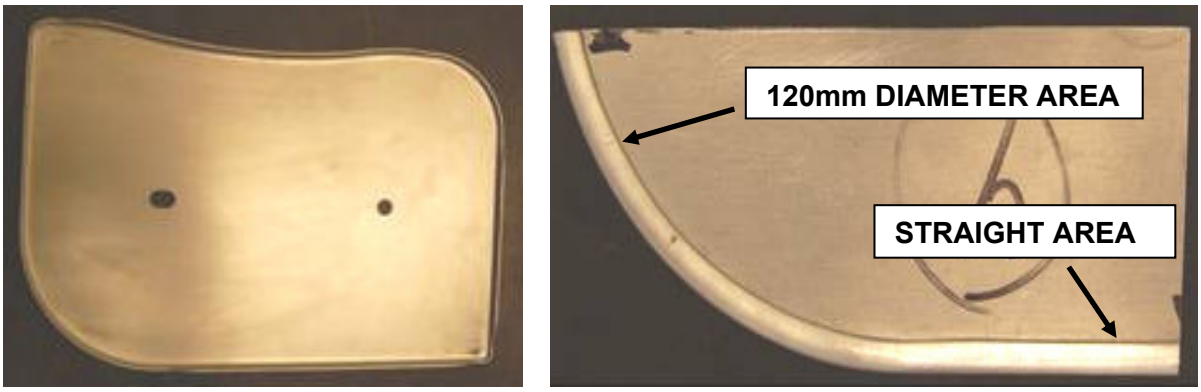

***Figure 7**: Complex part with 5 different diameter on it (left) and the chosen area to be improved applying the methodology developed in this study (right).*

The resulting hem union geometries are shown in Figure 8. The goal of this whole process is obtaining a good hemmed union on different areas of a complex part using one single coil by only changing the EM impulse application percentage over the flange height. Improvement was obtained on the deformation of the straight area while maintaining the same union quality on the 120mm diameter area by only changing the percentage of the flange height where the EM impulse is applied parameter.

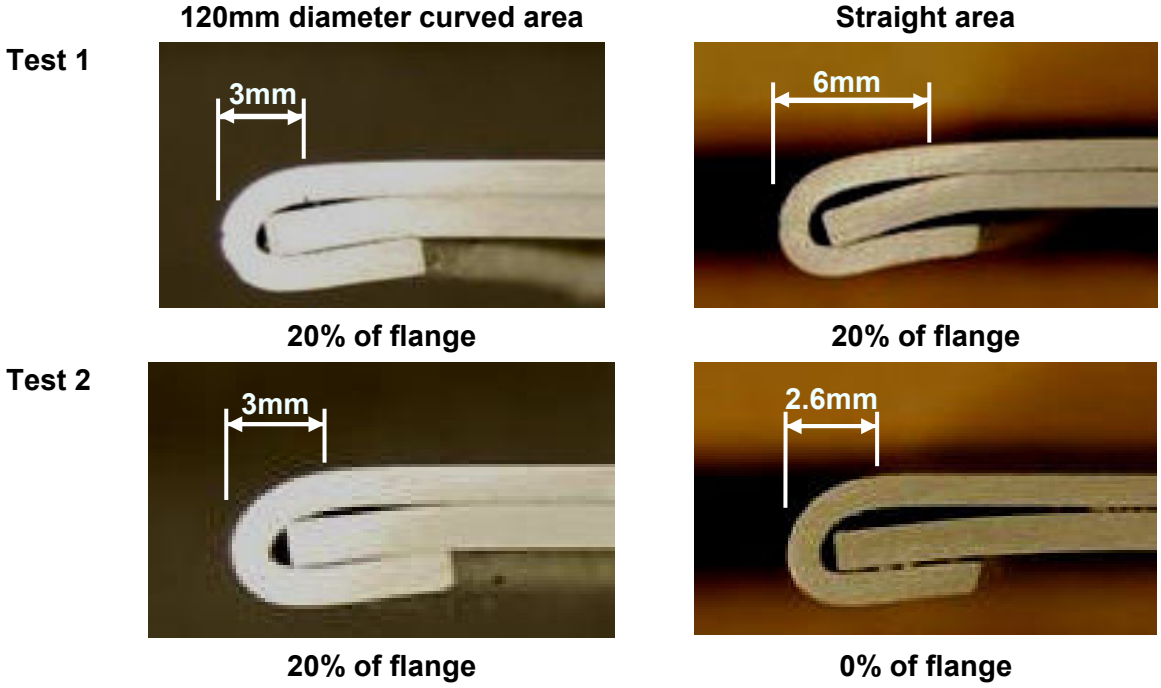

***Figure 8**: Deformation of the hem union for the straight area (left column) and the 120mm diameter curbed area (right column) of the complex part for the First test (upper row) and the Second test (lower row).*

Conclusions for the complex part:

- The methodology for the design of EM hemming coils developed in this study has been applied to the design of a coil for a complex part.
- An improvement in the studied area has been observed after adjusting the percentage of the flange height where the EM impulse is applied, results shown in the graph in the Figure 5.
- By adjusting this parameter, the same hemmed union geometry has been obtained on different geometrical areas of the part using one single coil and one single EM discharge of the capacitor bank.

6 General Conclusions

- The first steps for developing two new process applications for the emerging EMF technology have been established.
- The main process parameters have been studied and relationships have been developed.
- These conclusions have been applied to a complex part giving satisfactory results.
- Good agreement between experimental samples and prediction with the fully coupled simulation method was achieved

7 Future Work

- A complex part will be designed to further prove the conclusions arrived at from these experiments. This methodology will continue to be studied and improved for designing EM coils for hemming operations. This part will contain different diameters and straight areas always moving towards real auto body panels.
- Fully coupled simulations will be used to design the coil for this more complex hemming operation.

8 References

[1] *Haydar Livatyali, M.S.* : Computer aided process design of selected sheet metal bending processes-Flanging and Hemming., Dissertation, The Ohio State University, 1998

[2] *Carsley, J. E.*: Microstructural evolution during bending: *Conventional Vs. Roller hemming*, Trends in materials and manufacturing Technologies for transportation industries and powder metallurgy research and development in the transportation industry, Materials Processing & manufacturing division, 6th global Innovations

Proceedings, TMS Annual Meeting, San Francisco, California, USA, February 13-17, 2005.pp 169-174

[3] *Lin, G.*.: Quality and formability of automotive aluminium alloys, Dissertation, The University of Michigan, 2006

[4] *Golovashchenko, S.:* Sharp flanging and flat hemming of aluminum exterior body panels, Journal of materials engineering and performance, Vol. 14, August 2005, pp 508-515

[5] *Krajewski, P.E.; Carsley, J.E.:* Heat treatment effects on bending in AA6111, Aluminum 2003, ed: S.K. Das, TMS, 2003, pp25-35

[6] *Jimbert, P.; Eguia, I.; Perez, I.; Gonzalez, B.; Daehn, G*.: Hemming of aluminum sheet panels using the electromagnetic forming technology. Proceedings of International Deep-drawing Research Group IDDRG 2007 International Conference 21-23 May 2007, Győr-Hungary

[7] *Jimbert, P.; Eguia, I.; Daehn, G*.: Straight hemming of aluminum sheet panels using the electromagnetic forming technology. Proceedings of SHEMET 2007 Palermo, ITALY

Research in Impulse Joining of Self Pierce Riveting*

O. Hahn[1], R. Neugebauer[2], G. Leuschen[1], C. Kraus[2], R. Mauermann[2]

[1] Laboratory of Materials and Joining Technologies, LWF, University of Paderborn, Germany
[2] Fraunhofer Institute for Machine Tools and Forming Technology IWU, Chemnitz, Germany

Abstract

Results are shown in impulse joining of aluminium sheets with self-pierce-riveting. Two institutes are testing impulse-riveting with different setting velocities of the punch – up to 10 m/s by using pneumatic cylinders and about 100 m/s by using a propellant charge.

One aim focus consists in riveting without a C-frame against a flat anvil instead of using a C-frame with a contoured die. So accessibility is increased and disadvantages of occurring misalignments are avoidable.

The strength properties of the realised joints are tested.

Keywords

Mechanical joining, Impulse-joining, Self-pierce riveting, Aluminium

1 Introduction

Mechanical joining of metal sheets has become more and more important in the automotive industry. One major part concerning joining in the automotive industry is self-pierce-riveting (SPR).

---

* *This work is based on the results of the AiF research project 14888BG; the authors would like to thank BMWi for its financial support*

The standard tool is based on a C-frame. With increasing throat depth and joining forces the C-frame has to be built in a massive manner. Otherwise misalignments occur between die and punch what leads to decayed joints. With these massive constructions, robot-handling of C-frames is often not feasible anymore. At the moment realised deep-throats for C-frames are about 600 mm. Additional accessibility is limited with C-frames.

An alternative is the use of the impulse technology for joining rivets. By using the inertia of the system it is possible to work with low-stiff C-frames or without C-frames. If one works without C-frames, one must get the occurring misalignments under control.

Riveting with different joining velocities is studied by two institutes.

2 SPR-Setting

The standard SPR-procedure is based on setting velocities of about 0.005 to 0.01 m/s using a punch / contoured-die system on a C-frame. There are four steps to be proceeded:

1. The sheets are positioned to be joined together,
2. The punch pushes the rivet, which cuts through the upper-plate
3. Rivet spreads in the bottom-plate
4. Tool opens and plates are ejected

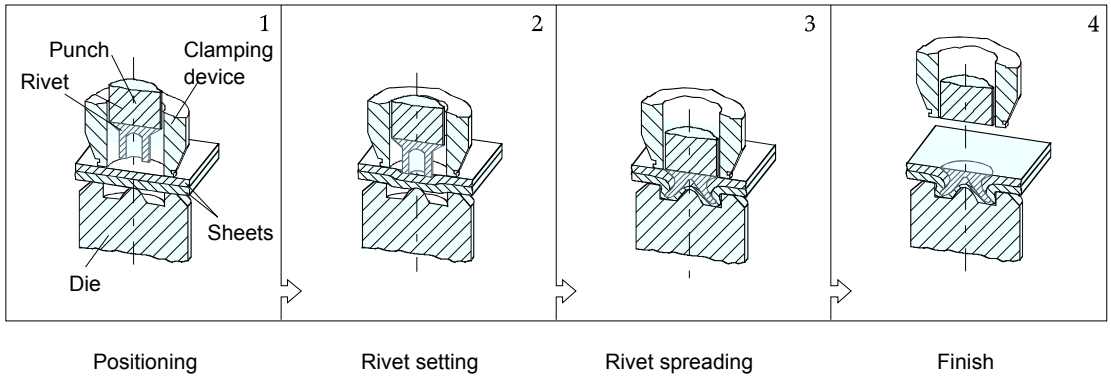

***Figure 1**: SPR-procedure [1]*

As mentioned above the aim is to work without a C-frame. In order to avoid decayed joints with misalignments > 0.2 mm, one works against a flat anvil. Replacing the contoured die by the flat anvil there are only minimal eccentricity requirements (< 1 mm). There are two main advantages in using a flat anvil:

1. One “flat die” for different joining operations, instead of one for each
2. High tolerances against misalignments between punch and die
3. The state of stress is predominantly compression. Thus also less ductile materials can be joined.

An attempt to eliminate the contoured die by using the flat anvil with the conventional setting speed (0.005 m/s) does not lead to functional and respectively optimal results as shown in figure 2, left image. As you can see the rivet set with the significant lower setting velocity did not even cut through the upper-plate. The right image shows a joining result with setting speed of about 120 m/s. The conventional set rivet has been strongly compressed, while with the impulse-technique set rivet has cut the upper-plate and spread rightly in the bottom-plate.

Conventional velocity v = 0.01 m/s

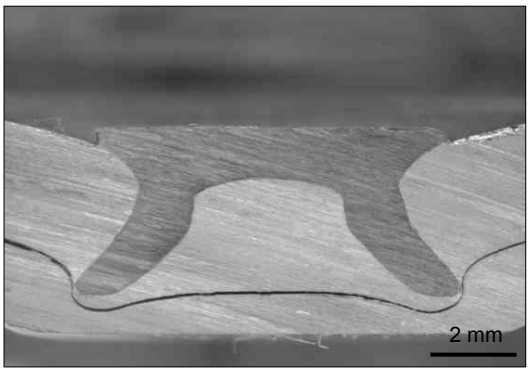

Upper plate: AlMg4.5Mn; thickness 2.5 mm
Bottom plate: AlMg4.5Mn; thickness 1.5 mm
Rivet: C5.3x6H4

High velocity v > 100 m/s

Upper plate: AlMg4.5Mn; thickness 2.5 mm
Bottom plate: AlMg4.5Mn; thickness 1.5 mm
Rivet: C5.3x6H4

***Figure 2**: Influence of the setting speed to the quality of the joint by using a flat anvil*

3 Experimentals

The research at the Laboratory of Materials and Joining Technologies (LWF) in Paderborn is based on propellant charges for riveting with setting speed greater than 100 m/s while the Fraunhofer Institute for Machine Tools and Forming Technology (IWU) uses pneumatic cylinders for accelerating the punch to about 10 m/s. Figure 3 shows the difference between the two acceleration principles.

Two different material-combinations were examined [2]. The first represents the preferred combination for Standard-SPR: “thin to thick” - a thin upper-plate is jointed with a thick bottom-plate. In

Figure *4* the influence of the different velocities to the riveting process is shown. By using the same rivet, the difference is small.

The second material combination (“thick to thin”) shows in

Figure *5* small differences. The higher velocity induced a hardly smaller undercut and a slightly lesser compression of the rivet than the lower velocity.

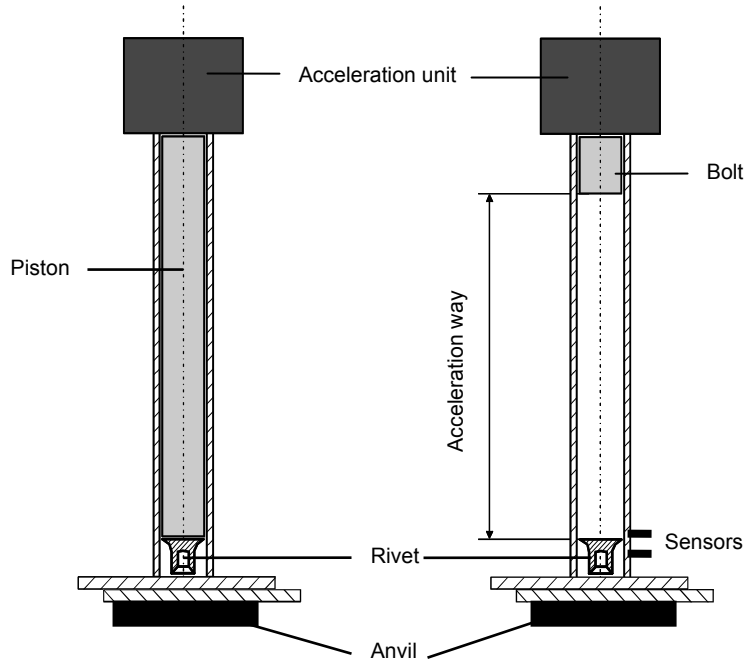

***Figure 3**: Comparison of the two acceleration principles, the left image shows the "piston" system (v < 10 m/s), the right image shows the "bolt" system (v > 100 m/s)*

Setting velocity: < 10 m/s

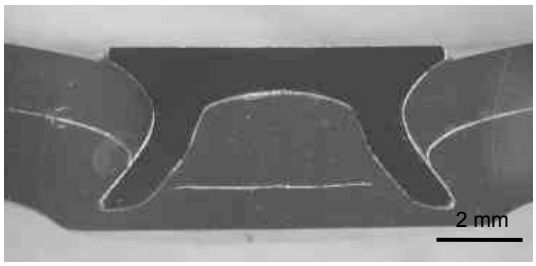

Upper plate: AlMg4.5Mn; thickness 1.5 mm
Bottom plate: AlMg4.5Mn; thickness 2.0 mm
Rivet: C5.3x5H4

Setting velocity: > 100 m/s

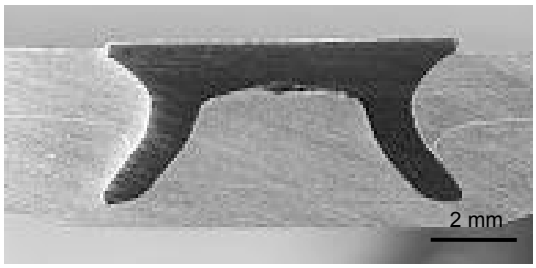

Upper plate: AlMg4.5Mn; thickness 1.5 mm
Bottom plate: AlMg4.5Mn; thickness 2.0 mm
Rivet: C5.3x5H4

***Figure 4**: Influence of different setting velocities to the quality of the joint*

The strengths of the impulse set rivets against the flat anvil are on akin levels to these conventional set against a contoured die. In Figure 6 the results are shown of a shear strength analysis under quasi-static load. There are only low differences between the extreme high (> 100 m/s) and the high velocity (< 10 m/s). The higher performance of the conventional procedure "thick to thin" is based on the higher width of the joint caused by the contoured die.

Setting velocity: < 10 m/s

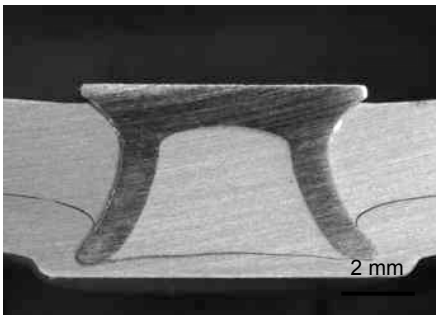

Upper plate: AlMg4.5Mn; thickness 2.5 mm
Bottom plate: AlMg4.5Mn; thickness 1.5 mm
Rivet: C5.3x6H4

Setting velocity: > 100 m/s

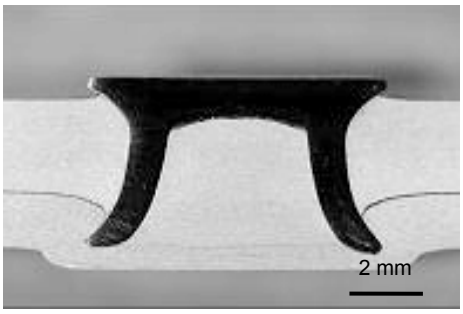

Upper plate: AlMg4.5Mn; thickness 2.5 mm
Bottom plate: AlMg4.5Mn; thickness 1.5 mm
Rivet: C5.3x6H4

Figure 5: *Influence of different setting velocities to the quality of the joint*

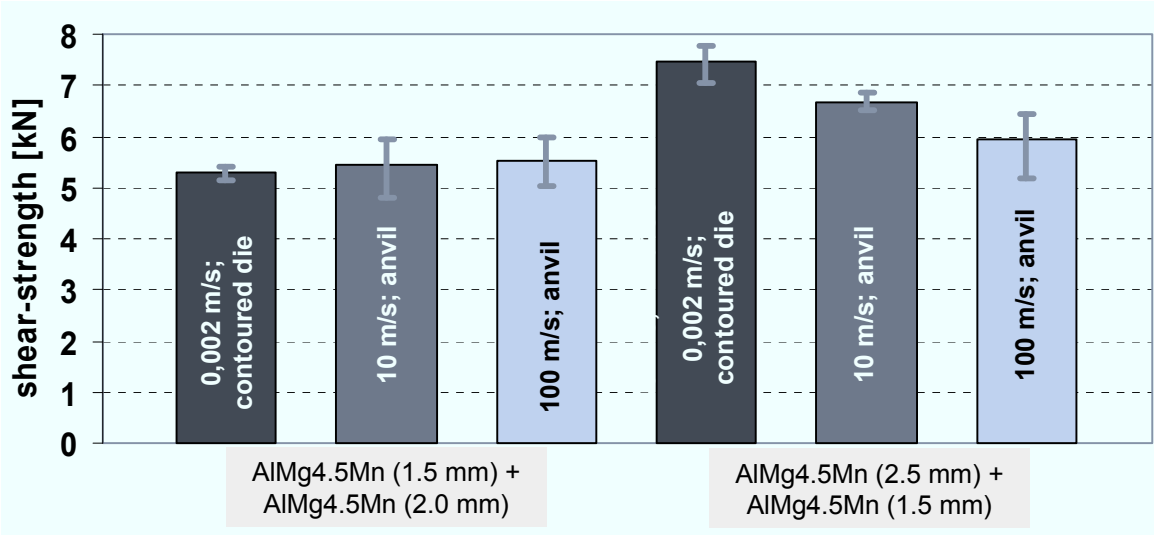

Figure 6*: Comparison of shear-strength under quasi-static load*

4 FE-Analysis

FE-Analysis for different velocities is problematic on the one hand because of missing data for strain-rate-depending flow curves and on the other hand it is no central question. Much more interesting is the question of the rivet geometry. It is improbable that standard SPR-geometry is also the correct one for impulse joining. A rivet development as before usually "trial and error" is extremely time consuming and expensive. At this point FE - analysis has clear advantages.

A goal of the investigation is to meet a statement about numeric modeling the high-speed joining process described sufficiently exactly, in order for the process development a computational predicting of new process parameters to make possible. That applies particularly to rivet geometry, since the experimental variation of these process parameters is the central point.

SPR-FE-Analysis is state of the art [4]. The simulation of the impulse riveting makes special demands:

- Material data for very large material deformations depending of strain-rate
- Material separation with the cutting process

A simple formula for material data is used, [5]:

$$k_{f_2} = k_{f_1} \left(\frac{\dot{\varphi}_2}{\dot{\varphi}_1} \right)^m \tag{1}$$

$i = 1$ quasi-static load

$i = 2$ $\dot{\varphi}$ = 20,000s-1

k_{f_i} yield stress

$\dot{\varphi}_i$ strain rate

m for aluminum m = 0.05, [6].

The following crack criterion was used [7]:

$$\varphi_B = \varphi_{BT} . e^{-b\left(\frac{\sigma_M}{\sigma_V}\right)} \tag{2}$$

φ_B strain until crack

σ effective stress (v. Misses) / hydrostatic stress

The sizes φ_{BT} and b are material constants. They were measured on the basis of existing material data [7] and by test calculations. For the upper sheet metal b = 1.0 and φ_{BT} = 3.0 were used. The validity of these values has to be confirmed in deep-going investigations.

In Figure 7 different crack-criteria are shown.

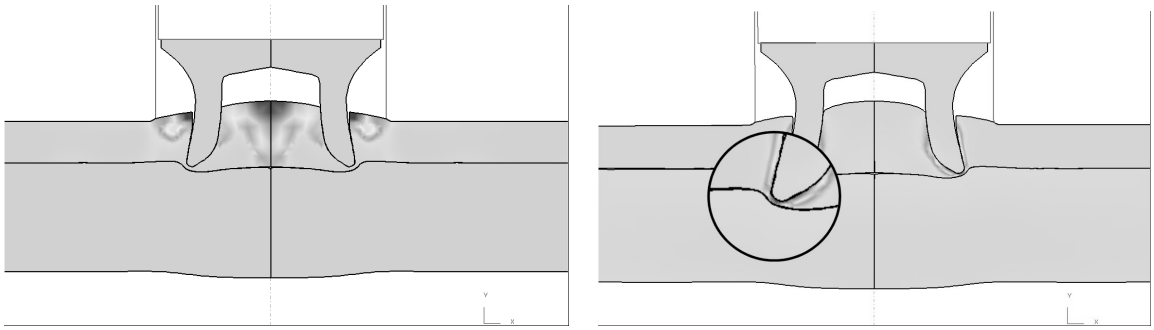

Standard criterion Cockroft & Latham Frobin-criterion [7]

***Figure 7**: Comparison of different crack-criteria*

In Figure 8 is shown the distribution of effective strain with impulse-SPR with flat anvil.

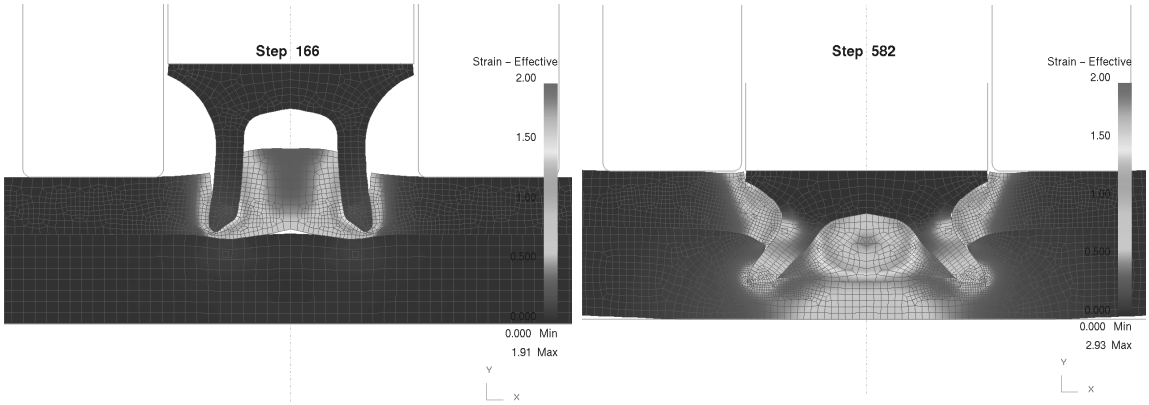

***Figure 8**: Distribution of effective strain with impulse-SPR*

5 Conclusions

The experiments prove the positive influence of high velocities in SPR-process. Using a flat anvil as counter-die leads to advantages in process stability (no contoured die; high stability against misalignments), accessibility without C-frame, joinability of brittle materials. The experiments proved the feasibility of joining especially of aluminium alloys with the standard rivet geometry. Changes of the rivet-geometry are imaginable in FE-analysis. Thus if necessary a new rivet geometry can be developed.

6 References

[1] *Hahn, O.; Klemens, U.; Hahn, O.; Klemens, U.*: Fügen durch Umformen. Nieten und Durchsetzfügen. Innovative Verbindungsverfahren für die Praxis. Dokumentation

707, Studiengesellschaft Stahlanwendung e. V., Verlag und Vertriebsgesellschaft mbH, Düsseldorf, (1996)

[2] *Hahn, O.; Leuschen, G.; Neugebauer, R.; Kraus, Ch.*: Impulsfügen; Zwischenbericht; EFB-Arbeitskreis

[3] *Lagler, K.; Mauermann, R.*: Robotergestütztes Impulsnieten im Fahrzeug-Rohbau; IIR Fachforum „Fügetechnologien im Fahrzeug-Rohbau"; Dresden; 09. März 2004

[4] *Stühmeyer, A.*: Simulation of self-piercing riveting process; 22. CAD-FEM User's meeting Dresden; 2004

[5] *Hensel, A.; Spittel, T.*: Kraft- und Arbeitsbedarf bildsamer Formgebungs-verfahren. VEB Deutscher Verlag für Grundstoffindustrie, Leipzig, 1978

[6] *Eberlein, L.* in: Verfestigung und Entfestigung metallischer Werkstoffe, Bd. 1. Bergakademie Freiberg

[7] *Frobin, R.*: Abhängigkeit des Umformvermögens vom Spannungszustand und Möglichkeiten zur Umformung spröder Werkstoffe. 2. Sächsische Fachtagung Umformtechnik, Freiberg 1995

Process Analysis and Physical Simulation of Electromagnetic Joining of Thin-Walled parts

V. Psyk[1], G. Gershteyn[2], O. K. Demir[1], A. Brosius[1], A. E. Tekkaya[1], M. Schaper[2], F.-W. Bach[2]

[1]Institute of Forming Technology and Lightweight Construction, Technische Universität Dortmund, Germany
[2]Institute of Materials Science, Leibniz Universität Hannover, Germany

Abstract

To avoid typical problems when connecting different metallic materials as aluminum and titanium as e.g. the formation of intermetallic phases, electromagnetic welding represents an alternative technology to conventional (i.e. usually thermal) joining processes. Although feasibility and potential of this technique are already proved, the fundamental correlations of part- and process-parameters have not yet been investigated systematically. As an approach to examine these, the performance of model experiments and supplementary technological tests is suggested. The resulting connection quality is evaluated using metallographic methods.

Keywords

Electromagnetic welding, Model experiment, Metallographic evaluation

1 Introduction and Principle of Impulse Welding

The demand for implementing lightweight construction concepts e.g. in the automotive or aircraft industry has been steadily increasing over the last years. A constructive approach to reduce the product weight can be realized by decreasing the number of part components by combining their functions. However, following this approach leads to a higher complexity of the remaining components, because they now have to fulfil different and sometimes contradictory functions [1]. Thus, in many cases, the application of one single material is no longer sufficient, and a sophisticated material mix realizing the desired technological characteristics is required. It could e.g. be necessary to combine the corrosion resistance and strength of steel or titanium with the high electrical and thermal conductivity of aluminum or copper. When connecting these materials, the application of conventional (i.e. usually thermal) joining technologies often implicates problems, because

at elevated temperatures in the range of 300°C and more, titanium shows a high affinity to the atmospheric gases oxygen, nitrogen and hydrogen. The chemical compound of titanium and these gases results in metalloid phases, which are extremely hard and brittle, so that part failure can occur. For this reason, autogenous welding is not applicable at all for titanium and titanium alloys. And even shielding gas arc welding technologies as MIG or WIG make special preconditions necessary, as e.g. the application of particularly pure gases, the maintenance of the shielding gas atmosphere even during the cooling-down of the part, and a careful preparation of the welding seam [2].

The welding of dissimilar materials as e.g. the combination of titanium and aluminum is even more difficult, because, here, the forming of intermetallic phases as TiAl3, TiAl2, TiAl, and Ti3Al, which also reduce the ductility of the material significantly, has to be avoided. Therefore, only special technologies as friction welding, which often results in reduced strength of the welding seam compared to the base material, or, in case of thin sheets, laser welding can be applied. Large and even connections of titanium and other metallic materials are often realized by means of explosive cladding [2], but, here, restrictions due to occupational safety have to be considered. Therefore, the development of innovative technologies suitable for the joining of these material combinations is necessary.

Here, one promising technology is electromagnetic forming (EMF), which can be used for forming operations as well as for the production of force-fit, form-fit, and welded material joints. EMF is a non-contact high-speed forming technology using the energy density of pulsed magnetic fields in order to apply a so-called magnetic pressure to workpieces made of electrically highly conductive materials. As soon as the resulting stresses in the workpiece exceed the yield stress of the material, plastic deformation starts. Depending on the geometry and setup of workpiece and tool coil, the technology can be used to compress or expand tubes and hollow profiles as well as to form flat or preformed sheet metal parts. A detailed description of the process principle and the pressure development is given in [3].

First approaches to use EMF in order to weld components were already realized in the nineteen-sixties [4]. At that time, the analysis focussed on the processing of tubular semi-finished parts while over the last years, investigations regarding sheet metal components have increasingly been carried out [5, 6]. For electromagnetic welding, the two joining partners are positioned at a defined distance and angle. Analog to explosive bonding, one partner is accelerated so that the two components approximate each other in the range of inter-atomic distance causing a bonding process on atomic scale. During collision, the workpieces are brought to a highly viscous liquid condition so that a wavy contact area is formed which can be laminar or turbulent [7]. The process is usually carried out at room temperature. Heat is produced only directly in the collision zone, i.e. there is no large-area heating of the workpiece. The weld seam is built within microseconds and no additive is required [8]. The feasibility and the potential of electromagnetic welding was already shown in several international publications, but, nevertheless, the fundamental correlations of part- and process-parameters responsible for the onset and formation of the connection development have not yet been investigated systematically [8, 9].

One explanation might be the complexity of the interdependencies between workpiece, tools/equipment, and process parameters during electromagnetic forming. The possibility to directly adjust process parameters is usually limited to the choice of the

capacitor charging energy, while e.g. the temporal course and the local distribution of the magnetic pressure and the resulting forming velocity are significantly influenced by the process setup and the equipment.

2 Investigations on a Model High-Speed Joining Experiment

2.1 Principle and Experimental Setup

In order to allow a basic analysis of the significance and influence of separate parameters describing the collision, a model experiment was built up at the Institute of Materials Science, Leibniz Universität Hannover (IW). The principle setup of this high-speed joining device consists of a joining unit and a pneumatically driven acceleration unit as schematically depicted in Figure 1. At the process beginning, the pressure chamber (10) is pressurized and a mass (7) is positioned at the end of the acceleration tube (6) that is connected to the acceleration chamber (8). Opening a high speed valve (9) pressurizes the acceleration chamber and a section of the acceleration tube so that the mass is sped up through the tube and bounces against the dynamic support (5) carrying the dynamic joining partner (4). The impact leads to a sudden relative movement (x) in the magnitude of some millimetres between the joining partners, which results in a welding process, provided that the chosen process parameters are suitable. In this way, the impact velocity of the mass, which is expected to be a decisive aspect, can be influenced via the dimensioning of the mass and/or via an adaptation of the initial pressure in the pressure chamber.

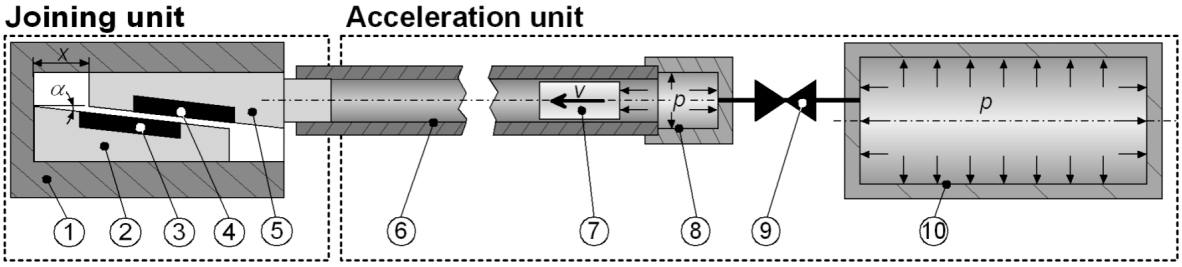

1 - Mounting device
2 - Static support
3 - Static joining specimen (length: 30 mm; width: 8 mm; thickness: 0.1 mm)
4 - Dynamic joining specimen (length: 30 mm; width: 8 mm; thickness: 0.1 mm)
5 - Dynamic support (weight: 0.337 kg)
6 - Acceleration tube (length: 1000 mm)
7 - Mass (weight: 0.052 kg)
8 - Acceleration chamber
9 - High-velocity valve
10 - Pressure chamber (volume: 0.05 m³; max. pressure: 1.6 MPa)

***Figure 1**: Principal setup of the high-speed joining device*

2.2 Evaluation of Welding Quality Achieved Using the Model Experiment

In order to investigate the influence of the impact velocity, experiments regarding the weldability of titanium and aluminum were carried out using the described high-velocity joining setup. For this purpose, aluminum (Al99.5) and titanium (TiAl6V4) samples with a size of 30 mm x 8 mm and a thickness of 0.1 mm were prepared by milling a rib profile. The surfaces were sanded in order to remove oxides and cleaned using acetone. The

aluminum samples were positioned as static joining specimen in the static support while the titanium samples were mounted to the dynamic support which was positioned at a distance (*x* compare Figure 1) of 5 mm in relation to the static support. The application of different initial pressures caused impact velocities in the range of 10 m/s up to 130 m/s, while the impact angle α was 5° in all trials.

The evaluation of the joining quality was done at IW using metallographic methods. These investigations showed that for velocities in the range of 10 m/s up to 25 m/s, no bonding on atomic scale could be achieved, whereas in case of higher impact velocities, at least sections of the specimens were impact welded. In Figure 2 representative micrographs are shown. Here, the contact area of specimens, joined with an impact velocity of approximately 30 m/s, approximately 100 m/s, and approximately 130 m/s is compared and it is clearly shown that an increase of the impact velocity leads to a higher ratio of the welded area and contact surface, an effect which is comparable to the material behaviour during explosive welding (compare [10, 11]). Statistic interpretations of the microstructural data suggest a linear correlation between this ratio and the impact velocity in the regarded span of values (compare Figure 2), but to be able to make a more reliable conclusion, additional experiments are required.

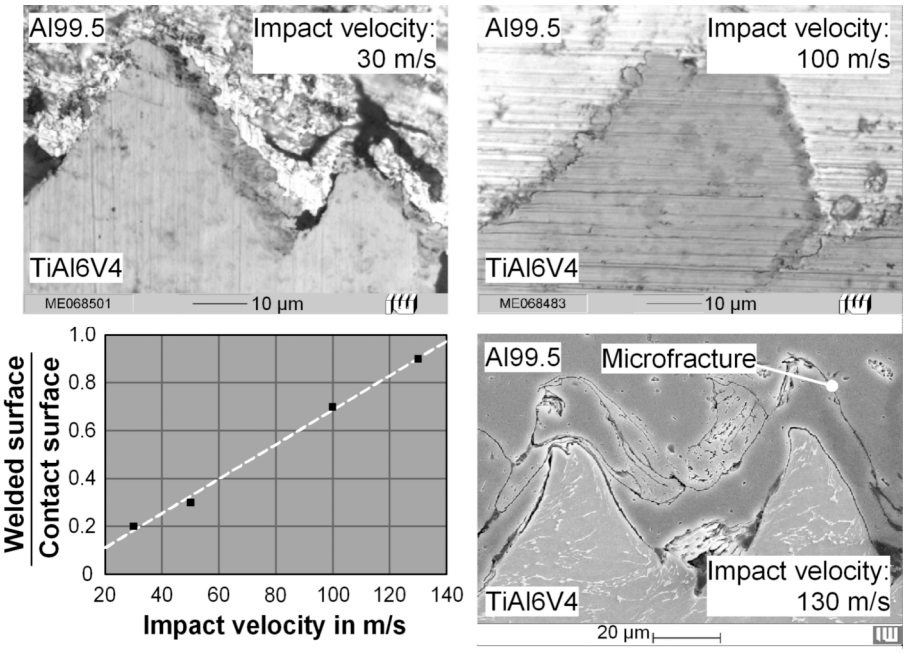

***Figure 2**: Influence of different impact velocities on the contact area of joined specimens*

However, when evaluating the welding quality, the proportion of the welded area is not the only criterion that has to be taken into account. Considering e.g. the intactness of the microstructure in the contact area, the micrograph of the joint area produced with an impact velocity of approximately 130 m/s shows microfractures in the aluminum running approximately parallel to the contact surface of the two joining partners. This effect indicates a deterioration of the joining quality, if a critical value of the impact velocity is exceeded. Thus, with respect to the microstructural investigations, it can be concluded that there exists an optimum value for the impact velocity that is high enough to maximize

the ratio of the welded area and contact surface but not too high, in order to avoid any damage of the microstructure. For the regarded material combination and setup, this optimum is between 100 m/s and 130 m/s.

Another evaluation criterion for the welding quality is given by the resulting phases in the joining area. In order to determine if metalloid or intermetallic phases are formed in the joints produced by using the high-velocity joining device, polished and etched specimens were investigated by means of an energy dispersive x-ray (EDX) and microanalysis. This method allows the detection of the element distribution in the welding area. As shown in Figure 3 the titanium and the aluminum base material can be distinguished and an extremely thin titanium-rich transition area of less than 1 µm thickness can be detected in-between the two. According to [12], intersection layers consisting of different phases in this magnitude can be regarded as subcritical and will not deteriorate the joint quality significantly.

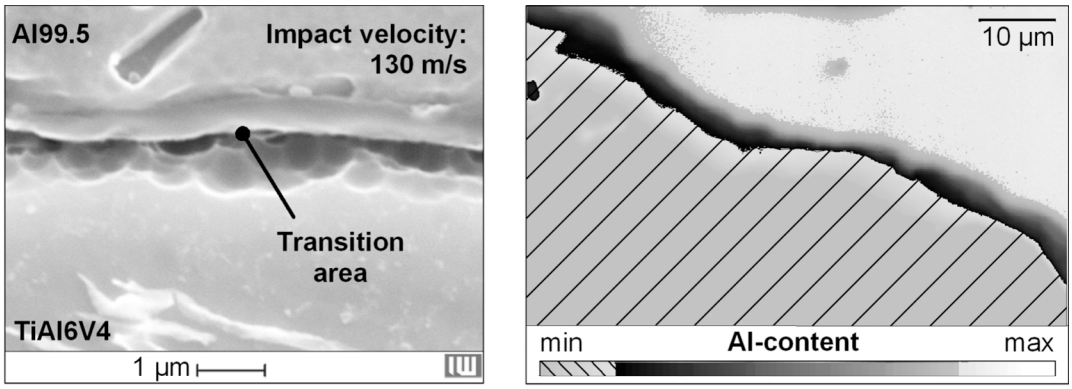

***Figure 3**: Phases in the transition area of joined aluminum and titanium samples*

3 Investigations on Electromagnetic Forming

3.1 Setup and Process Dimensioning of the Electromagnetic Compression

In the next step, comparative technological experiments applying the electromagnetic compression process were carried out. For this purpose, aluminum (Al99.5) tubes with a diameter of 20 mm and a wall thickness of 1 mm, produced by turning, were sanded in order to remove oxide films and cleaned in acetone using an ultrasonic cleaning device. Titanium (TiAl6V4) tubes with an outer diameter of 15 mm and a wall thickness of 2.5 mm were prepared in an analog manner and the aluminum and the titanium tubes were positioned coaxially in the compression coil so that the initial gap width between the two joining partners was 1.5 mm.

In order to achieve an impact velocity of approximately 100 m/s, which was determined as a desirable value in the model experiments, suitable process parameters have to be chosen. As already mentioned, the capacitor charging energy is the only directly adjustable variable. For this reason, preparative investigations on the correlation between this value and the resulting deformation behaviour for the regarded setup were carried out. Exemplary results are shown in Figure 4.

In free forming operations (i.e. without a joining partner inside), the time-dependent radial displacement of the smallest cross section of the aluminium tube, which is typically

located in the middle of the tool coil, can be quantified applying an optical measurement system based on the shadowing principle as described in [3]. By differentiating the displacement over time curve, the time dependent forming velocity can be determined and it can be associated to the according radial displacement. Provided that the parameters of the workpiece and the applied equipment (tool coil and forming machine) are the same, it can be assumed that the impact velocity of the middle cross section during an electromagnetic joining process is approximately the same as the forming velocity in a free electromagnetic compression at that special radial displacement (here 1.5 mm). However, this measurement technique is limited to recording the displacement of the smallest cross section of the tube, and the measurement uncertainty rises with increasing workpiece deformation and the related increasing wrinkling effect during free electromagnetic compression (compare photos in Figure 4). For the current investigations, it can be concluded that in case of an initial gap width of 1.5 mm between the joining partners, the impact velocity of the smallest cross section amounts to 100±15 m/s in case of 500 J charging energy and 80±10 m/s in case of 400 J.

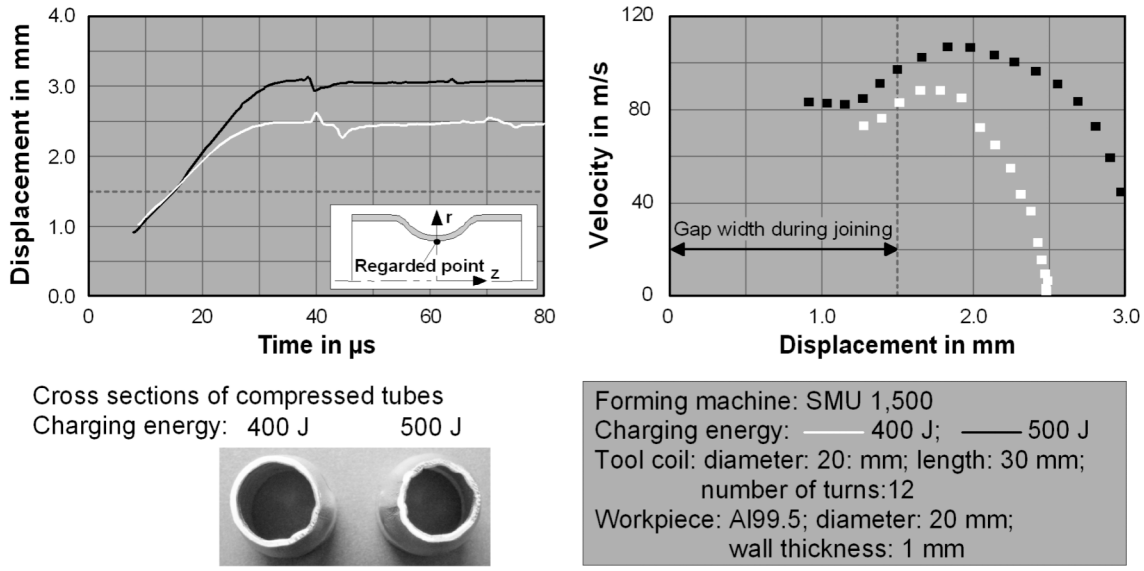

***Figure 4**: Displacement courses and corresponding radial velocities in free electromagnetic compression experiments applying different charging energies*

3.2 Evaluation of Welding Quality Achieved by Electromagnetic Forming

Considering these measurements, first electromagnetic joining experiments with a capacitor charging energy of 500 J and comparative tests applying higher energies of 1,000 J and 1,500 J were performed. It turned out that the charging energy of 500 J caused a joint merely basing on force-fit, i.e. an elastic plastic bracing of tube and mandrel (compare [14]) and no bonding on atomic scale occurred. However, in case of higher charging energies (1,000 J and 1,500 J), welding could be realized at least locally.

Micrographic investigations done by IW show that considering the axial length of the interface between aluminum and titanium, zones of different joint qualities can be identified, which are representatively shown in Figure 5. For both charging energies, a minor joint quality (characterised by gaps between the joining partners) occurs in the

middle of the compression area (*z*≈0 mm), although small adhesions of material particles welded on each other can be found. The length of this region spans 4 mm in both directions from the middle of the compression area in case of a charging energy of 1,000 J, and 2-3 mm in both directions in case of 1,500 J charging energy. This zone is directly followed by an area of high joining quality characterized by a wavy interface between the two materials. In case of 1,500 J charging energy, this zone continues to the end of the compression area, i.e. for a length of approximately 10 mm, and the transition between aluminum and titanium is extremely narrow (width 0.5-1 µm), while in case of 1,000 J charging energy, the length of this area is only about 2 mm and also the transition is slightly wider (2-3 µm). Subsequent to this high-quality joint zone, another region, characterized by a strongly inhomogeneous layer in-between the aluminum and the titanium, can be identified in case of the lower charging energy. This area extends to the end of the compression zone and, again, indicates an inadequate joining quality.

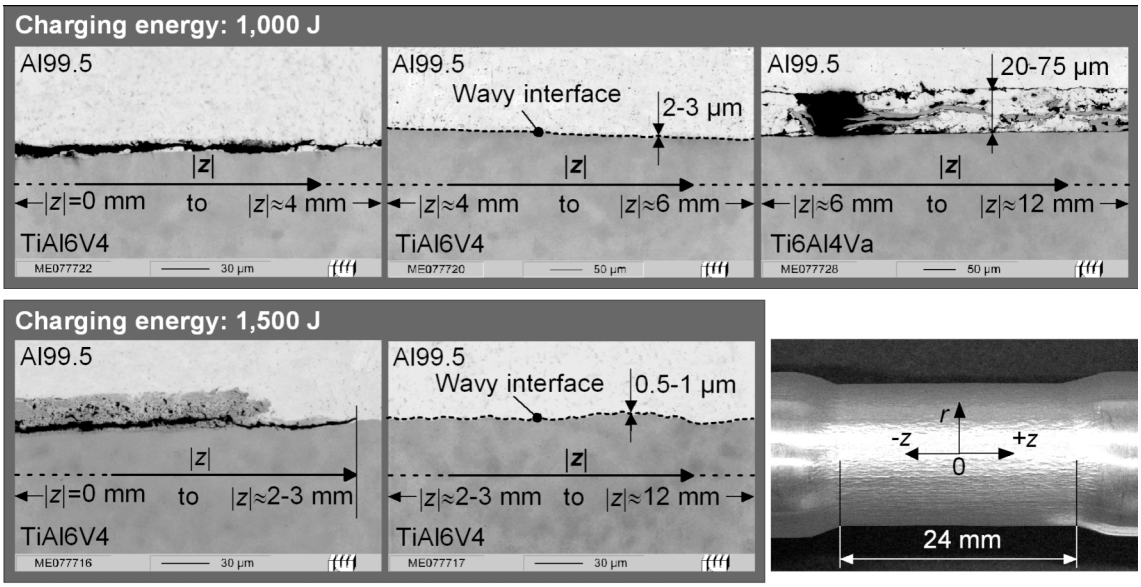

***Figure 5**: Microstructural state of joints produced by EMF*

One possible explanation for the described condition of the joints could be given considering the axial distribution of the workpiece velocity $\vec{v}_{wp}$ associated to the corresponding impact angle α_{impact}. In Figure 6, the qualitative axial distribution of the impact velocity and the angle between the joining partners, determined by an FE-analysis, is shown. Considering the experimental results described above, the impact velocity for a charging energy of 500 J is in the range of 100 m/s for z-values close to the centre of the compression zone (i.e. in the region of *z*≈0 mm) and decreases for higher z-values. On the other hand, it is obvious that especially for small z-values the impact angles are much higher during the electromagnetic compression tests than the 5° chosen for the model experiments. This derivation between the technological tests and the model experiment is a reasonable explanation for the absence of any bonding on atomic scale in case of using 500 J charging energy during electromagnetic compression.

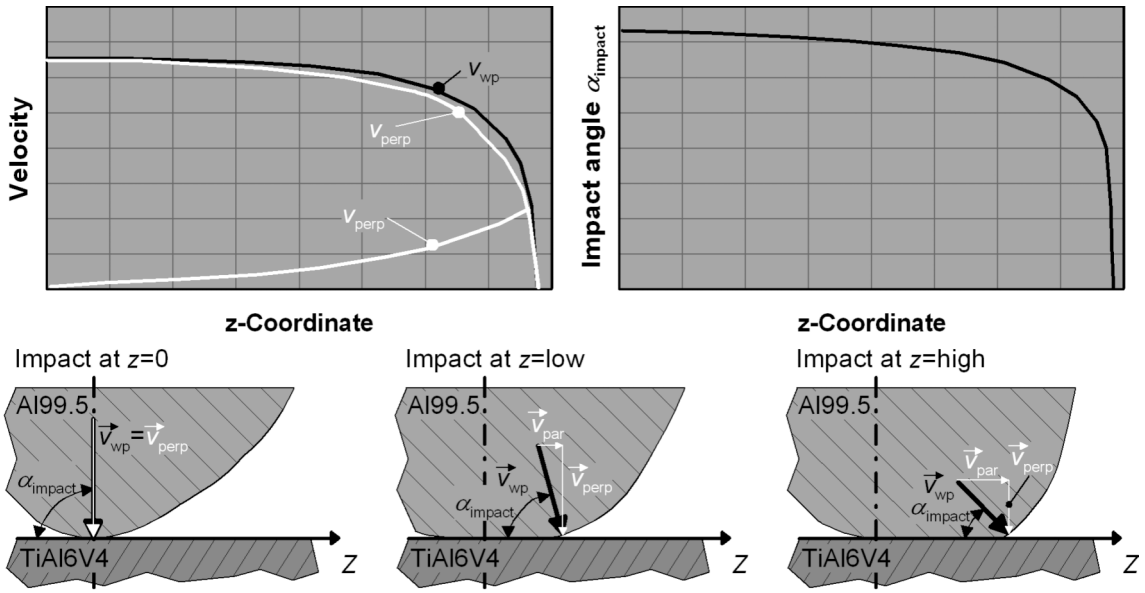

Figure 6: Distribution of impact velocity and angle along the workpiece axis

Regarding the condition of the joints in case of higher charging energies and the described zones of different welding quality, a possible explanatory approach can be given considering the velocity components parallel $\vec{v}_{par}$ and perpendicular $\vec{v}_{perp}$ to the joining interface and the surface of the inner joining partner, here the titanium tube, respectively. These values can be calculated on the basis of the local workpiece velocity and the corresponding impact angle. They are also qualitatively shown in Figure 6.

In the center of the compression area, the highest workpiece velocity, which is much higher than 500 m/s, here, occurs. Due to the extremely high impact angle (90° in the center) the corresponding perpendicular velocity components are high, too, while the parallel ones are very low (0 m/s in the center). This means that the high impact forces and pressures, which are mainly determined by the perpendicular velocity, are very high, but there the relative movement between the joining partners, which depends on the parallel velocity components are extremely low. This combination seems to be unsuitable for the generation of proper welds. For higher values of |*z*|, the workpiece velocity decreases and, due to the likewise decreasing impact angle, the parallel velocity component and thus the relative movement between aluminium and titanium rise. Thus, matching conditions, resulting in the described high joining quality, could be realized. In case of the lower charging energy (1,000 J), the combination of low impact angles and lower workpiece velocities lead to lower perpendicular and parallel velocity components, compared to the sample compressed with 1,500 J. This, again, seems to be a disadvantageous parameter constellation, and an unfavourable welding quality for |*z*|-values of 6 mm and higher occurs. This approach suggests that not only high workpiece velocities are required for the generation of good welding properties, but also matching conditions of local impact velocity and angle have to be granted. In order to determine such parameter constellations, the model experimental setup can be used, because thereby the impact velocity and impact angle can easily be modified separately.

4 Summary and Outlook

Summarizing, it can be said that the model high-velocity joining setup as well as the electromagnetic compression process in general are suitable for impact welding aluminum (Al99.5) and titanium (TiAl6V4). In the model experiment, the impact is realized between small rectangular samples applying a selectable impact angle and velocity. Microstructural investigations have shown that an optimum value of the impact velocity can be identified, which is high enough to maximize the ratio of welded area and contact surface but not too high, in order to avoid any damage of the microstructure. In the regarded case, this optimum is in the range of 100 m/s for an impact angle of 5°. Investigations of the transition area between aluminum and titanium have shown that this area is extremely thin, proving an advantage of the impact welding process in comparison to thermal joining technologies.

In addition, technological joining tests were carried out using the electromagnetic compression setup. A microstructural evaluation of the resulting welding quality has shown that it is inhomogeneous along the tube axis. An explanation for this effect is suggested, considering the velocity components parallel and perpendicular to the impact surface, which can be calculated on the basis of the impact velocity value and the angle between the joining partners. This approach proposes that in order to establish a proper weld, high workpiece velocities only are not sufficient, but also matching parameter conditions, taking the distribution of the impact velocity and angle along the workpiece axis into account, have to be provided.

For the determination of suitable parameter constellations, the model experiment is advantageous, because here, impact velocity and impact angle can be modified easily and, what is even more important, separately. Thus, numerous additional model experiments are planned, which will also involve the use of different specimen materials and thicknesses. First spot checks applying samples with a thickness of 500 µm have already shown that in this case higher impact velocities are required than in case of the 100 µm thick specimens. In order to transfer the results from these investigations to the electromagnetic welding process, parallel research work regarding the process analyses of this technology is planned. In order to determine the axial distribution of the impact velocity and angle quantitatively, a coupled electromagnetic and mechanic finite element analysis (FEA) following the style of BROSIUS as described in [13] shall be accomplished. Thus, both approaches will be exploited complementarily in order to allow a target-oriented process dimensioning for the electromagnetic welding technology.

References

[1] *Kleiner, M.; Geiger, M.; Klaus, A.:* Manufacturing of Lightweight Components by Metal Forming, Annals of the CIRP "Manufacturing Technology", 53rd General Assembly of CIRP, Vol. 52/2, Montreal, Kanada, August 24-30, 2003, pp. 521-542.

[2] *N.N.:* Hinweise zum Schweißen von Titan und Titanlegierungen, http://www.isoarc.ch/Info_Datenbank/Hinweise_zum_schweissen_von_Titan.pdf Deutsche Titan, 2000.

[3] *Beerwald, C.:* Fundamentals for Process Dimensioning and Design of Electromagnetic Forming (in German), PhD.-Thesis, Dortmund, Germany, 2004.

[4] *Lysenko, D. N.; Ermolaev, V. V.; Dudin, A. A.:* Method of pressure welding, Patent US 3520049, 1970.
[5] *Aizawa, T.; Okagawa, K.; Henmi, N.:* Impulse magnetic pressure seam welding of aluminium, copper and steel sheets, Proceedings of the 7th Int. Conf. on Theory of Plasticity (ICTP), 28.-31. October 2002, Yokohama, pp. 1687-1692, 2002.
[6] *Aizawa, T.:* Magnetic pressure seam welding method for aluminium sheets, Journal of Light Metal Welding and Construction, Vol. 41-3, pp. 20-25, 2003.
[7] http://www.iwf.tu-berlin.de/fachgebiete/wzm/forschung/forschung8/schweissen, state: 14.01.2008.
[8] *Shribman, V.; Tomer, Y.:* Magnetic pulse technology for improved tube joining and forming, In: Tube & Pipe Technology, 2006, S. 91-95.
[9] *Kore, S. D.; Date, P. P.; Kulkarni, S. V.:* Effect of process parameters on electromagnetic impact welding of aluminum sheets (2006), doi: 10.1016/J.ijimpeng.2006.08.006.
[10] *Deribas, A. A.:* Strengthening mechanisms and Explosive welding, Novosibirsk, 1980, p.222.
[11] *Grignon F., Benson D., Vecchio K.S., Meyers M.A.:* Explosive welding of aluminum to aluminum: analysis, computations and experiments, Int. J. of Impact Engineering 30, pp. 1333–1351, 2004.
[12] *M. Kreimeyer, F. Wagner, I. Zerner, G. Sepold:* Laser beam joining of aluminium with titanium with the use of an adapted working head (in German), Löt '01, Aachen, DVS-Berichte, Band 212, DVS-Verlag Düsseldorf 2001, pp. 317-321.
[13] *Brosius, A.:* A method for the Determination of Strain-Rate-Dependent Flow Curves by Means of Electromagnetic Tube Forming and Iterative Finite-Element-Analyses, (in German), PhD.-Thesis, Dortmund, Germany, 2005.
[14] Al-Ahmad, N.: Das Fügen rotationssymmetrischer Formelemente durch Umformen mit Impulsmagnetfeldern. Dissertation Ingenieurhochschule Zwickau 1980.

Electromagnetic Forming of AZ31B Magnesium Alloy Sheet: Experimental Work and Numerical Simulation*

I. Ulacia[1], J. Imbert[2], C.P. Salisbury[2], A. Arroyo[3], I. Hurtado[1], M.J. Worswick[2]

[1] Department of Manufacturing, Mondragon Goi Eskola Politeknikoa, University of Mondragon, Spain
[2] Department of Mechanical and Mechatronics Eng., University of Waterloo, Canada
[3] Automotive unit, Labein-Tecnalia Research Centre, Spain

Abstract

In the first stage of this work, polycrystalline specimens of AZ31B magnesium alloy have been characterized by uniaxial tensile tests at quasi-static and dynamic strain rates at room temperature. The influence of the strain rate is outlined and experimental results were fitted to the parameters of Johnson-Cook constitutive material model.

In the second stage of the present study, sheets of AZ31B magnesium alloy have been biaxially formed by electromagnetic forming using different coil and die configurations. Deformation values measured from electromagnetic formed parts are compared to the ones achieved with uniaxial tensile tests and also with the values obtained by conventional forming technologies.

Finally, numerical simulations have been carried out using an alternative method for computing the electromagnetic fields in the EMF process simulation, a combination of Finite Element Method (FEM) for conductor parts and Boundary Element Method (BEM) for the surrounding air (or more generally insulators) that is being implemented into commercial code LS-DYNA®.

Keywords

Electromagnetic sheet metal forming, Magnesium alloy, Formability, Numerical modelling

---

* *This work is based on the results of the project FORMAG; the authors would like to thank the Basque Government for its financial support*

1 Introduction

Recently there is a clear tendency of reducing the weight of vehicles since lightening the final weight of the vehicle provides clear benefits in fuel economy [1]. For this reason, magnesium alloys are generating interest in the automotive and aeronautic industries, due to their low density in comparison to aluminium and steel alloys thereby reducing gross vehicular weight. In addition, the low density improves dent resistance and shell resistance behaviour by increasing thickness in structural sheet applications [2]. Currently, the use of magnesium alloys in a car is approximately 0.3% of the total weight of the vehicle; however, it is estimated that for the year 2020 the use of magnesium alloys in vehicles will increase to up to 12.2% of the total weight, mainly to the detriment of steel, iron and aluminium, as it is shown in Figure 1 [3].

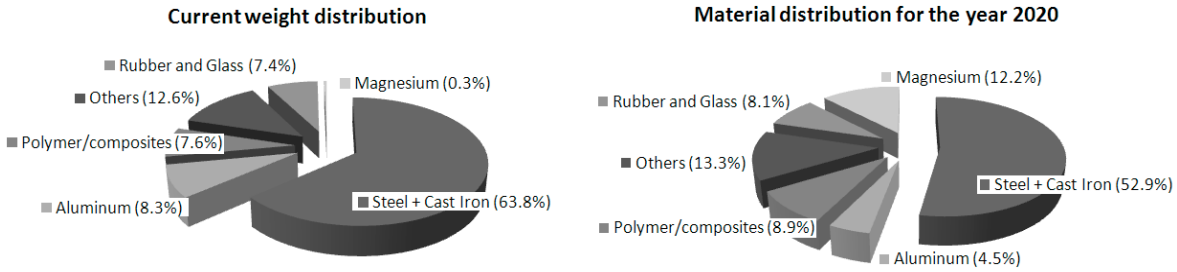

***Figure 1**: Current and estimated weight distributions in a car [3]*

Some limitations appear when forming magnesium alloys due to the hexagonal close-packed (hcp) microstructure. It is for this reason that casting and forging technologies have traditionally been used to manufacture magnesium parts. It is a well known fact that the mechanical properties of parts obtained by deformation operations are higher than the properties obtained by casting. Consequently, if the formability of magnesium alloys could be improved, there would likely be a considerable increase in the use of this under-utilized material. Therefore, there is a clear need of new forming methods in order to overcome this limitation. One way of increasing the formability of magnesium alloys is to increase the forming temperature. This is due to the activation of prismatic $\{10\bar{1}0\}<11\bar{2}0>$ and pyramidal $\{10\bar{1}1\}<11\bar{2}0>$ slide planes which begins at temperatures around 200-225ºC leading to a considerable improvement of formability and reduction of the anisotropy [4,5]. Some studies [5,6] show interesting maximum limit drawing ratios (LDR) of 2.5 in a temperature range between 200-250ºC for AZ31 alloy.

Another way to increase the formability of magnesium alloys would be to employ high velocity forming technologies, such as electromagnetic forming. El-Magd *et al.* stated that for AZ80 magnesium alloy elongation increases under dynamic loading [7]. Very little work has been done in the field of high speed forming of magnesium alloys [8-11]; however, all the investigations agree that higher deformation values are achieved using electromagnetic pulses to deform magnesium alloys, concluding that EMF is a promising technology for processing magnesium parts, even at room temperature. The idea of combining inductive heating and pulsed magnetic forming for EMF at elevated temperatures was suggested by Uhlmann et al. [11]; unfortunately, they did not report any values of the achieved deformations.

Consequently, in the current work the suitability of electromagnetic forming to produce magnesium alloy parts is evaluated. In the first stage of the present work, AZ31B alloy is characterized under a wide range of strain rates in order to identify the effect of strain rate on the mechanical behaviour of this magnesium alloy. Furthermore, the experimental data is fitted to the Johnson-Cook constitutive model for the numerical simulation. After the material characterization, experimental work is shown. Different free forming configurations were employed in order to obtain a wide range of biaxial deformation state values. The final deformation values of the formed parts were measured by means of photogrammetric methods and a comparison with the limits obtained with conventional forming technologies is performed. In the final part of the current contribution, a coupled numerical model for the process simulation is presented and the results are compared with experimentally obtained parts.

2 Material Characterization

The material employed in this study was 1 mm thick sheet commercial available AZ31B-O magnesium alloy. Quasi-static and dynamic tensile tests were carried out in the strain rate range of $0.001\ s^{-1} < \dot{\varepsilon} < 1500\ s^{-1}$. The reader is referred to [12] for a more detailed description of the testing. In the current work, only the tests at room temperature are considered, neglecting the softening effect that occurs in the material due to the temperature rise from the adiabatic nature of the dynamic deformation.

2.1 Uniaxial Tensile Tests at Different Strain Rates

The material was tested in the laboratories of the University of Waterloo at three different strain rate ranges using three different testing techniques: i) quasi-static strain rate tests (0.001, 0.1 s^{-1}) were conducted in a conventional electromechanic drive INSTRON testing machine ii) for intermediate range (50, 80, 100 s^{-1}) an IMATEK Instrumented Falling Weight (IFWI) apparatus was used and iii) for high strain rate (500, 1000, 1500 s^{-1}) a tensile split Hopkinson bar (TSHB) was employed. The testing was done for both rolling and transversal direction. The experimental results for the different strain rate ranges are shown in Figure 2 (only typical curves are shown for clarity reasons). It can be clearly seen that for both directions increasing the strain rate also increases the flow stress.

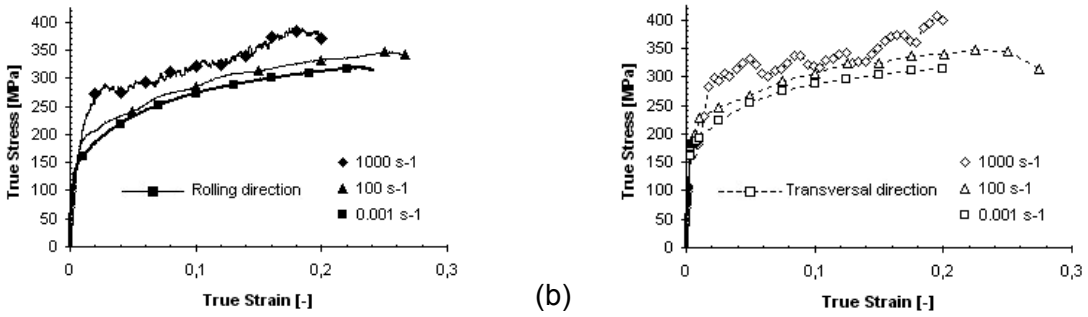

Figure 2: *Flow curves for AZ31B tests at different strain rates**

**The reader is cautioned that in the high strain rate tests the loading to failure was not monotonic and therefore, the 1000 s-1 curve does not reach the real strain at fracture [12].*

The measured elongations at fracture are illustrated in Figure 3. It can be seen that initially, at quasi-static strain rate range, the ductility of the material decreases when increasing the strain rate. However at intermediate and high strain rate the elongation at fracture increases when the strain rate is also increased. The influence of the specimen direction in the ductility is less noticeable at high strain rates than at quasi-static range.

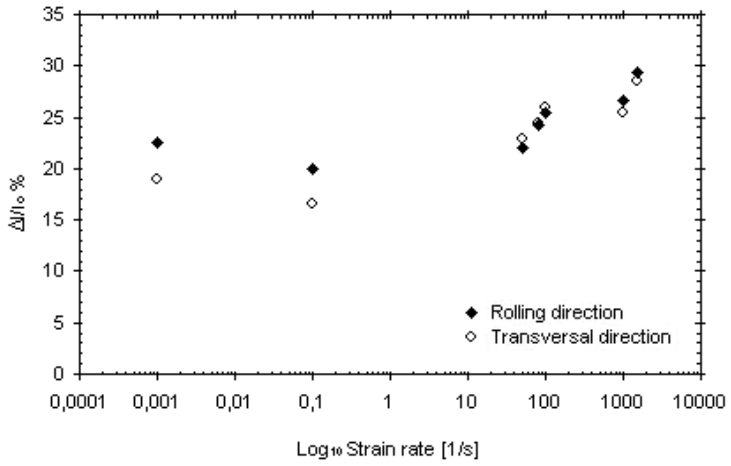

***Figure 3**: Elongation at fracture as a function of strain rate for AZ31B sheet*

2.2 Constitutive Modelling

In order to model the constitutive response of the material for a wide range of strain rates, the flow stress can be determined as a function of effective plastic strain, strain rate and temperature using the constitutive equation of Johnson-Cook [13]:

$$\sigma = \left(A + B \cdot \varepsilon_{eps}^{n}\right) \cdot \left(1 + C \ln \frac{\dot{\varepsilon}}{\dot{\varepsilon}_0}\right) \cdot \left(1 - \left(\frac{T - T_{room}}{T_{melt} - T_{room}}\right)^{m}\right) \quad (1)$$

where ε_{eps} is the effective plastic strain, $\dot{\varepsilon}$ is the strain rate, $\dot{\varepsilon}_0$ is the reference strain rate, T, T_{room}, T_{melt} are respectively the current material temperature, room and melting temperature for the material. A, B, C, n and m are the five material constants. The final term in Equation 1 corresponding to thermal effects is not taken into account since temperature influence is neglected.

The constitutive parameters required by the Johnson-Cook constitutive model are fitted to the experimental results using a non linear regression technique. The estimated values of the parameters, for both rolling and transversal directions, are tabulated in Table 1 with their upper and lower bounds for a 95% confidence interval.

Parameter	**Estimate**	**95% Confidence**	
		Lower Bound	**Upper Bound**
Rolling direction			
A (MPa)	180.002	152.028	207.977
B (MPa)	344.548	309.940	379.156
n	0.554	0.329	0.613

C	0.012	0.010	0.013
Transversal direction			
A (MPa)	220.891	176.558	265.223
B (MPa)	205.583	182.989	228.178
n	0.370	0.144	0.596
C	0.011	0.010	0.013

Table 1: *Johnson-Cook parameters for AZ31B*

In Figure 4 constitutive model for AZ31B is shown. Good agreement is seen between experimental results and constitutive models. It is also observed that for the rolling direction the strain hardening rate is higher than for transversal direction.

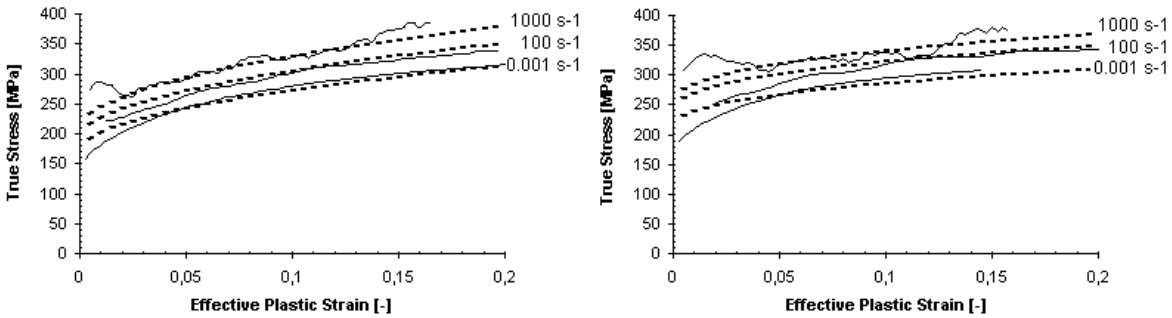

Figure 4*: Comparison of Johnson-Cook model predictions (dashed lines) with experimental results (solid lines) for rolling direction (left) and transversal direction (right)*

3 Experimental Work

3.1 Experimental Procedure

Different EMF experiments were carried out in the laboratories of Labein-Tecnalia with the aim of obtaining a wide range of deformations in the AZ31B magnesium sheets of 175 mm x 250 mm x 1 mm. Furthermore, electromagnetic forming experiments with an open die were performed in order to be recorded by means of a Photron FASTCAM-APX RS 250K high speed camera at a sampling rate of 37500 fps.

The multi-turn coil used for these experiments is made from copper as illustrated in Figure 5(a). Three different dies were employed in the experiments: i) a free forming square die with an 82 mm width and 160 mm in length, Figure 5(b); ii) a circular die with 80 mm in diameter, Figure 5(c); and iii) an elliptic die with the major and minor axis of 80 mm and 40 mm respectively, Figure 5(d). The die radius is 4 mm in all the cases. In some experiments with the circular and elliptic geometry, a driver of AA1050-0 aluminium alloy sheet of 1 mm thickness was used in order to reduce the discharged energy from a maximum value of 22 kJ to 7.5 kJ. In the case of square free forming die no driver was used due to the sheet-coil configuration (this point will be analysed with more detail in the numerical model section). A maximum energy of 4 kJ was discharged to form safe parts. A closing force of 60 kN was applied in all the cases by means of a hydraulic press. The discharged currents were measured at a sampling rate of 1.25 MHz by means of an oscilloscope connected to the Rogowsky coil of the EMF machine.

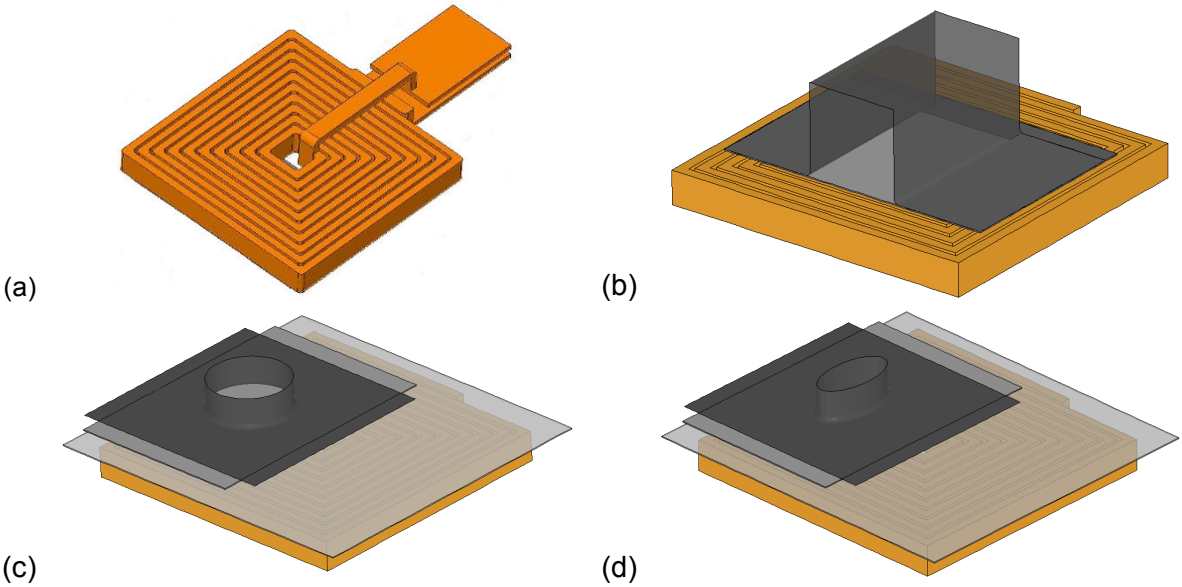

***Figure 5**: Experimental set-up for the different configurations used. (a) geometry of the coil, (b) square free forming set up, (c) circular and (d) elliptic dies with the driver*

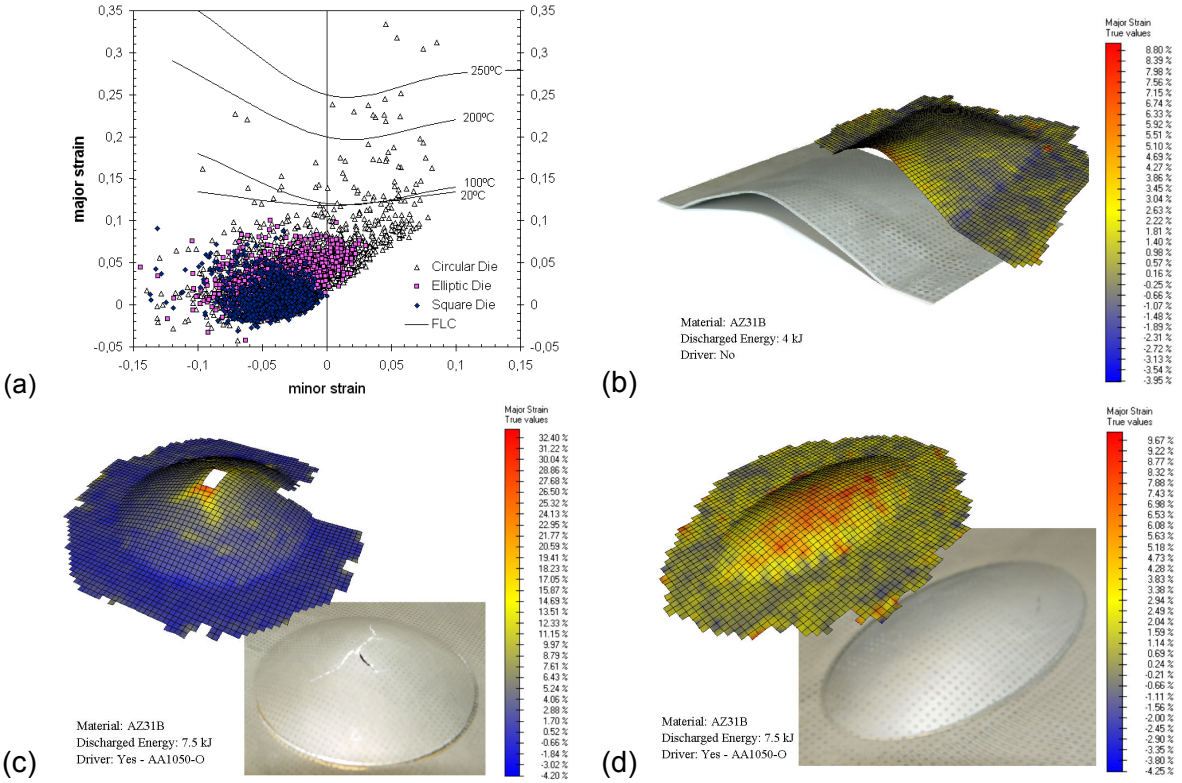

***Figure 6**: Deformation measurements of the different samples. (a) FLD for the different geometries formed, the FLC curves correspond to [6,14]; formed specimens and measured major strains for (b) square free forming, (c) circular and (d) elliptic dies*

3.2 Formability Results of AZ31B Sheet at High Strain Rates

AZ31B sheets were electrochemically etched with a 2 mm x 2 mm square grid before being formed by means of electromagnetic pulses. Once the specimens were formed, the deformation was measured using photogrammetric techniques with the software PHAST® as shown in Figure 6.

The specimens formed using each configuration and the measured major strains are displayed in Figure 6. The different maximum safe deformation states are shown in Figure 6(a) for each die configuration. It can be seen that for circular die forming the maximum deformation values of safe points clearly exceed the conventional Forming Limit Curve (FLC) obtained at room temperature by Palumbo *et al.* [14], showing a positive strain rate sensitivity. The general tendency of increasing the ductility at high strain rates seen for uniaxial tests (Figure 3) is also applicable for biaxial deformations. It is also remarkable that some safe maximum deformation states are close to the FLC curve established by Zhang et al. [6] for warm forming conditions of AZ31B. In the case of the elliptic die forming fracture occurred at the base radius, and so it was impossible to measure higher biaxial deformation values in the top of the geometry. In the case of square of square forming, the material flowed to the deformed part resulting in smaller deformation values.

4 Numerical Model

The analysis of EMF process involves the combined study of electromagnetic, mechanical and thermal fields. Consequently numerical simulations of the process must couple these related fields. There are different coupling strategies as explained in [15] and a sequentially coupling method is used in the current work. (Equations of the model are not shown here for briefness and reader is referred to [16] for more information).

Historically, Finite Element Method modelling has been predominantly used for EMF simulations [17], where other methods, such as Smooth Particle Hydrodynamics (e.g. [18]), have not succeeded. In the current study an alternative method is used for computing the electromagnetic fields in the EMF process simulation. A combination of the Finite Element Method (FEM) for conductor parts and the Boundary Element Method (BEM) for the insulators (including air) as implemented in the LS-DYNA commercial code [19], were used to simulate the forming process.

The principal advantage of using the BEM for the air analysis is that it does not need an air mesh. Thus it avoids the meshing problems associated with the air, which can be significant for complicated conductor geometries. EMF simulations include, very small gaps between conductors, leading to a large number of very small and distorted elements which then require re-meshing techniques to be employed as the air mesh moves around the conductors. Another advantage of the BEM is that it does not need the introduction of somewhat artificial infinite boundary condition.

On the other hand, the main disadvantage of the BEM is that it generates full dense matrices in place of the sparse FEM matrices. This causes an *a priori* high memory requirement as well as longer CPU time to solve the linear systems. In order to improve these requirements, a domain decomposition coupled with low rank approximations of the non diagonal sub-blocks of the BEM matrices has been introduced.

The purpose of the numerical study of the current paper is to predict and optimise the final deformed part as well as to outline the influence of different input variables on the final results.

The coil shown in Figure 5(a) was modelled for the EMF process simulation. Firstly the disposition of the workpiece with respect to the coil was studied in order to optimise the discharged energies. Figure 7(a) shows the maximum induced forces for each configuration subjected to an identical input discharged current (Figure 7(b)). It can be seen that when the currents induced in the workpiece form a closed loop, the forces induced in the material are higher. However, the induced currents (i.e. forces) in the sheet location corresponding to the central point of the coil are so small that it does not deform.

Once the suitable configuration was established for each experiment, a comparison between the experimental deformation and the numerical deformation was performed and the results are shown in Figure 8. From the figure, it can be identified that the predicted numerical and experimental temporal shape profiles are in good correspondence. This also indicates that the isotropic material behaviour assumption made in this study (employing constitutive equation explained in section 2) is acceptable, although it is well known the anisotropy on the mechanical behaviour of magnesium alloys at room temperature (e.g. [4]). A possible justification for the difference between experimental and numerical results for the circular die forming experiment (Figure 8(b)) could be the assumption of considering AZ31B sheet as an insulator in the EM analysis, since a driver was used. In the case of temporal study (Figure 8(a)) the reason for the difference could be a result of the excessive material flowing due to incorrect modelling of the friction conditions.

The influence of the conductivity of AZ31B alloy was numerically analysed. The values for conductivity used were those presented in reference [9] where a conductivity range of 9-11 MS/m was measured for AZ31B alloy. In Figure 8(a) it can be seen that the difference between the two conductivities is not very significant.

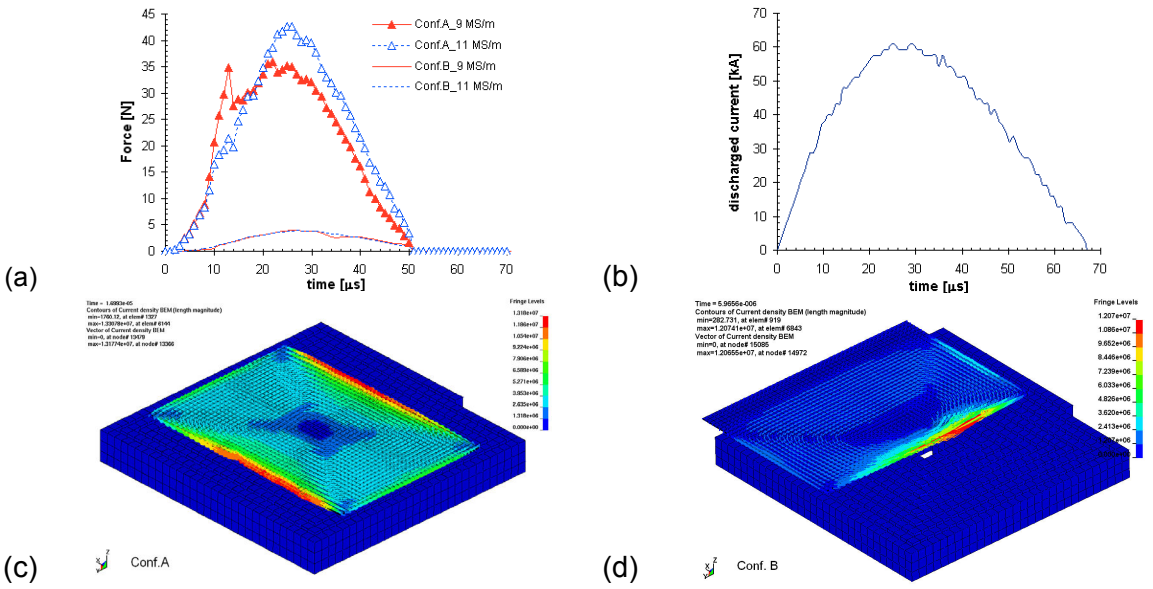

***Figure 7**: Numerical results. (a) Influence of the configuration and electrical conductivity of the sample on the induced force; (b) discharged current; vectors of induced current densities (values are in mA/mm^2) for (c) Conf.A, (d) Conf.B*

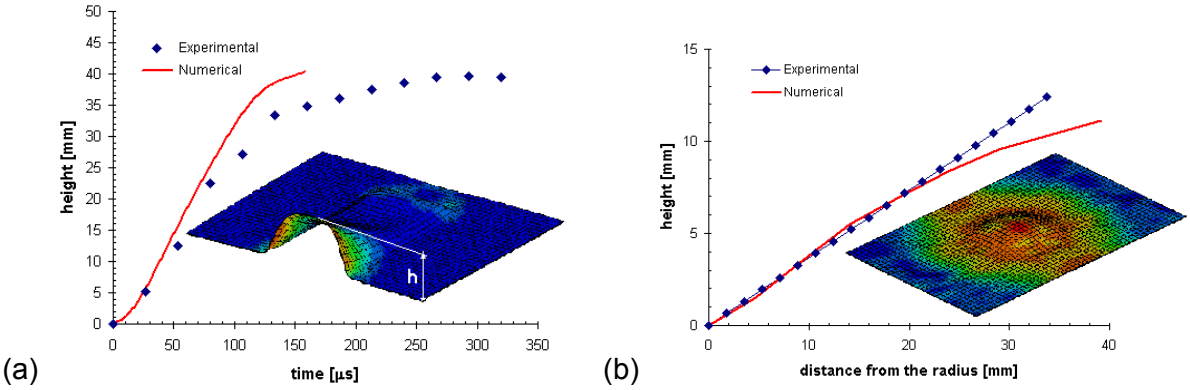

***Figure 8**: Comparison between experimental and numerical results. (a) time evolution of the maximum height for the square forming; (b) final shape for the circular die forming.*

5 Conclusions

Magnesium alloy AZ31B exhibits significant strain rate sensitivity, with increases in both ductility and flow stress at high strain rates. The estimated parameters for the simplified Johnson-Cook constitutive model fit reasonably well with the experimental data.

Furthermore, biaxial formability tests show that magnesium alloy AZ31B shows improved formability when formed at high strain rates using EMF. It has been suggested that at high strain rates twinning is the most active deformation system [20]. In the future, warm electromagnetic forming will be analysed in order to achieve proper process parameters.

The coupled numerical model suggested in the present contribution allows for the optimization of process parameters, such as sheet-coil configuration and the discharged current values. The numerical results of the deformed parts show relatively good results in comparison with experimental data. In order to obtain more accurate results, a more exhaustive tribological response of the material should be studied. Furthermore, in the case of simulating electromagnetic forming aided with a driver sheet, the AZ31B magnesium sheet should be considered as conductor and induced forces should be computed.

References

[1] *Vinarcik, E.J.:* Opportunities of Magnesium Sheet in Automotive Lightening. Light Metal Age, v.55, 1997, p.24-28.

[2] *Kleiner, M., Geiger, M., Klaus, A.:* Manufacturing of Lightweight Components by Metal Forming. 53rd CIRP General Assembly, Montreal, Canada, 2003, p.521-532.

[3] Magnesium Vision 2020: A North American Automotive Strategic Vision for Magnesium. USAMP report, 2007.

[4] *Agnew, S.R., Duygulu, Ö.:* Plastic anisotropy and the role of non-basal slip in magnesium alloy AZ31B. International Journal of Plasticity, v.21,2005, p.1161-1193.

[5] *Doege, E., Dröder, K.:* Sheet Metal Forming of Magnesium Wrought Alloys – formability and process technology. Journal of Materials Processing Technology, v.115, 2001, p.14-19.

[6] *Zhang, K.F., Yin, D.L., Wu, D.Z.:* Formability of AZ31 magnesium alloy sheets at warm working conditions. International Journal of Machine Tools & Manufacture, v.46, 2006, p.1276-1280.

[7] *El-Magd, E., Abouridouane, M.:* High Speed Forming of the Light-Weight Wrought Alloys, Proceedings of the First International Conference on High Speed Forming, Dortmund, 2004, p.3-12.

[8] *Jimbert, P., Ulacia, I., Fernández, J.I., Eguia, I., Gutierrez, M., Hurtado, I.:* New Forming Limits By Means Of Electromagnetic Forming And Numerical Simulation of The Process. 10th ESAFORM Conference on Material Forming. AIP Conference Proceedings, v.907, 2007, p.1295-1300.

[9] *Psyk, V., Beerwald, C., Klaus, A., Kleiner, M.:* Characterisation of extruded magnesium profiles for electromagnetic joining. Journal of Materials Processing Technology, v.177, 2006, p.266-269.

[10] *Revuelta, A., Larkiola, J., Coronen, A.S., Kanervo, K.:* High Velocity Forming of Magnesium and Titanium Sheets. 10th ESAFORM Conference on Material Forming. AIP Conference Proceedings, v.907, 2007, p.157-162.

[11] *Uhlmann, E., Jurgasch, D.:* New Impulses in the Forming of Magnesium Sheet Metals, Proceedings of the First International Conference on High Speed Forming, Dortmund, 2004, p.229-241.

[12] *Ulacia, I., Salisbury, C.P., Hurtado, I., Worswick, M.J.:* High strain rate characterization of AZ31B magnesium alloy sheet. In preparation. 2008.

[13] *Johnson, G.R., Cook, W.H.:* A constitutive model and data for metals subjected to large strain, high strain rates and high temperature. 7th International Symposium on ballistics, 1983, p.541-547.

[14] *Palumbo, G., Sorgente, D., Tricarico, L., Zhang, S.H., Zheng, W.T., Zhou, L.X.:* Formability Evaluation in Warm Conditions of AZ31 Magnesium Alloy. Proceedings of the IDDRG Conference, Porto, 2006, p.59-66.

[15] *Kleiner, M., Brosius, A., Blum, H., Suttmeier, F.T., Stiemer, M., Svendsen, B., Unger,J., Reese, S.:* Benchmark Simulation for Coupled Electromagnetic-Mechanical Metal Forming Processes. Production Engineering, v.XI, 2004, p.85-90.

[16] *Ulacia, I., Imbert, J., L'Eplattenier, P., Hurtado, I., Worswick, M.J.:* Numerical simulation of electromagnetic forming process using a combination of BEM and FEM. Submitted to Numisheet08, September 1-5, 2008, Interlaken, Switzerland.

[17] *El-Azab, A., Garnich, M., Kapoor, A.:* Modeling of the electromagnetic forming of sheet metals: state-of-the-art and future needs. Journal of Materials Processing Technology, 2003, v.142, p.744-754.

[18] *Panshikar, H.M.:* Computer modeling of electromagnetic forming and impact welding, M.S. Thesis, Ohio State University, 2000.

[19] *L'Eplattenier, P., Cook, G., Ashcraft, C., Burger, M., Shapiro, A., Daehn, G., Seth, M.:* Introduction of an Electromagnetism Module in LS-DYNA for coupled Mechanical-Thermal-Electromagnetic Simulations. Proceedings of the 9th International LS-DYNA Users Conference, Dearborn, 2006, p.17/1-17/8.

[20] *Kintana, J., Ulacia, I., Salisbury, C.P., Hurtado, I., Worswick, M.J.:* Comportamiento de la aleación de magnesio AZ31B a altas velocidades de deformación y elevadas temperaturas. To be published in the proceedings of the X Congreso Nacional de Materiales, June18-20, 2008, Donostia, Spain.

Design and Analysis of a Deep Drawing and In-process Electromagnetic Sheet Metal Forming Process*

D. Risch[1], G. Gersteyn[2], W. Dudzinski[3], C. Beerwald[4], A. Brosius[1], M. Schaper[2], A. E. Tekkaya[1], F.-W. Bach[2]

[1]Institute of Forming Technology and Lightweight Construction, Technische Universität Dortmund, Germany
[2]Institute of Material Science, Leibniz Universität Hannover, Germany
[3]Institute of Materials Science and Applied Mechanics, Wrocław University of Technology, Poland
[4]Poynting GmbH, Dortmund, Germany

Abstract

The design as well as the subsequent analysis of a deep drawing and in-process electromagnetic sheet metal forming calibration will be described in this paper. Due to the quite different forming processes concerning the occurred strain rates, an investigation on the microstructure of the formed workpieces will be pointed out. Furthermore, the design steps regarding the integrated tool coil will be presented and the resulting examples discussed. Finally, the setup of the integrated process as well as the feasibility will be shown on an exemplary semi-industrial workpiece.

Keywords

Electromagnetic sheet metal forming, Process integration, Microstructure

---

This work is based on the results of the Research Unit FOR443; the authors would like to thank the German Research Foundation for its financial support

1 Introduction & Motivation

The demands for lightweight construction become more and more important, for example in order to decrease fuel consumption in the transportation industry and thus the CO_2 emission as an environmental aspect. One possibility to realize such a concept is to optimize the design of the components on the one hand and, one the other hand, to apply “light” materials like aluminum.

Due to the smaller density and the comparably high strengths of aluminum alloys, for example the family of the 5xxx alloys are suitable for the use in lightweight car bodies instead of steel. The following diagram illustrates the increase of the weight proportion of aluminum within the European automotive branch over the last years [1].

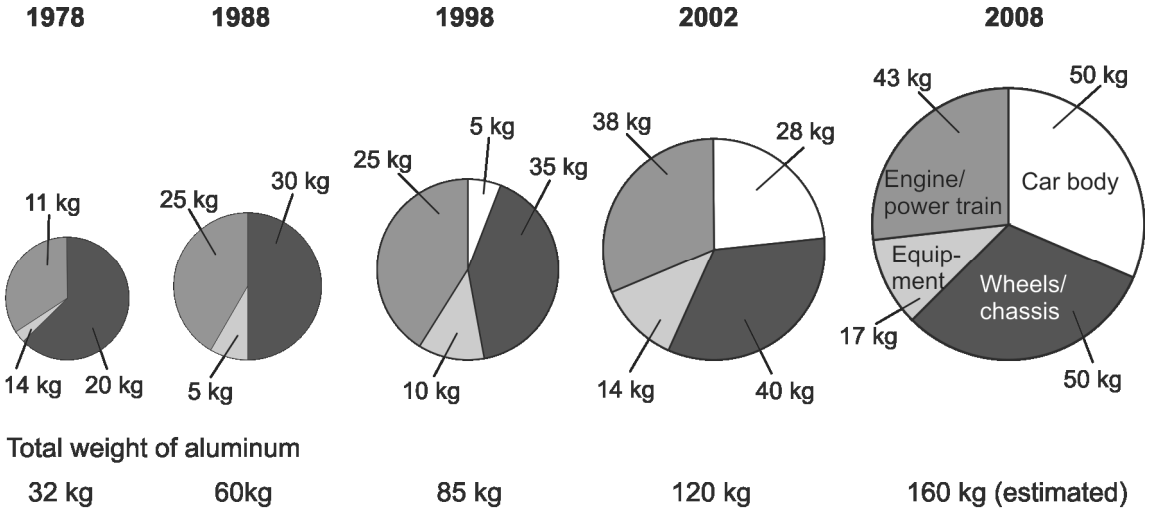

Figure 1: *Weight proportion of aluminum within the European automotive engineering [1]*

However, the formability of these materials is lower than that of common forming materials like carbon steels. Therefore, the realization of minor forming elements, as for example a door handle in an automotive door panel, can be quite difficult, so that a lot of drawing stages are necessary or even impossible with the conventional deep drawing process. Hence, the development of innovative technologies is indispensable.

An example of such an innovative technology is a combination of conventional deep drawing with electromagnetic sheet metal forming, where the electromagnetic calibration step is integrated in the deep drawing process. Due to this special combination the advantages of both processes can be merged.

In order to prove the potential of this combined process, investigations were performed on a semi-industrial demonstrator, which is based on the mentioned door handle.

2 Description of Deep Drawing and In-Process Electromagnetic Calibration

Deep drawing is one of the most important processes for forming sheets. Thereby, a wide range of different production sectors, like automotive parts, aircraft components,

household articles or white goods, are covered. The deep drawing process is a process to manufacture a product, especially hollow bodies, from sheet metal. During the deep drawing process, an initially flat blank, which is clamped between the die and the blankholder, is usually pulled over the punch into the die to deform the clamped blank into the desired shape. Thereby, the blankholder prevents any wrinkling in the flange area and facilitates a controlled material flow into the die radius [2]. Due to the fact that extensive research work was done in the deep drawing technology over the last hundred years, a considerable amount of knowledge regarding the process parameters as well as their interactions could be established. Therefore, a lot of strategies to produce a desired geometry are known. However, the limits in the deep drawing process, especially when using materials with poor formability, are inter alia to be found in the realization of small minor forming elements as, for example, a door handle in an automative door panel. Here, the manufacturing is quite difficult, so a lot of drawing steps are necessary or even impossible with the conventional deep drawing process. The advantage of the electromagnetic sheet metal forming is the high potential for the calibration of such geometrical elements.

The process principle of electromagnetic sheet metal forming is described in detail in [3]. With regard to the in-process electromagnetic calibration, the tool coil has to be integrated in the deep drawing die, while the minor forming element is placed in the punch, as shown in Figure 2. According the process principle of the electromagnetic forming, the magnetic pressure which is needed to deform the workpiece acts only in the area, where the winding is located. Due to the defined position of the tool coil in the drawing die and geometrical element in the punch, special effort was put on the positioning to each other in order to achieve the desired geometry.

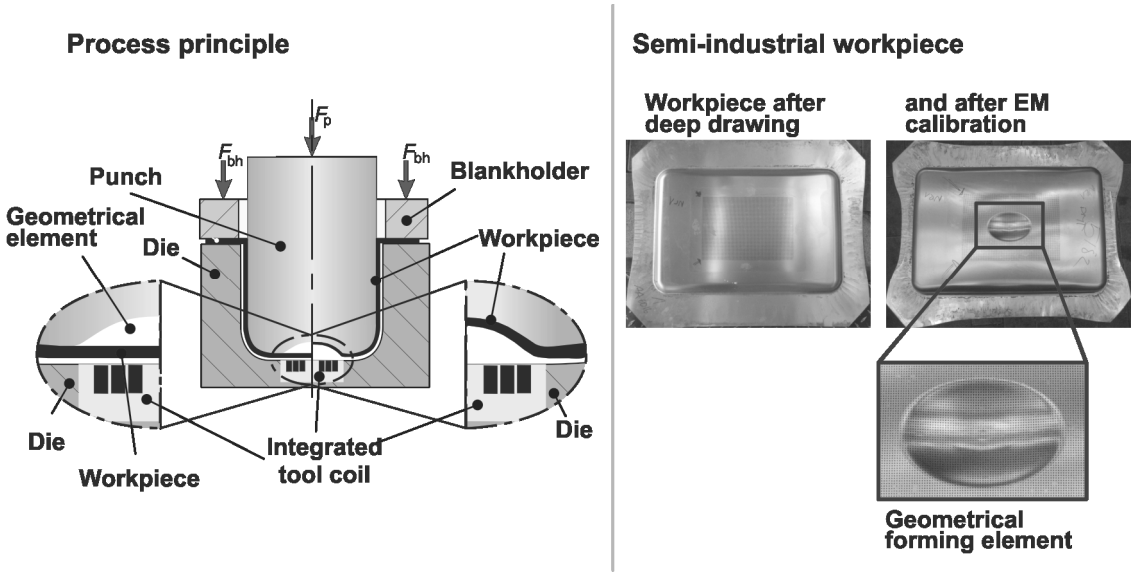

Figure 2: *a) Principle of the integrated process b) semi-industrial workpiece*

In order to design such a combination of deep drawing and in-process electromagnetic calibration and finally to show the feasibility as well as potential of this special combination, the following investigations are carried out. The analysis starts with the investigation of the microstructure of each single process and is followed by the

design of the special tool coil geometry separately on the basis of the electromagnetic forming process alone.

3 Influence of the Strain Rate on the Material Microstructure

In order to identify the different forming mechanism of each single process within the process combination, a detailed analysis of the microstructure was carried out. Thereby, a light optical microscopy as well as a scanning electron microscopy (SEM) was performed in order to investigate the macrostructure of the samples and the grain boundary. Furthermore, a transmission electron microscopy allows the analysis of the dislocation structure. These different investigation options offer the possibility to establish an understanding of the forming mechanisms. All investigations are done on the aluminum alloy AA5182.

The investigated specimens were formed with different strain rates: quasistatic bulge tests and dynamic electromagnetic sheet metal forming, respectively. Thereby, a regular dot pattern was applied to the workpiece surface in order to characterize the strain distribution after the forming operation with the optical measurement system Argus developed by GOM [4]. So, it was possible to detect positions with equal strains in both workpieces. Furthermore, selecting the regarded specimen sections also the loading condition has to be also considered as the same. The photos taken with the light optical microscope are presented in Figure 3.

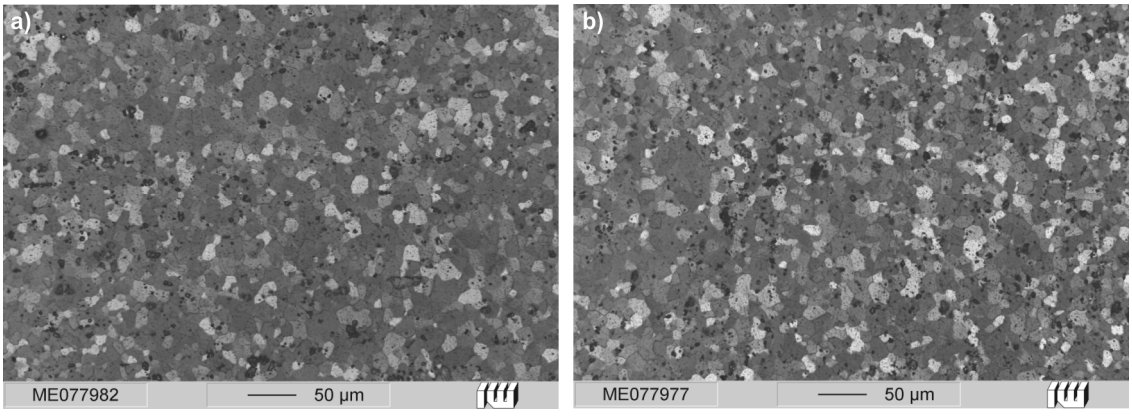

Figure 3: *Microstructure of the a) quasistatically and b) dynamically formed workpieces made of AA5182*

The grain size of the formed workpieces is determined on the basis of DIN EN ISO 643. The grain size of the electromagnetically formed specimen is 9, while the grain size of the quasistatically formed workpiece could be determined as 8.5. Due to having the same strain on the analyzed specimen, only a small difference of the grain size was observed. Nevertheless, the grain size of the dynamically formed parts is smaller than the quasistatic ones (compare Figure 3a), indicating that the forming mechanism of both processes differ from each other.

In order to obtain a deeper understanding of the dominating forming mechanism, an investigation on a microstructural level is necessary. Therefore, a transmission electron microscopy (TEM) was carried out. The specimens were prepared by means of wire-cut

electrical discharge machining (EDM) in order to have the best sample quality and no influencing parameters (e.g. local heating) on the dislocation structure.

The aim of this analysis is the identification of microstructural phenomena, for example the preferred slip planes within the crystal, so that, on the one hand, the dislocation structure can be described depending on the forming parameters and on the other hand, the different forming mechanism can be explained.

On this basis a comparison on the microstructural level of different forming operations is also possible. As known from literature [5], the aluminum alloys have a face-centered cubic system and the preferred planes are (110), (100), (211), (111), (310), and (123). Due to the face-centered cubic system, parallel planes in the crystal, which interact with each other, can exist. Hence, the following approach, which can be described on the basis of Figure 4, was used for the analysis.

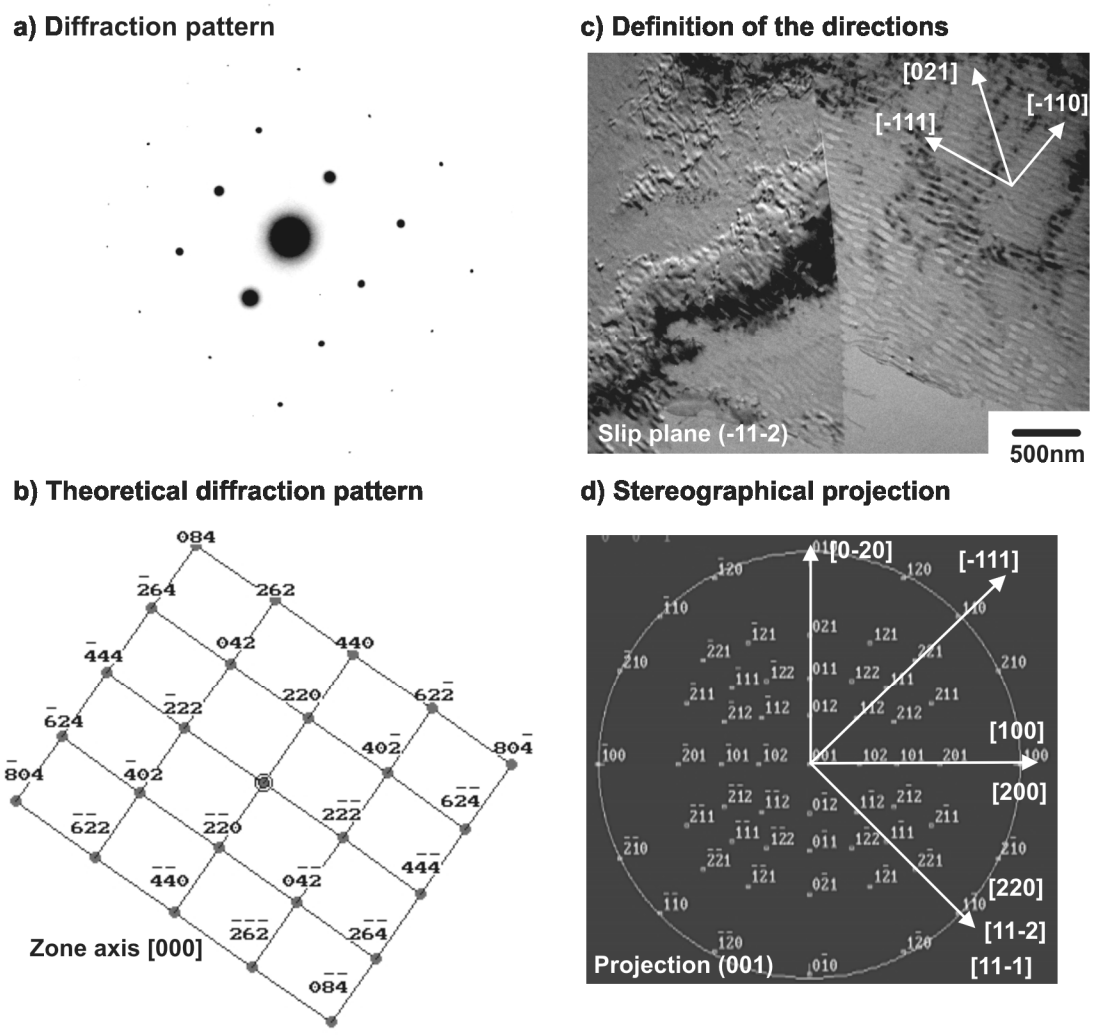

***Figure 4**: Approach to analyze the samples*

Due to the extremely small specimen size of one or two grains, a transmission electron microscope was applied for the analysis. Thereby, the reflected electrons are projected on a detector screen, and the diffraction pattern of the crystal (see Figure 4a), indicating the crystallographic orientations of the investigated samples, is received. Then,

the Miler indices of the crystal, which indicate the directions, can be defined. Knowing the distance and the angle of different planes obtained by the diffraction pattern and their mathematic correlations, the theoretical diffraction pattern can be determined (compare Figure 4b). Now, the achieved directions are transferred to the observed grain (see Figure 4c), and a stereographical projection is performed. This stereographical projection allows a well arranged two-dimensional description of directions and orientation of planes. This orientation is presented through the surface normal. Due to this, it is possible to detect parallel planes within the crystal. The orientations of the analyzed crystal in the standard (001) stereographical projection are presented in Figure 4d. Thus, the parallel planes within the crystal as well as the correlations between the planes could be identified.

The results obtained by using the described approach are shown in Figure 5. In Figure 5a the microstructure of the quasistatically formed workpiece is presented, while the electromagnetically formed sample is given in Figure 5b. In this investigation, the preferred direction of the sample taken from the quasistatic formed workpiece is the [100] direction. This means that the texture is oriented also in [100] direction. Contrarily, the electromagnetically formed specimen has three preferred directions [111], [110] and [100], which could be observed during the analysis. This means, that more dislocation motion occurs on the one hand and, on the other hand, a marginal texture could be detected.

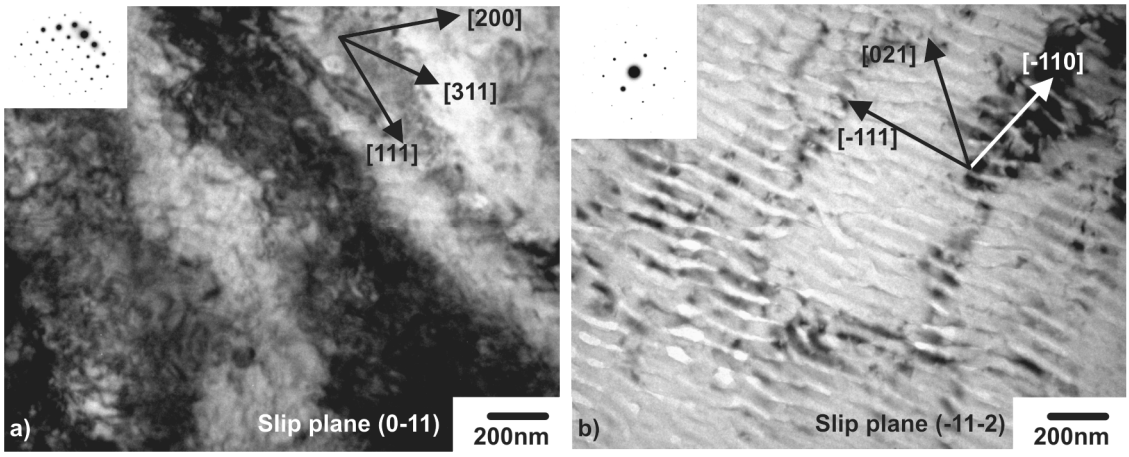

***Figure 5**: a) quasistatically formed sample b) electromagnetically formed sample*

In Figure 5b, some wavelike lines with a width of about 10 up to 40 nm can be perceived, while this wavelike structure in Figure 5a has a width of much more than 40 nm. Furthermore, this phenomenon is rare in the microstructure of the quasistatically formed workpiece, whereas approximately 30% of the grains belonging to the electromagnetically formed sample show this wavy formation. This wavelike structure is the result of the evolution of the gliding planes due to the dislocation motion. Investigations concerning the localization of plastic strain as well as the formation of waves of plastic flow are described in [6, 7]

Seen from the microstructrural point of view, the following forming mechanisms can be distinguished according to [8]

- Change in the resistance to motion of dislocation
- Increase of temperature
- Concentration of dislocations

But in case of parallel planes occurring by the electromagnetically formed workpiece, only one of these forming mechanisms is responsible for the deformation.

However, in case of the electromagnetically formed samples, parallel planes could be detected by means of the described stereographical projection. Consequently, more dislocations could slide. All mentioned aspects enhance the quality of the forming process so that the formability of the material could be increased.

4 Pre-Experiments to Design the Integrated Tool Coil

Preparing the combined process, pre-investigations regarding the electromagnetic forming step separately and using a plane tool coil were carried out. The major function of the coil winding is to apply an appropriate pressure pulse as well as pressure distribution onto the surface of the workpiece [3, 11, 12]. In this context, the influences of different pressure distributions resulting from different coil geometries on the quality of the forming results were analyzed at the Technical University of Dortmund. All tool coil and winding geometries had been designed and realized at Poynting GmbH. In this close collaboration several loops have been performed.The forming task here is an elliptical geometry, which is comparable to a door handle (shown in Figure 2). The investigation starts with a tool coil with an elliptical winding of eight turns. The outer dimensions correspond to the forming task, as shown in Figure 7a. Thereby, the turns of the winding have a constant cross section and the distance between two adjacent turns is equal. All experiments are done with the aluminum alloy AA5182 with a sheet thickness of 1.2 mm. The resulting workpiece geometries achieved by different charging energies are measured with an optical three-dimensional digitizer (ATOS I by GOM) and compared with the desired shape. The occurring deviations are presented in Figure 6.

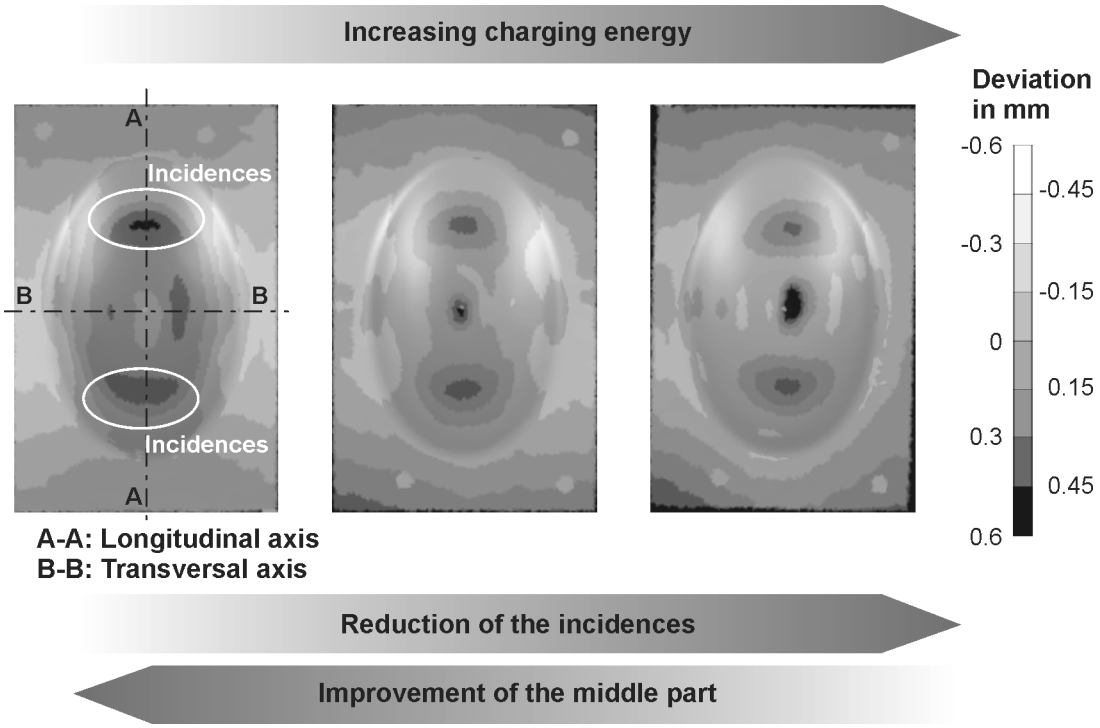

***Figure 6**: Contour courses of workpieces achieved with different charging energies*

A comparison of these geometries shows that by adapting the charging energy, either the middle of the workpiece can be reached in a good order or the incidences on the longitudinal axis (marked in Figure 6) are minimized, but no overall satisfying result is achievable.

In order to optimize the forming result, the pressure distribution has to be adapted. Therefore, a tool coil, which consists of eight turns with variable cross section as well as variable distance between the turns, was built and analyzed. This strategy, namely changing the turn density of the tool coil, was successfully applied in [12]. Both tool coils are presented in Figure 7a+b.

Position of the winding to the die

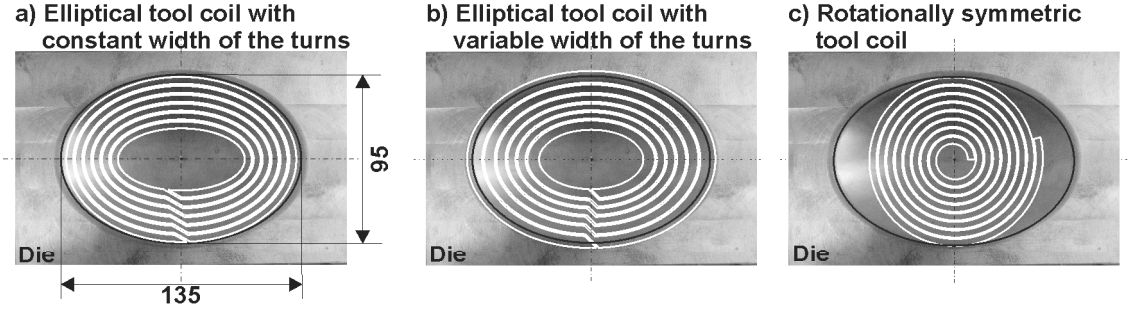

Data of the different tool coils

	a)	b)	c)
Number of turns	6	6	8
Height of the turns	14	16	7
Width of the winding	30 mm transversal 30 mm longitudinal	33.5 mm transversal 40.9 mm longitudinal	38 mm
Length of the longitudinal axis	130 mm	140 mm	98 mm
Length of the transversal axis	95 mm	190 mm	98 mm
Manufacturing of the winding	Water jet cut	Water jet cut	Manual wound

***Figure 7**: Description of the different tool coils*

Unfortunately, the desired geometry optimization regarding the elliptical geometry could not be achieved with this material (compare Figure 8). In general, the same effects occur using the tool coil with constant width of turns. Providing approximately the same geometric quality in the middle of the part, the occurring incidences are even stronger in case of the tool coil with variable width of turns.

The next iteration, the pressure distribution is optimized on the basis of the forming result of the previously described tool coils. Due to the incidences on the longitudinal axis, the pressure has to be increased to complete the form filling. One possibility to do so is to move the pressure maximum, which is usually located in the middle of the coil winding. Consequently, the length of the longitudinal axis of the tool coil has to be reduced. To

ensure a pressure near the die's edge, the width of the winding has to be increased simultaneously. Taking these actions results in a nearly rotational symmetric tool coil (compare Figure 7c). One advantage of this tool coil geometry regarding manufacturing aspects is the easy producibility in contrast to the elliptical tool coils. The forming results of this tool coil geometry are included in Figure 8, too.

In contrast to the elliptical tool coils, the rotationally symmetric one shows significantly lower deviations. The form filling is more homogenous and no incidence could be detected by an optical evaluation. Comparing all pictures, it can be seen that the best results could be achieved with the rotationally wound tool coil. Therefore, this coil geometry was chosen for the investigation of the combined deep drawing and electromagnetic sheet metal forming process.

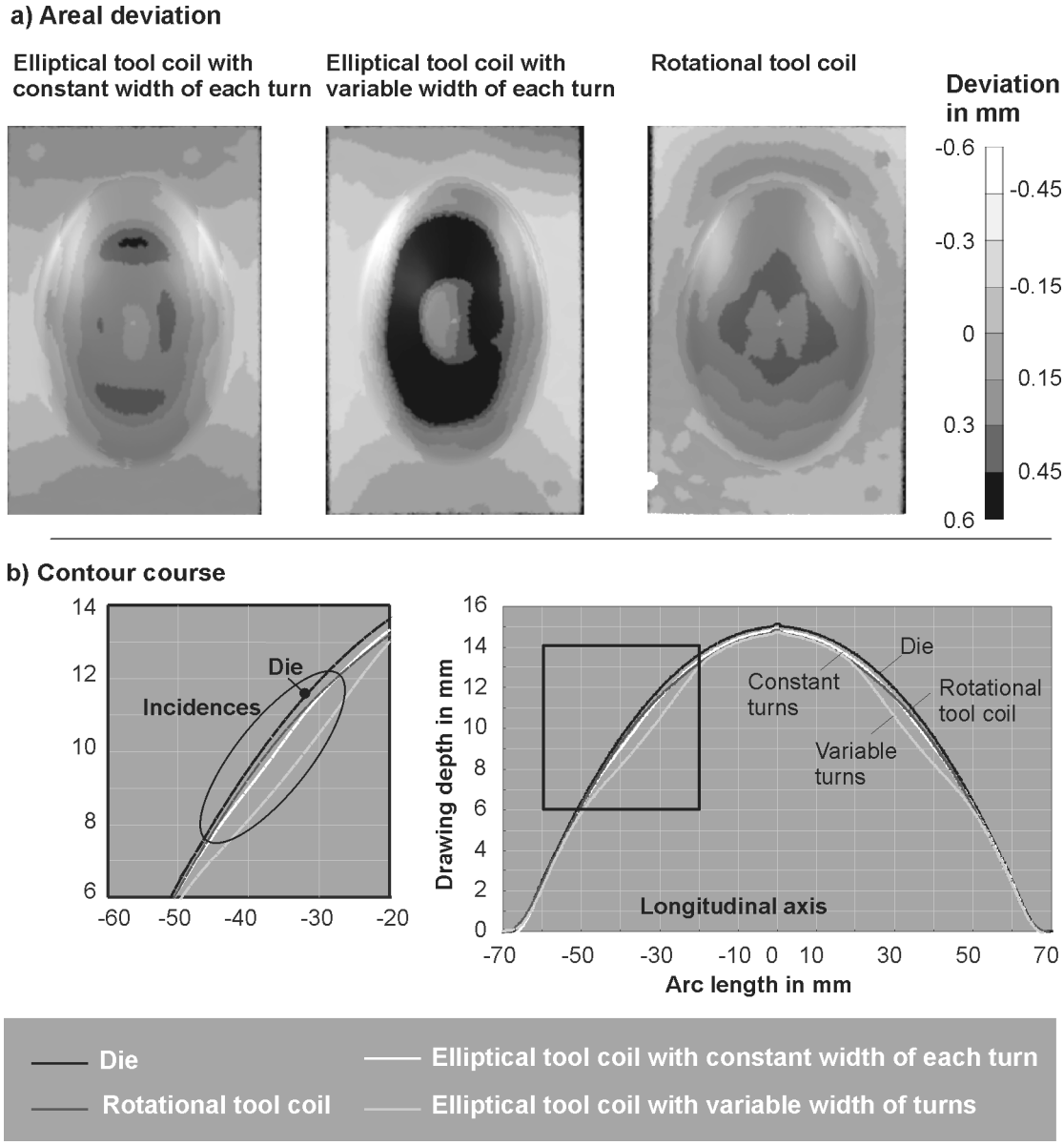

***Figure 8**: a) Areal deviation b) Contour course*

5 Discussion of the Results of the Deep Drawing and In-Process Electromagnetic Calibration Process

Apart from the feasibility of the electromagnetic calibration itself, there are additional restrictions regarding the deep drawing process. One impotant aspect is the remaining formability for the electromagnetic calibration operation, which will be reduced by all previous forming operations due to strain hardening and thinning effects.

However, in contrast to the plane tool coil, which was used in the pre-investigations, at Poynting GmbH a die with integrated tool coil has been adapted to the three-dimensional surface of the punch (resp. the workpiece).Therefore, the integrated tool coil has to be slightly curved, compare Figure 9. Furthermore, special measures have to be taken on the drawing die, especially on the embedding, as well as on the including winding: high voltage insulation between the single turns as well as between the winding and the workpiece; high strength to resist the deep drawing forces and to resist the impulse load of the winding during electromagnetic calibration; high wear resistance of the surface and adaptability to the forming press.

These demands require special and different materials in order to fulfill the described tasks. For the purpose of stability and adaptability to the forming press, a hardwood plate is used as a fixture, to which the curved tool coil is mounted. The slightly curved surface of the deep drawing die was realized by means of casting polyurethane (PU) to ensure the wear resistance during deep drawing. Within the prototypical testing of about 50 experiments, there is no significant abrasion of the polyurethane die.

The special deep drawing die including the tool coil as well as the necessarily modified EMF equipment was designed and manufactured at Poynting GmbH. The realized experimental setup is presented in Figure 9.

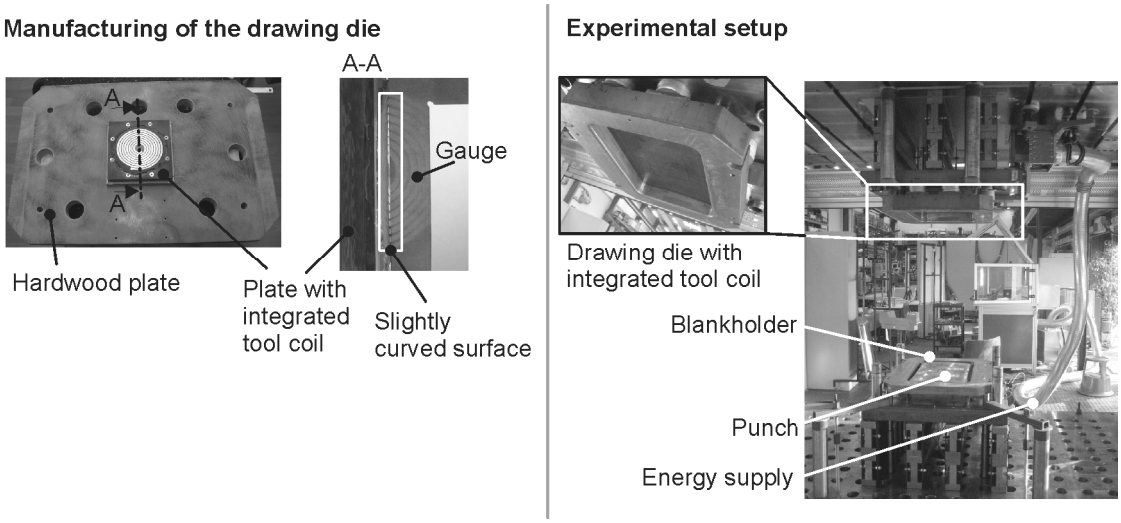

***Figure 9**: Experimental setup*

Representative results of the deep drawing and in-process electromagnetic forming operation using the described equipment is presented in Figure 10. Applying a charging energy of 2.6 kJ, the geometrical forming element could be realized without cracking.

The resulting strain distribution of the workpiece was determined by using the optical measurement system Argus developed by GOM. Using this evaluation tool, the maximum

Mises strain of the formed workpiece is approximately 17%. As known from literature the strain at failure by quasistatic loading of the aluminum alloy AA5182 is higher, namely in the range of 23-30% [9, 10], and additionally, the strain at failure increases with higher strain rates [11]. This means, that the formability of the used material is not exhausted and the described process strategy is arranged in a reliable process window. Furthermore, the geometry of the whole part could be achieved with good accuracy and without any significant deviation from the desired shape, as shown by the contour courses of the longitudinal as well as transversal axis. Moreover, no visible incidences could be detected comparable to the pre-investigation with the plane rotational symmetric tool coil.

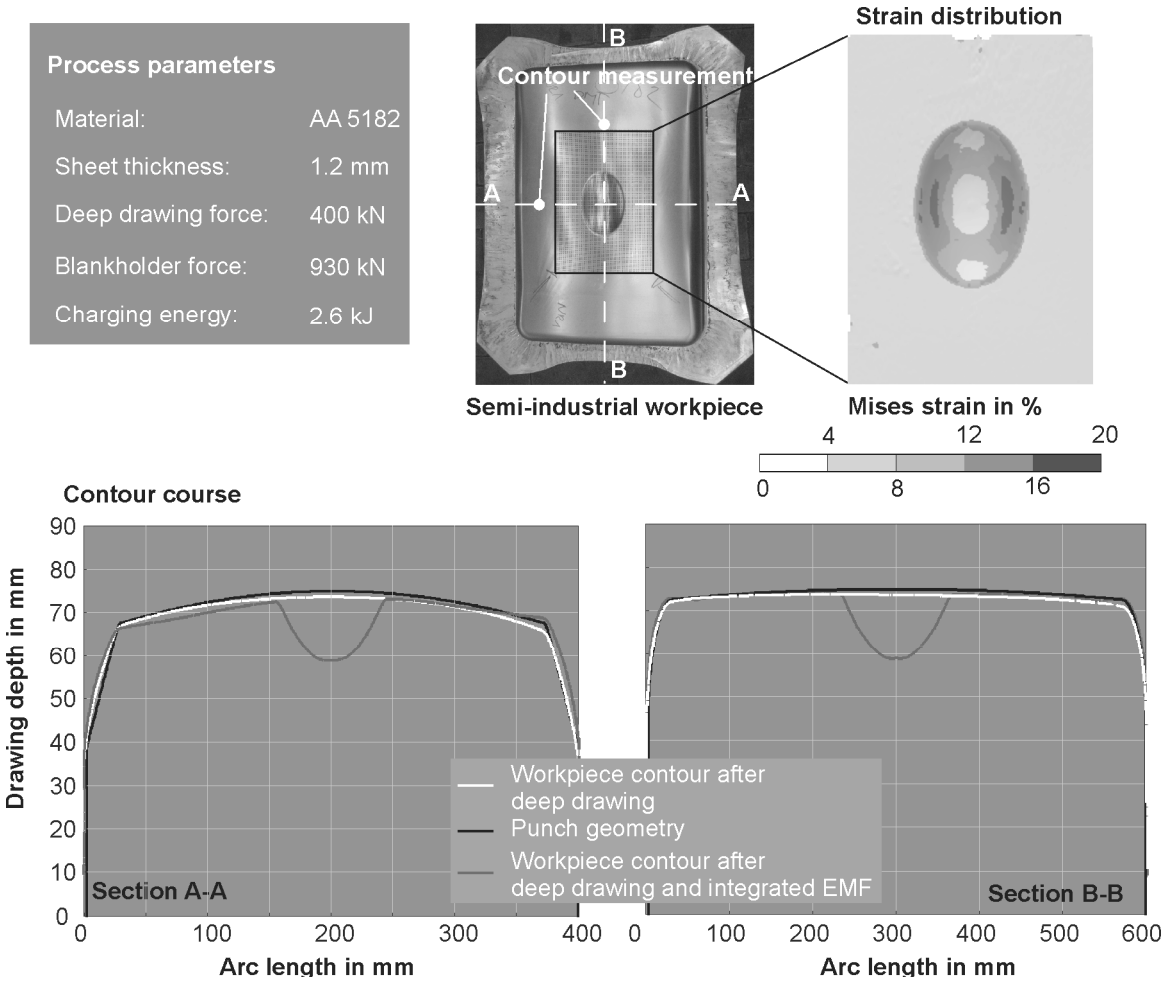

***Figure 10**: Results of the combined process*

All investigations were also carried out with the aluminum alloy A6016 and the results show qualitatively comparable results.

6 Conclusion & Outlook

In order to analyze the integrated process of deep drawing and in-process electromagnetic forming, both processes were investigated separately on a microstructural level. Thereby, the differences caused by the varying strain rates are described. Further investigation of the microstructure could consider the determination of

the temperature by means of an EDX-Analysis in TEM which are attained during the forming process. Moreover, the microstructural development in the combined process will be analyzed.

Regarding the integrated process, different tool coils were designed and tested on plane workpieces in order to achieve a homogenous form filling. Here, a rotationally symmetric tool coil showed the best results, although the desired die shape describes nearly an ellipse. These investigations will be extended to other complex geometries and other materials.

Finally, the feasibility of the described process combination of deep drawing and in-process electromagnetic calibration could be successfully proved. The analysis shows that the remaining formability was sufficient for the following calibration process and the achieved strain was lower than maximum strain of failure in quasistatic loading. So, the potential regarding forming more complex geometries is available and will be analyzed in detail in future work.

References

[1] *Jopp, K.:* Aluminiummotor in einem Guss. VDI nachrichten, 08/2003

[2] *Lange, K.:* Umformtechnik, Blechbearbeitung, Band 3, ISBN 3540500391

[3] *Beerwald, C.:* Grundlagen der Prozessauslegung und –gestaltung bei der elektromagnetischen Umformung (in German), Ph.D.-Thesis, Dortmund, Germany, 2004, ISBN 3-8322-4821-2

[4] www.gom.com

[5] *Hirsch P. B., Howie A., Nicholson R. B. at all:* Electron microscopy of thin crystals, London, Butterworths, p.503, 1965

[6] *Zuev, L.:* On the waves of plastic flow localization in pure metals and alloys, Ann. Phys. (Leipzig) 16, 4, p.p.286 – 310, 2007

[7] *Panin V. E., Grinyaev V. L, Danilov V. L. at all:* Mehrskalige Strukturstadien bei plastischer Umformung und Bruch, Novosibirsk, Wissenschaft. Sibir. Niederlassung, S. 255, 1990

[8] *Starenchenko, V. A.; Solov'eva, Y. V.; Abzaev, Y. A.; Kozlov, E. V.; Shpe°zman, V.; Nikolaev, V. I.; Smirnov, B.I.:* Evolution of dislocation structures having various orientations in strained single crystals of the alloy Ni3Ge. Physics of the Solid State, USA * vol 40 (April 1998), no 4, p 618-25, 19 refs. Translation of: Fizika Tverdogo Tela, Russia, vol 40 (April 1998), no 4, p 672-80

[9] *Ayres, R. A.; Wenner, M. L.:* Strain and strain-rate hardening effects on punch stretching of 5182-O aluminium at elevated temperatures. Metallurgical Transaction A, Vol. 10A, pp. 41-46, 1979

[10] *Takata, K.; Ohwe, T.; Saga, M.; Kikuchi, M.:* Formability of Al-Mg-Alloy at Warm Temperature. Materials Science Forum, Vols. 331-337, pp. 631-636, 2000

[11] *Vohnout, V. J.:* A Hybrid Quasi-Static-Dynamic Process for Forming Large Sheet Metal Parts from Aluminum Alloys, Ph.D.-Thesis, Ohio State University, Ohio, USA.

[12] *Psyk, V.; Beerwald, C.; Henselek, A.; Homberg, W.; Brosius, A.; Kleiner, M.:* Integration of Electromagnetic Calibration into a Deep Drawing Process of an Industrial Demonstrator Part, Key Engineering Materials Vol. 344 (2007) pp. 435-442, 2007, Trans Tech Publications, Switzerland

Forming Behaviour in Laser Shock Drawing*

H. Wielage, H. Schulze Niehoff, F. Vollertsen

BIAS - Bremer Institut für angewandte Strahltechnik GmbH, Klagenfurter Str. 2, 28359 Bremen, Germany

Abstract

Through the continuing trend of miniaturization new cost efficient and fast methods for processing small parts are required. In this paper a new non-mechanical process for the forming process of micro deep drawing is presented. This new deep drawing process utilizes a laser initiated plasma shock wave at the target, which forms the sheet. Several pulses can be applied at one point and therefore high forming degrees can be reached without increasing the energy density. In this paper the pressure of the shock wave is measured in order to enable optimizations of the process in future. Furthermore a distribution of the thickness over the deep drawn cups will be introduced. Finally laser deep drawing of samples made out of Al99.5, Cu and stainless steel sheet metal with thicknesses of 20 µm and 50 µm are shown.

Keywords

Micro forming, Laser forming, Deep drawing

1 Introduction

Within the ongoing demand of miniaturization of high precision components in electronics, precision mechanics, micromechanics and mechanical engineering the commercial relevance of the micro industry rises more and more. Read and write heads, inkjet printers, pressure sensors or micro fluidic chips are typical micro products in these industries. Within this increasing market the demand on productivity, efficiency, complexity and accuracy is growing. To this regard the well known advantages of high production rates, minimized material loss, excellent mechanical properties and close tolerances of the final product show the large potential of metal forming for micro parts [1]. Thus,

* *The presented work is part of the project VO 530/19-1 „Hochgeschwindigkeitsumformen durch laserinduzierte Schockwellen“. The authors would like to thank the Deutsche Forschungsgemeinschaft for their financial support within the project.*

investigations and improvements of conventional micro forming processes are needed, but also the invention of new processes is desirable. In this paper a new process of micro deep drawing by laser induced shock waves is introduced.

Laser shock treatment is already well known as a process for the modification of surfaces. Shot peening, i.e., got an increasing interest in the last years, since this technique can be used for the hardening of surface layer of components and especially for inducing residual compressive stresses. The modification of the material and its characteristics after laser shock treatment is already discussed in some basic works [2]. However, just some applications are known in the literature. This laser shock treatment was now extended to laser shock forming.

2 Principle of the Forming Method

Laser shock forming is a process, where the laser induced shock waves are used for a working step. While conventional laser forming is a process, where different thermal mechanisms cause bending of the sheet metal [3], laser shock forming takes place by a non-thermal mechanism. In this case the shock wave is used as a punch for the deep drawing process. At the laser shock forming the work piece is supplied with a laser pulse of high power density. The temporary pressure on the surface initiates an elasto-plastic shock wave onto the work piece and in consequence the shock wave pressure creates a forming of the work sheet. After the shock wave treatment no thermal effects on the surface of the sample can be detected [4]. This effect is taken beneficial for the laser shock forming.

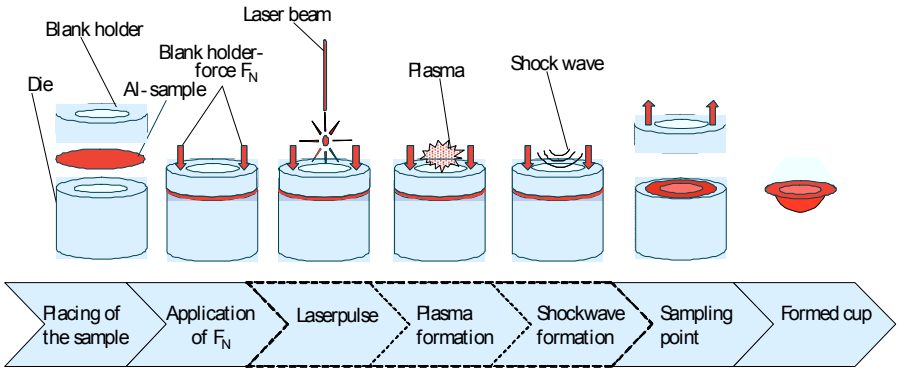

***Figure 1**: Principle of the laser deep drawing process*

The layout of the test blank for laser deep drawing is described by the following. A laser cut circular sheet metal is placed on a drawing die. The blank holder is placed onto the blank with a defined blank holder force below the clamping force. In a next step one or several short laser pulses of a TEA-CO_2-laser hit the specimen with the focus located at the blank surface. The high energy density of the laser radiation initiates ionization of the close-by atmosphere and thus plasma formation takes place. The propagation of the plasma causes a shock wave, if the energy density of the laser pulse exceeds a certain threshold. The principle of the laser shock forming can be seen in Figure 1.

3 The Shock Wave as a Tool

3.1 Pressure Measurement of the Shock Wave

The acting pressure of the plasma on the surface produces a shock wave at the solid body. The pressure caused by the laser introduced shock wave is the basic physical parameter for the plastic forming of the work piece. For the evaluation of the laser shock method the pressure is measured. The evaluation shown in this chapter can be used for future investigations to optimize the laser-caustic on the basis of the measured pressure. The pressure values can also be used for future simulations of the process or for an analytic model.

In order to detect the pressure under the surface of the target the following measuring method from Hintz [5] is used. For that a piezoelectric polyvinylidine fluoride (PVDF) sensor with an active area A of 1 mm², embedded in a PTFE foil, is bonded on the surface of a PMMA body, see Figure 2. The response rate is up to 10^{-9} Hz and therefore suitable for shock wave measurement. The 75 µm thick sensor film is located between the sample and a plexiglas body. For the calculation of the pressure the following term is used [5]:

$$p(t) = \int_0^t U(t')dt' \cdot \frac{1}{R} \cdot \frac{1}{C} \cdot \frac{1}{A} \qquad (1)$$

A high resistance is applied to preserve the piezosensor:

- Resistance R = 1 MΩ

The following data of the piezosensor are used:

- Capacity C = 22.5 pC/N
- Active area A = 1 mm²
- Voltage signal U(t')dt' = [Vs]
- Pressure p(t) = [Pa]

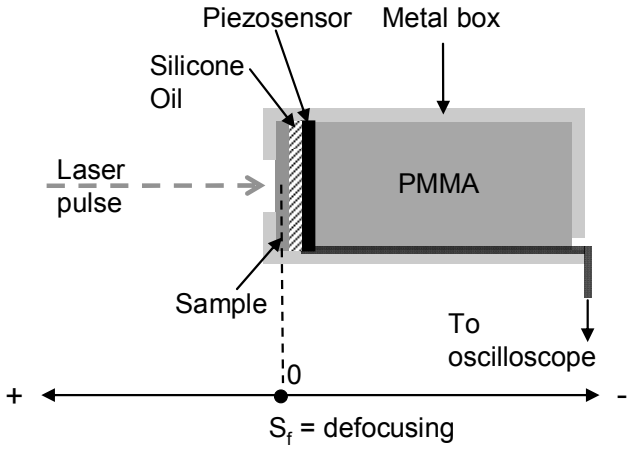

***Figure 2**: Schema of the pressure measuring with the piezosensor [5]*

Acoustic impedances are essential for the calculation of the absorbed intensity of the shock wave at the transition from one medium to another. The acoustic impedance of a material is determined by the density ρ of the material and the phase velocity c of a wave in this medium:

$$Z = \rho \cdot c \tag{2}$$

For a better coupling of the shock wave into the sensor, silicone oil is placed between sensor and sample. The PMMA body is hold in a metal box, which consists of a cylinder with a top to eliminate high frequency interferences, see Figure 2. The top is fixed by screws, which are tightened with defined 10 Ncm each. The PMMA body offers the development of the experiments without disadvantageous reflexions of the produced pressure wave. The laser beam is converged by a focused tilted mirror and the sensor signal is read by a digital storage oscilloscope.

At the two interfaces between sample, silicone oil and sensor reflexion losses of the shock wave occur. Hence, the pressure on the piezosensor is less than the pressure under the surface of the sample. A correction factor Z_U is calculated out of the acoustic impedances of aluminium Z_{Al}, of PMMA Z_{PMMA} and silicone oil Z_{Oil} to compensate these losses. For the ratio of the intensity of the pressure wave under the sample and after passing the sensor Z_U is [6]:

$$Z_U = \frac{(Z_{Al} + Z_{Oil})^2}{4Z_{Al}Z_{Oil}} \cdot \frac{(Z_{Oil} + Z_{PMMA})^2}{4Z_{Oil}Z_{PMMA}} = 4.55 \tag{3}$$

with Z_{Al} = 1.38 g/(cm²s)
Z_{PMMA} = 0.37 g/(cm²s)
Z_{Oil} = 0.121 g/(cm²s)

Hence, the corrected pressure p_r under the sample is:

$$p_r(t) = p(t) \cdot Z_U \tag{4}$$

The derivations of the formulas can be seen in [5]. With the stated values the pressure under the sample surface is therefore:

$$p_r(t) = 2.022 \cdot 10^{11} \frac{Pa}{Vs} \cdot \int_0^t U(t')dt' \tag{5}$$

For the calculation of the pressure under the surface of the sample the voltage signal is numerical integrated over the time and the pressure p determined by formula (5).

It becomes apparent that this measurement method is a complex measurement system, which obtains a comparable high statistical spread.

3.2 Results of the shock wave pressure measurement

In the following results out of the shock wave measurement are presented. The curves of pressure and the piezosensor signal shown in Figure 3 are generated by a shock wave. The shock wave was applied by a TEA-CO_2-laser pulse with a power density of 0.86 GW/cm² on an Al-sample with a thickness of 50 µm. The curves show the voltage and the pressure characteristics of the first shot on a sample. Over a period of fewer than 25 µs a pressure maximum of 2.5 MPa is achieved.

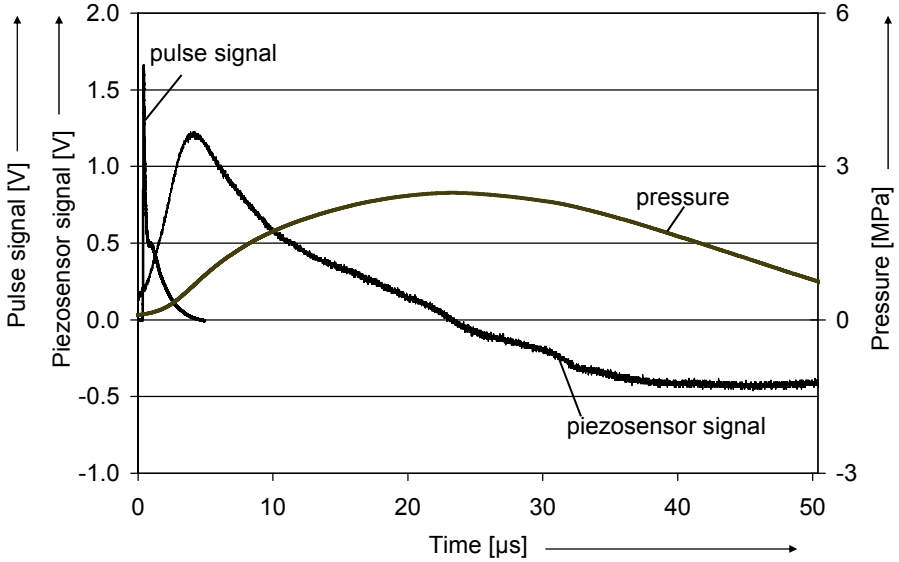

***Figure 3**: Typical signals of the pressure measurement; laser: TEA-CO_2; pulse energy: 3 J; spot size: 0.035 cm²*

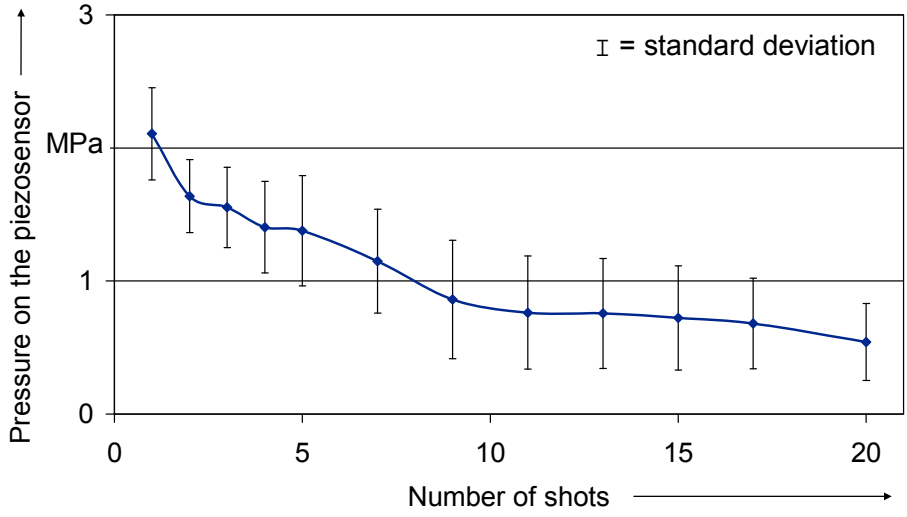

***Figure 4**: Influence of multiple exposure of one Al-sample on the measured pressure; laser: TEA-CO_2; pulse energy: 3 J; Al-Sample thickness: 50 µm; spot size: 0.035 cm²; number of experiments for each parameter: 5*

Furthermore, the influence of several pulses on an Al-sample on the pressure signal is investigated. Multiple exposures on Al-samples show that the first shot on a new sample achieves the highest maximum pressure value, whereas the measured pressure decreases for the following shots. This behavior is illustrated in Figure 4. The reason for this behavior is not found yet, but will be investigated in near future. In order to ensure consistent conditions for all measurements the target is renewed after the first shot in the following investigations.

Another potential influencing factor of the measurement process is the thickness of the used Al-sample, which is neglected in the correction factor in section 3.1. In order to investigate this influence on a potential difference between the real pressure values above the target and the measured values, experiments with different sample thicknesses were made. Figure 5 shows the measured maximum pressures under samples with thicknesses of 30, 50 and 100 µm. But a significant influence can not be identified. This might be caused by the comparable small sample thicknesses, which were used for laser shock forming: Within this sheet thickness range just a few grains are placed in the effective direction of the shock wave propagation. Therefore the sheet thickness in the investigated µm-area is not evaluated as a main influencing factor on the shock wave measurement.

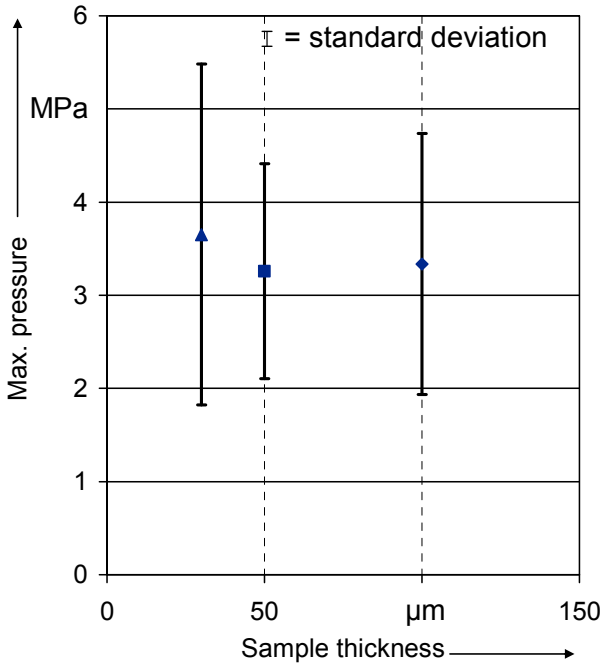

***Figure 5**: Maximum pressure under Al-samples with different thicknesses; laser: TEA-CO_2; pulse energy: 3 J; spot size: 0.035 cm²; number of experiments for each parameter: 10*

The influence of the distance between sample and laser beam focus s_F (see Figure 2) is determined for a future optimization of the pressure impulse. Thus, the piezosensor is positioned between 3 mm under (focal position s_f < 0 mm) and 60 mm above the focus in different steps.

Figure 6 shows the spot size for different focal positions and the corresponding measured maximum pressures. All pressures of the shock wave initiated 3 mm under to 7 mm over the focus position are at the level of 3.5 MPa. At a defocusing of 8 mm above

the target, the measured pressure decreases, it stays above 2.5 MPa, even at a focus to target distance of 40 mm. It becomes apparent that the process itself is stable: The shock waves initiated above the focus show constantly values of 2.5 and 3.5 MPa up to 40 mm defocusing. Even when the spot size increases the pressures are at a high level. Due to the constant pressure for a defocusing above s_F = 0 mm a correction of the focal position during deep drawing with multiple pulses is not necessary. Also the adjustment of the focal position does not play an essential part.

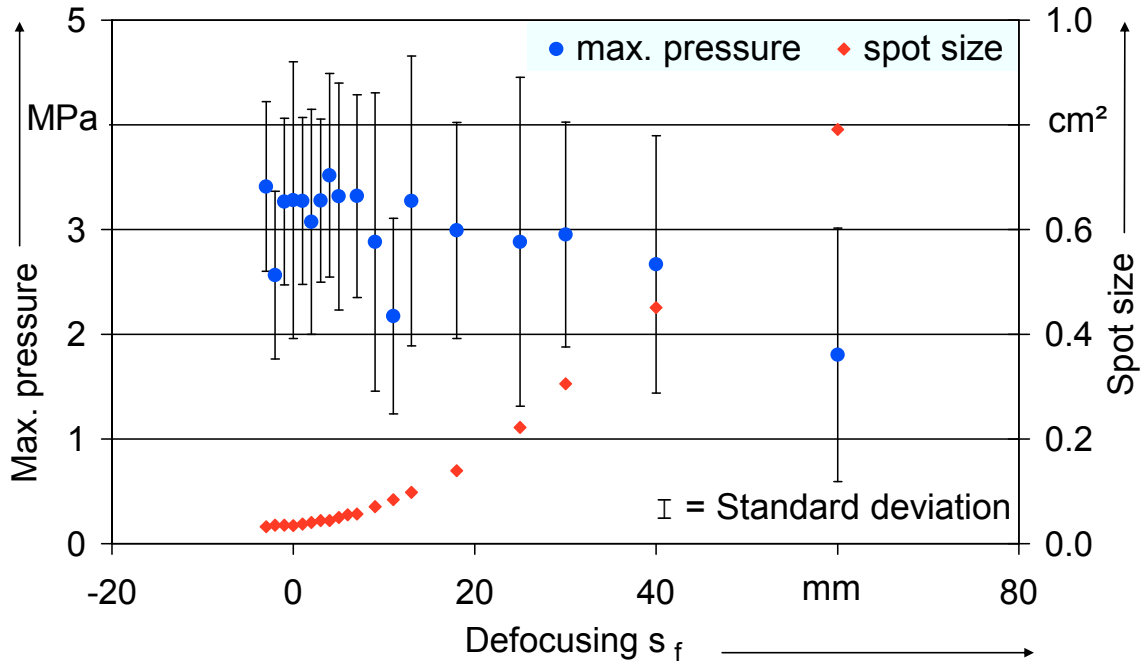

***Figure 6**: Pressure depending on defocusing; laser: TEA-CO_2; pulse energy: 3 J; Al-Sample thickness: 50 µm; number of experiments for each parameter: 10*

For a classification of the achieved pressures in the literature, the presented results are compared to results from Hintz [5] and a calculation of Hein [7, 8]. Hintz used the same pressure measurement system, but under different conditions. Hintz achieved pressures of 70 MPa at a pressure measurement of the shock wave initiated at free ablation. In comparison to the presented pressure values of 3.5 MPa a factor of 20 can be discovered by the same spot diameter. Hintz used an Excimer-laser (wave length 308 nm) with a laser beam energy of 2 J with a pulse duration of 45 ns and a pulse rising time of 1-3 ns. In contrast to that, the pulse duration of the TEA-CO_2-laser (wave length 10600 nm) is 100 ns and the pulse rising time is 35 ns. With the longer pulse duration and the longer rising time, the TEA-CO_2-laser the energy part, which is coupled into the plasma is less and thus the pressure of the shock wave is less. Hence, the measurement values are realistic.

A further classification can be made by the formula of Hein [7, 8] for the bursting pressure of a spherical cap in the hydroforming. The comparison makes sense, since the hydroforming process of forming spherical cups is the same like in the shock forming process. The calculated maximum pressure for a spherical cap in the presented case is 1.4 MPa. Thus, the measured pressures are located at a reasonable level.

4 Forming behaviour

4.1 Analyse of forming behaviour of deep drawn cups

In comparison to the presented method the deformations in the mechanical deep drawing process are affected by the die. The result is a distinctive deformation gradient at local positions, which implicates a smaller sheet thickness. For a further development of the laser shock forming it is significant to see how the initiated forming is located in the laser shock formed sheets.

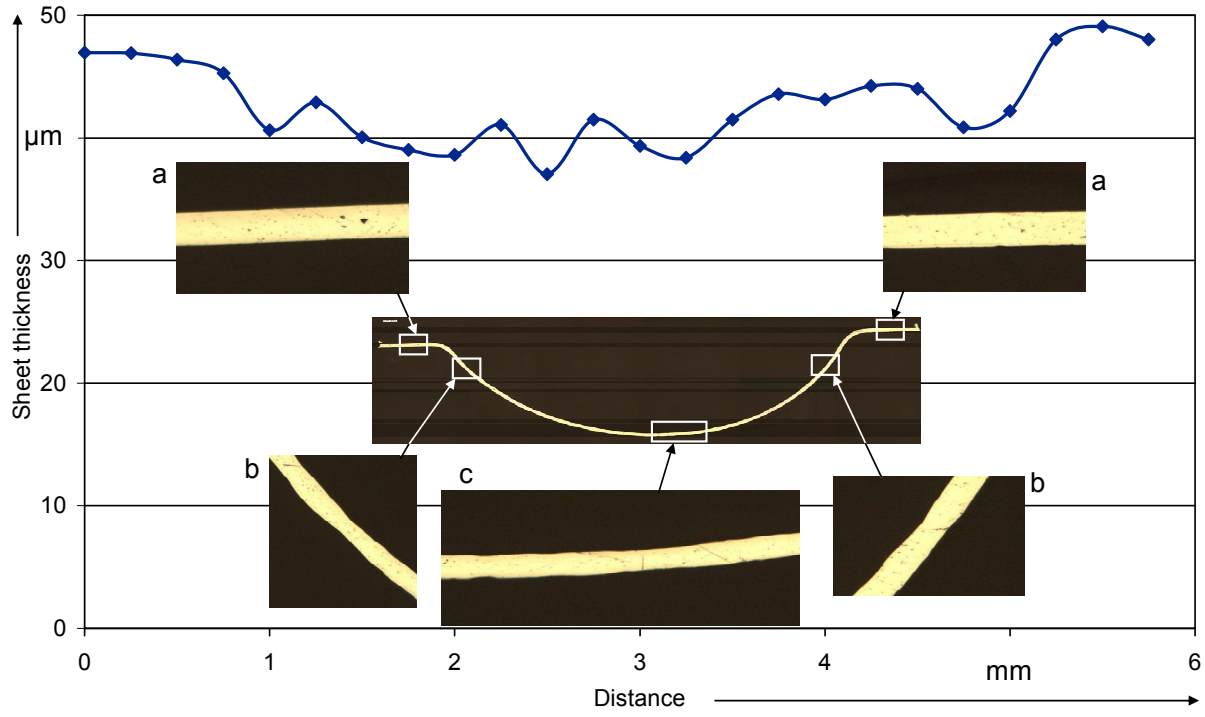

Laser:	TEA-CO_2	Initial thickness:	47 µm	Change in diameter:	1.7 %
Wavelength:	10600 nm	Initial diameter:	6 mm	Blank holder force:	10.2 N
Pulse energy:	600 mJ	Drawing ratio:	1.5	Number of shots:	120
Material:	Al99.5	Drawing radius:	0.25 mm	Uncertainty of measurement:	2 µm

***Figure 7**: Distribution of the thickness of a characteristic laser deep drawn cup*

Therefore the sheet thickness is plotted over the length of a characteristic deep drawn cup (Figure 7). The flange area (a) shows a uniform behaviour, while the escape of the drawing radius (b) on the left and the right side shows a necking of the sheet. In the bottom area (c) the sheet thickness varies in a wave form. This wave formed bottom is due to the orange peel that can be detached at the surfaces of the samples (i.e. Figure 9 b). Furthermore the comparably small change in the sample diameter after the forming process of 1.7 % shows that the process has a higher stretch-forming component than a deep drawing one. The global decrease of the thickness shows that within the forming

process the yield stress is achieved over the whole length of the cup. The material for the forming is taken from the entire width of the sample.

4.2 Forming behaviour of different materials

In order to investigate the applicability of the laser shock forming beyond Al 99.5, first results of processing stainless steel (1.4301) and copper were shown in this chapter.

In Figure 8 images of samples out of stainless steel with a thickness of 20 µm and 50 µm and in Figure 9 images of samples out of copper and aluminium with a thickness of 50 µm are shown. The samples are treated with similar parameters, whereas the stainless steel and copper samples are stretch formed and the aluminium is deep drawn.

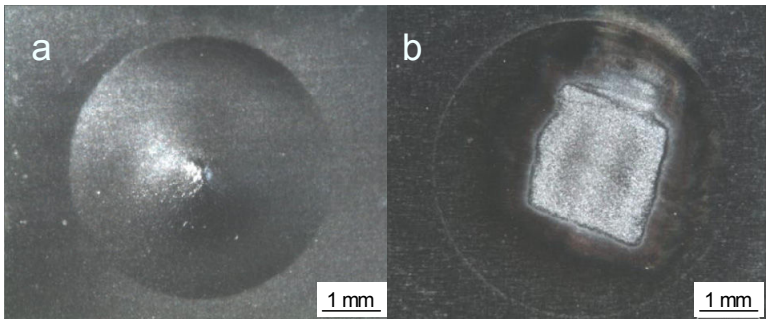

Laser:	TEA-CO2
Wavelength:	10600 nm
Pulse energy:	3 J
Material:	1.4301
Blank holder force:	4 N
a) Thickness:	20 µm
# pulses:	25
b) Thickness:	50 µm
# pulses:	700

***Figure 8**: Stainless steel samples out of with different number of pulses*

The sample out of stainless steel with 20 µm thickness (Figure 8a) shows a minimal deformation of 100 µm in cup height. The sample with 50 µm thickness (Figure 8b) shows no visible deformation after it was subjected to a 700 pulses. After 700 pulses a high damage of the material is noticeable, but still no deformation occurs. In contradiction to that the 50 µm copper sheet can be formed as well as aluminium (Figure 9a). With the same parameters copper shows a 1.5 times smaller cup high than the aluminium (Figure 9b), which is due to the higher yield strength of the material. However, high forming degrees up to the forming limit can also be reached with copper by the use of more pulses.

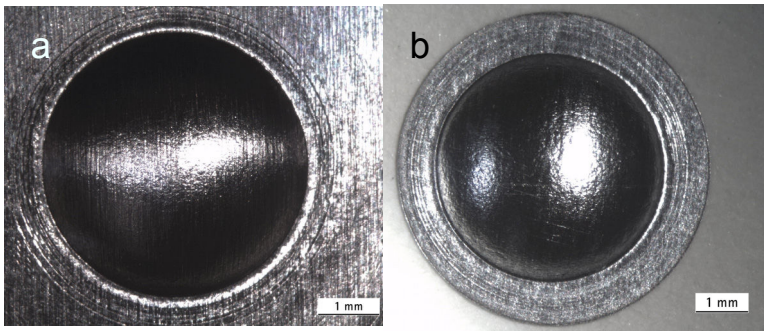

Laser:	TEA-CO2
Wavelength:	10600 nm
Pulse energy:	3 J
Thickness:	50 µm
a) Material:	SE-Cu
Blank holder force:	4.56 N
# pulses:	9
Cup height:	0.66 mm
b) Material:	Al99.5
Blank holder force:	4.1 N
# pulses:	9
Cup height:	1 mm

***Figure 9**: Copper (a) and aluminium (b) samples with the same parameter*

In contradiction to that, the yield strength of the used stainless steel was obviously too high. The calculated pressure after Hein [7, 8] for bursting is here 240 MPa (for s_0= 20 µm, cup height 100 µm). Therefore the reached forming pressures of laser shock waves of about 3.5 MPa (chapter 3) are not sufficient. An increase of the forming pressure will probably not bring better results, since the surface of the stainless steel is already damaged by the used shock wave pressure. Thus, further investigations with steel are not effective with the present setup.

Since the yield stress of copper is comparably low, the forming of copper is much easier to achieve. The higher ductility of copper in comparison to aluminium results in a smaller elongation ratio, but later crack formation than aluminium. This shows a further potential for copper in the laser shock forming. Thus, the application of laser shock forming with copper makes the process especially interesting for the electronic industries.

5 Conclusions

- Pressure measurement of the created shock wave was introduced, showing that pressures at the level of 3.5 MPa can be created with TEA-CO_2-lasers.
- An influence of the thickness of the Al-samples in the measurement process of the pressures is not detectable.
- An increasing number of exposures of one sample decrease the measured pressures.
- The pressure of the laser induced shock wave is not sensitive to defocusing during the deep drawing process in arrange of -3 mm to 7 mm.
- The distribution of the thickness of a characteristic laser deep drawn cup shows necking at the left and right side of the cup and a non-uniform behaviour at the bottom.
- The investigation of the applicability of the laser shock forming shows a good suitability not only for aluminium, but also for copper.

References

[1] *Geiger, M., Kleiner, M., Eckstein, R., Tiesler, N., Engel, U.:* Microforming. CIRP Annals, Vol. 50/2, 2001

[2] *Peyre, R. , Fabbro, R.:* Laser Shock Processing: A Review of the Physics and Applications. Optical and Quantum Electronics 27, p. 1213-1229, 1995

[3] *Vollertsen, F.:* Laserstrahlumformen - Lasergestützte Formgebung: Verfahren Mechanismen, Modellierung. Meisenbach Verlag, Germany, 1996

[4] *Schulze Niehoff, H., Vollertsen, F.:* Non-thermal Laser Stretch-Forming. Sheet Metal 2005, Advanced Materials Research, Vol. 6-8, p. 433-440, 2005

[5] *Hintz, G.:* Untersuchung der Druckerzeugung und der Strahl-Stoff-Wechselwirkung an einem Excimerlaser-System für die Schockbehandlung von Metallen, Dissertation, University of Erlangen-Nurnberg, 1997

[6] *Eisner, K.:* Prozeßtechnologische Grundlagen zur Schockverfestigung von metallischen Werkstoffen mit einem kommerziellen Excimerlaser, Dissertation, University of Erlangen-Nurnberg, 1998

[7] *Hein, P.*: Innenhochdruck-Umformen von Blechpaaren: Modellierung, Prozessauslegung und Prozessführung, Dissertation, University of Erlangen-Nurnberg, Meisenbach Verlag, Germany,1999

[8] *Hein. P., Vollertsen, F.:* Hydroforming of Sheet Metal Pairs, Journal of Materials Processing Technology 87, p. 154 – 164, 1999

Action of Pulse-Magnetic Fields on Liquid and Crystallizing Metal. Prospects for Development of New Technologies

V. A. Glouschenkov[1], D. G. Chernikov[1], A. J. Igolkin[1], F. V. Grechnikov[2], R. J. Jusupov[2]

[1] Samara State Aerospace University, Russia
[2] Volga Branch of the A. A. Baykov Metallurgical Institute, Russia

Abstract

Pulsed-magnetic fields are used for execution of a whole complex of technological processes: dividing, forming, assembling, welding and others. In all these technologies half-finished products from sheets, sections and tubes are used as billets.

Action of magnetic fields on a cast metal is known in the metallurgy production, for example, casting to an electromagnetic crystallizer. In spite of a high electrical resistance of a melt and owing to low mechanical resistance of a liquid metal the use of high-intensity pulse-magnetic fields (PMF) in technologies of mechanical engineering is of interest. Even the first exploration experiment showed high efficiency of such action. At energy of 1, 2 kJ a portion of the melt under the action of the PMF has flown more than 4 m, spread in the form of a thin film on the ceiling and solidified.

The paper presents three basic technological schemes of such action: with influence through a wall of a magneto-transparent crucible; by an immersion inductor; and action from the surface.

Factors accompanying such action are:

- *added sources of heat – as a result of flowing of induced eddy currents through the melt;*
- *force action on the melt responsible for passage of waves of stress and metal flows.*

Action of these factors is controllable both in intensity and in direction.

The temporal action of the pulse-magnetic field on a liquid and crystallizing metal (LCM) is to be matched with a curve of cooling the melt: either on the portion above the crystallization area or on its different portions, that is, at different relationships of solid and liquid phases.

Factors of action of the pulse-magnetic field change temperature conditions of crystallization influence on the number of centers of crystallization and, as the consequence, change structure and properties of cast metal.

The paper presents results of first studies on action of the pulse-magnetic field on a LCM which testify that such action is real and good. This has determined the prospects for development of new technologies in metallurgy (forming of an ingots' structure, stirring of a material, rolling of cast metal and so on) and in mechanical engineering (in casting, stamping, welding and others).

Keywords

Casting, Impact, Grinding

1 Introduction

Pulsed-magnetic fields are used for execution of a whole complex of technological processes: dividing, forming, assembling, welding and others. In all these technologies half-finished products from sheets, sections and tubes are used as billets.

Many researchers treated a possibility of using the action of the high-intensity PMF on a liquid and crystallizing metal skeptically. This is primarily associated with that the efficiency of pulse-magnetic processing reduces when electrical resistance of the processed material (solid metal – melt) increases. There are many other technical difficulties on the way to realization of such processing, for example, provision of performance of the inductor at elevated temperatures. But on the other hand, it is tempting to use the effect of decrease of mechanical resistance to deformation down to "zero" – for a metal melt. Moreover the positive experience of application of magnetic fields to cast metal in metallurgy production is known, for example, casting to an electro-magnetic crystallizer [1].

All these urged the authors on carrying out the first exploration experiment, the essence of which was in the following. The crucible, containing a melt of an aluminum alloy, was placed inward of the multiturn inductor for reducing. The giver of the level of the energy of the pulse-magnetic installation (МИУ-10) was moved to the lowest position appropriate to the minimum level of energy. After discharge of the МИУ-10 the melt was missed in the crucible. Having flown four meters, the metal "solidified" on the ceiling in a thin layer form. The experiment showed the efficiency of pulse-magnetic processing and good prospects for development of this direction.

2 Factors of Action of High-efficiency Pulse-magnetic Field on Liquid and Crystallizing Metal

The authors determined that basic interrelated factors of action of the PMF on a metal melt are: current intensity (I) in the discharging circuit, pressure (P) of the PMF on the liquid metal, which is specified by magnetic field intensity (H_0) and its related value of the skin layer (δ), a number of pulses of action (n), duration of pulses of action (t), temperature range of action (Tp) (before beginning of crystallizing or at the stage of crystallizing).

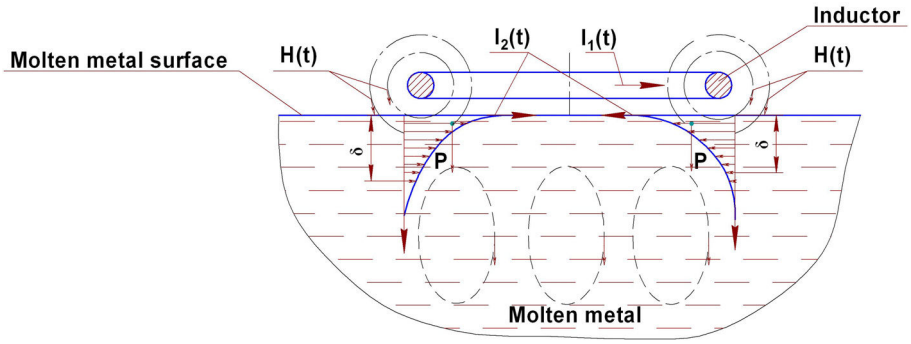

Figure 1: *Scheme of action of pulse-magnetic fields on a liquid and crystallizing metal*

One possible scheme of action of pulse-magnetic fields on a liquid and crystallizing metal is shown in Figure 1.

Under the magnetic field action the eddy currents are induced in the melt which are added internal sources of heat. Also electro-dynamic stresses appear which give rise to wave effects and metal flows. Propagation of shock waves has a beneficial effect on the process of thickening the metal, degasification, forming of a fine-grained structure. The arising metal flows intensify crystallization and change conditions of crystallization. Directionality of the metal flows is primarily dependent on a shape and disposition of inductor systems.

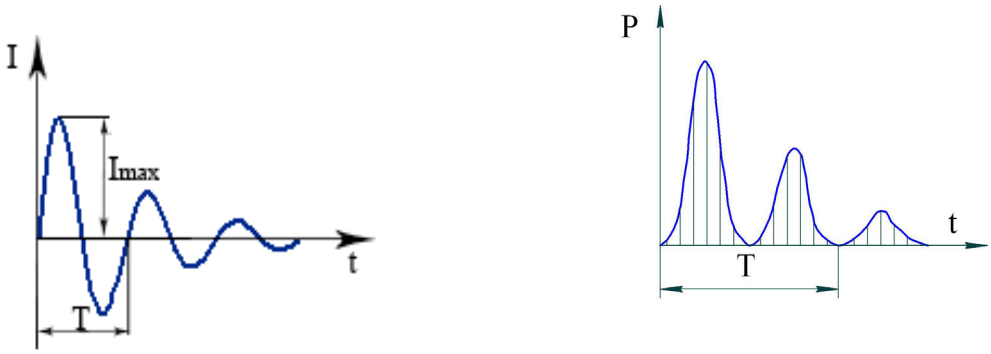

a) b)

Figure 2: *Discharging current of an inductor*

Electro-magnetic pulses of current are sinusoidal damping signals with the duration (t) of 50…150 μs and with the current amplitude of 10…50 kA (Figure 2).

The net pressure of the PMF is defined by the following expression:

$$p = \frac{\mu_0 \cdot H^2}{2} \qquad (1)$$

where H – magnetic field intensity at the surface of metal melt from the side of the entry of the field.

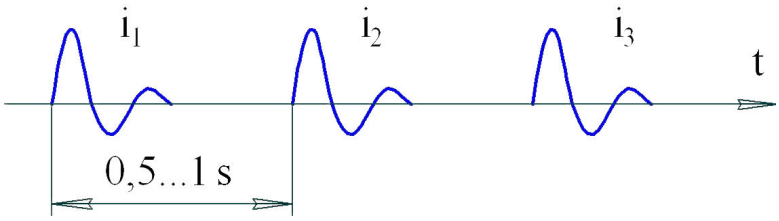

Figure 3: *Diagram of discharger pulses*

Such force and heat action can be repeated (n) with the temporal interval between pulses of 0,5…1 s (Figure 3).

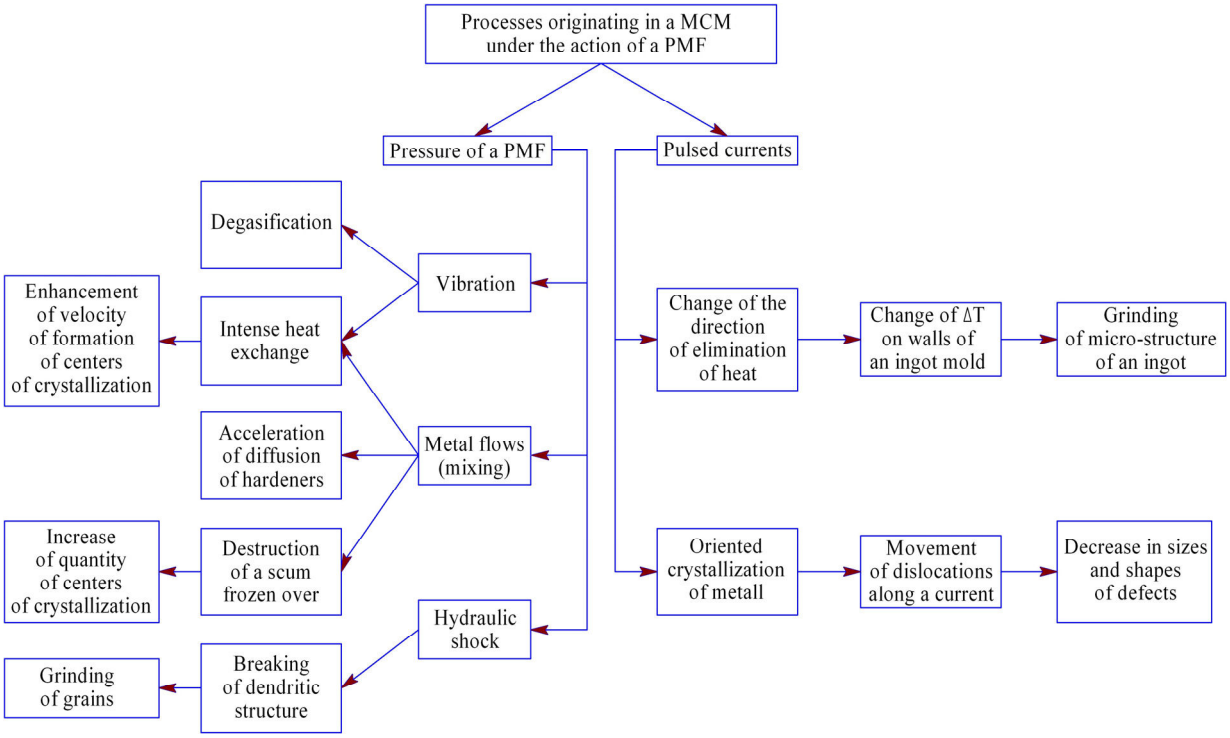

Figure 4: *Assumed mechanisms of action on a metal melt*

Analysis of the influence of these factors allowed making some assumptions about mechanisms of action on a metal melt which appear under the effect of the pulse-magnetic field of high intensity (Figure 4).

3 Technological Schemes of Pulse-magnetic Action on Cast Metal

Purposes of pulse-magnetic action on cast metal can be different, for example, stirring of a metal melt for intensification of a process of solution of hardeners, production of a homogeneous structure, production of a fine-grained structure, new technologies. Three standard technological schemes were developed for realization of these purposes (Figure 5):

- with the radial action of the PMF on a metal melt (Figure 5a);
- with the axial, surface action of the PMF on a metal melt (Figure 5b);
- three-dimensional pulse-magnetic processing of a metal melt with an immersion inductor (Figure 5c).

For performing the first scheme (Figure 5a) use can be made of inductors similar the inductors which are applied in pressing of metals by the PMF but either with the additional insulation of turns to offer the prospects of operation at elevated temperatures or being cooled. For this scheme a crucible must be made of a magnetically transparent material.

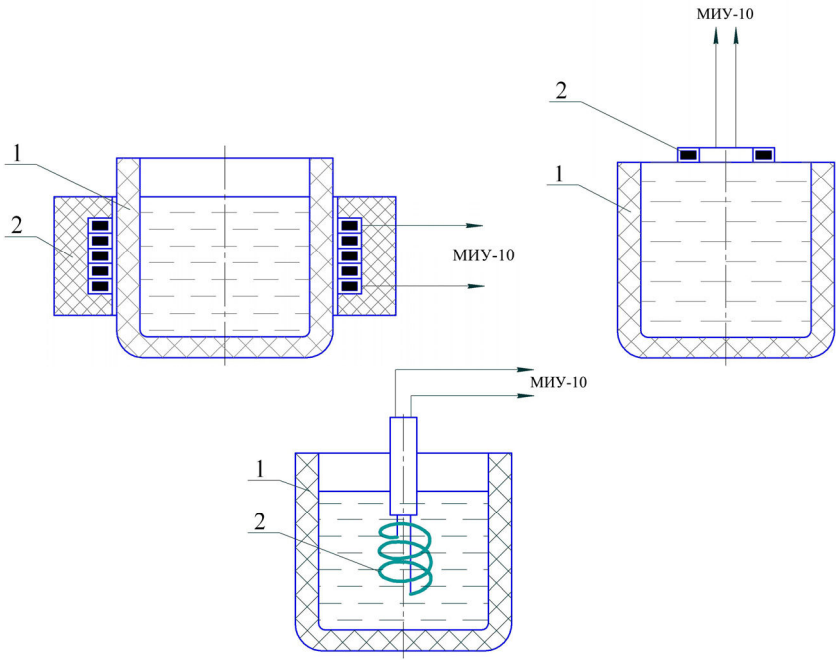

a) b) c)

1 – a crucible; 2 – an inductor.

Figure 5: *Standard technological schemes of pulse-magnetic processing of a metal melt*

The second scheme of pulse-magnetic action on a metal melt (Figure 5b) corrects the fault of the first scheme. The distance between the inductor and the surface of the melt is a minimum providing heat resistance of insulation.

The third scheme (Figure 5c) has the similarity to the scheme of processing a melt by ultrasonic oscillations but with the considerably more intensive action. In this case the following demands are made on an inductor: it must have the reasonable resistance to fire and be made of a chemically neutral material relative to the melt. Such scheme makes it possible to process the melt over all volume or in individual zones. For the directional action inductors can be placed asymmetrically, at an inclination; several inductors can be used in accordance with the set task.

4 Results of Experimental Investigations

The influence of parameters of the action of the high-intensity pulse-magnetic field on physico-mechanical properties of binary silumins was assessed in this exploration work with two first standard technological schemes.

For pulse-magnetic processing by the first scheme, three types of alloys were used which have a silicon content of 1,2%, 6% and 12%. A macro-crystalline stock was used which was produced while crystallizing a melt in the graphite crucible in the sand fill.

The procedure of performance of the experiment consisted in the following. The crucible and a weighed portion of a particular alloy were heated at the crown of the furnace up to 200 ºC after which they were charged into the smelting resistance furnace. Temperature in the furnace was maintained constant, 780 ºC. At the specific temperature the melt was removed from the furnace and was located in the heat chamber with a multi-turn inductor. The chamber was covered by a cap with a thermocouple built-in.

As soon as the temperature of the melt reached a prescribed value, pulse-magnetic processing was performed at different energies of 1,14…4,56 kJ according with the first technological scheme. Parameters of processing are given in Table 1. After processing by the PMF the melt was poured into the chill mold heated to 250 ºC to produce separately founded samples. Then the feedhead was removed from the samples and the samples were tested on a tensile testing machine.

Composition of an alloy	Parameters of pulse-magnetic processing (PMP)		
	Temperature of PMP, ºC	Energy of discharge of the pulse-magnetic installation, kJ	Temperature of pouring to the chill mold, ºC
Al+1,2%Si	740	1,14÷4,56	720
Al+6%Si	730	1,14÷4,56	720
Al+11,7%Si	670	1,14÷4,56	660

Table 1: *Parameters of processing of melts by the pulse-magnetic field*

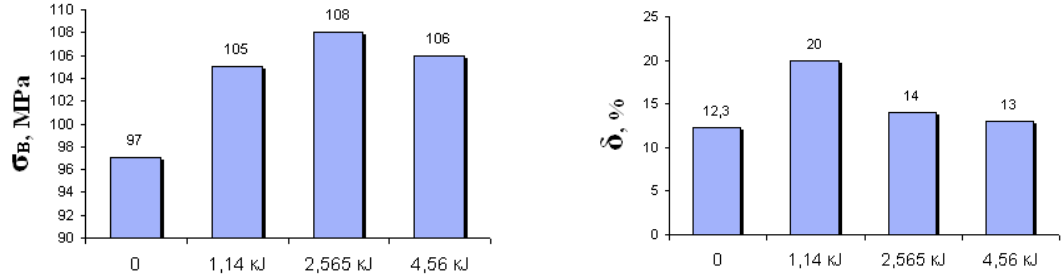

a) Influence of parameters of PMP on mechanical properties of the alloy Al+1,2%Si.

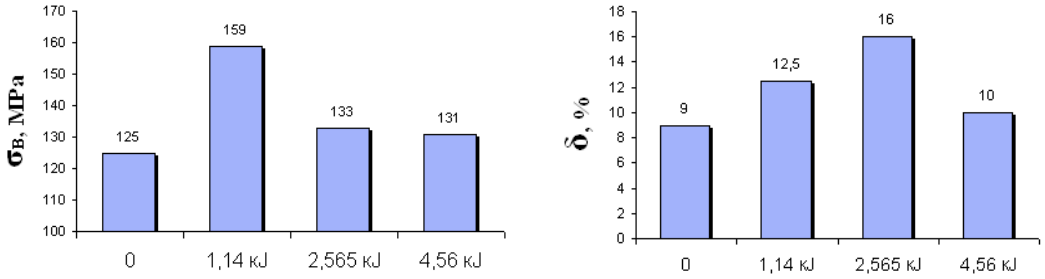

в) Influence of parameters of PMP on mechanical properties of the alloy Al+6%Si.

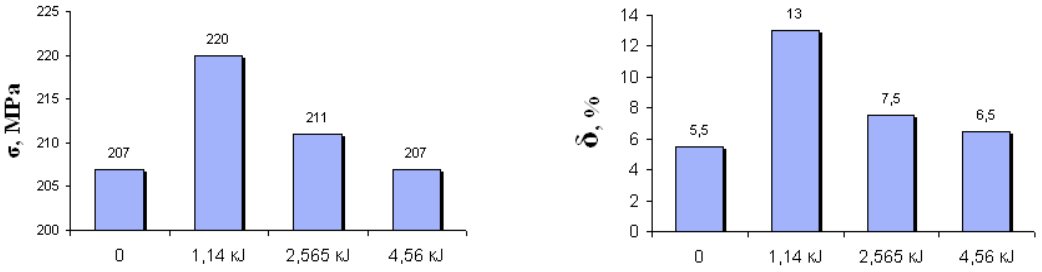

c) Influence of parameters of PMP on mechanical properties of the alloy Al+11,7%Si.

Figure 6: *Influence of parameters of PMP on mechanical properties of binary silumins*

The results of mechanical tests of alloys depending on regimes of PMP are presented in Figure 6.

As the result of the exploration experimental investigations the following conclusions may be deduced.

1. The positive influence of PMP on mechanical properties of binary silumins was determined.
2. Depending on a silicone content and parameters of PMP, a maximum in increase of mechanical properties comprised (Table 2):

Al+1,2%Si	(2,565 kJ)	σ_B	11%
	(1,14 kJ)	δ	62%;
Al+6%Si	(1,14 kJ)	σ_B	27%
	(2,565 kJ)	δ	78%;
Al+11,7%Si	(1,14 kJ)	σ_B	6%
	(1,14 kJ)	δ	by the factor 2,4.

Table 2: *Maximum in increase of mechanical properties comprised depending on a silicone content and parameters of PMP*

For PMP by the second standard scheme the alloy АК9ч of Al-Si system was chosen as the subject of investigation.

For the study and control over physical processes taking place during the pulse action, the procedures of experimental investigations of parameters of a process were developed. Among such parameters are:

- the value and distribution of temperature fields with height of the cast;
- the value of the pressure pulse passed through the LCM;
- the value and distribution of pressure of the PMF in the system “inductor – LCM’s surface”;
- values of currents being induced in the LCM; and others.

It should be noted also that a peculiarity of the process of the pulse action is its fast progression and singleness. In this connection added demands are imposed upon the procedures being developed, main of which is the interrelation of temperature, energetic, force parameters of the process of crystallizing a metal and parameters of the magnetic field acting on it.

Figure 7 presents a scheme of action of the PMF on a melt and arrangement of thermo-electric transducers and pressure sensors.

It is possible to acquire a familiarity in more detail with the description of procedures of experimental investigations of parameters of action of the PMF on a LCM, with the results of these experimental investigations as well as with technique of the experiment in the work [2].

Analyzing the results of mechanical tests of check samples and samples processed by the PMF it is possible to note the following: maximum values of ultimate strength (σ_B) and specific elongation (δ) were reached at the energy of discharge W=2,565 kJ and a number of pulses n=3, increment of properties is 20% for σ_B and 56% – for δ. Moreover pulse-magnetic processing of the melt reduced porosity of casts from 2-3 down to 1-2 point, aided to equalization of content of key components (Si, Mg) through the height of a

cast and, at the same time, to their movement to the upper zones. Nature of distribution of heavier components (Fe, Mn) is reverse, enriching of the lower zones.

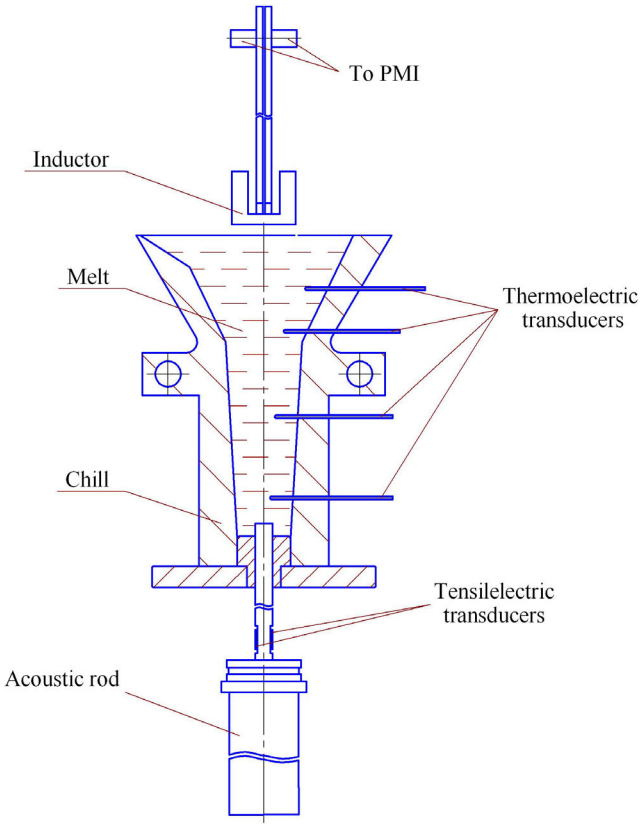

Figure 7: *Scheme of action of the PMF on a metal melt*

Such high efficiency of pulse-magnetic processing of cast metal made it possible to determine the areas of possible application of this type of force and heat action in different technologies of mechanical engineering (Figure 8).

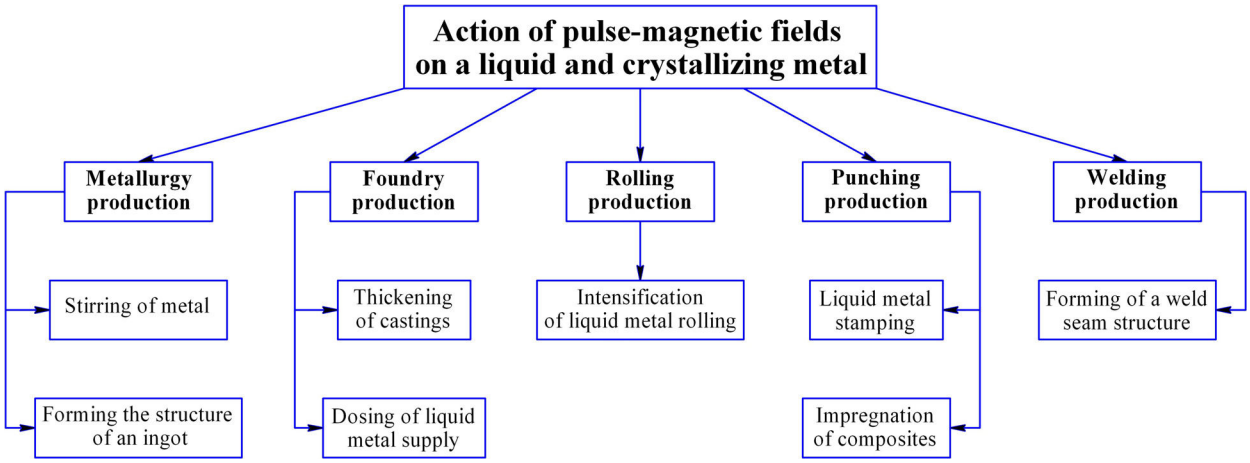

Figure 8: *Application of pulse-magnetic processing in different technologies of mechanical engineering*

5 Conclusion

The present project is supported by the Russian Fund of Fundamental Research. Authors see the subject-matter under discussion as a promising direction and consider that it is necessary to continue more system and in-depth investigations.

References

[1] *Getselev, Z.N.; Balahontsev, G.A.; Kvasov, F.I.; Cherepok, G.V.; Varga, I.I.; Martynov, G.I.:* Uninterrupted cast to an electromagnetic crystallizer. M.: Metallurgy, 1983, p.152.

[2] *Glouschenkov, V.A.; Igolkin, A.Ju.; Chernikov, D.G.; Nikitin, V.I.; Vyalov, B.V.:* Multi-phase and multi-component materials under dynamic loading. 10th European Mechanics of Materials Conference (EMMC10), 2007

Electromagnetic Pulse Forming of Carbon Steel Sheet Metal

R. Andersson, M. Syk

Swedish Tool & Die Technology, Luleå, Sweden

Abstract

Electromagnetic pulse forming is a promising direct method for a high speed sheet metal forming of materials with high conductivity, like Al- and Cu-alloys. For metallic sheet with low conductivity, like carbon steel sheets, the frequency of the current through the forming coil must increase to create the same forming properties as for materials with high conductivity. Usually this frequency is not easy to change in an existing electromagnetic pulse system without exchanging of the capacitors.

Anyway, this project have analysed the formability of two high strength steel sheet material, a carbon steel DP60 and a austenitic stainless steels, with and without a copper driver. The experiments were made on commercial electromagnetic pulse system from Poynting with a predefined current frequency through the forming coil.

The geometries that were used for the electromagnetic pulse forming analysis were a cone, rectangular parts, and spherical dome. All physical parts were 3D digitised and the deviation were analysed against nominal reference objects.

The spherical dome experiment was used to analyse the increase in formability of the high strength steel sheets compared with conventional stamping in an Erichsén sheet metal testing machine.

Keywords

Steel sheet formability, Geometrical deviation, 3D analysis

1 Introduction

This project deals with high velocity deformation of steel metallic materials using electromagnetic pulse as driving mechanism for the forming force. Electromagnetic pulse forming is a high velocity process where a coil creates a magnetic field which repels the sheet material and pushes it down to a die. The most important parameters that influence the process are: energy level, induced current, electrical conductivity and the mechanical properties of the sheet material and the geometry. This means to get a successful

electromagnetic pulse forming process is that the current will flow as close as possible to the surface of the material to be deformed. The higher the electrical conductivity in the sheet material the less is the induced current thickness. This is easily described by the magnetic skin depth as a function of frequency, which is mathematically described by

$$\Delta = \sqrt{\frac{\rho}{\pi f \mu}} \tag{1}$$

where *f* is the frequency, ρ is the resistivity of the sheet material and μ is the absolute magnetic permeability of the metallic sheet [1]. To achieve a good forming process the magnetic skin depth should not become larger then the sheet metal thickness. Equation 1 shows clearly that the frequency is a very important parameter to create a successful electromagnetic pulse process. The frequency of an electromagnetic pulse system comes mainly from the type and the amount of capacitors. Equation 1 shows also that different type of metallic sheet materials get different values of the magnetic skin depth at same frequency due to differences in resistivity. Some metallic materials resistivity is found in table 1 below.

Material	Conductivity		Resistivity
	[10^6 Siemens/m]	[% IACS]	[10^{-9} ohm-m]
Silver (pure)	62,87	108,40	15,91
Copper (pure)	60,09	103,60	16,64
Gold (pure)	40,60	70,00	24,63
Aluminium (99.99%)	37,67	64,94	26,55
Aluminium 6062-T6	27,32	44,70-49,50	36,61
Aluminium 6062-T4	25,38	43,50-44,00	39,41
Magnesium (pure)	22,39	38,60	44,67
Iron (Casted 99.9%)	9,048	15,60	110,5
Magnesium (Casted)	8,70	15,00	114,9
Steel (Casted)	6,21	10,70	161,1
Steel (High-alloyed)	1,68	2,90	594,5
Stainless Steel 316	1,33	2,30	749,6
Titanium (6AL-4V)	0,58	1,00	1724

***Table 1**: Conductivity and resistivity for some metallic materials [2]*

Table 1 shows together with equation 1 that for specific system with prescribed frequency the magnetic skin depth will be much higher for materials with high resistivity. This means that materials like steel and stainless steels become more difficult to achieve with low frequency system. One way to overcome this problem is to use a foil of low resistive material on top of the steel sheet material and that foil will act as a driver to push the steel sheet into the die cavity.

This paper will investigate the electromagnetic forming process of steel metallic sheets with and without a driver material. The objective will be to analyse the difference of

the formability with or without driver, the deviation and springback from the nominal geometry and also the increase in formability.

2 Material and Experiments

2.1 Sheet Metallic Materials

The materials used in this study are one austenitic stainless steel and one high-strength carbon steel, both in the as-received condition. The thickness and strength levels are tabulated in table 2.

Grade	Thickness (mm)	Rp02 (MPa)	UTS (MPa)
Stainless Steel EN1.4401	0.25	319	635
Carbon Steel DP600	0.7	432	640

Table 2: The sheet materials in this study

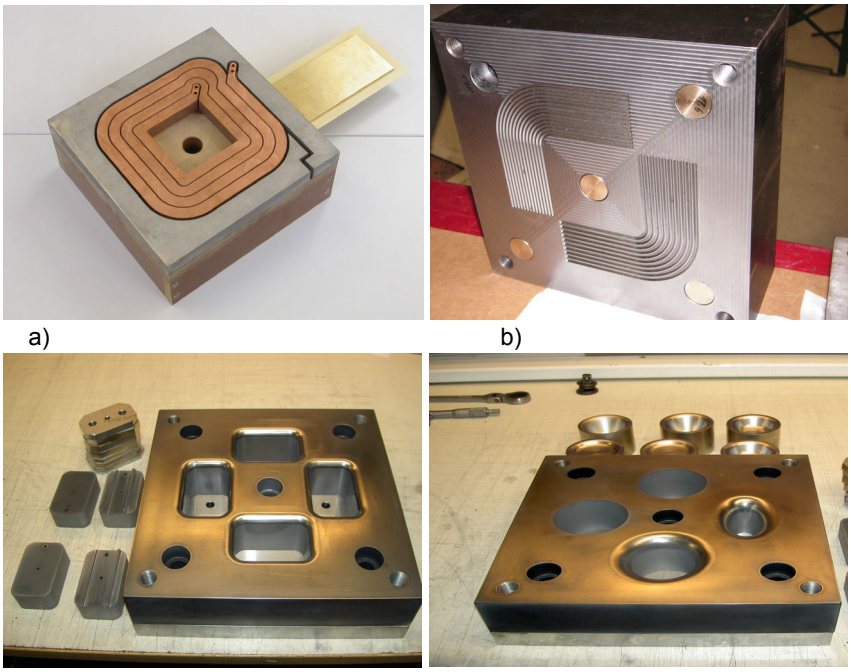

***Figure 1**: a) shows the coil b) the die with a specific pattern c) the die with rectangular inserts and d) the die with oval and round inserts.*

2.2 Coil and Dies

The electromagnetic coil that was used for the experiments were designed in collaboration with the company Poynting [3], Dortmund, Germany. The design was made so a homogenous pressure should occur on the sheet metal during the electromagnetic pulse forming process. Three dies were used in this study. Two of the dies had exchangeable inserts, one with inserts for conical parts and hemispherical domes and the other for

rectangular parts. The third die was designed to analyse a forming process to create a surface pattern of a sheet metal similar to what can be found on heat-exchanger or bipolar plates. The electromagnetic coil and dies is shown in figure 1.

2.3 Electromagnetic Pulse Experiments

All electromagnetic pulse forming experiments were done at a Magnaform Maxwell 60kJ system located at Poynting. The technical data of the system is found in table 3.

Characteristics	
Max charging energy E	60 kJ
Max Charging voltage U	8.3 kV
Capacitance C	1742 µF
Max permitted current	1800 kA
Short circuit frequency	25-29 kHz

Table 3*: shows the characteristics of the electromagnetic pulse system Magnaform Maxwell 60kJ that was used in this study.*

To improve the efficiency of the electromagnetic pulse forming process for sheet metal material with low conductivity is to use a high conductivity foil between coil and sheet metal. This foil will then act as pressure device on the sheet metal during the electromagnetic pulse process. This trick improves the formability process of low conductivity materials.

The first experiments was to make a comparison study of the difference of forming process of the carbon steel DP600 with and without a copper foil as a driver. The energy level and current-trace curves for this experiment are found in appendix 1.

The second experiment was to compare the improvement of formability for DP600 in equivalent biaxial tension between electromagnetic pulse process and conventional Erichsen test. The energy level and current-trace curves for this experiment are found in appendix 1.

The third experiment was to analyse the geometrical deviation and springback after the electromagnetic forming process of the stainless steel grade with copper foil as a driver. The energy level and current-trace curves for this experiment are found in appendix 1.

2.4 Erichsen Sheet Metal Forming Test

Quadratic samples of 250x250 mm width were stretched with a loading path of equivalent biaxial tension over a hemispherical punch with a diameter of 50.8mm until fracture occur in an Erichsen 40 tonne hydraulic press [4]. For the subsequent strain analysis all sheet metal specimens were electrochemical etched with a square pattern of 2x2 mm.

3 Analysis and Results

3.1 Analyse of Experiment Nr 1

The first experiments were to make a comparison study of the difference of forming process of the carbon steel DP600 with and without a copper foil as a driver. The foil had a thickness of 0.6 mm. After the electromagnetic forming processes of the two deformed blanks they become digitised by 3D scanning with an ATOS III system from GOM [6]. Subsequently a best fit algorithm has been used to compare the 3D deviation between the deformed sheets and 2D cuts have been used to make a detailed comparison. The cut position and the comparison are shown in figure 2-5.

Figure 3-5 show the major impact a copper driver has on the formability of high strength steel sheets with the current-trace curve that is described in appendix a1. The conclusion is: to improve the sheet metal forming performance without using a copper foil as a driver a high frequency electromagnetic pulse system must be used. This conclusion can also be drawn from the description of equation 1.

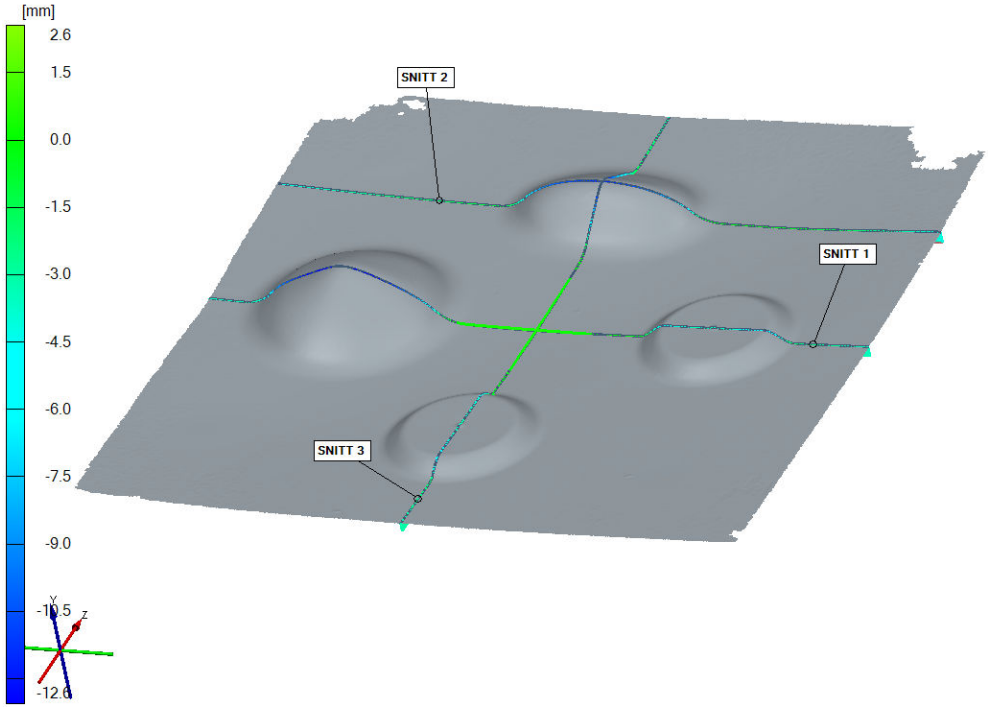

***Figure 2** shows the three 2D cuts for the comparison study.*

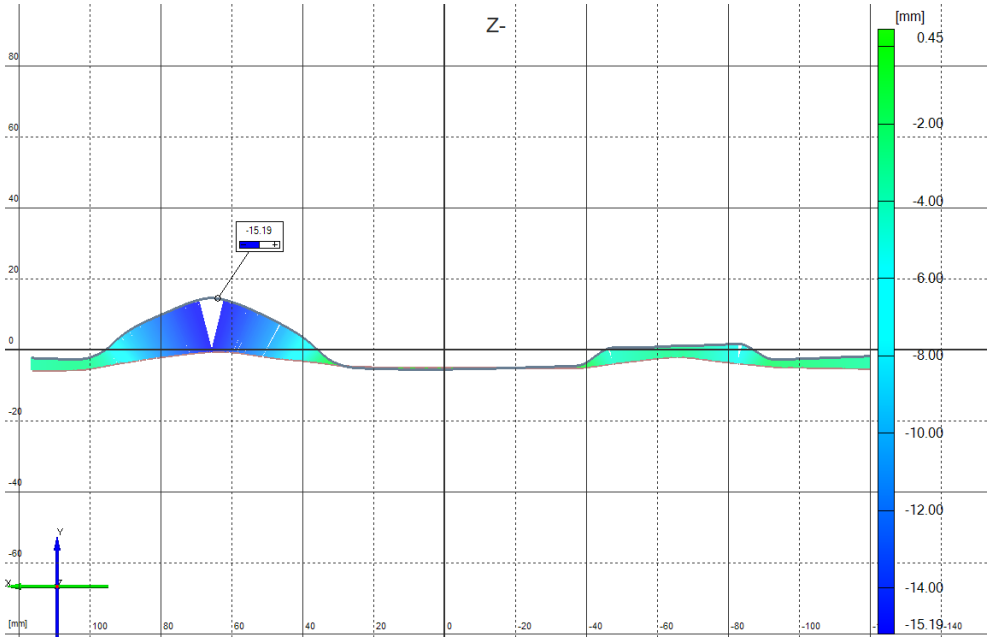

Figure 3 *shows the deviation between the shape of DP600 with and without copper driver at cross-cut 1.*

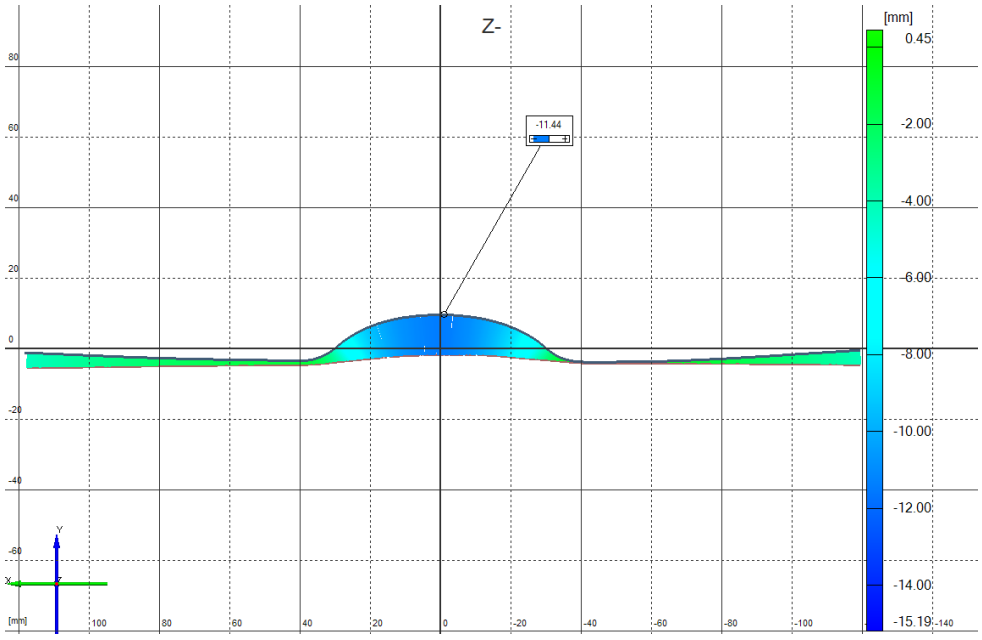

Figure 4 *shows the deviation between the shape of DP600 with and without copper driver at cross-cut 2.*

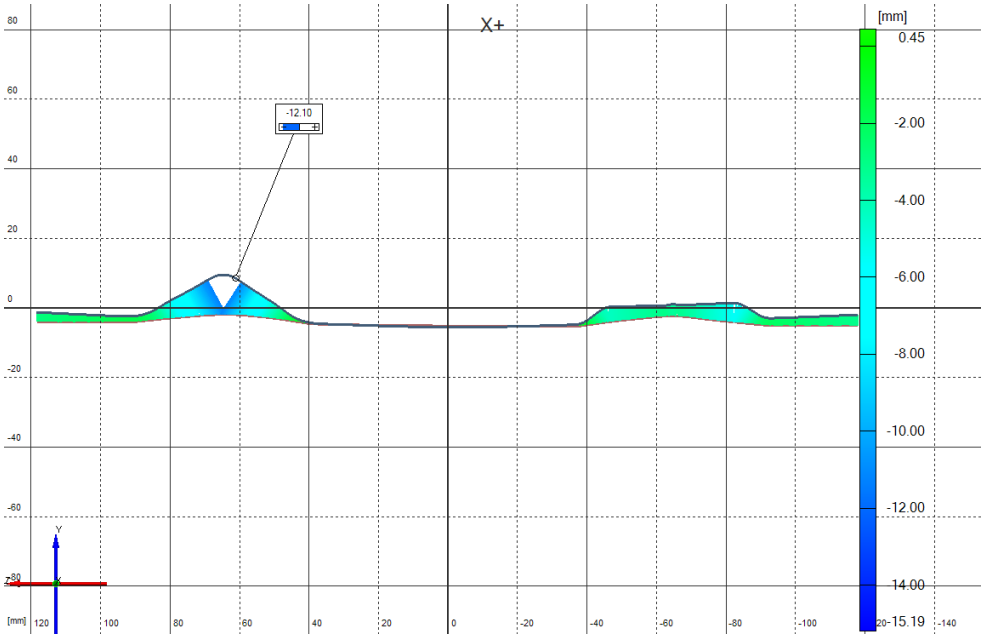

Figure 5 *shows the deviation between the shape of DP600 with and without copper driver at cross-cut 3.*

3.2 Analyse of Experiment Nr 2

The second experiment was to compare the improvement of formability for DP600 in equivalent biaxial tension between electromagnetic pulse process and conventional Erichsen test. For the electromagnetic pulse experiment a copper foil with thickness of 0.6 was used as a driver. All specimens were stretched to fracture or close to fracture and three samples for each test method were used to get a statistical security of the result. The strain field of the sheet metal specimen formed with the two methods is shown in figure 6 and the location in a forming limit diagram is shown in figure 7.

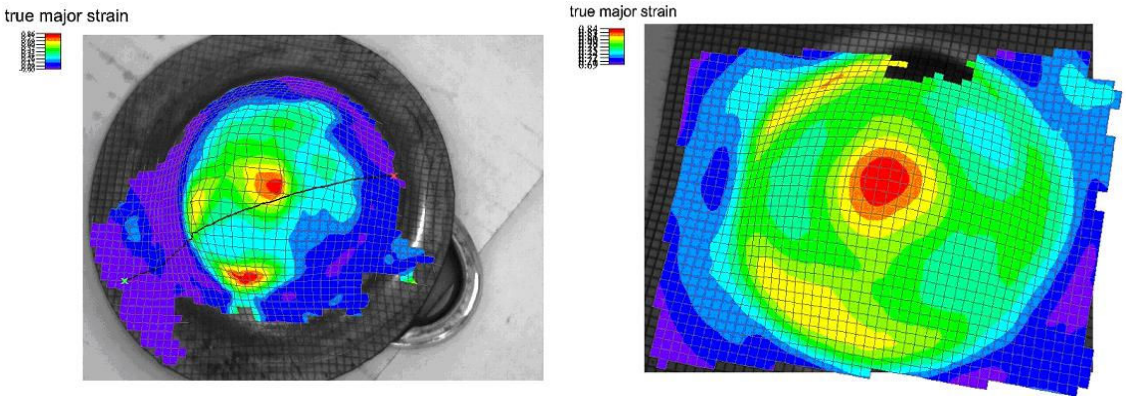

a) b)

Figure 6 *shows the strain field over the equivalent biaxial tension specimen made by a) the Erichsen test and b) electromagnetic pulse.*

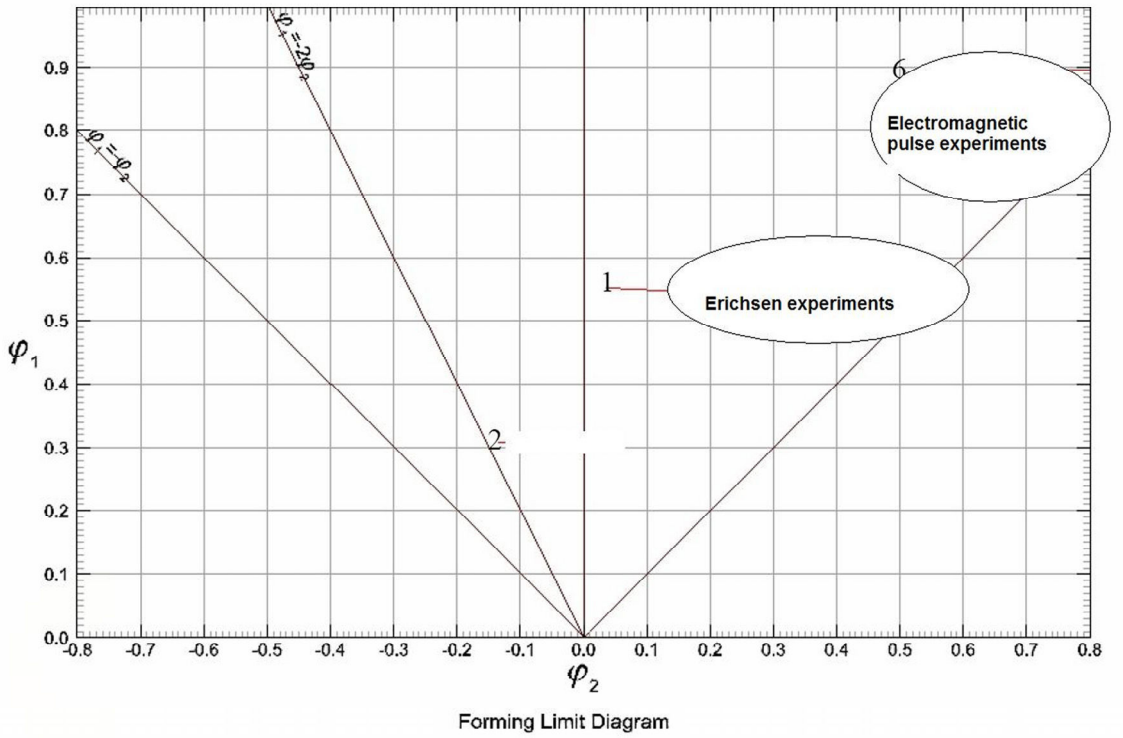

Figure 7 *shows the strain region at fracture either through conventional Erichsen sheet metal testing or through electromagnetic pulse forming.*

Figure 6 and 7 show that we can get an increase in formability with more then 50% of high strength steel sheets if a copper driver is used compared to standard formability tests with a hydraulic press.

3.3 Analyse of Experiment Nr 3

The third experiment was to analyse the geometrical deviation and springback after the electromagnetic forming process of a sheet metal of stainless steel with thickness of 0.25 mm together with a copper foil with thickness of 0.1 mm, which acts as a driver. The final formed part were digitised by 3D scanning with an ATOS III system from GOM [6] and the comparison were made against the nominal CAD data. The result is shown in figure 8.

Figure 8 shows that the springback and geometrical deviation is very low. One reason for this minimal geometrical deviation after electromagnetic pulse forming is that the sheet metal hit the die surface with really high speed and this causes a plastic deformation through the sheet thickness which minimise the tendency for springback.

There has also been experimental test with thicker stainless steel sheets together with thicker copper foil as driver and the tendency is similar i.e. minimum springback tendency. Increase in thickness demands of course higher energy levels from the electromagnetic pulse system.

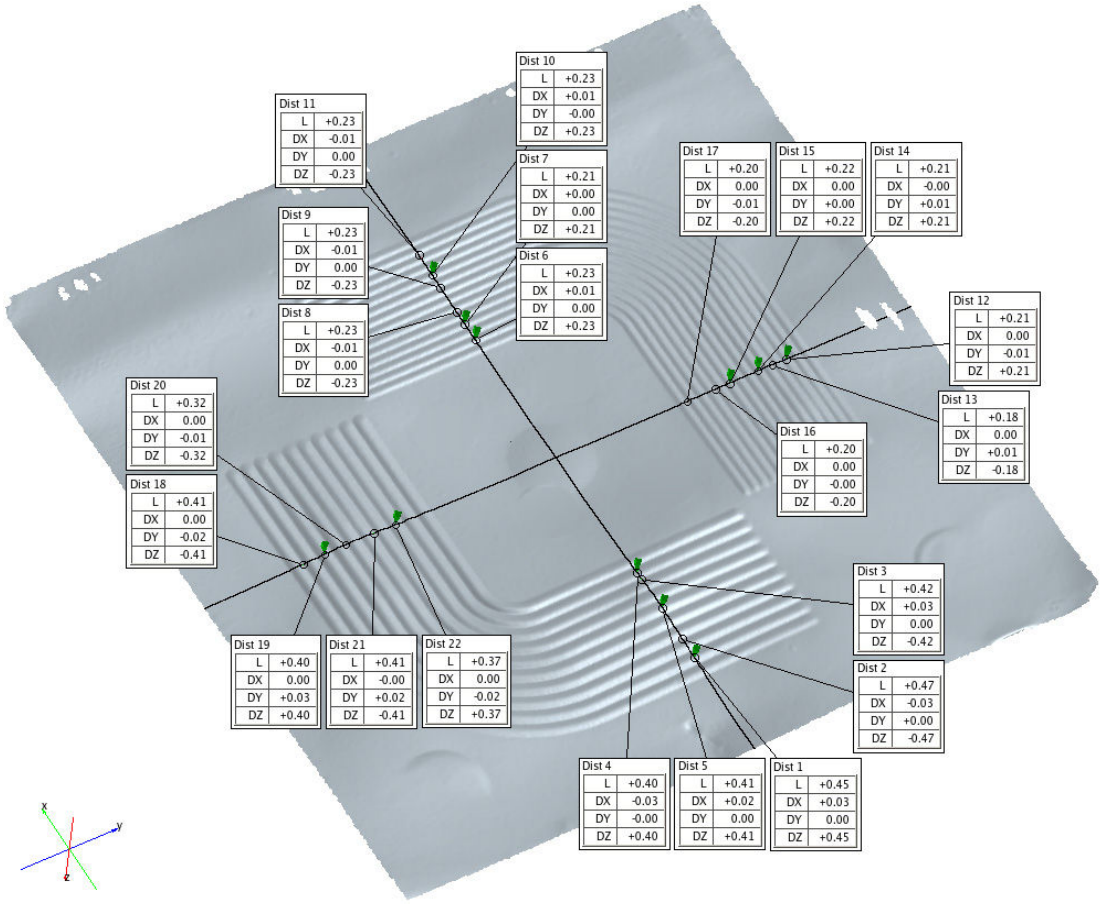

Figure 8 *shows the deviation of the electromagnetic pulse formed part and the nominal geometry.*

4 Conclusion

The major conclusion from this study are that electromagnetic pulse forming of steel sheets without using any high conductive material that acting as a pressure device must be done on a high-frequency electromagnetic pulse system. The reason for this can be found in equation 1 and table 1, which shows if the resistivity of the sheet material is increasing then an increase in frequency is needed to get an efficient process.

If it should be possible to develop and manufacture a electromagnetic pulse system that have same performance as for low resistivity material i.e. increased system frequency then we see from the experiments 2 and 3 in this study that we could achieve both an increase in formability of high strength steel sheet materials as well as a decrease in springback.

References

[1] *Hayt W. H.:* Engineering Electromagnetics Seventh Edition,(2006), McGraw Hill, New York ISBN 0-07-310463-9
[2] *Syk, M:* Electromagnetic Pulse Processes – A literature survey (2004), Svensk Verktygsteknik
[3] www.poynting.de (2008-01-25)
[4] www.erichsen.de (2008-01-25)
[5] www.autogrid.de (2008-01-25)
[6] www.gom.com (2008-01-25)

Appendix A Energy Levels and Current Trace Curves

A.1 Experiment Nr 1

The energy level was 14 kJ and the current trace curve is shown in figure 9.

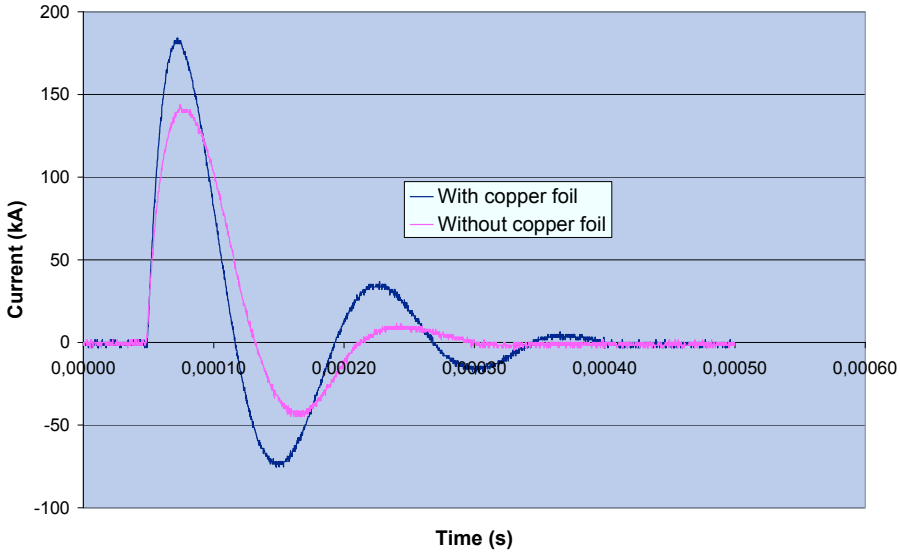

Figure 9 *shows the current-trace curve for experiment 1.*

A.2 Experiment Nr 2

The energy level was 14 kJ and the current trace curve is shown in figure 10.

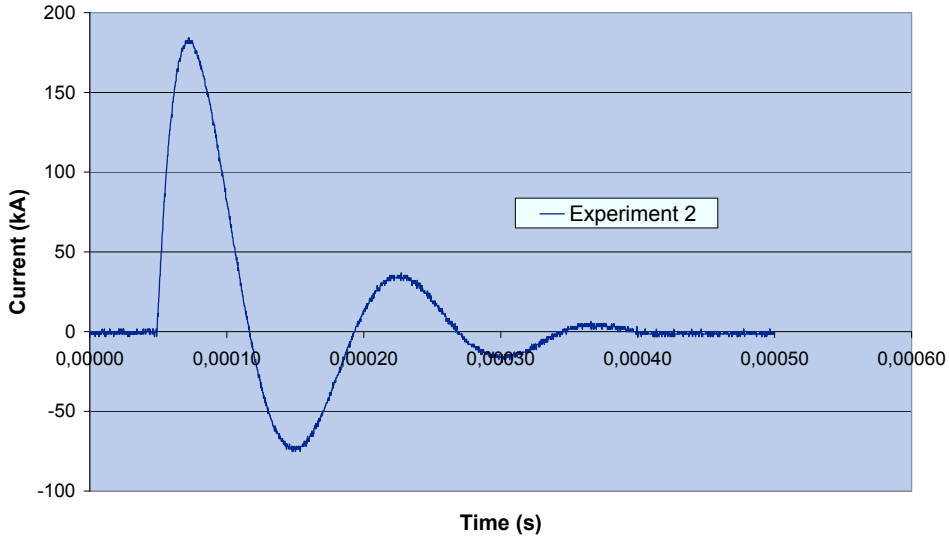

Figure 10 *shows the current – trace curve for experiment 2*

A.3 Experiment Nr 3

The energy level was 3 kJ and the current trace curve is shown in figure 11.

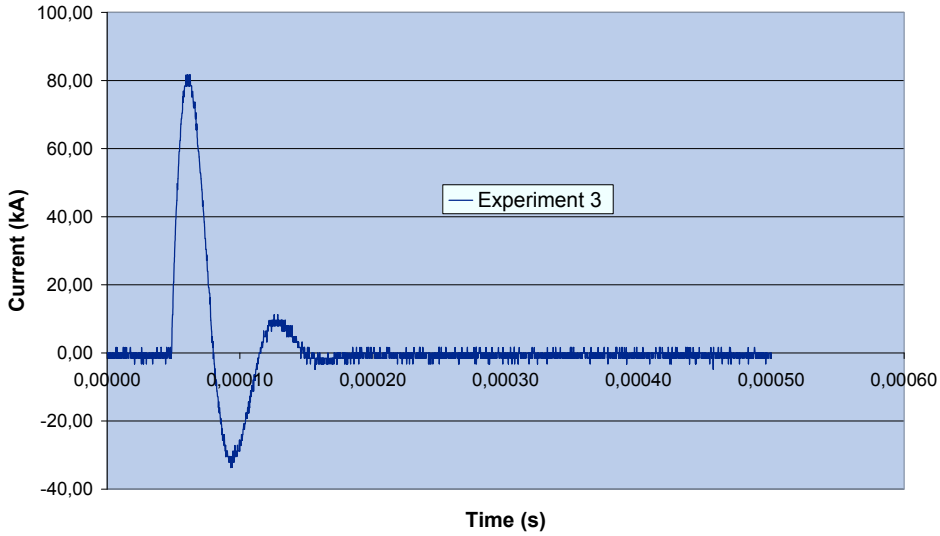

Figure 11 *shows the current – trace curve for experiment 3*

Influence of Mandrel's Surface on the Mechanical Properties of Joints Produced by Electromagnetic Compression*

T. Hammers[1], M. Marré[3], J. Rautenberg[4], P. Barreiro[2], V. Schulze[1], D. Löhe[1], A. Brosius[3] and A. E. Tekkaya[3]

[1]Institute of Materials Science and Engineering I, Universität Karlsruhe (TH), Kaiserstr. 12, Karlsruhe 76131, Germany
[2]now: EnBW Kraftwerke AG, Kernkraftwerk Philippsburg, Philippsburg 76652, Germany
[3]Institute of Forming Technology and Lightweight Construction, Technische Universität Dortmund, Baroper Str. 301, Dortmund 44227, Germany
[4]Institute of Machining Technology, Technische Universität Dortmund, Baroper Str. 301, Dortmund 44227, Germany

Abstract

Electromagnetic compression of tubular profiles with high electrical conductivity is an innovative joining process for the manufacturing of lightweight structures. Taking conventional interference fits into account, the contact area's influence on the joint's quality seems to be of significance, as e.g. the contact area and the friction coefficient between the joining partners determine an allowed axial load or torsional momentum proportionally. Therefore, different contact area surfaces were prepared by shot peening and different machining operations and strategies. The mandrel's surfaces were prepared by shot peening with glass beads and Al_2O_3 particles. Alternatively, preparation was done using simultaneous five axis milling, because potential joining partners in lightweight frame structures within the Transregional Collaborative Research Centre SFB/TR10 would be manufactured similarly. After that, the manufactured surfaces were characterized by measuring the surface roughness and using confocal whitelight microscopy. After joining by electromagnetic compression, the influence of different mandrel's surface conditions on the joint's mechanical properties were analyzed by tensile tests. Finally, conclusions and design rules for the manufacturing of joints by electromagnetic compression are given.

Keywords

Electromagnetic compression, Joining, Shot peening, Milling

---

* *This paper is based on investigations of the Transregional Collaborative Research Centre SFB/TR10, which is kindly supported by the German Research Foundation (DFG)*

1 Introduction

One major objective of the Collaborative Research Center SFB/TR10 is the flexible and competitive production of frame structures, which fulfill the condition of lightweight constructions as structural parts, cabins or chassis frames. To achieve this common aim, the application of innovative joining technologies as well as joining strategies are necessary. Joining by electromagnetic forming (EMF) as a cold joining process is an attractive alternative solution compared to conventional welding or riveting processes [1]. Targeting the introduction of joining by electromagnetic compression into a manufacturing process chain, the joining process, pre-stages, and post-stages of production have to be taken into account. For example, previously raw or semifinished parts can be used after manufacturing as connecting elements (nodes) in order to assemble tubes to frame structures. They are mandatorily machined before joining by e.g. milling processes. As the shape of the nodes is usually very complex, the machining procedures may be done by simultaneous five-axis milling. The milling of lightweight aluminum nodes and the preparation of areas for joining described require adequate milling strategies in order to be efficient and to manufacture a high quality product. Moreover, the quality of the surface layer results from the chosen milling strategy and its parameters, taking e.g. cutting tools, cutting rate and feed rate into account. In turn, the resulting surface characteristics influence the mechanical properties of the joint as known from manufacturing conventional interference fits. Consequently, the influences of the surface on the mechanical properties of joints manufactured by electromagnetic compression were investigated, characterizing the surface by the average surface roughness and by scanning electron microscope (SEM).

2 Joining by Electromagnetic Compression

As the energy density of a pulsed magnetic field is used for the contact-less forming of a workpiece, the resulting deformation is closely related to the electromagnetic properties. The process model (Figure 2) can be described as an oscillating circuit which includes the capacitor *C*, the resistance *R*, and the inductance *L* of the pulse generator as well as the consumer load consisting of tool coil (solenoid) and workpiece (tube). After the capacitor bank has been charged it is suddenly discharged by the closing of a high current switch. As a result, a damped oscillating current flows through the coil, generating a corresponding magnetic field. According to Lenz's law, a current in the workpiece is induced flowing in the opposite direction to its cause. Due to the skin effect, the current and the magnetic field penetrate the workpiece wall in the course of the process progresses. The resulting pressure pulse acts orthogonally on both the field strength and the induced current, i.e. in a radial direction on tube and tool coil, as shown in Figure 2 [2].

In contrast to quasi-static forming procedures the pressure pulse in EMF causes high strain rate effects in the formed material [4]. The resulting magnetic pressure *p(t,r,z)* is determined by the energy density of the magnetic field outside H_a and inside H_i of the workpiece and can be calculated on the basis of the measured coil current as described in detail in [2].

$$p(t,r,z) = \frac{1}{2} \cdot \mu_0 \cdot \left(H_a^2(t,r,z) - H_i^2(t,r,z) \right) \quad (1)$$

If the yield strength of the tube is exceeded, a permanent reduction of diameter occurs.

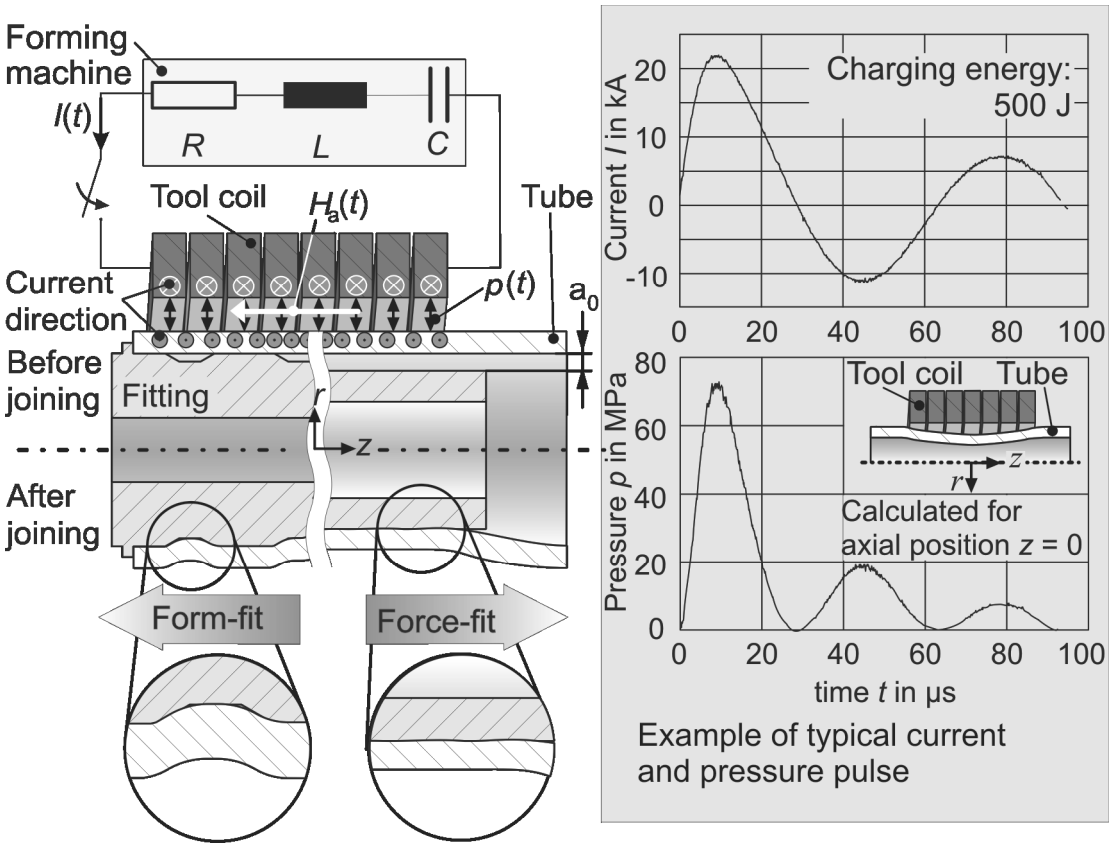

***Figure 1**: Process principle of joining by electromagnetic compression with a directly acting tool coil*

At the same time as electromagnetic compression can be used for forming, joining operations are feasible as well. In general, joints produced by electromagnetic tube compression can transmit forces by dominating force-fit or dominating form-fit. Moreover, if a very high specific energy is supplied a so called magnetic pulse welded connection can be produced as well [4,5].

As described in detail in [6], the constriction velocity of a tube being compressed as well as its mass determines the kinetic energy at the moment of impact and therefore the force which acts on the mandrel. Assuming a massive mandrel, during this deformation process the tube is deformed plastically and the mandrel's deformation remains purely elastic. During the decrease of the forces, a corresponding elastic relaxation of mandrel and tube occurs. If a full relaxation of the mandrel is prevented by the tube, a permanent pressure in the joining area (in the radial direction) is established [7]. This pressure is a balanced condition on the one hand of the mandrel's stress relief, and on the other hand the resulting interference fit (caused by the elastic recovery of the mandrel) in the tube. The strength of interference fits manufactured so far strongly depends on the area of the contact zone, the friction coefficient, and the remaining residual stresses in the contact zone. The last depend on material parameters like yield point and Young's modulus [8] as well as on the geometrical stiffness of the parts to be joined [9]. In Figure 4, the influence of the compression velocity (determined by the charging energy) on the strength of the joints is presented.

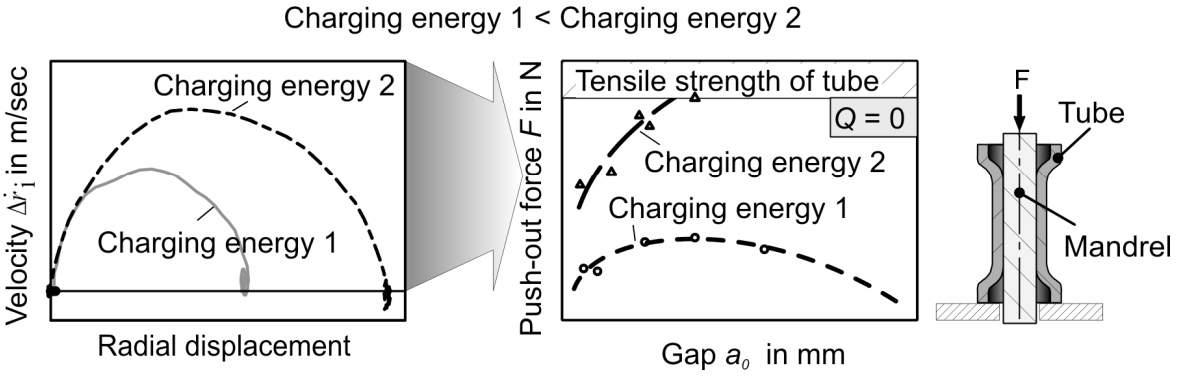

***Figure 2**: Principle of joining by electromagnetic compression*

3 Manufacturing and Testing of Joints

3.1 Preparation of Joining Partners

The material of both tube and mandrel was made of AA6060. The outer diameter of the tube was 20 mm with a wall thickness of 1 mm. The gap between tube and mandrel was 1.2 mm. Since the influence of the mandrel's surface on the mechanical properties of joints was intended to be analyzed, the mandrel's topography was first modified by shot peening or by milling. Then, the specimens were joined with tubes by electromagnetic compression.

The preparation of surfaces for electromagnetic forming was done by five-axis CNC machining on a Deckel-Maho milling machine (DMU 50 Evolution). This multi-axis machining set-up was chosen to provide a flexible possibility for an efficient process of manufacturing lightweight components and to fulfill the requirements of geometric accuracy and a high surface quality. The main importance was to create a reproducible roughness in a flexible finishing process. The NC-data were generated by a common CAM-system as used for the manufacturing of complex parts like dies and moulds. During these surface finishing processes, high process forces as they occur in the machining of hard and hardened materials [10] were not expected, so that a deformation of the specimen could be excluded. Although the mandrels could have been turned, milling finishing strategies were chosen because they are necessary to be integrated within the manufacturing process chain of a node with several extends for adapting. Figure 3 shows the principle of milling a surface. There are two different basic ways of structuring a surface of a joining zone. The macro-structure allows the profile to fit into the structured areas of a mandrel or a node, to increase the strength of the connection. The micro-structure/surface roughness is important for a grouting between the inner and the outer part. Although the transition between both types of surface characteristics is smooth, a measurable surface roughness (e.g. smaller than 50 µm) and a structure which can have the form of a groove or a pocket and a visible depth (e.g. greater than 0.05 mm), can be distinguished. Both factors have a particular influence on the strength of an electromagnetically joined connection. While the microstructure, according to the influence on the friction and the transferable tangential stress between both joining partners, leads to a more force-fit based connection, macrostructured elements offer a high potential to increase the form-fit. To reduce the complexity of the workpieces for basic research, the

relevant joining part of the node is substituted by a simple mandrel. The use of standard tools is inevitable for a later adaption of a flexible and efficient manufacturing of a complete node. Ball end mills with a diameter of 6 mm with a coating that reduces the adhesive behavior of the ductile aluminum alloy were used to cover a wide range of micro- and macro-structures with process-safe strategies. The main difficulties in a simultaneous machining of the mandrels segment are similar to those in the machining of cavities in dies and moulds [11]. Collisions between the tool or the tool holder and the workpiece need to be avoided and, therefore, the range of angles of inclinations which also depend on the length of the tool and the geometry of the tool holder has to be chosen carefully. Oscillations that can occur due to the length and thinness of the mandrels and the appearing process forces during milling were reduced to a minimum within an area that was not used for the joining process by choosing a minimum length when clamping the mandrel.

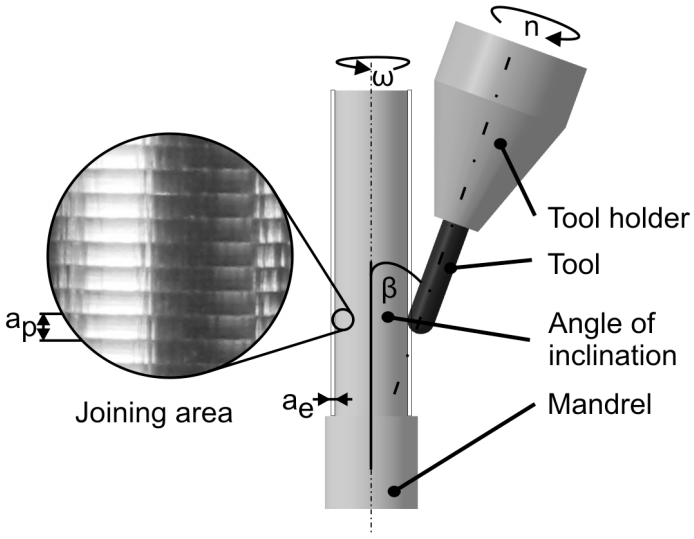

***Figure 3**: Principle of milling the mandrels*

For the alternatively used shot peening process, a micro peening device (IEPCO Peenmatic 770), an Al_2O_3 shot with a mean diameter of 20 - 30 µm (EKR 320 A), and glass beads with a mean diameter of 20 – 30 µm (MS 550 B) were applied. In addition, the shot pressure was varied from 0.5 up to 1.5 bar. A 10 mm distance to the surface as well as a feed of 0.5 mm/s were kept constant [12].

3.2 Joining by Electromagnetic Compression

The forming machine SMU1500 with a maximum charging energy of 1.5 kJ was used for joining by electromagnetic compression. At first, joining was done preliminarily with charging energies of 0.9 kJ, 1.1 kJ and 1.5 kJ, to determine adequate process parameters for force-fit joining. The measured current and the calculated magnetic pressure for the mentioned charging energies are indicated in Figure 4.

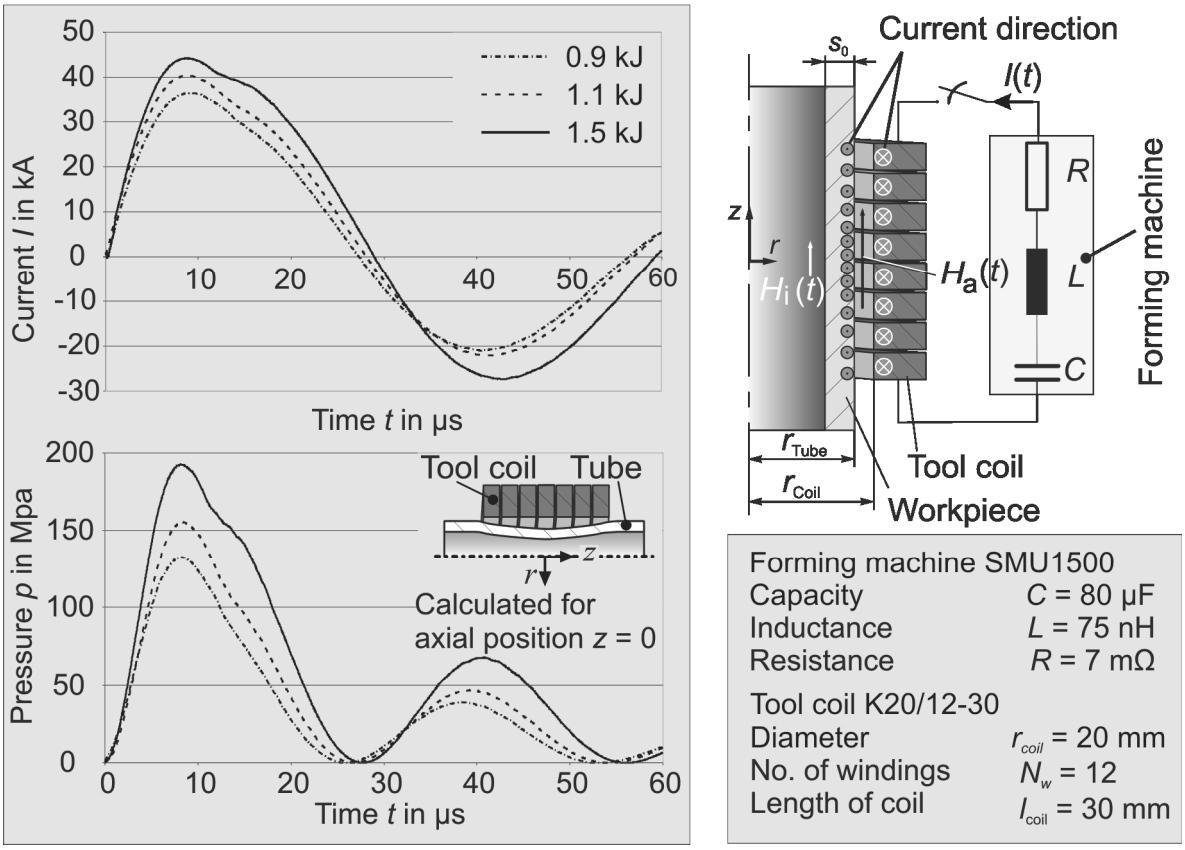

***Figure 4**: Experimental set-up for joining by electromagnetic compression*

The experimental setup for joining was built up of a tool coil and a guiding device with an expandable mandrel for clamping the tube at a top crossbar and a mounting with a corresponding standard fit to the joining partner (mandrel) at a bottom crossbar. The alignment of toolcoil to the specimens is provided by gimbal-mounting the guiding device to the machine.

3.3 Characterization of Joining Partners and Joint

In order to analyze the influence of the mandrel's surface on the mechanical properties of the joint, the initially turned surface was altered by shot peening or milling. The strength of the joints was determined by tensile tests using a universal tensile testing machine Zwick 1478 with a maximum force of 100 kN. The crosshead velocity during tensile testing was adjusted to 2 mm/min. The quantities measured were force and strain, in both axial and tangential direction in the joining area, using strain gauges. In addition, light optical microscope and scanning electron microscope (SEM) investigations were done to characterize the interface between tubes and mandrels after shot peening or milling and before joining.

4 Experimental Results

4.1 Surface Characterization before Joining

Fig. 5 shows the average surface roughness as a function of the shot pressure for both shot media. The mandrel's roughness is strongly increased by peening at small shot pressure already. Beyond 0.5 bar the influence of shot pressure on the surface roughness is rather small. This behavior can be observed for both shot media.

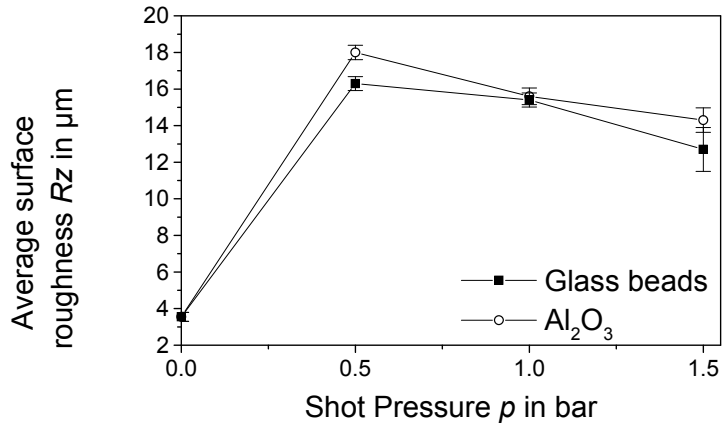

***Figure 5**: Average surface roughness depending on shot peening pressure and media*

The milling process parameters were chosen according to the findings of several experiments about manufacturing surfaces for products made of AA6060. A helical tool path along the mandrel was chosen in order to avoid marks that appear in strategies that work with a constant z-level movement of the tool. Moreover, this strategy is more time efficient and guarantees a more constant surface quality, because infeed movements and toolpaths without cutting are reduced to a minimum. The milling process was done without any lubrication, which is more ecological, but increases the risk of adhesive aluminum being stuck within the small chip flutes of the tool. Figure 6 shows four sets of milling parameters exemplarily chosen and the resulting average surface roughnesses in comparison to the theoretically feasible values. The determining factor for the theoretical surface roughness is the line width or axial depth of cut (a_p) of the process. The theoretical roughness can easily be calculated with the knowledge of this line width (b_r) and the diameter of the tool (D_k).

$$R_{th} = \frac{D_k}{2} - \sqrt{\frac{D_k^2 - b_r^2}{4}} \tag{2}$$

The real measurements differ due to the varying engagement conditions along the cutting edge. Therefore, the following parameters prevent an exact allocation of the single influencing factors: change of cutting speed from center of the ball end mill to the shaft of the tool, the different initial oversizes before the finishing process allowing the variation of the radial depth of cut a_e, and the different radii of the cutting edge which especially have a high influence at minor axial depths of cut [13]. This leads to the conclusion that for the provision of a reproducable roughness for joining areas within a narrow range, the really

occurring average surface roughnesses have to be measured. Even for greater line widths, when the theoretical surface roughness approaches the real measured values, the calculated factors cannot be used as a basis for a prediction.

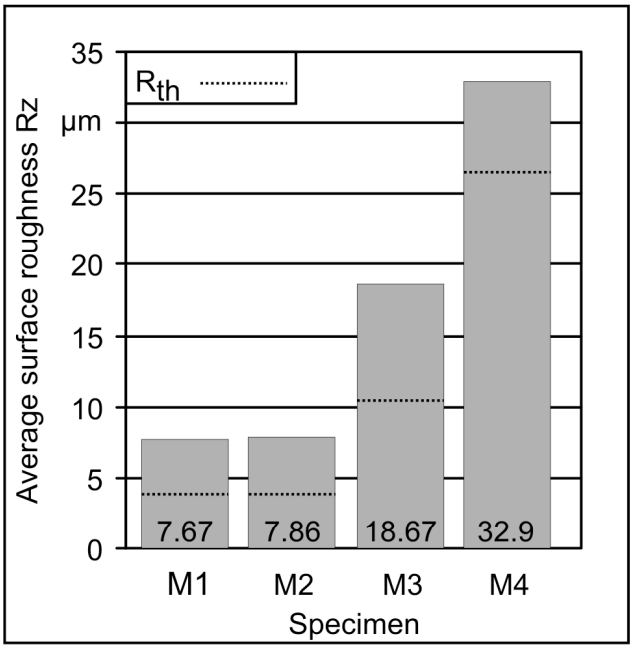

Material:	EN-AW 6060 (AlMgSi0,5)
Tool:	Ball-end mill, D = 6 mm
Coating:	TiAlN
Strategy:	Simultaneous 5-axis finishing

M1	
Cutting speed:	v_c = 300 m/min
Feed rate:	f_z = 0.1 mm
Angle of inclination:	β = 15°
Axial depth of cut:	a_p = 0.3 mm
Rad. depth of cut:	a_e = 0.1 mm
M2	
Cutting speed:	v_c = 300 m/min
Feed rate:	f_z = 0.05 mm
Angle of inclination:	β = 15°
Axial depth of cut:	a_p = 0.3 mm
Rad. depth of cut:	a_e = 0.3 mm
M3	
Cutting speed:	v_c = 300 m/min
Feed rate:	f_z = 0.05 mm
Angle of inclination:	β = 15°
Axial depth of cut:	a_p = 0.5 mm
Rad. depth of cut:	a_e = 0.1 mm
M4	
Cutting speed:	v_c = 300 m/min
Feed rate:	f_z = 0.05 mm
Angle of inclination:	β = 30°
Axial depth of cut:	a_p = 0.8 mm
Rad. depth of cut:	a_e = 0.2 mm

***Figure 6**: Average surface roughness depending on milling parameters*

It can be seen that the differing oversizes between the mandrels of the first series (M1) and the mandrels of the second series (M2) have no influence on the resulting average surface roughness. The measured data above represent the roughnesses of different mandrels manufactured in each case with the same parameters and within the same clamping as those used for joining. The difference of 0.19 µm is within the variation of different measurings of the tactile roughness measuring system that was used (Mahr Perthometer) and is insignificant. While the specimen of the series M3 represents a medium roughness, M4 expresses, on the one hand, the maximum roughness that can be manufactured with the chosen tools and process parameters and, on the other hand, a smooth transition to a macrostructured surface and, therefore, the upper end of a microstructured joining area. After manufacturing, the mandrels were electromagnetically joined with the tubes and the properties during tensile loading were tested.

4.2 Analysis of the Mechanical Properties of the Joints

Taking preliminary joining into account, two typical characteristics occurred during tensile testing, as shown in Figure 7 a + c. In Figure 7 a, the force increases and then suddenly drops. After that, the tube starts to slip off the mandrel showing a typical seize effect. Consequently, the pull-out force increases again until the tube is pulled off the

mandrel [14]. The mandrel's surface of force-fit joints showing seizing in tensile tests is shown in Figure 7 b. In Figure 7 c, the force shows a straight increase until plastic deformation of the tube occurs, which finally leads to an abrupt fracture of the tube in the area next to the joining area as shown in Figure 7 d.

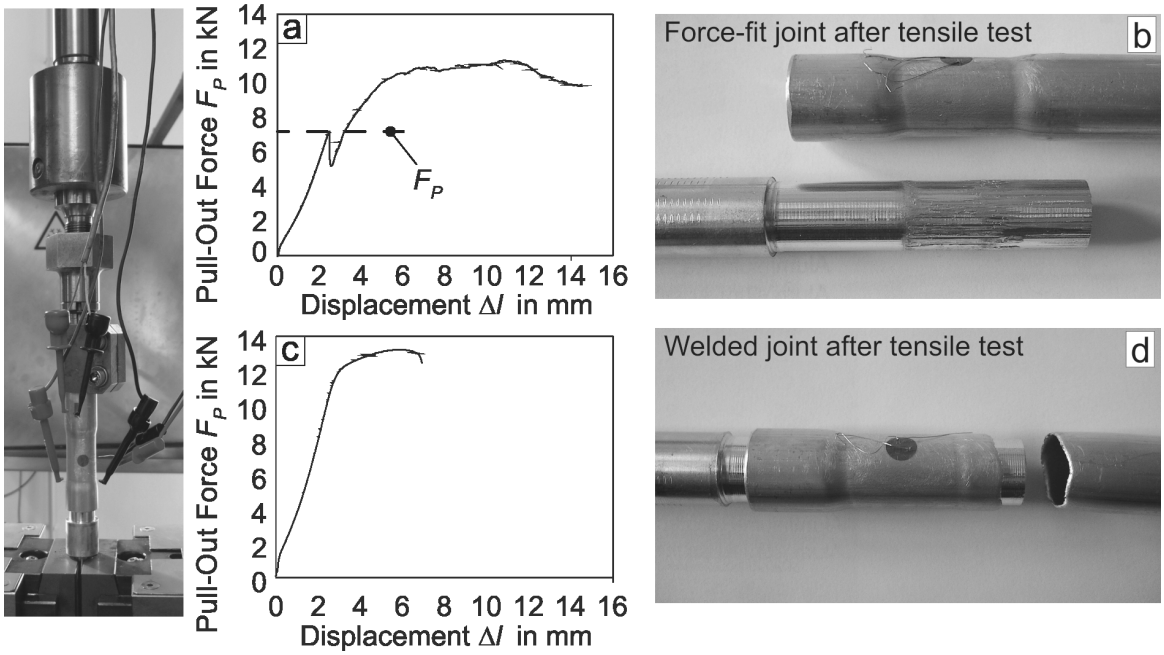

***Figure 7**: Typical characteristics of force against displacement in tensile tests of force-fit joints (a) and impulse-welded joints (c)*

Concerning the joints manufactured with a charging energy of 1.5 kJ, the impact velocity [4] leads to an impulse-magnetic welding of tube and mandrel as shown in Figure 8. The force-vs.-displacement characteristic given in Figure 7 c occurs inevitably and independent of the joint's surface characteristic.

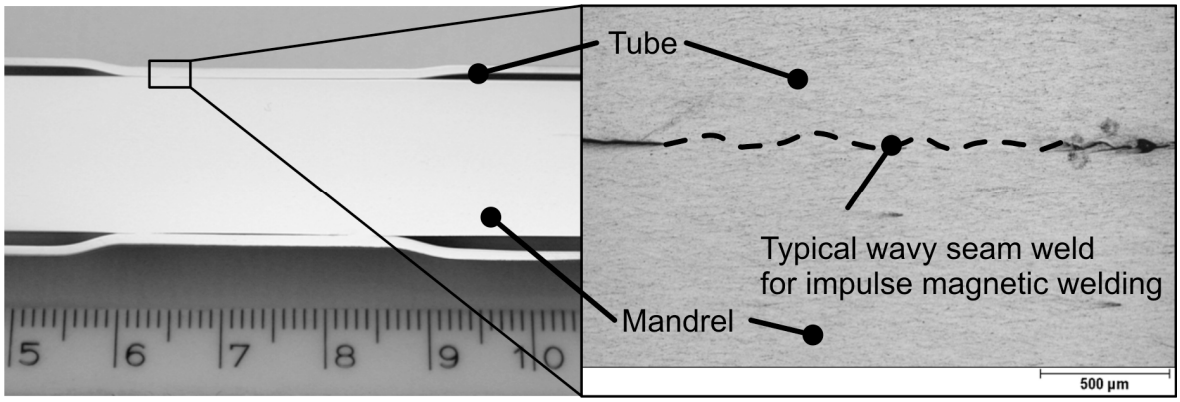

***Figure 8**: Joining area cut in axial direction (left), micrograph of welded area (right)*

Therefore, a charging energy of 1.5 kJ was inapplicable for determining the surface's influence on force-fit joints. Joints manufactured with a charging energy of 0.9 kJ

and the according gap width a_0 generally result in rather low pull-out forces. Therefore, joining was done with a charging energy of 1.1 kJ.The pull-out force versus the used shot pressure for the shot peening of the mandrels for Al_2O_3 and glass beads as shot media is shown in Figure 9. The effect achieved with the glass beads is much lesser than with Al_2O_3 particles. While the specimens shot peened with glass beads merely reach a maximum pull-out force of less than 2.5 kN, the pull-out force can be increased up to 4 kN by shot peening with Al_2O_3 particles.

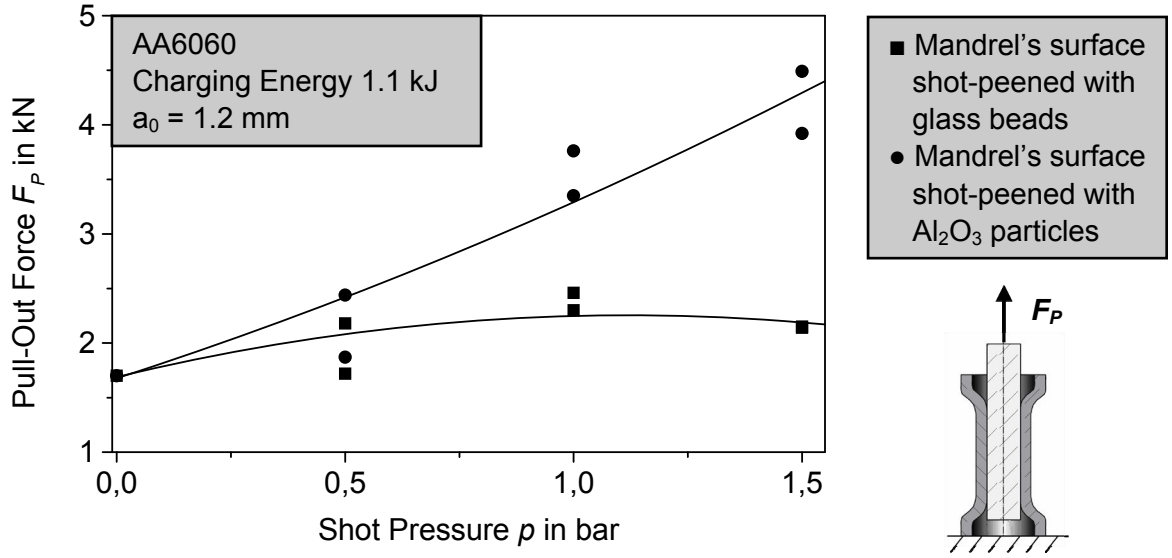

***Figure 9**: Pull-out-forces as a function of the shot pressure after shot peening*

The increase of the pull-out force by shot peening with Al_2O_3 is based on micro form fit in the contact area between tube and mandrel because the surface morphology is very different as shown in Figure 10 [14].

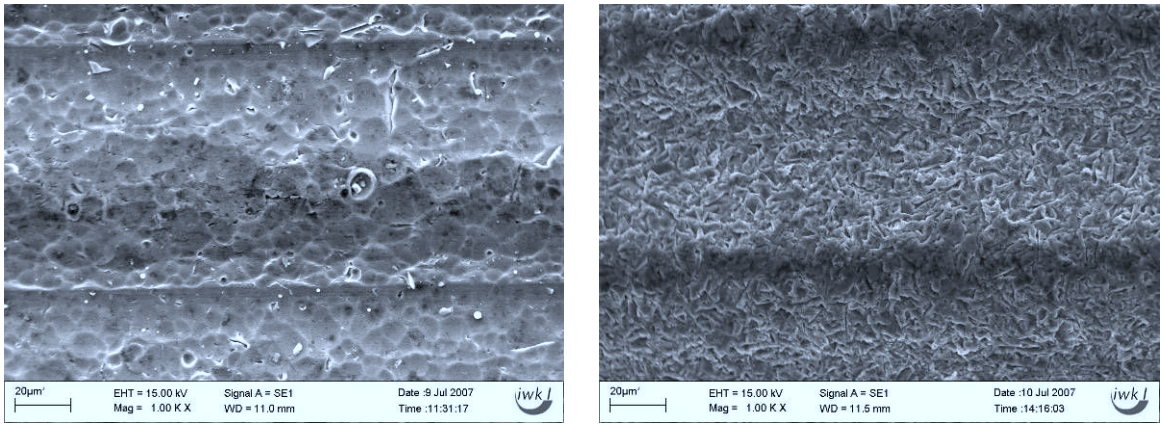

***Figure 10**: Surface of shot-peened mandrels (air pressure 0.5 bar). Left: glass beads, 20 - 30 µm. Right: Al_2O_3, 20 - 30 µm*

Figure 11 shows the correlation between pull-out forces and the average surface roughness Rz of the mandrel's surface induced by milling. The pull-out forces of the milled mandrels increase with the roughness to a maximum force of app. 8 kN. This is a result of

the roughness itself and the resulting micro form-fit (squares). An additional effect can be seen on the mandrel's surfaces after the milling process M2 (circles), which leads to an increased work hardening compared to the other processes. Furthermore, this leads to a higher interference fit in the contact area and a significantly higher pull-out force. A further explanation could be the different percentage contact area which is not considered by measuring the average surface roughness. These assumptions need to be proved in further research work which will be focusing on larger roughness values.

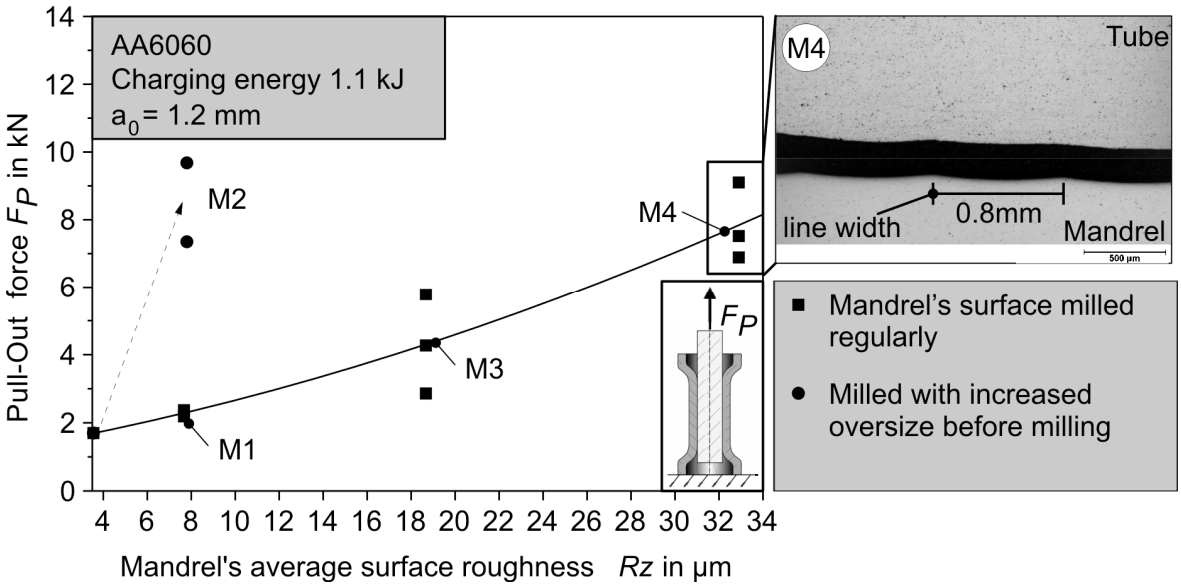

***Figure 11**: Pull-out-forces as a function of the mandrel's roughness after milling and micrograph of the joint area in axial direction*

In addition, micrographs in axial direction were investigated to evaluate the contact's characteristic of the joining zone. Consequently, the penetration of the mandrel's surface layer to the tube's surface was analyzed. As displayed in Figure 11, the roughness of the M4 surface left an impression in the tube's surface. This effect could not be observed with the other surfaces. The gap between mandrel and tube is caused by cutting for metallographical preparation leading to tangential elastic relaxation.

5 Summary

To improve the transmission of forces between mandrels and tubes in force fit joints manufactured by EMF, two surface treatments were investigated. At first, shot peening of the mandrels with high-shot pressure and square-cut shot media leads to a maximum pull-out force of 4 kN. The pull-out force can be increased up to 8 kN by structuring the mandrel's surface through milling, introducing significant roughness to the surface. This is done, on the one hand, by increasing the roughness or, on the other hand, by increasing work hardening in the surface layer of the mandrel caused by a higher remaining oversize before the finishing milling process of M2. Further investigations will be done to determine the oversize's influence on the strength of a connection. In future, with the knowledge from these investigations, it will be possible to precisely set up the strength of a connection up to its pull-out force, according to the characteristics of the mandrel and its

joining area. Furthermore, this knowledge allows to transfer desired surfaces to the manufacturing of lightweight nodes within an economic and flexible process chain.

References

[1] *Homberg, W.; Marré, M.; Beerwald, C.; Kleiner, M.:* Joining by forming of lightweight frame structures, In: Advanced Materials Research: Flexible Manufacture of Lightweight Frame Structures, Band 10 (2006) S. 89-100

[2] *Beerwald, C.*: Grundlagen der Prozessauslegung und -gestaltung bei der elektromagnetischen Umformung. Universität Dortmund - IUL, Dr.-Ing. Diss., Reihe Umformtechnik, Shaker Verlag, Aachen 2005, ISBN 3-8322-4421-2.

[3] *Zhang, P.; Kimchi, M.; Shao, H.; Gould, J. E.; Daehn, G. S.*: Analysis of the Electromagnetic Impulse Joining Process with a Field Concentrator, In: Materials Processing and Design: Modeling, Simulation and Applications Proceedings of the 8th International Conference on Numerical Methods in Industrial Forming Processes

[4] *Kojima, M; Tamaki, K.*: Factors affecting the result of electromagnetic welding of aluminum tube. Transactions of the Japan Welding Society, 19:53–59, 1988.

[5] *Shribman, V.; Tomer, Y.:* Magnetic pulse technology for improved tube joining and forming, In. Tube & Pipe Technology, 2006, S. 91-95

[6] *Barreiro, P., Schulze, V., Löhe, D., Marré, M., Beerwald, C., Homberg, W., Kleiner, M.*: Strength of tubular joints made by electromagnetic compression at quasi-static and cyclic loading, In: 2nd International Conference on High Speed Forming, 20.3.-21.3.2006, Dortmund, Germany, Proceedings, pp.107 -166, ISBN 3-00-018432-5

[7] *Al-Ahmad, N.*: Das Fügen rotationssymmetrischer Formelemente durch Umformen mit Impulsmagnetfeldern. Dissertation Ingenieurhochschule Zwickau 1980.

[8] *Kleiner, M.; Marré, M.; Beerwald, C.; Homberg, W.; Löhe, D.; Barreiro, P.; Schulze, V.*: Investigation of force-fit joints produced by electromagnetic tube compression, In: Annals of the German Academic Society for Production Engineering, WGP, Vol. XIII/1 (2006), S. 227-230

[9] *Bühler, H.; v. Finckenstein, E.*: Fügen durch Magnetumformung, Werkstatt und Betrieb, 101. Jahrg., Heft 9 (1968) S. 209-215

[10] *Becze, C. E.; Clayton, P.; Chen, L.; El-Wardany, T.I.; Elbestawi, M. A.*: High-speed five-axis milling of hardened tool steel. International Journal of Machine Tools and Manufacture, Vol. 40, Issue 6, May 2000, pp. 869-885

[11] *Weinert, K.; Rautenberg, J.; Surmann, T.; Mehnen, J.*: Simulation of the Milling Process for Lightweight Aluminum Connectors. Annals of the German Academic Society for Production Engineering, XII (2005) 1, ISBN 3-9807670-6-x, pp. 125-128

[12] Barreiro, P.; Schulze, V.; Löhe, D.: Influence of Process Parameters on Structure and Mechanical Properties of Joints produced by Electromagnetic Forming and Friction Stir Welding. Submitted to Advanced Material Reasearch 2007.

[13] *Weinert, K.; Kahnis, P.; Koehler, W.; Rautenberg, J.:* Gratwanderung zwischen Stabilität und Labilität. MM Maschinenmarkt, 110 (2004) 14, S. 28-32

[14] *Schulze, V.; Barreiro, P.; Löhe, D.*: Investigation of the Influence of Process Parameters on the Structure and the Mechanical Properties of Joints Produced by Electromagnetic Compression. In: Advanced Materials Research: Flexible Manufacture of Lightweight Frame Structures, Band 10 (2006) S. 79-88

Corrosion Protection of the Zone of Thermal Action (Zone of Butt of Tubes While Welding) from the Inside When Laying Multifunctional Pipeline Systems

V. A. Glouschenkov, V. F. Karpukhin

Samara State Aerospace University, Russia

Abstract

The work is aimed at handling a main problem of corrosion protection of the pipeline's interior section adjacent to a weld butt. It is proposed to execute fastening of elements of the protective system of pipes by application of the pulse-magnetic technology which has essential technical and economical advantages over other methods. Protection of end sections of pipes is performed by pulse-magnetic pressing-in of a bush made from stainless steel or by pulse-magnetic welding of rings from a protective material. Commercial tests of the pipelines produced by the technology being proposed supported good prospects of this technology use.

Keywords

Corrosion, Welding, Assembly

1 Introduction

Experience of operating of pipelines shows that most of the accidents with pipelines are associated with the corrosion breakdown of tubes. So, while assembling and operating pipelines much attention is given to the corrosion protection of them.

Corrosion protection of pipelines from inside is performed in two directions. The first direction concerns the use of pipelines with a protective coating from the high corrosion-resistant materials. The second – use of cathodic protection wherein as a result of electrochemical processes, the protective material, preventing corrosion of the pipeline's material, dissolves in the course of operating of the pipelines.

In practice, both directions are widely used. Paint, varnish, polymeric, enamel and other coatings are used as protective ones.

At the present time while laying steel multifunctional pipeline systems only tubes with an inner anticorrosive coating are used. But during butt electric- arc welding of pipes, heat of the end sections of the pipes greatly exceeds their heat resistance. Therefore the subsequent protection of the pipes' sections adjacent to the weld butt is a complicated problem.

A draft of a zone of a pipeline's weld butt is shown in Fig.1. A weld butt is placed at a distance of 10-15 m from a free face, therefore applying a protective coating in this zone after welding is rather difficult to perform.

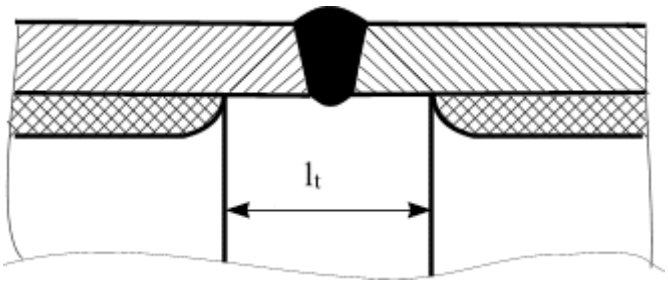

l_t – zone of thermal action

***Figure 1**: A draft of a zone of a pipeline's weld butt*

One of the presently most abundant methods of protection of the zone of thermal action is the method of setting of TUBOSCOPE sealing bushes (US). But this technology has disadvantages: the process is conducted in-the-field, requires high accuracy of diameters to be butt-joined, it is rather labor-intensive because of use of hand work when applying a hermetic and setting a bush.

2 Research Results

The following methods of protection of the zone of thermal action with use of pulse-magnetic technologies were developed [1]:

- Welding of rings from aluminum alloys on pipes (cathodic protection);
- Pressing of thin-walled bushes from stainless steel in the zones adjacent to faces of pipes.

View of the zone of a weld butt with fastening of elements by the processes of pulse-magnetic technology is shown in Fig.2.

The advantages of pulse-magnetic loading are super-little machine time, high velocities of deformation, low power consumption, ecological safety of the processes. The processes of pulse-magnetic fastening the elements of corrosion protection of pipes are performed in stationary, working conditions with the rather simple technological attachments. They don't require close fitting the parts being joined. Therewith the technologies of applying the inner protective coating on pipes and of butt -welding pipes are essentially unchanged.

Figure 3 presents the process of fastening the protective rings in pipes with a help of pulse-magnetic welding [2].

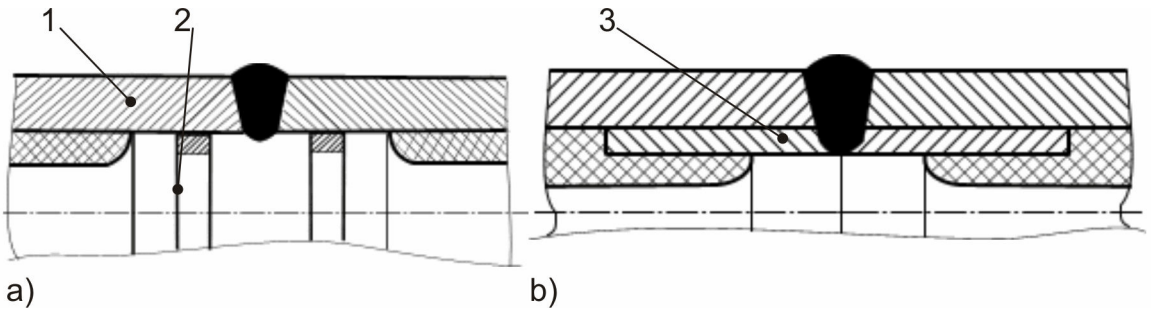

1 – pipe, 2 – protective ring, 3 – bush.

***Figure 2**: Zone of a pipeline's weld butt with corrosion protection by protectors (a) and with bushes from stainless steel (b).*

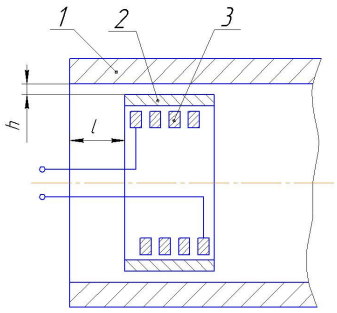

1 – pipe; 2 – ring; 3 – coil

***Figure 3**: Scheme of process of welding protective rings with a pipe*

Minimum values of a distance from the pipe face to the protective ring face l are selected such lest during welding a butt of pipes, the temperature of the zone of joining of the protective ring with the pipe exceeds 350° C. The reliable joining of the parts being welded is formed by a high-speed collision of the protective ring 2 with the pipe inner surface 1. The protective ring is accelerated in the gap "h" to the speed, required for formation of joining of the materials being welded, under the action of radial electro-dynamic forces appearing when an intense pulse current flows along the inductor 3.

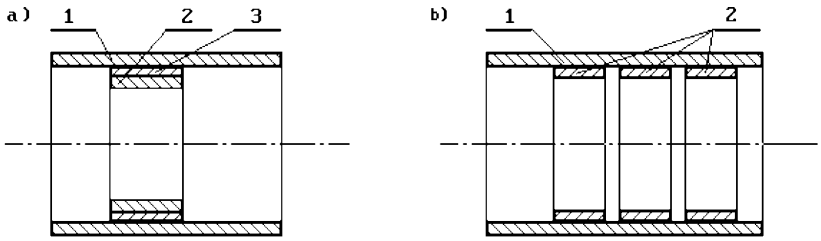

1 – pipe; 2 – ring; 3 – sublayer

***Figure 4:** Protection of end sections of pipes with one protective ring (a) and with several rings (b)*

Aluminum alloys alloyed with magnesium are used as protective materials. Joining such materials with steels by methods of welding under conditions of high-speed collision is impracticable [3]. Therefore the pipe's inner surface is cladded with technically pure

aluminum by the method of pulse-magnetic welding and then the ring from a protective material is welded with the cladded surface of the pipe. View of such joint is shown in Figure 3a.

It is rationally to use pulse-magnetic welding for formation of welded joints of length no more than 20…25 mm [4] with ring's thickness of 2…3 mm. So length of the protective ring may not exceed 20…30 mm. To increase protector's mass several protective rings should be welded successively in a row [2] as it is shown in Fig. 4b.

In deciding on the technological parameters of the process of pulse-magnetic welding a protective ring with a pipe, it should be taken into account that pipes have a wide zone of tolerance on sizes. As a result a value of the initial gap between the surfaces being welded may differs essentially from the nominal value. To compensate for possible departures of the initial gap's value (at small values of the gap) it is necessary to increase considerably the energy of discharge as compared with the rated level. This greatly enhances the load on the inductor and reduces its life time. Moreover as the value of the initial gap increases the magnetic field pressure level, required for acceleration of the protective ring to the velocity providing formation of a welded joint, decreases. Therefore parameters of the process of pulse-magnetic welding must be selected in relation to the condition of collision of the parts being welded during the second quarter of the period of oscillations of the discharging current. Recommended value of epy initial gap is defined by the following expression:

$$h_{min} > \frac{V_{min}}{12f}, \tag{1}$$

Where V_{min} is the minimum collision velocity providing formation of a welded joint, f is the operating frequency of the discharging current.

The maximum value of the initial gap is limited by two conditions. In the first place, a value of plastic deformation of the ring may not exceed a limiting value δ_p for the protective material. This condition is described by the expression:

$$h_{max} < \delta_P R, \tag{2}$$

where R – the initial radius of the protective ring.

In the second place, the value of forces applied to the inductor's inner surface as a result of action of the "coil effect" may not exceed forces of interaction between the inductor and a billet. This condition is described to sufficient accuracy by the expression [5]:

$$h_{max} = \sqrt{R_C + R_i} - \left(R_C + \delta_i\right), \tag{3}$$

where R_C and R_i are the inductor's outer and inner diameters, respectively and δ_i is a value of the insulating gap between the inductor and billet.

It is of prime importance to take into account conditions (2) and (3) when developing the technology of welding of protectors with pipes in diameters up to 130 mm.

Use of sufficiently large gaps makes it possible to perform welding of protective rings of one standard size with pipes of a variety of standard sizes different in wall thickness. For welding protectors with pipes of the same outer diameter with the wall thickness from 4 mm to 10 mm it will suffice to have two standard sizes of protective rings and, accordingly, two inductors.

The amplitude value of pulse-magnetic field pressure P, needed for acceleration of a protective ring of thickness "s" at the close of the first half-period of the discharging current to the velocity providing formation of a welded joint, is described by the expression:

$$P = 4V_{min} \cdot f \cdot \rho \cdot s \,, \tag{4}$$

where ρ -density of the protective ring's material.

Pulse-magnetic pressing-in of a stainless steel bush is conducted by the scheme similar to the scheme shown in Figure 2. It differs in that the faces of a bush and pipe coincide (l=0), value of the gap h is minimum, because it is not necessary to accelerate the bush to high velocities; moreover in connection with low electric conductivity of stainless steel, a layer of a high electric conductivity material is placed between the inductor and the bush, it may be made for example by winding of aluminum foil. Thickness of the layer must comprise about 1 mm.

Value of pulse-magnetic field pressure necessary for pressing-in is defined by the expression:

$$P = \frac{6\sigma_s \cdot k \cdot s}{D} \quad , \tag{5}$$

where σ_s - yield limit of the bush's material; D and s – diameter and thickness of the bush, respectively; k – dynamic coefficient of the yield limit of the bush's material which is computed from the formula [6]:

$$k = 3.006 \cdot \exp(-0.036 \cdot 10^{-7} \cdot \sigma_s), \tag{6}$$

Calculation of parameters of the inductor and the pulse-magnetic installation's charging energy needed for fastening elements of corrosion protection is performed by the known procedure presented in the work [7]. The expression (4) is used when calculating a process of welding protectors with pipes, the expression (5) – for pressing bushes in pipes.

The fragments of tubes welded with new technology of protection of the zone of thermal action were put to rapid and production tests and showed high quality of protection.

References

[1] Glouschenkov V.A.: Corrosion protection of weld seam in pipe joint when laying oil field pipelines // Proceedings of the international conference on the joining of materials JOM- 8. - Helsingor (Denmark), 1997. – p. 547-551.

[2] Karpuhin V.F.; Glouschenkov V.A.; Voinov A.K.; Al-Erhayem O.: Pulse-magnetic welding of rings from aluminium alloys with steel pipes for cathodic protection of welded butts of pipelines // Proceedings of the international conference on the joining of materials JOM- 8. - Helsingor (Denmark), 1997. – p. 565-566.

[3] Кудинов В.М.; Коротеев А.Я.: Сварка взрывом в металлургии. – М.: Металлургия, 1978. – 168 с.

[4] Дудин А.А.: Магнитно-импульсная сварка металлов. – М.: Металлургия, 1979. – 128 с.

[5] Карпухин В.Ф.; Воинов А.К.: Использование технологии магнитно-импульсная обработка материалов на современном этапе: Труды 1-й Международной научно-технической конференции «МЕТАЛЛДЕФОРМ – 99», Секция 4, Самара, 1999. – С. 62-66.

[6] Мазуровский Б.Я.; Сизев А.Н.: Электро-гидравлический эффект в листовой штамповке. – Киев: Наукова думка, 1983. – 192 с.

[7] Белый И.В.; Фертик С.М.; Хименко Л.Т.: Справочник по магнитно–импульсной обработке металлов. – Харьков: “Вища школа”, 1977. – 168 с.

SESSION 5

TOOLS AND EQUIPMENT

High-current Capability of Coaxial Cables in Magnetoforming Applications*

M. Römheld, F. Pohl, W. Hartmann

Siemens AG, Corporate Technology CT PS 5, Günther-Scharowsky-Str. 1
91052 Erlangen, Germany

Abstract

Magnetoforming technology often requires impulse current amplitudes of several hundred kiloamps, at pulse durations between 30 µs and >100 µs. Often, it is required to provide the impulse via a flexible transmission line (cable) in order to allow the forming coil to be positioned correctly. These cables have to withstand the high pulse currents without deterioration for a large number of pulses. In addition, it is necessary to minimise the inductance of the cable connection, as an increase in inductance negatively influences the efficiency of the installation as a whole, whence low-inductance coaxial cables are required which are able to fulfil all of these requirements simultaneously.

Manufacturers normally do not specify the impulse current capability of coaxial cables, as this is not necessary for most standard applications. Therefore, experiments were performed to explore the limits of commercial medium high voltage cables in regard of their impulse current withstand capability for these specific impulse parameters.

A coaxial medium voltage cable has been tested at single pulses of ca. 100 µs duration, at amplitudes between 30 and 140 kA. The radial deformation (expansion) of the cable was detected with a high-resolution, high-speed camera. At a frame rate of 9000 frames/s the expansion of the cable has been determined as a function of the current amplitude. We observed dynamic changes of the cable diameter at currents above 81 kA, reaching up to 1.26 mm increase in diameter at 142 kA pulse amplitude. Above 100 kA, part of the deformation becomes irreversible, with cumulated permanent changes of up to 1 mm. The measurements are used to estimate the operating range of these cables.

Keywords

Magnetic forming; impulse current; coaxial cable; operating range

---

* *This work has been funded by the Sächsische AufbauBank SAB, Saxonia, Germany within the scope of the project "Grundlagen zur elektromagnetischen Formgebung flächiger Karosseriebauteile", project number 8942/144,9 as part of a collaboration with the Fraunhofer Gesellschaft (FhG) Chemnitz, Germany; the authors thank T. Koch from the FhG Chemnitz for his support of this work.*

1 Introduction

Magnetoforming technology often requires impulse current amplitudes of several hundred kiloamps, at pulse durations which are typically between 30µs and >100 µs. In practical applications, it is often required to provide the impulse via a low-impedance, flexible transmission line (cable) in order to allow the forming coil to be positioned according to the forming process / work piece requirements. These cables have to withstand the high pulse currents without deterioration for a large number of pulses, which in some applications can reach millions. Additionally, it is necessary to minimise the inductance of the cable connection, as an increase in inductance negatively influences the efficiency of the installation as a whole, whence low-inductance coaxial cables are required; these cables have to fulfil all of these requirements simultaneously.

Manufacturers normally do not specify the impulse current capability of coaxial cables, as this is not necessary for most standard applications. Therefore, experiments have been performed to explore the operating range and limits of commercial medium high voltage cables in regard of their impulse current withstand capability for these specific impulse parameters.

In particular, the measurements described hereafter have been made to determine the radial deformation (blow-up) of the cable, i.e. the outer conductor of the coaxial cable, which is pushed outward by the magnetic field inside the cable during a high-current pulse. Distinction has been made between dynamical (reversible) deformation, and irreversible deformation, i.e. a permanent increase in the outer diameter (OD) of the cable sheath.

2 Experimental Setup

2.1 Pulse Generator

The tests of the pulse cables were performed using a high-current, all-solid-state pulse generator for magnetoforming at the Fraunhofer Gesellschaft (FhG) Institute for Forming Technology IWU at Chemnitz, Germany [1], [3]. The pulse generator has been developed by Siemens [2] and built by Highvolt GmbH, Dresden, Germany, and has the following electrical parameters:

capacitance	450 µF
charging voltage	2.5 … 21 kV
pulse energy	1.4…100 kJ
pulse current	20…200 kA_p nominal
	40…400 kA_p short circuited
pulse duration	100 µs typ.
pulse reprate	0.5 min^{-1}

The pulse generator (Figure 1) allows for a wide range of operating parameters and is used in a short-circuit mode in these experiments, as the short-circuited cable under test has a low impedance as compared to the internal generator impedance. The transmission line connecting the experiment and the pulse generator consists of a bundle of 6 parallel cables (see below) in order to reduce the transmission line impedance to an acceptable level.

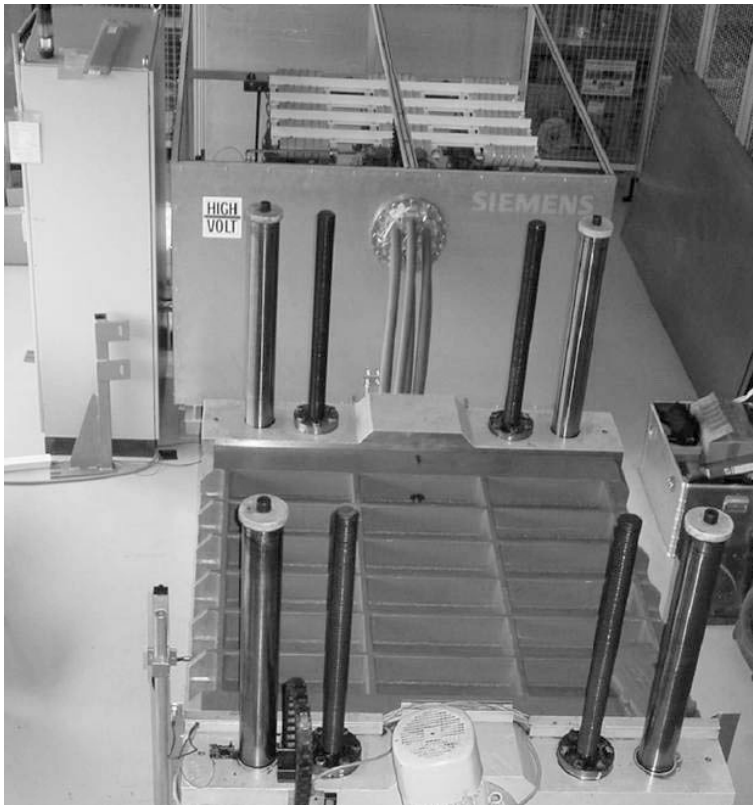

Figure 1: *Photograph of the pulse generator installed at the FhG IWU, Chemnitz, Germany. In the foreground the workstation with the vertically moveable mounting plate for the experiment can be seen.*

2.2 Coaxial Cable Test Setup

For the pulse generator installed at the FhG IWU Chemnitz, a mechanically rather stiff, high impedance high voltage cable of ca. 45 mm outer diameter (OD) has been used as a flexible transmission line. Its advantage is its high DC voltage capability of 200 kV, the large diameter of its outer conductor of 39 mm, and a large copper cross section. Its disadvantages are the stiffness, resulting in a large bending radius of >60 cm, and its high impedance; the specific cable inductance amounts to ca. 270 µH/m, resulting in a total TL inductance of 90 nH for the cables only. In the following, the test of an alternative medium voltage coaxial cable from Draka (Figure 2) (Draka NTMCWOEU Feltoflex 10 kV, 1x35/16, DC test voltage 42.5 kV, OD 24.5 mm) is reported. The diameter of the outer conductor is 17 m; the specific inductance is only 150 nH/m, and the cable is considerably more flexible than the cable originally used for the pulse generator.

The 110 cm long cable is fixed to the mounting plate of the magnetoforming workstation with a pair of V-shaped clamps (Figure 3), and the deformation of the cable caused by the magnetic pressure of the current pulse is measured in a clear section between the two clamps. On one side, the inner conductor of the cable is connected to the hot side of the cable bundle termination, while the outer conductor is connected to the ground side of the cable bundle. At the other side, the cable-under-test is short circuited by directly connecting the copper wire strands of the outer conductor to the inner conductor.

Figure 2: *Photograph of the Draka cable under test.*

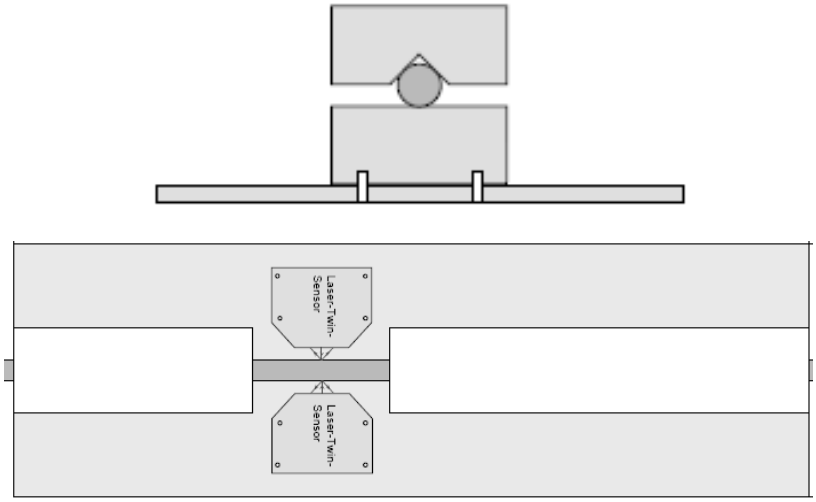

Figure 3: *Schematic drawing of the cable fixture during the experiments.*
Top: end-on view of the cable in the V-clamps; bottom: top view of the setup showing the clear section between the two clamps used to measure the cable deformation during the tests.

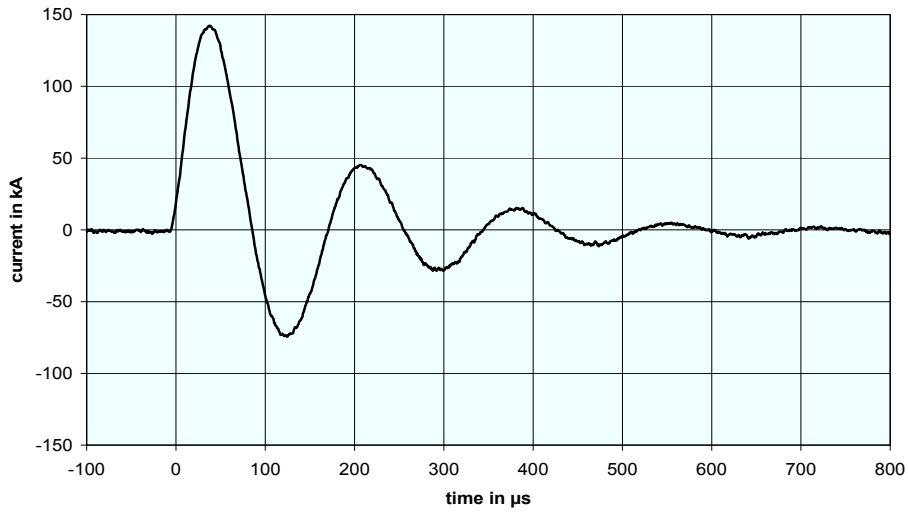

Figure 4: *Current pulse shape for a peak current of 142 kA.*

The cable is exposed to damped sinusoidal pulses of varying amplitude (Figure 4).

2.3 Diagnostics

The cable is clamped to the lower side of the mounting plate and viewed from below (Figure 5) using a high-speed video camera at a frame rate of 9000 fps (frames per second).

Figure 5: *Cable-under-test clamped to the mounting plate, illuminated with a cold-light lamp, and observed with a high-speed video camera.*

The spatial resolution of the video camera is 35 µm per pixel in the radial direction of the cable. At a frame rate of 9,000 fps, the time between frames is 111 µs, which is longer than the main current pulse. Therefore, the test system does not resolve the true dynamical movement (radial deformation) of the cable sheath during the current pulse, and only maximum values are used for further evaluation of the cable.

In order to determine the permanent cable deformation, the cable diameter was measured before and after each shot with a calliper. The absolute accuracy is comparable to that of the video camera measurements, and is of the order of 30...40 µm.

3 Experimental Results

The experimental results are summarised in the following graphs. Figure 6 shows the result from the video camera measurement, revealing that the dynamical deformation amplitude of the cable (blow-up) is of the order of 0.9 mm at the highest current of 142 kA_p. The long-term dynamical deformation is around 0.6 mm, while the permanent deformation caused by this shot is only 0.4 mm as determined from a calliper measurement (c. Figure 7). Permanent (non-reversible) cable deformation (expansion) starts above 60 kA peak current, indicating a permanent loss of the binding strength between outer conductor and cable dielectric at and above these current levels. Above a peak current of 120 kA, this expansion becomes noticeable growing to several hundred microns per pulse.

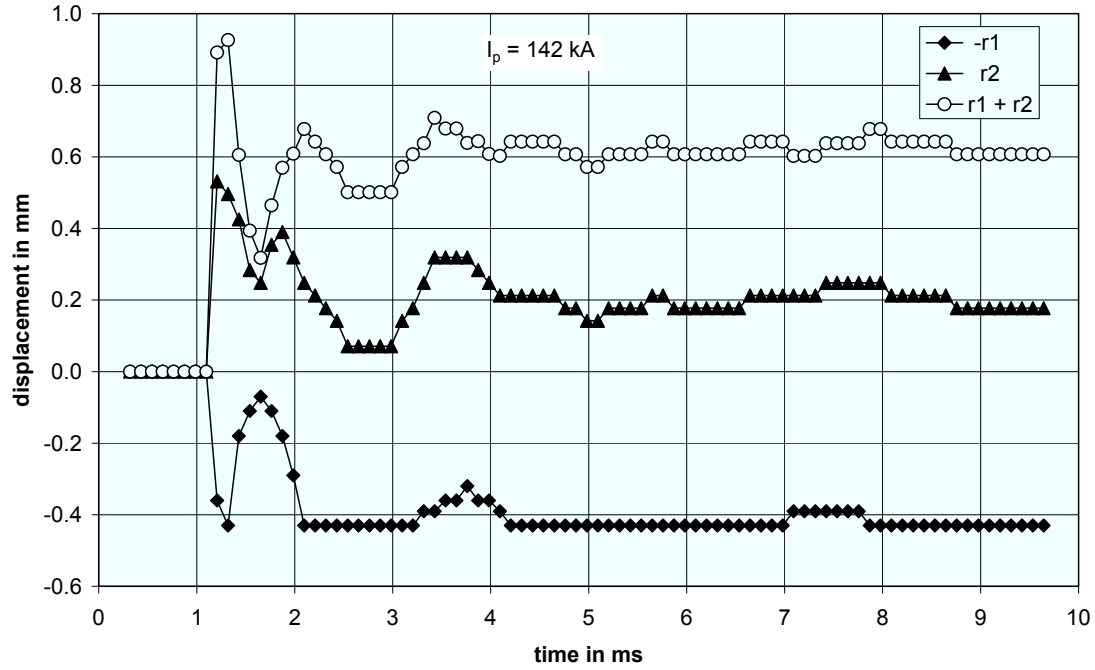

Figure 6: *Draka cable, dynamical deformation from high-speed video camera measurement, for a peak current of 142 kA (c. fig. 4).*

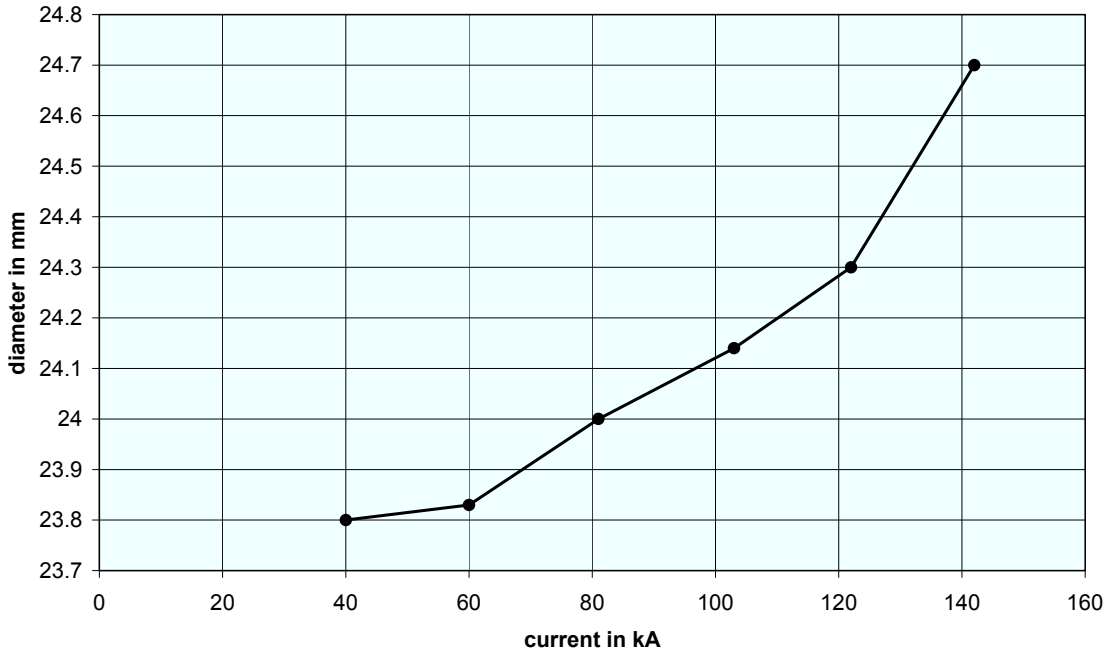

Figure 7: *Calliper measurement of the diameter of the Draka cable as a function of the current pulse amplitude after exposure to single pulses of increasing amplitude.*

4 Discussion

The experimental results as well as the calculation of the magnetic pressure leading to the observed cable expansion are summarised in figure 8.

The magnetic pressure inside a coaxial cable is calculated according to eq. 1:

$$p_{mag} = \frac{\mu_0 I^2}{8\pi^2 r^2} \tag{1}$$

where p_{mag} is the magnetic pressure between inner and outer conductor; μo is the permittivity of space; I is the momentary current; r is the effective radius (≈ inner contour) of the outer conductor.

Due to the small diameter of the Draka cable, the peak magnetic pressure amounts to ca. 8 bar at a peak current of 60 kA, and increases to over 45 bar at currents around 140 kA. Obviously, the threshold pressure for permanent damage to the cable sheath for this type of cable is of the order of 6...8 bar and should not be exceeded for an extended number of pulses if the cable is intended to survive thousands or even millions of pulses. Short-circuit phenomena, on the other hand, should be rare events in a production unit, whence the short-circuit load capacity of the cable can be designed to be in the range of over 100 kA to 120 kA.

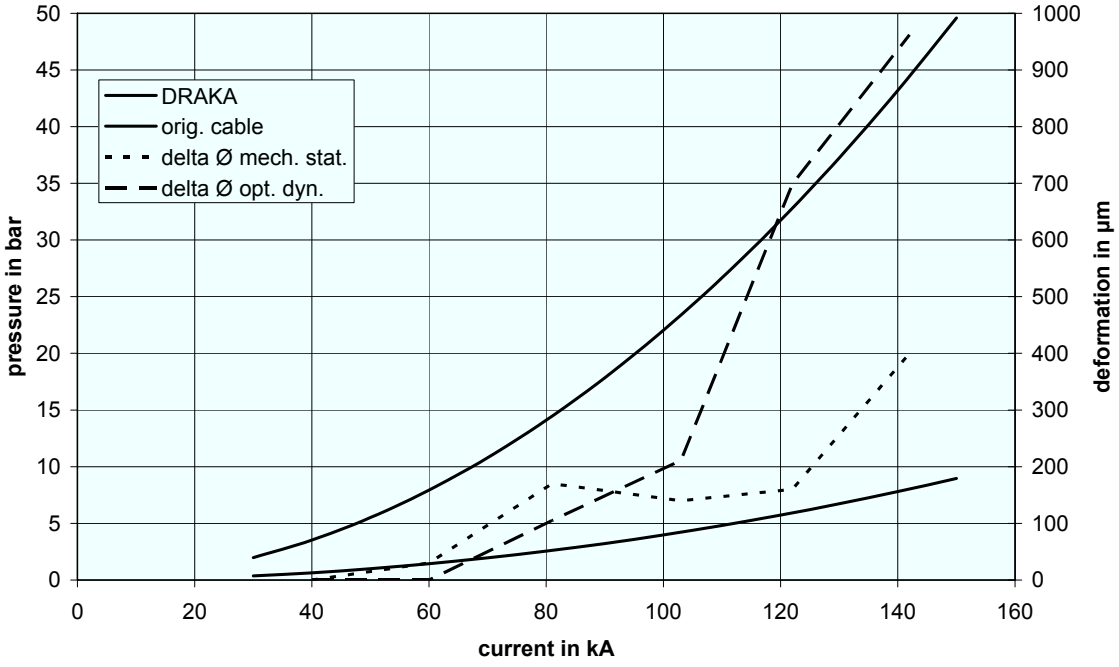

Figure 8: *Calculated magnetic pressure inside coaxial cables ("DRAKA": cable used in these experiments (upper full line); "orig. cable": cable used for the connection between magnetoforming pulse unit and the experiment (lower full line); c. figure 1) and reversible ("opt.dyn.", dashed line) and non-reversible ("mech.stat.", dotted line) diameter change per pulse of the Draka cable as a function of the pulse current amplitude.*

The magnetic pressure as calculated for the original cable used in the magnetoforming unit at FhG IWU is shown as the lower curve in figure 8. Owing to its larger outer conductor diameter, the magnetic pressure inside the cable is considerably lower than that of the Draka cable at the same current; assuming a similar threshold pressure for permanent diameter change (i.e., a similar strength of the outer cable sheath), a single cable is able to carry pulse currents of up to 100 kA without deterioration, and should be able to survive up to 200 kA_p for a limited number of pulses (i.e., in short-circuit events on the load side).

5 Conclusions

We have characterised the pulse current capability of a coaxial medium voltage cable in the current regime of 40 kA to 140 kA. Dynamical and static measurements of the cable deformation (expansion) have shown that a save operating range can be identified where permanent cable deformation is negligible, as well as a current threshold has been found above which a permanent damage of the cable has to be taken into account. Below this threshold, we assume that the cable can be used for a large number of current pulses, i.e. in commercial applications of magnetoforming apparatus, while above this threshold the cable can survive only a few rare events like short-circuit loads caused by a faulty load.

The maximum pulse current allowable for a specific cable mainly depends on two characteristics, namely, the strength of the outer conductor and cable sheath, and the outer conductor diameter. For a specific medium voltage cable, we have found a threshold of the order of 6 to 8 bar of the magnetic pressure above which a permanent, non-reversible deformation (expansion) of the cable can not be avoided. Assuming that similar cables have similar properties, the results found in this work can be used to safely design flexible, long lifetime, high voltage, high current connections for pulsed power applications requiring high current amplitudes and a large number of pulses at the same time.

References

[1] *Hartmann W., Römheld M., Donner A.*: A 100 kJ Pulse unit for electromagnetic forming of large area sheet metals, Proc. ICHSF 2006, Dortmund, Germany, p. 227-236, 2006.

[2] *Hartmann W., Römheld M.,:* Design of a high current pulse generator for magnetoforming, Proc. 26th IEEE Int. Power Modulator Conference, p. 310-313, 2004.

[3] *Hartmann W., Römheld M., Donner A.*: A 100 kJ Pulse unit for electromagnetic forming of large area sheet metals, Proc. 27th IEEE Int. Power Modulator Conference, p. 577-581, 2006.

Reversed Switch-On Dynistor Switches of Gigawatt Power Microsecond Pulses

Y. V. Aristov, I. V. Grekhov, A. K. Kozlov, S. V. Korotkov, A. G. Lyublinsky

Ioffe Physico-Technical Institute, Russian Academy of Sciences,
26 Polytechnicheskaya, St. Petersburg, 194021 Russia

Abstract

A high-power (250 kA and 25 kV) compact switch based on an assembly of reversed switch-on dynistors (RSDs) connected in series and a coaxial saturable-core choke, which is necessary for their effective switching, is described. An essential feature of this switch is a drastic reduction of the duration of RSDs control pulse, which allows using minimum dimensions and low inductance saturable core choke and obtain high rise rate (more than 30 kA/μs) of the switched current. The increased RSDs control pulse amplitude and rise rate that are required for RSDs switching on by reduced duration triggering pulse are attained by using a fast switch based on new type semiconductor devices—deep-level dynistors (DLDs).

Keywords

Semiconductor, Assembly, Switch

1 Introduction

Power silicon thyristors are conventional semiconductor switches in high power devices of pulsed power engineering. These thyristors are characterized by a low steady-state voltage drop after termination of the transient switching process and are comparatively inexpensive. Two-electrode semiconductor devices — reversed switch-on dynistors (RSDs) [1-3] that are switched on by control plasma layer — represent a promising alternative to pulsed thyristors.

Due to uniform over device area switching on process the switching capability of RSDs is 1.5 - 2 times higher than those of the best modern pulsed thyristors with the same diameter of semiconductor structure.

2 Reversely switch-on dynistor structure

Reversely switch-on dynistor (RSD) is a four-layer two-electrode silicon semiconductor thyristor-type device (Figure 1). The design of its anode emitter consists of alternating p^+ and n^+ sections with a characteristic size smaller than the thickness of the n-base.

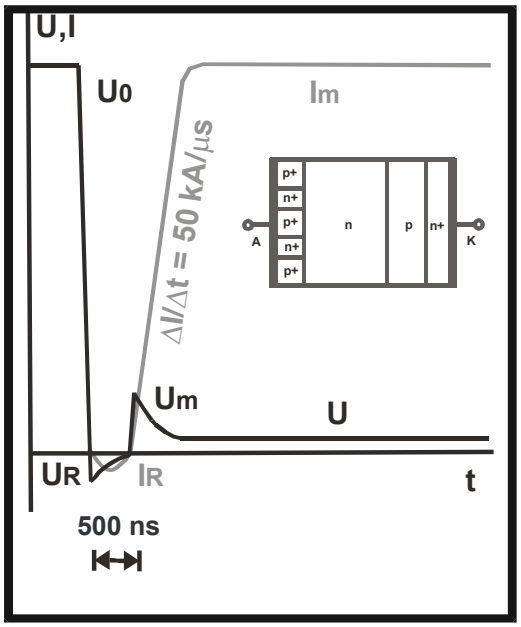

***Figure 1**: Schematic structure of reversely switch-on dynistor as well as voltage and current pulse forms during switching on process*

In the initial state, RSD blocks the voltage of power circuit U_0 (2…2.5 kV). To turn-on the device the low reverse voltage $U_R << U_0$ is applied across RSD for a short time while U_0 voltage is blocked by saturable core choke. As a result, the control current I_R flows through n^+-n-p-n^+ reverse conducting channels. This current provides the carrier injection into n-base uniformly all over the device area.

After the control current stops flowing and the initial voltage polarity restores, holes are being moved by the field from the plasma layers into the p-base, causing electron injection from cathode n^+-emitter and the fast turn-on of RSD.

Small peak voltage U_m occurs on RSD during the process of n and p bases modulation. The duration of this peak voltage is less than 1 μs and is determined by width of base layers and charge stored into the structure while control current flows through RSD. After that few volts steady-state voltage U remains on RSD.

Under the sufficient density of control current and sufficient density of injection reverse conducting channels RSD switching occurs uniformly all over the device area. As a result, the switching capability of RSD increases practically proportionally to the device operating area. RSD turns on without any delay between control and main current pulses, therefore in case of serial connection all RSDs are turned-on simultaneously and high reliability of RSD stack operation is guaranteed.

Power RSD switches are able to switch current pulses with amplitude of several hundreds kiloamperes and dI/dt of tens kiloamperes per microsecond under the voltage of

tens kilovolts. They have high efficiency, small dimensions and low cost. The latter is determined by simple manufacturing technology of reversely switch-on dynistors.

3 Main electronic design principles of RSD based switches

Two principal electrical circuits of power switches based on high voltage RSD assembly RSD1-RSDN and energy storage capacitor C0 are shown on Figures 2 and 3. MC is the main circuit, CS is the control system, RS is the remagnetization system for saturable core choke and Z is a load.

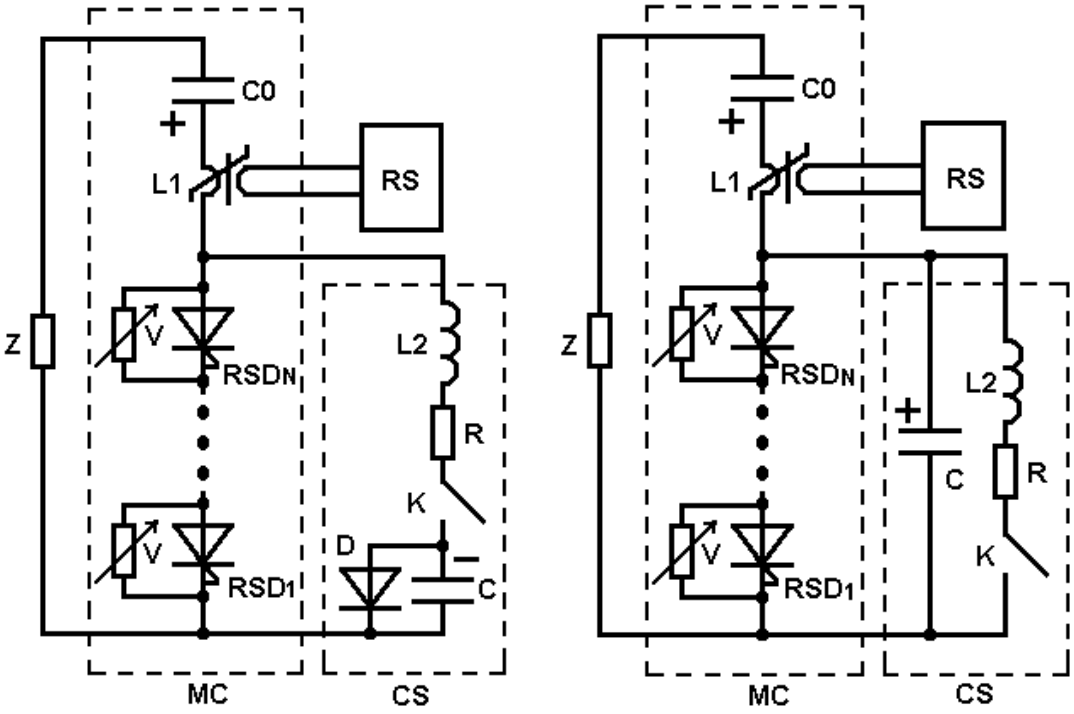

***Figures 2 (left) and 3 (right)**: Principal electrical circuits of power switches based on RSD stack and energy storage capacitor C_0*

In the circuit on the Figure 2 power capacitor C_0 and triggering capacitor C are charged initially up to U_0 and U voltages correspondingly (U_0>>U). RSD stack RSD_1-RSD_N blocks voltage U_0. Triggering switch K blocks voltage U_0+U. Varistors V equalize the voltage drops between RSDs in stack.

When triggering switch K is turned on capacitor C discharges through RSDs and reverse control current I_R passes through RSD structures. Negative voltage which occurs on capacitor C due to LC recharge is blocked by diode D and control current decays slowly with time constant L_2/R.

Saturable core choke L_1 blocks U_0 voltage during RSD switching on process and prevents passing of I_R current through load Z. Then inductance L_1 drastically reduces after saturation of the core, initial polarity U_0 voltage is applied to RSD stack, RSDs switch on simultaneously without delay and power capacitor C_0 discharges through load Z. Resistor R prevents discharge of C_0 capacitor through the control system circuit.

In the circuit on the Figure 3 power capacitor C_0 and triggering capacitor C are charged initially up to U_0 voltage. Then triggering switch K is turned on and capacitor C recharges through the circuit RL_2. RSD stack blocks negative voltage on capacitor C when the voltage on capacitor C changes the polarity. I_R triggering current forming by L_2 inductance passes through RSDs structures and decays slowly with time constant L_2/R. Saturable core choke L_1 has large inductance during this process and prevents discharge of C_0 capacitor through the load, but after saturation of the core U_0 voltage is applied to RSD stack and RSDs switch on simultaneously without delay.

The parameters of control system elements L_2, R, C in both circuits of Figures 2 and 3 provides the duration of I_R triggering current higher than time of L_1 choke core saturation. This is very important to prevent the delay between reverse triggering pulse current and main forward pulse current through RSD. Otherwise due to recombination process the charge stored into RSD structures by reverse current may decrease below the lowest acceptable limit.

Remagnetization system is necessary to put the core of L_1 choke into initial unsaturated state.

Single-turn coaxial construction of choke L_1 allows to obtain very low inductance of L_1 in saturated state and therefore obtain high increase rate of power current. The size of the choke may be reduced by using short triggering pulses. But the amplitude of triggering current in this case should be high. For example, for 500 ns duration of triggering pulse current and 3" diameter RSD the triggering pulse amplitude should be more than 1.5 kA. To obtain so high triggering pulse parameters and eliminate high loses we should use special semiconductor devices for triggering switch K.

4 Deep level dynistors – new nanosecond range power semiconductor devices.

It is possible to use pulsed thyristors for RSD triggering, but more promising devices are Deep Level Dynistors (DLD) which have been developed recently at Ioffe Physico-Technical Institute (Russia). The most advantages of DLD are subnanosecond switching on time, dI/dt capability up to 250 kA/μs, operating current up to few tens kA and relatively low cost provided due to simple technology process.

Deep Level Dynistors (DLD) is a four layers two electrodes thyristor type device (Figure 4) on the base of silicon doped by the impurities, forming deep levels at the middle of the band-gap.

In initial state the voltage U_0 (2…2.5kV) is applied across DLD forming the space-charge region near the collector junction. Switch-on process is initiated by short (1,5-2 ns) overvoltage pulse with dU/dt not less than one kilovolt per nanosecond applied to the dynistor. The electric field at the collector region in this case essentially exceed the critical value of static avalanche breakdown field because there are no free carriers which can cause the impact ionization of silicon lattice in this region.

When electric field exceeds ~$3 \cdot 10^5$ B/cm, the tunnel ionization of impurity centers occurs, electrons appear in the super-high field region and cause the intensive impact ionization. The front of impact ionization moves with velocity 3-5 times higher than saturated velocity, leaving electron-hole plasma behind itself. This plasma with a high

conductivity fills the base layer and causes fast DLD switching into conductive state. Typical duration of this process does not exceed several hundreds of picoseconds.

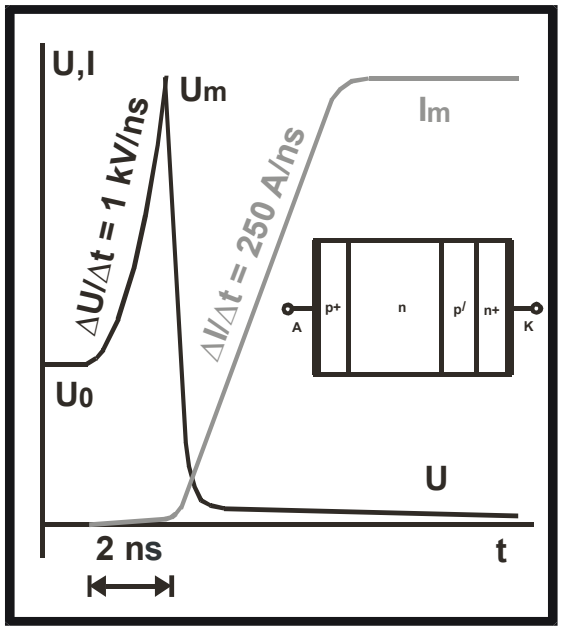

***Figure 4**: Schematic structure of deep level dynistor as well as voltage and current pulse forms during switching on process*

After switching, high conductivity state of dynistor is supported by carriers injection of from p^+ and n^+ injectors. Very fast switching time and low voltage across the device in the on-state lead to very low switching energy losses; as a result dI/dt capability of FID can be as high as several hundreds kiloampere per microsecond.

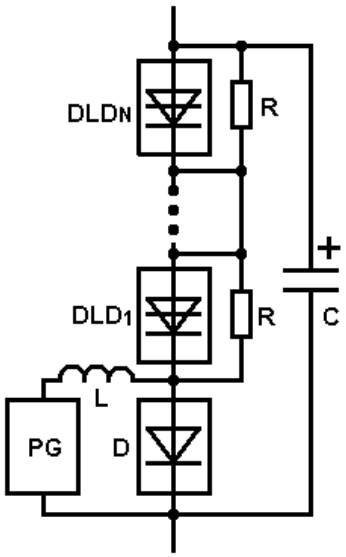

***Figure 5**: Principal electrical circuits of DLD based switch*

The principal electrical circuit of high voltage DLD based switch is shown on Figure 5. DLD_1-DLD_N are serially connected dynistors. Nanosecond pulse of overvoltage for DLD triggering is formed by inductance L, capacitor C and Drift Step Recovery Diodes (DSRD) assembly D.

DSRD is nanosecond high voltage (1-1.5kV) switching-off diode with deep diffusion pn junction. Nanosecond current interruption by DSRD is possible under special commutation conditions. At first 100 ns pulse of direct current formed by PG generator passes through DSRD, provides electron-hole plasma in base layer and store the charge inside diode structure. After that reverse pulse current pulls of plasma from the diode and result in very fast DSRD switching-off for a few nanoseconds. Nanosecond rise time high voltage pulse is applied to DLD_1-DLD_N -C circuit and result in DLD stack switching on.

Resistors R are used to equalize static voltage drops between DLD_1-DLD_N.

5 Design of RSD based switches and experimental results

Photo of power RSD switch with DLD based triggering system is shown on Figure 6. Principal electrical circuit of the switch is shown on Figure 3.

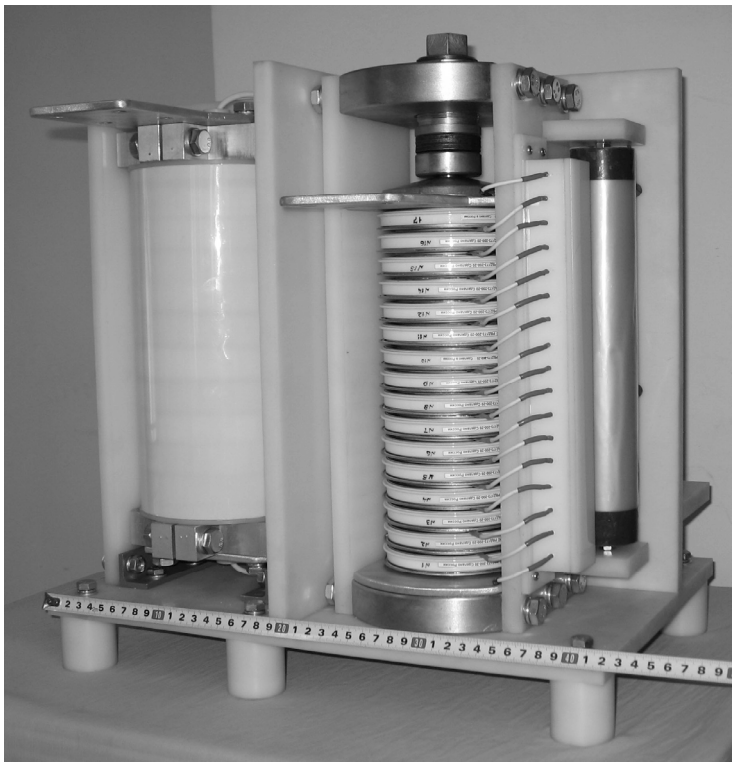

***Figure 6**: 250 kA 25 kV RSD based switch with DLD triggering system*

One can see at left side single-turn saturable core choke, at right side RSD stack with varistor divider and triggering capacitor C behind the RSD stack.

Main parameters of the switch are the following:

- Maximum pulse current 250 kA
- Pulse duration 300 μs
- Maximum operation voltage 25 kV
- RSD stack 16 RSDs with 3" diameter of semiconductor structure

Triggering DLD based switch has maximum operation voltage 25 kV. Triggering pulse current amplitude is 2.5 kA, pulse rise time is 200 ns. DLD stack consists of 12 serial connected 12mm diameter DLDs. Photo of DLD switch is shown of Figure 7.

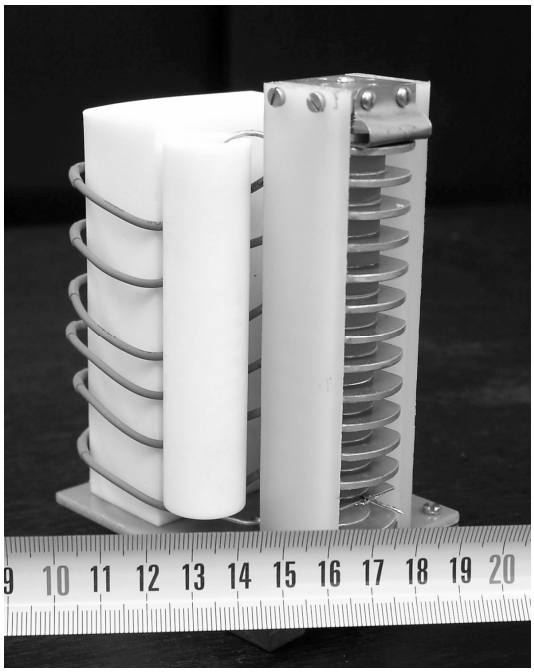

Figure 7*: 25 kV DLD based switch with few nanosecond pulse rise time*

Principal electrical circuit of DLD switch is shown on Figure 5. One can see at the photo DLD_1- DLD_{12} stack with diode overvoltage pulse former based on DSRD assembly (bottom device in the stack), triggering capacitor C. Resistors R and inductance L are placed into compound filled box (behind the stack and capacitor).

The oscillograms of RSD based switch pulse current I_0 and voltage drop U at RSD stack during commutation process are shown of Figure 8.

One can see that negative pulse voltage drop on RSD stack is relatively higher. Small total square of RSD reverse conductivity channels limits the maximum amplitude of reverse pulse current at 10-15% level of forward pulse current.

The circuit shown on Figure 9 is used to form slowly decay alternating-sign pulses in the load. Saturable core chokes L_1 and L_2 have high inductance during RSD triggering and separate control system CS from power circuit and diode stack D. Choke L_1 block U_0 voltage of capacitor C_0, choke L_2 blocks reverse voltage U_R on RSD which occurs in RSD stack during triggering process. The size of choke L_2 is small because U is much less than U_0. When core of choke L_1 saturates forward U_0 voltage is applied to RSD stack, RSD stack switches on and commutates power pulse current through the load R_0L_0.

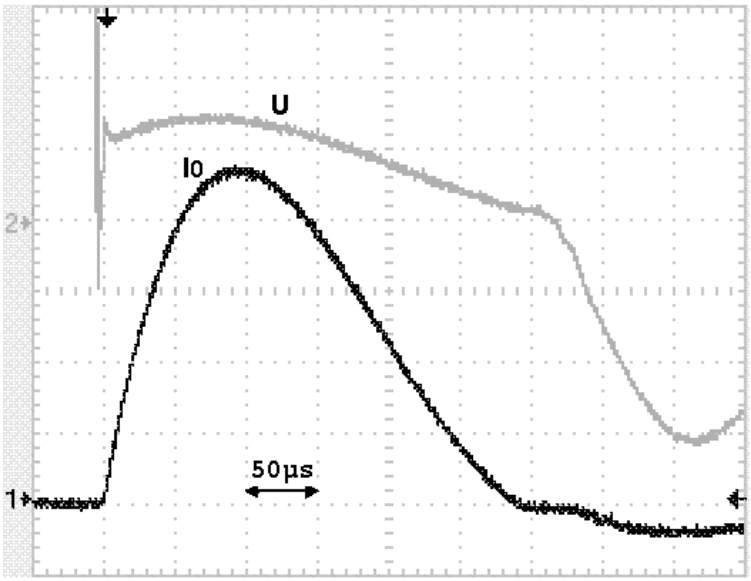

***Figure 8**: Oscillograms of RSD based switch pulse current I_0 and voltage drop on RSD stack during commutation process. Time scale of X-axes is 50 µs/div, Y axes scales are 50 kA/div and 5V/div.*

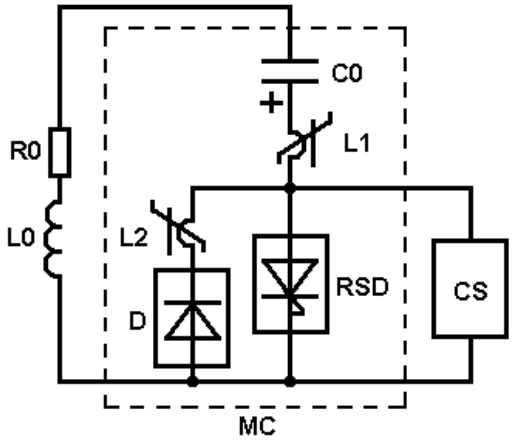

***Figure 9**: Principal electrical circuit of RSD based switch with additional diode stack to form slowly decay alternating-sign pulses on the load*

When capacitor C_0 recharges to negative polarity, chokes L_1 and L_2 block reverse voltage and after saturation of L_1 and L_2 cores negative pulse current passes through parallel connection of RSD stack and diode stack D. Reverse power current through RSD stack is low because conductivity of diodes in open state are higher than reverse conductivity of RSD. But this small current keeps RSDs in open state and prevents RSD stack switching off. Therefore slowly decay alternating-sign pulses passes through the load.

Power current rise rate for all described above RSD switches is determined by saturated inductance of L_1 choke and stray inductance of RSD stack. The coaxial construction of choke L_1 is used to increase the power current rise rate (see Figure 10).

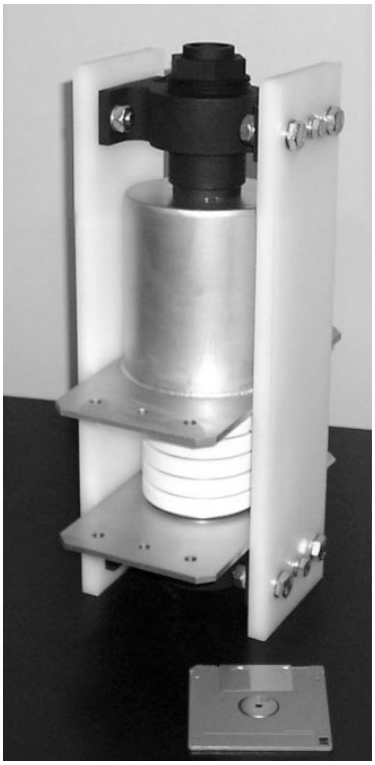

***Figure 10**: 200kA 12 kV RSD based switch with coaxial saturated core choke. dI/dt=30kA/μs*

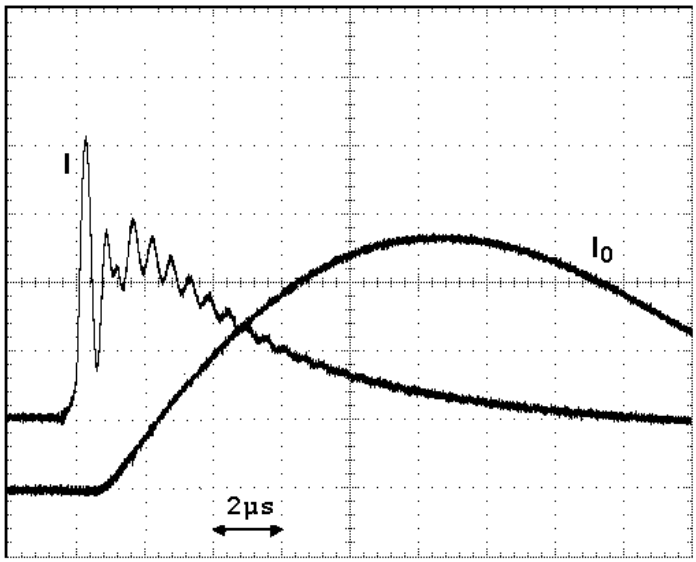

***Figure 11**: Oscillograms of RSD based switch with coaxial choke pulse current I_0 and triggering pulse current I. Time scale of X-axes is 2 μs/div, Y axes scales are 50 kA/div and 500A/div correspondingly.*

Main parameters of RSD based switch with coaxial saturated core choke are the following:

- Maximum pulse current 200 kA
- Pulse duration 30 μs
- Maximum operation voltage 12 kV
- Current rise rate 30 kA/μs
- RSD stack 7 RSDs with 2" diameter of semiconductor structure

The oscillograms of power pulse current through the load I_0 and triggering pulse current I are shown of Figure 11.

It is possible to increase energy of the pulses commutated by RSD switches by increasing operation voltage U_0 or by increasing pulse current I_0. Both are possible. Reliability of RSD stack, simple construction and simultaneous switching on series connected RSDs allow to increase operation voltage up to 50 kV and more. Maximum pulse current commutated by 4" diameter RSD is more than 400 kA. The simple parallel connection of RSD stacks is possible to increase pulse current additionally.

6 Conclusion

Up to gigawatt pulse power compact switches with up to 50 kA/μs current increase rate is possible to build based on assembly of series connected reversed switch-on dynistors (RSDs) and coaxial saturable-core choke. Due to uniform over device area switching on process the switching capability of RSDs is 1.5 – 2 times higher than those of the best modern pulsed thyristors with the same diameter of semiconductor structure. Simple and reliable construction of RSD based switches are designed and described in the article.

The possible area of RSD switches application are pulsed electromagnetic and electro hydraulic technologies, laser technologies, nuclear research, purification of industrial gases and water by electrical discharge etc.

References

[1] *Gorbatyuk, A.V., Grekhov, I.V., Korotkov, S.V., and Yakovchuk,N.S.,* USSR Inventor's Certificate no. 1 003 699, Byull. Izobret., 1983, no. 39, p. 259.

[2] *Gorbatyuk, A.V., Grekhov, I.V., Korotkov, S.V., et al.*, Pis'ma Zh. Tekh. Fiz., 1982, vol. 8, no. 11, p. 685 [Sov. Tech. Phys. Lett. (Engl. Transl.), vol. 8, no. 6, p. 298].

[3] *Korotkov, S.V.*, Prib. Tekh. Eksp., 2002, no. 4, p. 5 [Instrum. Exp. Tech. (Engl. Transl.), 2002, no. 4, p. 437].

Assessing the Effective Energy for Magnetic Forming Processes by Means of Measurements and Numerical Calculation*

P. Werdelmann[1], J.Rosendahl[2], D. Peier[1], S. Kulig[2]

[1]Institute of High Voltage Engineering and Electromagnetic Compatibility,
Dortmund University of Technology, Germany
[2]Institute of Electrical Drives and Mechatronics,
Dortmund University of Technology, Germany

Abstract

The efficiency of magnetic sheet metal forming processes is strongly depending on the facility's overall design. This mainly includes the geometric layout of forming tool, work piece and matrix but, however, will also expect the energy storage device being taken into consideration. Apart from field theoretic models the energy storage is describable by its terminal traits which the electric load - tool coil and work piece - is connected to. The paper presents a measuring method for the tool coil's terminal quantities, current i(t) and voltage u(t), which are used to provide the electric power p(t) being transferred to the load. Thus, it is possible to determine the entire energy which is dissipated by the work piece, provided that the coil's resistance is known. Besides the measurement, this approach is supported by numerical calculation intending to take a closer look at the inner losses of the work piece which are not accessible from measuring the system's terminal traits directly. Dividable into separate parts of the total energy, this information is applied to assess the forming process by means of the facility's energetic performance and to draw an overall energy balance.

Keywords

Electromagnetic Forming, Energetic Efficiency, Measurements

---

* *The authors want to thank the* Deutsche Forschungsgemeinschaft *who founded the research group FOR 443 for the financial support, which made the presented investigation possible.*

1 Introduction

Electromagnetic sheet metal forming facilities typically consist of a tool coil, the workpiece and a primary energy store, which itself is built of capacitive elements just because they are very easy to handle and do not need comprehensive switching efforts compared to inductive energy stores. However, the efficiency of energy transfer will differ depending on the storage facility's layout as the load will evidently show resistive-inductive behaviour [1]. The load which is connected to the energy store in this work is pictured in figure 1 and shows a spiral coil positioned in parallel under a thin conducting metal sheet.

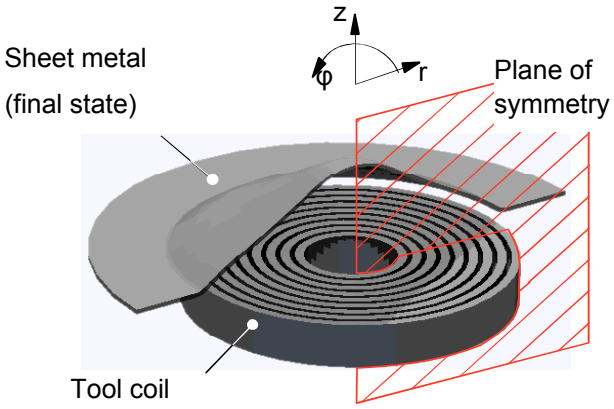

***Figure 1**: Scheme of the geometric setup of the load configuration which is connected to the energy store. The numerical model is based on this setup and the measurements of voltage and current were performed at the tool coil's terminals.*

The induced eddy currents inside the work piece will interact with the coil's excited flux density making the plate bulge into a new shape. This mechanic work is to be transferred into the sheet metal by transforming the initially stored electric energy into magnetic energy. These types of energy conversion have different efficiency factors and will have to feed energy drains like eddy current heating losses [6]. The assessment of these losses compared to the initially stored energy is performed by measurements of the tool coil's terminal quantities and completed by numerical simulations in the following.

2 Measurement of the Tool Coil's Terminal Quantities

The tool coil's and work piece's electric characteristics can be determined in total by measuring the terminal quantities at the coil's input clamps which are the current $i(t)$ and the voltage $u(t)$.[†] The multiplication of both represents the electric power $p(t)$ which itself delivers the totally dissipated electric energy when being integrated with respect to time. The current is measured by making use of a Rogowski inductive current sensor which is already integrated into the facility setup. The more difficult challenge is to identify the

[†]*The measurements have been carried out at the sheet forming facility Maxwell7000 , IUL, Dortmund University of Technology.*

correct voltage at the forming tool's clamps; apart from the ability to withstand the occurring voltage stress, synchronicity between the current and the voltage signals has to be guaranteed. For these reasons, an ohmic-capacitive voltage divider is designed and mounted in close vicinity to the current signal's pick-up. Because of the symmetric structure its layout is optimized to minimize inductively coupled signals due to very high magnetic field strengths in it is surrounding. The voltage divider as well as the corresponding equivalent circuit diagram is pictured in figure 2.

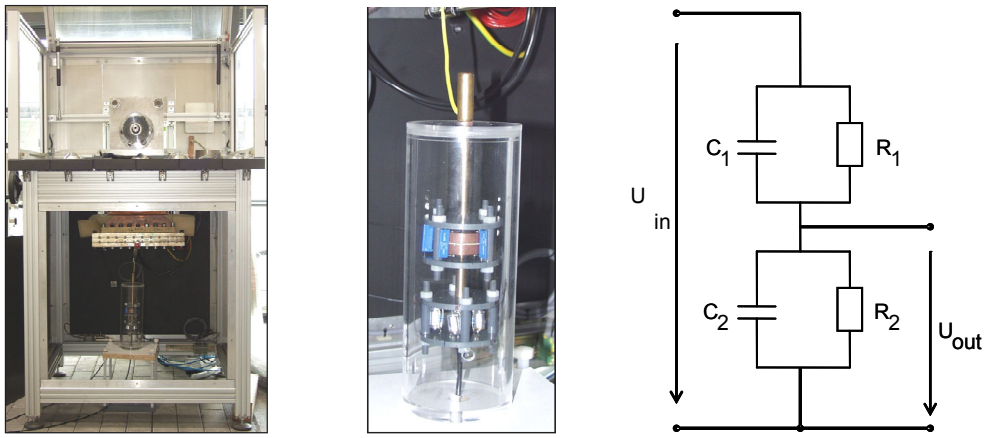

***Figure 2**: The resistive-capacitive voltage divider is placed in the tool coil's close vicinity and is coaxial symmetrically designed to minimize current-induced failure voltages.*

The intended impedance in the upper and lower branches are designed to R_1 = 50 kΩ, C_1 = 50 pF and R_2 = 50 Ω, C_2 = 50 nF to obtain a divider ratio of T = 1000 which is not a function of the frequency. However, due to parasitic influences of the surrounding the divider's ratio between input voltage to output voltage is depending on the frequency and amounts T = 983 for a frequency of f = 15 kHz. Figure 3 gives an overall view on the forming facility to show where the measuring sensors have been mounted.

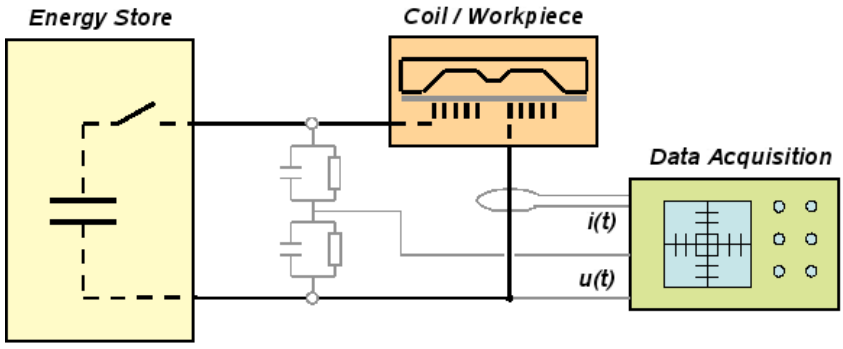

***Figure 3**: Schematic block diagram of the forming facility consisting of energy store, tool coil and work piece. To obtain the input power a voltage divider and an inductive current sensor provide the signals which are picked up by the data acquisition setup.*

Both, the current i(t) and the voltage u(t) at the coil's terminals have been recorded synchronously and are used afterwards to determine the electric input power p(t) which is transferred into the system 'tool coil – work piece'. The following figure 4 reveals the

measured current and voltage for an electromagnetic forming process as well as the resulting electric power *p*(t).

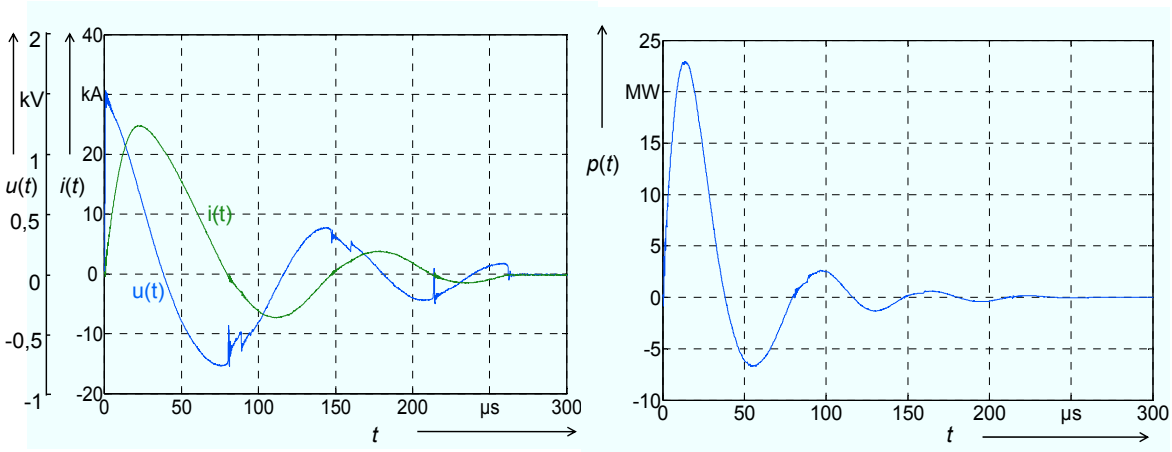

***Figure 4**: Current i(t) and voltage u(t) (left figure) measured at the tool coil's terminals while forming an aluminum sheet (AlMgSi0.5, d = 1.2 mm, W_{charge} = 556 J) from which the electric power p(t) (right figure) is calculated.*

The voltage at the tool coil's terminals for $t = 0$ represents the capacitor bank's charging voltage as there is no voltage drop along the connecting wires. This value amounts $U_{charge} = 1483$ V in this experiment and therefore the charging energy is determined by knowledge of the energy store's capacity of $C = 505.2$ µF to

$$W_{charge} = \frac{1}{2} \cdot C \cdot U_{charge}^2 = 556\ J \qquad (1)$$

The measured voltage shows some unsteady and repetitive leaps which may be caused by sudden cut-offs of the ignitron switching devices as this effect happens for the current crossing zero. However, this phenomenon is smoothened regarding the electric power and will therefore only have little effects on the totally transferred energy.

3 Assessment of the Effective Energy

3.1 Assessing the Effective Energy Transfer by Measurement Data

The electric power *p*(t) which enters the tool coil's terminals is integrated with respect to time in order to obtain the total energy which is transferred into the system 'tool coil – work piece'. A classic energy balance only uses the values for the electric process having completely finished; disregarding this, figure 5 reveals the different parts of energy as functions of time, because especially in the current waveform's beginning there are huge parts of energy temporarily being stored in the magnetic field. This energy is given back to the primary capacitive energy storage device as long as the product of coil current and voltage is negative. In the beginning of the impulse current the energy that enters the coil's terminals is higher than the finally transferred energy. The exponentially damped but freely oscillating discharge causes irreversible losses in the conducting structures of the

entire facility but even though, a part of it is used to support the aim of bulging the aluminium sheet into it's new shape.

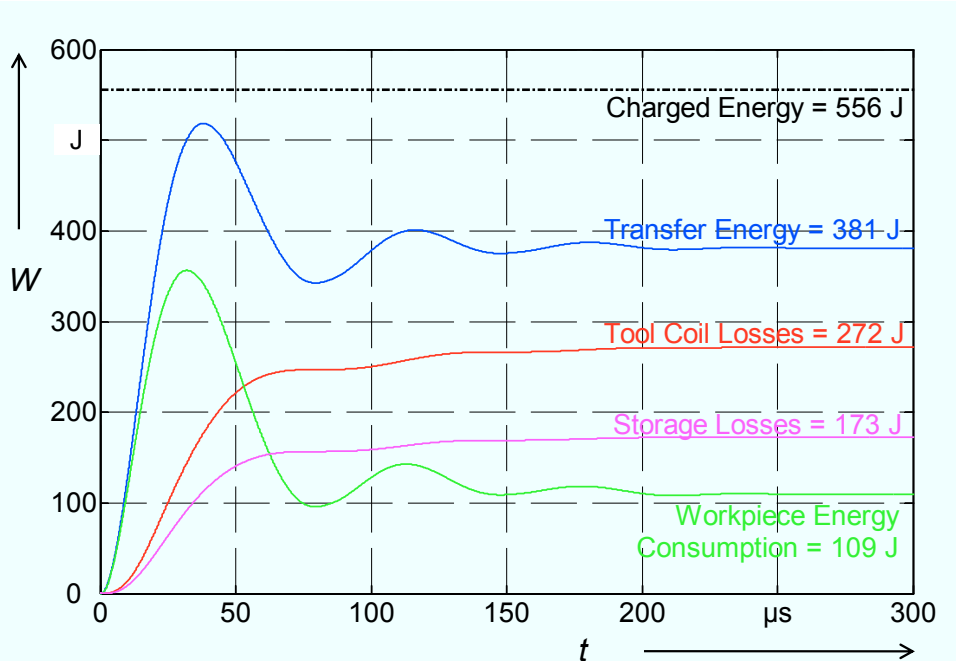

***Figure 5**: The cumulative parts of energy calculated from measured terminal quantities draw a complete energy balance of the energy transfer.*

In the beginning of the impulse current the energy that enters the coil's terminals is higher than the finally transferred energy, which is due to the fact, that this amount of energy is stored in the magnetic field temporarily and pushed back to the capacitor.

The part of energy which passes the tool coil's terminals is dividable into tool losses and the effective energy which is dissipated by the work piece. The storage losses are calculated from the initially stored energy and the part of energy which has been totally transferred to the tool coil and the work piece. However, the energy storage does not discharge completely on the tool coil; there is still some voltage ($U_{t=260\mu s}$ = 85 V) left on the capacitors at t = 260 µs and the ignitron devices do not switch again, which is evident as the current falls to zero and does not rise again (see fig. 4). Therefore, this part of energy, which is definitely not transferred to the load, is taken into consideration for reasons of accuracy which reveals the storage losses to:

$$W_{storage} = \frac{1}{2} \cdot C \cdot \left((1483V)^2 - (85V)^2 \right) - W_{transfer} \approx 173\,J \qquad (2)$$

With this value it is possible to determine the inner ohmic resistance $R_{storage}$ of the energy storage. The dissipated energy can be expressed by the current and reveals a conditional equation for the storage loss resistance:

$$W_{storage} = \int R_{storage} \cdot i(t)^2 \, dt \quad \Rightarrow R_{storage} = \frac{W_{storage}}{\int i(t)^2 \, dt} = 6.98 \, m\Omega \tag{3}$$

In earlier works [2], the coil's network elements have been identified from which in detail the ohmic coil resistance R_{coil} = 11.2 mΩ is of particular interest in this case. With this value the tool coil losses are calculated as cumulatively shown in figure 4 reaching an end value of 272 J.

The amount of energy which is dissipated by the work piece contains the mechanical energy but also the part being responsible for joulean heating of the aluminum sheet and amounts 109 J after the electric process has finished at approximately t = 260 µs. There is no direct access to the current density within the work piece making it not possible to distinguish between both from the measurements.

3.2 Assessing the Effective Energy Transfer by Numerical Calculation

Numerical field calculation methods are useful to get a deeper insight into the forming process. An electromagnetic field calculation system like FELMEC 2 ½ D calculates the magnetic vector potential on the cross section of an axially symmetrical arrangement as in figure 1. From the vector potential the remaining magnetic field quantities as well as the forces on the work piece can be calculated. A structural mechanic simulation system like SOFAR calculates the movement of the forming object from the exerted forces. The programs FELMEC and SOFAR have been developed at Dortmund University of Technology by the research group FOR 443 as well as the coupling of both. The coupled programs use the time stepping method to allow transient calculation of the forming process. The explicit coupling alternately determines the electromagnetic forces and the movement of the work piece during each time step. Since the methods are already presented in the literature ([3], [4] and [5]), just the most important aspects are described here.

In many previous investigations a measured current is used as an excitation for the simulation of the forming process in coupled simulations. The necessity of preceding measurements is reasonably unsatisfying when simulation tools are applied to predict the forming result. The coupling of SOFAR and FELMEC is able to follow that procedure, but nevertheless a further coupling of electric networks allows the consideration of equivalent network elements for the capacitor bank. The results presented in this chapter are based on numerical field calculations of the forming process by only giving the initial voltage and capacity of the energy storage device. By this approach the current is a degree of freedom in the calculation and preceding measurements are not required for the simulation of a forming process. Thus, arbitrary combination of capacities and initial energies may be simulated for parameter studies with respect to the efficiency like presented in [6].

However, measurements are useful to enhance the accuracy of any simulation. Using the results presented above, an ohmic resistance can be calculated which represents the total losses in the capacitor bank and the power lines to the tool coil for this special example. It is used as a lumped element in the coupled numerical field calculation of the example set up in chapter 2 with a capacity of 505 µF and an initially stored energy of 556 kJ.

The evaluation also focuses on the different influences of the forming facility's modules on the process in terms of energy drains. Now a complete energy balance may be drawn because the thermal losses can be calculated by knowledge of the current

density on the cross section of the tool coil in the *r*,*z*-plane. The mechanical power absorbed by the work piece is determined by (4) since the force and the velocity are known quantities of the field calculation.

$$p_{mech}(t) = \int f(t) \cdot v(t)\, \mathrm{d}A \tag{4}$$

The ohmic losses due to the resistance of the storage device can be directly calculated by equation (5).

$$p_R(t) = i(t)^2 \cdot R \tag{5}$$

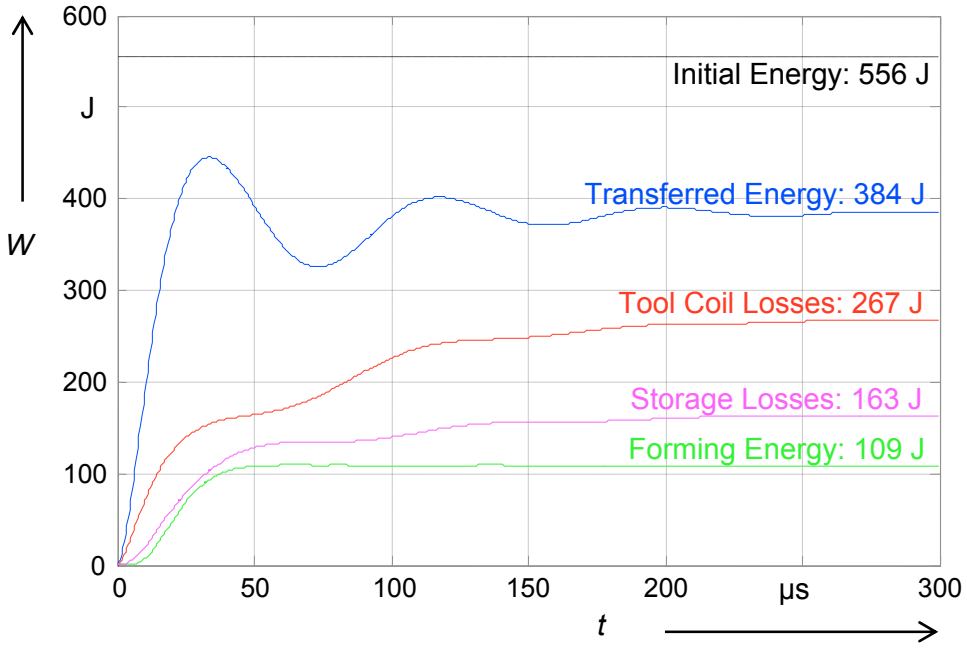

Figure 6: *Variation of the different kinds of energy over time determined by the numerical field calculations for a forming process with a capacitor bank of 505 µF and an initial energy of 556 J.*

The apparent power transferred into the sub system tool coil and work piece is given by the multiplication of the voltage and current as in the case of the measurements. The energy at each time step is determined by integrating the power with respect to time. The curves in figure 6 are the cumulative sums of the energy calculated at each time step and show the energy dissipation of the different modules of the facility as results of the simulation.

The ohmic loss energies represent the dissipation into thermal energy of the storage device and the tool coil. The effects are not reversible in this application and the curves are continuously increasing as can be seen for the mechanical energy. The transferred energy instead may temporarily be higher than the totally transferred energy at the end of

the forming process, since the reactive energy oscillates between the tool coil and the work piece. The results show quite good accordance with the measurements.

4 Summary and Conclusions

This work focussed on assessing magnetic sheet metal forming facilities regarding the effective energy which is transferred from a primary capacitive energy storage device to a time-variant load consisting of forming coil and workpiece. The results are obtained by measuring the tool coil's terminal quantities current and voltage from which the totally transferred power as well as the energy are calculated. Different parts of energy can be separated which makes it possible to draw a comprehensive energy balance for the forming process as a function of time.

The experiments are compared to simulation results where both, the measured results as well as the numerically obtained match each other exactly in revealing the fact, that the main part of the initially stored energy is used to cover any unwanted drains and energy losses and only less than 20 % can be used mechanically. Almost half of the energy is needed for heating up the tool coil; this shows the necessity to design a forming tool which is appropriately fitted to the demands of the volume forces' radial distribution and even more to optimize existing energy storage devices including innovative and appropriate switching technologies.

References

[1] *Werdelmann, P.; Peier, D.*: Purposive Design of a Magnetic Sheet Metal Forming Facility. 2nd International Conference on High Speed Forming, Dortmund, 2006

[2] *Werdelmann, P.; Peier, D.*: Approaching Parameter Identification of Magnetically Coupled Systems by Means of Optimization Procedures. Proceedings of the 10th International Conference on Optimization of Electrical and Electronic Equipment. May 18th - 20th, 2006, Brasov, Romania, Vol. 1, pp. 71-77

[3] *Kost, A.*: Numerische Methoden in der Berechnung elektromagnetischer Felder. Springer-Verlag, Berlin, Heidelberg, New York 1994

[4] *Stiemer, M.; Klocke, M.*: Validation of different Approaches to Coupled Electro dynamical-Structural Mechanical Simulation of Electromagnetic Forming. 1st International Conference on High Speed Forming, Dortmund, 2004

[5] *Kleiner, M.; Brosius, A.; Blum, H.; Suttmeier, F. T.; Stiemer, M.; Svendsen, B.; Unger, J.; Reese, S.*: Benchmark Simulation for Coupled Electromagnetic-Mechanical Metal Forming Processes. Annals of the WGP, Production Engineering Vol. XI/1, 2004

[6] *Rosendahl, J., Werdelmann P., Azer S., Klocke, M.*: Qualifizierung unterschiedlicher Energiespeicher bezüglich einer Optimalen Energieübertragung. Springer Verlag, Werkstatttechnik online Jahrgang 98 H. 1/2, Düsseldorf, 2008

Reliability of Solid State Switches Used in High Current Discharge Applications

A. Welleman, B. Backlund

ABB Switzerland Ltd, Semiconductors, Fabrikstrasse 3, CH-5600 Lenzburg / Switzerland
(adriaan.welleman@ch.abb.com)

Abstract

The presentation will give information about the long term reliability of semiconductor components which are used in high current, high di/dt discharge switches as they are used in systems for electro-magnetic forming. Prototype equipment for laboratory use has shown the capability of the switches and equipment to fulfil the requirements requested by the end-users. This however is not enough to be used in the industrial production lines under continuous and repetitive heavy load conditions. Because of the relative high life-time expectations of the durable equipment used for magnetic forming in the automotive industry the life-time of the semiconductor switches, the inductive loads and the capacitor banks are becoming an issue. The presentation will only describe the semiconductor reliability.

A prototype system for 21 kVdc and pulse current of 210 kA was designed and built in the year 2005 by Siemens for the Fraunhofer Institute in Chemnitz, Germany. The semiconductor switch was supplied by ABB Switzerland Ltd. For this experimental machine only low repetition rates of one shot per several minutes and a limited expected life-time of approx. 15.000 – 20.000 shots was acceptable for the experimental work. The requirement from the automotive industry however is at least one shot per 15 seconds and an operational life-time of ≥ 2 Mio shot at the mentioned power level. During the last year ABB has done extensive tests to evaluate the behaviour of the semiconductor components used in high current solid state switches under the specific application conditions for production processes.

In the presentation the test results of high current semiconductor devices are described for 250.000 shots and 1 Mio shots, and recommendations for reliable solid state switch designs are given.

Keywords

Semiconductor Device, Solid State Switch, Life-time, Switch reliability

1 Introduction

Semiconductor devices have made dramatic progress in power handling during the last decade. The today's technology and production capabilities make it possible to produce devices with high blocking voltage combined with very high current handling. Depending on the design and the device structure also very high current rise rates in the range of up to several tenths' of kA/µs are possible. Especially for single pulse or medium pulse repetition rates semiconductor devices are getting more and more competitive to conventional technologies like Thyratrons, Ignitrons, Spark-Gaps and Mechanical Switches. The main advantages are the reliability, lifetime and almost no maintenance of the semiconductor switches if the characterization is done right. Main advantages like longer life-time, environmental friendly (no mercury etc.) and flexible mounting position are compensating the higher initial cost of a solid state design. The type of semiconductor used and the rating of the device are extremely important for a reliable operation and need an in-depth know-how of the application and the switching device. ABB has developed over the years a specific range of semiconductor devices and adapted standard products which can fulfil the requirements for pulsed applications. Based on the 21 KV / 210 kA switch assembly, supplied for an experimental system, which was described at the ICHSF 2006 [1] further reliability tests were done to evaluate the behaviour of the semiconductor devices under the given application conditions. This paper will show some of the results of tests.

2 Device Technology

Semiconductor devices for pulsed applications can be divided in Turn-On and Turn-Off devices. Turn-On devices are Thyristors structures and in the group of Turn-Off devices we find the GTO's (Gate-Turn-Off Thyristor), IGCT's (Integrated Gate Controlled Thyristor) and IGBT's (Insulated Gate Bipolar Transistor). For high energy short pulse discharge applications, like high speed forming, mostly thyristor technology is used. The table below gives a short overview of the different possibilities.

Device Type	Max. Forward Blocking Voltage	Max. Peak Pulse Current Capability	di/dt	Switch-On	Switch-On/Off
Thyristor	≤ 8500 V	120 kA	1.5 kA/µs	Yes	No
GTO-Like Thyristor	4500 V	150 kA	50 kA/µs	Yes	No
Integrated GTO-Like Thyristor	4500 V	150 kA	50 kA/µs	Yes	No
GTO	4500 V	4 kA	3 kA/µs	4 kA	4 kA
IGCT	≤ 6000 V	4 kA	2 kA/µs	4 kA	4 kA
IGBT (Wire bonded module)	≤ 6500 V	1 kA	5 kA/µs	1 kA	1 kA
IGBT (Press Pack Module)	4500 V	2 kA	5 kA/µs	2 kA	2 kA

***Table 1**: Overview of different semiconductor device technologies.*

For High Speed forming the use of capacitor discharge switching is very common because high energy has to be switched into a load in a very short time. The capacitor can be discharged completely, and means that devices with high switch-on capability

were selected. The devices used for the reliability test were Integrated GTO-like Thyristors which are used in the 21 kV / 210 kA discharge switch. The driver unit is integrated with the device and the freewheeling diode is monolithic integrated on the same silicon wafer as the switching part to minimize induction.

2.1 GTO-like Devices

Thyristor (SCR) technology is a well proven solution which is used for high current, relative long pulses and low current rise rates in capacitor discharge applications. Standard commercial of-the-shelf devices can be used as long current rise rates stay clearly below 700 A/µs. Depending on the application, the pulse current, current rise-time, pulse length and pulse repetition rate, different wafer designs can be selected to fulfil the requirements. Figure 1 shows a variety of Ø 51 mm thyristor wafers with different capabilities. Most of the designs are available in different diameters for different current capabilities. Blocking voltages can be from 1800V till up to 8500V per device for the thyristor designs and up to 6000V for the highly interdigitated designs (GTO-like structure). For higher voltage, devices are stacked in series connection.

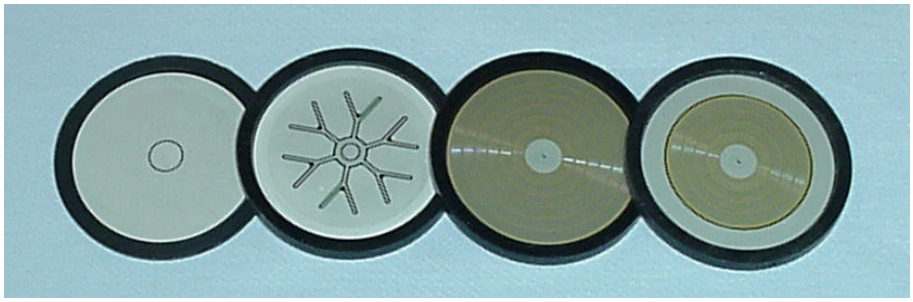

***Figure 2**: Si-Wafers Ø51 mm for di/dt < 0.1kA/µs, 1kA/µs, 18kA/µs and 15kA/µs. The right one is with a monolithic integrated freewheeling diode.*

The two wafers on the right side of the picture are representing the GTO-like wafer structure, of which the right one is the reverse conducting version with monolithic integrated diode. These GTO-Like structures use a lot of small thyristor segments on one silicon wafer, and have a very high di/dt and fast switch-on capability.

2.2 Device Design

In the year 2005 a reverse conducting solid state switch was designed and supplied for 21 kV / 210 kA and up to 400 kA under short circuit conditions. Devices used were of the GTO-like technology, reverse conducting and using 3 parallel devices with 91 mm wafer size, ABB P/N 5SPR 26L4506. Figure 2 shows the semiconductor part built-up.

***Figure 2**: Low Inductive Housing, GTO-Like wafer and Complete Device*

The semiconductor part is combined with a driver unit which is powered by a closed loop current source power supply and optical triggered. This construction enables easy series connection as the isolation voltage of the closed loop high voltage cable is the isolation between the device levels in the switch. This technology is possible for voltages up to 40 kVdc. Figure 3 shows the complete switching device with integrated driver unit.

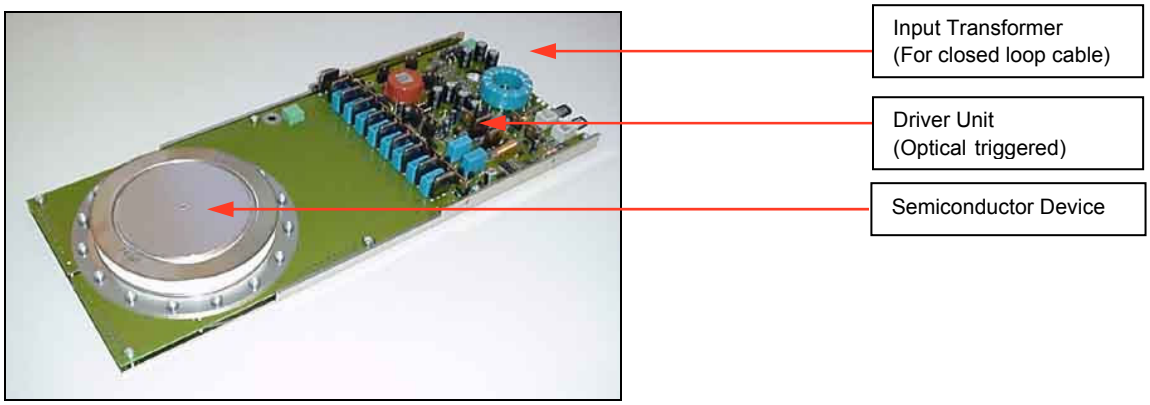

***Figure 3:** Discharge Device p/n: 5SPR 26L4506, Vdrm=4500V complete with driver unit.*

Because of the required current capability, devices with 4500V blocking voltage are used. Higher blocking voltages will reduce the current capability.

3 Switch Assembly

3.1 Reverse Conducting Discharge Switch 210 kA / 21 kVdc / 100 µs

Table 2 shows the basic specification of the complete switch assembly for the 100 kJ discharge system [2], using reverse conducting devices.

To reach the required life-time of 20.000 shots it was calculated that three (Np=3) devices in parallel and eight (Ns=8) devices in series connection have to be used to share the current and voltage. The switch was built-up with three independent stack assemblies each having 8 devices in series connection. The current per device is therefore limited to about 70 kA under normal conditions and 140 kA under short circuit conditions. The last one should happen only maximum 1000 times. Figure 4 shows the circuit diagram of the

switch assembly with 3 stacks in parallel, each stack has its own power supply and one light distribution box will fire each stack independent or all 3 stacks simultaneously.

Parameter	Normal Condition	Short Circuit Condition
Max. Charge Voltage	21 kV	21 kV
Peak Pulse Current Forward	210 kA	420 kA
Peak Pulse Current Reverse	90 kA	150 kA
Current Rise Rate (di/dt)	3 kA/µs	9 kA/µs
Pulse Duration	100 µs	50 µs
Pulse Form	Damped Sine Wave	Damped Sine Wave
Pulse Rep. Rate	1 Shot / Min.	1 Shot / 10 mins
Lifetime	20.000 Shots	1.000 Shots

Table 2. *Specification for Reverse Conducting 210 kA / 21 kV switch assembly.*

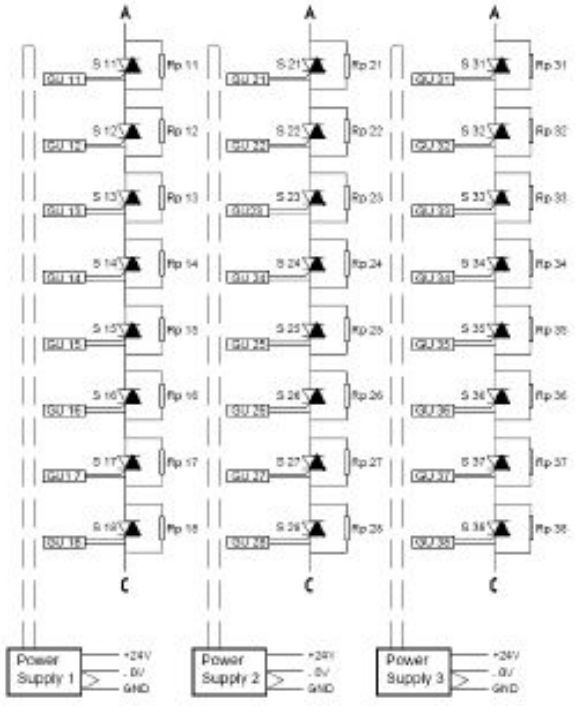

Figure 4: Circuit diagram 21 kV switch

Figure 5: Picture of <u>one</u> stack assembly

Because of reverse conducting devices are used and no switch-off is required no snubber circuit is needed. Only voltage sharing resistors are connected over each device level. Three independent stacks were used in parallel to avoid hard parallel connection of 3 devices. This configuration allows also the use of one single stack if less power is required. Every stack can handle the 70 kA nominal and the 140 kA short circuit condition. The driver units are optical triggered from a light distribution box and this box can be selected to fire 1, 2 or all 3 stacks simultaneously or sequential. The figures below show measurements on one of the stack assemblies.

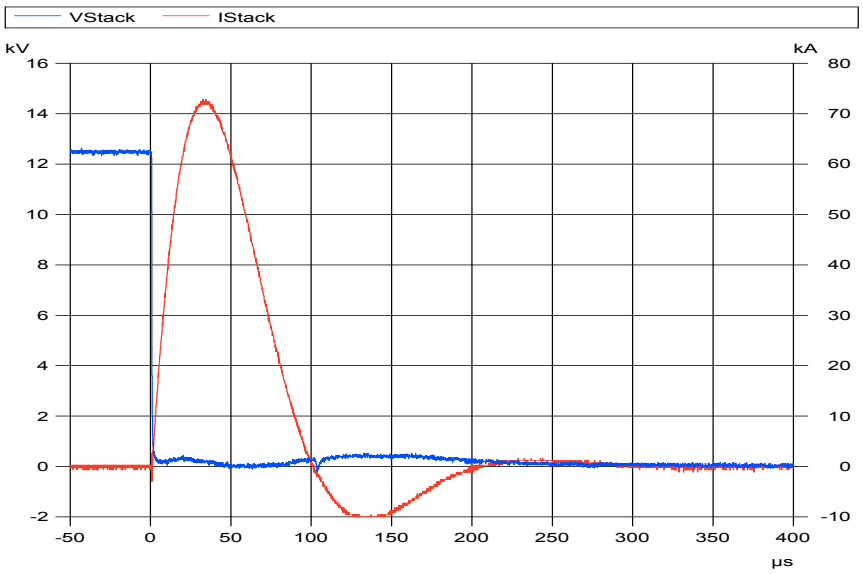

***Figure 6**: Single Stack Pulse Test*

4 Reliability

4.1 Reliability of Devices

Compared to Ignitrons and Spark Gaps, solid state switches have very good life times, but have not infinite life. For a semiconductor device the design and the production processes are most important. Quality- and Process management in the Waferfab are of vital importance. The life-time of a semiconductor is in the application mostly limited by mechanical stress or cosmic ray. Mechanical stress is caused by temperature steps in the silicon due to current pulses. The temperature of the silicon can increase more than 100°C within some micro seconds and the larger these temperature steps are the shorter life-time is expected. Therefore it is important to avoid large temperature steps if long life and high reliability is required. To accomplish this high reliability systems will have more or larger size devices which means often higher costs. Important is also the influence of cosmic ray [3] on the silicon wafer. To reach an acceptable FIT rate (1 FIT is 1 failure in 10^{-9}h) per device of ≤100 it has to made sure that the DC voltage on the device is maximum 65% of the device blocking capability. This means that a device with Vdrm=4500V should not be charged with higher DC voltage as 2900Vdc. In case of higher DC voltage the device will have a reduced life-time. The semiconductor manufacturer can calculate the expected life-time of devices if the application conditions are known in detail. The experimental system was designed for 20.000 shots with a repetition rate of 1 shot per minute but a production line in the industry will need ≥ 2 Mio shots with a repetition rate of one shot every 15 seconds. Therefore ABB has made calculations and several tests to verify the difference.

5 Tests

5.1 Test Conditions

The test was performed with an application oriented damped sine wave of 100 µs duration and I-peak = 70 kA for the first test, later for the second and third test with I-peak = 31 kA.

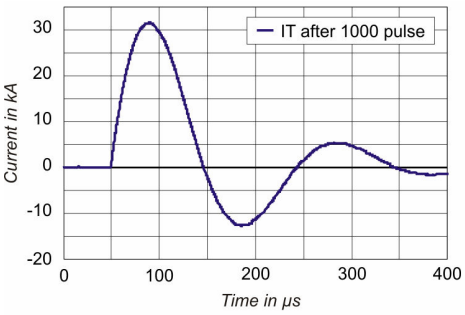

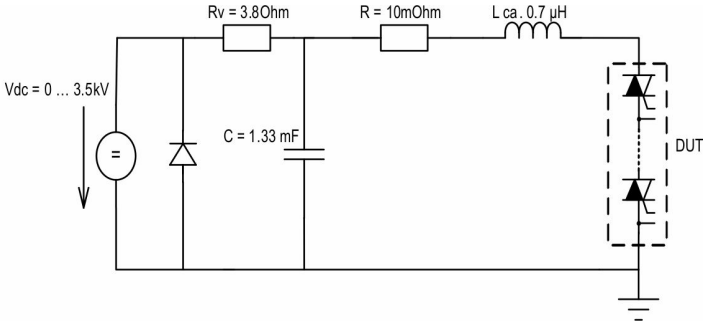

***Figure 7**: Damped Sine wave 100µs* ***Figure 8**: Test circuit*

The test was done with two series connected reverse conducting devices 5SPR 26L4506. Vdc 5.6kV (2.8kVdc per device level) Peak pulse current for the first 20.000 shots was 70kA, later reduced to 31 kA for 250.000 and 1 Mio shots. All devices survived these tests and finally the wear-off at wafer level was analysed.

Test No.	Devices	Date	Vdc charge	I-pulse	t-pulse	Rep. Rate	Shots
1	5SPR 26L4506	27.04.2007	2.8 kV	70 kA	100µs	1 shot / 6 sec	20260
2	5SPR 26L4506	20.06.2007	2.8 kV	31 kA	100µs	1 shot / 6 sec	252600
3	5SPR 26L4506	26.08.2007	2.8 kV	31 kA	100µs	1 shot / 6 sec	1040000

***Table 3:** Overview of tested devices and shots*

The test was done with a pulse repetition rate of 1 shot per 6 seconds, which is 2.5 times more as the specified one shot per 15 seconds. Still the devices did not need active cooling and could be cooled with convection air. Investigations were done, optically at cathode and anode side, with IR camera and Electron microscope REM/EXD.

5.2 Test No. 1 - Device Test 20.000 shots @ 70 kA

After the test the devices were still functioning but leakage current was increasing at a level of 2.8kV and higher. Changes were found at the cathode contact fingers and some molten craters on the aluminium metallisation on the anode side of the wafer. These changes are indicating that the end-of life for the wafer is very near.

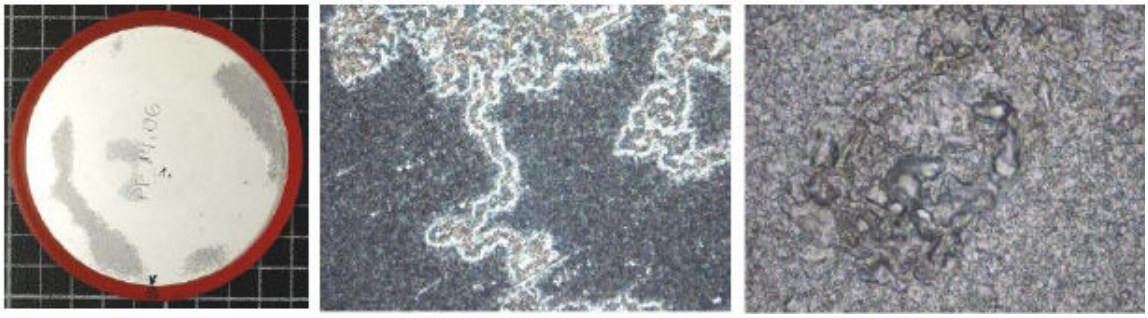

Figure 9: *Anode side of wafer with partly melted aluminium contact layer. Middle picture is enlarged 45x, right picture 440x*

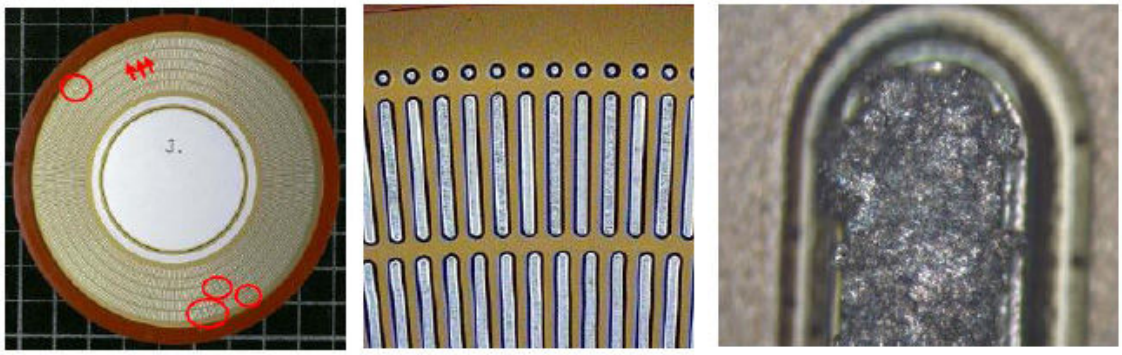

Figure 10: *Cathode side of wafer, middle picture shows contact finger arrangement, right picture shows burned contact finger with almost an cathode-anode short*

5.3 Test No. 2 - Device Test 250.000 shots @ 31 kA

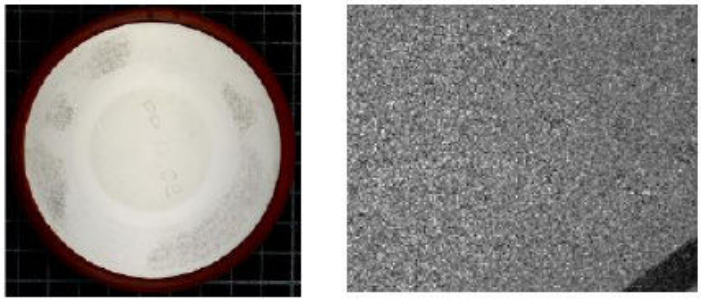

Figure 11: *Anode side of wafer shows uncritical small spots in aluminium contact layer.*

Four additional devices were used for the second test run, but with current reduced to 31 kA at the same pulse width of 100 µs. After 250.000 shots two of the devices were taken out of the switch assembly and dismantled for inspection of the wafer. Both devices were still functioning and the leakage current at 2.8 kVdc was not increased. Very small changes were found at the cathode contact fingers and some melting spots on the aluminium metallisation equally spread over the silicon wafer. The results shows that the damage to the wafers was visible but clearly less as in test No.1, after the device had

seen 12x more shots. With the remaining 2 devices the test was continued, see results under test No.3.

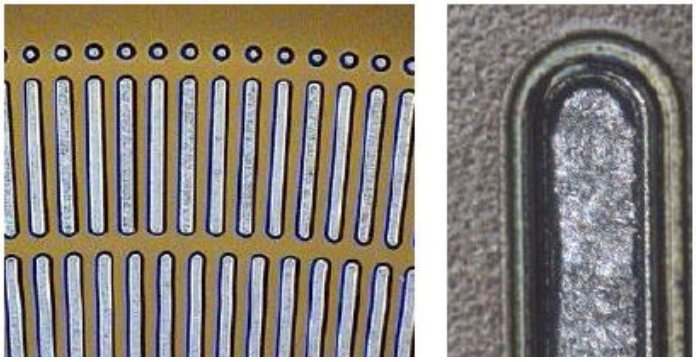

***Figure 12**: Cathode side, contact fingers show very little wear-off and some burned spots, which are uncritical*

5.4 Test No. 3 - Device Test 1.040.000 shots @ 31 kA

Test No.2 was continued with the two remaining devices till a total of more than 1 Mio shots had been performed under the same condition. After 1.04 Mio shots the test was stopped and the wafers analysed. Both devices were still functioning and the leakage current at 2.8 kVdc had not increased. Changes were found at the contact fingers and melting spots on the aluminium metallisation of the wafer. There was no damage, only wear-off which is not critical compared to the result of test No. 1. The small spots on the anode side are dense but not deep in the aluminium layer. It is expected that about 40 – 50% of the life-time was consumed. This will result that a device failure under the given condition of 31 kA @ 100 µs pulse width is not expected before 2.5 Mio shots, which is more than 50x the result of the original experimental design. It has to be mentioned that the tests were done on a limited quantity of random selected devices.

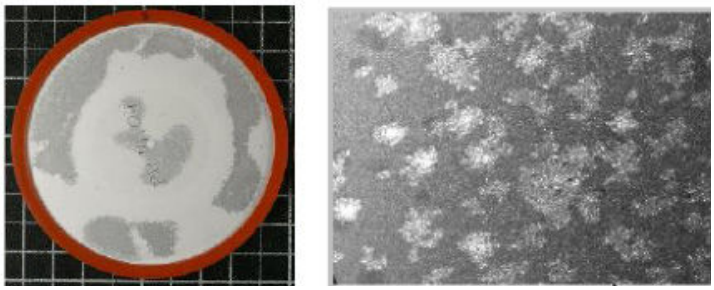 (Enlarged 220x)

***Figure 13:** Anode side of wafer with small molten spots on the aluminium contact layer.*

6 Conclusion

It can be concluded that the devices used for the experimental 100kJ / 21kV / 210kA discharge system are a reliable solution as enough silicon area is used. For industrial use the life-time has to be increased substantially. The test result with the 200kA switch using Np=3 devices (70kA per device) compared to a 210kA switch using Np=6 devices (31kA per device) shows that by almost doubling of the silicon area, an increase in life-time by a factor of 50 can be reached. This also means that a 50x higher reliability will double the cost of the semiconductor switch assembly. The test was performed to give the end-user proven results for industrial applications. Based on the results, it can be stated that the reliability of proper designed solid state switches is clearly superior to ignitrons and spark gaps. Despite the initial higher costs, the solid state design offers much higher reliability, longer life-time and lower operation costs. ABB is striving to further improve the performance, the reliability and reduce the cost for this type of solid state switches.

References

[1] *A. Welleman, W. Fleischmann,* “High Power Semiconductor Devices and Solid State Switches for Pulsed Discharge Applications”, 2nd International Conference on High Speed Forming ICHSF2006, Dortmund, Germany, March 2006

[2] *W. Hartmann, M. Römheld, A. Donner,* „A 100kJ Pulse Unit for Electromagnetic Forming of Large Area Sheet Metals”, 2nd International Conference on High Speed Forming ICHSF2006, Dortmund, Germany, March 2006

[3] ABB Switzerland Ltd Application Note 5SYA 2046 “Cosmic Ray on IGCT”

Novel Layers for Dies Used in Electromagnetic Sheet Metal Forming Processes *

E. Vogli[1], F. Hoffmann[1], J. Nebel[1], D. Risch[2], A. Brosius[2], W. Tillmann[1], A. E. Tekkaya[2]

[1]Institute of Materials Engineering, Dortmund University of Technology, Germany
[2]Institute of Forming Technology and Lightweight Construction, Dortmund University of Technology, Germany

Abstract

Due to the high forming velocities during electromagnetic sheet metal forming processes, a high impact force acts between workpiece and die. Here, the die surface sustains high damages shown by high wear and galling of the workpiece on the die surface.

To enhance the die lifetime, a novel coating concept based on the PVD (physical vapour deposition) process was developed. In doing so, the hardness and the toughness of the designed layers were varied and adjusted to the demands of AlMg-sheet forming process.

Keywords

Electromagnetic sheet metal forming, Tool design, Physical Vapour Deposition (PVD)

1 Introduction

The electromagnetic forming (EMF) process is a highly dynamic process using pulsed magnetic fields to form metals with a high electrical conductivity. A typical setup (see Figure 1) consists of a tool coil, a workpiece, and a form defining tool (die). In this case, a modular die consisting of a drawing ring and cover plate is applied.

* *This work is based on the results of the Research Unit FOR 443; the authors would like to thank the German Research Foundation (DFG) for its financial support.*

During the deformation the workpiece is accelerated to more than 300 m/s, which reflects the highly dynamic character of the EMF process [1-2]. Here, high contact forces between workpiece and die, or more precisely the cover plate, occur during impact. As a result of the temporarily and locally non-uniform velocity distributions caused by an elliptical tool coil, an oval-shaped imprint can be detected in the area where the workpiece touches the die first and with maximum velocity (see Figure 1). Due to this, the tool surface is exposed to significant wear during the service time because of the high forces associated with large damages as well as deteriorated surface roughness.

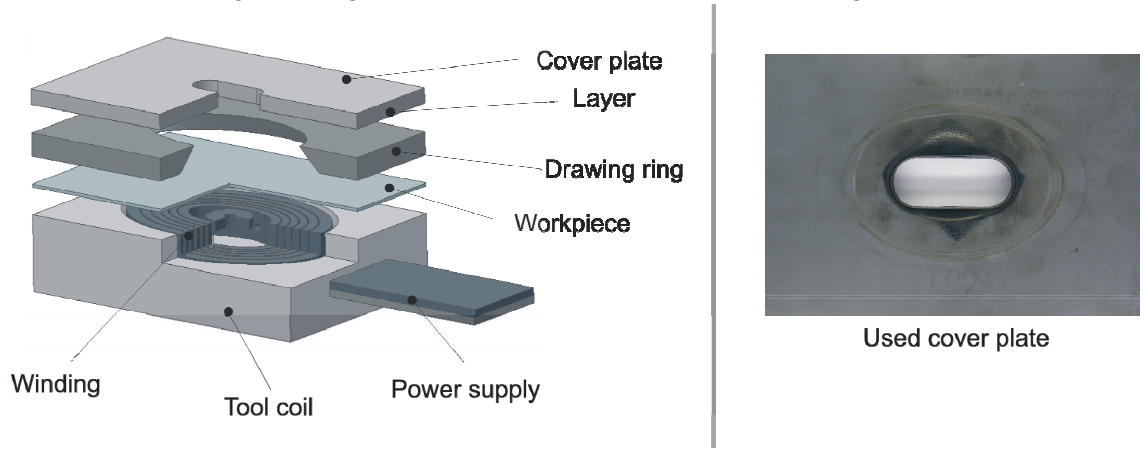

***Figure 1**: Draft of the experimental setup and an exemplary cover plate*

Another aspect of reducing tool lifetime is galling or cold welding – adhesion of sheet metal on the tool surface after forming [3-5]. These effects can be reduced by the application of fluid lubricants, but this can lead to geometrical deviations of the formed workpiece due to the accumulation of the lubricant.

In materials science the trend is targeted at the modification of tool surface with custom-made characteristics for complex requirements [6]. In this regard, the thin film technologies offer a large potential by designing layers with defined structures and tailored-made characteristics [7]. Monolayer, nanostructured layer systems as well as multilayer systems, such as TiAlN, TiN/AlN, TiN/VN, TiN/ZrN etc., exhibit a high potential due to their high hardness of more than 40 GPa [8-10]. In order to be able to use their advantages optimally, the layer's properties must be adjusted to the process features, such as forming velocity, the material to be formed, forming temperature, etc.. Podgornik et al. [11] found out that with the decrease of the tool's surface roughness both friction and tendency to galling can be reduced by cold steel forming. They observed that the carbon-based low friction coatings of DLC (diamond-like carbon) type possess a higher galling resistance compared to the hard TiN coatings. To the same conclusion came Murakawa et al. [12] by deep-drawing of aluminium. Whereas CrN and TiAlN hard coatings improved the dies lifetime up to three times, employing DLC coatings on deep-drawing dies increased the die's lifetime ten times.

In order to enhance the resistance of the forming tool employed by EMF against wear and impact as well as to extend the lifetime of the die, an innovative concept concerning the die surface modification has been developed and will be presented in this research work. In this context, different PVD layer systems have been designed and deposited, in which the hardness and toughness of the layers have been adjusted related to the soft aluminium sheets and high forming velocity. Corresponding metallographic,

mechanical, and microscopic investigations of the coated layers have been conducted to understand the relation between layer microstructure and tribological properties. To evaluate the behaviour of the coatings under dynamic impact conditions, which are comparable to the EMF process, a custom-made impact testing device including measurement systems was designed and utilized. Additionally, a finite element simulation was carried out in order to estimate the occurring contact forces between the workpiece and the forming tool. Based on these results, accompanying electromagnetic forming experiments have been performed to establish the correlations between developed layers and real forming conditions.

2 Description of the experiments

2.1 Experimental setups

In this work, two kind of coating systems were designed and deposited - hard and low friction carbon-based layers (DLC) and hard multilayer systems (Ti / TiAlN) containing ten individual layers with different layer thicknesses. Layer depositions were carried out in a high ionization magnetron sputtering PVD-device (CC800-9sionx, CemeCon, Germany). Cylindrical specimens (diameter of 40 mm and thickness of 12 mm) of tempered steel (1.3502) were employed as substrates and were used to analyze as well as to optimize layer systems related to the electromagnetic forming process demands. Prior to the coatings the specimens were polished up to 1 µm and cleaned in an ultrasonic bath with acetone for 15 min. The last cleaning treatment occurred in the PVD-device during etching, where the substrates surfaces were activated at the same time to enhance the adhesion between substrate and coatings. In order to deposit DLC-layers, two carbon and two chromium targets were employed in a pulsing mode and C_2H_2 atmosphere. Thereby, bias-voltage was varied to adjust the features of carbon-based layers to electromagnetic forming process demands. For $(Ti/TiAlN)_5$ layers one Ti target and three TiAl 60:40 targets were sputtered in inert atmosphere to deposit Ti-layers and in nitrogen atmosphere to deposit TiAlN-layers. In doing so multilayers with varied Ti monolayer thickness from 10 to 100 nm and constant TiAlN layer thickness with approx. 500 nm were analyzed regarding their capability of being adjusted to EMF. The best adjusted layers were deposited on cover plates (diameter of 120 mm and thickness of 12 mm) to investigate the improvement of galling resistance. The deposited layers and PVD deposition parameters are summarized in Table 1.

The layer thickness and morphology were investigated by means of SEM (JXA840, JSM 35, Japan). The layer adhesion was analyzed by means of scratch tests with a maximum load of 100 N. A ball-on-disk tribometer (CSEM, Switzerland) was employed to test the friction and sliding wear characteristics of the layers. The tests were performed using a WC-Co ball (1880 HV0.1) with 6 mm diameter and a load of 5 N with a constant track speed of 0.4 m/s. The layer hardness and Young's modulus were acquired by nanoindentation tests (NANO indenter XP, MTS Nano Instruments, USA).

Coating systems	DLC	Ti	TiAlN
Thickness	ca. 3 µm	10-200 nm	ca. 500 nm
Deposition Parameters			
Etching	650 V, 240 kHz, 200 mln Ar, 50 mln Kr, 45 min		
Cathode number	4 (2 Cr; 2 C)	1	3
Gas	Ar, Kr, C_2H_2	Ar, Kr	Ar, N_2
Power [W]	4000	4000	5000
Bias-Voltage [V]	25-150	100	100
Mode	Pulsing	DC	DC

Table 1: *Coating parameters.*

To evaluate the behaviour of the coatings on the EMF process, a custom-made impact tester (see Figure 2) with a velocity of 30 m/s was utilized (see [4]). A ball is fixed on the plunger and this plunger- unit is positioned at the upper end of the acceleration pipe. The test is started by dropping the plunger unit. In order to achieve velocities up to 25 m/s, which are higher than those realized by gravity (approx. 10 m/s), an additional pressure supply can be used. At the lower end of the acceleration tube the upper plunger is suddenly stopped by an anvil, where the specimen is located. In order to determine the fall velocity, a light barrier, which is integrated in the using the effect of shadowing a light beam, is applied.

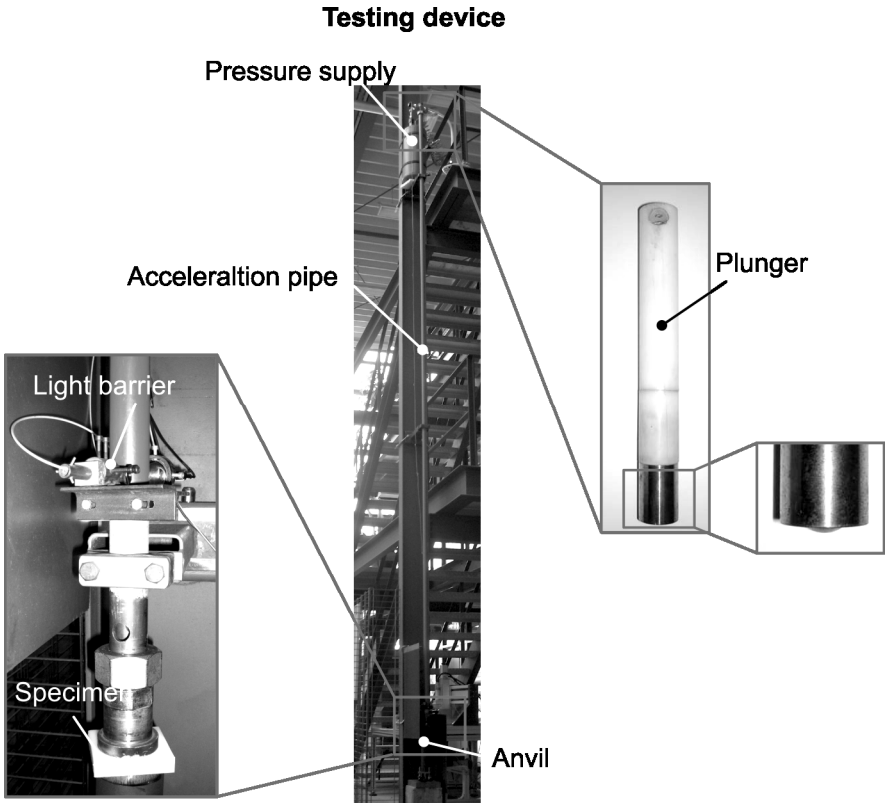

Figure 2*: Impact testing device*

The surfaces of the tested samples were analyzed by an optical 3D-profilometer (Infinite Focus, Alicona Imaging GmbH, Austria). Aimed to investigate the designed coating in the EMF process, 40 forming processes were carried out in a pulse generator device (Maxwell Magneform 2000, USA) with a charging energy of 2.560 J, inductance of 44 nH, capacity of 960 µF, and an eigenfrequency of 23 kHz. The setup is shown in Figure 1. The employed workpiece material was an aluminium alloy AlMg3 with a thickness of 1 mm and nearly pure aluminium Al99.5 with a thickness of 2 mm.

2.2 Analyzing method to estimate the impact force

An experimental setup for estimating the contact force between workpiece and die is really difficult. On the one hand the sensors, have to bear a high and short impact and, on the other hand, the design implementation of the sensor into the die is quite complex. Therefore, the finite element analysis (FEA) is used to estimate the acting contact force during the forming process.

A mass-spring-damper system is implemented into the structure-mechanical simulation instead of a meshed die to represent the die's physical behaviour. The chosen arrangement of the elements of the mechanical analog model influences the response behaviour of the model. A first approach is a parallel connection of the damper and the spring (Kevin-Voigt-Model) to which the substitute mass is connected in series (see Figure 3).

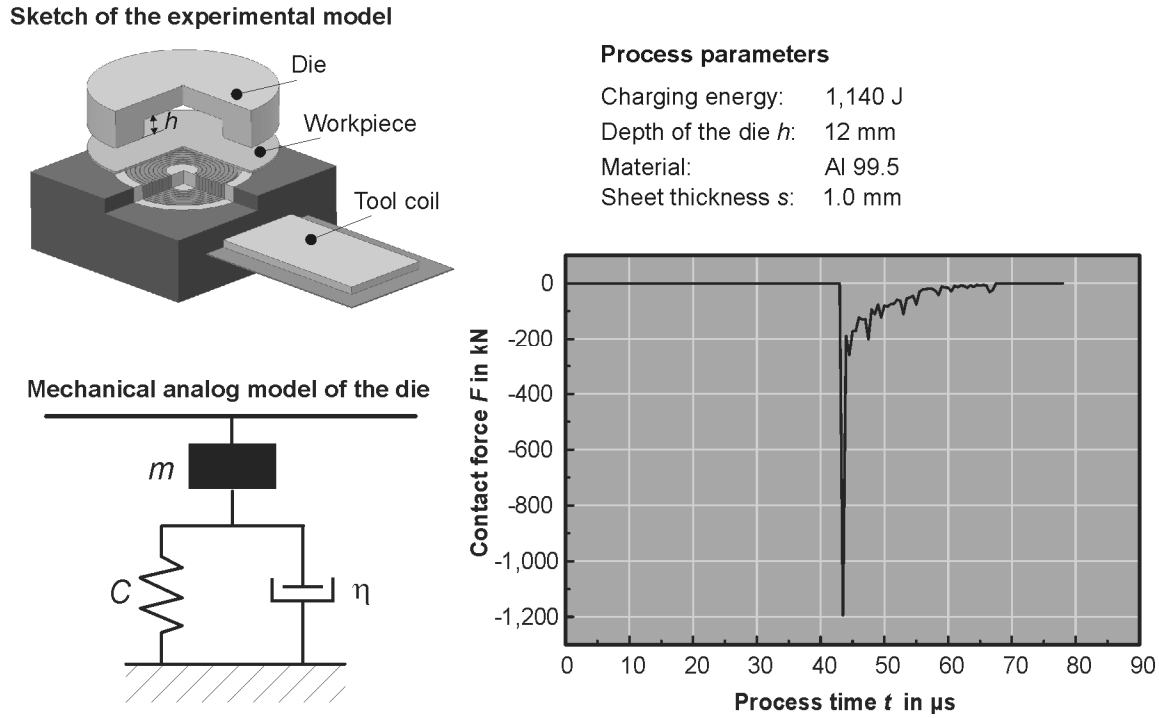

Figure 3: *Mechanical analog model: "Mass-Spring-Damper"*

The stiffness of spring *C* represents both, the material stiffness (Young's modulus) as well as the geometrical stiffness (e.g. the height of the die). In the same way the damping coefficient η represents the material damping property as well as the constructive change, such as the use of an additional shock absorber. The mass *m* within

this model could be calculated based on the die geometry. The mechanical analog model as well as an exemplary force distribution established by the described model in a FEA is displayed in Figure 3 together with the simulation parameters used.

This diagram shows the qualitative trend of the contact force between workpiece and die. It can be clearly seen that the force impact reaches 1.2 MN for a short period of time. This is important with respect to the coated cover plates, which have to sustain this impact.

3 Results and discussion

3.1 Damages of uncoated tools

Typical damage tool surfaces being exposed to very high contact forces, where the counterpart material was a AlMg3-alloy, are shown in Figure 4. At the radius of the contact zone between die and workpiece a material transfer with a thickness of approximately 20 µm was detected.

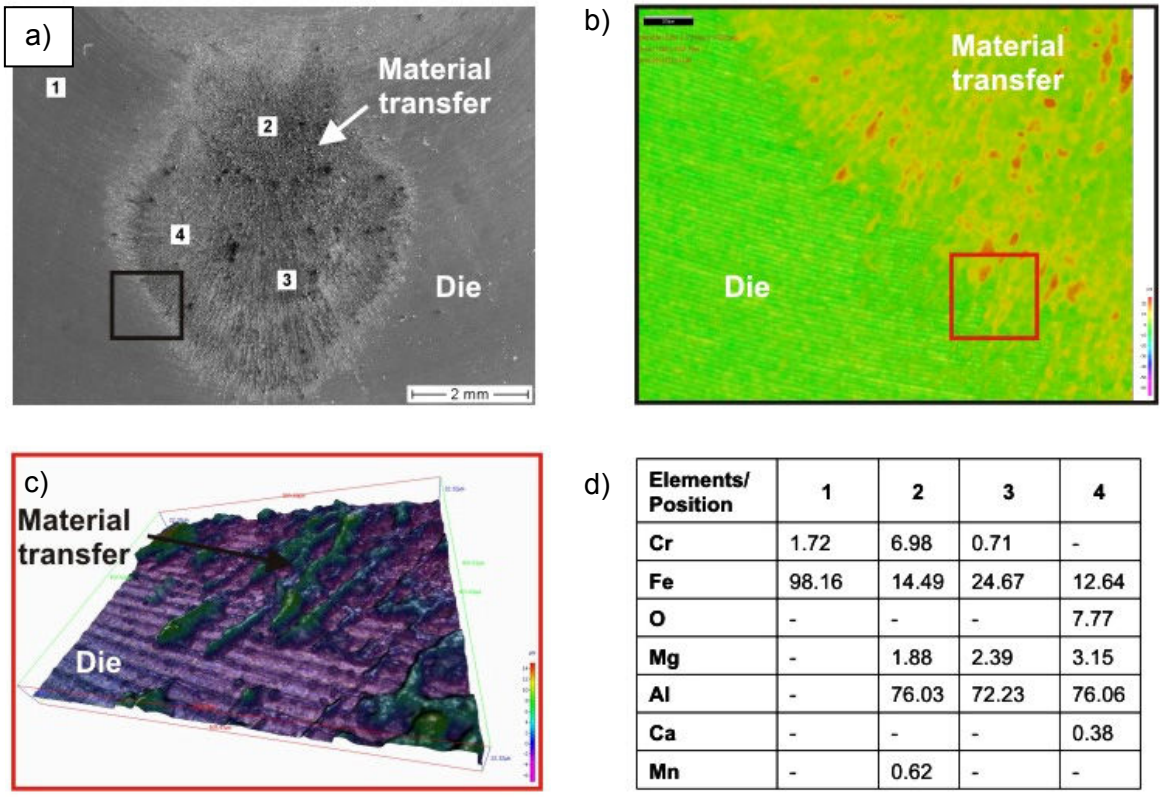

d)

Elements/ Position	1	2	3	4
Cr	1.72	6.98	0.71	-
Fe	98.16	14.49	24.67	12.64
O	-	-	-	7.77
Mg	-	1.88	2.39	3.15
Al	-	76.03	72.23	76.06
Ca	-	-	-	0.38
Mn	-	0.62	-	-

Figure 4: *a) SEM- , b)-c) 3D-profilometer and d) EDX-analysis of damaged tool*

EDX-analyses of these areas indicate the existence of Al and Mg, which support the galling phenomena during the forming process. AlMg3 alloy sheets are exposed to high pressures and velocities employed on the forming process leading to cold welding between workpiece and tool surface [13]. Springback effects tear apart the cold welded areas. The consequences are grave formation and fretting wear of both tool and workpiece [14].

3.2 Characterization of the different layers

In order to develop an appropriate layer system for the electromagnetic forming processes with high wear and impact resistance, the layer systems have firstly been investigated with standard tests. SEM images of coatings fracture surfaces reveal a good adhesion between substrate and coatings as well as a good cohesion within the layers for all systems (Figure 5). Dense structures for all coatings were observed. While a textured columnar morphology was detected in the multilayer systems, amorphous, “glassy” structures were found for carbon-based coatings.

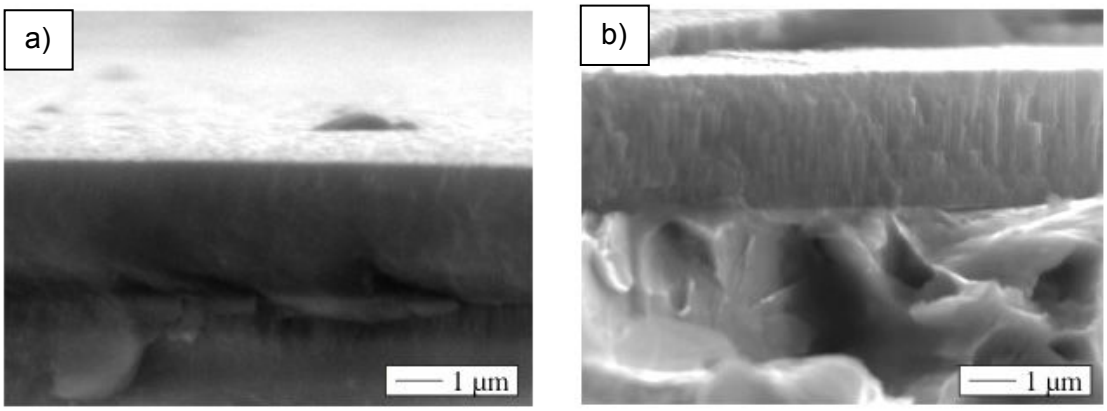

***Figure 5**: SEM images of a) DLC-coating and b) Ti/TiAlN multilayer*

The hardness and Young’s modulus of the deposited layers are presented in the Figure 6. It is observable that by reducing the metallic monolayer thickness the hardness of the Ti/TiAlN multilayers was increased, whereas the Young’s modulus did not change. Consequently, the layer toughness remained constant by an increase of the layer hardness. Bemporad et al. [15] and Evans et al. [16] found a rise in the hardness and adhesion through a reduction of the metallic layer thickness within the multilayer systems due to a better interface toughness and lower residual stresses. This explains the improved adhesion of multilayers with reduced metallic layer thickness.

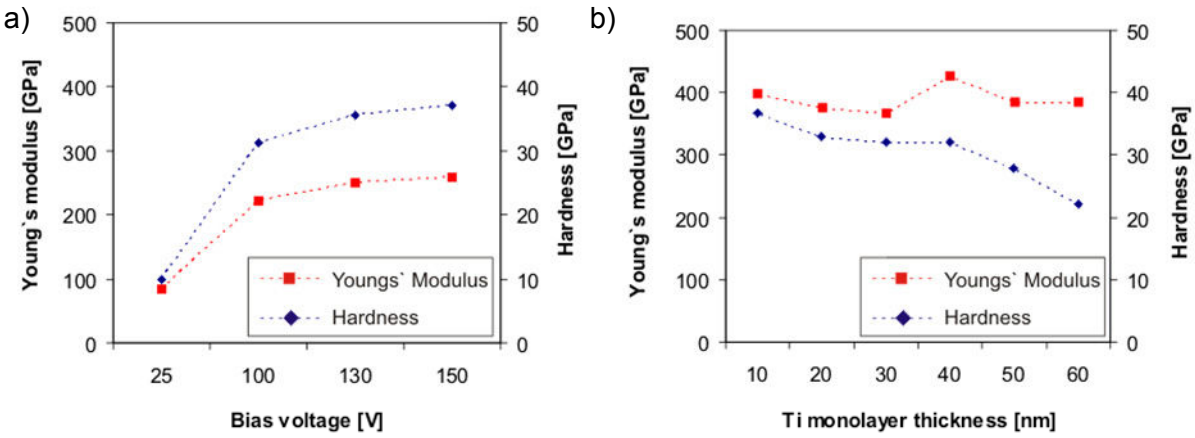

***Figure 6**: Young`s Modulus and hardness results of a) DLC-coating and b) Ti/TiAlN-multilayer*

A hardness improvement of approximately 4 times was detected fore DLC layers by increasing the bias voltage from 25 to 150 V. This leads to a higher Young`s modulus and thereby higher stiffness of the DLC-layers. However, the Young's modulus of DLC coatings is lower (max. 250 GPa) compared to the Ti/TiAlN multilayers (min. 380 GPa), which supports a higher toughness of DLC coatings compared to the Ti/TiAlN multilayers.

Figure 7 compares friction coefficients as well as the progress of abrasive behaviour of both layer systems in a sliding test. It is obvious that the mechanism of layer failure is different. DLC coatings wore slowly. The initial friction is higher than 0.2, but reduces very quickly to remain stable at 0.05 for all deposited DLC coatings and is independent from the applied bias voltage. On the contrary, Ti/TiAlN-multilayers show a progressive wear associated with high friction coefficients. This is in accordance with further studies [18], where low friction coefficient values for DLC coatings were explained with the existence of graphite as lubricant film.

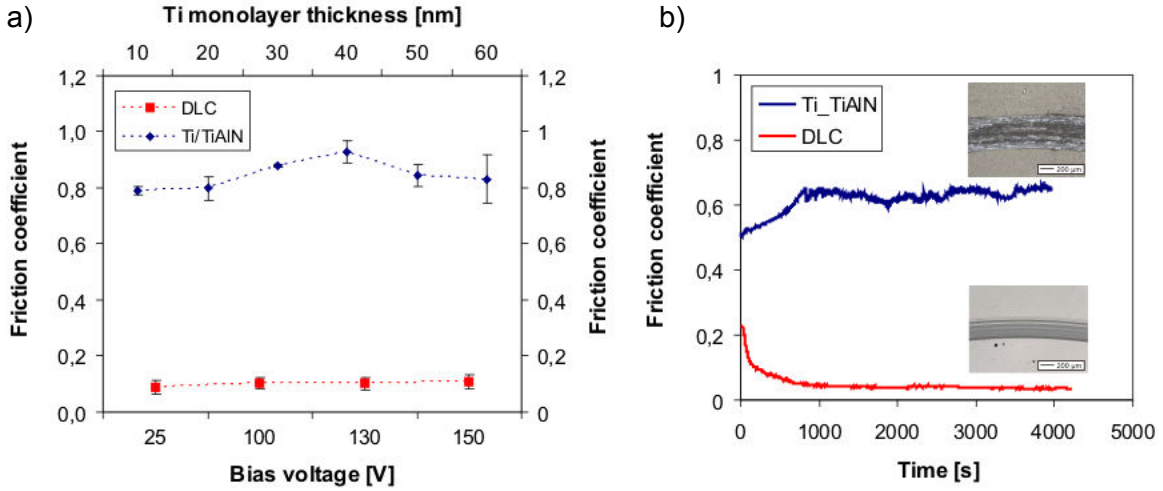

***Figure 7**: a) Friction coefficient and progress of abrasive behaviour of deposited coatings*

Figure 8 shows the different failure modes of the coated samples in scratch tests. Since DLC coatings possess a high portion of graphite an acoustic measurement during scratch tests is more difficult than for Ti/TiAlN multilayers.

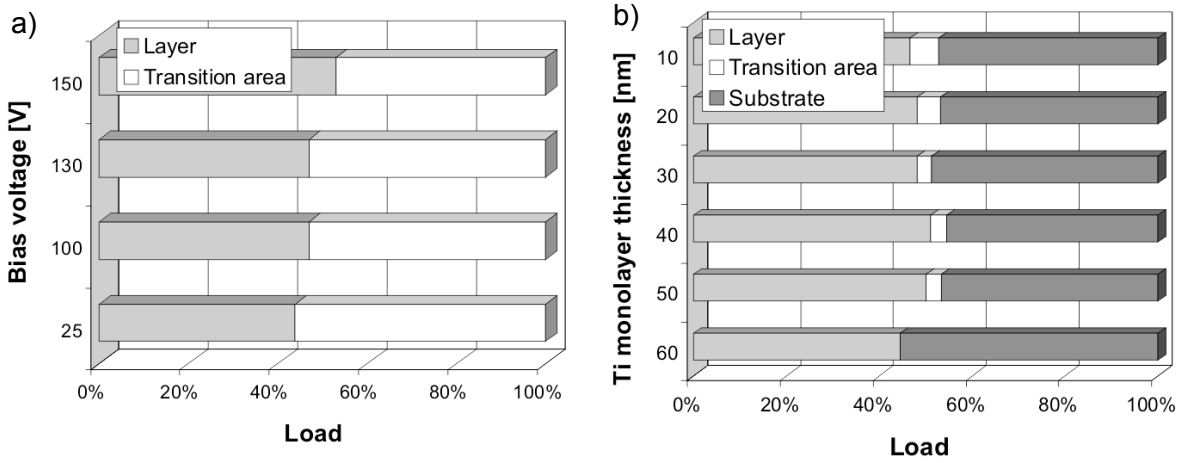

***Figure 8**: Adhesion results of a) DLC coatings and b) Ti/TiAlN multilayers*

Graphite in the DLC coatings lubricates and does not chip off. Under the optical microscope a large transition area between the cracking of DLC coatings and substrate was observed. Thereby the exact failure position, and thus the critical load, could not be determined. However, the first critical load L_{C1} for both systems is in the same range between 40 and 50 N. Scratch tests on DLC-coatings showed no debonding up to loads of 100 N. In contrast to that, multilayer systems had a small cracking transition zone between the first layer and substrate. This area was enlarged by decreasing the Ti monolayer thickness. These results clearly indicate that the DLC coatings are harder and tougher than the Ti/TiAlN mutlilayers, whereas in Ti/TiAlN multilayers both hardness and toughness are enhanced by decreasing the Ti monolayer thicknesses.

Additional tests with the custom-made impact device, shown in Figure 2, were performed on Ti/TiAlN multilayers to evaluate them under EMF process conditions. None of the layers shows macrocracks or spallations, even though all tested systems could not eliminate a plastic deformation of the substrate materials (Figure 9).

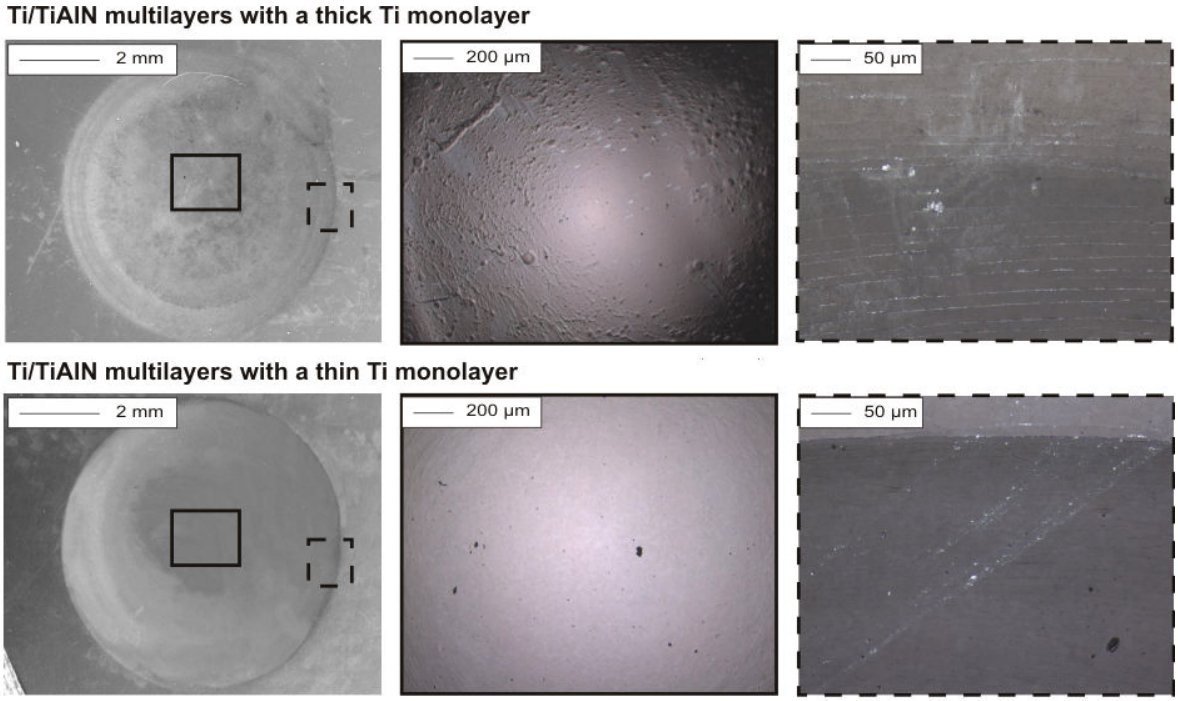

***Figure 9**: Impact test results*

The plastic deformations had a diameter of 3.1 to 3.6 mm and a depth of 0.3 to 0.5 mm. The high resistance against this impact test indicates a high adhesion of multilayers on tempered steel and a high cohesion within the multilayers. It is noteworthy that the thinner the Ti monolayers are the larger is the resistance of the systems against impacts.

Based on the results taken from standard tests it can be established that DLC coatings deposited at high bias voltage and Ti/TiAlN layer systems with 10 nm Ti monolayer thickness show the best performance. Therefore, dies were coated with these systems and evaluated in the EMF process.

3.3 Forming experiments employing coated tools

Dies coated with DLC and Ti/TiAlN multilayer systems were firstly investigated during electromagnetic forming of aluminium sheets after 40 impacts (Figure 10). The characteristic round groove was detected in both dies, while no fretting wear was found. 3D profilometer analyses of these areas show a light damaging in the form of wear of coated die surfaces. These damages are higher for Ti/TiAlN than for DLC coated die. This can be explained by the lower friction coefficient of DLC layers compared to Ti/TiAlN multilayers, which thereby improve the wear resistance of dies. To the same conclusion came Podgornik et al. [13] by cold forming of austenitic steels.

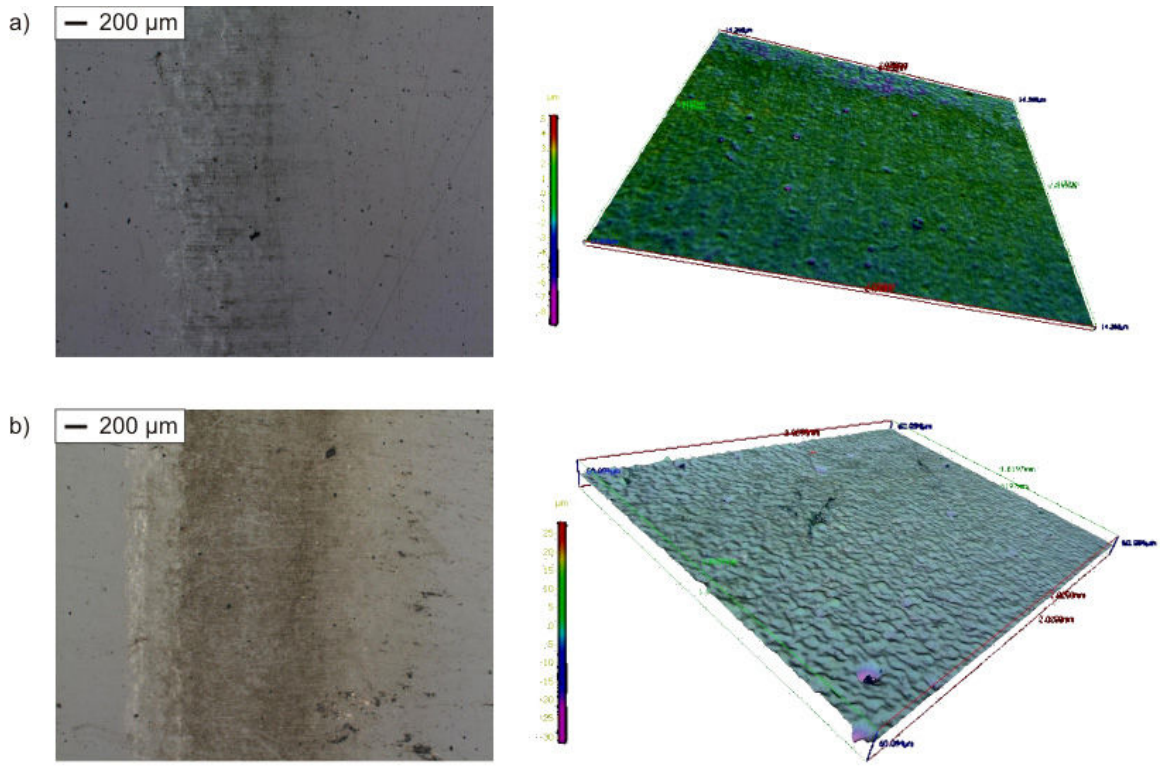

***Figure 10**: 3D profilometer analyses of a) Ti/TiAlN and b) DLC coated die in real and false colours after forming of Al-sheets*

When forming AlMg3 alloy sheets next to round grooves the fretting wear on coated dies was observed. The thickness of material transfer varied from 2 µm for Ti/TiAlN coated dies to only 1 µm for DLC coated dies (Figure 11). Based on the results attained, the fretting wear was reduced approximately 10 to 20 times by employing coated dies (see chapter 3.1). However, it is noteworthy that AlMg3 sheets cause more damages on dies than Al sheets.

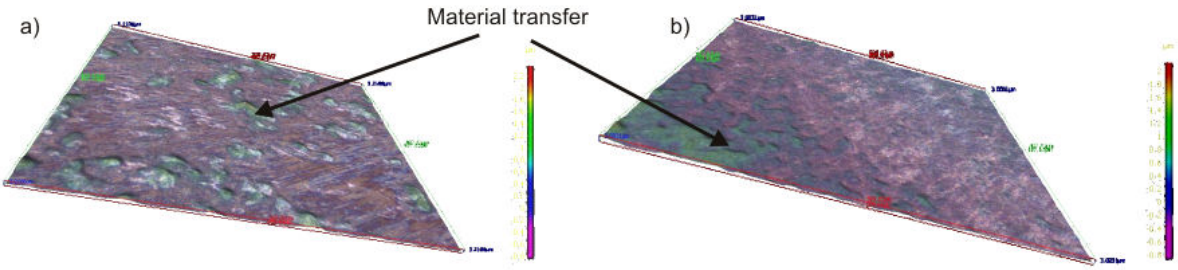

Figure 11: *3D profilometer analyses of a) Ti/TiAlN and b) DLC coated die in false colours after forming of AlMg3 sheets*

4 Summary & outlook

In this research work an approach to enhance the galling resistance of dies employed by electromagnetic forming processes was presented. Two different kinds of coatings - low friction DLC layer and Ti/TiAlN multilayers - were studied and adapted to the EMF process demands. It was detected that the DLC layers feature lower friction coefficients at high hardness and lower Young's modulus than the Ti/TiAlN multilayers, while the hardness of the multilayers increases when reducing the Ti monolayer thickness by a constant steady-state Young's modulus. Based on the level of Young's modulus, DLC layers have a higher ductility than Ti/TiAlN multilayers. Consequently, the hardest DLC layer and Ti/TiAlN multilayer with the thinnest Ti monolayer (10 nm) were chosen for further investigation in the EMF process. Coated dies show no galling after forming Al sheet, while after forming AlMg3 sheets a slight material transfer was observed. However, the galling resistance for both coated dies was enhanced compared to the uncoated ones. The wear resistance of DLC coated dies was higher than the Ti/TiAlN coated dies independently of the materials to be formed.

References

[1] *Risch, D., Beerwald, C., Brosius, A., Kleiner, M.:* On the Significance of the Die Design for Electromagnetic Sheet Metal Forming, Proc. of the ICHSF 2004 - 1st Int. Conference on High Speed Forming, 31.3.-1.4.2004, pp.191-200, Dortmund, 2004 ISBN 3-00-012970-7.

[2] *Beerwald, C.:* Fundamentals for Process Dimensioning and Design of Electromagnetic Forming (in German), PhD Thesis, Dortmund, 2004.

[3] *Risch, D., Vogli, E., Baumann, I., Brosius, A., Beerwald, C., Tillmann, W., Kleiner, M.:* Aspects of Die Design for the Electromagnetic Sheet Metal Forming Process, Proc. of the ICHSF 2006 – 2nd Int. Conference on High Speed Forming, 20.-21.3.2006, Dortmund, pp. 189–200, ISBN 3-00-018432-5.

[4] *Tillmann, W., Vogli, E.*: Adjusted thin layers for the electromagnetic sheet metal forming die, Advanced Engineering Materials 10 (2008) 1-2, pp. 79-84.

[5] *W.R.D. Wilson:* Tribology in cold metal forming. Journal of Manufacturing Science Engineering, 119 (1997) pp. 695-701.

[6] *Hovsepian, P.Eh., Lewis, D.B., Münz, W.D.*: Recent progress in large scale manufacturing of multilayer/superlattice hard coatings, Surface Coatings Technology, 133-134 (2000), pp. 166-175.
[7] *Musil, J.:* Hard and superhard nanocomposites coatings, Surface and Coatings Technology, 125 (2000) 1-3, pp. 322-330.
[8] *Boutos, T.V., Sanjines, R., Karimi, A.:* Effects of deposition temperature and bilayer thickness on the mechanical properties of AlN/TiN multilayer thin films, Surface and Coatings Technology, 188-189 (2004), pp. 409-414.
[9] *Erkens, G.*: New approaches to plasma enhanced sputtering of advanced hard coatings, Surface and Coatings Technology 201 [9-11] (2007), pp. 4806-4812.
[10] *Imbeni, V., Martini, C., Lanzoni, E., Poli, G., Hutchings, I.M.:* Tribological behaviour of multi-layered PVD nitride coatings, Wear, 251 (2001), pp. 997-1002.
[11] *Podgornik, B., Hogmark, S.:* Surface modification to improve friction and galling properties of forming tools, Journal of Materials Processing Technology, 174 (2006), pp. 334-341.
[12] *Murakawa, M., Koga, N., Takeuchi, S.:* Diamond-like carbon-coated dies for deep drawing of aluminium sheets, Trans. ASME, 121 (1999), pp. 674-678.
[13] *Story, J.M., Chandorkar, K.V.:* Hinweise zur Werkzeuggestaltung für die Aluminium-Blechumformung, Tagungsband zum Kolloquium „Neuere Entwicklungen in der Blechumformung“, Fellbach, 7.-8. Mai 1996, pp. 215-247.
[14] *Girschewski, B., Hoffmann, H., Lang, S.:* Einsatzpotential von AlMg-Blechen in der Karosserieaußenhaut, Blech Rohre Profile, 12 (1997), pp. 42-45.
[15] *Bemporad, E.; Sebastiani, M.; Pecchio, C.; De Rossi, S.:* High thickness Ti/TiN multilayer thin coatings for wear resistant applications, Surface and Coatings Technology, 201 (2006), pp. 2155-2165.
[16] *Evans, A.G., Hutchinson, J.W.:* The thermomechanical integrity of thin films and multilayers, Acta Metall. Mater. 43 (1995), pp. 2507-2530.
[17] *Reiter, A.E., Brunner, B., Ante, M., Rechberger, J.:* Investigation of several PVD coatings for blind hole tapping in austenitic stainless steel, Surface & Coatings Technology, 200 (2006), pp. 5532-5541.

ISBN 3-9809535-3-X